SCUOLA DI DOTTORATO

UNIVERSITÀ DEGLI STUDI DI MILANO-BICOCCA

Department of Earth and Environmental Sciences (DISAT)

PhD program in Chemical, Geological and Environmental Sciences, Cycle XXIX

Geological Sciences curriculum

DAMAGE-BASED LONG-TERM MODELLING OF PARAGLACIAL TO POSTGLACIAL EVOLUTION OF ALPINE ROCK SLOPES

Riva Federico

Registration number: 701372

Tutor: Prof. Federico Agliardi

Co-tutor: Prof. David Amitrano

Coordinator: Prof. Maria Luce Frezzotti

ACADEMIC YEAR 2016/2017

CONTENTS

PREFACE

Large mountain slopes in alpine environments undergo a complex long-term evolution from glacial to postglacial environments, through a transient period of paraglacial readjustment. During and after this transition, the interplay among rock strength, topographic relief, and morpho-climatic drivers varying in space and time can lead to the development of different types of slope instability, from sudden catastrophic failures to large, slow, long-lasting yet potentially catastrophic rockslides.

Understanding the long-term evolution of large rock slopes requires accounting for the time-dependence of deglaciation unloading, permeability and fluid pressure distribution, displacements and failure mechanisms. In turn, this is related to a convincing description of rock mass damage processes and to their transition from a sub-critical (progressive failure) to a critical (catastrophic failure) character. Although mechanisms of damage occurrence in rocks have been extensively studied in the laboratory, the description of time-dependent damage under gravitational load and variable external actions remains still difficult.

This PhD project aims at studying the long-term evolution of alpine rock slopes through their glacial, paraglacial and postglacial stages of evolution. In particular, I investigate the mechanisms driving the transition from a relatively undisturbed, deglaciating slope to a paraglacial rock slope affected by initial development of large slope instabilities, and finally to a mature, hydraulically coupled postglacial rockslide or Deep Seated Gravitational Slope Deformation (DSGSD). To do this, I developed a novel approach able to overcome the limitations of existing numerical modelling techniques and capture the long-term evolution of real, large rock slopes. In this perspective, starting from a time-dependent model conceived to reproduce laboratory rock deformation experiments by combining damage and time-to-failure laws, we pointed at reproducing both diffused and localized damage, meanwhile tracking long-term slope displacements from primary to tertiary creep stages. The adopted approach is completed by taking into account rock mass heterogeneity and property upscaling, time-dependent deglaciation and damage-dependent fluid pressure occurrence.

1 LARGE ALPINE ROCK SLOPES

1.1 WHAT IS AN "ALPINE SLOPE"?

The definition of "alpine" environment is not straightforward, but derives from different classification criteria. Former (possibly cycling) glaciation and deglaciation, occurrence of glacial and periglacial geomorphological features, occurrence of permafrost, and vegetation types and trim line elevation and evolution have been used to define alpine environment and to extend its meaning from the European Alps to other similar contexts (Caine, 1971; Matsuoka, 1994; Gruber et al., 2003; Wienhöfer et al., 2007; Cossart et al., 2008). Trying to include these different aspects and apply them to slopes, we define "alpine" a slope which experienced the full set of hydro-mechanical conditions typical of glacial, paraglacial and postglacial environments, as well as their transitions.

Large rock slopes in such morpho-climatic conditions evolve under the influence of several processes, acting with changing magnitude and timing over different timescales, from years to thousands of years (Ballantyne, 2002). Alpine slopes are thus extremely complex systems with respect to topographic, geological, geomorphological, hydrogeological and geomechanical features. Moreover, the evaluation of both present and past conditions of a slope is further complicated by the poor knowledge of long-term processes and the uncertainties in reconstruction of mechanical and hydraulic properties in formerly glaciated environments. Several processes were recognized to have a role in controlling evolution of alpine slopes, including: rock mass strength, active tectonics, climatic conditions, weathering, deglaciation, glacial and fluvial erosion, permafrost degradation, surficial hydrology and groundwater recharge and flow (Ballantyne, 2002; Clague and Stead, 2012; Crosta et al., 2014). Since extended dissertation of all these processes is not the purpose of this brief review, only glacial and paraglacial processes and slope groundwater circulation will be reported, as they were pointed out to have a major control on long-term behavior of alpine slopes. In the next paragraphs, these processes and their implications on slope stability will be reviewed.

1.2 GLACIAL AND PARAGLACIAL CONTROLS ON SLOPES

The transition from glacial to postglacial environments is a key-point in the evolution of alpine slopes, and occurs through a period of transient conditions referred to as "paraglacial". The term "paraglacial" was firstly used by Church and Ryder (1972) to group "non-glacial processes that are directly conditioned by glaciation", thus referring to landscapes whose evolution is directly affected by glacially-condition on topography, hydrology, vegetation and mechanical properties of involved materials. For slope processes, the exact nature, magnitude and duration of paraglacial processes are still debated, as well as the paraglacial controls on the initiation of large rocks slopes (Cruden and Hu, 1993; Ballantyne, 2002; Agliardi et al., 2009).

Glaciation and deglaciation had extremely important impacts on slopes in the European Alps, because of the large extent of glaciation during the Last Glacial Maximum (LGM, ≈ 26.5-19 Kyr ago; Clark et al., 2009) and later re-advances (Florineth and Schluchter, 1994; Ehlers and Gibbard, 2004; Ivy-Ochs et al., 2008; Wirsig et al., 2016). LGM is commonly recognized as the last extensive glacial pulse, in which glaciers filled main valleys and reached piedmont areas in both Northern and Southern flank of the chain (Fig. 1.1), obliterating valley morphologies related to previous large-scale glaciations.

The erosive power of ice flows contributed to carving valley flanks and landscapes by deepening and steepening, thus affecting relief production and valleys shape (Meigs and Sauber, 2000; Tomkin and Braun, 2002; Herman et al. 2011). The topography reshaping resulted in the redistribution of gravitational stresses in the valley profile (McColl, 2012; Crosta et al., 2013), depending on the glacier shape, flow velocity and temperature, the initial relief magnitude, the mechanical properties and the structure of rock masses forming the valley flanks (Savage et al., 1985; Harbor, 1992; Augustinus, 1995; Li et al., 2000; Olvmo and Johansson, 2002; Brook et al., 2004). Augustinus (1995) observed that, for same topographic and mechanical settings but increasing horizontal stress, the distribution of tensile zones throughout slope is greatly affected (Fig. 1.2), with remarkable consequences on potential instabilities nucleation and development (Savage et al., 1985). Rock mass structure and strength are key-factors in controlling glacier erosion and the resulting valley profile. In typical and simplified V-shaped fluvial valleys, glacier erosion starts from toe and progressively steepen valley flanks depending on mechanical properties, presence of weakened zones, glaciation duration and ice thickness. The interaction among these factors determines the postglacial valley topography, thus influencing subsequent stress redistribution and oversteepening (Harbor, 1995).

Following loading and erosion processes related to glacial environment, glacier retreat (i.e. deglaciation) introduces major perturbations of rock slope state, mainly related to "slope debuttressing". The latter term refers to the progressive removal of supporting ice from slope during downwastage (Ballantyne, 2002). Carlsson and Olson (1982) highlighted that glacier weight can induce higher stress regime along valley profiles with respect to ice-free conditions, in which stresses usually consists in the sum of topographic, tectonic and exhumation-generated components (Crosta et al., 2013 and references therein). The excess stress is stored in rock masses as residual strain energy. During deglaciation, the stress perturbation caused by progressive downwastage and the residual energy release can induce the formation and reactivation of tensile and shear fractures leading to rock mass damage. This results in a decrease of rock mass strength whereas the decrease in confining pressure causes also reduction of shear strength along joints and interlocking between blocks (Crosta, 1996; Eberhardt et al., 2004; McColl, 2012).

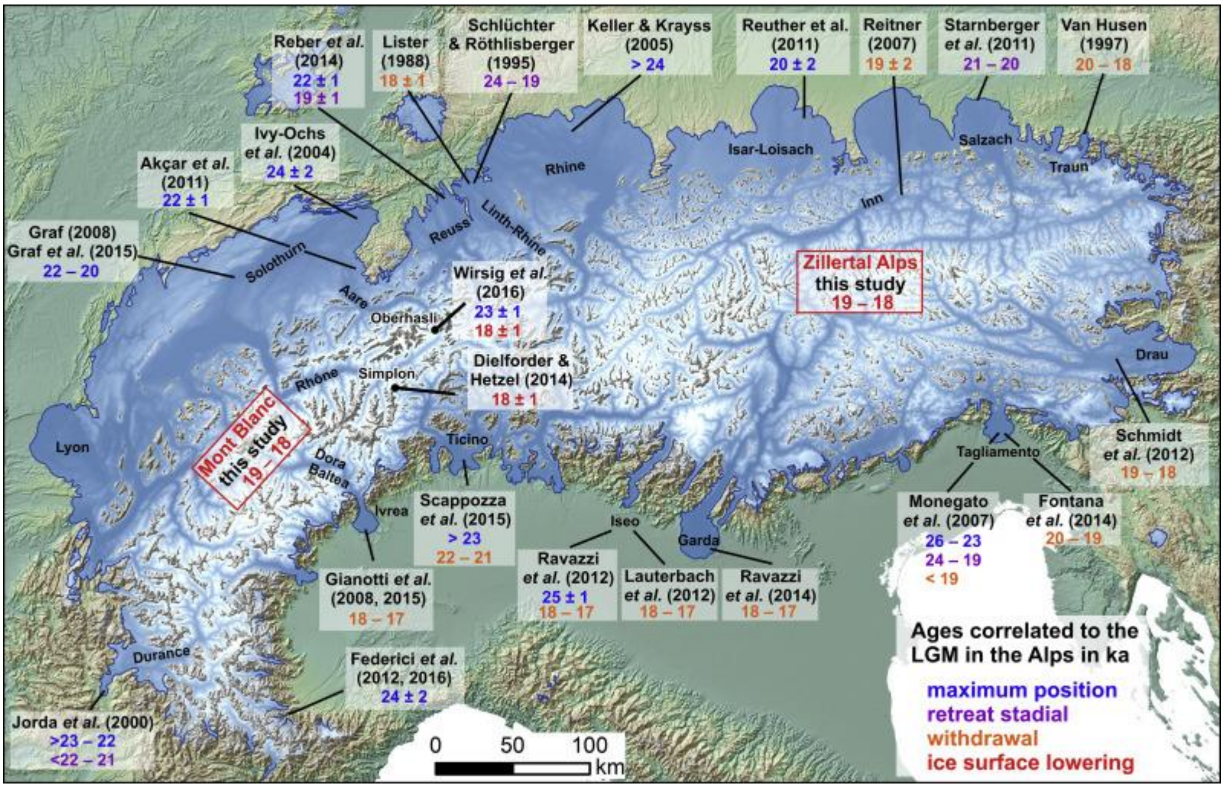

Figure 1.1: Ice covering extent in the Alps during the Last Glacial Maximum (LGM). Absolute dates (ka) for different deglaciation stages in different alpine regions are also indicated (Wirsig et al., 2016).

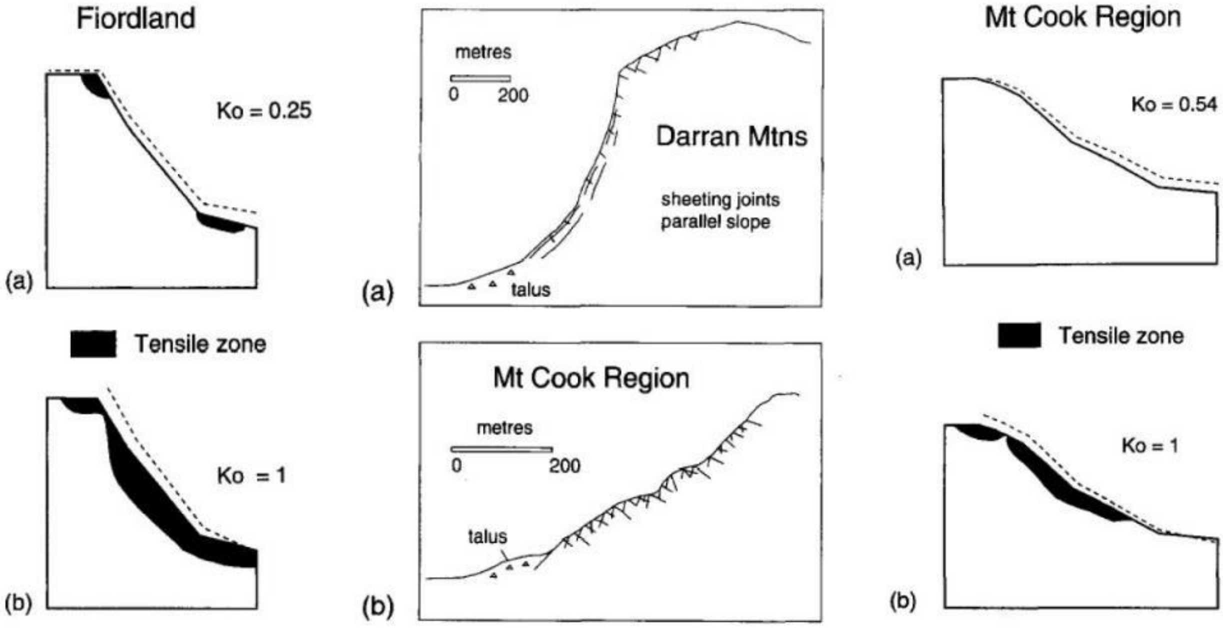

Figure 1.2: Tensile zones in slopes with gravitational load (a) and applied horizontal stress (b) computed by Finite Element numerical modelling (from Augustinus, 1995).

Increase of fracturing eventually affects hydraulic rock mass behavior through increasing connectivity, permeability and joints opening. This in turn makes the rock mass prone to enhanced physical and chemical weathering (Hoek and Bray, 1981). This ensemble of processes can interplay with tectonic or locked-in stresses (Savage et al., 1985; Miller and Dunne, 1996), lithology (Harbor, 1992), fluvial incision and static fatigue processes (Molnar, 2004; Pariseau and Voight, 1979; Eberhardt et al., 2004), and leave clear geomorphic imprints in the long- and cross-profile steepness and shape of alpine valleys (Brocklehurst and Whipple, 2004; Sternai et al. 2011). Main processes determining slope modifications and related effect on stability at the transition from glacial to paraglacial conditions are resumed in Table 1.1.

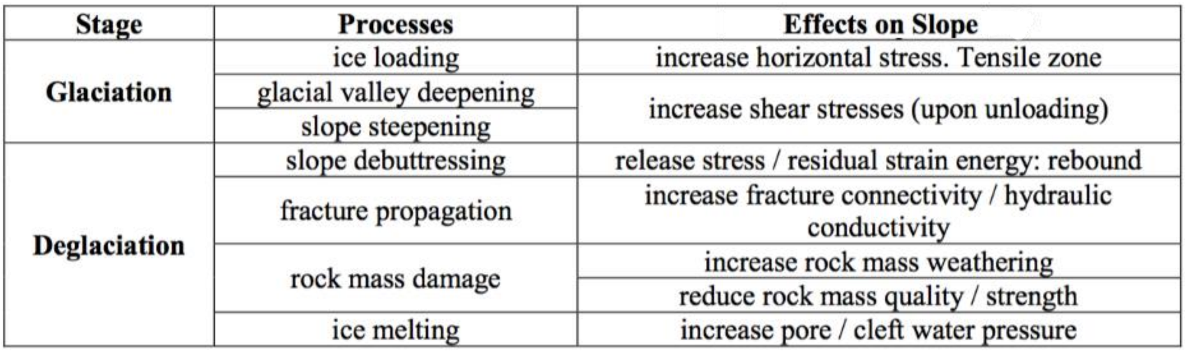

Stage	Processes	Effects on Slope
Glaciation	ice loading	increase horizontal stress. Tensile zone
	glacial valley deepening	increase shear stresses (upon unloading)
	slope steepening	
Deglaciation	slope debuttressing	release stress / residual strain energy: rebound
	fracture propagation	increase fracture connectivity / hydraulic conductivity
	rock mass damage	increase rock mass weathering
		reduce rock mass quality / strength
	ice melting	increase pore / cleft water pressure

Table 1.1: Main processes involved in glacial and paraglacial slope modifications (from Crosta et al., 2012)

During the "paraglacial" period the hydro-mechanical processes acting in a slope reflect a transient exhaustion of the perturbation induced by former deglaciation, in terms of slope geometry, stress distribution, rock mass strength and permeability (i.e. slope groundwater hydrology), surface erosion rates, and vegetation. The duration of the paraglacial period and the magnitude of associated readjustment is still debated, making accurate quantification of effects difficult, especially in a long-term framework. The perturbations induced by glaciation and deglaciation, depending on the interplay of topography, rock strength and climate might take a variable time (and involve variable mechanical/hydraulic effects) to completely "dissipate" in the slope. Depending also on site-specific conditions, periglacial readjustment might result into instability nucleation or, on the other hand, into increase of stability conditions.

In any case, the term "paraglacial" does not refer to a time period, but to a complex of stress, hydrological, mechanical and biological transient states directly triggered by deglaciation and progressive glacier downwasting. In the Alps, the main paraglacial phase was recognized at the end of LGM, when extensive deglaciation resulted in the glaciers retreat from the main valleys. After that, a progressive recessional phase occurred, matched with downwasting of main valleys lobes in a relatively (and still debated) short span of time (≈ 1-4 Ka, Ivy-Ochs, 2015; Wirsig et al., 2016). Following re-advances involved only the areas immediately surrounding the cirques headwalls, being thus localized only in tributary valleys at relatively high altitudes (Preusser and Schlüchter, 2004; Ivy-Ochs et al., 2008). Geomorphological features, paleoclimatic evidence and exposure data permitted to constrain their spatial and temporal extension, distinguishing at least four stadials during Lateglacial: Gschnitz (Older Dryas, 15.4±1.4 kyr BP), Clavadel (Older Dryas, before Bølling warm phase, 14.7 kyr BP), Daun (Older Dryas, before Bølling warm phase, 14.7 kyr BP) and Egesen (Younger Dryas, 11.2±0.9 kyr BP in the Italian central Alps, Hormes et al., 2008). During the Holocene, further warming constrained glaciers to higher altitudes, although other limited readvances occurred, the last one known as Little Ice Age (600-300 yr BP).

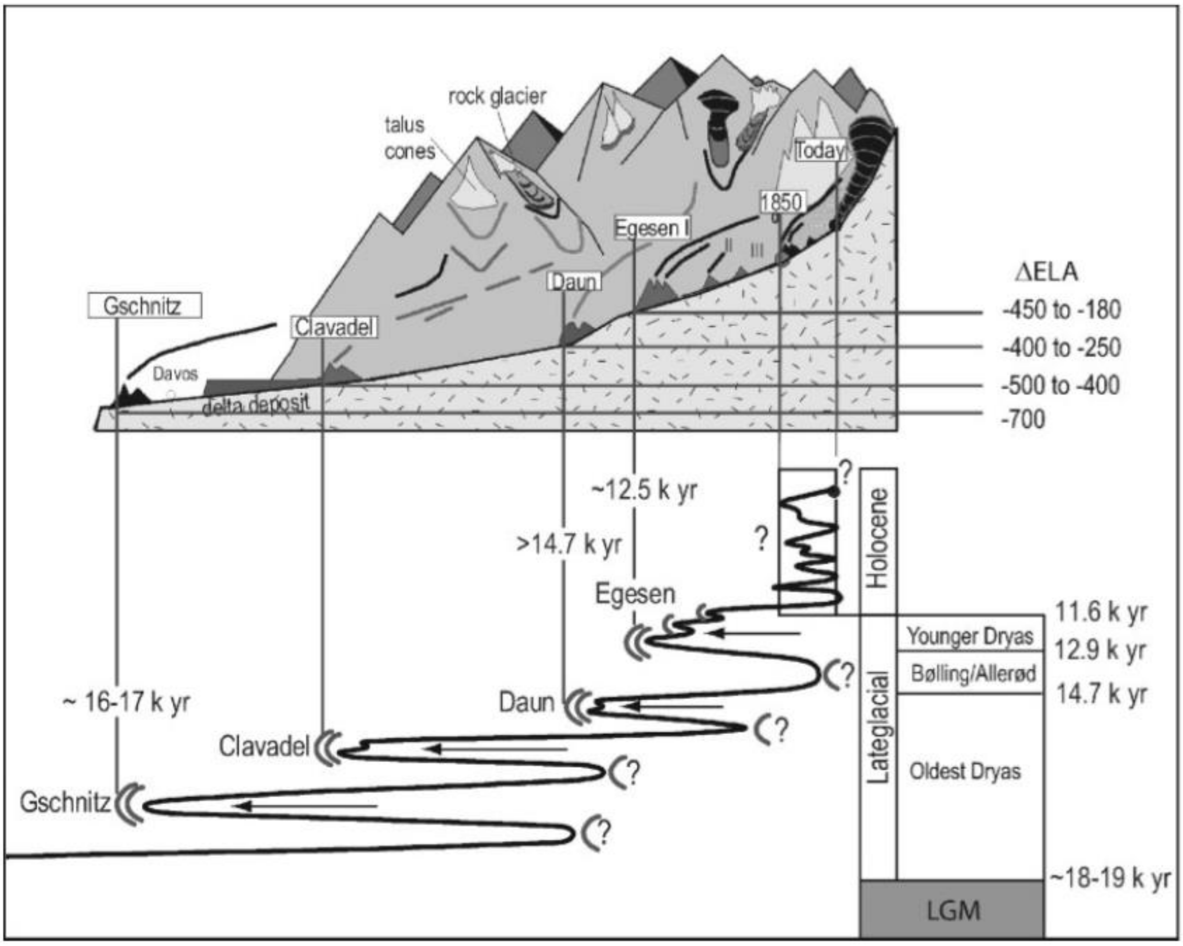

Figure 1.3: Lateglacial stadials recognized in the surrounding of Davos, showing the absolute chronology and the depression of the Equilibrium Line Altitude (ELA) attained with respect to the reference value of Little Ice Age (from Ivy-Ochs et al., 2008).

1.3 LONG-TERM STABILITY OF ALPINE SLOPES

The interaction between the morpho-climatic processes described above, the site-specific mechanical and topographical features and the inherited geological structure determines the long-term evolution of a certain slope. The European Alps, extending for over a thousand kilometers along-axis and hundreds of kilometres across the range, are characterized by an extreme variability of combinations between different topographies, rock types, tectonic settings and climatic forcing (Bigi et al., 1990; Frei and Schär, 1998; Schmid et al., 2004; Korup et al., 2007). These result in a variety of slope geometries and processes, eventually resulting in different slope failure types and timing. The risk posed by different types of slope instabilities motivated extensive research for assessing long-term mechanisms and triggering factors, in the aim of civil protection and early-warning purposes (Casagli et al., 2010; Clague and Stead, 2012; Agliardi et al., 2013).

Beyond classical landslide classification schemes (Cruden and Varnes, 1996), we may classify the types and styles of instabilities involving alpine rocks slopes depending on involved rock mass volume and time-dependent behavior. Enhanced rockfall activity frequently occurs in steep slopes characterized by rock masses made of hard rock with relatively spaced and persistent discontinuities, which largely control the size and kinematics of the instability (i.e. structurally-controlled instabilities). Rockfall activity can occur just after the deglaciation as consequence of unloading and stress redistribution or protracting with episodic events, depending on rock structure, weathering and erosion processes, eventually forming talus deposits at slope toe. On the other hand, large rock mass volumes characterized by several sets of closely spaced discontinuities (i.e. “equivalent continuum” rock masses), both sudden (catastrophic) failures or slow rock slope deformations can occur depending on rock mass mechanical properties, presence of inherited weak zones, slope profile (relief, slope angle, oversteepening and hypsometry) and magnitude of external actions (Ballantyne, 2002; Cossart et al., 2008; McColl, 2012; Deline et al., 2015): in favorable condition, deformation by shear can follow deglaciation (Figs. 1.4a, b), resulting in the nucleation of a potential instability. Slopes differentiation in postglacial environment is characterized by well-developed basal shear zones and highly fractured and permeable unstable masses, in which perched water table could develop, as testified by springs occurrence at slopes toe and by borehole data obtained from geotechnical slope investigations (Fig. 1.4c). In this mature condition, the most distinctive patterns of displacement feedback to hydrological triggers are observed (Angeli et al., 1996; Corominas et al., 2005; Crosta et al., 2014; Vallet et al., 2015).

Catastrophic failures in weak or extensively damaged rock masses can also be triggered during or just after deglaciation phase, as a direct consequence of slope oversteepening and stress redistribution (Fig. 1.5a). Events reported by McSaveney (1993) (Fig. 1.5b), Sigurdsson and Williams (1991) (Fig. 1.5c), Evans and Clague (1994) and Oppikofer et al. (2008) (Fig. 1.5d) are representative of this type of short-term instability. On the other hand, alpine rock slopes can evolve towards failure for thousands of years, due to the long-term effects of mechanical properties degradation in sub-critical stress conditions, also referred as progressive failure (Bjerrum, 1967; Chigira 1992; Eberhardt et al., 2004; Brideau et al., 2009).

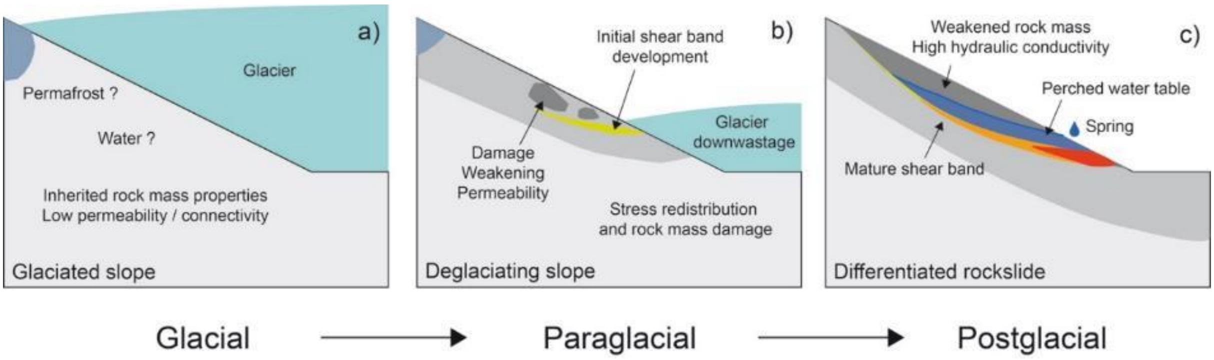

Figure 1.4: Conceptual glacial to postglacial slope evolution: In glacial conditions (a) rock mass are supposed to be poorly damaged and hydraulically interconnected. In paraglacial conditions (b) progressive brittle damage leads to weakening and permeability increase. Rockslide differentiation (c) occurs through the development of a mature basal shear band and a weak, permeable rockslide mass hosting perched aquifers.

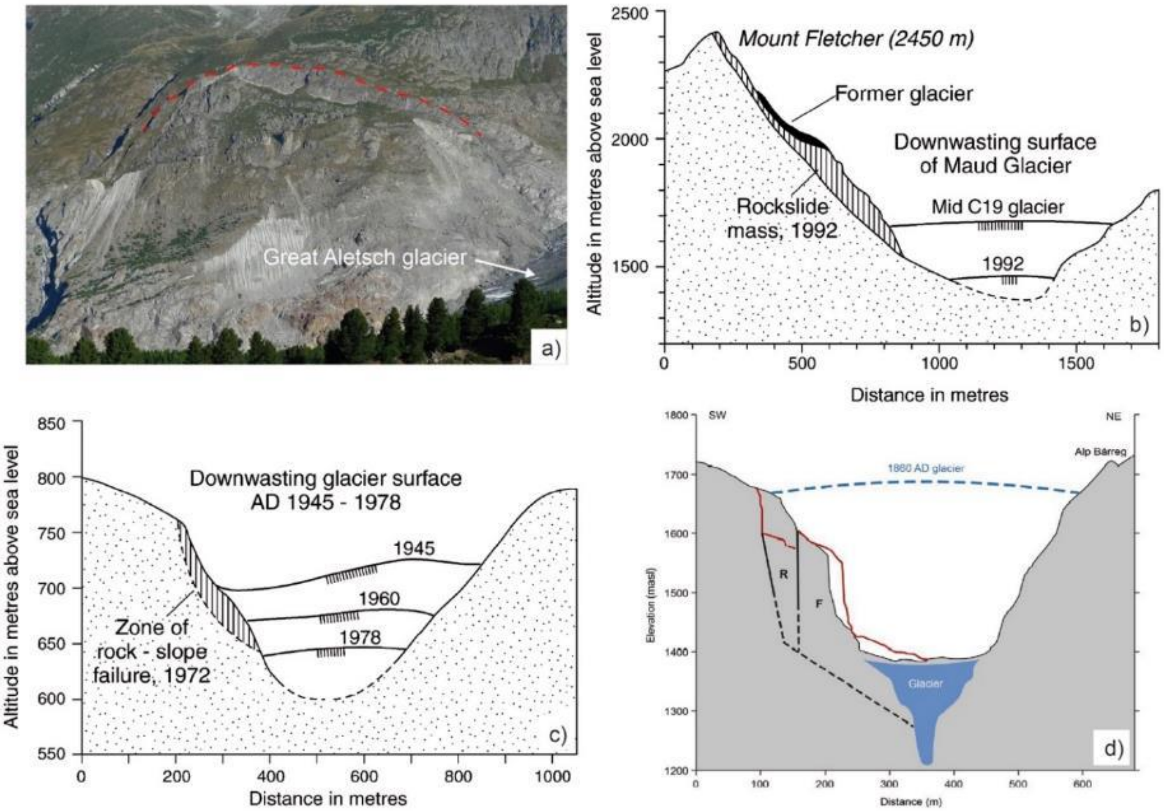

Figure 1.5: Examples of failure occurring during or immediately after glacier downwasting: (a) Driest rockslide (Vogler et al., 2016), (b) Mount Fletcher rockslide (McSaveney, 1993), (c) Myrdalsjokull rock slope failure (Sigurdsson and Williams, 1991) and (d) Schlossplatte/Alp Bäregg collapse (Oppikofer et al., 2008). Photo b and c from Ballantyne, (2002)

In these conditions, slope evolution can be characterized by progressive or transitional temporal patterns of long-term displacement, representing different activation and regression phases (Fig. 1.6), which eventually result in long-term stability or delayed catastrophic collapse (Fig. 1.7) (Bovis, 1982; Broadbent and Zavodni, 1982; Ballantyne, 2002; Hormes et al., 2008; Zerathe et al., 2014). This displacement pattern is typically expressed by large rockslides, widespread through the Alps and constituting notable threats for villages and anthropic activities. Finally, slopes can undergo long-term deformation lasting tens of thousands years without global catastrophic failure, as expressed by Deep Seated Gravitational Slope Deformations (DSGSD; Hippolyte et al., 2009; McColl, 2012; Crosta et al., 2013). In the present work, I deal with the long-term evolution of large, slow rock slope instabilities, which can be classified as “large rockslides” and “Deep-Seated Gravitational Slope Deformations” as describes in the following sub-sections.

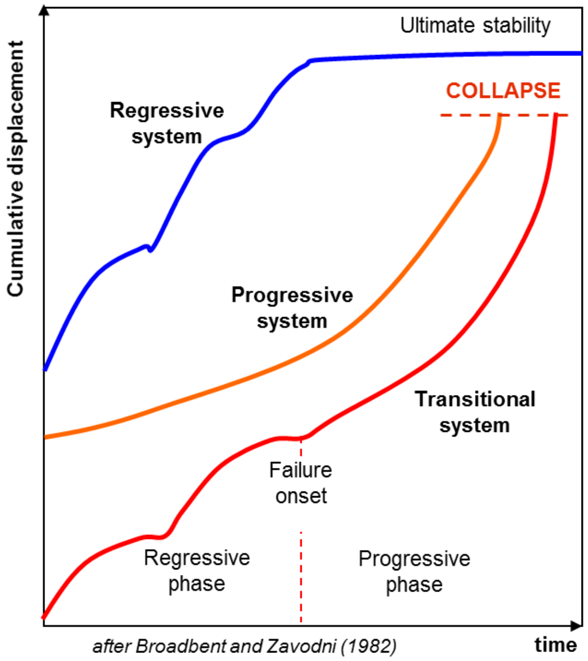

Figure 1.6: Possible long-term slope evolutions (modified after Broadbent and Zavodni, 1982)

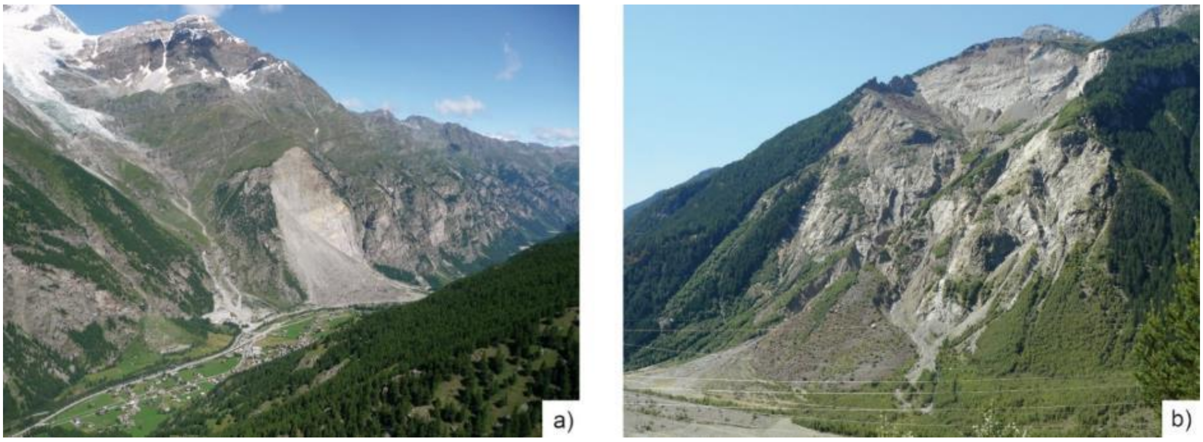

Figure 1.7: Delayed catastrophic collapses: Randa rockslide (a) and Val Pola rock avalanche (b).

1.3.1 Large rockslides

Large rockslides represent instabilities that, in some cases, could evolve into delayed catastrophic collapses, representing a major threat in alpine environment. They consist of large unstable rock mass volumes, usually involving the middle-lower portion of valley flanks, which extension ranges from hundreds square meters to several square kilometers. Agliardi et al. (2012) performed an Alpine scale inventory (Fig. 1.8) collecting a modal value of 0.5 Km^2 and a maximum value of 6 Km^2, after which transition to DSGSD is encountered. Rockslides spatial distribution and density were related to several morphoclimatic factors: Pedrazzini (2012) compiled a regional inventory of gravitational slope deformations for the upper Rhone catchment (Fig. 1.9), discerning between rockslides, DSGSDs and roto-translational rockslides. Obtained results point to valley oversteepening, stress redistribution due to deglaciation, occurrence of large-scale tectonic features and active tectonics as the main influencing factors in predisposing instability conditions. Moreover, lithology strength and structure were recognized to have a minor control on rockslide occurrence, although playing a major role in differentiation and style of slope instability.

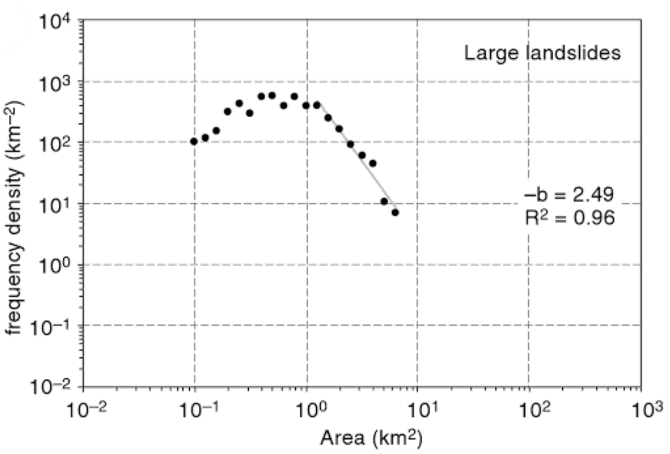

Figure 1.8: Frequency density distribution of large landslides area, showing modal value of 0.5 km^2. Inventory consists of 791 samples collected throughout the entire Alpine orogeny (from Agliardi et al., 2012)

Surface evidence of rockslides mainly consists of scarps and trenches, corresponding to the emergence of main or secondary shear bands along the slope, which often separates unstable portions with different displacement rates or activation timing. Lower boundary consists of a basal shear band, which depth can often exceed one hundred meters from topographical surface, mainly describing a translational kinematics. Rockslides can be constituted by rock mass with different degree of damage and strain localization, depending on rock mass mechanical properties and shear deformation experienced. Typically, shear band material ranges from intensively fractured rock mass to brecciated layers with clay and silt matrix, characterized by complex mechanical and hydraulic behavior (Zangerl., 2010; Loew and Strauhal, 2013; Strauhal et al., 2016). Rockslides are often perched above the valley floor, with basal shear band emergence often highlighted by springs outflows, which occurrence results from hydraulic conductivity contrast between rock mass within the rockslide and crushed material constituting basal shear band. Groundwater circulation largely affects rockslides behavior, especially in mature stage of evolution, where hydro-mechanical coupling phenomena are frequently observed. They mainly consist in mechanical rockslide response to external hydrologic triggers constituted by high groundwater recharge episodes due to snow melting or intense precipitations. This displacement component is usually superimposed to a slope creep movement cause by progressive rupture in subcritical stress regime.

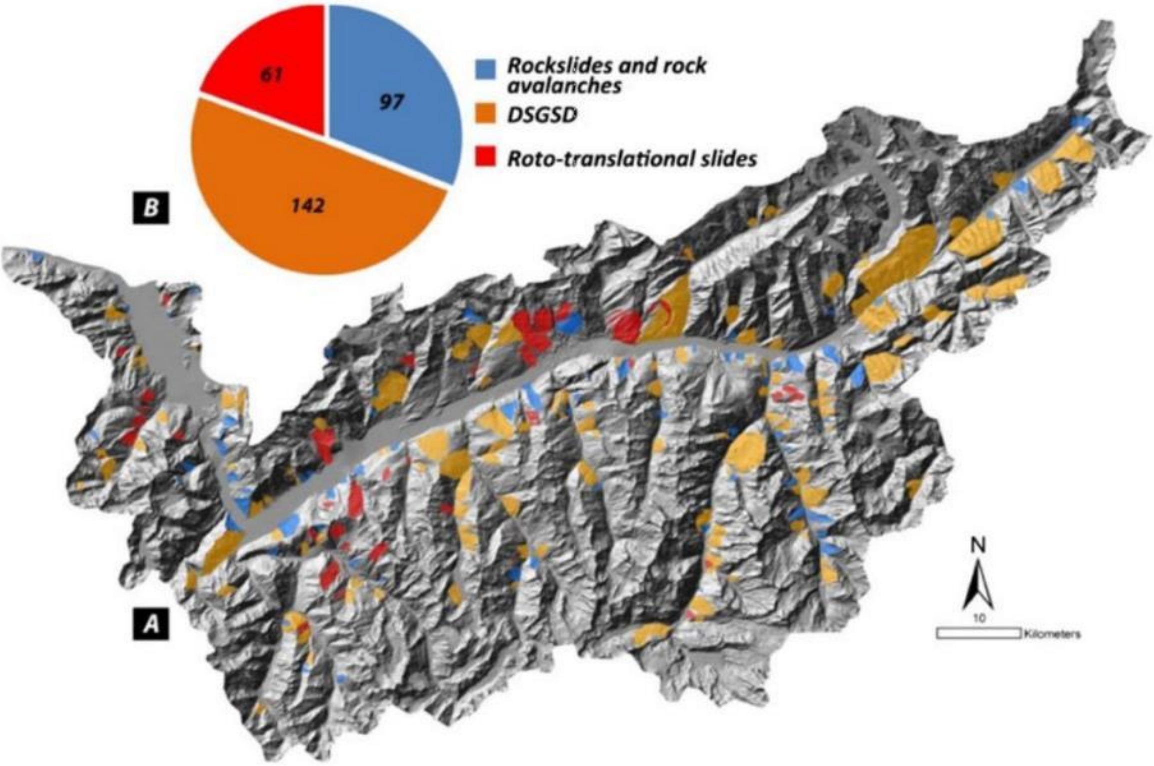

Figure 1.9: Gravitational slope deformation inventory for the upper Rhone catchment compiled by Pedrazzini (2012).

Large rockslides occur not only as a direct consequence of deglaciation and slope debuttressing, but several thousand years might pass since nucleation and acceleration of the unstable body are registered, with implication for slope stability and delayed potential catastrophic collapse. Zerathe et al. (2014) performed a comprehensive inventory of dated landslide at the Alpine-scale and inferred temporal clustering of large failure events plotting them in a time diagram (Fig. 1.10). Particularly, two different clusters were recognized: the first ranges from around 11 to 8 kyr BP and was related to deglaciation with consequent paraglacial effect. The second was located from around 5 to 3 kyr BP, thus corresponding to the Subboreal period, which in paleoclimatic reconstructions appears as characterized by intense hydrological perturbations and large surface water availability (Magny et al., 2013). Widespread occurrence of large scale instability in this time span was thus linked to slope response to intense hydrological triggers.

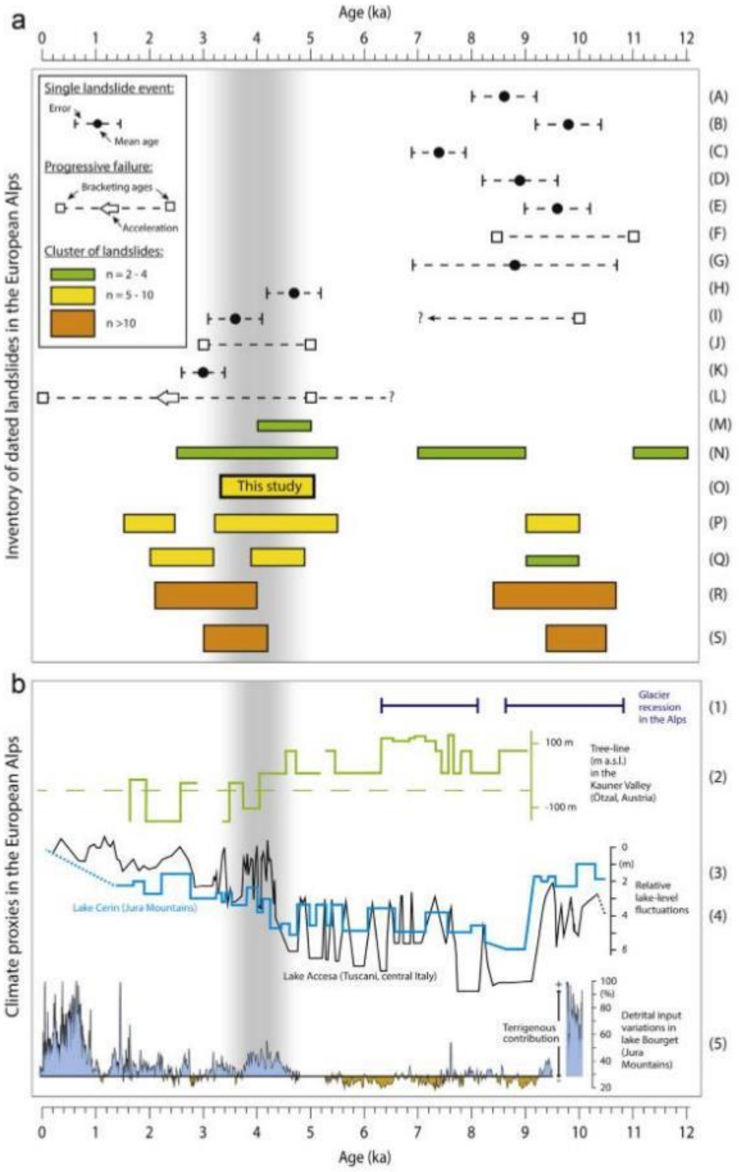

Figure 1.10: Diagram showing the chronological distribution of large Alpine dated landslides (a). Corresponding paleoclimatic proxies of temperature and hydrologic regime are reported in diagram (b). The shaded gray area refers to the landslide clustering identified between 5 and 3 kyr BP (from Zerathe et al., 2014)

1.3.2 *Deep Seated Gravitational Slope Deformations*

Long-term interaction between alpine rock slopes, morpho-climatic processes and paraglacial readjustment can also result in the development of Deep Seated Gravitational Slope Deformations (DSGSD). These extremely large mass movements can involve entire valley flanks and are commonly characterized by high relief energy, deep basal shear band, large volumes involved and lateral boundaries sometimes hard to clearly identify (Zischinsky 1969; Bovis, 1982; McCalpin and Irvine, 1995). The size of DSGSDs can be extremely variable, ranging from hundred square meters to hundred square kilometers (Fig. 1.11, inset), with modal area of 5 Km^2. The analysis of width/downslope length ratio on censed DSGSDs permitted to assess the mainly equidimensional nature of these phenomena. Notably, DSGSDs tends to develop in width rather than downslope, which is due to the relative small distance between crest and valley floor in respect to the width of alpine valleys, which often exhibit similar geomechanical and lithological features for several kilometers. Lithology and tectonic settings proved to be strong controlling factors in DSGSDs development: instabilities nucleates mainly in metapelites, paragneiss and flysch-type rocks, meanwhile being clustered around main tectonic features, probably due to long-term stress regime and the damage and rock mass properties degradation induced by such regional-scale lineaments.

DSGSDs are also characterized by low to extremely low displacement rates, ranging from mm to tens of mm per year, but due to the long-term state of activity can strongly imprint landscape geomorphological evolution through valley narrowing and damming, drainage network modifications and associated landslide catastrophic events (Crosta et al., 2012; Crosta et al., 2014). DSGSDs are widespread in the entire Alps, where more than one thousand phenomena were censed, covering an area of 5.6% in respect to the total investigated (Fig. 1.11; Mortara and Sorzana, 1987; Trigila et al., 2010; Crosta et al., 2014).

Long-term cumulated displacements are expressed on slope surface by distinctive morphostructures (Fig. 1.12), which orientation, occurrence and sizing are strongly influenced by pre-existent brittle and ductile structural features (Agliardi et al., 2001; Ambrosi and Crosta, 2006; Agliardi et al., 2012; Hippolyte et al., 2012; Crosta et al., 2014). Morphostructures extent ranges from few meters (e.g. trenches, open fissures) to several hundred meters (e.g. doubled crest ridges) and can express tensile, shear or mixed style of deformation through sintethic or antitethic slip surfaces. In the upper part of the slope extensional features as trenches, graben, multiple ridges and downthrown blocks usually dominate. Moving to middle-lower sectors, morphostructures related to compression and shear became more frequent and bulging, folding and intensely fractured rock masses are commonly recognized. Compression regime can result in excess of material at toe and slope steepening, which combined to erosion, groundwater circulation and mechanical properties degradation can bring to the occurrence of nested secondary instabilities within DSGSDs. These often consist of active rockslides potentially capable of catastrophic evolution, thus representing a major concern for antrophic activities involved. Ruinon (Agliardi et al., 2001; Crosta and Agliardi, 2003; Agliardi et al., 2011), La Saxe (Crosta et al., 2014) and La Clapière (Guglielmi and Cappa, 2010) rockslides are a few examples of this geohazard in alpine environment (Fig. 1.13).

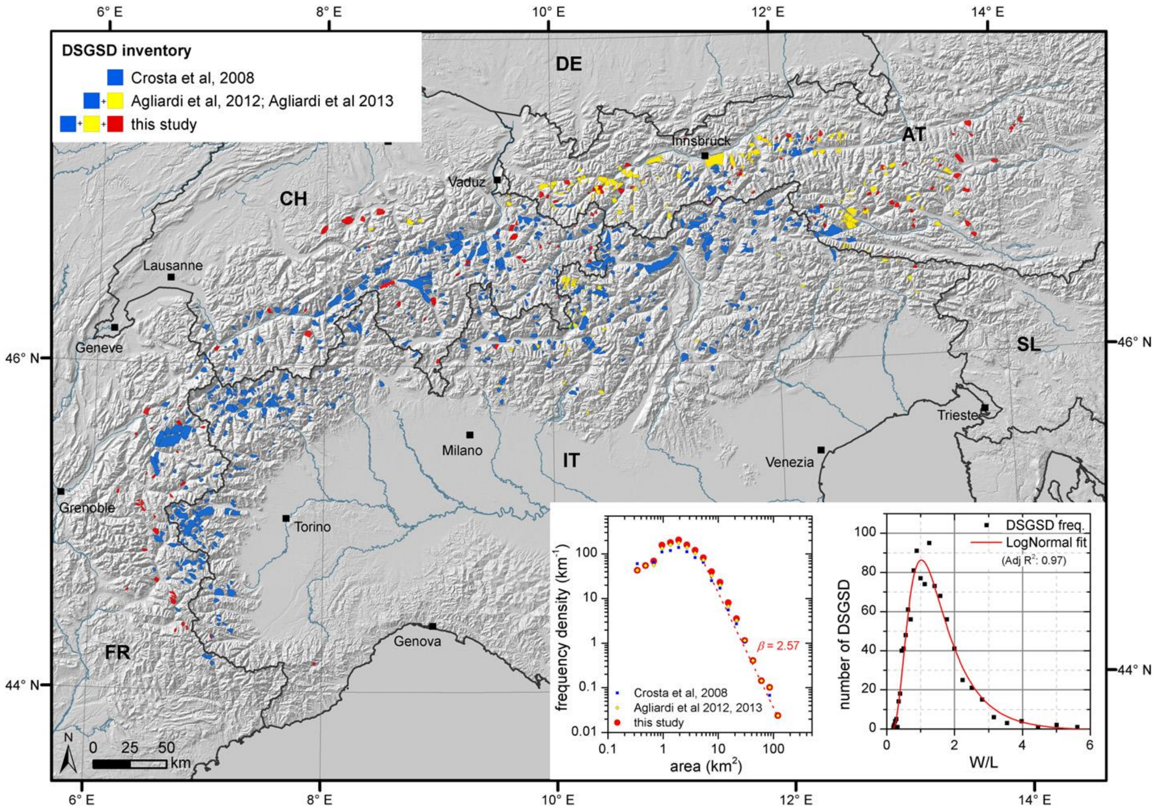

Figure 1.11: Alpine DSGSD inventory. Size frequency distribution and Width/downslope length ratio are also reported, showing the in areal extension heterogeneity and the predominance of DSGSD wider than longer (from Crosta et al., 2013).

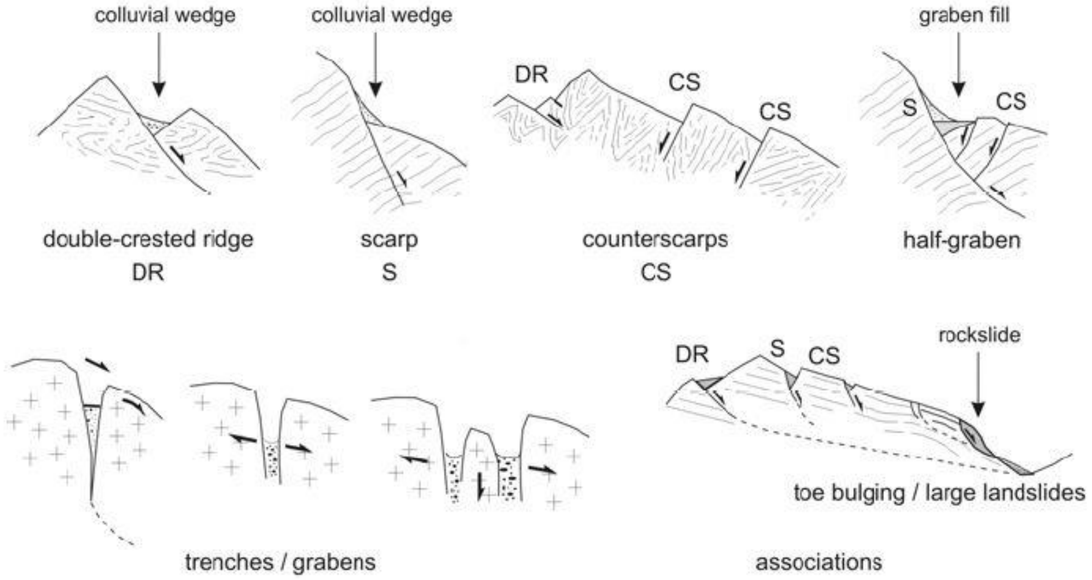

Figure 1.12: Main morphostructures observed in Deep Seated Gravitational Slope Deformations (from Agliardi et al., 2012)

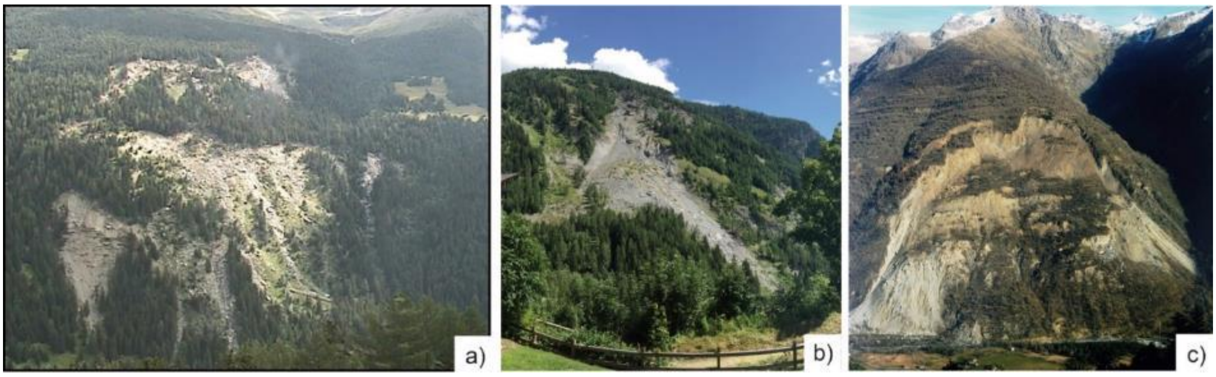

Figure 1.13: Secondary instabilities nested in the lower part of Deep Seated Gravitational Slope Deformations. Ruinon (a), La Saxe (b) and La Clapièere (c) rockslides.

Several processes were pointed out as potential predisposing, preparatory and triggering factors of DSGSD (Crosta et al., 2014): rock mass strength and structure (Zischinsky 1966; Agliardi et al., 2001; Ambrosi and Crosta, 2006; Barbarano et al., 2014), active tectonics (Radbruch-Hall, 1978; McCalpin, 1999; Crosta and Zanchi, 2000; Agliardi et al., 2009; Riva et al. 2016), long-term exhumation (Agliardi et al., 2013), deglaciation and slope debuttressing (Augustinus, 1995; Agliardi et al., 2001; Ambrosi and Crosta, 2006; Cossart, 2008), climate with associated hydrological-hydrogeological pulses (Evans and Clague, 1994; Crosta, 1996; Ballantyne, 2002; Agliardi et al., 2013), topographic and tectonic stresses (Savage et al., 1986; Varnes et al., 1989; Miller and Dunne, 1996; Ambrosi and Crosta, 2011), toe erosion (Crosta and Zanchi, 2000) and anthropic interference (Zangerl et al., 2010). However, in the long-term period, the major control on slope evolution might be exerted by progressive failure mechanisms and hydraulic properties evolution, even if the multitude of processes involved certain results in a complex interaction of causes and triggers during DSGSD development. Despite DSGSD occurrence was also recognized for unglaciated slopes (Crosta and Zanchi, 2000) and the relationship with pre-existing tectonic features is clear, glacial erosion and paraglacial readjustment are considered important processes in formerly glaciated slopes, predisposing by debuttressing and stress redistribution the development of deep seated instabilities by rock mass damage. This is in accordance with reported activation during the Lateglacial, resulting from the application of dating techniques on DSGSDs associated morphostructures (Agliardi et al., 2009). Hippolyte et al. (2012) performed extensive Cosmic Ray Exposure dating on the Rognier DSGSD (Western Alps) in the aim of understanding, through the reconstruction of activity periods for different morphostructures along the slope, the genetic mechanism and the evolution of the DSGSD. Their results constrained slope activity since at least 14 kyr BP up to present time (Fig. 1.14), proving the extremely long slope lifetime in respect, for example, to catastrophic evolution sometimes associated with large active rockslides. Moreover, collection of several samples from the same morphostructure provided the esteem of displacement rates, which for the Roigner DSGSD are comprised in the range 0.3-3 mm per year, thus testifying the slow displacement rates to which the rock mass is subjected.

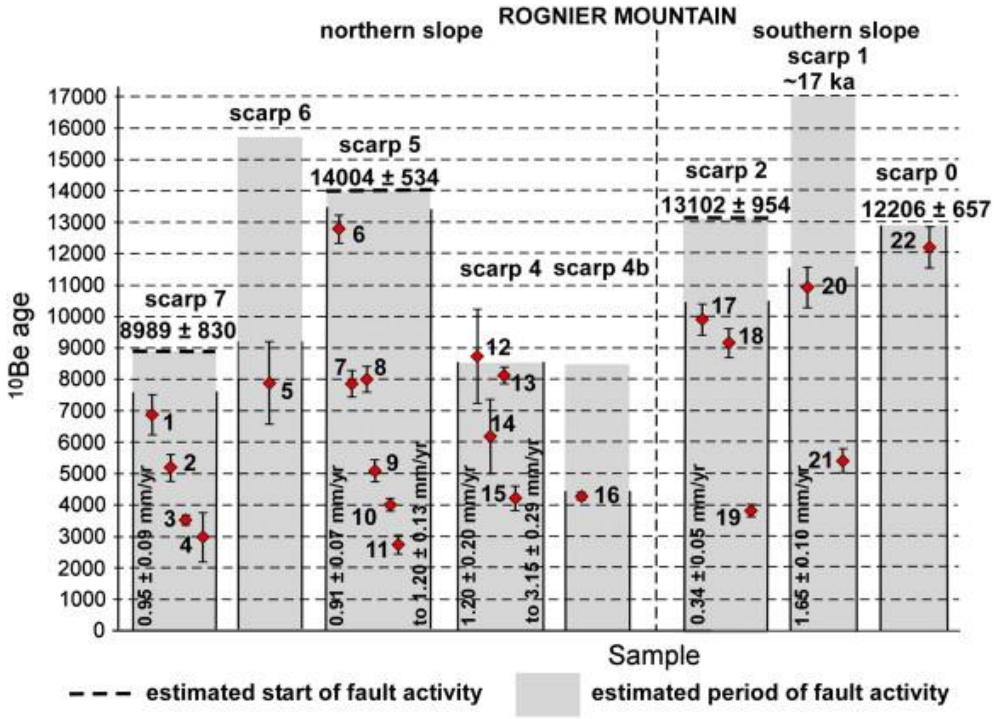

Figure 1.14: Exposure ages and mean displacement rates derived from the CRE dating of different morphostructures on the Rognier slope (from Hippolyte et al., 2012)

1.4 HYDROLOGY OF GLACIATED AND DEGLACIATED SLOPES

During paraglacial and postglacial evolution, different hydrological triggers to which slopes have different sensitivity, including rainfall, surface runoff and snowmelt, can promote and favor rock slope instabilities involving relatively small rock volumes or entire valley flanks, with severe potential impacts on human lives, activities and infrastructures (Dortch et al., 2009; Crosta and Agliardi, 2003; Helmstetter and Garambois, 2010; Zangerl et al., 2010; Agliardi et al., 2012; Crosta et al., 2014 Leith et al., 2014; Deline et al. 2015). Observed slope creep patterns, especially for active rockslides, often result by superimposed long-term and seasonal components (Crosta and Agliardi, 2003; Vallet et al., 2015). While the long-term component is often regarded as evidence of (sub-critical) progressive rock mass failure processes (Eberhardt et al. 2004; Amitrano and Helmstetter, 2006; Lacroix and Amitrano, 2012; Stead and Eberhardt, 2013), the latter is usually interpreted as evidence of hydromechanical coupling between hydrological triggers and landslide systems (Crosta et al., 2014; Vallet et al., 2015; Preisig et al., 2016).

Several studies were carried out to evaluate groundwater flow in mountainous terrains, both at regional and local scale (Gleeson and Manning, 2008; Welch and Allen, 2012; Welch and Allen, 2014), even if knowledge about long-term circulation in glacial, paraglacial and postglacial conditions remains an extremely complex task. Especially for glaciated conditions (Fig. 1.4a), the almost total lack of studies, which concentrates mainly on supraglacial and subglacial water circulation (Boulton and de Marsily, 1996; Flowers and Clarke, 2002; Boulton et al., 2005), makes the reconstruction of slope groundwater regime extremely difficult. During paraglacial readjustment, all the aforementioned processes related to deglaciation and slope debuttressing results in stress redistribution, rock mass damage and progressive increase of fracture intensity (Fig. 1.14b). Despite also during this stage no direct observations of slopes behavior exist, consequent increase in rock mass permeability and fracture interconnection is expected, corresponding to the comparison of local damage-induced aquifers within the deglaciating slope. In mature stage, characterized by well-developed basal shear zone and permeable unstable rock mass, hydro-mechanical interaction between hydrological inputs and slope displacements is often observed and supported by geotechnical slope investigations. The coupling degree was ascribed to rock mass permeability, which controls the sensitivity of slope to oscillations in fluid pressure (Loew and Strauhal, 2014; Strauhal et al., 2016): for highly-fractured and conductive rock masses, low response to variations in groundwater table are observed, while for less permeable rock masses strong hydro-mechanical coupling is expected. Such different sensitivity could be one of the main factors in determining potentially various coupling regimes in large rockslides with respect to DSGSDs, characterized by different scale but also by different cumulated displacement and strain. These could result in different rock mass damage pattern, fracture density distribution, shear bands comminution and hydraulic properties, taking also into account the important role of geomorphological features in driving groundwater circulation within slopes.

Indeed, especially in DSGSDs, the effect of morphostructures is not only topographical, but also condition the distribution and circulation of water within the slope. Modification can involve (a) enhanced percolation of water favored in upper slope due to trenches, scarps and counterscarps, (b) increase of hydraulic conductivity through open fracture networks, (c) localization of preferential flow-paths through the slope and (d) deep circulation system into rock-mass along base displacement surface. Crosta et al. (2014b) analyzed the effect of DSGSDs on the slope drainage networks and aquifers of Upper Valtellina valley (Italian Central Alps) through field surveys, sampling campaigns, photointerpretation and review of existing data about springs location and hydro-chemistry. Results suggest that DSGSDs strongly control springs spatial distribution and superficial drainage density, with higher spring density but lower development of superficial network encountered within unstable areas. Moreover, a clustering of springs is recognized for DSGSD areas: springs tend to concentrate on distinct parts of the slope, such as in the middle sector and along lateral boundaries of DSGSD (Fig.1.15), suggesting the development of localized flow-paths driving groundwater in specific slope portions.

Conceptual model of water circulation into a DSGSD-affected slope was also reconstructed (Fig. 1.16), identifying different circuits and residence times. The geochemical imprint of waters and their flowpaths into rock mass were related to three different types of springs: (a) shallow springs located in the upper part of the slope, characterized by low mineralization, subsuperficial circulation in debris cover and short residence time, (b) intermediate springs located in the middle part of the slope, characterized by higher mineralization, longer residence time and mixing between shallow and deep circuits under the influence of morpho-structures (i.e. scarps or counterscarps) and (c) deep springs located in the lower part of slope, characterized by higher mineralization and fed by deep circulation within the slope, driven by the development of DSGSD's failure surface.

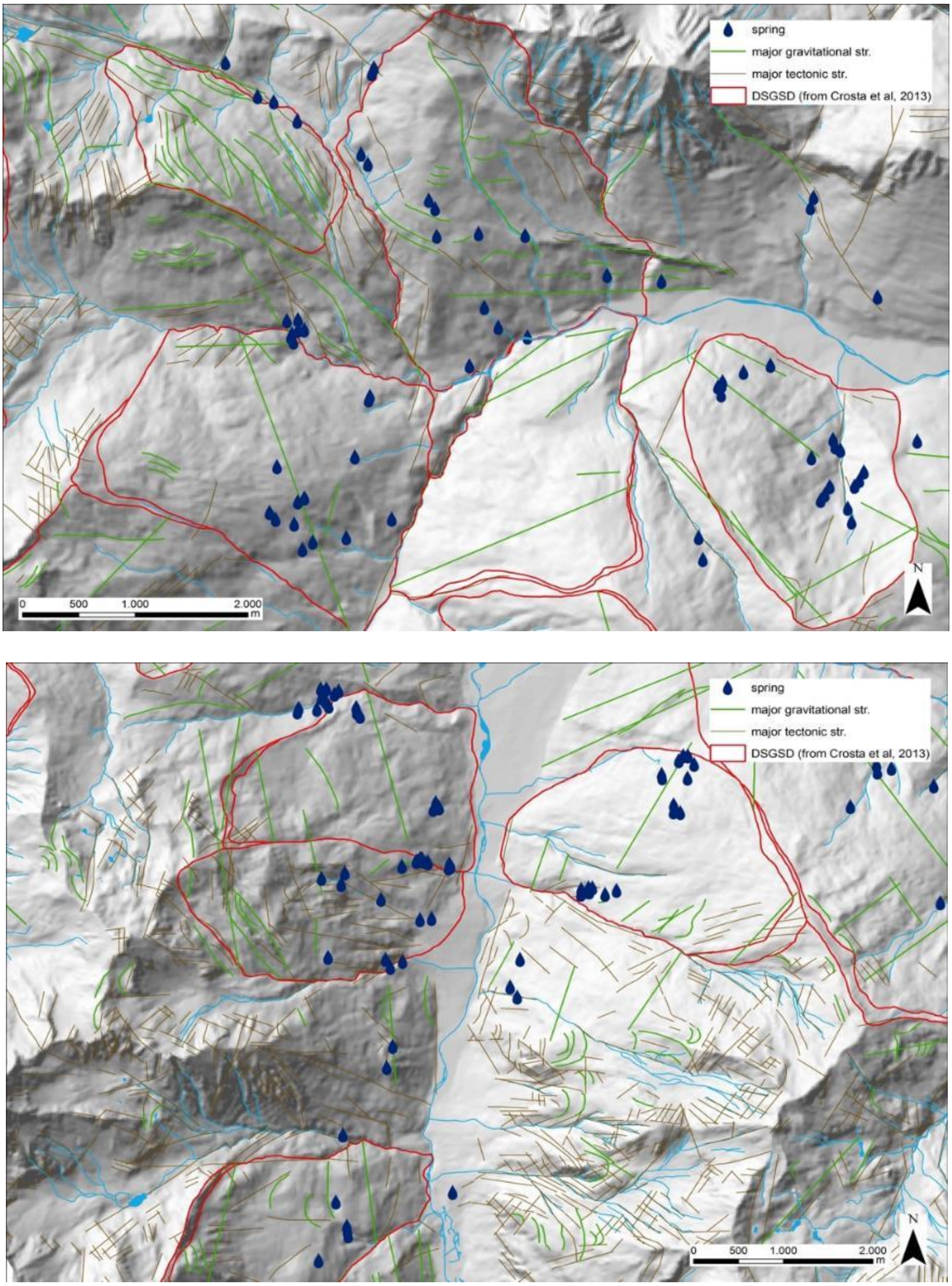

Figure 1.15: Spatial distribution of springs within DSGSD areas. Purple circles indicate mid-slope springs while purple squares

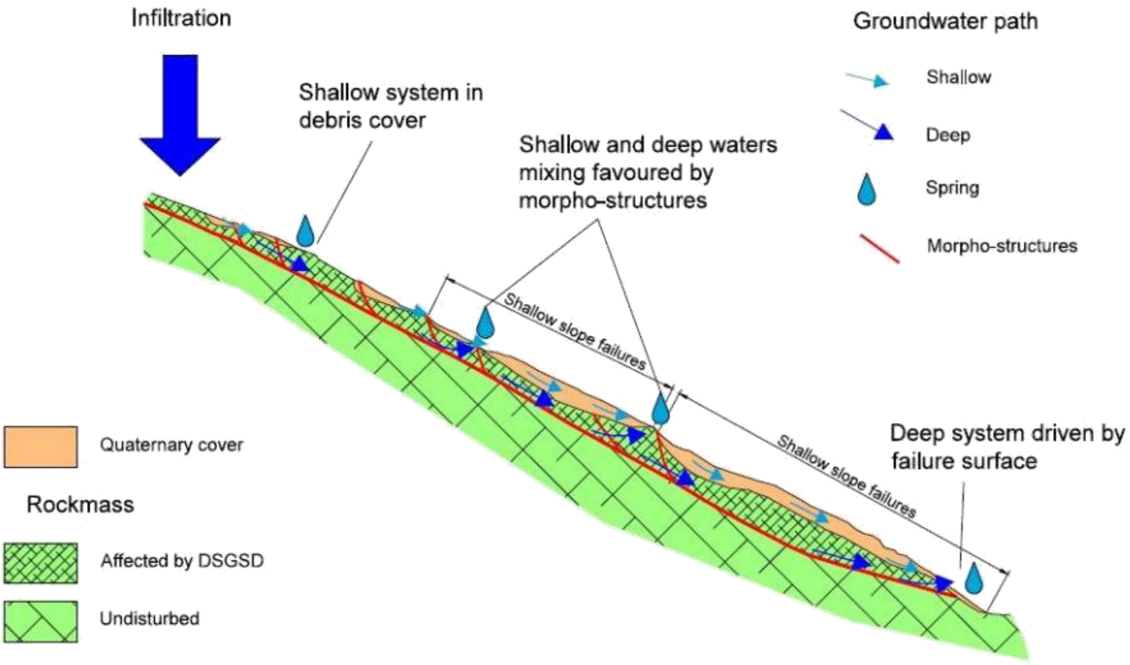

Figure 1.16: Conceptual model of water circulation into a DSGSD affected slope.

2 LARGE ROCK SLOPE INSTABILITIES: ISSUES AND APPROACHES

Modelling the time-dependent behavior of large rock slope instabilities is key to understand their long-term evolution and controls, predict future displacements and potential catastrophic evolution for risk analysis, Early Warning and civil protection purposes (Crosta et al., 2014). In addition, forecasting the evolution of alpine rock slopes requires the ability to properly track their mechanical and hydrological history from a glaciated condition (Fig. 1.4a) to the occurrence of a “mature” instability (Fig. 1.4c), through a variably long period of readjustment (Fig. 1.4b).

In practice, landslide forecasting mostly relies on analytical, statistical or numerical models which account for the slope mechanical response to hydrologic triggers as rainfall, snowmelt, deep drainage remediation or artificial water reservoir fluctuations (Cappa et al., 2004; Guglielmi et al., 2005; Eberhardt et al., 2007; Zangerl et al., 2010; Crosta et al., 2014; Vallet et al., 2015; Preisig et al., 2016). These models, simulating typical and site-specific pore pressure fluctuations, permit to evaluate the hydro-mechanical landslide sensitivity and simulate the induced displacement field within unstable slope. Information derived from such modelling are then used for accurate assessment of stability conditions and expected slope evolution in the short-term period.

In these approaches, the geological model of the analyzed slope is often derived from present-state geotechnical and geophysical characterization, which are based on point-like investigations covering only a small portion of the unstable volume. Nevertheless, large alpine rock slopes experiencing glaciation, deglaciation and paraglacial readjustment usually exhibit slow creep-like movements that, lasting for thousand years, bring to cumulated displacement of several tens of meters accompanied by the evolution of geometry, internal structure, strength and hydrology, even if magnitude and timing of adjustment are rarely well known.

On the other hand, existing models of long-term rock slope instability are usually not time-dependent and focus on the analysis of initial onset mechanisms of failure and their topographic, lithological, structural and climatic controls (Agliardi et al., 2001; Eberhardt et al., 2004; Ambrosi and Crosta, 2006). Interestingly, these models predict major role of slope deglaciation and brittle creep process in the initiation of slope instability while a link between early and mature stages is rarely provided. Also hydromechanical coupling and fluid pressure effect are often omitted due to almost complete lack of knowledge about slope hydrological constraints in glacial environment besides their evolution during paraglacial and postglacial stages.

Therefore, attempts to comprehensive model different stages of long-term alpine rock slope evolution must face several *caveats*, including:

a) limitations of rheological approaches in the time-dependent modelling of slope evolution, unless a landslide shear zone is pre-determined and its viscous parameters calibrated (De Caro et al., 2016);

b) mostly unknown spatial and temporal evolution of surficial hydrology and groundwater occurrence in the slope during and after deglaciation (McColl, 2012; Crosta et al., 2013,);

c) limited knowledge of the relationships between brittle failure processes and permeability on the large scale and under changing stress conditions typical of rock slopes (Leith, 2012; Preisig et al., 2012; Rutqvist, 2015; Ziegler et al., 2016);

d) limited understanding of hydro-mechanical controls on instability development, sensitivity to hydrological triggers and long-term evolution, as a major input to the development of slope forecasting (Preisig et al., 2016).

Trying to successfully reproduce the slope long-term evolution in a unique framework, damage is the key process linking in a common ground all these issues.

In this chapter, features of damage process will be analyzed, ranging from microscopic to macroscopic scale and resuming empirical descriptors and modelling approaches exploited in literature to assess its behavior. Moreover, numerical approaches used in large rock slopes modelling will be reviewed, focusing on the long-term processes and the role of fluid pressure in determining instability conditions.

2.1 ROCK MASS BEHAVIOR AND PROPERTY UPSCALING

Real slopes are constituted by rock masses, which in turn consists of intact rock (i.e. “rock matrix”) subdivided in discrete blocks by discontinuities (bedding, foliation, fractures), resulting in a discontinuous, heterogeneous and anisotropic material. Fractures intensity and orientation depend on the former action of different geological processes (Pollard and Haydin, 1988), often resulting in sets of discontinuities, with spacing and length varying according to relatively simple probability density functions (e.g. negative exponential; Priest and Brown, 1995) or constrained by primary geological feature (e.g. strata-bound fractures), and by different roughness and weathering conditions affecting discontinuity strength (Barton et al., 1974). The mechanical and hydraulic behaviors of rock masses depend on the interaction between intact rock strength, the geometry, strength and deformability of discontinuity, and the stress state, with rock mass strength decreasing with increasing sample volume (Hoek and Brown, 1980 and Fig. 2.1).

The scale of the problem is a key control on rock mass properties (i.e. intact rock strength is scaled by size) and on the way rock mass behavior is represented in order to set up or select the most suitable modelling techniques (Hoek, 1988; Edelbro, 2003). Small volumes of rock masses characterized by widely-spaced, persistent discontinuities, individual fractures and their properties will constrain the size and mechanisms of rock mass deformation and failure, according to a “discontinuum medium” scheme. This structural configuration can be associated with planar failure (Fig. 2.2a), especially in rock masses characterized by a highly-persistent discontinuity set (e.g. bedding) oriented in a cinematically admissible way. For two or more sets, wedge instabilities (Fig. 2.2b) can occur, with shape and volume of unstable blocks controlled by the discontinuities pattern. Instead, toppling (Fig. 2.2c) is observed in slopes with persistent and steeply dipping discontinuities set, also depending on the intact rock tensile strength in giving flexural component to the rock mass slabs.

On the opposite, large-scale problems (e.g. large rock slopes) in rock masses constituted by several sets of closely-spaced discontinuities (no dominant structural patterns) are characterized by small rock blocks with respect to the problem size. In these case, the global behavior of the rock mass can be regarded as that of an “equivalent-continuum” medium with strength, deformability and hydraulic properties representative of the global rock mass behavior. Circular failures (Fig. 2.2d) are representative of rock masses constituted by randomly-oriented discontinuities, which makes the kinematics resembling a soil slope behavior. In such cases, rock mass properties are derived by upscaling intact rock properties, taking into account the characteristics of discontinuities though the approaches described in the following paragraphs.

An accurate definition of intact rock properties can be obtained, at different levels of complexity, by performing laboratory tests on intact rock samples (direct and indirect tension, uniaxial and triaxial compression, others). These allow to quantify rock strength, deformability, physical properties and fabric controls on their variability. Observed behavior permitted the development of several failure criteria and constitutive models (Griffith 1921, 1924; Fairhurst, 1964; Bieniavski, 1974; Hoek and Brown, 1980; Sheorey et al., 1989; Hoek et al. 1992). Also discontinuities were tested in laboratory conditions, mainly by shear tests on decimetre-scale samples, to investigate peak and residual strength on smooth joints (Hoek, 2007), simulated

(Patton, 1966) and real discontinuities (Barton, 1976; Barton and Choubey, 1977). Results allowed establishing failure criteria accounting for joint roughness and strength.

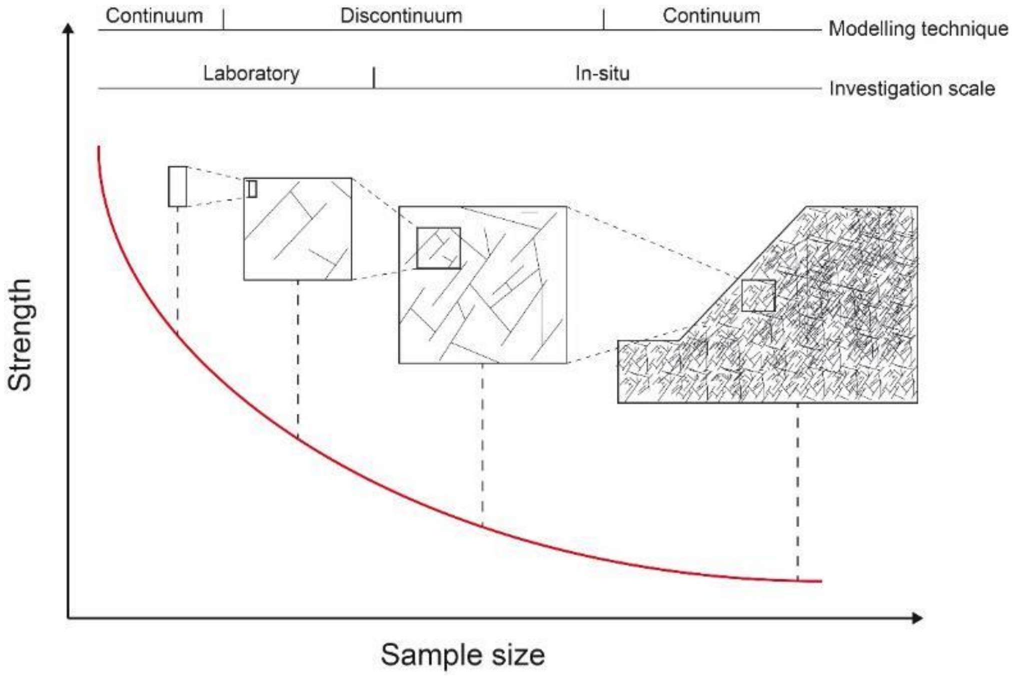

Figure 2.1: Sample size effect on strength and modelling technique adopted (modified from Krauland et al., 1985 and Edelbro, 2003).

Instead, the complex mechanical and hydraulic behavior of rock masses cannot be characterized by mechanical testing, although large-scale tests in boreholes or excavation allow investigating rock masses on the scale of cubic meters. Therefore, empirical approaches were developed to quantify equivalent rock mass strength starting from intact rock values, based mainly on numerical modelling, back-analysis, and rock mass classification (Krauland et al., 1985). Numerical modelling, which in the last decades has exponentially grown due to increase in computational efficiency, represent an extremely powerful tool to assess rock mass properties. Nevertheless, the choice of modelling approach is critical, as different formulations are based on different simplified assumptions on rheology, rock mass properties and physical processes involved. Moreover, input parameters are fundamental in determining affordable results. Back-analysis and large-scale testing are options not always suitable for practical application, due to lack of previous knowledge or the high logistic and economic efforts needed to perform large-scale tests. Few experimental data exist in literature for large rock masses, except for in situ test executed for determination of strength (Bieniavski and Van Heerden, 1975; Thorpe et al., 1982), deformability (Palmstrom and Singh, 2001) and permeability (Brace, 1984; Witherspoon, 2000).

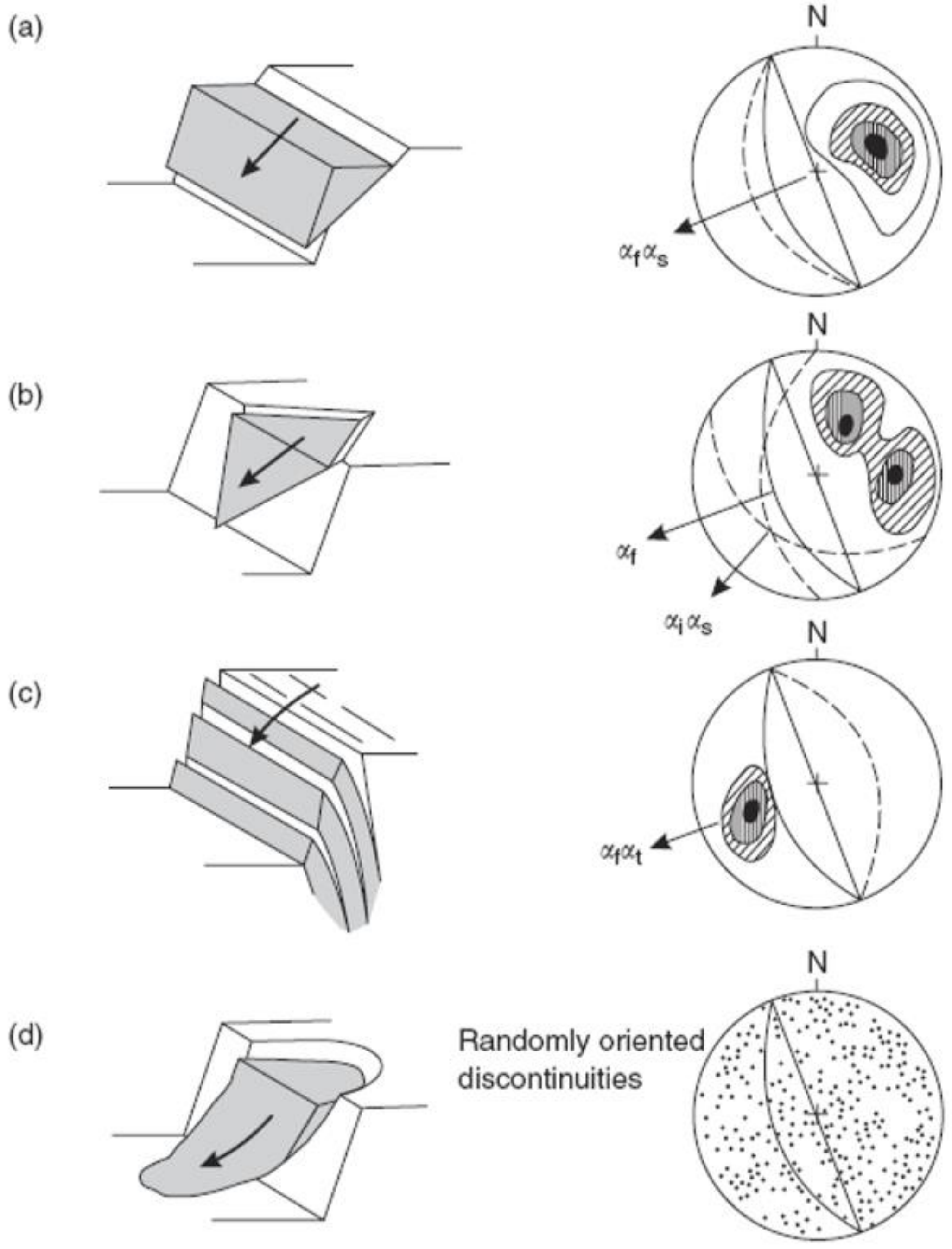

Figure 2.2: Main types of rock slope failures according to structural conditions. Typical stereo plots associated are also reported (from Hoek and Bray, 1981)

Empirical rock mass classification schemes provide estimates of expected rock mass behaviour for specific engineering applications (tunnelling, excavations, and foundations). Starting from the pioneering work of Ritter (1879), several classification methods were developed, mainly starting from empirical observation performed for specific rock masses and for specific engineering purposes (Palmstrom, 1985; Edelbro, 2003). Terzaghi (1946) proposed an empirical rock load theory for underground railway tunnels, in which rock mass is subdivided into nine categories based on rock mass structure and observation subsequent to tunnel advance. Despite being a qualitative classification, rock load theory represents one of the first attempts made for the rock mass classification. Later, Deere et al. (1967) introduced Rock Quality Designation index (RQD) to quantify rock mass quality and fracture intensity from core logs, given by the percentage of recovered core pieces longer than 100 mm. Despite affected by evident orientation and scale bias, RQD is nowadays frequently used in core logging for its simplicity and constitute an input value in subsequent multi-parametric analysis like for example Rock Mass Rating (RMR). The RMR (Bieniawski 1976, 1989) was initially conceived for shallow tunnels and mining operations and rely on the contribution of different parameters for establishing the global quality of rock mass, namely intact rock strength, spacing, orientation and weathering of discontinuities and water occurrence. Rock mass is subdivided into five categories, from very good to very poor, including also indications regarding support system to be adopted. The RMR was later extended with the introduction of coefficients related to slope geometry, failure mode and excavation technique, making the classification suitable to slope stability problems (Slope Mass Rating; Romana, 1985). Another method, developed for underground excavation in Scandinavian granites, is the rock Quality Index (Q-index) of Barton et al. (1974). This classification method is based on three fundamental ratios, representing block size, frictional strength and stress regime, described by six different parameters collected through outcrop or core logs analysis. The Q-index, also recurring to dimension and category of excavation, gives practical indications about rock mass quality and reinforcements during engineering operations.

A groundbreaking step toward a quantitative parametrization of rock mass strength and deformability was made by Hoek and Brown (1980). They proposed a non-linear empirical failure criterion for intact rock, and later extended its use to rock masses, based on the assumption that increasing problem scale until discontinuities are included in the “sample” adds another scale effect to the assessment of sample strength. Thus, they proposed an empirical method to scale intact rock (lab) properties values based on the spatial pattern of discontinuities (rock mass structure) and their conditions, derived from detailed site characterization on outcrops or rock cores (Hoek and Brown, 1988, 1997; Marinos and Hoek, 2000). In order to support the practical adoption of this approach, Hoek et al. (1995) introduced the Geological Strength Index (GSI). Related with the parametrization of the empirical failure criterion proposed by the same author in 1980 (Hoek et al., 1995; Hoek and Brown, 1997), the GSI permits to describe rock mass with an index ranging from 5 to 95, relying only on visual description of structure and joints weathering and avoiding multi-parametric classification schemes (Fig. 2.2). The easiness in its application permitted a large diffusion of GSI, which was later adapted for description of weak, heterogeneous and complex rock masses and related to quantitative descriptors (Marinos and Hoek, 2000; Hoek et al., 2002; Hoek et al., 2005; Marinos et al. 2005;Cai et al., 2004; Hoek et al., 2013). GSI was also applied on characterization of slopes, particularly regarding stability evaluation, and engineering projects (Brideau et al., 2009; Agliardi et al., 2013). Recently, Agliardi et al. (2016) proposed a method to evaluate the GSI from rock cores starting from relationship between P-wave velocity and rock mass structure and weathering. This method, based on quantitative description of structure and joint conditions (Fig. 2.3 and Table 2.1) permitted to evaluate GSI also for rock masses located at depth, thus being useful in the characterization of equivalent continuum properties for practical applications.

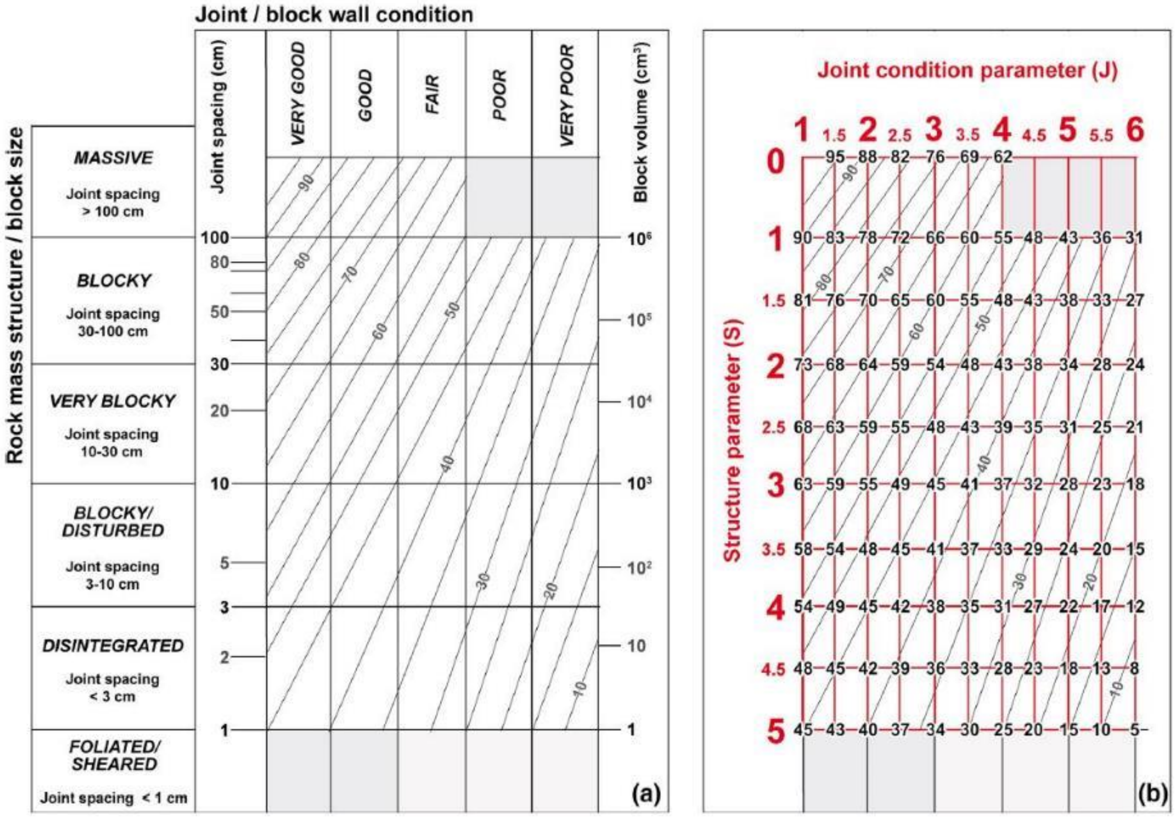

Figure 2.3: (a) GSI chart based on quantitative joint spacing (from Cai et al., 2004) (b) GSI chart for borehole logging: Structure and Joint condition parameters are derived from Table 2.1 (from Agliardi et al., 2016).

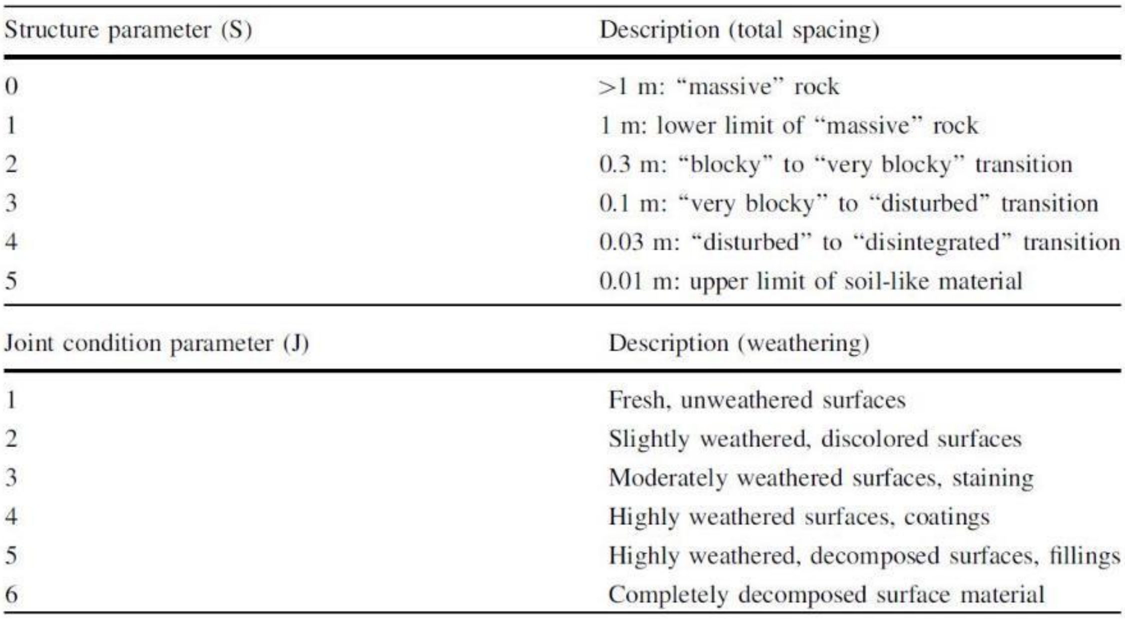

Structure parameter (S)	Description (total spacing)
0	>1 m: "massive" rock
1	1 m: lower limit of "massive" rock
2	0.3 m: "blocky" to "very blocky" transition
3	0.1 m: "very blocky" to "disturbed" transition
4	0.03 m: "disturbed" to "disintegrated" transition
5	0.01 m: upper limit of soil-like material
Joint condition parameter (J)	**Description (weathering)**
1	Fresh, unweathered surfaces
2	Slightly weathered, discolored surfaces
3	Moderately weathered surfaces, staining
4	Highly weathered surfaces, coatings
5	Highly weathered, decomposed surfaces, fillings
6	Completely decomposed surface material

Table 2.1: Relationships between structure parameter and joint spacing and between Joint condition parameter and weathering (from Agliardi et al., 2016).

2.2 BRITTLE FAILURE OF ROCKS: DAMAGE

During loading, macroscopic behavior of rocks is characterized by mechanical properties evolution. Particularly evident from the analysis of stress-strain diagram, the elastic modulus behavior changes with applied stress, passing from an elastic phase to progressive decrease until rock peak strength, where failure occurs in form of tensile and/or shear fractures. This macroscopic behavior is the expression of micromechanical processes consisting in microcrack nucleation, propagation and coalescence, which are recognized also for stress levels well below the peak strength, contributing to the progressive damage of rock and the evolution of mechanical properties. Thus, describing damage contributes to the understanding of processes governing failure throughout the entire loading history.

Damage depends on geometry and intensity of cracks and defects, that in rocks are recognized at micro, meso and macro scale (Fig. 2.4). Rock microcracks were classified depending on location in intergranular, intragranular and along grain boundary (Kranz, 1983), and mainly originate from rupture of interatomic bonds in response to stress application.

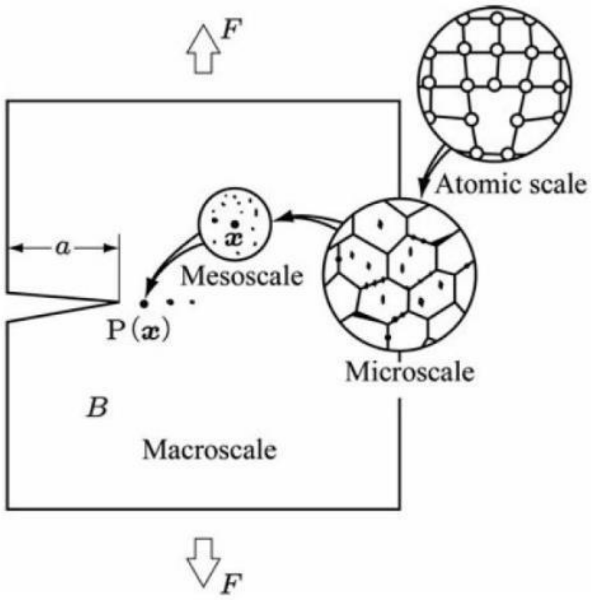

Figure 2.4: Microscopic to macroscopic expression of damage in isotropic material (from Murakami, 2012)

2.2.1 Damage processes: experimental evidence and descriptors

Laboratory compression tests (uniaxial and triaxial) on intact rock specimens were used to quantify the mechanisms of progressive microcracking (damage) of low-porosity rocks during standard or cycling loading by measuring strain and acoustic emission behaviors (Martin and Chandler, 1994; Eberhardt et al., 1999). In this respect, five different regions were recognized in the stress-strain curves, corresponding to changes in mechanical behavior due to progressive damaging and brittle rupture of the rock specimen (Fig. 2.5). The first stage refers to crack closure, corresponding to closure of cracks initially occurring within the rock and favorably oriented with respect to the direction of loading (i.e. perpendicular to σ_1). Crack closure depends on the textural and physical characteristics of the tested rock, and is expressed by a concave-up stress-strain curve. Further increase in the applied load leads to a linear increase in deformation, marking the beginning of elastic region (region II in Fig. 2.5), where the typical elastic moduli of rocks are measured. The transition to inelastic stable crack growth occurs above a stress threshold value, which corresponds to the onset of dilatancy (Crack Initiation stress, σ_{ci} in Fig. 2.5). Crack initiation is a fundamental point in stress-strain curve, as it marks the initiation of damage process, expressed by increase of specimen volume due to microcracks nucleation and growth. Since this stress threshold does not have a clear evidence on stress-strain curve, several methods were proposed to accurate establish the Crack initiation stress, mainly accounting for volumetric or lateral strain (Nicksiar and Martin, 2012). For example, Brace et al. (1966) identified Crack Initiation with deviation of volumetric strain from linear trend, while Martin and Chandler (1994) proposed to identify σ_{ci} by comparing elastic volumetric strain (i.e. derived using elastic E and ν) with the correspondent experimental value. Within stable crack growth regime, increase in microcracks density is strictly dependent on the increase in applied load: if the stress is kept constant, microcracks growth stops (Bieniavski, 1967). The onset of dilatancy is usually recognized for stresses corresponding to the 40-60% of the rock instantaneous (peak) strength. Approaching the rock peak strength (around 70-80%), transition from stable to unstable cracking is observed at a stress threshold value called Crack Damage Stress (σ_{cd} in Fig. 2.5). Reversal in total volumetric strain curve is observed due to interaction and coalescence of microcracks, reaching critical microcracks density and resulting in the development of macroscopic fractures within the sample. Martin and Chandler (1994) demonstrated that crack damage threshold strongly depends on accumulated damage within the sample. Damage process is no more dependent on applied load and continues until global failure is reached (σ_{peak} in Fig. 2.4). After the macroscopic rupture, the post-peak part of the stress-strain curve can be reconstructed by the use of stiff servo-controlled testing frames, and is characterized by rapid fall of stress versus strain and the advent of residual strength.

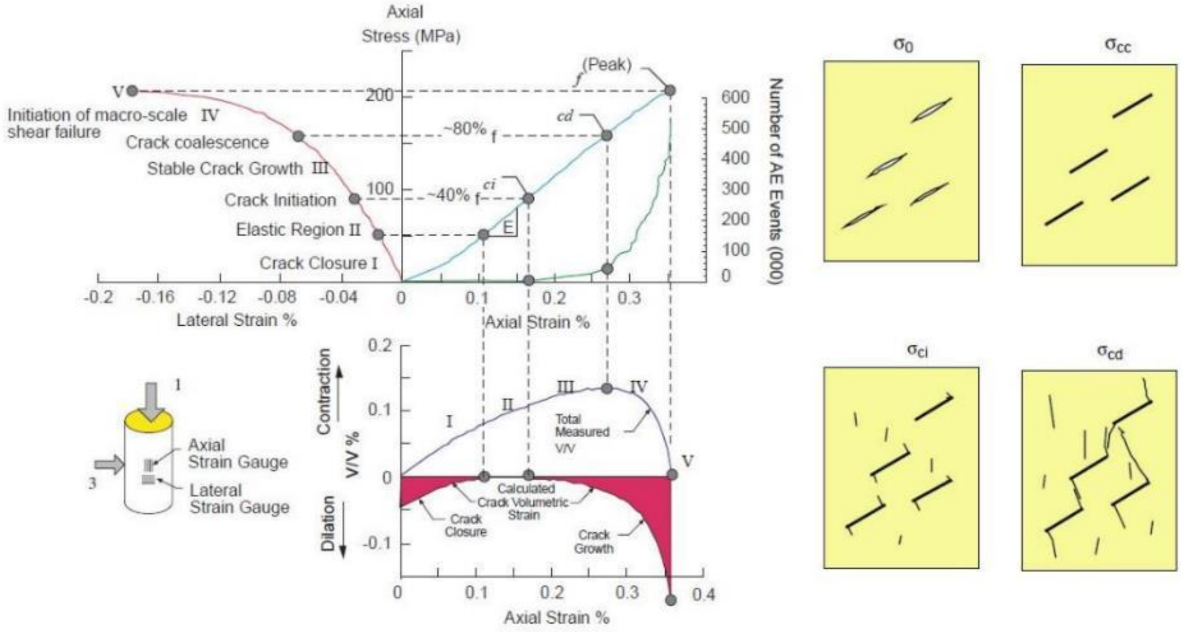

Figure 2.5: Typical triaxial testing on intact rock. Stress strain curve, acoustic emission counts and volumetric versus axial strain are reported, highlighting main stages involved in microcracks initiation, growth and coalescence. Microcracks conceptualized patterns in most significative stress thresholds are also indicated (from Cai et al., 2004).

Several microscale phenomena contribute to crack nucleation and growth (i.e. crack damage) at stresses far below the rock peak strength. These include: atomic diffusion, stress corrosion and microplasticity (Atkinson and Meredith, 1987), commonly grouped under the process of “subcritical crack growth”. Laboratory creep tests showed that subcritical crack growth evolves in time at constant applied stress, and can eventually result in delayed macroscopic rock failure. Such time-dependent behaviour is named “brittle creep”, because it is related to brittle damage processes and not to crystal plasticity typical of ductile creep processes occurring at high temperature and/or confining pressure. Due to practical limitations (i.e. test duration and related practical issues), creep tests are usually performed for applied stresses closer to rock peak strength, even if subcritical crack growth is encountered for any applied stress above crack initiation threshold (σ_{ci} in Fig. 2.5). The typical creep deformation curve consists of three distinct stages in a strain versus time diagram: (a) primary or decelerating stage, (b) secondary or steady-state stage, (c) tertiary or accelerating stage (Fig. 2.6). The physical meaning and the existence of the secondary stage are still debated in literature, as it may be considered only the flex point in the strain-time curve. Several environmental conditions influence brittle creep process, thus controlling the timing of macroscopic failure: temperature, water content and effective pressure, differential stresses and initial microstructure of the sample are among the most influencing (Brantut et al., 2013 and reference therein).

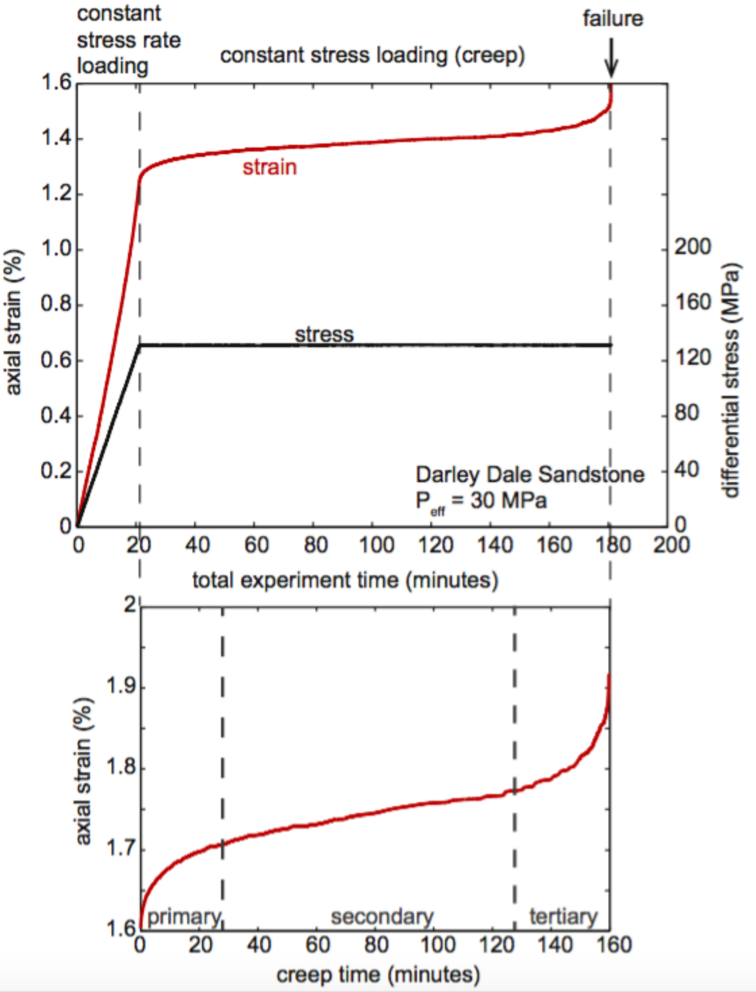

Figure 2.6: Strain and stress versus time curves for laboratory test on Darley Dale sandstone. The sample is loaded until a stress lower than peak rock strength, which is then maintained constant. The sample start creeping through primary, secondary and tertiary stages until failure (from Brantut et al., 2013).

Crack damage processes are key drivers of brittle failure processes and of the evolution of rock properties at microscopic, mesoscopic and macroscopic scale, including strength, deformability and permeability (Paterson and Wong, 2005). Thus, several efforts were made to measure damage and its evolution versus strain and time using direct estimated of fracture density or indirect (proxy) damage descriptors (Kachanov, 1986; Katz and Reches, 2004).

Regarding direct microstructural observation, Katz and Reches (2004) conducted microcracks density mapping on granite thin sections at different loading stage during triaxial loading, observing progressive growth and coalescence, while other authors described microfracturing evolution recurring to computerized tomography (CT) and Scanning Electron Microscopy (SEM) techniques (Tapponnier and Brace, 1976; Feng et al., 2004). Moreover, damage state could be also related to evolution of several physical properties typically measured during laboratory tests: despite the aforementioned method using the ratio between experimental and elastic volumetric strain, several other techniques were developed (Paterson and Wong, 2005). Acoustic emissions provide an affordable and well-tested correlation with damage (Fig. 2.7), being physically related to the process of microcracking and easy to measure. Occurrence of acoustic emissions was clearly recognized since the crack initiation threshold, also showing an increasing rate of events while approaching macroscopic failure (Lockner, 1993; Eberhardt et al., 1999; Martin et al., 2001; Cai et al., 2004; Heap et al., 2009). Interestingly, this concept was upscaled using microseismic events to assess spatial and temporal damage evolution due to deep underground tunneling projects (Martin and Chandler, 1997; Cai et al., 2001). Triaxial tests conducted by Stanchitz et al. (2006) on granite and basalt highlighted anisotropic nature of damage and its dependence on fabrics, documented by anisotropy of P-wave velocity and shear wave birefringence during deformation. Decrease in seismic wave velocity was recognized as response to damage increase, due to enhanced fracture density and in turn to a “slower” media for the waves to cross (Fig. 2.7; Schulze et al., 2001). Indeed, hydraulic permeability usually increases while damage progresses, mainly due to two different complementary mechanisms: the growth of microcracks density, which increase interconnection and possible pathways, and the onset of dilatancy, which basically corresponds to open fractures availability (Zoback and Byerlee, 1975; Shulze et al., 2001; Rutqvist and Stephansson, 2003).

Martin and Chandler (1994) proposed the Crack Volumetric Strain (CVS) as a proxy of crack damage in intact rock laboratory tests, starting with the assumption that dilatancy is a proxy of micro and meso-crack growth. The CVS, that is defined as the difference between elastic volumetric strain and measured experimental volumetric strain, permits to accurately assess the point in stress-strain curve in which crack initiation begins (Fig. 2.5). Moreover, cumulated value of CVS permits to assess rock dilatancy up to the peak stress, thus resulting in indirect measure of the critical microcrack density needed for triggering macroscopic failure. As microcracking is strictly related to damage, the CVS can be also used to as a mesoscopic proxy to describe microscopic damage evolution through analysis of deformation curve.

Regarding the stiffness, Young Modulus and Poisson’s ratio shows an opposite behavior in respect to damage, indicating progressive softening throughout microcracking process. Lemaitre (1977) demonstrated the role of rock elastic response as a measure of the experienced damage according to the relationship:

$$D = 1 - E/E_0 \quad (2.1)$$

where D is the damage, E the observed Young Modulus and E_0 the initial Young modulus.

This observation was confirmed by other authors (Kachanov, 1982; Zhang, 1992), among which Eberhardt et al. (1999) observed decrease of Young Modulus and progressive growth of Poisson's ratio during monocyclic loading tests on Lac du Bonnet granite (Fig. 2.8). In particular, the authors suggest the different variation rate observed between two parameters as evidence of predominant axial cracking during the damage of rock specimen. All these observations were later confirmed by Heap et al. (2010) for other litotypes, meanwhile stressing the anisotropic nature of crack damage process.

Moving to the rock mass scale, different approaches were used to assess damage in rock masses. Among these, GSI was successfully applied to describe different damage domains, progressive decrease in mechanical properties and kinematics in rock slope failures (Brideau et al., 2009): starting from undamaged and stable rock mass outcropping in a porphyry quarry site, Agliardi et al. (2013) recognized the imprint of damage process and quantified it through widespread GSI mapping. The obtained results show progressive decrease of GSI values for different slope sectors, characterized by increasing instability conditions, meanwhile resulting in a clear "damage path" in which failure kinematics at different scales appears related with occurrence of certain degree of damage within rock mass (Fig. 2.9). Other damage descriptors reported in literature are basically related to the ratio between fracture persistence and rock bridges occurrence or the reactivation of pre-existing fractures and their propagation within intact rock (Eberhardt et al., 2003; Stead and Eberhardt, 2013; Preisig et al., 2016).

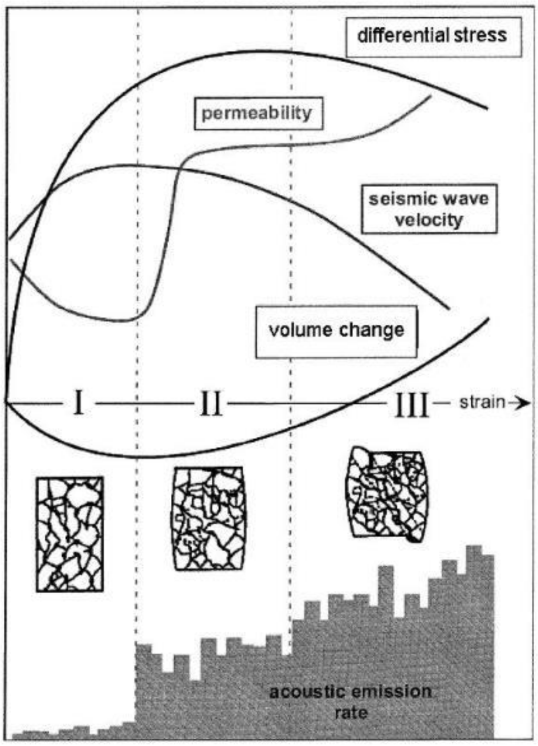

Figure 2.7: Evolution of rock physical properties during deformation of rock salt (from Schulze et al., 2001)

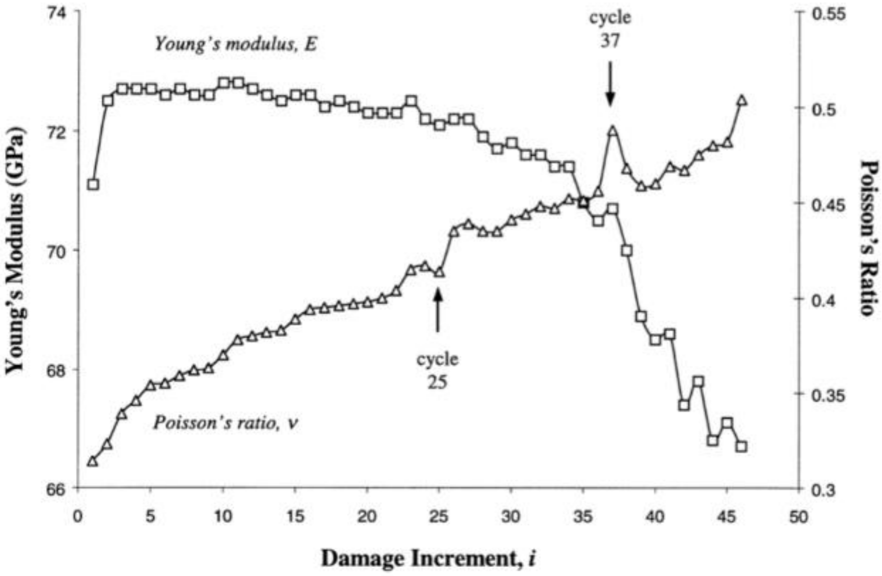

Figure 2.8: Evolution of Young's Modulus and Poisson's Ratio during monocyclic loading tests (from Eberhardt et al., 1999)

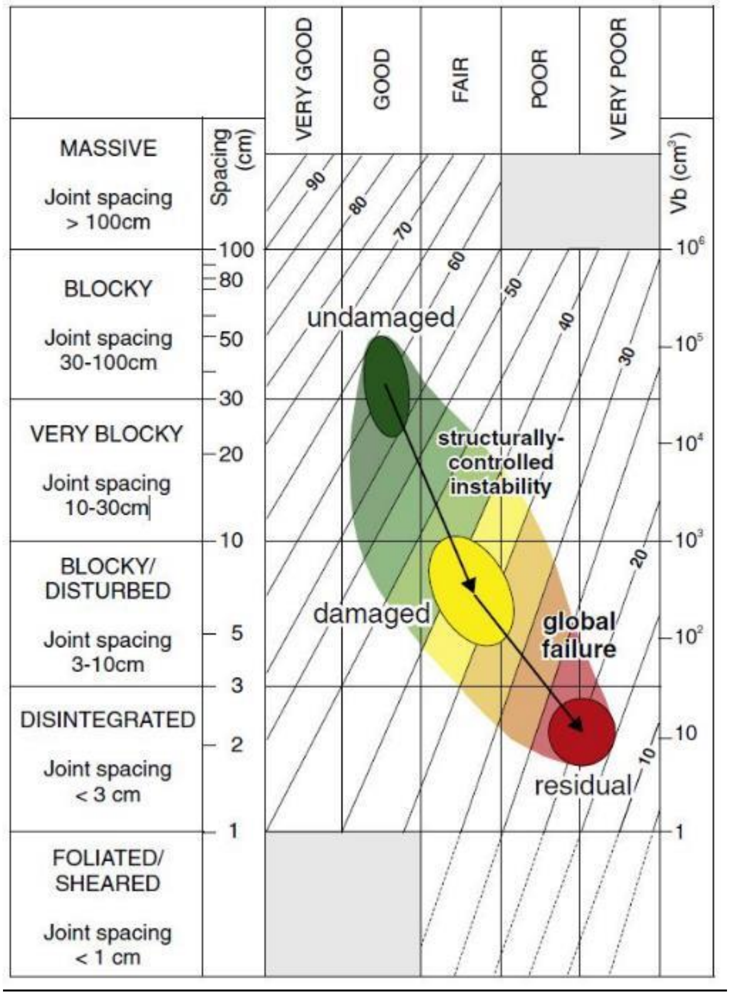

Figure 2.9: Rock mass "damage path" derived from field data on porphyry quarry. Decrease of GSI is observed moving from undamaged to variously damaged rock mass. In turn, failure mechanism registered throughout the slope appears related to the damage experienced by different slope sectors (from Agliardi et al., 2013)

2.2.2 Damage modelling approaches

To explain and simulate the behavior observed in laboratory tests, different models of brittle damage were developed since early 20th century. In particular, damage processes have been described by discrete fracture mechanics approaches (Griffith, 1921, 1924; Paterson and Wong, 2005) and in a continuum damage mechanics framework (Kachanov, 1958; Rabotnov, 1968; Lemaitre, 1984).

Regarding fracture mechanics, the theory proposed by Griffith (1921, 1924) argues that flaws and microcracks act as stress concentrators, particularly if favorably oriented in respect to applied stress. Fracture develops by tensile rupture at the crack tip, where the local stress overcome the local cohesive material strength. Griffith theory was applied to uniaxial tension (Griffith, 1921), uniaxial compression (Griffith, 1924), biaxial stresses (Griffith, 1924) and general stress state (Orowan, 1941), later extended to rocks by Murrell (1958). Orientation of crack in respect to applied stress, confining pressure and tensile strength of the rock are main parameters in determining propagation, orientation and length of induced tensile crack (Fig. 2.10). Despite the rigorous physical background, Griffith's theory is applicable only at microscopic crack initiation, when no interaction and coalescence among neighbor cracks is observed: experimental strength and deformability evolution observed during unstable macroscopic cracking are not well described (Paterson and Wong, 2005).

To overcome these limitations, several authors tried to represent in a unique framework the effect of mechanical degradation, from microcracks nucleation to macroscopic failure though mesoscopic growth and coalescence. This resulted in the development of Continuum Damage Mechanics (CDM), in which material degradation is represented by an equivalent continuum, with properties expressed by statistical average of the mechanical state and decreased by introducing a proper damage variable (Murakami, 2012). Kachanov (1958) was the first to propose a scalar continuity variable to describe the effect of properties degradation, accounting for a phenomenological but rather realistic description of brittle creep rupture under uniaxial tension. His theory was later extended to multiaxial stresses (Rabotnov 1968, 1969), also introducing the damage variable D, ranging from 0 (undamaged state) to 1 (completely fractured material). The damage variable, which is based on the concept of effective stresses (i.e. the stress is applied only to undamaged portion of material), represent the failed material, thus reflecting the macroscopic effects of microscopic processes like microcracks nucleation, propagation and coalescence. Due to the anisotropic nature of many materials (including rocks) damage variable was suggested to be better described by a tensor (Murakami and Ohno, 1981; Krajcinovich and Foneska, 1981), even if scalar approach resulted in simpler formulation and affordable prediction of material behavior (Lemaitre, 1984). Moreover, Katz and Reches (2004) demonstrated that the use of scalar damage factor could eventually result in anisotropic damage at macroscopic scale.

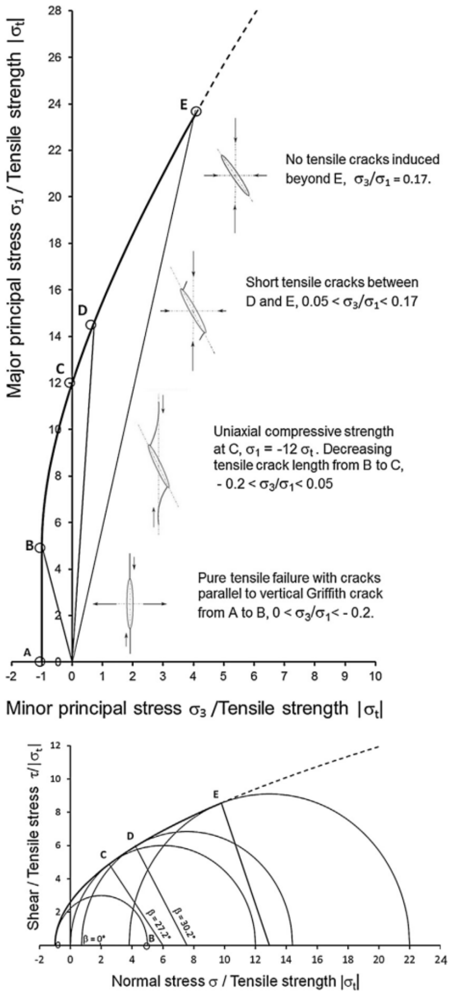

Figure 2.10: Different modes of tensile microcrack propagation in pure tensile (A), tensile (B), uniaxial compressive (C) and compressive (D and E) conditions. Corresponding stress states are also indicated (from Hoek and Martin, 2014).

Moreover, starting from micromechanical background and experimental observation on subcritical crack growth and creep failure, several authors tried to develop numerical models able to reproduce brittle cracking and damage. Starting from the theoretical approach used, three main categories of models can be distinguished: (a) fracture mechanics, (b) continuum damage mechanics (CDM) or (c) statistical (Yuan and Harrison, 2006; Brantut et al., 2013). Hybrid models, combining concepts coming from different frameworks, were also developed trying to conjugate main strengths of different approaches.

Models based on fracture mechanics have the advantage of explicitly described micromechanics processes underlying brittle cracking recurring to open crack model or sliding crack model (Brantut et al., 2012). Kemeny and Cook (1987) analyzed a homogenous cracked solid and its rupture under strain-controlled and displacements-controlled boundary conditions. They analytically demonstrate two different fracture models, the non-interacting crack model and the external crack model, explaining also fracture extension first using the “non-interacting” and then with the “external” crack model. Using a simplified microcracks distribution within rock sample, their model was able to correctly reproduce experimental behavior observed on Westerly granite (Fig. 2.11) Disadvantages of this approach are related to the difficulty in reproducing intrinsic complexity of the rock structure, with variously oriented and interacting cracks, and the microcracks coalescence with subsequent strain localization.

On the other hand, continuum damage mechanics have the advantage of proposing a less physically rigorous but rather simpler approach to the problem: through the definition of damage variable (or variables) and constituting laws relating it to stress and strain, the material is represented as a continuum with averaged mechanical properties (Valanis, 1985; Ofoegbu and Curran, 1992). By changing stiffness and physical properties of rock in respect to accumulated strain, dilatancy and microstructure variations models were able to reproduce several aspects of damage as stress-strain curves and softening behavior (Fig. 2.12).

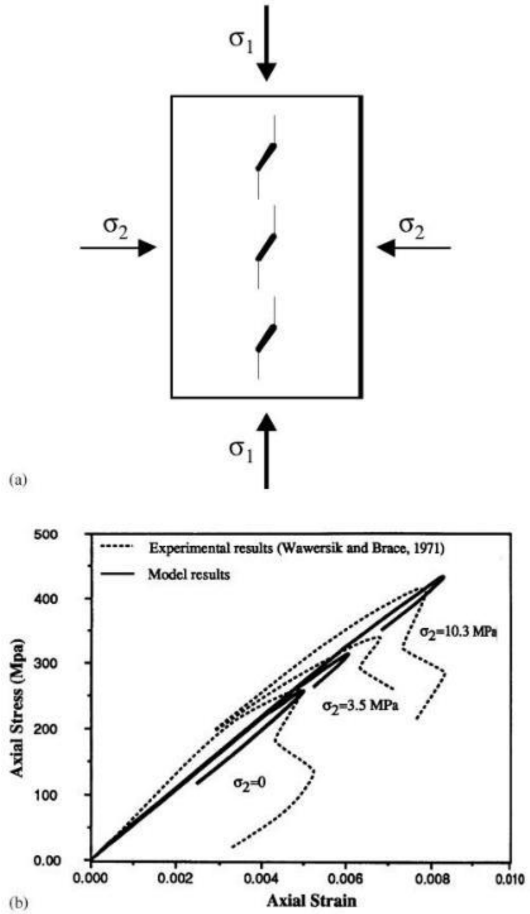

Figure 2.11: Idealized crack pattern and experimental versus modeled stress-strain curves for tests on Westerly granite at different confining pressures (from Kemeny and Cook, 1987)

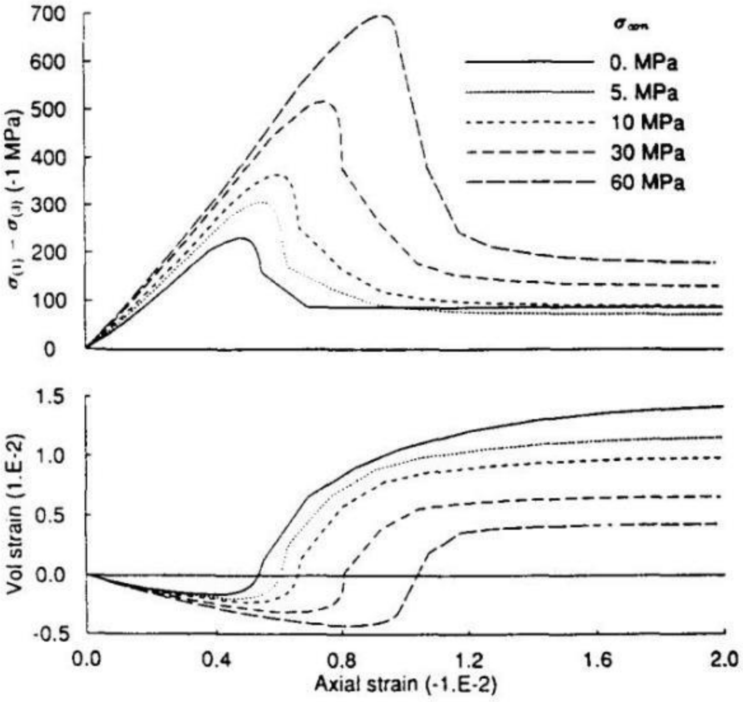

Figure 2.12: Differential stress versus axial strain and volumetric versus axial strain curves obtained for numerical simulations with different confining pressures on Creighton norite (from Ofoegbu and Curran, 1992)

Statistical models aim at reproducing the intrinsic heterogeneity of rocks with statistical approach, subdividing the model domain in representative elements with different mechanical properties. Scholz (1968) developed this concept in a time-dependent framework, being able to partly reproduce strain behavior but not subsequent localization and tertiary creep.

Combining statistical approach with continuum damage mechanics, several authors attained a complete representation of creep behavior and strain localization (Fig. 2.13; Turcotte et al., 2003; Amitrano and Helmstetter, 2006; Xu et al., 2012). These models statistically describe the rock heterogeneity with statistical distribution, meanwhile introducing a damage coefficient related to empirical observation on laboratory experiments. Due to relation observed between crack increase and stiffness, variation in Young modulus was often used at this purpose (Chaboche, 1977; Lemaitre and Chaboche, 1978; Hudson and Harrison, 1997; Amitrano and Helmstetter, 2006; Xu et al., 2012). The main concern in the application of these models to real rock masses consists in the choice of phenomenological damage parameter, as it has to be upscaled without any experimental evidence regarding crack density increase or physical processes involved in rock mass brittle failure. Moreover, the assumption of a static law is another simplification in respect to the main role of stress corrosion (i.e. groundwater effect) in failure process and the changing morphoclimatic conditions encountered for example in real large rock slopes (Brantut et al., 2013).

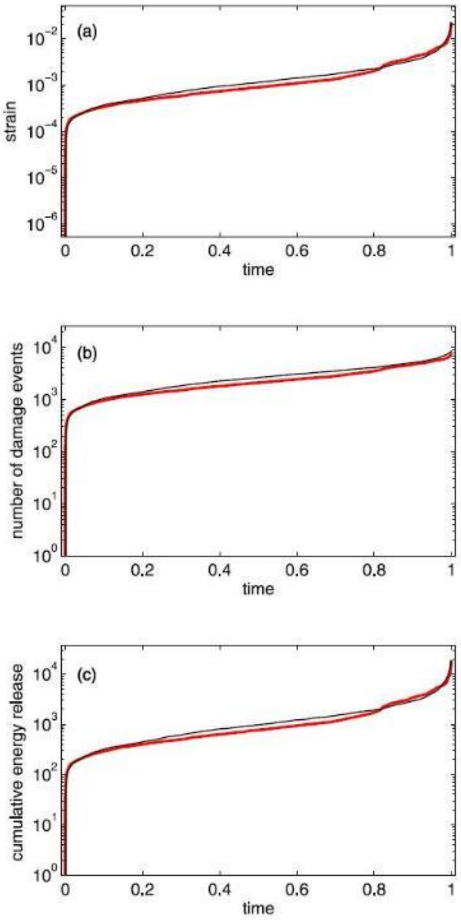

Figure 2.13: Strain (a), cumulated rupture events (b) and cumulated energy release (c) dependency on time for modelled creep tests, proving the model capability in capturing the entire creep curve of the material (from Amitrano and Helmstetter, 2006**)**

2.3 FLUID-ROCK INTERACTION: HYDRO-MECHANICAL COUPLING

Mutual interplay between pore/cleft fluid pressure and material stress and strain, which deeply influences the behavior of geomaterials, has been recognized since the earliest studies in soil and rock mechanics (Terzaghi, 1923). This interplay occurs through a series of physical interactions collectively referred to as “hydromechanical coupling”. Starting from a century ago, several authors studied hydromechanical coupling and its implication on geological processes. The main studies are summarized in the comprehensive reviews by Tsang (1991), Rutqvist and Stephansson (2003) and Neuzil (2003).

The ensemble of processes involved in hydromechanical coupling (HMC) can be conceptualized in direct vs. indirect and fluid-to-solid vs solid-to-fluid HMC (Fig. 2.14; Rutqvist and Stephansson, 2003). Direct coupling occurs when a change in applied stress induces a change in pore fluid pressure (solid-to-fluid coupling, i in Fig. 2.14) or a change in pore fluid pressure induces a change in volume (fluid-to-solid coupling, ii in Fig. 2.14). Indirect coupling involves changes in physical properties of the geologic media, such as variation of hydraulic properties in response to changing stress (solid-to-fluid coupling, iii in Fig. 2.14) or variation of mechanical properties in response to changing pore fluid pressure (fluid-to-solid coupling, iv in Fig. 2.14). Hydromechanical coupling is thus related to the rock mechanical properties and their spatial heterogeneity, which in turn depend on microscopic and macroscopic structure and porosity, directly conditioning fluid pressure occurrence and distribution.

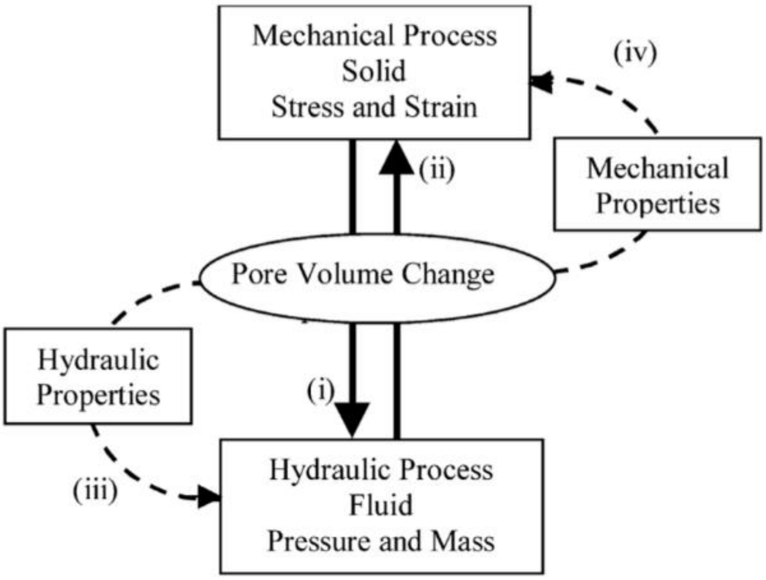

Figure 2.14: Direct and indirect hydromechanical coupling in geological media (from Rutqvist and Stephansson, 2003)

The basis of coupled hydromechanical interaction were drawn by Terzaghi in 1923 (and with a parallel study by Meinzner in 1928), when his theories of effective stresses and pore pressure diffusion were published. Terzaghi observed that the total stress can be subdivided into two different components, one transmitted to the solid structure (effective stress) and another bear by pore fluid pressure. This concept is expressed by the well-known relationship that expresses the soil consolidation as a direct consequence of fluid pressure dissipation in the form:

$$\sigma'_{zz} = \sigma_{zz} - p \tag{2.2}$$

where σ'_{zz} is the effective stress, σ_{zz} is the total vertical stress and p is the pore fluid pressure.

Later, Biot (1948) developed a poroelasticity theory to explain three-dimensional consolidation and to relate elastic response of modelled medium to variation in pore fluid pressure, meanwhile generalizing the Terzaghi effective stress law as:

$$\sigma'_m = \sigma_m - \alpha p \tag{2.3}$$

where σ'_m is the mean effective stress, σ_{zz} is the total mean stress and α is a coefficient taking into account the effect of variable porosity in considered medium. As experimentally proven, α is usually close to 1 for soils but lower values can be encountered for rocks, in which low crack density and consequent low porosity can be observed (Nur and Byerlee, 1971).

Several laboratory tests were performed on intact rock samples, mainly to extrapolate poroelastic parameters and to investigate intact rock behavior with varying confining stress and pore fluid pressure (Heiland, 2003 and reference therein). Results indicate a complex behavior, strongly affected by rock porosity (including shape of pores), applied stresses and fluid pressure. During loading tests, usually permeability decreases as response to crack closure stage, then followed by an increase due to microcracks development and interconnection in subcritical regime (Fig. 2.7). The increase of fluid pressure in turn causes transient decrease of effective stress, thus reducing rock strength and promoting slip along preexisting fractures. However, establish a universal trend to evaluate permeability evolution is impossible, and hydraulic parameters have to be assessed for each specific case based on rock micro and macro structure, deformation history, stress applied and fluid pressure.

Quantitative description of hydromechanical coupling in rock masses is even more complicated: the orientation, aperture, roughness and connectivity of joints dramatically affect fluid circulation and related effect on mechanical parameters and stress state. Several authors tried to assess permeability modification caused by fracture aperture and roughness, under varying normal or shear stress (Witherspoon et al., 1980; Makurat et al., 1990; Rutqvist, 1995; Olsson and Barton, 2001). Fracture pattern in a specific rock mass is the result of deformation and stress fields experienced, which in the long-term period is subject to transient conditions that may results in rock mass structure modification and properties evolution. For this reason, establish rigorous stress-permeability relationships is nearly impossible without site-specific investigations. However, general trends were recognized through site investigations performed in different contexts and for different rock types. Permeability is mainly determined by mechanical properties of fractures as normal stiffness, shear strength and cumulated displacement. This is evident especially in faults zones, where the large movement along slip surface often results in the formation of large conduit with high permeability (Rutqvist and Stephansson, 2003). Observation performed for underground tunneling shows the effect damage induced by excavation, which often bring to the development of cracks with consequent enhance of hydraulic permeability. Dramatic increase (up to 6 order of magnitude) were recognized for host rocks with small initial permeability (Wang et al., 2001), while in some cases both increase and decrease in initial permeability were associated to damage zone, thus highlighting the uncertainties in governing processes and the importance of site-specific characterization (Backblom and Martin, 1999).

In fractured rock masses, major fluid fluxes often tend to be concentrated in a few, highly conductive and open fractures, which constitute a small part of the entire fracture network. They are usually characterized by broad aperture derived from roughness, shear displacement or stress state, and are grouped in clusters, which extension depends on fracture density and spatial pattern of the host rock. Occurrence of less permeable fractures within interconnecting cluster is important as they can represent bottlenecks, conditioning both the hydraulic properties of the entire cluster and the fluid pressure distribution, which in turn influence hydromechanical coupling. Indeed, the response at stress variations is different between highly conductive and less conductive joints (Fig. 2.15): widely open fractures are usually less affected by stress variation, while less conductive fractures can experience substantially changes also for little stress variations, consisting in either permeability increase or decrease. Confining pressure (i.e. depth) also influences hydraulic response to stress variations, with progressive sensitivity decrease as confining stress increase.

As for mechanical properties, the scale of the problem with respect to fracture density is a key control on the rock mass behavior and on the most suitable modelling approach to be adopted: small volumes characterized by persistent and well-spaced discontinuities will behave predominantly as a discontinuum medium, with intact rock portions characterized by dry conditions juxtaposed to discontinuities filled by water, resulting in pressure peaks along and at the tips of persistent fractures. On the other hand, rock masses constituted by an interconnected, closely-spaced and well-developed fracture network will be better characterized as a soil-like continuum medium, for which equivalent hydraulic properties can be extrapolated.

Failure surfaces in rockslides and DSGSDs are constituted by deformation bands in which the effect of shear and gravitational displacement resulted in an extremely damaged rock mass, often crushed in breccia layers with silty and clay matrix. Understanding the hydraulic behavior of such elements is extremely important due to the high influence that exert on slope groundwater circulation and landslide development. Few studies exist on hydraulic characterization of shear bands induced by gravitational displacement (Strauhal et al., 2016). However, despite some substantial differences in scale, deformation mechanism, confining stress and texture, shear bands can be somehow compared to tectonic faults, for which behavior was studied from both structural and hydrogeological points of view (Chigira, 1992; Caine et al., 1996; Bense et al., 2013).

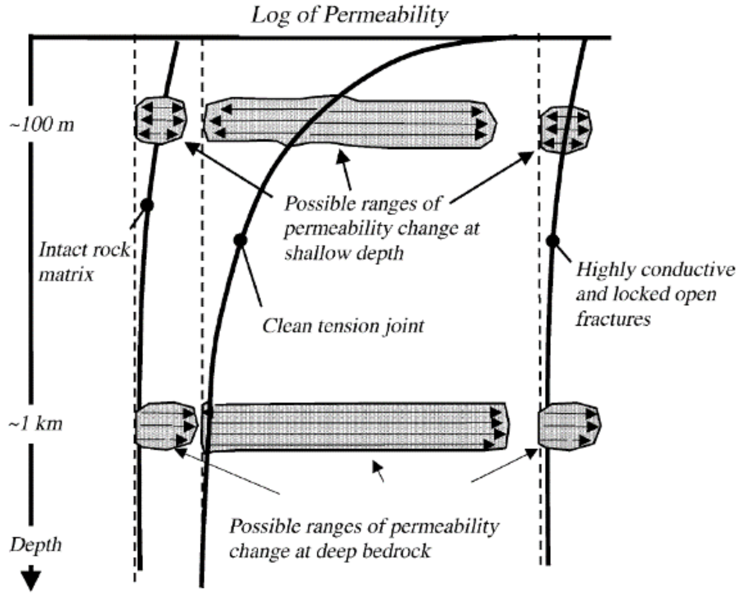

Figure 2.15: Expected ranges of permeability variation for intact rock matrix, low-conductive fractures and highly-conductive fractures at different depths (from Rutqvist and Stephansson, 2003).

Fault influence area in hosting rock mass is usually expressed as the sum of the fault core, in which the strain is mainly concentrated, and the damage zone, the volume in which rock mass structure was altered by fault due to enhanced fracturing (Fig.2.16a, b, c). Conceptual models proposed in literature usually distinguish among a zone of enhanced permeability, caused by increase in fracture density and interconnection (i.e. damage zone), and a low-permeability fault core sealed by fine-grained material (Fig. 2.16d, e; Bense et al., 2013). Moreover, a conduit-barrier effect is recognized, related to marked anisotropy for fluxes directed parallel to fault direction, which are favored in respect to undisturbed portions of rock mass. On the other hand, fluxes across the fault core are strongly limited or even inhibited, due to the low hydraulic permeability and barrier effect (Chester and Logan, 1986). Interaction between rock mass properties and applied load determine the relative extension of damage zone and fault core, deeply influence in turn also hydraulic behavior (Fig. 2.16f; Caine et al., 1996). The application of these concepts to landslides basal shear band, highlight the key-role of comminution and shear deformation magnitude in the definition of hydraulic properties. For low cumulated shear displacement and strain, an increase in permeability could be expected due to enhanced fracture density but no occurrence of fine material or brecciated levels. For mature shear bands, conduit-barrier concept could be applied, as confirmed by abundance of field data which testifies occurrence of fine material along main surfaces, with thickness ranging from centimeters to several meters. The permeability contrast between fractured rock mass and shear bands could also explain the formation of perched aquifers hosted within unstable bodies, with consequence on hydromechanical coupling and time dependent evolution. Site investigation recently performed by Strauhal et al. (2016) assessed hydraulic conductivity variations of several order magnitude between basal shear band and overlying rockslide mass. Interestingly, gravitational deformation also caused an increase of hydraulic permeability of the entire rockslide body, if compared to surrounding and stable rock mass.

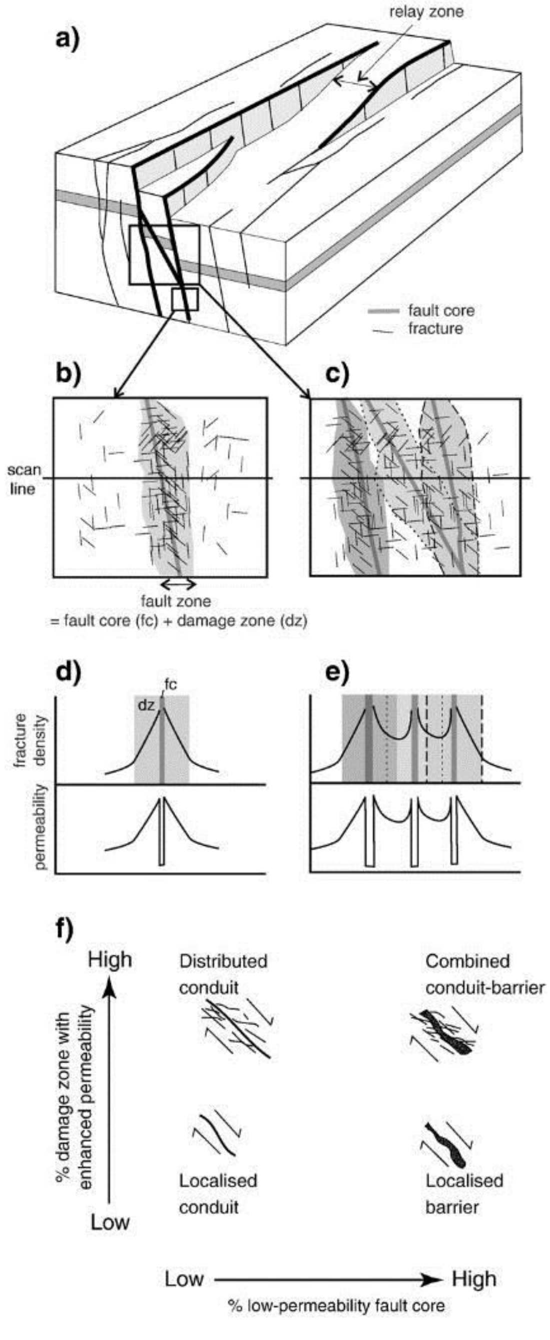

Figure 2.16: Effect of faulting on rock mass hydraulic properties (a): extension of fault core and damage zone for a single fault (b) and neighborhood interacting faults (c); expected variations of permeability in respect to fault distance for a single fault (d) and neighborhood interacting faults (e); hydraulic behavior in respect to relative extension of fault core and damage zone (f) (from Bense et al., 2013).

2.4 LARGE ROCK SLOPES: NUMERICAL MODELLING

To reproduce the multitude and intrinsic complexity of processes involved in long-term slope evolution (Cf Chapter 1), the choice of modelling approach and boundary conditions is fundamental. The modelling strategy must be able to capture the initiation and propagation of instability at a suitable scale, meanwhile taking into account all the processes involved. To investigate slope behavior, mainly three modelling approaches have been developed: continuum methods, discontinuum methods and hybrid continuum/discontinuum methods (Jing, 2003; Stead and Eberhardt, 2013).

Continuum methods are based on the continuous representation of rock mass, with mechanical and hydraulic equivalent properties derived from intact rock and discontinuities characterization. Usually, equivalent parameters are evaluated through rock mass characterization techniques directly applied to in-situ rock mass (Cf. Chapter 2.1). Continuum approach was widely used to investigate long-term evolution of slopes and evolution of mechanical properties induced by gravitational creep, active tectonics, deglaciation and changing hydrogeological regimes (Fig. 3.17; Agliardi et al., 2001; Ambrosi and Crosta, 2006; Brückl and Parotidis; 2005; Barbarano et al., 2015).

Discontinuum approaches as Distinct Element Methods (DEM; Cundall, 1971) explicitly take into account joints occurrence, representing the rock mass as formed by intact rock blocks bounded by discrete discontinuities. Blocks can be either represented by polygons, as in UDEC formulation (Itasca, 2010), or by circular features, as in PFC formulation (Itasca, 2007), bounded (and eventually bonded) by surfaces with specified behavior, to simulate real discontinuities properties such as normal stiffness, shear stiffness, cohesion and friction angle.

The application of discontinuum approach to rock slope stability problems is particularly suitable for cases in which kinematic is largely controlled by discontinuities (Benko and Stead, 1998; Eberhardt et al., 2003; Lorig et al., 2010; Havaej et al., 2015). At this aim, the flexural toppling analysis performed by Alzo’ubi et al. (2010), in which experimental versus predicted behavior fits well regarding strain pattern and rupture surface location, demonstrates the importance of intact rock tensile strength in controlling failure. Nichol et al. (2002) conducted a similar analysis on toppling, investigating the interaction between brittle and ductile mechanisms in the development of large instabilities. Relationship between rock strength, joints distribution and toppling behavior was founded, proving the role of rock mass conditions in determining type and occurrence of slope failure. Other applications of discontinuum approach to large rock slope permitted to assess the influence of groundwater regime, thermo-mechanical effects and seismic fatigue in determining instabilities in real (Gischig, 2011) and simplified alpine slopes (Fig. 2.18; Gischig et al., 2016).

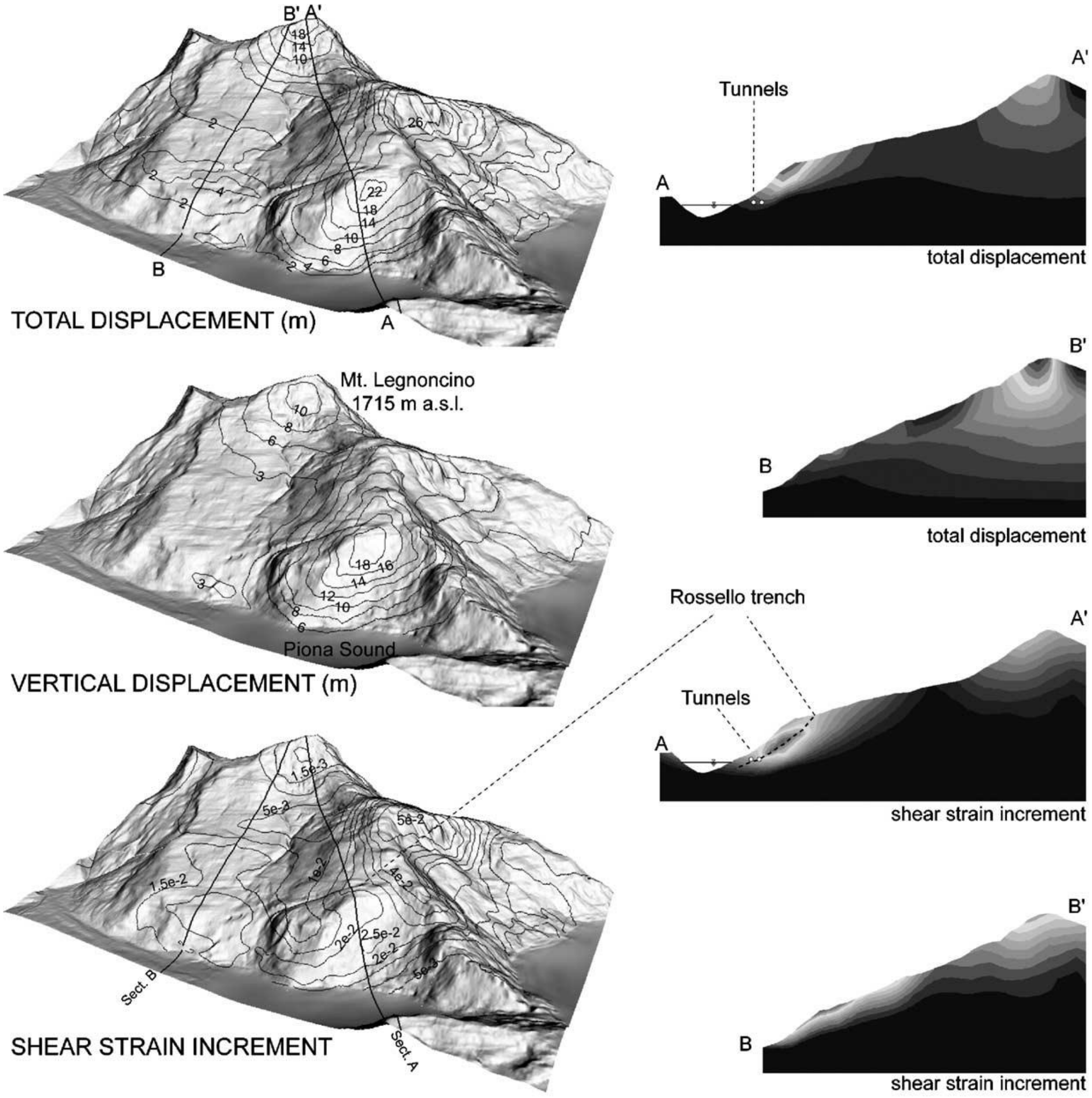

Figure 2.17: Results of 3D continuum numerical modelling of the Mt. Legnoncino DSGSD. Patterns of total displacement, vertical displacement and shear strain increments are shown both on 3D maps and along the cross-sections A-A’ and B-B’ (from Ambrosi and Crosta, 2006).

Hybrid approaches combines continuum and discontinuum formulation to reproduce in a unique framework the intact rock deformation, the sliding on pre-existent discontinuities and, most of all, the initiation and propagation of new cracks as a consequence of applied stress. Indeed, intact rock is represented as a continuum bounded by discontinuous joints: as the rock failure criterion is reached, new fracture is initiated and meanwhile a corresponding discrete feature with joint mechanical properties is created. Despite the high computational load requested by such types of numerical code, they proved to accurately reproduce the process of brittle failure at micro, meso and macro scale, particularly for mining purposes (Fig. 2.19.; Cai and Kaiser, 2004; Elmo, 2006; Elmo and Stead, 2010; Vyazmensky et al., 2010; Hamdi, 2015).

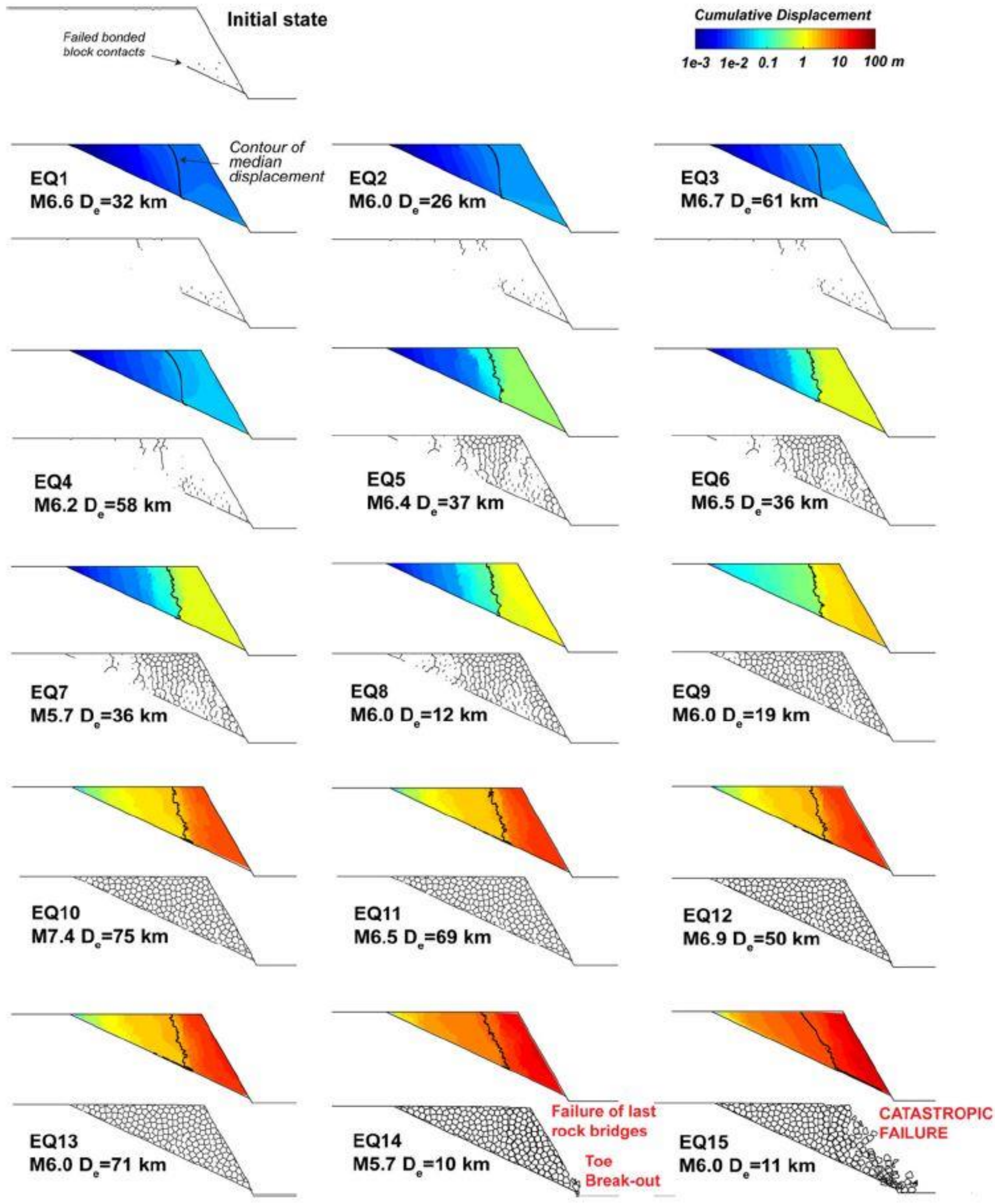

Figure 2.18: Seismic fatigue effect on simplified slope discontinuum model in terms of cumulated displacement and failed discontinuities. Slope collapse occurs after the 15th event. (from Gischig, 2016)

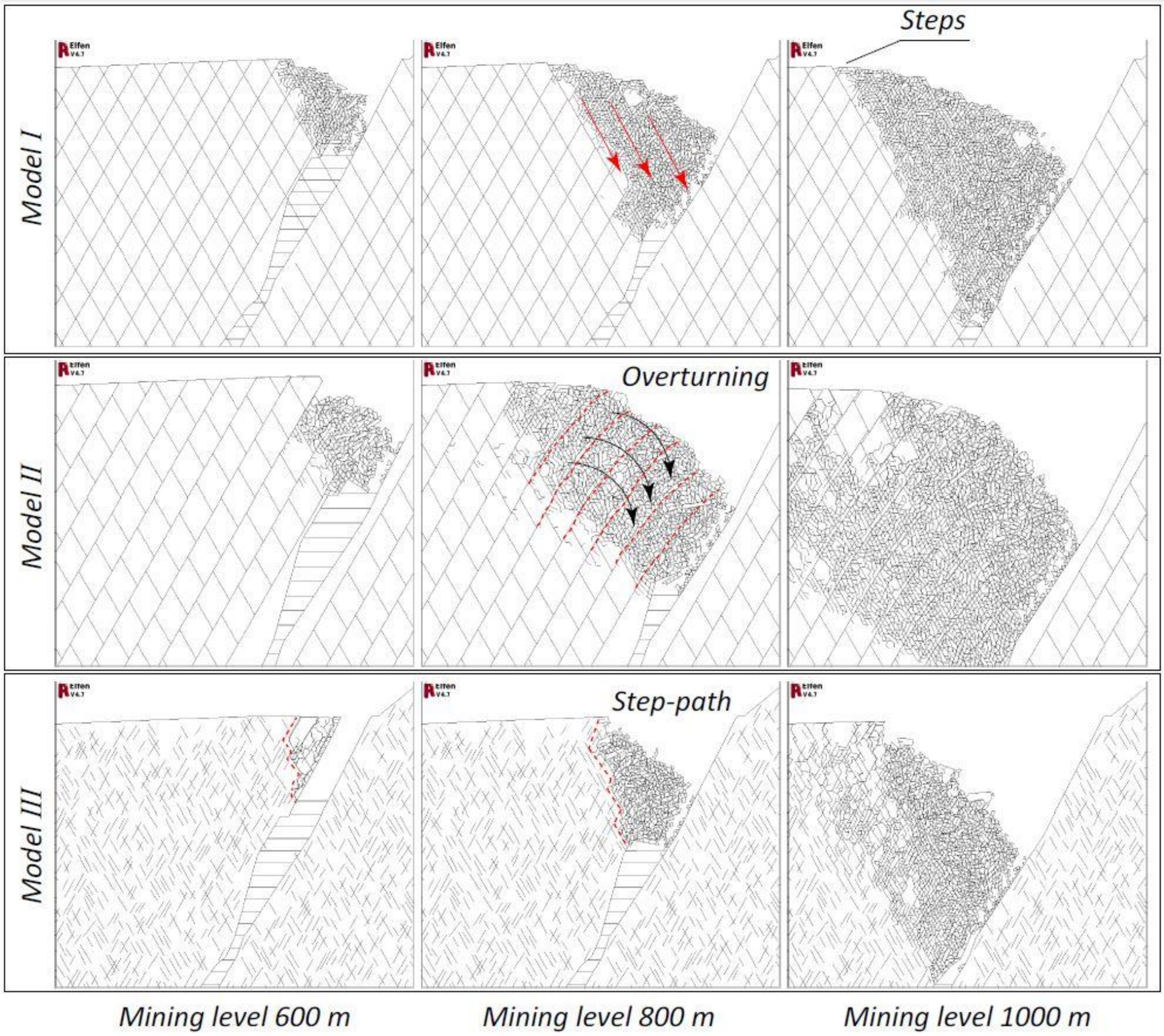

Figure 2.19: Use of hybrid modelling approach for mining applications. Different failure mechanisms are reproduced as a function of discontinuity persistence and spacing (from Hamdi, 2015)

Despite the adopted modelling approach, brittle failure, subcritical crack growth and hydro-mechanical coupling are fundamental in the assessment of slope stability, especially in investigating long-term slope behavior with underlying progressive rock mass damage. For single unstable block or slopes largely controlled by discontinuities, discontinuum and hybrid approaches offer a better account for the observed mechanisms, being able to reproduce large displacements along discrete features and formation of new cracks. On the other hand, for large and quasi homogeneous rock slopes continuum models are usually preferred (Fig. 2.1) due to the simple but rather affordable formulation and the minor uncertainties in the input values, as representative volume of rock mass could be described with continuum equivalent parameters regarding both mechanical and hydraulic properties.

2.4.1 Time-dependent progressive failure

As observed in the previous chapter, subcritical crack growth contribute to the progressive damage at laboratory scale since a critical fracture density is reached, coinciding with the macroscopic rupture of the rock sample. These concepts are often upscaled to large rock slopes, where progressive rupture and mass creep are pointed out as fundamental processes in long-term rockslide nucleation and differentiation (Bovis, 1990; Ballantyne, 2001; Eberhardt et al. 2004; Crosta et al., 2012; Stead and Eberhardt, 2013). In this framework, rock mass strength is usually represented as the sum of two different components, the frictional shear strength of rock mass joints and the cohesion due to the intact rock bridges located between non-persistent discontinuities ("effective cohesion"; Terzaghi, 1962; Einstein et al., 1983). In subcritical stress conditions (i.e. under rock mass peak strength) and focusing only on a single pre-existing joint, failure propagation is modelled through subsequent progressive events in which shear stress is concentrated at the crack tip until the local peak strength is overcome. Then, rupture propagation and stress redistribution in the surrounding area occurs (Fig. 2.20; Bjerrum, 1967; Eberhardt et al., 2004).

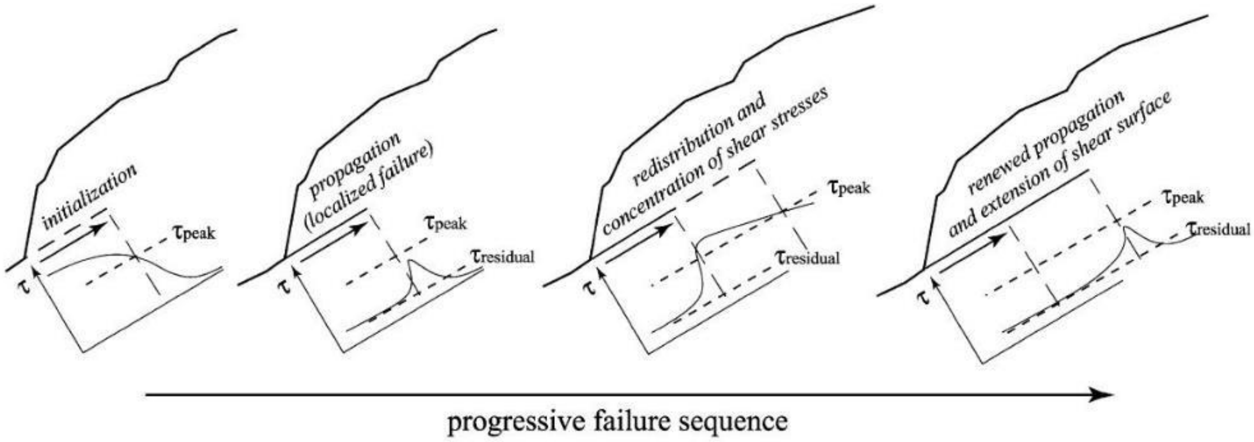

Figure 2.20: Progressive failure sequence for a single discontinuity (Eberhardt et al., 2004)

As real rock slopes are constituted by an ensemble of non-persistent and variously oriented discontinuity, progressive failure sequence propagates within rock mass through time until a continuous and kinematically favorable surface is developed, thus resulting in potential slope instability. The interplay between joints geometry and intensity in respect to the intact rock bridges percentage, intact rock strength and internal deformation of rock mass condition the occurrence of different kinematics, shear band geometries and potential development of secondary scarps and counterscarps within the slope (Fig. 2.21; Eberhardt et al., 2004). The macroscopic evidence of these local processes results in the commonly observed "slope creep" movements (Emery, 1972), characterized by rather constant, low displacement rates to which seasonal accelerations of different magnitudes are often superimposed (Crosta and Agliardi, 2003; Vallet et al., 2015).

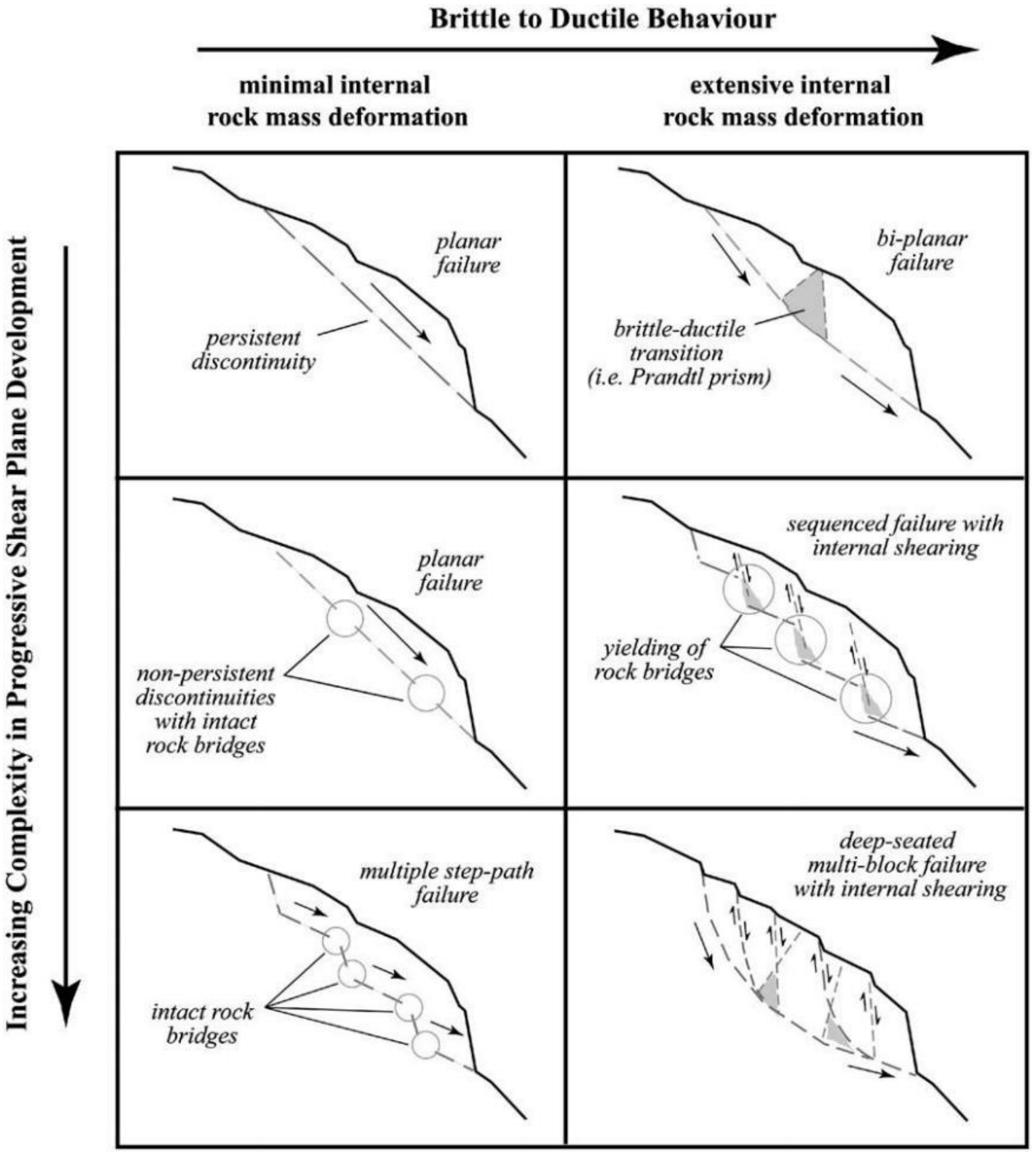

Figure 2.21: Effects of fracture pattern and brittle vs. ductile behavior on development and geometry of instabilities (from Eberhardt et al., 2004)

Eberhardt (2004) applied these concepts in the back-analysis of Randa slope progressive failure using hybrid continuum/discontinuum approach. Obtained results reproduce rockslide development through tensile cracks initiation, growth and coalescence consequent to slope deglaciation, meanwhile predicting the rockslide episodic nature (Fig. 2.22).

With a complete different approach based on damage and brittle creep laws applied to a finite-element model, Lacroix and Amitrano (2013) described the long-term evolution of simplified rock slopes, capturing in a unique environment the degradation of mechanical properties, the strain localization within a basal shear band and the complete creep behavior since slope collapse (Fig. 2.23).

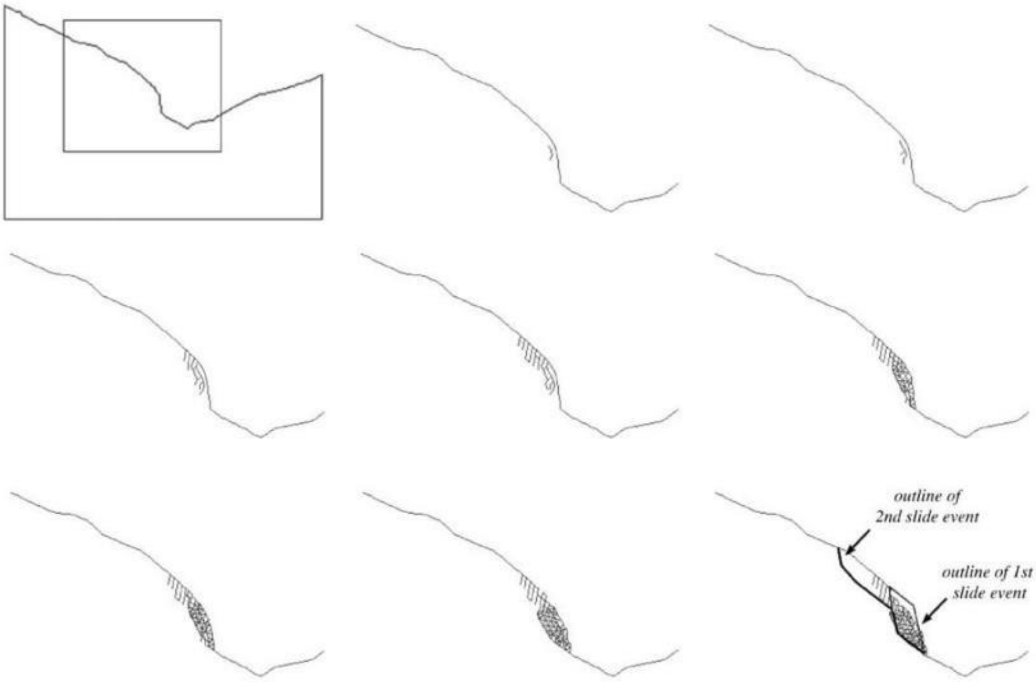

Figure 2.22: Progressive development of internal deformation and rupture surface of Randa rockslide. The hybrid modelling approach is able to reproduce the staged failure observed on real slope (from Eberhardt, 2003)

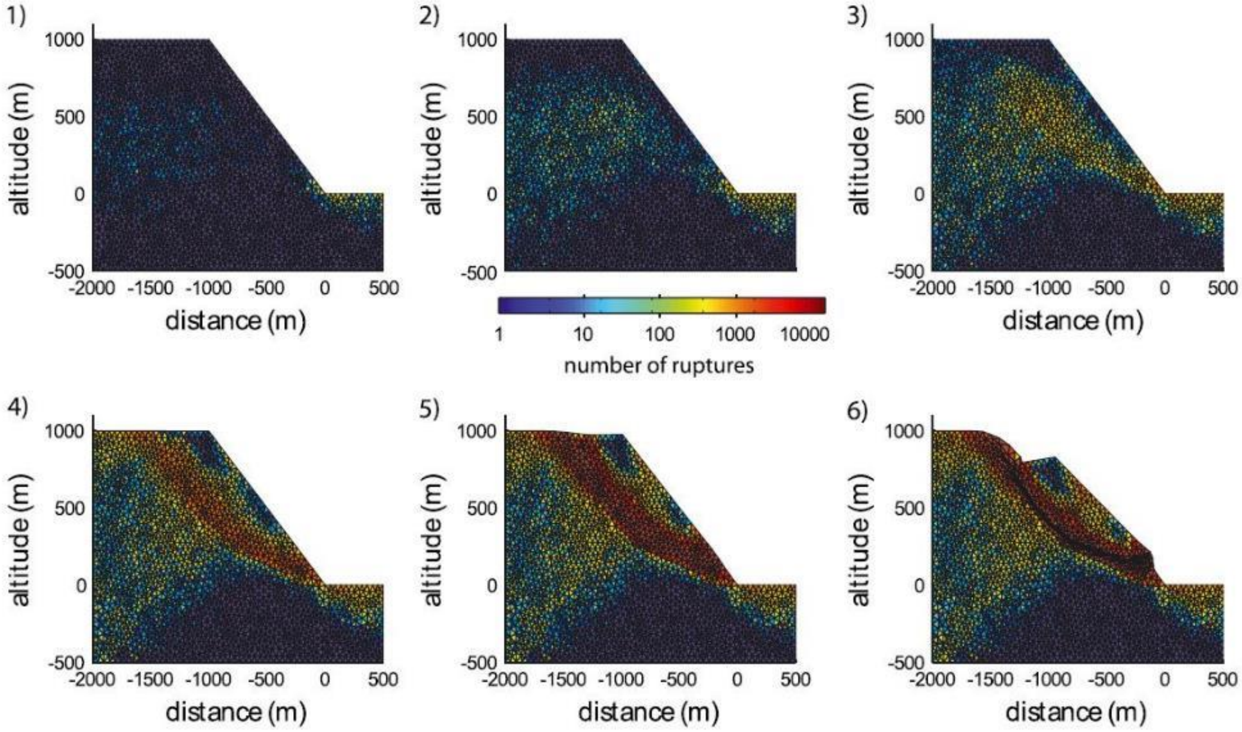

Figure 2.23: Evolutionary steps of a simplified rock slope subjected to damage process. The color scale represents the number of damage events per element (from Lacroix and Amitrano, 2013)

Time-dependency has a fundamental role in the development and evolution of alpine instabilities. Thus, several authors tried to link slope mechanical state with time, particularly focusing on short-term prediction for forecasting and early-warning purposes. Starting from the accelerating creep approach of Fukuzono (1985) and Voight (1988,1989), Crosta and Agliardi (2003) proposed a method to evaluate, in respect to observed displacement patterns, threshold values of velocity directly applicable to early warning assessment of active rockslides. Including to the displacement patterns also the observed precipitations, Vallet et al. (2015) developed a method based on wavelet analysis to assess the hydro-mechanical coupling and the evolution of deep-seated landslide particularly sensitive to hydrologic triggers.

Another approach focused on visco-plastic modelling to reproduce rock slope behavior through time (Angeli et al., 1996, Secondi et al., 2013; Crosta et al., 2014; De Caro et al., 2016). This can reproduce downslope movement relying on the assumption of a rigid block overlying a viscous shear band, in which all the strain and displacement are concentrated. Despite the accurate results obtained by the application of this approach, one concern is represented by the difficulties in calibration of viscous parameters, which are basically not comparable with field-measurable indexes. Otherwise, this approach often doesn’t consider the evolution of mechanical properties as a consequence of strain and fracturing experienced by the simulated rock mass. In addition, the role of fluid pressure is rarely taken into account, due both to the uncertainties in long-term slope groundwater circulation and the not obvious interaction with discontinuous and heterogeneous rock mass material.

2.4.2 Deglaciation and long term-evolution

Deglaciation is a fundamental process in the evolution of large alpine rock slopes, in terms of both slope carving/erosion and stress redistribution related to ice downwasting. Despite this, few modelling approaches focused on slope response consequent to deglaciation phase and its effect on stability. Agliardi et al.(2001) and later Ambrosi and Crosta (2006) modelled the postglacial evolution of DSGSDs in the Italian Central Alps using two-dimensional finite difference method, showing how plastic deformation and displacement in the slope occurs immediately after deglaciation and proving the role of paraglacial readjustment in promoting large slope instabilities. Leith (2012) used a long-term finite-difference model to assess the cyclic effect of endogenic and exogenic processes on the long-term evolution of typical alpine landscape, proving the interplay of tectonics, rock mass mechanical properties and glacial erosion in determining observed alpine slopes fracture patterns and topographies (Fig. 2.24). Agliardi et al. (2014) instead focused on a specific case study and tried to assess rock mass damage induced by deglaciation and slope debuttressing, recurring to finite element modelling to explain rockslide differentiation and occurrence on the Spriana slope (Fig. 2.25). Despite rock mass is represented as continuous medium, numerical model succeeds in reproducing a tensile damage zone due to stress redistribution, affecting the entire slope up to 150 m from surface and resulting in weakened band predisposing for further damage development and rockslide differentiation.Despite the good accounting for deglaciation effects and nucleation of slope instabilities, these modelling approaches have often limitations in describing mature stage of slope evolution and the evolution of rock mass in terms of mechanical and hydraulic parameters.

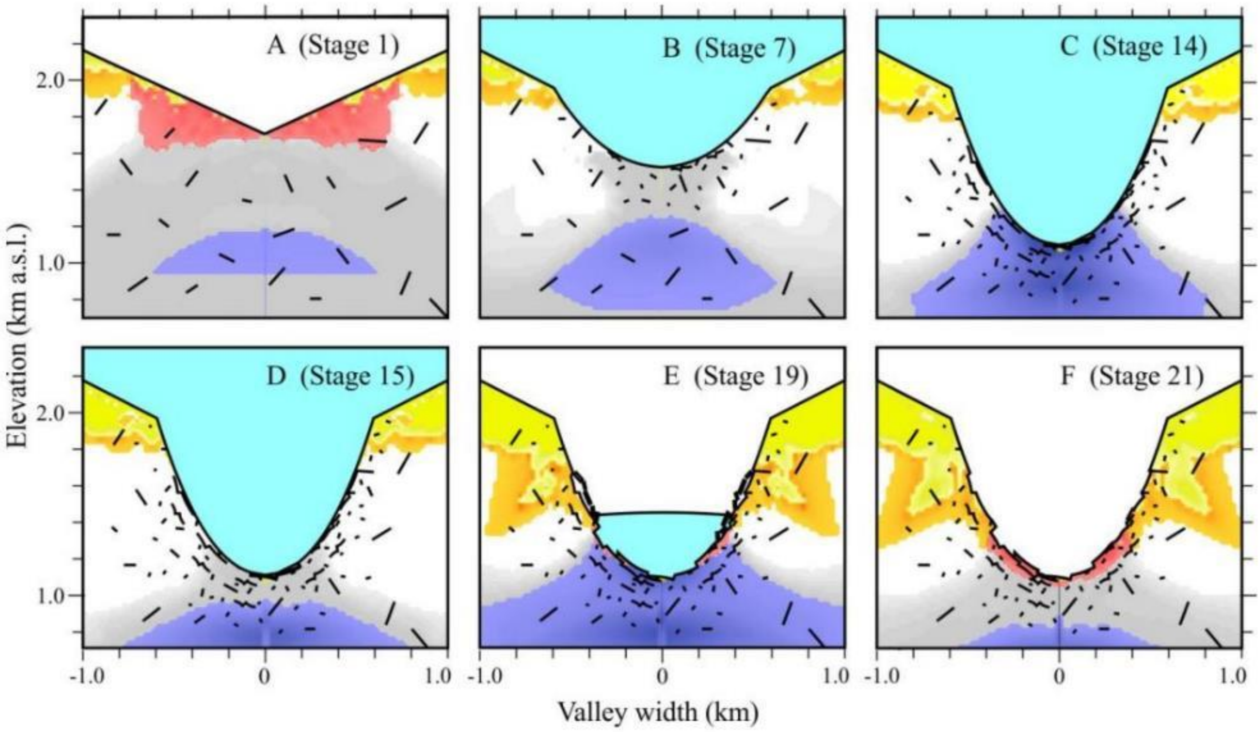

Figure 2.24: Fracture pattern evolution for a typical alpine valley subject to glacial erosion (stages 1 to 14) and progressive ice downwasting (stages 15 to 21). Fracture are drawn based on stress orientation and regimes predicted by the numerical model (from Leith, 2012)

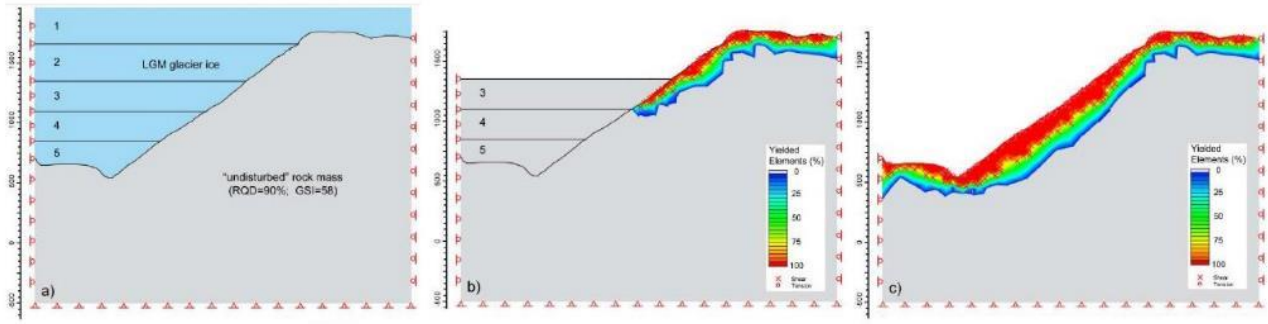

Figure 2.25: Damage evolution as a function of progressive glacial debuttressing, resulting in a damage band extending over 150 m within the Spriana slope and predisposing to slope instability (from Agliardi et al., 2014)

2.4.3 Role of fluid pressure

Although movements critically accelerating until catastrophic collapse may result by rock mass progressive failure without any external forcing (i.e. tertiary creep; Saito and Uezawa, 1961; Zavodni and Broadbent, 1980; Voight, 1989; Rose and Hungr, 2007), hydro-mechanical coupling has been recognized to play an increasingly important role as rockslides attain mature stages of evolution (Crosta et al., 2014). In glacial environment, even if slope undergone erosion and steepening by glacier flow, rock mass is supposed to be quasi-undisturbed, except for the shallower portions. Low fracture intensity and sealed joints are expected to be associated with low hydraulic conductivity and poor fracture interconnection at slope scale (Fig. 1.4a).

Several techniques were exploited to numerically model fluid circulation and hydromechanical coupling in geological media, starting from traditional frameworks to progressively exploit more advanced techniques (Hudson, 2002). Models based on equivalent continuum were developed based on well-known simple equations originally conceived for hydrogeology (Oda, 1982) and adapted for including effect of hydromechanical coupling. Despite the simple formulation, continuum models are affected by great uncertainties mainly related in the definition of hydraulic parameters, given the discontinuous nature of fluid flow in rock masses. As a comprehensive discrete description of large scale rock mass fracture pattern is unfeasible, statistically-based Discrete Fractures Networks (DFN) conjugate discontinuum description of geological media with sounding statistical description of rock mass anisotropy and heterogeneity. In the last years, efforts in this direction provided encouraging results in modelling of rock mass hydraulic and mechanical behavior for various engineering applications (Elmo et al., 2014; Sturzenegger et al., 2014; Dershowitz, 2015; Elmo et al., 2015).

As in real slope these hydrologic pulses has a seasonal occurrence related to surficial water and groundwater availability, i.e. in spring during snowmelt and in summer/fall during intense and prolonged meteoric events (Hansmann et al., 2012), authors described the mechanical effect of such cycling as “hydromechanical fatigue” (Preisig et al., 2016), also identifying site specific thresholds for triggering of slope acceleration phases (Bonzanigo, 1999; Agliardi and Crosta, 2014). The degree of hydromechanical coupling depend on the slope specific conditions, being affected by superficial topography, hydraulic properties of materials involved and fracture spatial distribution and density. Either way, trigger could be represented by intense or prolonged hydrological input, results in different acceleration periods and cumulated displacement also depending on slope damage state and associated rock mass properties evolution (Preisig et al., 2016). Several authors used the capability offered by UDEC of modelling groundwater flow along discontinuities to investigate the role of hydrologic controls and hydromechanical coupling on slope mechanical behavior (Fig. 2.26; Guglielmi et al., 2005; Bonzanigo et al., 2008; Fischer et al., 2010).

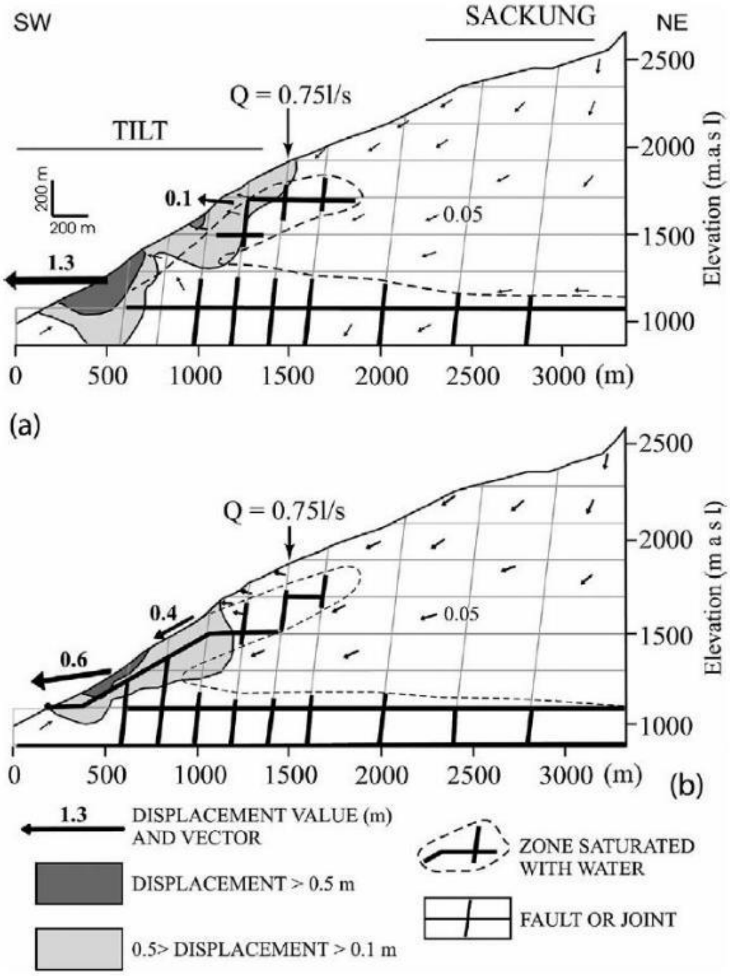

Figure 2.26: Results of hydromechanical simulation performed with only pre-exisisting faults (a) and with the inclusion of pre-existent failure surface (b) (from Guglielmi et al., 2005).

3 DADYN-RS: TIME-DEPENDENT DAMAGE-BASED SLOPE MODEL

Trying to overcome the caveats expressed and reviewed in the previous chapter, we attempted to capture the main stages of the alpine rock slope lifecycles within one continuum modelling framework, including the effects of time-dependent deglaciation, rock mass heterogeneity, evolving strength and permeability, and fluid pressure occurrence. Due to the large scale and the uncertainties in the definition of both mechanical and hydraulic parameters, we represented rock mass as an equivalent continuum, starting from a damage-based, time-dependent approach initially proposed to simulate laboratory rock deformation experiments (Amitrano and Helmstetter, 2006).

We tested the performance of the new model components, specifically designed for reproducing real rock slopes behavior, through a parametric analysis on simplified slope profiles (Cf. Chapter 4). Obtained results permitted to evaluate the effect and the sensitivity of different parameters on slope geometry, damage localization, strain pattern and time-dependent behavior.

Later, we simulated the long-term evolution of two alpine slopes, Spriana (Cf. Chapter 5) and Confinale (Cf. Chapter 6), subjected to a rockslide and a Deep Seated Gravitational Slope Deformation, respectively. The Spriana rock slope (Valmalenco, Italian Central Alps) is affected by an active, potentially catastrophic rockslide characterized though a wealth of geological, site investigation and monitoring data. Indeed, the Confinale slope (Upper Valtellina valley, Italian Central Alps) consists of a deep seated landslide slowly creeping and conditioning the evolution of “Ruinon” rockslide, a nested instability threatening the valley floor and extensively studied through the last decades due to the likelihood collapse. We also used numerical modelling to evaluate the potential of damage-based modelling in the understanding of long-term rock slope instability and contribute to a more general discussion of the mechanisms and timing of alpine valley evolution since the Last Glacial Maximum.

3.1 BRITTLE CREEP MODEL:

We developed our model starting from a 2D, plane strain, time-dependent, Finite Element modelling framework, proposed by Amitrano et al. (1999) and Amitrano and Helmstetter (2006), later applied by Lacroix and Amitrano (2013) to simple slope problems in intact rocks. The model was initially conceived to simulate different aspects of laboratory rock deformation experiments (i.e. microcrack damage, localization, acoustic emissions, brittle creep and energy release) within a continuum damage mechanics framework (Kachanov, 1986). In this approach, the brittle failure processes underlying macroscopic progressive failure and creep behavior are described in terms of degradation of the instantaneous "effective" elastic modulus (Fig. 3.1a), a macroscopic proxy of increasing crack density (i.e. damage; Amitrano and Helmstetter, 2006). A combination of a damage law (time independent component) and a time-to-failure law based on subcritical crack growth theory (Atkinson, 1984; Atkinson and Meredith, 1987; Prager et al., 2008) was initially tested on laboratory creep tests on intact rock proving the ability of completely describing macroscopic creep behavior, from primary to tertiary stages (Amitrano and Helmstetter, 2006; Fig. 3.1b).

This interplay results in two different ways a finite element can undergone failure, respectively (a) when the mobilized (instantaneous) stress exceeds the material instantaneous strength (time-independent damage; stress state 1 in Fig. 3.1c) or (b) when the available time-to-failure is entirely consumed in subcritical stress conditions (time-dependent damage; stress state 2 in Fig. 3.1c).

The continuum-based approach allows overcoming the computational and parametrization issues typical of explicit models based on fracture-mechanics (Eberhardt et al., 2004; Elmo, 2006; Elmo and Stead, 2010), and applying the model on any problem scale from laboratory to large mountain slopes. Our model formulation is based on "macroscopic" (global) damage and time-dependence laws, which are implemented as micro-mechanical (local) rules at the scale of individual finite elements. Although implying some over-simplification of the involved physics, this multi-scale formulation allows complex macroscopic phenomena to be captured by the model in the form of emerging properties, as already pointed out by Amitrano and Helmstetter (2006) and further discussed in the next paragraphs.

3.1.1 *Time-independent damage law*

The model simulates damage mechanics according to an elastic interaction model which reproduces the progressive mechanical degradation underlying a brittle creep behavior. A "damage event" occurs in a given finite element when the mobilized stress exceeds the material instantaneous strength, which is described by a Mohr-Coulomb failure criterion with tensile cutoff. At each damage event *n* and within each element *i*, the effective deformation modulus E_i is decreased depending on an incremental damage parameter D, according to:

$$E_i(n) = \left(1 - D_i(n)\right)E_{0,\mathrm{i}}(n) \qquad (3.1)$$

where: $E_{0,i}$ is the initial (elastic) deformation modulus and $D_i(n)$ is a proxy of crack density progressively accumulated within the element after n damage events (Kemeny and Cook, 1986; Fig. 3.1a).

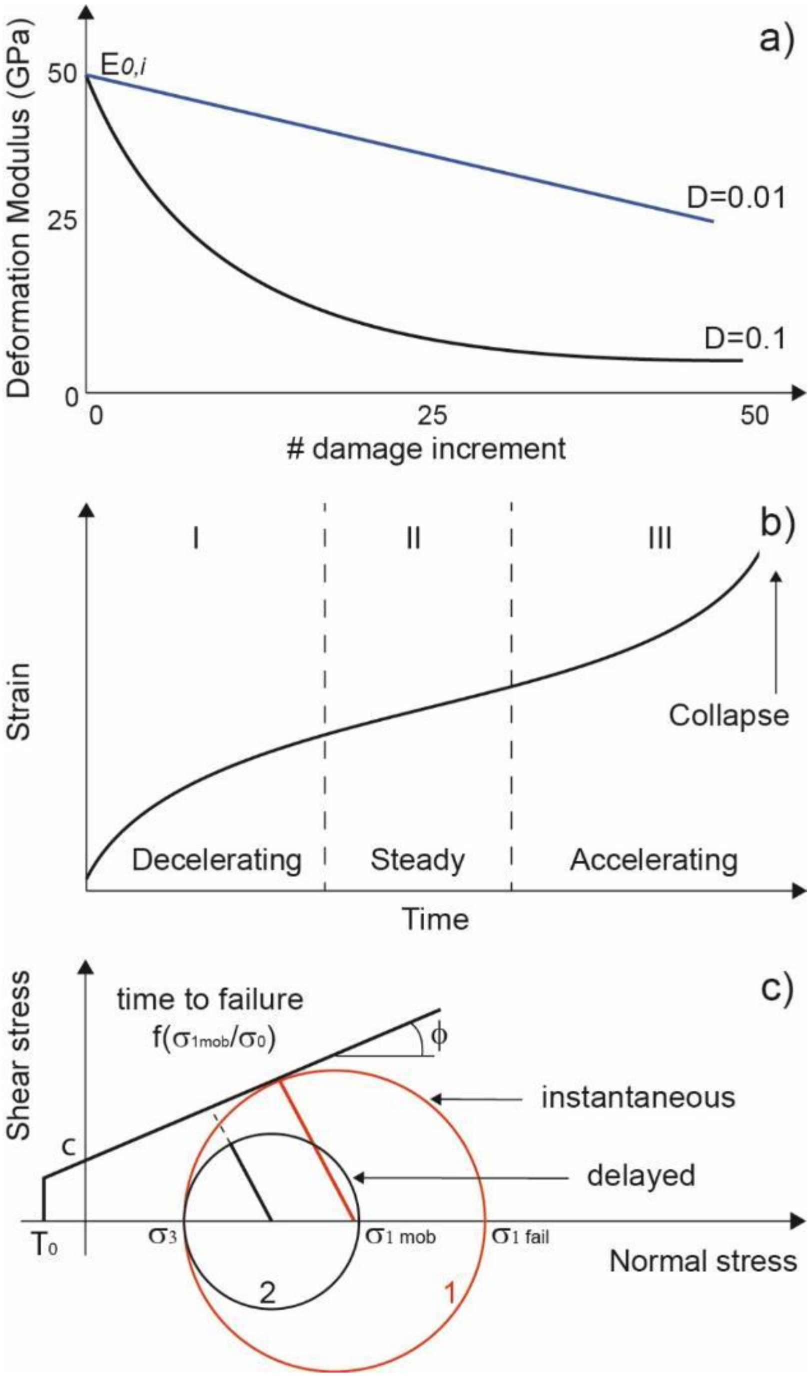

Figure 3.1: Progressive damage effects leading to macroscopic brittle creep. (a) Decrease in deformation modulus corresponding to damage accumulation in a continuum damage mechanics framework; (b) complete creep curve observed in slopes (modified after Saito and Uezawa, 1961); (c) Instantaneous failure (stress state 1) versus progressive failure occurring in subcritical stress conditions (stress state 2).

3.1.2 Time-dependent component

When, in every finite element used to discretize the model domain, the mobilized stress is not sufficient to cause instantaneous failure and consequent damage, delayed failure resulting from subcritical crack growth (intact rock) or progressive fracture damage (rock mass) is simulated using a time-to-failure law, depending on the ratio of locally mobilized stress and instantaneous (peak) strength as represented in Fig. 3.1c (stress state 2 in).

The time-dependent creep law simulates failure by static fatigue and is derived from fracture mechanics studies on subcritical crack growth and stress corrosion (Wiederhorn and Bolz, 1970; Das and Scholtz, 1981; Atkinson, 1985; Atkinson, 1991). Failure is assumed to occur when a critical microcrack density is reached, resulting in coalescence and development of a macro-failure surface. Time-to-failure is related to instantaneous stress with an exponential form:

$$t_{f,i} = T_0 exp\left(-b\frac{\sigma i}{\sigma_{0,i}}\right) \qquad (3.2)$$

where: $t_{f,i}$=time to be consumed to reach failure in the element i; σ_i is the mobilized effective stress and $\sigma_{0,i}$ is the instantaneous strength at i (Fig. 3.1c); T_0 and b are empirical parameters derived for intact rocks by laboratory creep tests published in literature, which were reviewed by Amitrano and Helmstetter (2006) (Fig. 3.2 and table 3.1). They fitted experimental values with exponential time-to-failure law (2) to evaluate the correlation coefficient and quantify the effect of rock type (petrography, texture) and boundary conditions on timing. The comparison between laboratory creep test observations and the failure trends predicted by the time-to-failure law showed a good match. Regarding T_0 and b, the exam of creep test data resulted in a strong correlation between these two parameters, expressed by the relationship $log(T_0) \approx b$ (Lacroix and Amitrano, 2013 and Table 3.1). Regarding boundary conditions, an increase in the b value is observed at higher confining stress (Kranz, 1980; Baud and Meredith, 1997) and lower temperature (Kranz et al., 1992). Fluid occurrence seems to affect T_0 and b (Scholz, 1972; Kranz et al., 1982) by accelerating failure through stress corrosion and decrease in effective stresses, even if lack of experimental data makes the quantification of this effect difficult. Time-to-failure law reproduces rock behavior observed during laboratory creep tests, in which mobilized stress is close to instantaneous strength (σ/σ_0>0.75; Fig. 3.2). For very low mobilized stresses the relation (3.2) results in very long predicted time-to-failure. This behaviour is consistent with the mathematical formulation of the time-to-failure law, but is difficult to support experimentally due to practical issues (laboratory test duration). It may be argued that, for low mobilized stress microcrack nucleation and propagation still occur, but are counterbalanced by sealing and healing phenomena (Atkinson and Meredith, 1981; Atkinson and Meredith, 1987). A practical implication of using a time-to-failure law at every mobilized stresses is that the numerical model never reach a true equilibrium state, thus requiring a threshold conditions to stop the model calculation loop at a certain point during slope evolution. Moreover, the lack of equilibrium state prevents the calibration of slope mechanical parameters through back-analysis.

Another important issue related to the application of time-to-failure law to large-scale problems regards the lack of data on rock masses and criteria to upscale T_0 and b. These need to be calibrated. Our approach to the problem will be discussed in next paragraphs.

The application of (3.2) during the simulation run allows computing, at each model timestep, the time-to-failure of each finite element. The lower computed value identifies the finite element closer to failure. Model time is then updated so that failure at this element occurs and the consumed time is subtracted from the remaining lifetime of the other elements. At this point, the failed element is "damaged" according to the damage law (3.1), as previously explained the reduction of deformation modulus in an element undergoing damage leads to stress redistribution around the element, possibly resulting in an "avalanche" of instantaneous failures in surrounding elements. Avalanches are made possible by the elastic modulus heterogeneity imposed at the element scale, that permits the formation of "stress concentrators" within the model domain (Amitrano et al., 1999; Amitrano and Helmstetter, 2006; Lacroix and Amitrano, 2013). In the original model formulation, heterogeneity is conceived as uniform distribution of elastic moduli calculated into a predefined range. When instantaneous failure does not occur after stress redistribution, the calculation cycle proceeds with recalculation of time-to-failure law.

According to this procedure, after n damage events, the time-to-failure for the element i after the n-th damage event or avalanche results from:

$$t_{f,i}(n) = t_n + t_f(\sigma_i, \sigma_{0,i})(1 - p_i(n))(1 - D_i(n)) \tag{3.3}$$

Where $p_i(n)$ is the proportion of consumed lifetime and $D_i(n)$ is the damage cumulated after n damage events. Every time an element is damaged, its proportion of consumed lifetime $p_i(n)$ is reset to zero.

Within the numerical model framework, three different ways to express time exist: two are directly calculated by the model during the simulations, while the latter is extrapolated *a posteriori* by scaling the simulation time with respect to the specific constrain available for the study site. They are classified as following:

- timestep: computational unit used by the explicit FEM algorithm to pass through progressive iterations. It can correspond to rupture in a single element or more (i.e. avalanche events);
- model physical time: calculated as the cumulative sum of the lower computed value obtained by the application of time-to-failure law (3.2) at every timestep. At the end of simulation, it defines the global lifetime of the slope;

scaled time: derived after the end of simulation by scaling the model physical time of a correction factor, which is constrained from the geochronological or paleoclimatic evidence (e.g deglaciation time, absolute or relative chronology) available for the study site.

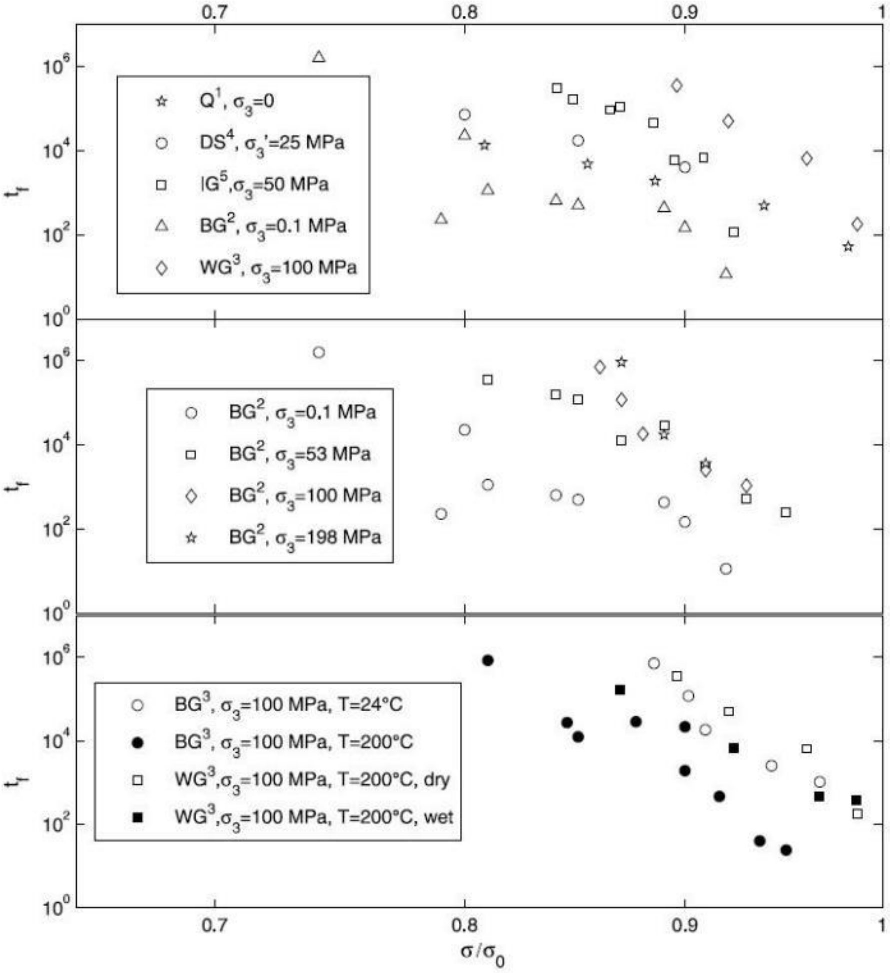

Figure 3.2: Failure times (in seconds) for laboratory creep tests performed at different loads and boundary conditions. Tested rocks correspond to: BG, Barre granite; WG, Westerly granite; IG, Indiana granite; DS, Darley Dale sandstone. Apexes refers to: (1) Scholz [1972], (2) Kranz [1980], (3) Kranz et al. [1982], (4) Baud and Meredith [1997], and (5) Masuda [2001]. From Amitrano and Helmstetter, (2006).

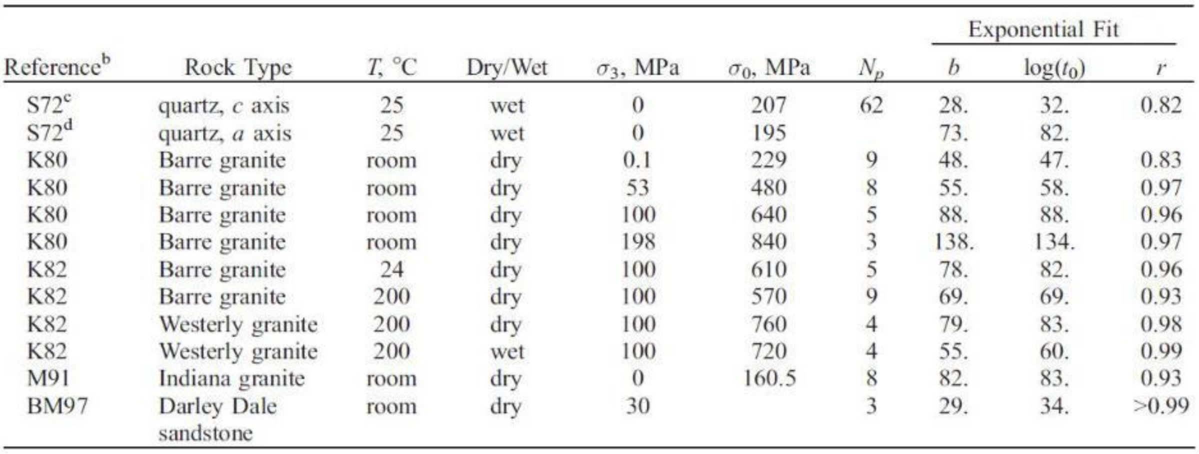

Reference[b]	Rock Type	T, °C	Dry/Wet	σ_3, MPa	σ_0, MPa	N_p	Exponential Fit		
							b	$\log(t_0)$	r
S72[c]	quartz, *c* axis	25	wet	0	207	62	28.	32.	0.82
S72[d]	quartz, *a* axis	25	wet	0	195		73.	82.	
K80	Barre granite	room	dry	0.1	229	9	48.	47.	0.83
K80	Barre granite	room	dry	53	480	8	55.	58.	0.97
K80	Barre granite	room	dry	100	640	5	88.	88.	0.96
K80	Barre granite	room	dry	198	840	3	138.	134.	0.97
K82	Barre granite	24	dry	100	610	5	78.	82.	0.96
K82	Barre granite	200	dry	100	570	9	69.	69.	0.93
K82	Westerly granite	200	dry	100	760	4	79.	83.	0.98
K82	Westerly granite	200	wet	100	720	4	55.	60.	0.99
M91	Indiana granite	room	dry	0	160.5	8	82.	83.	0.93
BM97	Darley Dale sandstone	room	dry	30		3	29.	34.	>0.99

Table 3.1: Creep test data from literature and fits for time-to-failure exponential relationship (2). References: BM97, Baud and Meredith (1997); M91, Masuda (2001); K80, Kranz (1980); K82, Kranz et al. (1982); S72, Scholz (1972) (from Amitrano and Helmstetter, (2006)).

3.1.3 Model emerging properties

Elastic interactions among elements with heterogeneous properties and damage states allow the model reproducing complex problem-scale macroscopic behavior as an emerging property (i.e. not directly accounted for by the model formulation at the scale of individual elements), including progressive damage localization, shear band formation, complete description of creep stages (decelerating to accelerating) and rupture event distributions (Amitrano and Helmstetter, 2006).

In this respect, damage parameter is fundamental to completely describe creep stages, also considering experimental observation relating time-to-failure and accumulated damage (Ray et al., 1999; Amitrano and Helmstetter, 2006). Poisson ratio is imposed as constant scalar value at element scale, thus representing an isotropic material. However, at macroscopic scale apparent ratio increase is reproduced by the model (Amitrano, 1999), in agreement with experimental observation on cyclic loading tests (Martin and Chandler, 1994; Eberhardt et al., 1999; Heap et al., 2010).

3.1.4 Model sensitivity to mechanical properties

Lacroix and Amitrano (2013) performed a sensitivity analysis on simplified slopes to assess the effect of rock mechanical parameters on time evolution, rockslide thickness and width of basal shear band. Regarding the time needed by the different simulations to reach ten meters of summit vertical downthrown (*t10*), they observed that increase in cohesion corresponds to longer slope lifetime, due to the occurrence of stronger rock mass (Fig. 3.3a). Increase in *t10* is also reproduced when internal friction angle is decreased, probably as a consequence of ductile mechanism onset and related diffused deformation, which takes more time to cumulate displacement within the slope (Fig. 3.3a). Increase in Poisson’s ratio cause a correspondent increase of slope lifetime (Fig. 3.3b), while time-to-failure parameter obviously have a strong effect: linear increase of b results in exponential increase in *t10* (Fig. 3.3c).

Definition of mechanical parameters has also major effect on the mean thickness (T) of resulting rockslide. Cohesion increase results in shallower instabilities, as its practical consequence is to move upward the Mohr-Coulomb failure criterion, thus making deep failures (i.e. at high confining stress) unfavorable (Fig. 3.4a). The effect of internal friction angle is unclear, as no evident trends in T are collected (Fig. 3.4a). Instead, Poisson’s ratio and time-to-failure parameter have a marked effect, since rockslide thickness strongly raise in response to increase in ν and decrease in b (Fig. 3.4b, c).

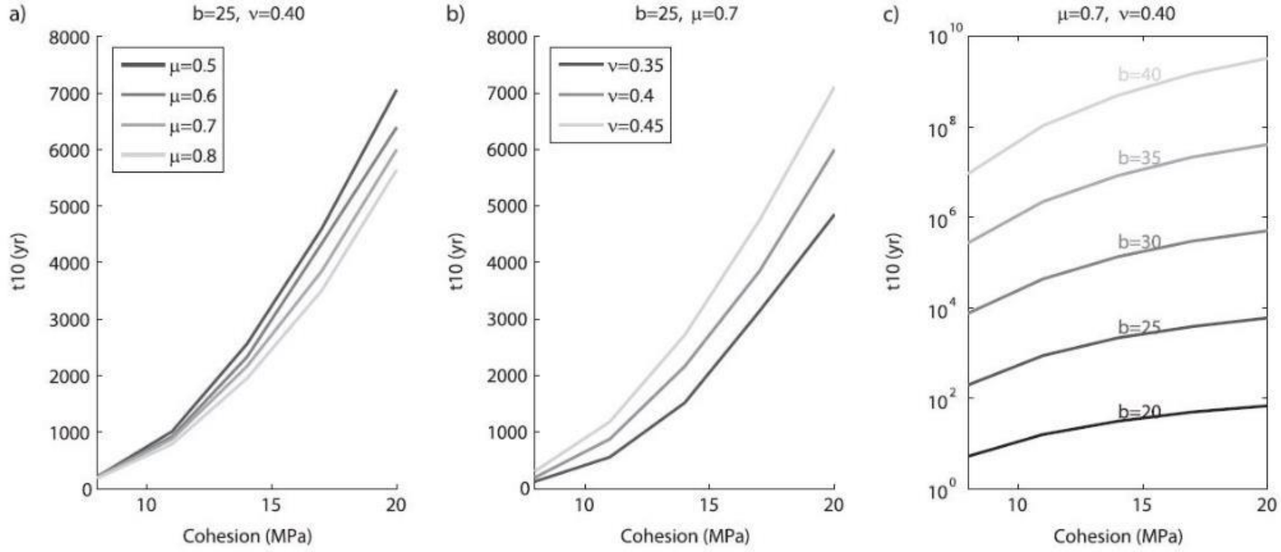

Figure 3.3: Time to reach ten meters of crest vertical downthrown versus slope cohesion for different values of (a) internal friction angle, (b) Poisson's ratio and (c) time-to-failure parameter (from Lacroix and Amitrano, 2013).

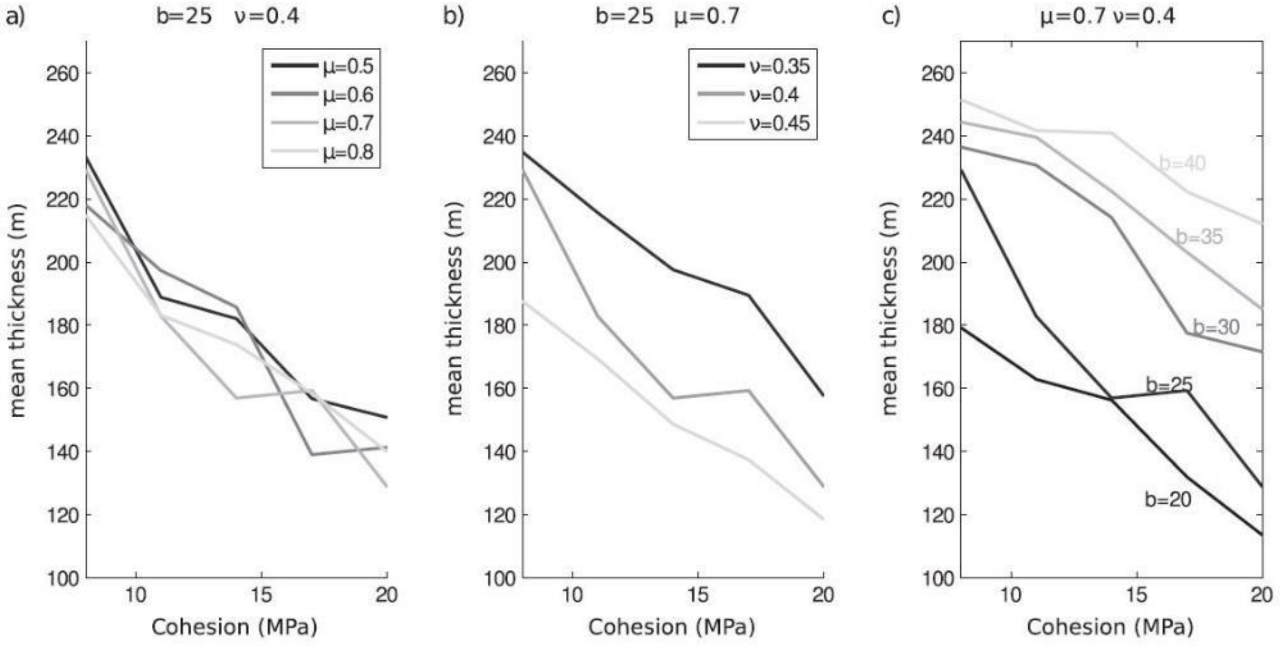

Figure 3.4: Mean rockslide thickness versus slope cohesion for different values of (a) internal friction angle, (b) Poisson's ratio and (c) time-to-failure parameter (from Lacroix and Amitrano, 2013).

Thickness of basal shear band (*W*) is an important descriptor of both damage and strain localization. For a given mesh accuracy, i.e. element size, wide bands correspond mainly to brittle-ductile transitional behavior, while sharp, localized bands are the expression of purely brittle rupture. Decrease in *W* are encountered for decrease in ν and increase in cohesion and friction angle (Fig. 3.5a,b). This testify how stronger rocks fail in a more brittle manner, thus resulting in a narrower and more localized shear band. Surprisingly, the effect of time-to-failure parameter is major also on the basal shear band width, as increase in *b* results in marked increase of *W* (Fig. 3.5c).

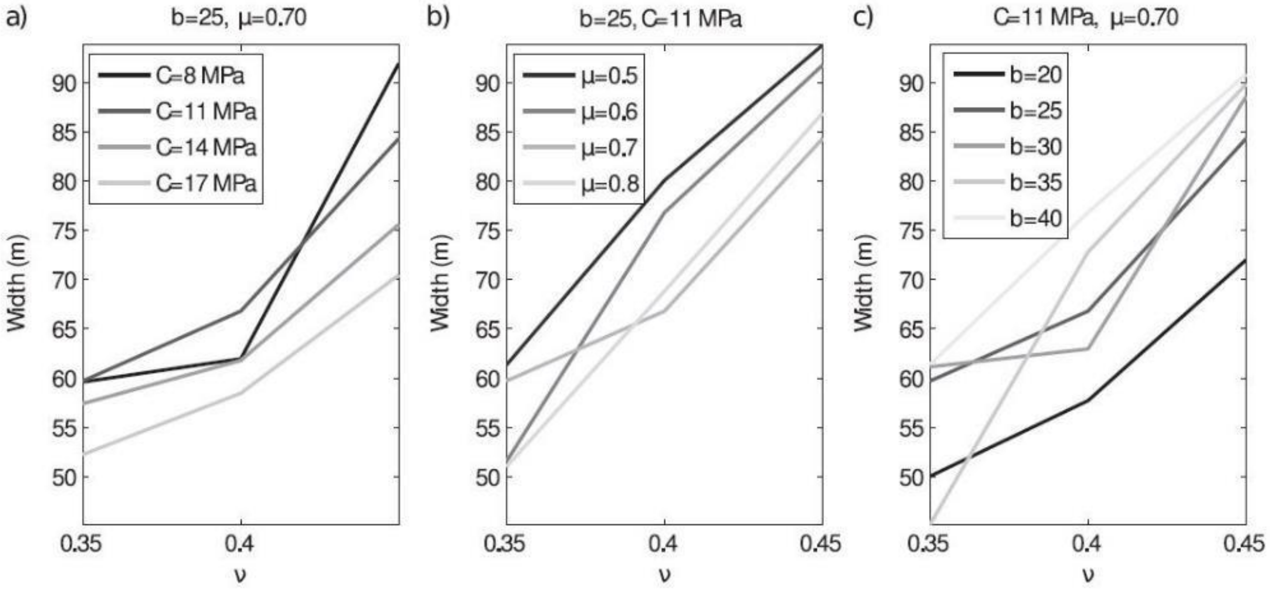

Figure 3.5: Width of rockslide basal shear band versus Poisson's ratio for different values of (a) cohesion, (b) internal friction angle and (c) time-to-failure parameter (from Lacroix and Amitrano, 2013).

3.2 DADYN-RS STRUCTURE AND FLOW DIAGRAM

The DaDyn-RS (Rock Slope) model is developed in Matlab^{TM} (MathWorks, Inc.) and consists of a main script which execute a series of nested functions, each one in charge of a specific operation in the calculation cycle. Amitrano et al. (1999) and Amitrano and Helmstetter (2006) developed their original model (and investigated its parameters) to simulate laboratory creep tests with dry, intact rock, whereas Lacroix and Amitrano (2013) simulated the behavior of idealized dry slopes shaped in intact rock. In order to deal with large, real rock slopes in fractured rock mass we developed new model components (Cf. subsections from 3.3. to 3.6), incorporated into the original model in the form of new nested functions (Fig 3.6). With respect to the original DaDyn formulation, the RS version of the model includes 16 nested functions and 28 variables including vectors, structured arrays and strings.

Model improvements have been conceived to meet the specific requirements of large rock slope modelling. Alpine valley flanks typically have huge size (Fig. 1.4) and host rock slope instabilities ranging in volume up to billions of cubic meters (Agliardi et al., 2013; Crosta et al., 2013), requires the upscaling of material properties from intact rock to rock masses equivalent-continuum with respect to strength, deformability and hydraulic properties (Hoek and Brown, 1980). In addition, as real alpine slopes underwent time-dependent deglaciation, we introduced the capability of simulating ice thickness in terms of transient hydrostatic load on slope surface. Finally, to reproduce the effects of changing groundwater regimes we developed a novel approach in which fluid pressure occurrence is taken into account relying on very simple but coherent hydrological boundary conditions. Model input parameters are resumed in Table 3.2.

The numerical code workflow (Fig 3.6) starts with the definition of the geometry, boundary conditions and rock mass properties of the model (Cf. subsection 3.3). The meshing algorithm consists first in the processing of input geometry to obtain disjoint minimal regions, constituting the base for the discretization process, which is conducted recurring to a 2-D Delaunay triangulation algorithm using a minimum edge side length, specified as input value during model set-up.

Then, before entering into the main calculation loop, gravity force and overlying glacier loading (Cf. subsection 3.4) are initialized in the slope. Resulting stress and strain are computed for each Finite Element, then fluid occurrence and connectivity are calculated (Cf. subsection 3.5). , thus obtaining real-time spatial pattern of groundwater within the slope. Fluid pressures computed at each element allow computing effective stresses, which in turn influence rupture location and timing at the element scale. Local element failure can occur instantaneously or delayed, eventually triggering avalanche through stress redistribution in surrounding elements. Rupture avalanches are reproduced through a secondary loop cycle that permits to refresh mechanical state and fluid pressure without time progression until a stable instantaneous stress state is reached. Output stresses, strains and simulation time permit to restart the main loop cycle and reproduce progressive evolution of the slope through subsequent time steps. The simulation stops as the imposed displacement threshold is reached, which is selected by the user for a specified observation point during input parameters definition, according to available monitoring data or field evidence. Emergency model “exit criteria” are also provided to avoid unrealistic model behavior, interrupting simulation in case of exceeding imposed threshold values. These include: the maximum number of rupture allowed in a single avalanche, the maximum number of ruptures allowed for a single element and the maximum number of rupture events in the entire model domain. Once the calculation loop is completed, last functions provide to the construction of model outputs in form of both graphical and numerical format. Among these, pattern of damage events, fluid pressure occurrence, maximum and minimum stresses, strain components, mechanical properties and displacement can be visualized (Fig. 3.7). Moreover, numerical code provides the capability of monitoring several observation points located in significant portions of model domain, to assess simulation behavior through time (Fig. 3.8). All the outputs can be exported for further data processing.

Parameter	**Symbol**	**Unit**
Unit Weight	γ	kN/m^3
Young Modulus (intact rock)	E_0	MPa
Tensile strength (rock mass)	T	MPa
Cohesion (rock mass)	C	MPa
Coefficient of internal friction (rock mass)	μ	-
Poisson ratio (rock mass)	ν	-
Rock mass GSI	GSI	-
Damage increment parameter	D	-
Time-to-failure law parameter	b	-
Permeable cluster water filling	w	%
Glacier maximum level	H	m a.s.l.
Starting of deglaciation	t_{d0}	years
Deglaciation duration	T_d	years

Table 3.2: Summary of numerical model input parameters.

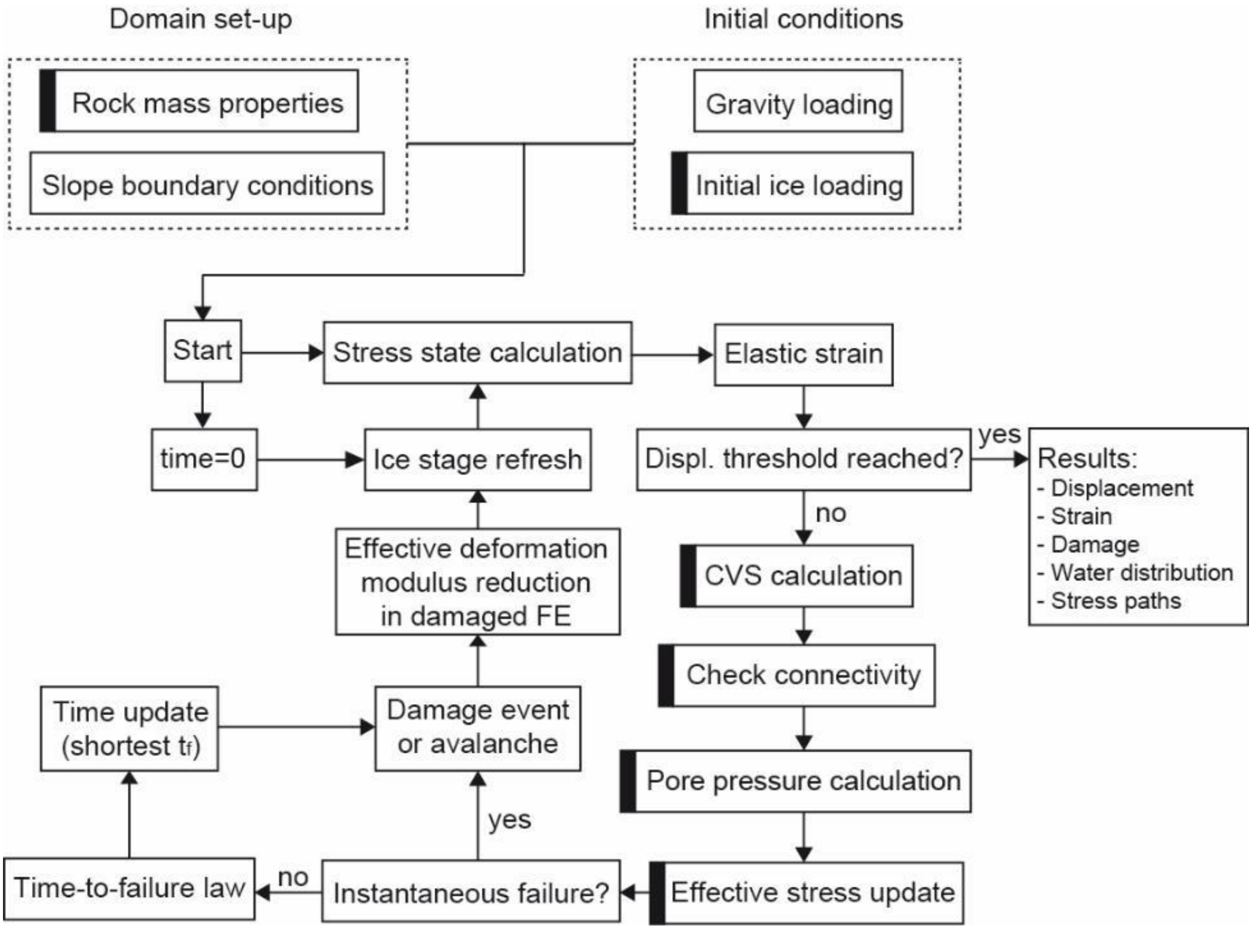

Figure 3.6: Dadyn-RS simplified structure. Components specifically developed for Dadyn-RS are outlined by a thick black mark.

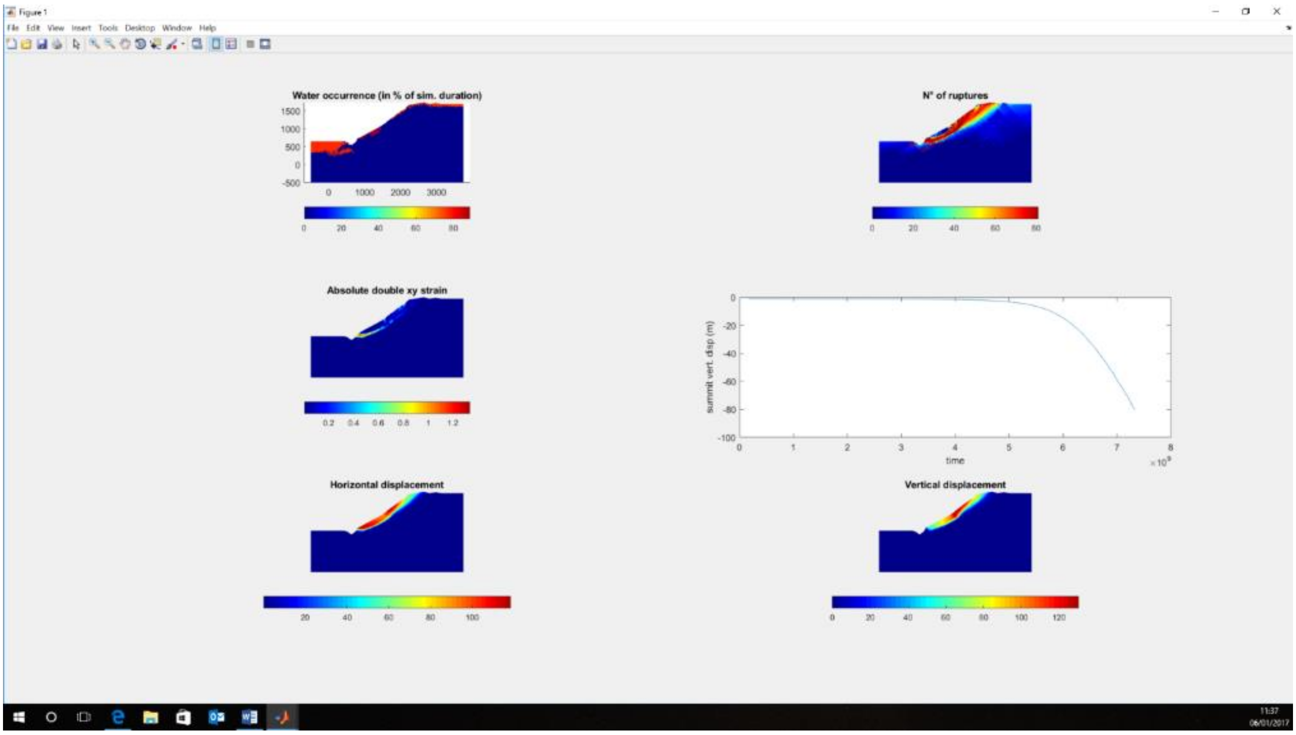

Figure 3.7: Dadyn-RS graphical output showing patterns of fluid pressure occurrence, damage, strain and displacement for the current simulation.

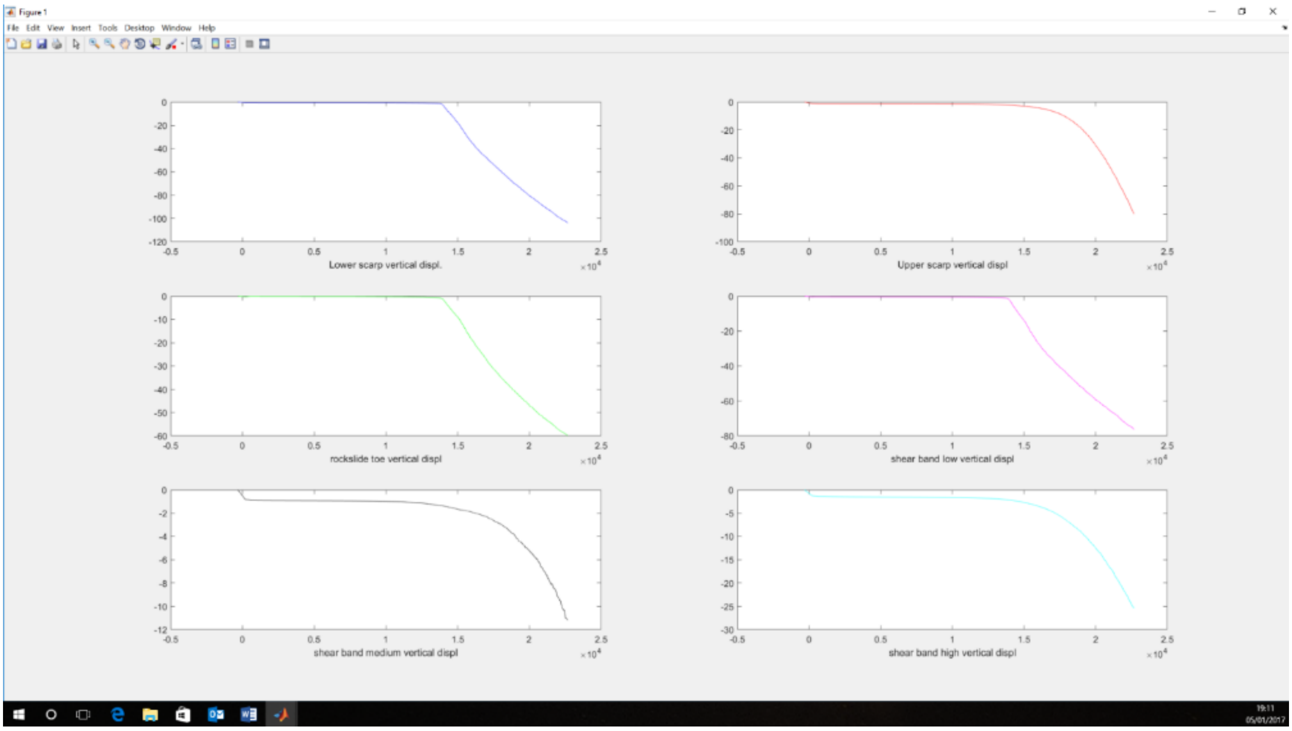

Figure 3.8: Dadyn-RS graphical output showing vertical displacement through time in six selected observation points

3.3 ROCK MASS PROPERTY UPSCALING

To account for the behaviour of real fractured rock masses, we used an upscaling strategy based on the Hoek-Brown approach (Hoek and Brown, 1980; Hoek et al, 2002). This relies on the observation that rock strength decrease when increasing the size of the "sample" from intact rock (containing microcracks, flaws and textural defects) to rock mass (made of rock blocks split by macro cracks/discontinuities; Fig. 2.1). Following this approach, intact rock properties measured in laboratory tests (Fig. 3.9a) are scaled to field conditions using the Geological Strength Index (GSI, Fig. 3.9b; Hoek et al., 1995; Hoek and Brown, 2002). This empirical parameter describes rock mass structure and discontinuities alteration, easily quantified in both outcrops (Marinos & Hoek, 2000) and borehole data (Agliardi et al. 2016). The GSI varies in the range 5-95 depending on rock mass structure and weathering of discontinuities. In modelling real rock slopes, parameter definition might take into account all the previous and "inherited" modifications to rock mass structure due to previously acting geological processes, thus referring GSI input distribution to the beginning of simulation (i.e. end of LGM). The use of GSI allows a first esteem of tensile strength and the equivalent Mohr-Coulomb cohesion and friction coefficient, which are then inserted in DaDyn-RS as rock mass input values. Heterogeneity can be attributed to friction angle and cohesion in form of uniform distributions calculated between ranges specified by the user.

The GSI also allows deriving initial values of rock mass deformation modulus E_0 at each element i, using the empirical relation proposed by Hoek and Diederichs (2005) for the undisturbed case (Fig. 3.9c):

$$E_{0,i} = E_{lab}\left(0.02 + \frac{1}{1+e^{\left(\frac{(60-GSIi)}{11}\right)}}\right) \tag{3.4}$$

where: $E_{0,i}$ is the initial rock mass deformation modulus in the element i, and E_{lab} is the Young modulus of intact rock (Hoek et al, 2002).

Calculation of rock mass equivalent deformation modulus is automatically performed within the numerical code by defining as input parameters the intact rock Young Modulus, the rock mass GSI mean value and the corresponding standard deviation. Assuming a normal distribution for real populations of GSI values, a randomly assigned value is attributed at each Finite Element. The GSI assignment can be totally random or controlled by a specified seed, thus assuring repeatability of properties attribution at the initial state of simulation. Then, equation (3.4) is used to generate corresponding lognormal distributions of E_0 to be introduced in initial model set up, accounting for material heterogeneity as close as possible to the real conditions (Fig. 3.9d).

During the attribution of rock mass properties the model domain can be divided into different subdomains with simple geometry, each one characterized by different mechanical properties. This permits to evaluate the effect of different geological materials or structures, for example stratigraphical boundary between two different formations or faults occurrence with associated damage zones, which can greatly condition slope evolution and instability development (Agliardi, 2001).

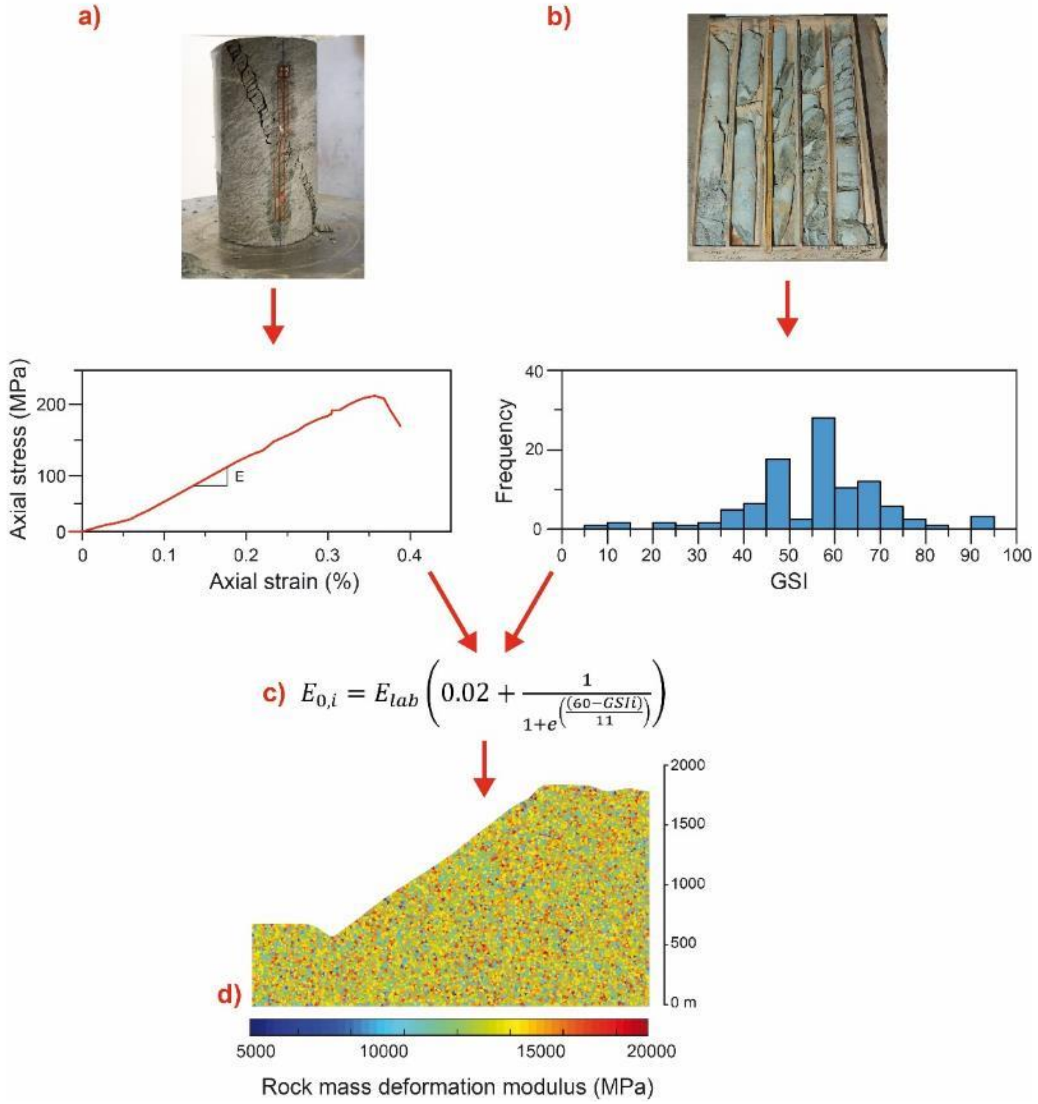

Figure 3.9: Rock mass property attribution. Data from laboratory tests performed on intact rock (a) are scaled by GSI coming from field characterization of boreholes and outcrops (b) to obtain rock mass parameters. Using the empirical relationships proposed by Hoek and Diederichs (2005) (c), initial model distribution of deformation modulus is obtained (d).

3.4 TIME-DEPENDENT DEGLACIATION

Deglaciation is assumed to be one of the most important conditioning factors in the long-term evolution of alpine slopes, although the exact nature of its effects is still debated. The extensive and elevated ice load to which valley flanks were exposed to at the end of Last Glacial Maximum and the consequent melting due to increased temperatures determined extensive stress redistribution and the development of widespread damage within the slopes. To simulate the effects of deglaciation we adapted the approach of Lacroix and Amitrano (2013) for use with complex slope topographies, by applying separated horizontal and vertical ice loads components in order to obtain an overall, transient "hydrostatic" ice load on FE mesh nodes at slope surface (Fig. 3.10). In our model, the timing of deglaciation is updated independently on the model creep time (governed by Eq. 2) and calibrated on available absolute or relative chronological constraints (Bini et al., 2009; Wirsig et al., 2016).

Two parameters control the time dependency of deglaciation, namely: the starting time of deglaciation (t_{d0}), and the deglaciation duration (T_d), which is expressed as:

$$h_{ice} = H \qquad if\ t \leq t_{d0} \tag{3.5}$$

$$h_{ice} = H\left(1 - \frac{t - t_{d0}}{T_d}\right) \qquad if\ T_d + \ t_{d0} > t > t_{d0} \tag{3.6}$$

$$h_{ice} = 0 \qquad if\ t > t_{d0} + T_d \tag{3.7}$$

With H glacier height at the end of LGM.

Glacier load calculation is included in the code structure through a dedicated function, which first step consists in the identification of slope surface nodes and corresponding elements through a searching polygon. Obtained coordinates are then sorted to calculate both slope angle and distance between connecting nodes, fundamental for determining horizontal and vertical components of glacier force applied. Simulation time is then checked to calculate glacier heigth h_{ice} with (3.5),(3.6) or (3.7) depending on the relative value of t. Once h_{ice} is obtained, relative heights are extrapolated by difference with vertical coordinate of each element center in order to calculate ice weight per unit area, assuming a constant value of ice density with depth (916 kg/m^3). Glacier load bear by each surface element is finally calculated by multiplying ice weight for corresponding element length, meanwhile extracting horizontal and vertical load components based on slope angle. Forces are finally transferred from elements to nodes by splitting force applied at the element in the three equal components to be applied at nodes constituting the element boundary.

Ice load is applied as an external force added to the gravitational stress depending on current ice thickness. At this aim, the glacier load function is called during stress state calculation to properly refresh forces acting on the slope at least every timestep. Indeed, under the assumption of constant deglaciation rate, T_d is discretized in time intervals ΔT_d, corresponding to 1 m of ice removal. The model is forced to refresh stresses at every ΔT_d, or less in case one or more damage events are predicted by the time-to-failure law during an ice removal stage. This condition prevents the model to skip considerable parts of deglaciation, especially during early deglaciation when the ice-buttressed slope is characterized by long times to failure. This allows a better account for deglaciation effects on progressive damage and failure, especially for contexts characterized by relatively high deglaciation rates, as the LGM European Alps (Ivy-Ochs et al., 2006; Wirsig et al., 2016).

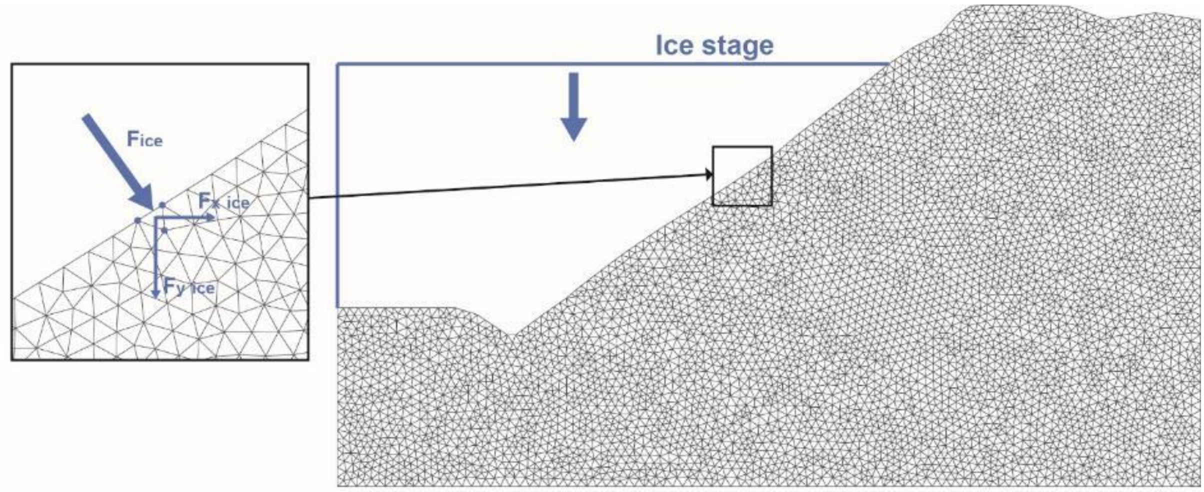

Figure 3.10: Time dependent deglaciation in DaDyn-RS. Glacier loading is applied at each element center by means of hydrostatic load, decomposed in horizonatal and vertical components depending on current ice thickness and local slope angle.

3.5 DAMAGE-DEPENDENT FLUID OCCURRENCE

Including the effects of hydro-mechanical coupling in the long-term evolution of alpine slopes is a necessary but extremely difficult task. This is due to the almost complete lack of knowledge about slope hydrology and hydraulic boundary conditions in deglaciating settings (Fig. 1.4), including the recharge contribution of melting glaciers, the role of permafrost on the availability and mobility of liquid water in slopes, and the geometry and extent of groundwater below the ice cover (Boulton and de Marsily, 1996; Bense et al., 2009; McColl, 2012; Crosta et al., 2013). In addition, while the influence of crack damage on the permeability of rocks has been studied in rock mechanics laboratory and underground field experiments (Zoback and Byerlee, 1975; Fortin et al., 2011; Rutqvist, 2015), the mechanisms and long-term development of rock mass permeability between deglaciation and complete rockslide development (Preisig et al., 2016) are not well known.

Therefore, we need a simplified yet mechanically-based model of fluid occurrence in the slope during its evolution. Starting from the observation that permeability in low-porosity rock is strongly related to crack density evolution associated to mechanical damage (Zoback and Byerlee, 1975; Mitchell and Faulkner, 2008; Faoro et al., 2013; Rutqvist, 2015; Violay et al 2015), we linked fluid occurrence to the rock mass dilatancy associated to progressive brittle damage (Martin and Chandler, 1994; Fortin et al., 2011) using a novel approach based on experimental evidence (Zoback and Byerlee, 1975; Rutqvist and Stephansson, 2003; Rutqvist, 2015). In our model, fluids can occur in a specific finite element if three conditions, which are checked for each element at each calculation timestep, are met, namely: damage, dilatancy, and connectivity.

First, the element needs to be damaged. Upscaling available laboratory-scale experimental observations, we assume that at least one rupture event must have occurred to increase crack density (according to the damage parameter D) at the element scale. This is a simplified assumption since: a) rock masses are fractured by definition also in an “undamaged” state, and b) inherited persistent fractures can locally occur in the initial slope state, potentially hosting fluid pressure. However, in view of the lack of constraints on initial slope hydrology in long-term applications, at this model development stage we assume that initial hydraulic aperture and connectivity are negligible. Model refinements accounting for initial rock mass porosity and damage-proportional crack density will be listed among future improvements. At this stage, our model is able to provide a lower-bound estimate of the spatial distribution of damage-dependent rock mass permeability. In the numerical code, damage condition is checked by searching for elements with no rupture accumulated, which are excluded from further calculations by assigning a value of fluid pressure applied equal to 0.

Depending on the stress path, deformation history and mechanical properties, at a given model stage an element can be characterized by net (cumulative) dilatancy (i.e. volume increase) or contraction (i.e. model decrease). Dilatancy (Fig. 3.11) is an established measure of crack growth and increased rock permeability in low-porosity brittle rocks at laboratory scale (Martin and Chandler, 1994; Eberhardt et al., 1999; Katz and Reches, 2004). We assume that this applies also to fractured rock masses in crystalline rocks. Fluids can occur in dilatant finite elements, which are identified in our model by computing the Crack Volumetric Strain (CVS) (i.e. the accumulated inelastic volumetric strain; Martin and Chandler, 1994) as a proxy of dilatancy and crack density. To obtain a spatially-distributed quantification of rock mass dilatancy, and thus identify the potential loci (finite elements) of pore pressure occurrence, at each element and at each model step we calculate the CVS_i as the difference between total computed volumetric strain (ε_V), and the elastic volumetric strain component, which depends on initial (undamaged elastic) values of the deformation modulus (E_0) and Poisson ration (Katz and Reches, 2004):

$$
\begin{aligned}
&CVS_i = (\varepsilon_V)_i - (\varepsilon_V)_{elastic,i} \\
&(\varepsilon_V)_{experimental,i} = \varepsilon_{1,i} + \varepsilon_{2,i} \qquad (3.8) \\
&(\varepsilon_V)_{E,i} = (\sigma_{1,i} - \sigma_{3,i})(1-2\nu)/E_{0,i}
\end{aligned}
$$

The total volumetric strain of each element is derived from the strain components computed by the model, and refreshed after every rupture event, by extracting the principal strains ε_1 and ε_2. The corresponding elastic volumetric strain $(\varepsilon_V)_{E,i}$ depends only on the calculated differential stress, as the Poisson's ratio and the initial rock mass deformation modulus remain constants throughout the entire simulation. After the subtraction between the two strain components, spatial pattern of CVS values within the slope is obtained: as fluids can occur only in elements with CVS<0, corresponding to net dilatancy, other elements (i.e. contractive) are excluded from further calculations by assigning a value of fluid pressure applied equal to 0.

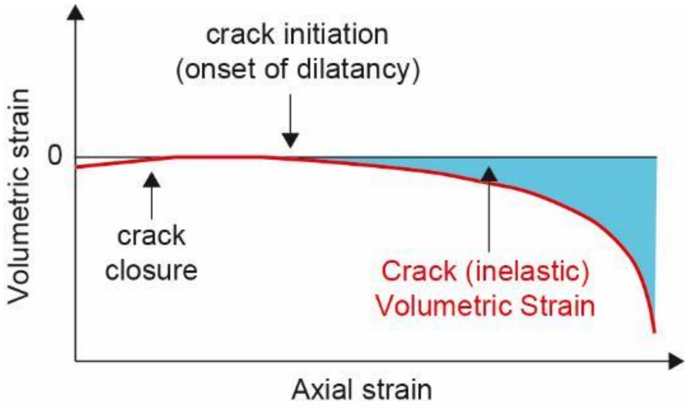

Figure 3.11: Experimental volumetric vs. axial strain curve for compression tests on intact rocks (modified after Martin and Chandler, 1994)

However, real rock slopes are characterized by the interconnection at different scale of rock mass discontinuity to host aquifers. To numerically reproduce this behavior, we assume that fluids enter the slope only by percolation from the topographic surface. This requires that dilatant elements are connected each other and to the topographic surface. In this way, slope aquifers are progressively developed during the model evolution through consecutive events, depending on both slope stress state and fluid pressure distribution. In our model, connectivity calculation is performed in two different steps: clustering and surface interconnection. Elements satisfying previous conditions (i.e. at least one rupture and net dilatancy) are checked and grouped in “permeable element clusters” by applying linkage and hierarchical clustering algorithms implemented in Matlab^{TM} (Fig. 3.12). The adopted clustering criterion is based on maximum distances measured between the centroids of each element. If computed values are lower than a threshold value, elements belong to the same permeable cluster, otherwise they are grouped differently and attributed a different cluster ID. In DaDyn-RS, the clustering threshold value is defined as the maximum element side length. If this assumption can be inaccurate for coarse meshes with refined elements at boundaries, for finer and homogeneous meshes typically adopted in our simulations distance criterion proved to be affordable in clusters grouping.

After that, surface connectivity is verified by searching, within each cluster, the presence of at least one surface element (clusters 3, Fig. 3.12): clusters not satisfying the condition of surface connectivity are excluded from the fluid pressure calculation (clusters 1 and 2, Fig. 3.12).

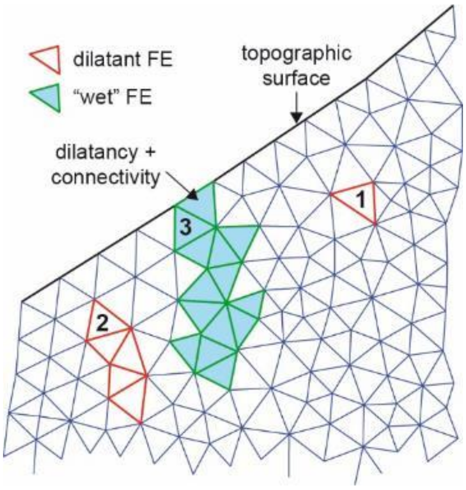

Figure 3.12: Permeable element cluster definition combining damage, dilatancy, and connectivity. Fluid pressure is applied only in cluster 3 (dilatant and connected with surface).

We assume that static water fills “permeable element clusters”, resulting in locally hydrostatic conditions. Fluid flow is not simulated at this stage of model development, thus avoiding the need to impose strong assumptions on the past hydraulic boundary conditions. As explained before, these are completely unsupported by experimental evidence in the long-term period during glacial and paraglacial stages. Fluid pressure is applied by imposing a specified degree of cluster filling (to be calibrated), indirectly accounting for partial drainage effects and ranging from 0 (empty cluster) to 1 (completely-filled cluster). To reproduce the possible effect of hydrologic pulses on slope behavior, time-dependent variations in fluid pressure can be simulated by defining cluster filling percentages and related timings. Simulated variations are instantaneous (i.e no rising of recession limbs are described), since the possibility of reproducing more realistic hydrographs is not yet implemented at current stage of the model. Once determined cluster filling from comparison with simulation time, height of fluid column is calculated for each element depending on the difference between element center and groundwater level. The corresponding value is then multiplied with water density to obtained fluid pressure.

Fluid pressures in permeable element clusters allow computing effective stresses at each model element (Fig. 3.13). Changes in effective stress distribution can results in both instantaneous failures or an update of the time-to-failure in subcritically stressed elements. Thus, damage-dependent fluid occurrence will affect further damage, dilatancy and water distribution, resulting in a simplified two-way hydro-mechanical coupling cycle (Rutqvist and Stephansson, 2003).

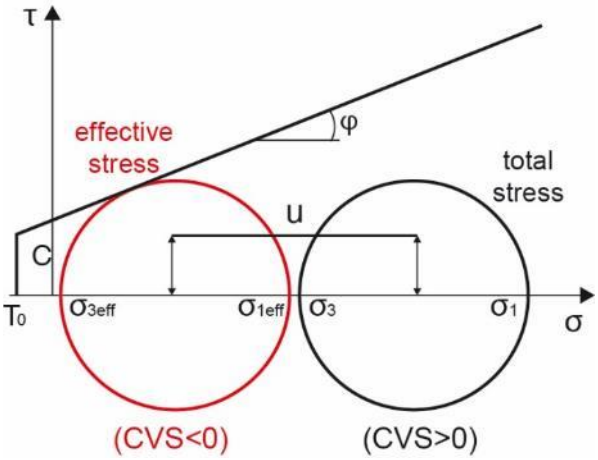

Figure 3.13: Effective vs. total stresses in “wet” element clusters.

3.6 ADDITIONAL COMPONENTS

Despite the major components introduced within the model structure, a number of minor improvements were also adopted to make to model suitable for the simulation of large real slopes. First, due to the large domain dimension and the elevated number of Finite Elements, the numerical code was vectorized and optimized in different portions to globally increase computational efficiency and calculation velocity.

Then, to reproduce topographies typical of alpine environments, the capability of introducing complex profiles derived from digital elevation models was included in DaDyn-RS. Slope profiles are initially defined as pairs of x and y coordinates, then discretization and mesh building are performed recurring to the Partial Differential Equation Toolbox implemented in Matlab^{TM}. The only parameter specified in model domain discretization is the maximum edge length, which is usually determined in respect of domain size by parametric analysis to balance between the simulation detail and the computational speed.

Output variables produced by the model were increased to better investigate long-term slope behavior. Besides new outputs related with the introduction of damage-dependent fluid occurrence, rock mass approach and time-dependent deglaciation, we introduced the capability of monitoring stress state and displacement for multiple points within the slope. Observation points are selected before the start of simulation, usually corresponding to significant portions of the slope (i.e. crest zone, rockslide toe, observed scarps). Monitoring results permit to investigate displacements trends and stress paths in different portions of the slope, better accounting for time dependent evolution of slope mechanisms, rockslide activation and differentiation. Observation points are used also during model validation, in comparison with observed displacements derived from geomorphological and geochronological evidence.

3.7 DADYN-RS CALIBRATION AND VALIDATION

Due to the large number of input parameters and the lack of knowledge about mechanical, hydraulic and environmental conditions of alpine slopes during glacial periods, model parameters are calibrated with a multi-indicator approach to reduce uncertainties in application to real cases.

Mechanical properties derive from in-situ geotechnical characterization and are scaled to represent rock mass equivalent continuum through Hoek and Brown approach (subsection 3.3). Permeable cluster filling represents an exception and is calibrated based on comparison between simulated versus observed slope behavior, since no data are available on long-term slopes hydrogeology. Moreover, to correctly reproduce the influence of rock bridges on strength and timing of slope, cohesion and tensile strength have to be calibrated ranging between intact rock and equivalent rock mass values. Modification in these parameters affect the geometry and kinematics of slope, also involving minor effects on damage localization. Time-to-failure law parameters are usually derived by creep tests on intact rock samples performed in controlled environment. Regarding rock masses, large uncertainties regarding both material upscaling and varying stress state make the esteem of b challenging. However, preliminary parametric tests on real slopes resulted in limited upscaling effect, making intact rock values directly suitable for slope-scale simulations. The damage increment parameter D regulates the discretization of mechanical properties reduction in respect to number of rupture events, meanwhile influencing diffused versus localized damage. D is calibrated based on simulated versus observed damage patterns and has a major influence on modelling results. Real time scaling depends mainly on glacier-related and time-to-failure parameters, which can be calibrated only in respect to available geochronological constrains, like relative or absolute dating. To evaluate the effect of main parameters on modelling results, an exhaustive sensitivity analysis on simple slope profiles is reported in chapter 4.

Multi indicator approach consists in iterative adjustment of main parameter involved to match simulated vs observed evidence of main slope features. Validation of modelling results mainly takes into account:

1) statistical distribution of simulated GSI values, back-calculated by distributions of effective deformation modulus in slope sectors corresponding to different “damage domains” and compared with observed GSI distribution obtained from geomechanical in-situ characterization
2) simulated rockslide geometry (size, depth, toe and crest locations) and morphological features (scarps, countercarps, toe bulging);
3) spatial and mechanical patterns of damage (localized vs. distributed damage) compared with in-situ surficial and deep data about rock mass comminution along shear bands, fracture density and GSI distribution;
4) slope kinematics and patterns of surface and deep displacements compared with available data on short-term and long-term slope displacement rates, coming from geomorphological, geotechnical or geochronological investigations;
5) time dependent behavior (i.e. total model lifetime vs. deglaciation time; displacement-time curves for different slope portions) compared with available absolute or relative chronological constraints.

The calibration process starts with the definition of time-to-failure and damage parameters (1 in Fig. 3.14), which are then checked for correspondence with observed damage pattern and slope kinematics. Once overall matching is reached, minor adjustment in depth of shear band and localized versus diffused damage distribution are performed with calibration of tensile strength and cohesion of rock mass (2 in Fig. 3.14). The last step comprise the verification of time-dependent behavior simulated by the model (3 in Fig. 3.14). As modification in one single parameter can influence both resulting geometry and time-dependency, iterative approach is adopted since a fitting simulation is obtained.

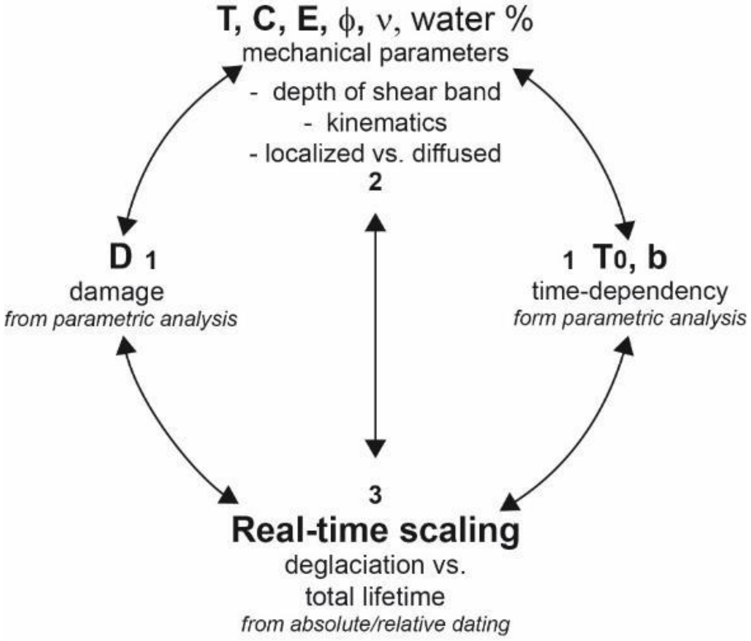

Figure 3.14: Multi-indicator approach used for calibration and validation of modelling results in DaDyn-RS

4 PARAMETRIC ANALYSIS

4.1 MODEL SETUP AND INVESTIGATED PARAMETERS

In the previous chapter, background theory and the new components introduced within DaDyn-RS were presented. We started testing the performance of the new model by assessing its sensitivity to the main parameters in long-term slope evolution, particularly observing their effects on the damage pattern, the strain distribution and the slope failure time, expressed as the model physical time required to the slope for reaching instability conditions. Thus, before dealing with real case studies, we performed a parametric analysis on simplified deglaciating rock mass slopes.

Two different profiles were investigated, respectively characterized by constant slope angle of 33° and 45° (Fig. 4.1). Local relief, from slope crest to toe, was established in 1000 m, which can be considered representative of typical alpine valley environments. A total domain length of 2500 m and total height of 1800 m were selected, allowing sufficient distance from the slope to the model boundaries to avoid boundary effects. Slope was discretized with a three-noded triangular finite element mesh, with maximum edge length equal to 50 m, resulting in xxxx elements and xxxx nodes. Mesh nodes along lateral boundaries were constrained in the horizontal direction, while at the model bottom was fixed in both vertical and horizontal direction.

A single set of mechanical properties typical of good-quality rock masses in crystalline rocks was selected and kept constant throughout the entire parametric analysis, since the effect of strength parameters on model behavior were already deeply analyzed by Amitrano and Helmstetter [2006] Lacroix and Amitrano [2013] (Cf. subsection 3.1.4 and figs. 3.3, 3.4 and 3.5) for simple rock slopes. In our simulations, imposed parameters roughly correspond to typical values found in gneissic rock type, scaled to equivalent rock mass values with the approach described in subsection 3.4 by imposing GSI values comprised in the interval 65-75. The GSI pseudo-random seed was maintained equal during the entire analysis to eliminate the effect of properties heterogeneity on simulation results, thus every simulation was performed starting from the same mechanical state.

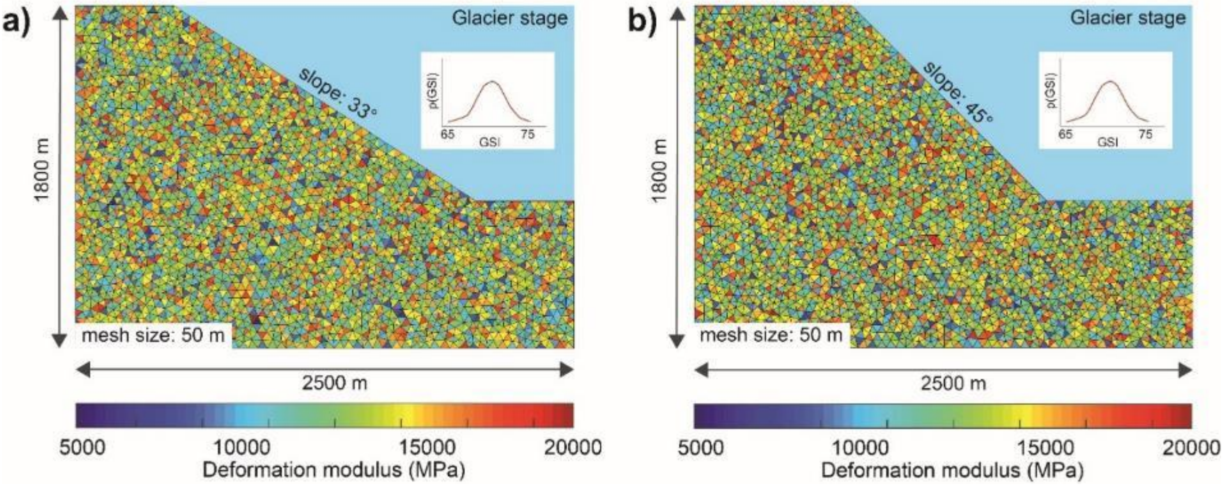

Figure 4.1: Simple slopes investigated in parametric analysis. Slope angle of 33° (a) and 45° (b) were tested maintaining rock mass mechanical parameters and deglaciation boundary conditions constant throughout the entire analysis.

For parametric analysis purpose, we did not scale model physical time into a real time. Initial ice stage for the simulation of deglaciation corresponds to the crest zone (1800 m). Deglaciation starts after 1×10^7 model physical time units from the start of simulation and lasts for further 1×10^7 units since complete slope deglaciation. Mechanical properties and deglaciation parameters are resumed in Table 4.1.

Parameter	Symbol	Unit	Value
Unit Weight	γ	kN/m^3	2700
Young Modulus (intact rock)	E_0	MPa	22700
Tensile strength (rock mass)	T	MPa	1
Cohesion (rock mass)	C	MPa	5.5
Coefficient of internal friction (rock mass)	μ	-	1
Poisson ratio (rock mass)	ν	-	0.4
Rock mass GSI	GSI	-	70±5
Glacier maximum level	H	m a.s.l.	1800
Starting of deglaciation	t_{d0}	yrs	
Deglaciation duration	T_d	yrs	

Table 4.1: Mechanical parameters and deglaciation constraints imposed during parametric analysis.

All the simulations were stopped once the vertical displacement of the slope summit reach 100 m. We observed that this value allows the complete development of landslide mechanisms in most simulations, as lower displacements resulted in incomplete development of instabilities, while higher brought to global slope collapse and excessive deformation of finite element mesh along shear zones. Thus, we supposed that slopes encountered global failure conditions corresponding to this threshold, meanwhile conventionally defining the time needed to reach this stage as “slope failure time”.

Parametric analysis was divided in three following phases: the first one regarded investigation of different mesh sizes, performed to evaluate the influence of Finite-Element dimension on slope geometry and time-dependency of the numerical model. Moreover, it was used to determine a suitable mesh size for the remaining part of the analysis, searching for a compromise between detail of simulation and computational load. The second part focused on the effect of rock mass heterogeneity on slope stability conditions, particularly assuming different distributions and variability of input GSI values. Finally, the third part of analysis comprehended sensitivity analysis on different key parameters including: slope angle, permeable cluster water filling, time-to-failure parameter and damage increment parameter. This resulted in 72 model simulations, whose extended outputs are reported in Annex 1.

4.2 INFLUENCE OF MESH SIZE

Mesh size influence was evaluated in simplified conditions as a preliminary stage in parametric analysis. We decided to investigate only the model set-up with slope angle of 33° (Fig. 4.1a) and value of time-to-failure parameter and damage coefficient respectively equal to 30 and 0.1. Empty permeable clusters were imposed to not include the effect of fluid pressure on calculation. Investigated mesh sizes range from 150 m to 25 m and simulations were performed every 25 meters, thus resulting in 6 different models. Details of performed simulations and results of analysis are reported in Table 4.2 and Figure 4.2. Simulations were performed by a computer equipped with Intel® Xeon® CPU 3.07 GHz, 8 GB RAM and running MATLAB R2015b 64bit.

Mesh size	N° of finite elements	Slope failure time	Calculation time
150	489	2.7×10^{11}	1 min
125	690	5×10^{11}	2 min
100	994	2.7×10^{11}	4 min
75	1903	3×10^{11}	9 min
50	4293	2×10^{11}	45 min
25	17217	1×10^{11}	25 h 30 min

Table 4.2: Number of elements, slope failure time and calculation time obtain for every simulation.

Obtained results show the dependence of the kinematics and thickness of slope instability, degree of damage localization and model lifetime on the mesh size. In particular, a finer mesh (i.e. smaller finite elements) results in the progressive deepening of unstable slope sector and transition from a translational to a roto-translational kinematics of slope instabilities affecting the entire slopes from crest to toe. Major changes in the style and strain localization of slope instability occur among simulations with mesh coarser and finer than 100 m. Coarser mesh size corresponds to more diffuse damage and no or little strain localization, resulting in a high degree of internal slope deformation (Fig. 4.2b and 4.3a). As in elasto-plastic modelling approaches, finer meshes lead to the transition to more localized shear strain, with damage and displacements concentrating in thinner shear zones. This also leads to the development of sharp surface morpho-structures (scarps) as already pointed out by Lacroix and Amitrano (2013) (Fig. 4.2e and 4.3b). In addition, maximum accumulated shear strain values reach more than double values in 25 m mesh (ε_{max}=0.6) with respect to 125 m mesh (ε_{max}=0.25).

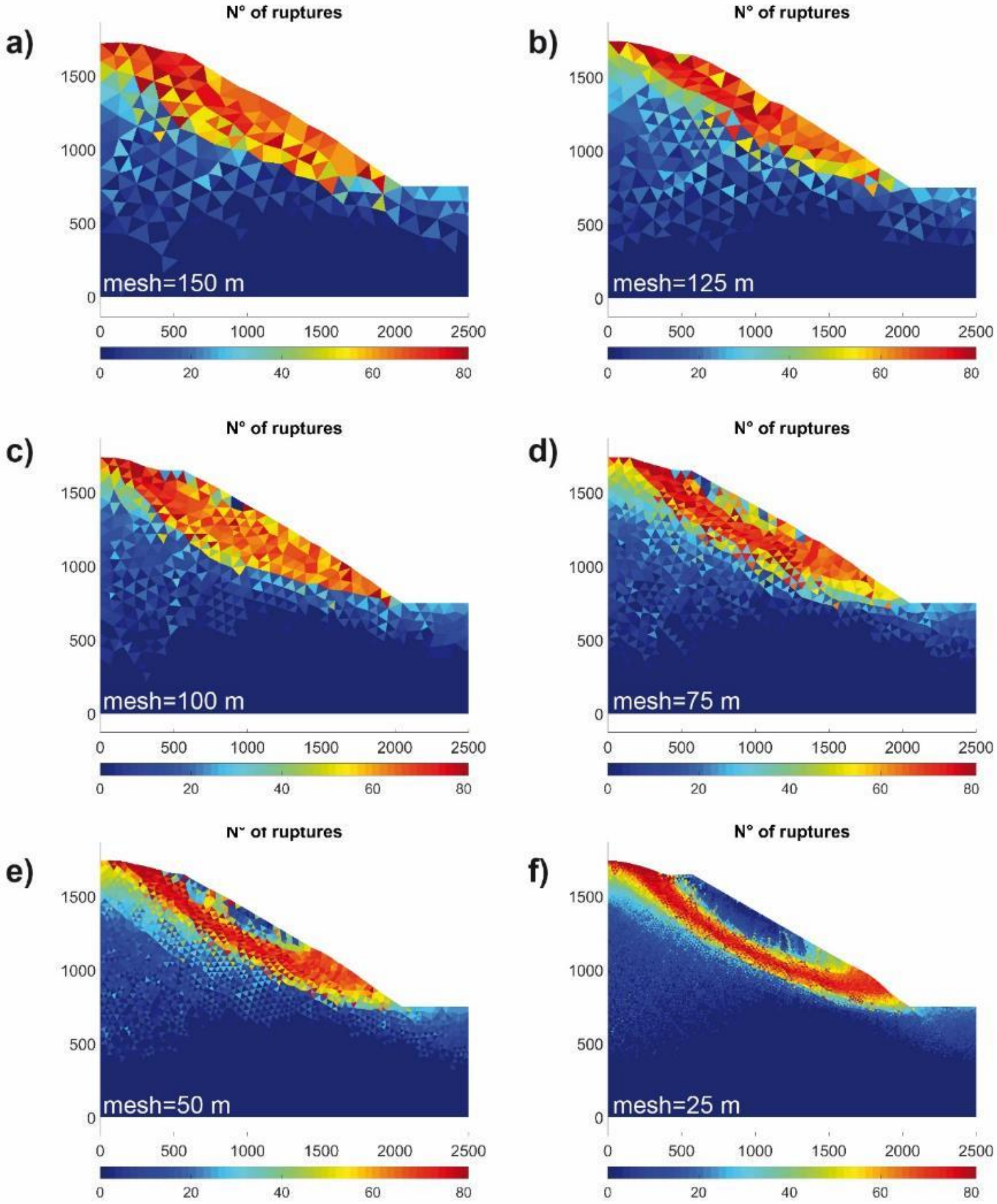

Figure 4.2: Mesh size effect on damage distribution within the slope.

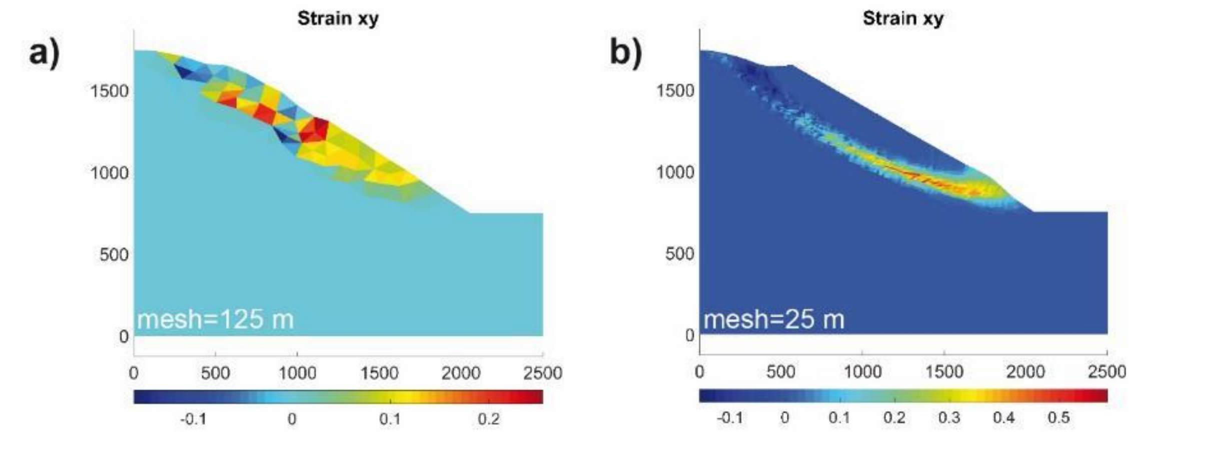

Figure 4.3: Mesh size effect on strain distribution within the slope. In the simulation with mesh size equal to 25 m strain is localized along shear band.

Another key control of mesh size is that exerted on slope lifetime (i.e. the physical time required to accumulate – in this case - 100 m of vertical crest displacement). A clear dependence of the global slope failure time on the mesh size was outlined by the simulations: the slope lifetime progressively shortens as the mesh element size decrease, corresponding to a more brittle and localized failure behavior. However, based on available data on deep-seated landslides, DSGSDs and rockslides, the simulations that better fit the observed behavior are those characterized by mesh size minor than 100 m. Above this threshold, evaluation of slope displacement appears difficult and kinematics simulated by the model differs from what observed on real rock slopes, resulting in unrealistic damage and strain patterns. Based on the results of different simulations and the aforementioned remarks, we decided to use mesh size value of 50 m (2.7% of the model vertical size) for the next part of parametric analysis. This value represents a compromise between modelling details, observed mechanisms and computational efficiency.

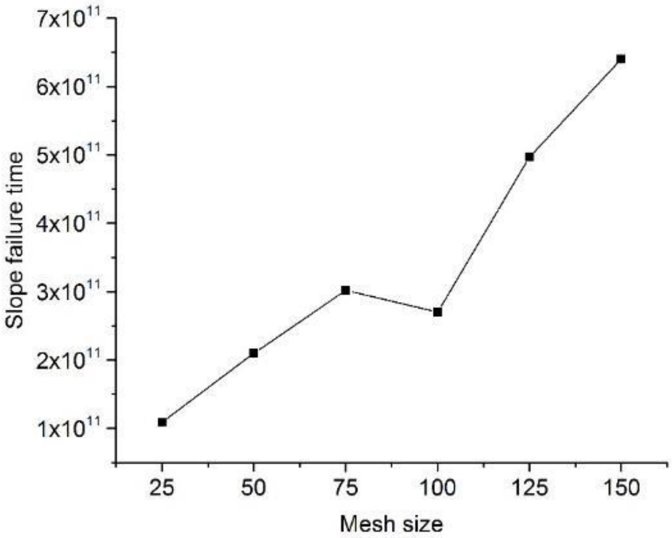

Figure 4.4: Slope failure time for different mesh sizes. Increasing the number of elements within slope domain, slope failure time progressively decrease.

4.3 INFLUENCE OF ROCK MASS HETEROGENEITY

Real slopes are constituted by heterogeneous rock mass, which locally influences the slope in terms of changing strength and mechanical properties: to assess the effect of such variability on the global slope behavior, we performed a model run characterized by different ranges of input GSI values. Heterogeneity was reproduced recurring to different probability density functions, respectively normal and uniform (rectangular). Moreover, for each analyzed distribution, we tested three different degree of heterogeneity. Starting for a mean GSI value of 65, we generated normal distributions by varying the standard deviation (σ=2, σ=5 and σ=10) and uniform distributions varying the minimum and maximum values (mean value ±2, ±5 and ±10) (Fig. 4.5). The other model boundary conditions and mechanical properties were maintained constant in respect to figure 4.1 and table 4.1, while the mesh size was established in 50m.

Performed simulations show minor differences regarding slope kinematics, damage distribution and depth of basal shear band (Fig. 4.6). The simulations with GSI normal distribution (Fig. 4.6a, b, c) and GSI uniform distribution (Fig. 4.6d, e, f) resulted in a rototranslational rockslides affecting the entire slope, with minor strain and damage within unstable body and basal shear band localized in the upper slope and progressively widening moving downvalley. The effect of rock mass heterogeneity slightly affect damage pattern, resulting only in minor variations within the rockslide body and in deep elements, more damaged for higher variability in input parameters. Notably, negligible changes occur switching between normal and uniform distributions.

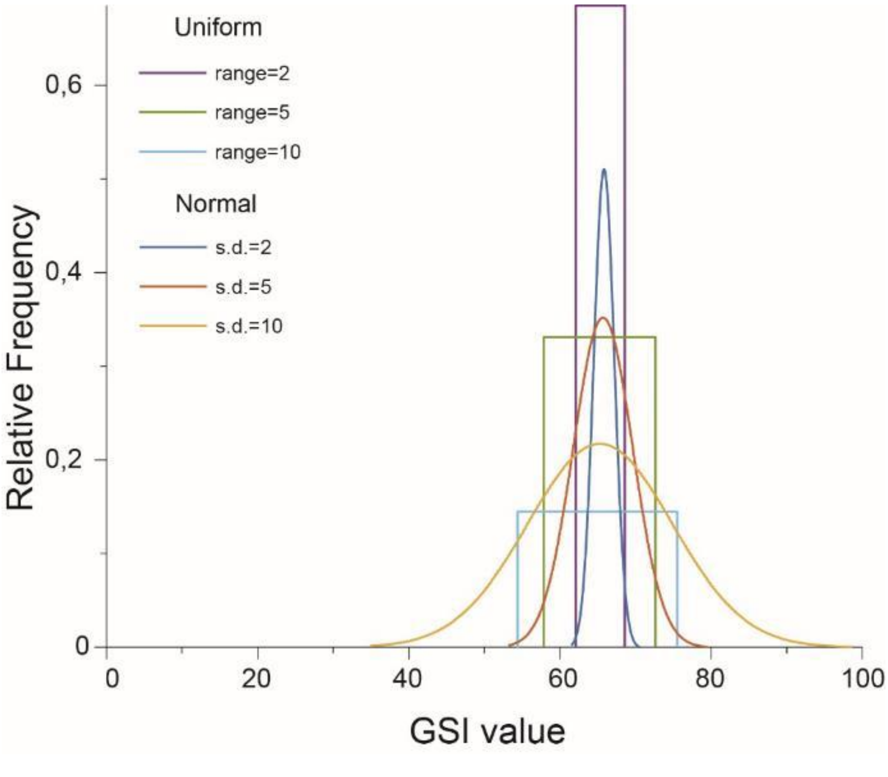

Figure 4.5: Different GSI distributions tested for assess the heterogeneity effect on slope behavior

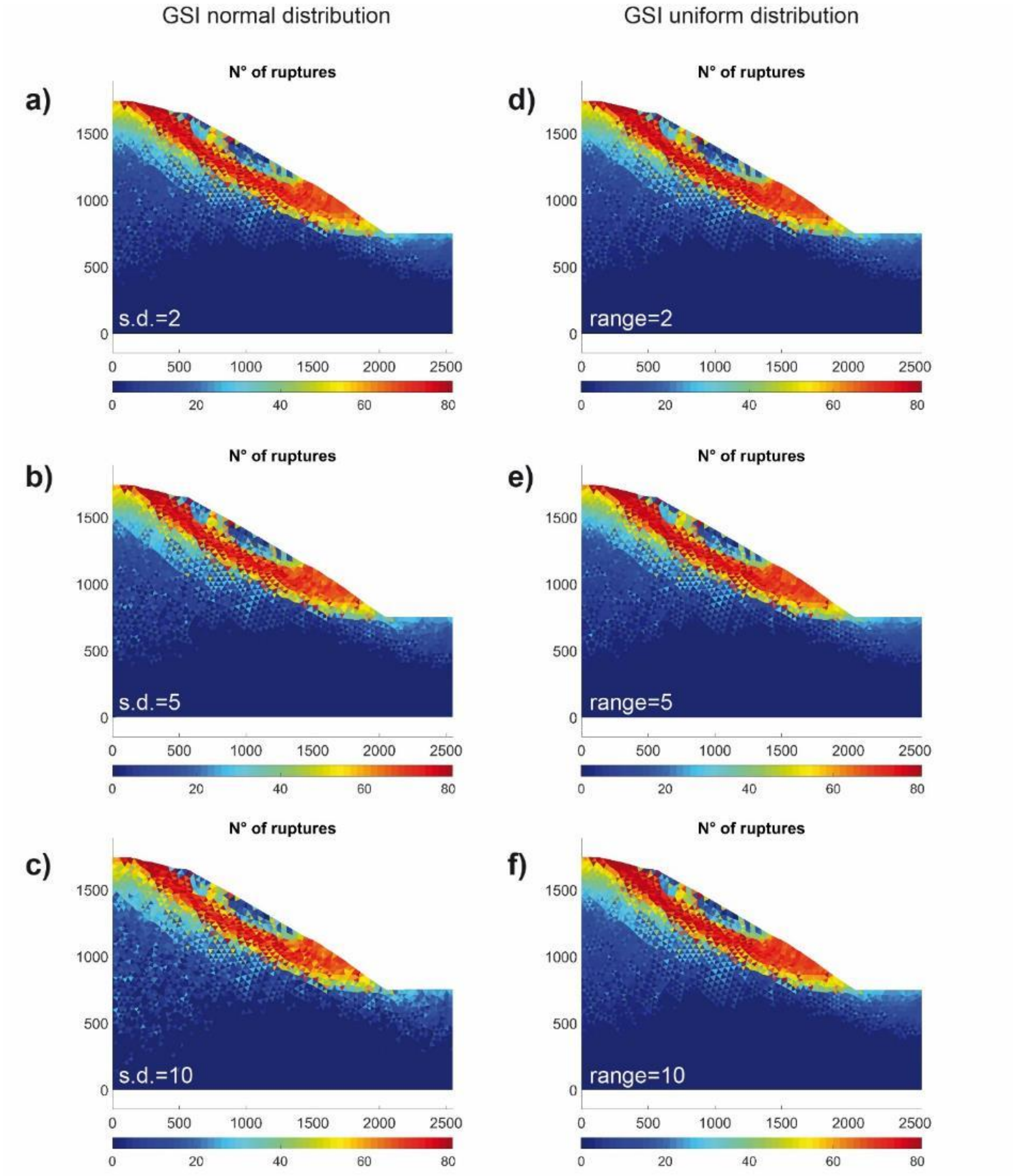

Figure 4.6: Final damage pattern for simulations with varying rock mass heterogeneity. The slope kinematics and the damage distribution are poorly affected by variations in initial GSI distribution.

Regarding the time component, the general slope behavior through time is coherent in all the simulations performed, even if variations in slope failure time occurred (Fig. 4.7). With low GSI variability, the slope failure time is very similar between the normal and uniform distributions tested, with variations comprised in 2.5% of the entire slope lifecycle. Moving to higher values, respectively σ=10 in normal distribution and range of ±10 in uniform distribution, departure from the aforementioned trend is observed. Shorter slope failure time is simulated for uniform distribution, while for the normal distribution the opposite behavior is observed, testified by the longer time to reach the threshold value of 100 m vertical displacement.

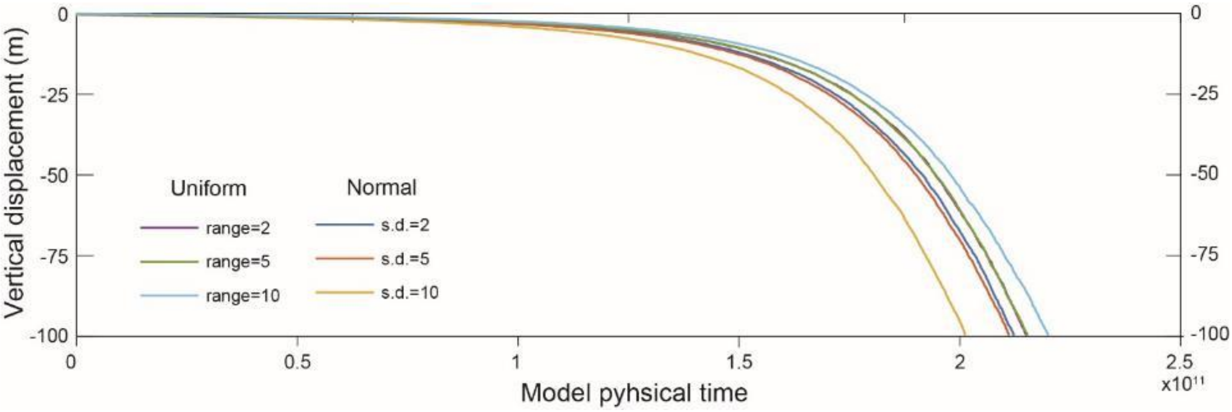

Figure 4.7: Time versus vertical crest displacement for the performed simulations. Although the general slope trend is maintained, variations in slope failure time were registered.

4.4 INFLUENCE OF SLOPE ANGLE

Slope angle depends on rock type, strength and inherited morphogenetic processes and, in combination with slope geometry (relief, curvature etc.), rock mass properties, structure and hydrological processes is an important control on the mechanisms of rock slope failure. For parametric analysis, we decided to test two different profiles, characterized respectively by 33° and 45° of slope angle with the same mechanical properties reported in table 4.1, to quantify the effect on instability development, geometry, timing and damage pattern.

Simulations with slope angle of 33° are characterized by shallower instabilities ranging from crest to toe, often with a dominant translational kinematics (Fig. 4.8a). Steeper slopes result in deeper and more curved basal shear bands, frequently suspended over the valley bottom (Fig. 4.8b). In both cases, most damage occur along the basal shear band, which for both tested slope angles underlie a less damaged rock mass. Damage extends below the unstable rock mass in both tested profiles, and reach deeper for models with 33° slope. Strain distribution accurately follow the damage pattern, reaching maximum values along the basal shear band, even if weak traces of forming secondary scarps and counterscarps are encountered in both set-ups in the middle slope sector (Figs. 4.8c, d). Slope surface appears more deformed for slope angles equal to 45°, while for simulations with 33° mainly consists in slope summit lowering and bulging at toe.

Regarding time spent to reach slope failure, a difference of almost 2 orders of magnitude exists between the two tested profiles: models with 45° slope develops instability much more rapidly under the same mechanical and creep conditions, thus proving the influence of slope angle on progressive rupture and long-term slope stability. Interestingly, the vertical displacement trend is similar, consisting in a slow and progressive acceleration until shear band is completely formed and slope failure is encountered (Figs. 4.8e, f).

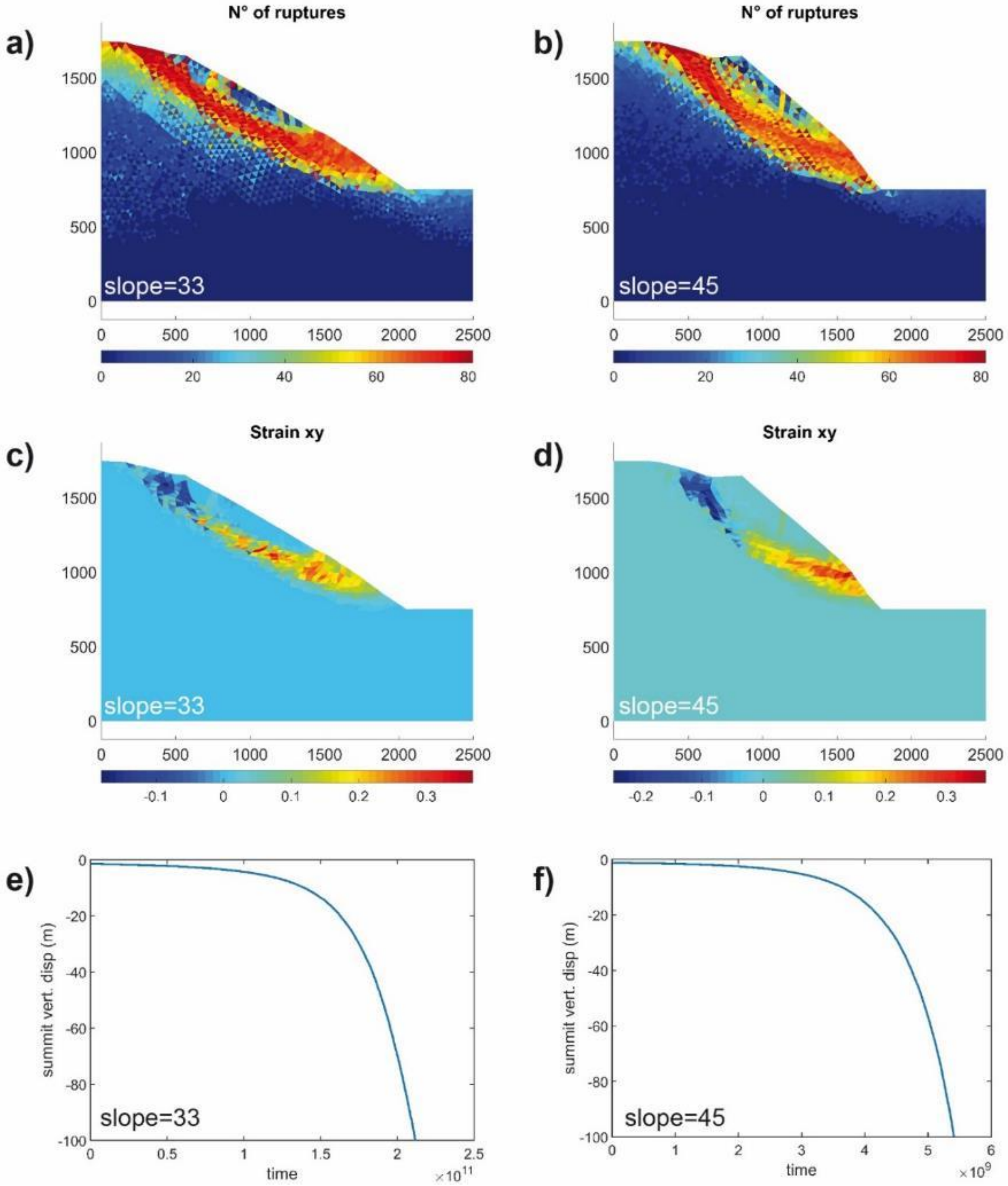

Figure 4.8: Variations induced by slope angle on damage distribution (a and b), shear strain (c and d) and trend of summit vertical displacement (e and f). Simulations were performed with b=30, w=0 and D=0.1.

4.5 INFLUENCE OF WATER (AMOUNT OF PERMEABLE CLUSTER FILLING)

Based on the approach described in chapter 4, DaDyn-RS has the capability to account for damage-dependent pore pressure distribution (and related hydro-mechanical coupling effects) in a simplified way. Fluid pressure application, besides the conditions assumed to its application (i.e. damage, dilatancy and surface connection), depends only on one input parameter, the permeable cluster filling. Cluster filling can range from 0 (clusters completely empty, i.e "dry" conditions) to 1 (clusters completely filled). We decided to test the model for dry conditions and for three different degrees of filling: 0.25, 0.5 and 0.75. The complete filling condition (w=1) was excluded from this analysis, as it is an unlikely condition and excessively severe condition for real rock slopes, especially in a long-term development perspective.

As expected, also in DaDyn-RS fluid pressure proved to have a major influence on simulations results. The kinematics and geometry of slope instability is deeply affected by changes in fluid pressure and substantial differences can be observed with respect to "dry" simulations. For a given slope slope angle and set of mechanical properties, dry models are characterized by deeper instabilities, more localizd damage and more curved basal shear zones with respect to models with fluid pressures accounted for. (Figs. 4.9a,b and 4.10a,b). These are characterized by shallower and more roto-translational rockslide mechanisms, more similar to the commonly observed real patterns of slope instability (Figs. 4.9b, c, d and 4.10b, c, d). Also strain and damage patterns experienced great difference between "dry" and "wet" simulations: when fluid pressure is taken into account, more strain is accumulated along shear bands but also within unstable masses, as it results from the comparison between simulations with increasing cluster filling (Figs. 4.9e, f, g, h). Models with fluid pressures are characterized by more diffused damage, and the amount of permeable cluster filling resulted a major control on the damage pattern (diffuse vs localized). This also has a significant impact on the topographic evidence of rock slope instability: while "dry" topography is rigidly lowered except from little bulging at toe, applying a value of w=0.75 results in hummocky slope profile, with major deformation localized in upper portion (Figs. 4.9d and 4.10d). All these consideration are supported by the observation of damage pattern, that is concentrated along shear bands in dry simulations to became widespread in the entire slopes as a consequence of fluid pressure occurrence. Moreover, in wet simulations the entire unstable body experience great damage from surface to basal shear band, caused by the progressive growth and deepening of slope groundwater system. The test of different cluster filling degrees permitted also to infer that major changes in damage pattern regard the transition from dry to wet simulations, while for different values of w variations occur, but with minor intensity.

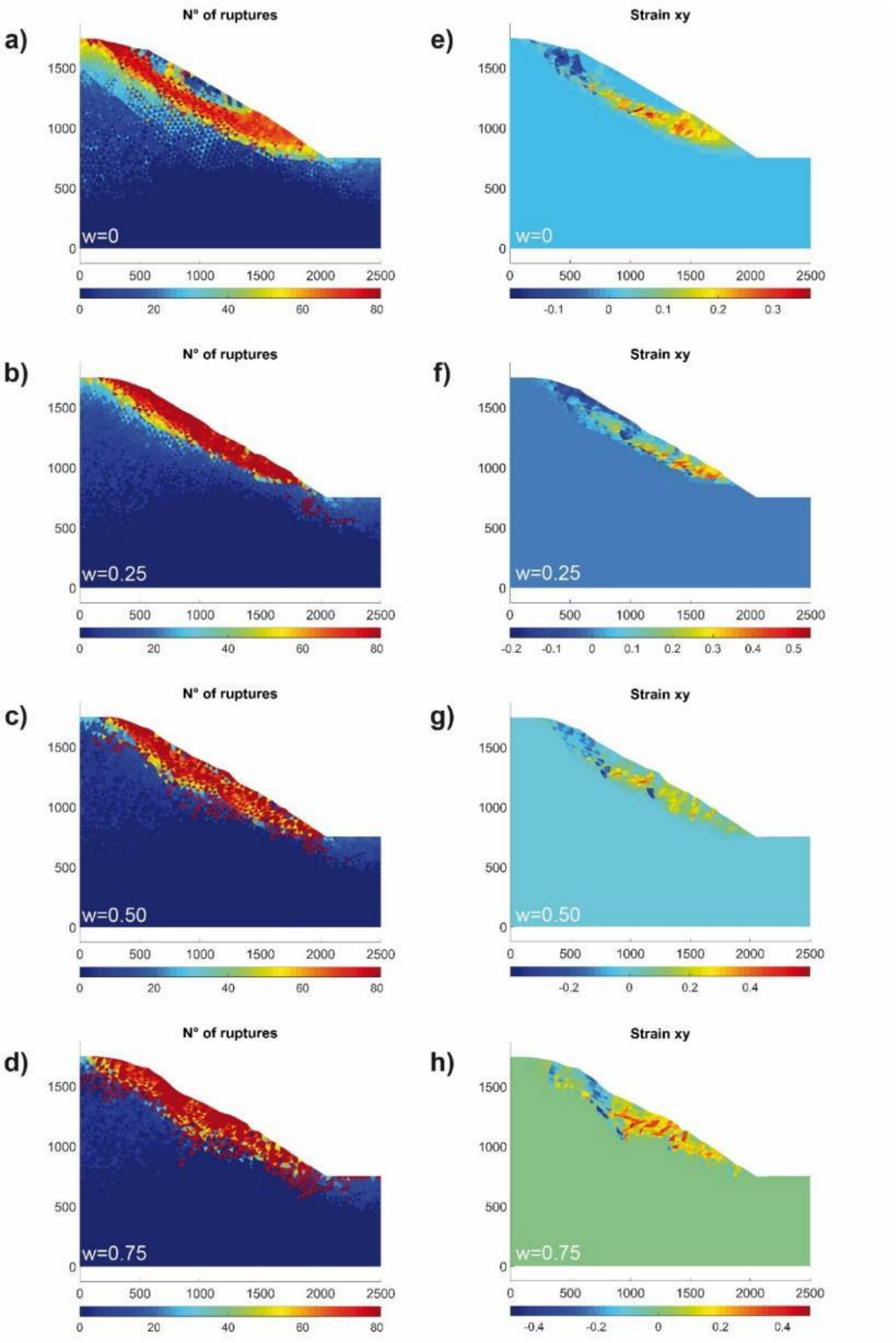

Figure 4.9: Effects of different cluster fillings on the damage and strain distribution for w=0 (a and e), w=0.25 (b and f), w=0.5 (c and g) and w=0.75 (d and h). Models were performed with slope=33°, b=30, and D=0.1.

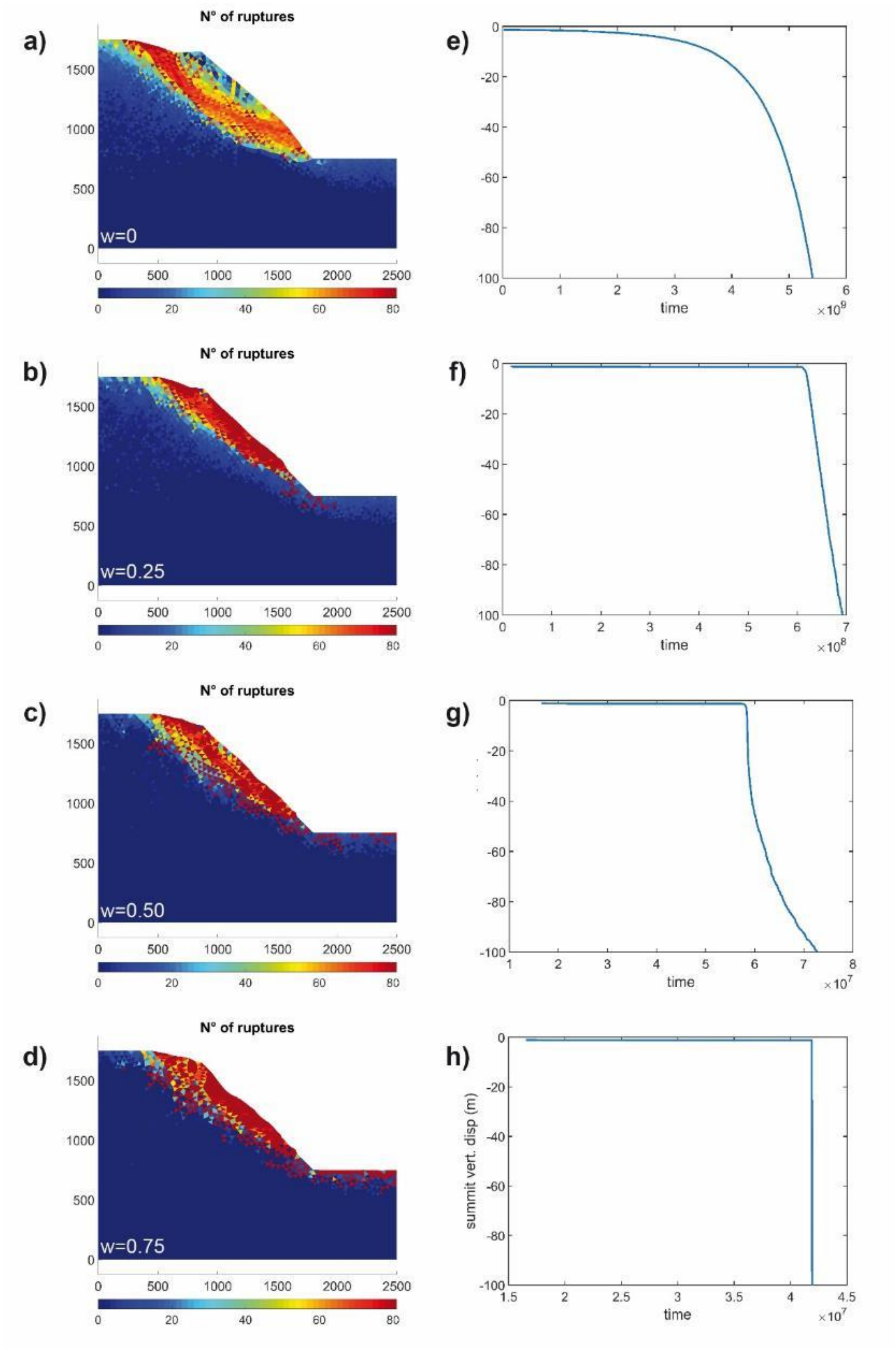

Figure 4.10 Effects of different cluster fillings on the damage pattern and summit displacement trend for w=0 (a and e), w=0.25 (b and f), w=0.5 (c and g) and w=0.75 (d and h).Models were performed with slope=45°, b=30, and D=0.1.

Accounting for damage-dependent fuid pressure occurrence has also a major impact on the time-dependent behaviour of simulated slopes (total lifetime and temporal patterns of displacements) . Water influences slope evolution by strongly shortening the slope life cycle: introducing a cluster filling of 0.25 results in the reduction of slope failure time by one order of magnitude (Figs. 4.10e, f and 4.11). Cluster filling degrees of 0.5 and 0.75 induce further shortening, up to more than two orders of magnitude.. Fluid pressure occurrence can also influence the displacement trend of the slope, which for dry simulations is expressed by a smooth and progressive acceleration since tertiary creep phase is reached (Fig. 4.10e). Increasing w to 0.25 results in a complete different behavior, consisting in a long quasi-steady state phase followed by an abrupt acceleration and consequent delayed slope collapse (Fig. 4.10f). Cluster filling of 0.5 exhibits a shorter steady-state phase, followed by an abrupt acceleration and a progressive deceleration of displacement rate at summit (Fig. 4.10g). Finally the model with the higher value of cluster filling (0.75) is characterized by an instantaneous and delayed catastrophic collapse, which abruptly occurs without notable cumulated displacements just after the end of deglaciation phase (Fig. 4.10h). The progressive increase of cluster filling parameter results in exponential decrease of slope failure time (Fig. 4.11) since values of w=0.50. Then, fluid pressure effect is mitigated for w=0.75, where a trend decrease is observed in both tested profiles. Models with slope angle equal to 45° exhibit more sensitivity to fluid pressure occurrence, especially for high cluster filling degree (Fig. 4.11), where a higher reduction of life cycle is registered in respect to similations with slope of 33°.

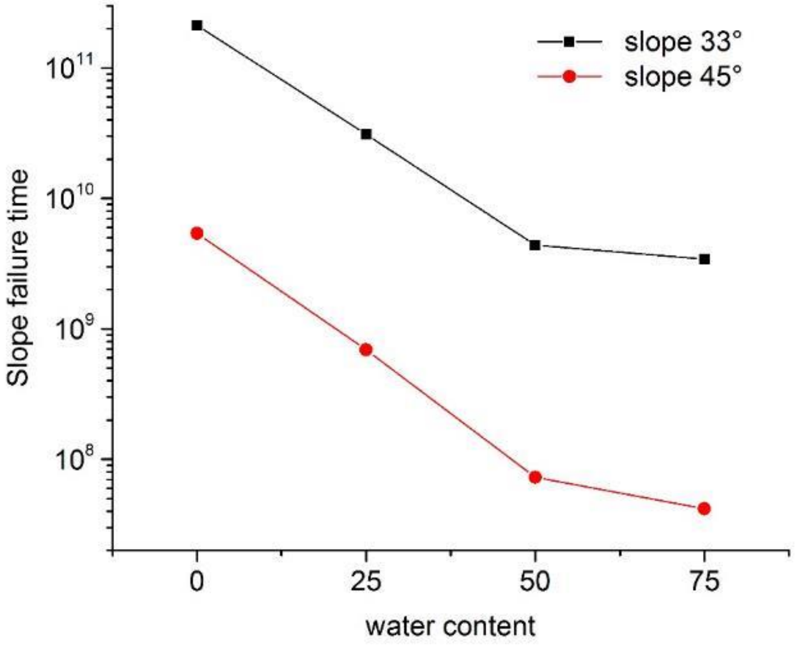

Figure 4.11: Effects of w on slope failure time for simulations with slope angle of 33° and 45°. Simulations were performed with b=30 and D=0.1.

4.6 INFLUENCE OF TIME-TO-FAILURE PARAMETERS

Time dependency within Dadyn-RS is mainly controlled by a time-to-failure law (subsection 3.2), which is a function of applied stress, instantaneous (peak) strength and the parameter *b*. As previously explained, typical *b* values for different intact rock types were derived by Amitrano and Helmstetter (2006) from experimental data (creep tests), whereas no experimental measurements are available to describe time-dependent behavior of fractured rock masses. Nevertheless, sensitivity analysis performed on *b* resulted in the exponential increase of time-to-failure for linear increase in such parameter (Fig3.3c; Lacroix and Amitrano, 2013). In order to get insights on the influence of *b* on the simulated behavior of large slopes in rock masses, we performed a parametric analysis using three different values of *b* (15, 30 and 45), which are in the range commonly observed for intact rocks.

Simulations show that increasing *b* values result in deeper rock slope instability, also influencing the occurrence and thickness of a less damaged unstable body (Fig. 4.12). This effect is more evident in “dry” models, whereas in simulations with fluid pressures it is overcome by the controls of damage-dependent pore pressures on damage patterns and the mechanisms of instability. In addition, lower value of *b* results in instabilities suspended on the valley bottom (Fig. 4.12a, b) while highest values results in the complete involvement of the slope, form crest to toe (Fig. 4.12e, f). Regarding damage and strain pattern, no major changes are encountered in simulations with b=30 and b=45, while for b=15 significant changes in unstable volume occur (Figs 4.12 c, d, e, f).

As *b* is the parameter that controls time-to-failure law, model time-dependency is strongly sensitive to variation of this input, resulting in a nonlinear increase of global slope failure time for linear increases of *b* (Figs. 4.13 and 4.14). For the same model set-up, increase of parameter *b* from 15 to 45 results in time increase up to 6 orders of magnitude for reaching 100 m of slope summit downthrown.

Also vertical crest displacement trend is affected by imposed value of b (Fig. 4.13). For the simulation with b=15 (Fig. 4.13a), the summit underwent a stage of quasi-steady displacement, followed by a quite abrupt acceleration and consequent collapse immediately after slope deglaciation. However, due to the different geometry of instability and its timing, a comparison with the other parametric simulations might be not reasonable. Otherwise, simulation with b=30 and b=45 (Fig. 4.13 b and c), despite the similar geometrical expression on slope, exhibit a slightly different displacement trend, particularly consisting in a smoother acceleration phase for the simulation with b=30.

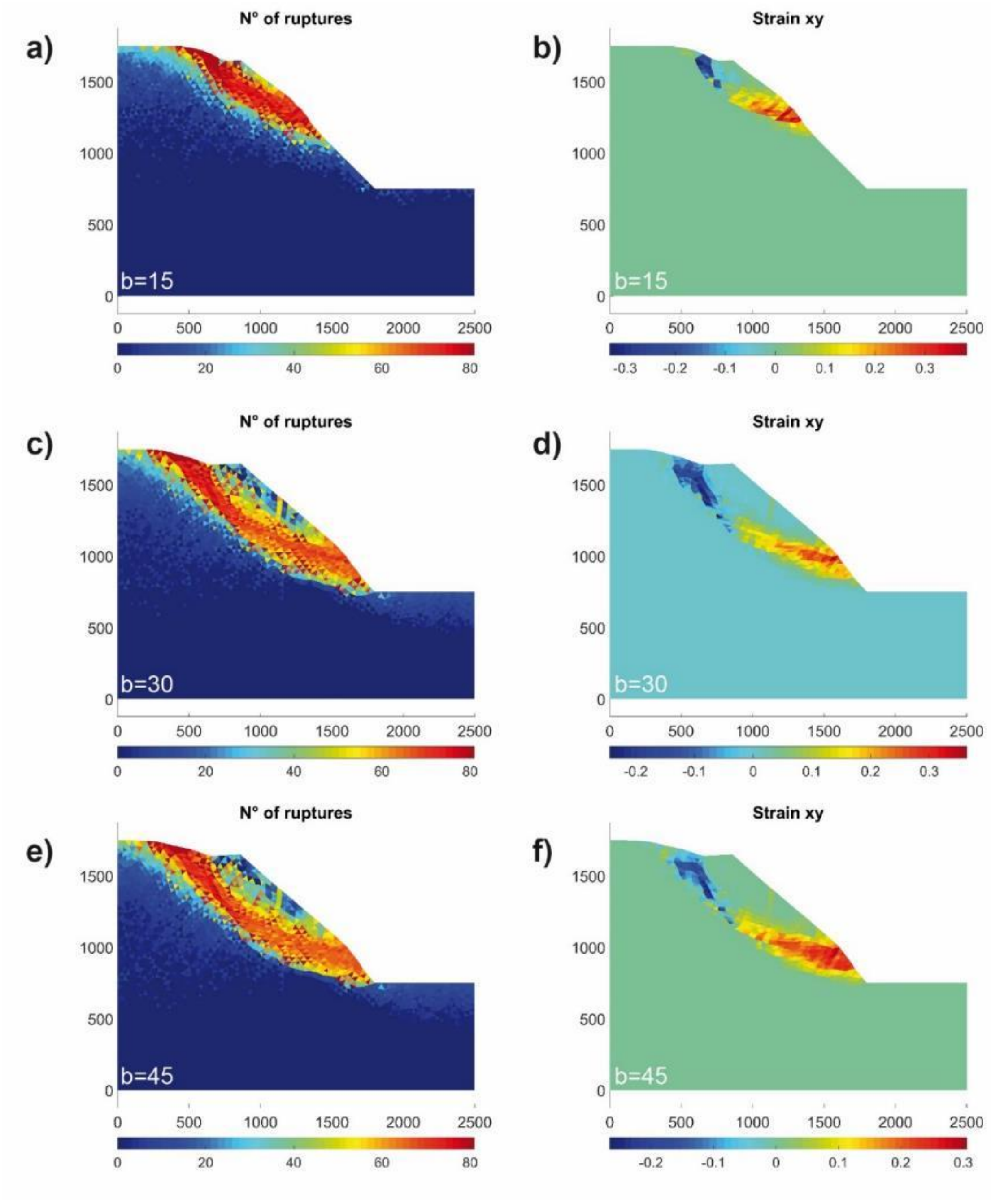

Figure 4.12: Effects of different values of time-to-failure parameter on the damage and strain distribution for b=15 (a and b), b=30 (c and d), b=45 (e and f). Models were performed with slope=45°, w=0 and D=0.1.

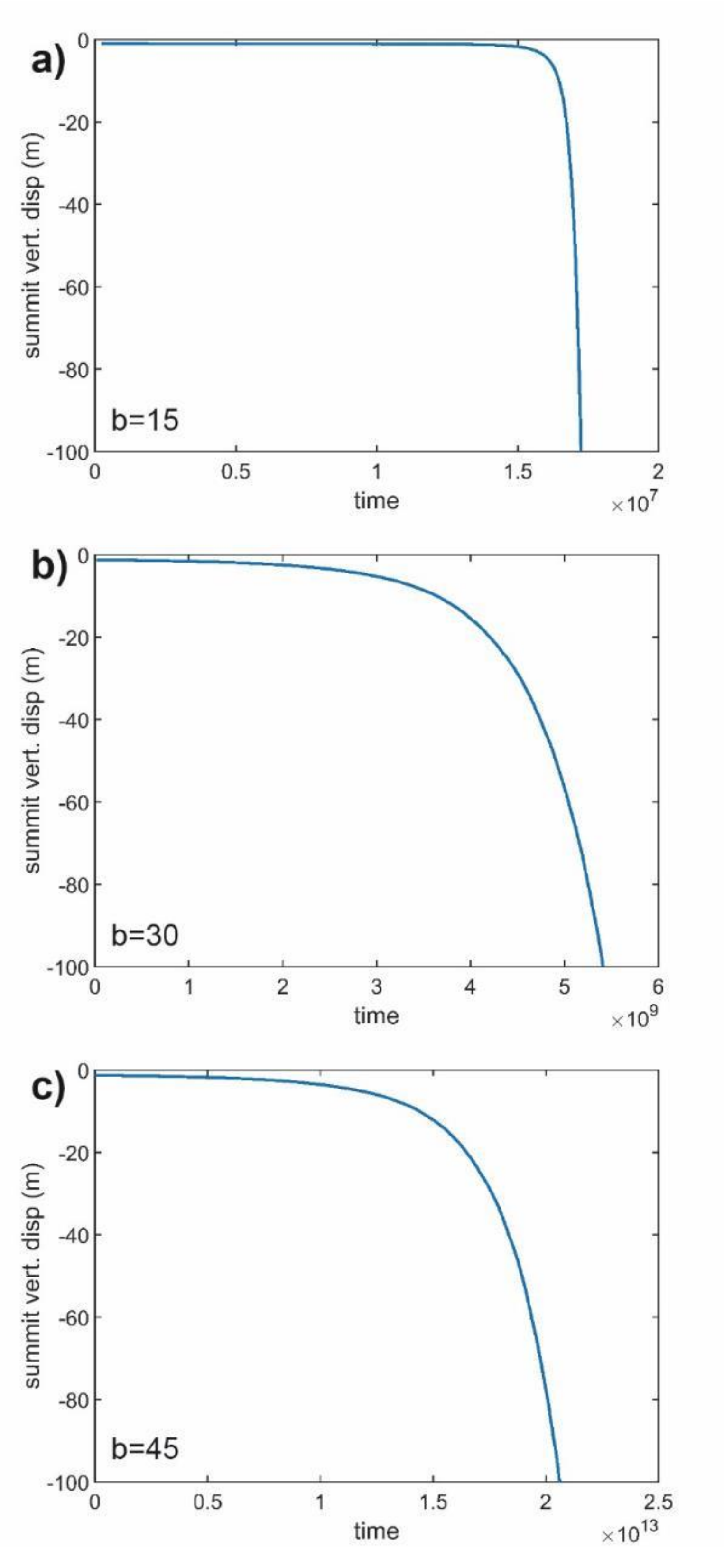

Figure 4.13: Effects of different time-to-failure parameter on the summit displacement trend. Models were performed with slope=45°, w=0 and D=0.1

The effect of the time-to-failure parameter *b* was evaluated also on simulation with or without fluid pressure occurrence. Comparing models with *w*=0 to simulations with half-filled permeable clusters (*w*=0.5), “wet” conditions resulted in shorter slope failure times, testifying increased slope sensitivity to variations in time to failure parameter. An exception is represented for b=15, as the unfavorably conditions for fluid pressure occurrence and the low slope lifecycle avoided the development of permeable clusters. This resulted in substantially “dry” conditions, testified by the equal timing in respect to simulation not accounting for damage-based fluid pressure (Fig. 4.14).

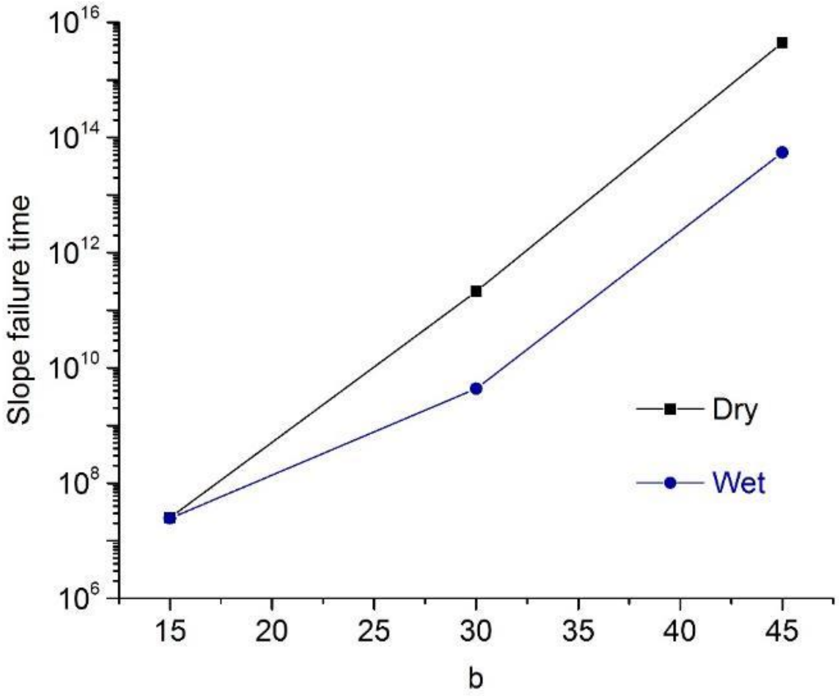

Figure 4.14: Effects of b on slope failure time for simulation without and with damage-based fluid pressure. Simulations were performed with slope=33°, D=0.1 and permeable cluster filling equal to 0 (Dry) and 0.5 (Wet).

4.7 INFLUENCE OF DAMAGE INCREMENT PARAMETER

The damage increment parameter D modulate the decrease of the deformation modulus E occurring at each damage event which occurs in a model finite element (and the related cumulative effects). D is a macroscopic proxy of incremental damage (e.g. incremental increase of crack density) in a continuum damage mechanics framework. Low values of D results into a more progressive fracturing behavior, while higher D results in a "coarser" discretization of the element path to brittle failure, resulting in a more abrupt brittle failure behaviour. We performed simulations for three different values of D, namely 0.05, 0.1 and 0.15. For each of these values, a different maximum number of ruptures per single element was imposed, to avoid unrealistically low deformation modulus in severely damaged elements. The imposed threshold corresponds to value typically observed in completely crushed and destructured rock mass (i.e. cataclastic breccia layers often observed in shear zones).

For D=0.05, the model reproduced a transitional slope behavior, characterized by diffused damage, low strain and limited damage localization (Fig. 4.15a, b). Moreover, damage extends well below the main shear band, especially in slopes with 33° (Fig. 4.16a) while in models with slope angle of 45° this effect is mitigated. Simulations with 0.15 are much more brittle, with marked damage localization and shallower basal shear bands (Figs. 4.15e, f and 4.16e). Surrounding unstable rock mass is characterized by intact or poorly damaged rock mass moving on basal shear band, along which the majority of strain is concentrated, reaching a double maximum value in respect to simulation with D=0.05.

The time-dependent behaviour of the models is also affected by D. Low values of D results into lower acceleration of the displacement-time curve at slope crest, meanwhile taking more time to reach slope failure (Figs. 4.16a, b and 4.17). Increasing to D=0.1 and then D=0.15 makes the slope behavior more "brittle", with a stage of low displacement rate followed by an abrupt non-linear acceleration stage leading to slope collapse. The abruptness of this transition is regulated by the value of D (Figs. 4.16c, d, e, f). Comparison between dry and wet simulations exhibited a major sensitivity to variation in D from models without fluid pressure occurrence, which registered higher decrease of slope failure time in response to increase of damage increment parameter (Fig. 4.17).

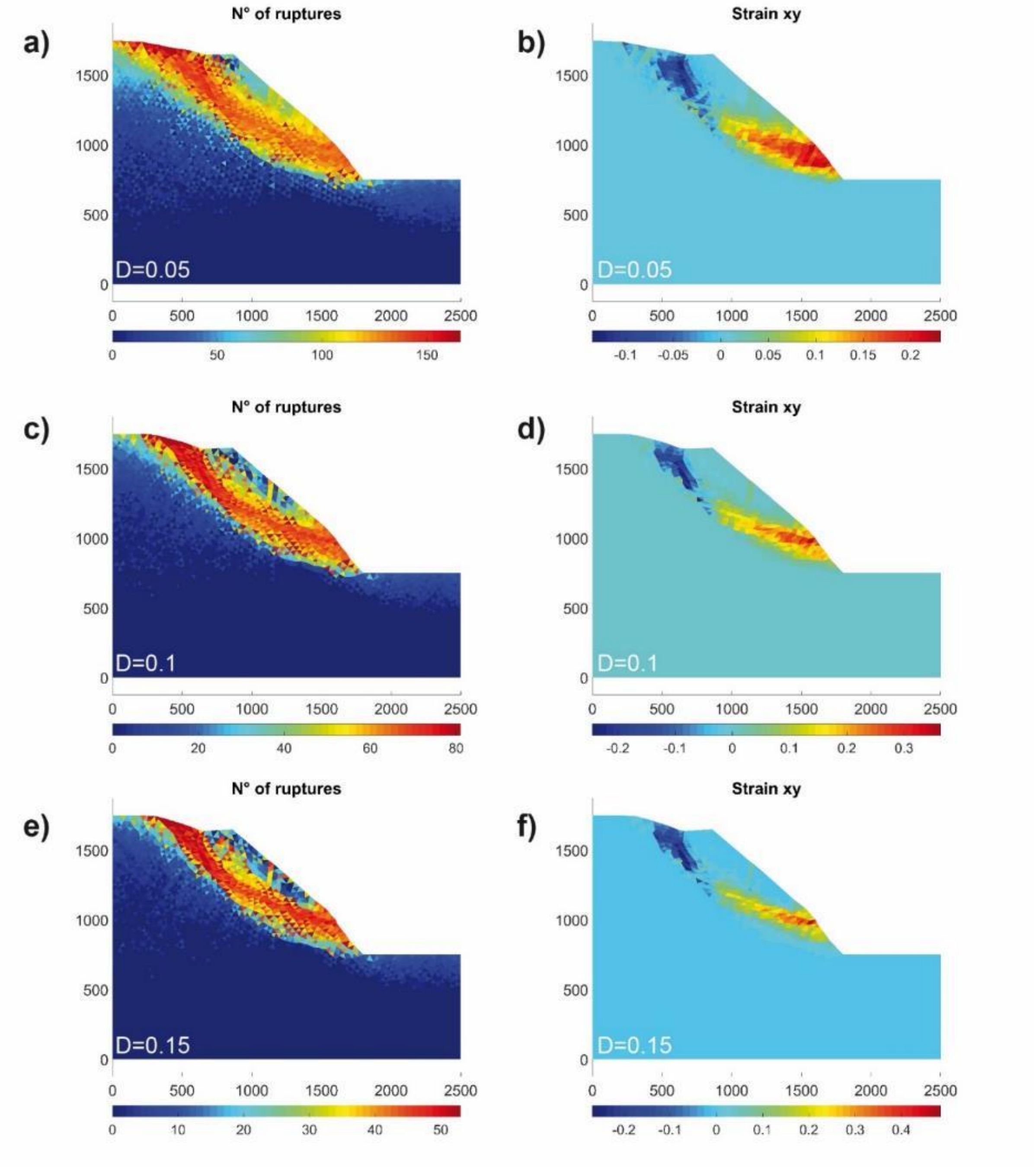

Figure 4.15: Effects of different values of damage increment parameter on the damage and strain distribution for D=0.05 (a and b), D=0.1 (c and d), D=0.15 (e and f). Models were performed with slope=45°, b=30 and w=0.

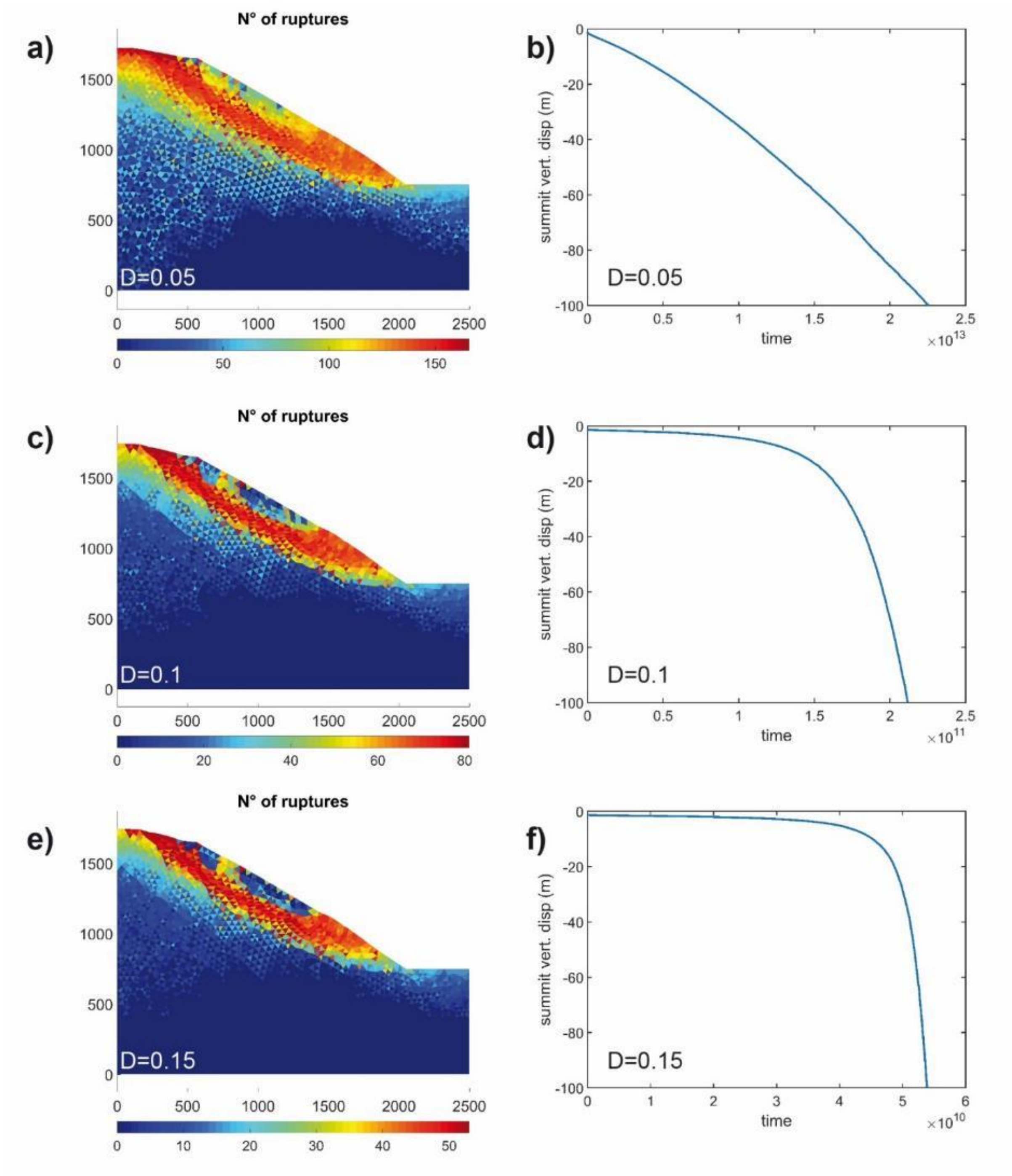

Figure 4.16: Effects of damage increment parameter on the damage pattern and summit displacement trend for D=0.05 (a and b), D=0.1 (c and d), D=0.15 (e and f).

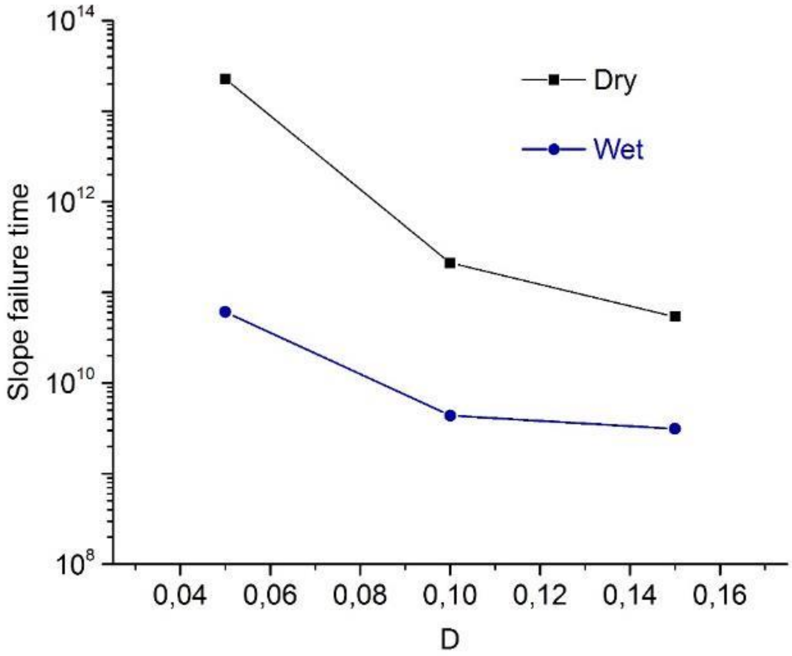

Figure 4.17: Effects of D on slope failure time for simulation without and with damage-based fluid pressure. Models were performed with slope=33°, b=30 and permeable cluster filling equal to 0 (Dry) and 0.5 (Wet).

4.8 SUMMARY AND CONCLUDING REMARKS

We carried out a parametric analysis of the sensitivity of DaDyn-RS to the main inputs parameters.Time-to-failure parameter (*b*) and cluster filling degree (*w*) are the variables that majorly influence model time-dependency and slope kinematics. Linear increase of b resulted in the exponential increase of slope failure time, exhibiting the strongest sensitivity in comparison to the other parameters analyzed (Figs. 4.18 and 4.19). Regarding cluster filling, the application of damage-dependent fluid pressure under the same model setup, takes differences in slope failure time up to 4 orders of magnitude between "dry" and "wet" simulations (Figs. 4.18 and 4.20). However, from comparison through 3D plots, is evident how this effect is subordinate in respect to the influence of time-to-failure parameter (Fig. 4.18). Regarding damage increment parameter, the strong influence on spatial distribution of damage is clear, as *D* controls the occurrence of localized or diffused patterns within the slope (Fig. 4.16). Moreover, its effect was also recognized regarding slope failure time, especially for dry conditions (Fig. 4.20), while introducing damage-dependent fluid pressure results in a minor effect.

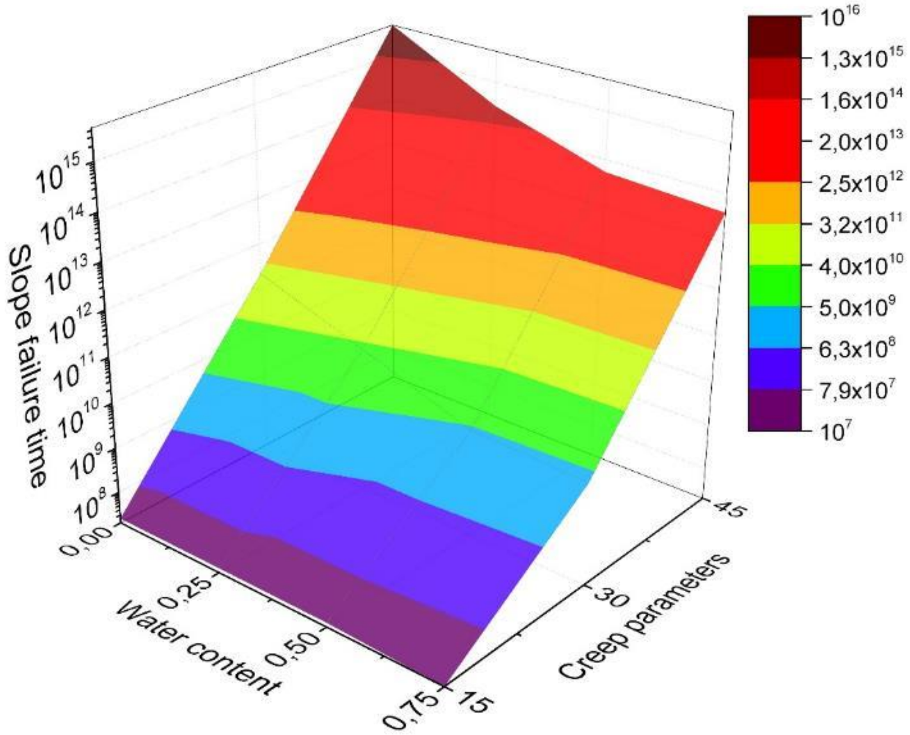

Figure 4.18: Three-dimensional plot representing the mutual influence of cluster filling parameter and time-to-failure parameter on slope failure time.

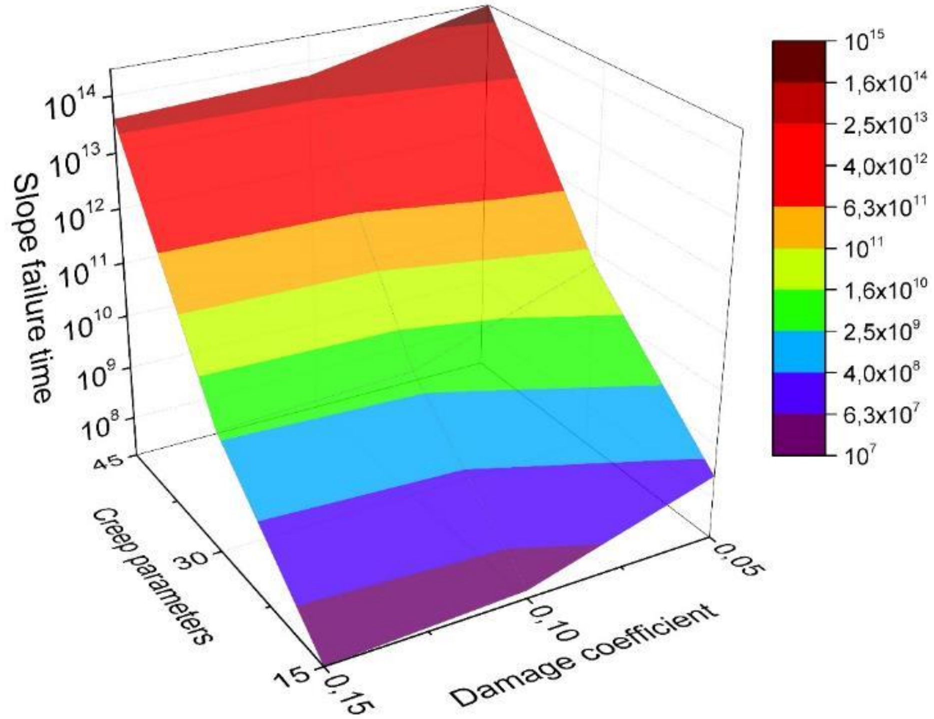

Figure 4.19: Three-dimensional plot representing the mutual influence of damage increment parameter and time-to-failure parameter on slope failure time.

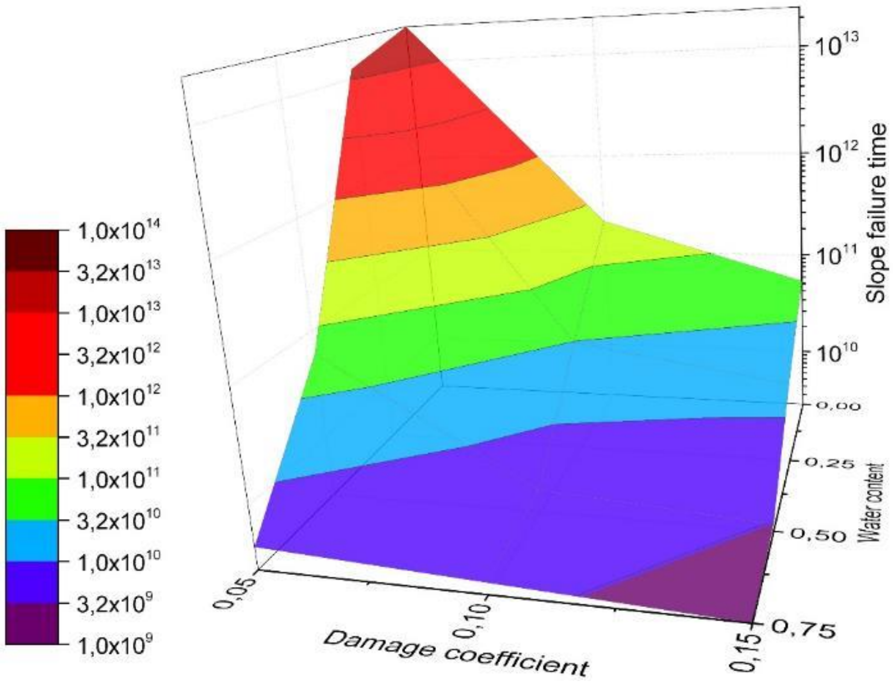

Figure 4.20: Three-dimensional plot representing the mutual influence of cluster filling parameter and damage increment parameter on slope failure time.

However, from the results of the parametric analysis seems that the simulations better resembling kinematics, damage distribution and timing observed on real slopes come from values of *D* and *b* of the same order of magnitude of those calibrated for laboratory application [Amitrano and Helmstetter, 2006]. Using these sets of parameter, balance between localization along basal shear band and diffused damage within the unstable rock mass are obtained, as reported from deep investigations on large rockslides and DSGSDs. This suggests that, for brittle rocks (e.g. granitoids, gneiss), no significant upscaling of *D* and *b* could be required for practical applications. The introduction of damage-dependent fluid pressure occurrence gave the chance to test its long-term effect on slope stability. Water has a major role in determining landslide geometry, particularly by strongly enhancing damage and deformation within unstable body. A clear effect of fluid pressure is also recognized on timing, with higher cluster filling degrees corresponding to shorter slope failure times. This prove the role of slope groundwater circulation in conditioning slope evolution in both short and long term evolution, providing also interesting constraints on the evaluation of both damage and strain pattern.

DaDyn-RS proved the ability to completely reproduce the typical case studies commonly encountered in real alpine environment. Collapse during or just after deglaciation is simulated particularly for weak rock masses and steep slopes (Fig. 4.12a,b), resulting in perched rototranslational rockslides triggered by slope debuttressing. Delayed catastrophic collapse is ascribed mainly to damage coalescence along basal shear band, which can occur long time after slope deglaciation and with different acceleration magnitudes. In our simulations fluid pressure seems to have a major role in determining such type of instability (Fig. 4.10). Long-term progressive creep without catastrophic failure is encountered particularly for non steep slopes with little water occurrence (Fig. 4.16a,b), being expressed by smooth and progressive movement downslope and ductile deformation and damage within the unstable body. In particular cases, such as simulations with low cluster filling degree and good mechanical properties, slopes require an extremely long time to reach failure. This can be compared to a regression phases, pointing out potential slope stability in long-term conditions (Fig. 4.12e and 4.13c). Results of parametric analysis gave interesting insights in the model behavior, provide test for new components introduced and permitted to evaluate the model sensitivity to the different input parameters. This results are extremely useful as could permit methodological constraints for the application of the model to real case studies.

5 THE SPRIANA ROCKSLIDE

5.1 GEOLOGICAL AND GEOMORPHOLOGICAL SETTINGS

The Spriana rock slope is located on the left flank of lower Val Malenco (Valtellina, Italian Central Alps) and range in elevation from 550 to 1800 m a.s.l. with a regular profile characterized by mean slope of 37°. The area is mainly constituted by granitic to granodioritic gneiss belonging to the “Monte Canale” tectono-metamorphic unit (Austroalpine Bernina Nappe) which experienced greenschist facies metamorphism and ductile deformation during both Variscan and Alpine orogenic cycles, although to the Alpine overprint was limited (Trommsdorf et al., 2005). Regarding mineralogical composition, quartz (30%-40%) and plagioclase (35%-45%) are the main components of this rock, that locally tends to schist composition due to increase in chlorite and white mica, while the rock fabric is characterized by a well-developed layering between quartz, plagioclase and K-feldspar layers (2 to 5 mm thick) and phyllosilicate-rich domains (up to 1.5 mm) resulting in strong strength anisotropy (Agliardi et al., 2014). Particularly, micaschists outcrops are detected in the middle portion of the slope, near the village of Case Piazzo (Fig. 5.1). In the Southern portion of the study area, augen gneiss facies and subordinate intercalations of porphiroids and calcareous-dolomitic lenses outcrop, marking the transition to the granitic gneisses of Monte Rolla. Monte Canale gneiss is also characterized by a complex anisotropic fabric, which a main gneissic layering folded at cm-scale (typical amplitude 3 cm, wavelength from 1 to 4 cm). This resulting in an heterogeneous mechanical behavior and strength, also depending on interaction with quartz-rich and pyllosilicate-rich domains Agliardi et al., (2014). Widespread Quaternary sediments occur in the area, including unsorted slope debris in the upper slope sector, discontinuous patches of glacial deposits in the middle slope sector and fluvioglacial and fluvial deposits in lower slope sector (Fig. 5.1).

Slope topography and geomorphological features testify the imprint of glaciation during the Last Glacial Maximum, when the Malenco glacier here reached a thickness of 800 m, completely covering the slope (Bini et al., 2009; Wirsig et al., 2016). Deposits related to glacier dynamics are widespread all throughout the slope since a maximum elevation of 1650 m a.s.l.. No evidence of later significant glacier pulses occurs in this sector of the Val Malenco valley and in similar alpine valleys (Ivy-Oechs et al., 2006; Ivy-Oechs et al., 2008), whereas the lower portion of the slope was reshaped by the fluvial dynamics of the Mallero River, as testified by the widespread gneiss outcrops along the river bed. Rock mass is extensively exposed also in the upper part of the slope, while in the middle-lower portion a debris cover with thickness up to 30 m mantle the bedrock.The analysis of aerial photos and Lidar Digital Elevation Models allowed detecting structural lineaments mainly oriented in NW-SE and NE-SW directions, also expressed at larger scale by the orientation of Malenco valley and its tributaries (Fig. 5.2).

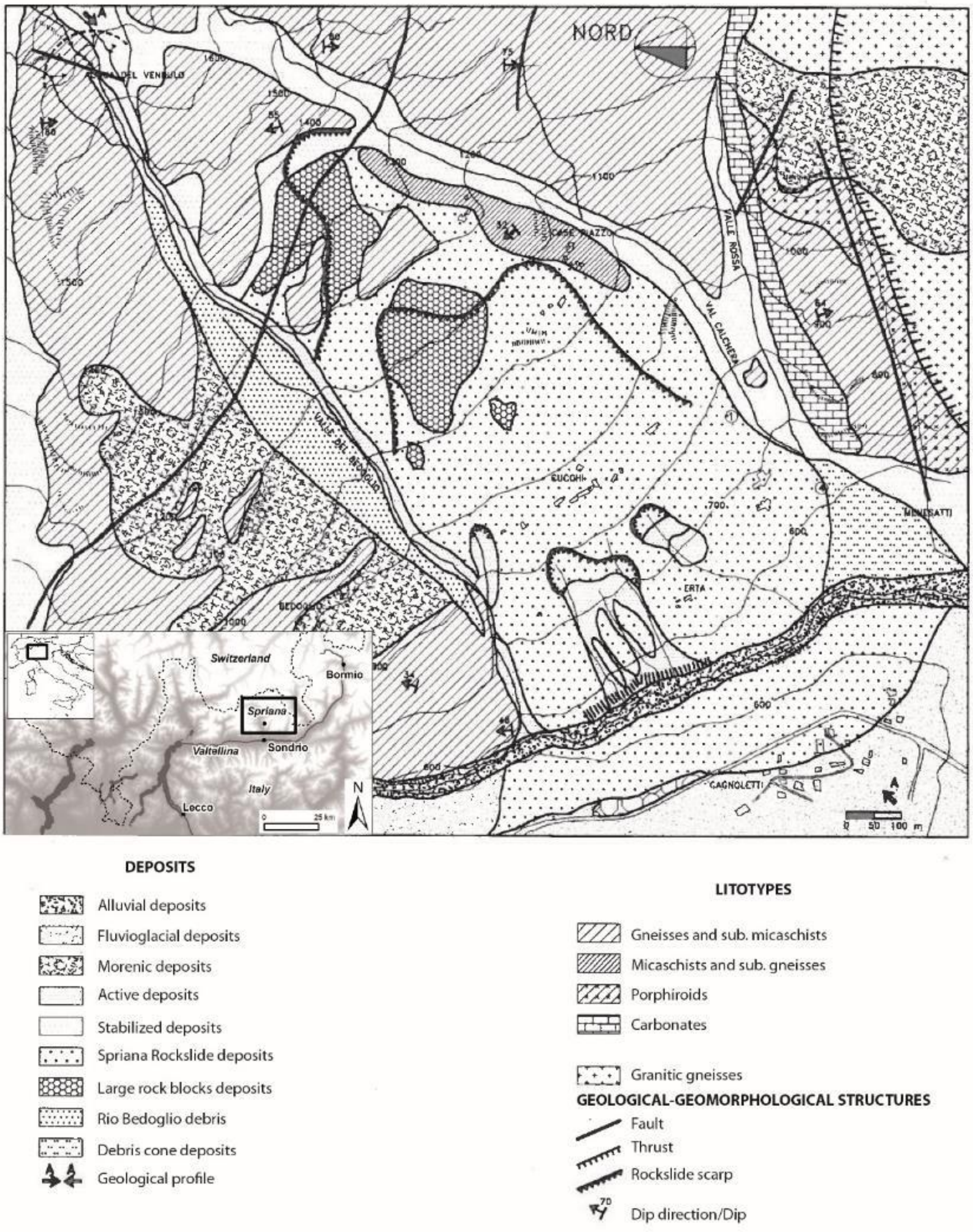

Figure 5.1: Geological sketch of the main deposits, litotypes and geological-geomorphological elements detected in the study area (from Belloni and Gandolfo, 1997).

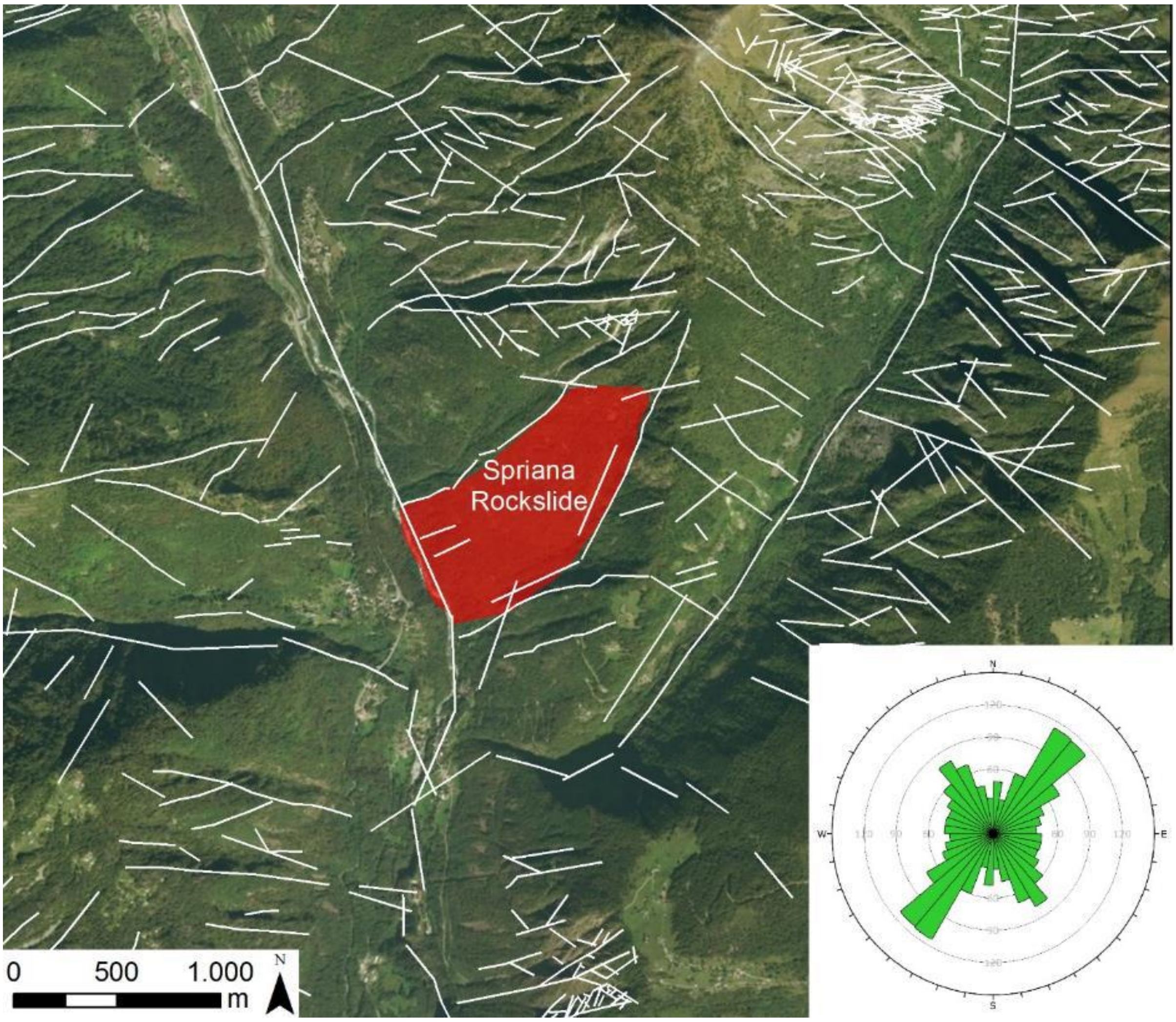

Figure 5.2: Structural lineaments derived from the interpretation of aerial photos and Lidar DEMs. The rose diagram permits to distinguish the main orientation, consisting in NE-SW and NW-SE directions.

5.2 THE SPRIANA ROCKSLIDE

The slope is affected by an important active rockslide (Figs. 5.1 and 5.3), characterized by a long and complex history (Belloni and Gandolfo, 1997; Agliardi and Crosta, 2014). The rockslide extends between 700 m and 1400 m. a.s.l., over an area of about 0.5 km^2, involving an estimated 50 Mm^3 of fractured rock mass and debris suspended on the valley floor of around 150 m. The lateral boundaries are roughly constituted by Bedoglio and Calchera valleys, which delimitate an unstable body width of 700-750 m. The basal shear band emerges perched on the valley floor at around 700 m a.s.l., highlighted by the occurrence of two bulging areas respectively at 750 and 700 m a.s.l., where springs alignment is observed (Fig. 5.3).

Site investigation data suggest that compound kinematics (mixed translational and rotational components) occurs along a basal shear band up to 130 m deep in the middle sector, although secondary shear zones were recognized in the main rockslide body. Hence, three main rotational scarps emerge from the basal shear band (Figs. 5.3 and 5.4), namely: the historic Lower Scarp (top at 1160 m a.s.l., major activity in 1960), the historic Upper Scarp (top: 1400 m a.s.l., major activity in 1977-78) and a prehistoric rockslide headscarp (top: 1600 m a.s.l.). No documented information is available for the latter, indeed characterized by a sharp geomorphological evidence with a vertical downthrown of about 80 m (Agliardi and Crosta, 2014). The prehistoric headscarp can be traced to the N outside the rockslide, along a less evident scarp located just upstream the Spriana rockslide and comprising the village of Bedoglio, thus suggesting that a wider area was affected by post-LGM long-term instability. This slope portion exhibit geomorphological evidence as bulging at valley bottom, a 200 m-long trench in the upper slope and occurrence of intensively fractured levels sampled during slope geotechnical characterization. Past activity in this portion could be related to the debuttressing immediately following the LGM deglaciation stage, with the formation of a coeval Post-LGM scarp. In the long-term period the site-specific conditions brought to the formation of the Spriana rockslide and to the ceased activity in the Bedoglio portion, which in the lights of conducted measurements appears stable. Further evidence of prehistoric rock slope instability also occur upslope the Spriana rockslide above 1700 m a.s.l., with a subdued slope sector with a total downthrown exceeding 100 m.

The displacement history of the Spriana rockslide is long and complex (Belloni and Gandolfo, 1997; Agliardi and Crosta, 2014). The first documented evidence dates back to the end of the 19th century, when shallow slope instabilities started occurring in the middle-lower slope sector, especially after the construction of a hydroelectric derivation tunnel in 1912.

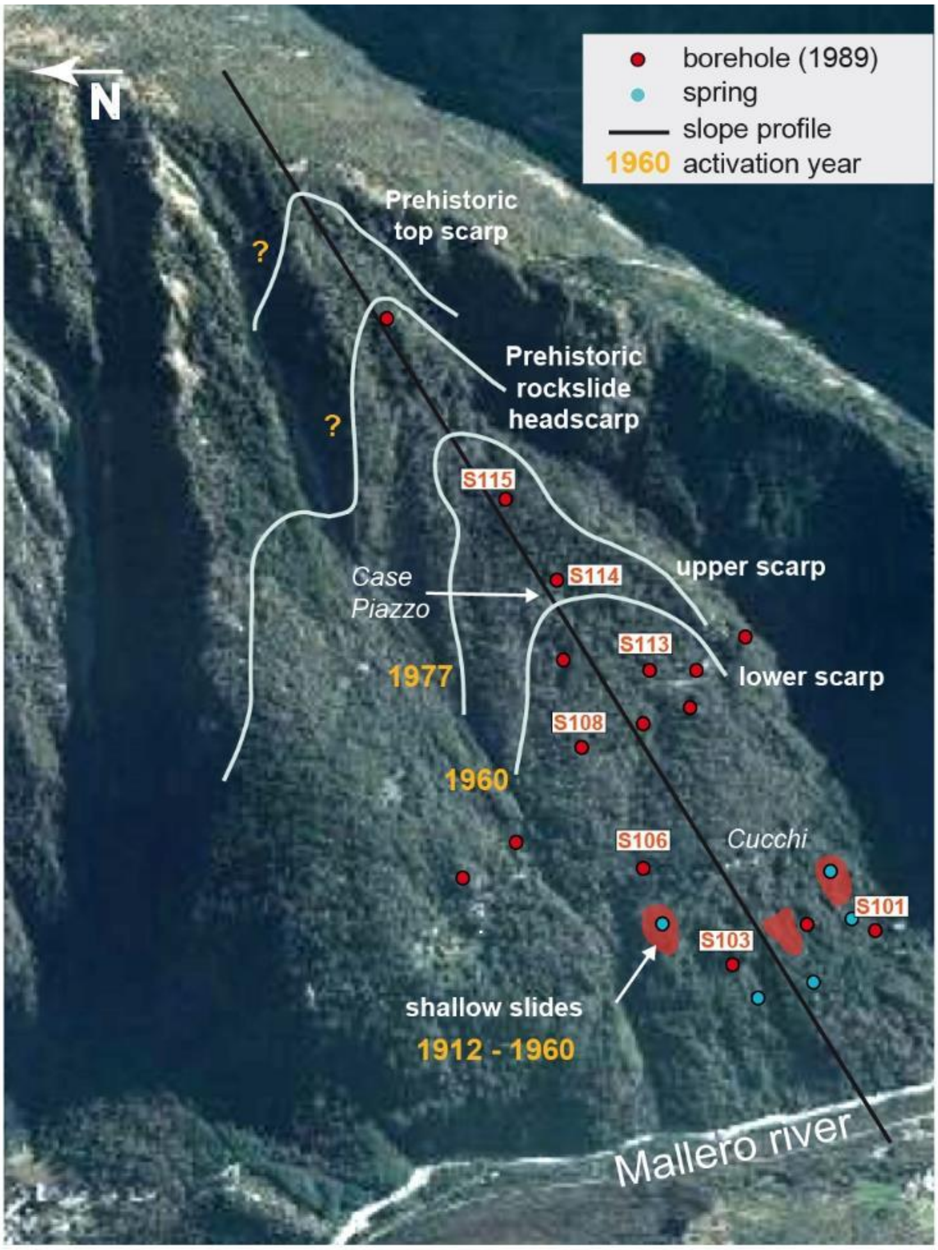

Figure 5.3: Spriana rockslide locations, main morpho-structural evidence and temporal evolutionary stages. Boreholes refers to the 1989 campaign and were used for the geotechnical characterization of the slope.

During the next decades, the lower slope sector experienced widespread shallow landsliding triggered by intense meteoric events, mainly consisting in mobilization of debris near the springs' emergence area. The first global activation event was registered in 1960, when a period of intense and prolonged rainfall caused a retrogressive activation of rock slope instability. Field evidence constrained the moving portion from 700 m a.s.l. up to the village of Cucchi (lower scarp, 1160 m a.s.l.), leading to its evacuation (Fig. 5.3). During 1977 and 1978, the rockslide experienced another retrogressive global reactivation, outlined by the displacements of the Upper Scarp located (1400 m a.s.l.) and culminated with the evacuation of Case Piazzo village. The eventuality of a massive slope failure threatening the city of Sondrio (few kilometers downstream), motivated extensive geotechnical investigations. These were carried out in two main stages in 1978 (Cancelli, 1980) and 1989 (Belloni and Gandolfo, 1997) and consisted of detailed topographic, geological and geophysical surveys, 20 full-core boreholes, 5 seismic lines, and a 140 m long horizontal adit in the middle sector (1040 m a.s.l.), aimed at the direct investigation of the inferred rockslide basal shear zone.

At the same time, monitoring activities started through an extensive monitoring network measuring surface displacements (topographic network, wire extensometers), subsurface deformation (borehole inclinometers and extensometers) and hydrological variables (meteo stations, standpipe and multipoint piezometers). The network was progressively improved, automated, and supported by space-borne observations by satellite In-SAR monitoring. The huge amount of information collected in decades was recently reviewed by Agliardi and Crosta (2014) to obtain an updated geological and geotechnical model of the slope (Fig. 5.4).

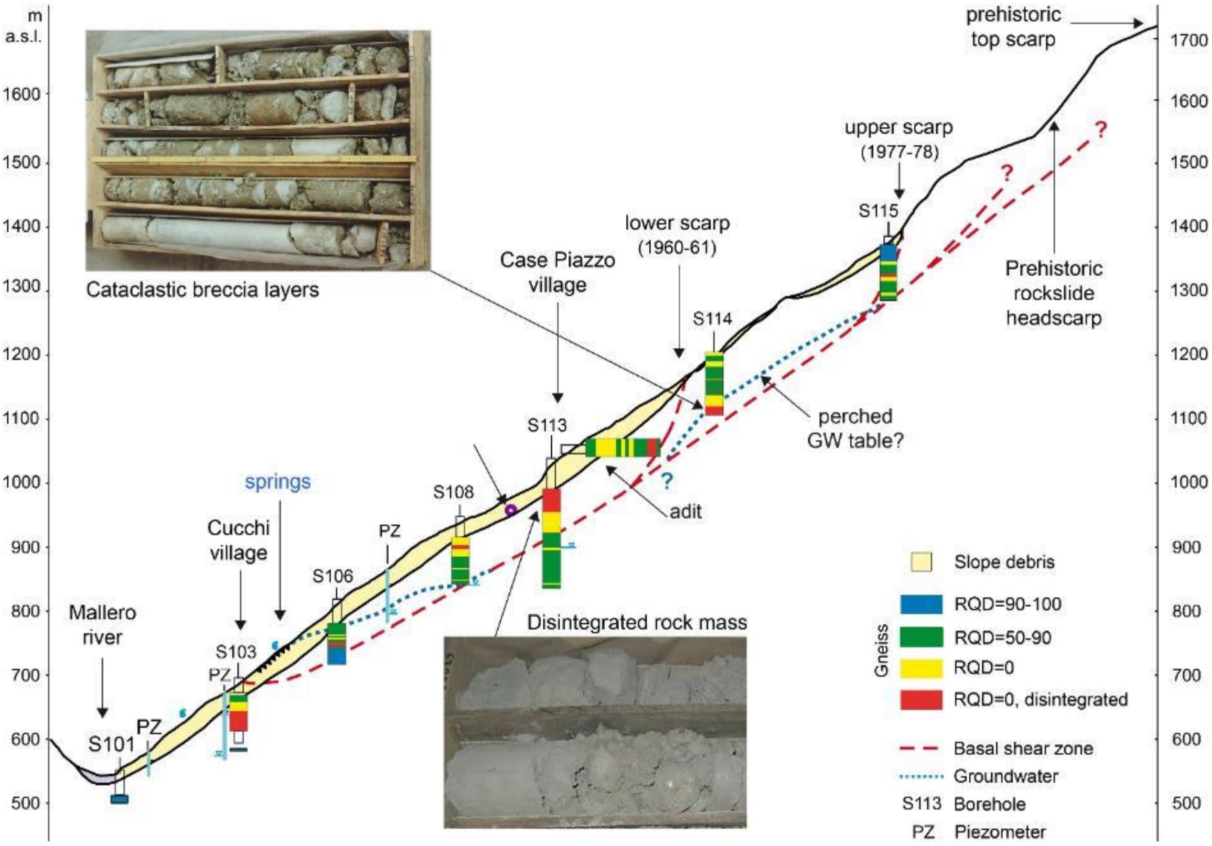

Figure 5.4: Geological and geotechnical model of the Spriana rockslide from field, site investigation and monitoring data (modified after Crosta and Agliardi, 2014). Examples of borehole evidence of diffuse and localized brittle damage patters are also reported.

5.3 GEOTECHNICAL INVESTIGATIONS AND MONITORING

Displacement monitoring carried out since 1978 (manual) and since 1990 (automated) with topographic, geotechnical and PS-InSAR measurements (1992-2007, reported in Agliardi and Crosta, 2014) testify continuing rockslide activity. This is characterized by long-term, steady-state slope creep, occurring at rates of 0.5-3 cm/yr.

The first historical datasets on rockslide activity derives from the benchmarks network, installed in 1977 and covering the entire slope with 43 measure points. They were periodically checked for almost 12 years, with lecture performed every two weeks. Obtained displacements permitted to constrain the lateral boundaries of the rockslide which, as stated before, correspond with Bedoglio and Calchera tributary valleys. Moreover, a marked difference in displacement rates appears in the Southern part of the rockslide, where abrupt decrease in movement is observed in correspondence to C11, C9 and C13 benchmarks (Fig. 5.5b). This could derive from different unstable bodies within the rockslide or boundary effects, related to the dragging of rock mass volumes closer to the rockslide limit (Belloni and Gandolfo, 1997).

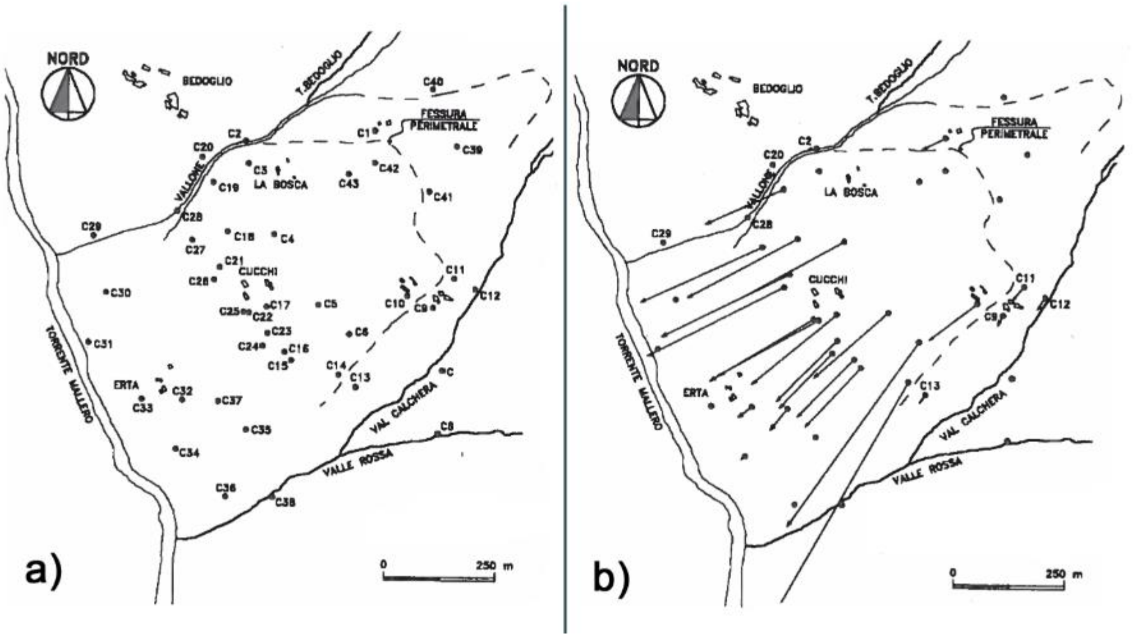

Figure 5.5: (a) Installed benchmarks network (1977) and (b) measured displacements: the vectors represent magnitude and direction of movements (from Belloni and Gandolfo, 1997).

Regarding subsurface deformation, boreholes inclinometers were drilled and monitored for two years, from 1990 to 1992. During this period, collected measures delineated different displacement trends for different portions of the rockslide. In particular, the medium portion registered the maximum displacement value, 5 cm/yr, followed by the upper portion (4 cm/yr) and by the lower one (1 cm/yr). Notably, from the exam of the deep displacement component, appears that the slope debris and the shallower rock mass are rigidly moving upon the basal shear band, where all the displacement is cumulated (I-115 in Fig. 5.6). Moreover, in I-111 profiles, the shallow portions appear dragged by the lower ones, with minor displacement at surface progressively growing with depth. For some inclinometers (I-115, I-114, I-111; Fig.

5.6) stable rock mass was not reached, and downslope movements were registered also at boreholes bottoms.

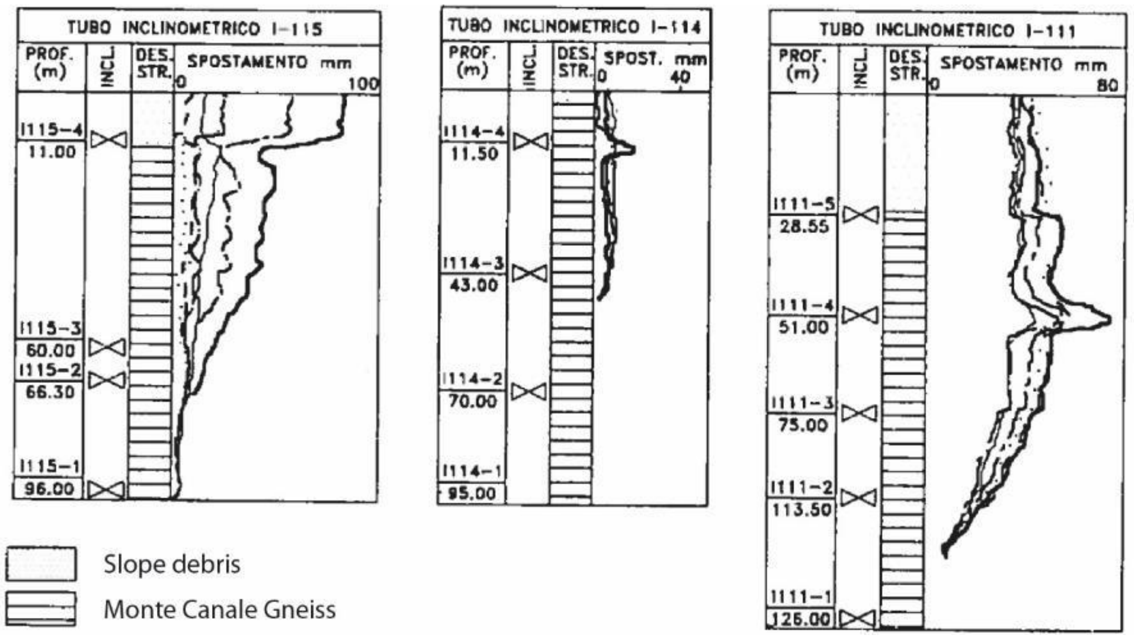

Figure 5.6: Two-year displacement patterns registered for I-115, I-114 and I-111 (from Belloni and Gandolfo, 1997).

Sudden or prolonged periods of increase of displacement rates (up to >20 cm/yr) are superimposed on this long-term trend (Agliardi and Crosta, 2014). Borehole piezometric data suggested the occurrence of a perched water table into the rockslide mass, likely above the basal shear zone (Belloni and Gandolfo, 1997). The water table is deeper in the upper slope sector, where depths of 90-100 m from the surface are collected. Moving downslope, progressively aquifer thickening and rising is observed, reaching slope surface close to the Cucchi village, where alignments of persistent springs were observed (Figs. 5.3 and 5.4).

Piezometric monitoring suggest maximum water table rise in the range of 3-5 meters, which trend is controlled by precipitations and snowmelt. Intense and prolonged recharge of the perched aquifer systems are considered responsible of rockslide acceleration periods through direct hydro-mechanical coupling effects, while for minor, daily precipitations only weak response is observed. Through the analysis of rainfall, groundwater and displacement data, Agliardi and Crosta (2014) suggested that two distinct behaviors occur for the Spriana rockslide. For rising in the water table comprised into 2 m, short acceleration events with minor cumulated displacement occurs (i.e. spring 2000; Fig. 5.7). On the other hand, particularly intense and /or prolonged recharge episodes with rise of slope groundwater table of 3 m, induce longer and faster acceleration phases with large cumulated displacements. This situation occurred in the autumn of 2000, where a flooding event resulted in a 7 months acceleration period with cumulated displacements up to 10 cm (Fig. 5.7).

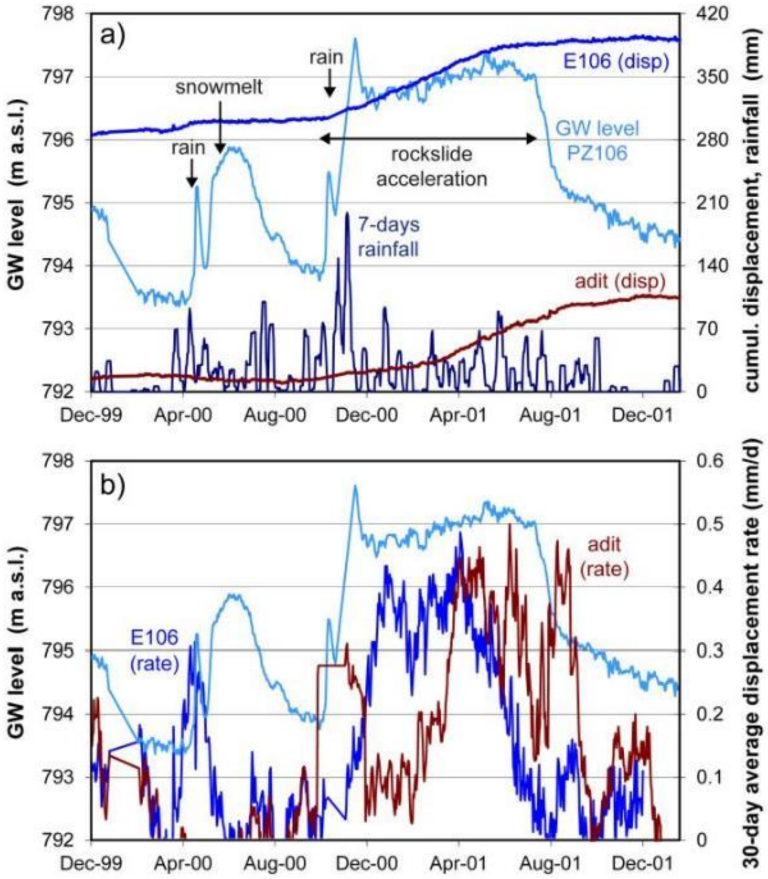

Figure 5.7: Cumulative displacements (a) and averaged displacement rates (b) associated with oscillations in groundwater level. Two different acceleration phases were recognized in spring and autumn of 2000, caused respectively by rise of around 2 m and 3 m in piezometric level (from Agliardi and Crosta, 2014).

5.4 GEOTECHNICAL CHARACTERIZATION

In the previous paragraphs, the geotechnical investigations conducted on the Spriana slope were briefly illustrated. Among the collected data, the borehole logs and the drilled rock cores represent fundamental information for the construction of rockslide geotechnical model, as they permit to investigate the rock mass quality and fracture density also at depth. To do this, we reclassified and digitalized all the data coming from the 17 boreholes of 1989 campaign, which results were scrupulously documented through a detailed log attached at the original report (ISMES, 1990), that included type of fracture, shape, roughness, weathering, dip angle, aperture and filling material for each of the joint encountered during the perforations (Fig. 5.8).

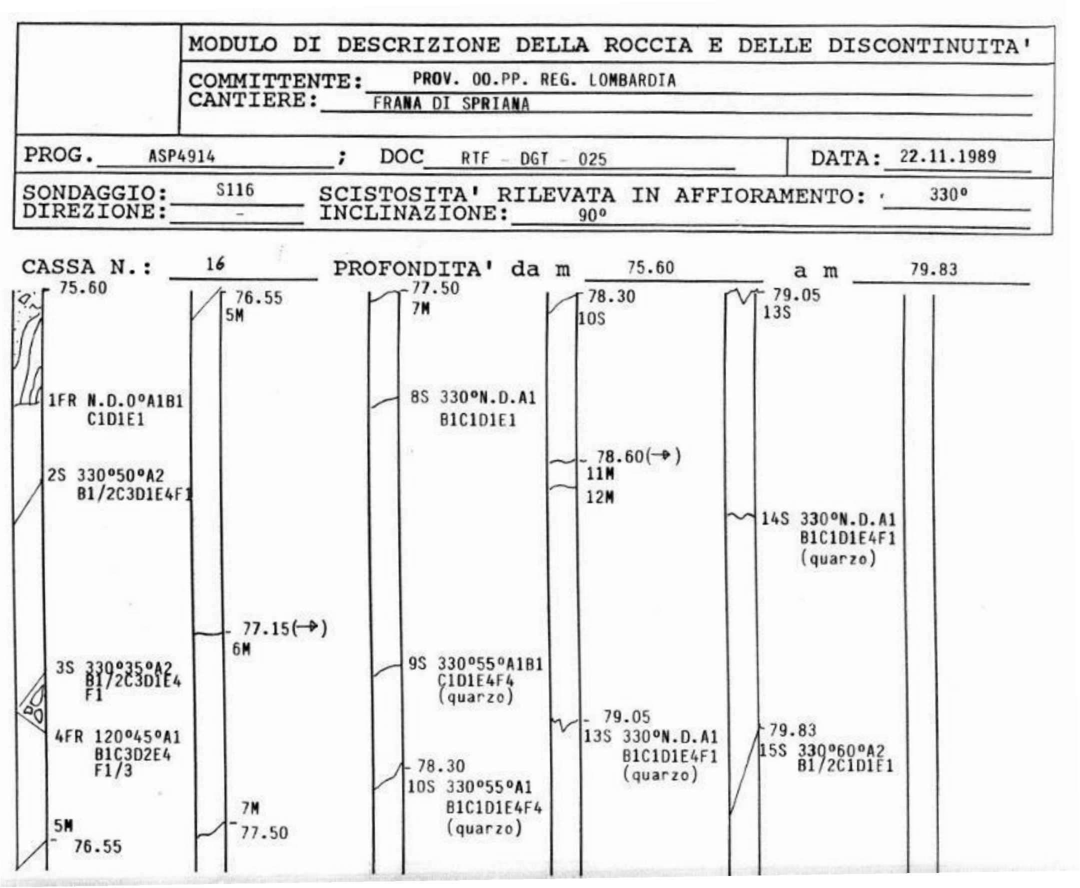

MODULO DI DESCRIZIONE DELLA ROCCIA E DELLE DISCONTINUITA'

COMMITTENTE: PROV. OO.PP. REG. LOMBARDIA
CANTIERE: FRANA DI SPRIANA

PROG. ASP4914 ; DOC RTF - DGT - 025
DATA: 22.11.1989

SONDAGGIO: S116
DIREZIONE: -
SCISTOSITA' RILEVATA IN AFFIORAMENTO: 330°
INCLINAZIONE: 90°

CASSA N.: 16 PROFONDITA' da m 75.60 a m 79.83

75.60
1FR N.D.0°A1B1 C1D1E1
2S 330°50°A2 B1/2C3D1E4F1
3S 330°35°A2 B1/2C3D1E4 F1
4FR 120°45°A1 B1C3D2E4 F1/3
5M
76.55

76.55
5M
77.15(→)
6M
7M
77.50

77.50
7M
8S 330°N.D.A1 B1C1D1E1
9S 330°55°A1B1 C1D1E4F4 (quarzo)
78.30
10S 330°55°A1 B1C1D1E4F4 (quarzo)

78.30
10S
78.60(→)
11M
12M
79.05
13S 330°N.D.A1 B1C1D1E4F1 (quarzo)

79.05
13S
14S 330°N.D.A1 B1C1D1E4F1 (quarzo)
79.83
15S 330°60°A2 B1/2C1D1E1

Figure 5.8: Example of original borehole log attached at the 1989 technical report. Each fracture is codified regarding dip and dip direction, shape (A), roughness (B), aperture (C), weathering (D) and filling (E and F) (from ISMES, 1990)

Different geotechnical parameters were applied, taking into account the intrinsic limitations in each of the considered method and referring to each core run as a geotechnical unit, thus calculating every parameter in respect to this interval. The main issue encountered during the whole reclassification work was represented by the core axis orientation: Indeed, borehole dip and dip direction bias the frequency of crossed discontinuities sets, depending on the geometrical association between the borehole axis and a certain set geometry. The original boreholes were oriented, thus dip and dip direction were provided for each crossed fracture. However, as we were not interested in defining properties for single sets but quantifying global rock mass state, we decided to not include this distinction in our reclassification.

To reclassify borehole data we used four different, commonly-used geotechnical parameters, namely:

- **Rock Quality Designation** (RQD; Deere, 1963): specifically conceived for borehole logs classification, the RQD permit to express with a value ranging from 0 to 100 the rock mass quality of a specified core run, defined as the percentage of core pieces with length major than 10 cm in respect to the total examined length (Fig. 5.9). This parameter is very easy and quick to measure, thus being widely applied and tested. However, RQD has some strong limitations: first of all, no information about core fragments with length minor than 10 cm are obtained. Moreover, joint conditions and weathering are not taken into account by RQD, which focuses only on the geometrical aspect. This can be a critical limitation in our reclassification since RQD cannot permit the discrimination between single fractures, intensively fractured portions or brecciated levels. Finally, centimetric variations in joints spacing (for example from 9 to 11 cm) results in high variation of RQD.

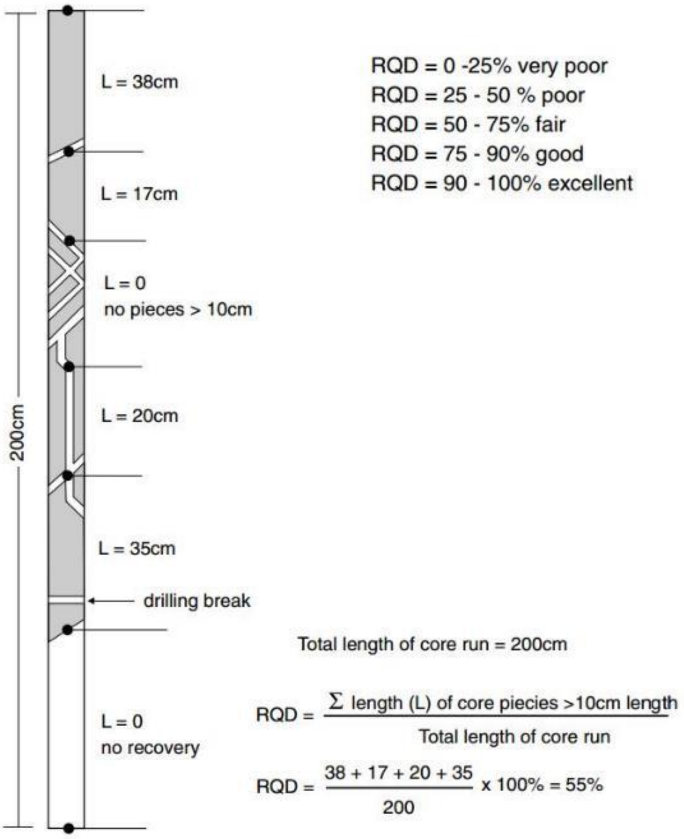

Figure 5.9: Example of RQD calculation in borehole logging (from Palmstrom, 2005).

- **Weighted Joint Density** (wJD; Palmstrom, 2005): this parameter accounts for joint density introducing a correction factor, which depends on the relative angle between the borehole axis and the crossed discontinuity (Fig. 5.10 and Tab. 5.1). In this way, a more robust representation of rock mass fracture density is obtained, even if this method doesn't permit a complete removal of orientation bias. The wJD can be applied to both cores and outcrops logging recurring to different equations (Fig. 5.9). Regarding a single borehole run, wJD is defined as the sum of the crossed joints (multiplied for the correction factor), divided by total core length. The disadvantage of this technique is represented by the conservative values obtained from its application. Moreover, during reclassification of Spriana core logs, we encountered troubles in the application of wJD to brecciated/highly-fractured portions due to the difficulties in identifying and determining single fractures and associated dip angles.

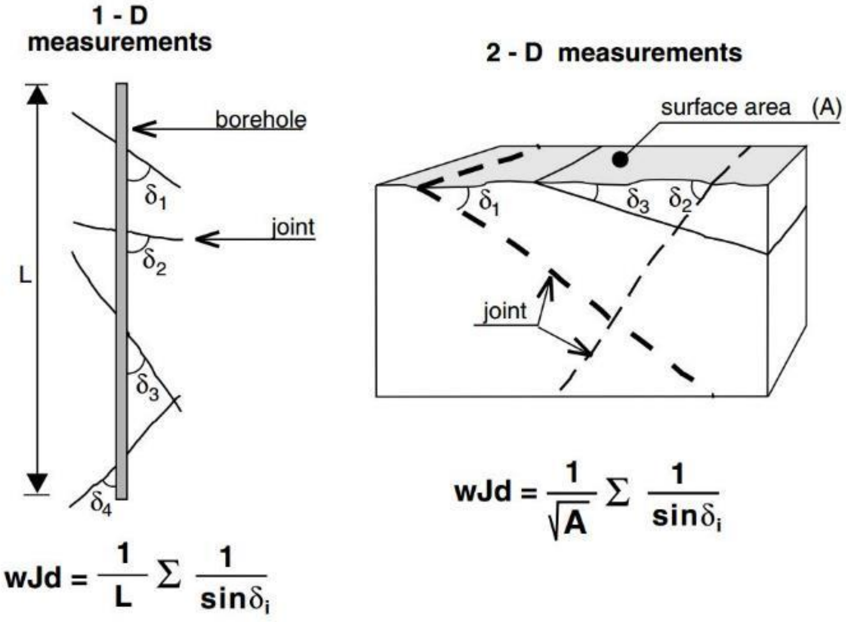

Figure 5.10: Weighted joint density (wJD) can be applied both for measuring joint occurrence in boreholes and on outcrops. In both cases, the apparent dip angle of the discontinuities in taken into account applying the correction factor reported in Table 5.1(from Palmstrom, 2005).

Relative angle	Correction factor
δ>60°	1
30°<δ<60°	1.5
15< δ<30	3.5
δ<15°	6

Table 5.1: Correction factors corresponding to different relative angles between the borehole axis (or the outcrop surface) and the sampled joint.

- **Geological Strenght Index** (GSI; Hoek et al., 1995): GSI was briefly introduced in chapter 2, where the theoretical background and the main strengths of this approach were enounced. The application of GSI to borehole logging was examined particularly by Cai et al. (2004) and later by Agliardi et al. (2016), trying to extrapolate information coming directly from rock cores in the aim of quantifying rock mass quality and structure. Despite the evident orientation bias if compared to three-dimensional outcrops application, another concern is represented by the little exposure of joint surface in rock cores, which makes evaluation of joint conditions difficult and poorly representative. Among the calculated parameters, the GSI is the only one that takes into account, despite the geometrical aspect, also the weathering and the degradation of discontinuities. This is a fundamental point in our reclassification work, since we were interested not only in the fracture density but also in quantification of damage experienced by the rock mass.

- **Number of fractures per unit length** (P_{10}; Dershowitz and Herda, 1992): this parameter was initially developed to provide an easy and quick measure of fracture intensity, represented by the ratio between the number of fractures and length of scanline (or core run). Nowadays P_{10} is frequently used as input parameter for Discrete Fracture Network simulations, to describe fracture intensity related to a considered rock mass. During reclassification of Spriana boreholes, no distinction between sets were performed, thus the calculated P_{10} is referred to all the fractures crossed for the considered core run. Unfortunately, joint dip and weathering are not taken into account by this parameter, which is suitable only for geometrical description of fracture density.

The 17 reclassified boreholes are well distributed along the entire slope and located both inside and outside the landslide area (Fig. 5.11), resulting in 882 core runs for a total length of 1048m. Obviously, data refers only for sampled rock mass, as cores crossing slope deposits were excluded from the analysis. Data were analyzed and plotted to calculate for each run the wJD, the P_{10} and the GSI, while the RQD was derived from original core logging data, where recorded. Complete recalculation of this parameter was not possible, since no detailed location of fractures in respect to borehole length was reported (Fig. 5.8). Thus, to not introduce inaccurate measures derived from interpretation of data, we decided to avoid RQD calculation except when explicitly reported. In the following paragraphs a brief description for each borehole is reported, while detailed geotechnical profiles are included in annex 2.

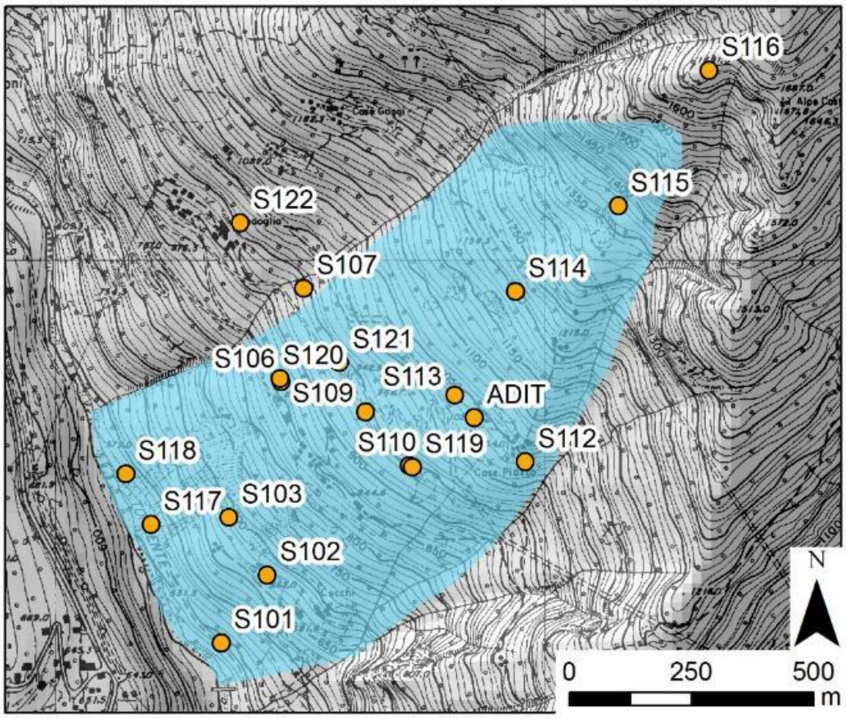

Figure 5.11: Location of boreholes drilled during the 1989 sampling campaign in respect to the rockslide extension

S101 is located in the southern part, lower portion of the slope and reaches 45 m of depth. The crossed rock mass is substantially of good quality, with GSI values comprised in the range 70-85. This is also testified by the low values of P_{10} and wJD. Unfortunately RQD was not available for this borehole.

S103 is located in the center of the rockslide, lower portion. It provides rock-mass core comprised in the interval 100-109 m of depth. The material encountered exhibited very high quality, mainly consisting of intact rock without discontinuities. This is testified by obtained GSI of 90 and RQD of 100, while P_{10} and wJD results closer to 0.

S106 is located in the Northern sector, middle portion of the Spriana slope, and is considered one of the most revealing boreholes. Indeed, in the almost 100 m investigated, two clear sectors can be distinguished (Fig. 5.12). The shallower one is characterized by fractured rock mass, with brecciated and intensively fractured portions, especially in the interval 70-75 m. In this first domain, GSI is characterized by a maximum value of 40, while the minimum value of 5 corresponds to completely crushed and comminuted rock mass. After 75 m of depth, a clear turning point is detected, with GSI increasing up 65-80 until the end of borehole. Meanwhile, also P_{10} and wJD registered an abrupt decrease, symptom of good quality rock mass. This transition corresponds to the passage of basal shear band, which divide unstable and stable rock mass. Unfortunately RQD was available only for two core runs in the entire borehole.

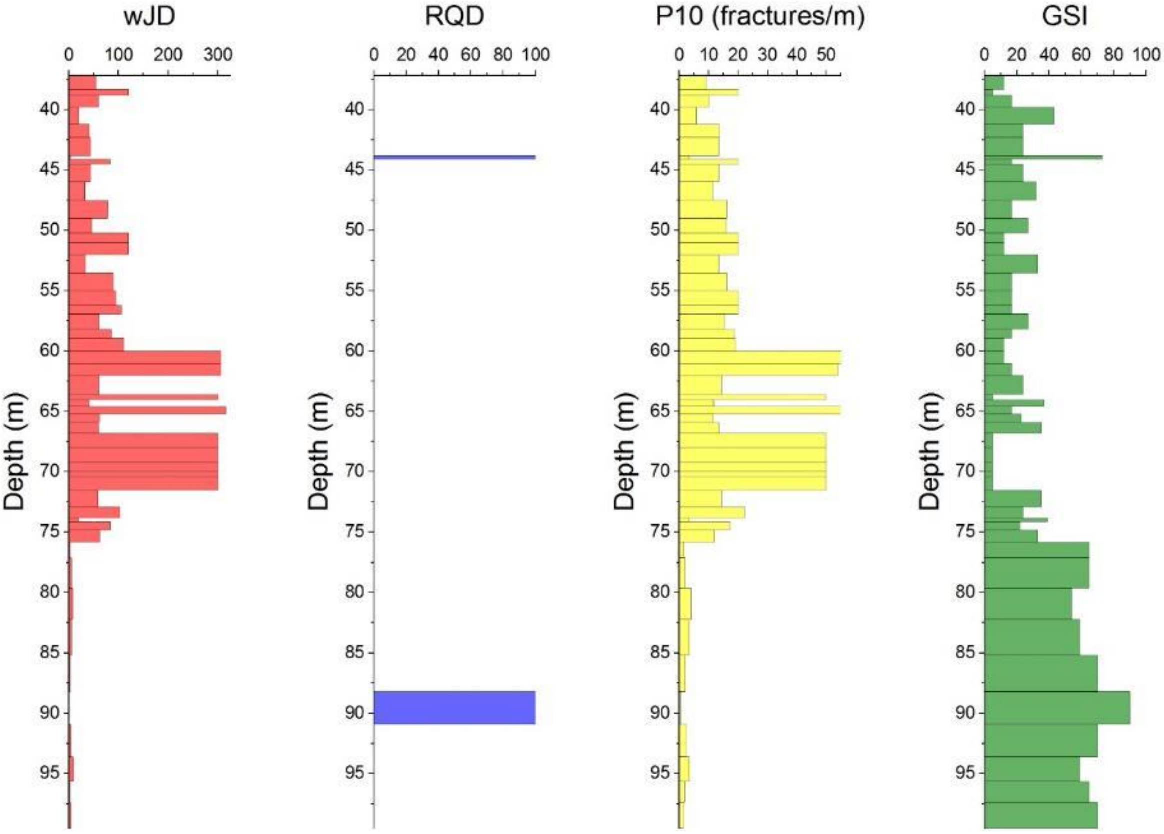

Figure 5.12: S106 characterization. Changes in geotechnical parameters are evident between the rock mass within or below the rockslide.

S107 is located in the middle slope sector, near the rockslide Northern boundary. Investigated rock mass, which depth ranges from 20 to 92 m, shows good mechanical properties, with modal GSI value around 55-60. This behavior is testified also by wJD, P_{10} and RQD, which exhibit coherent trends. However also in this borehole some intensively fractured levels are encountered, corresponding to local worsening in geotechnical parameters (intervals 47-49 m and 79-82 m).

S108 is located in the center of the slope, extending from 30 up to 100 m of depth. The crossed material is characterized by the alternation of good rock mass volumes, with GSI comprised in the range 60-80, and brecciated levels with poor mechanical properties. These are encountered especially in the shallower portion, where an interval of almost 10 m of crushed material is sampled. This borehole well testify the action of gravitational component on the slope, consisting in solid blocks disrupted by brecciated and intensively fractured levels. Unfortunately RQD was not available for this borehole.

S109 is located in the center of the slope, extending up to 100 m from the topographical surface. Among all the boreholes drilled, S109 exhibit the thickest level of poor quality rock mass: in the interval 44-64 m the geotechnical parameters highlight the occurrence of extremely fractured material, crossed by several and plurimetric levels of breccias. In this borehole basal shear band is not recognized, as breccias are encountered until the end of drilling. Unfortunately RQD was not available for this borehole.

S110 is located in the Southern part, middle portion of the slope and extends from 32 m to 55 m of depth. Despite the short sampled interval, this borehole crosses a brecciated level comprised between 33 and 37 m, resulting in low values of GSI (equal to 5) and RQD (equal to 0) accompanied with corresponding high intensities of wJD and P_{10} (respectively 300 and 50). The remaining part of the borehole is characterized by good mechanical properties, with GSI comprised in the interval 60-80 and wJD and P_{10} close to 0.

S111 is located in Northern part, middle portion of the slope, where reaches 125 m of depth. The crossed rock mass is characterized by the occurrence of metric, intensively fractured levels, alternating with good quality material (GSI from 45 to 80). The occurrence of breccias is registered also in depth, where a metric level is encountered at 125 m from topographical surface. Unfortunately RQD was not available for this borehole.

S112 is located in the Southern part, middle slope portion, and extends from 4 m to 97 m of depth. Also this borehole is characterized by the occurrence of several intensively fractured levels, which makes the log of geotechnical parameters fluctuating from poor quality material to GSI values of 50-60. The basal shear band is not clearly recognizable, since passage to a stable rock mass properties is not collected at the end of drilling. Unfortunately RQD was not available for this borehole.

S113 is located in the center of the slope, near the Case Piazzo village. It is the deepest borehole performed in the 1989 survey campaign, extending up to 190 m of depth. The pattern of geotechnical parameters is similar to S106, and can be subdivided in respect to the basal shear band, which location is not clearly identifiable, but probably comprised in the interval 90-100 m. Indeed, the rock mass below consists in good quality material with homogeneous fracturing, in contrast with the upper part of borehole, which continuously crosses disintegrated and brecciated levels (Figs. 5.4 and 5.13). Unfortunately RQD was only partially available for this borehole.

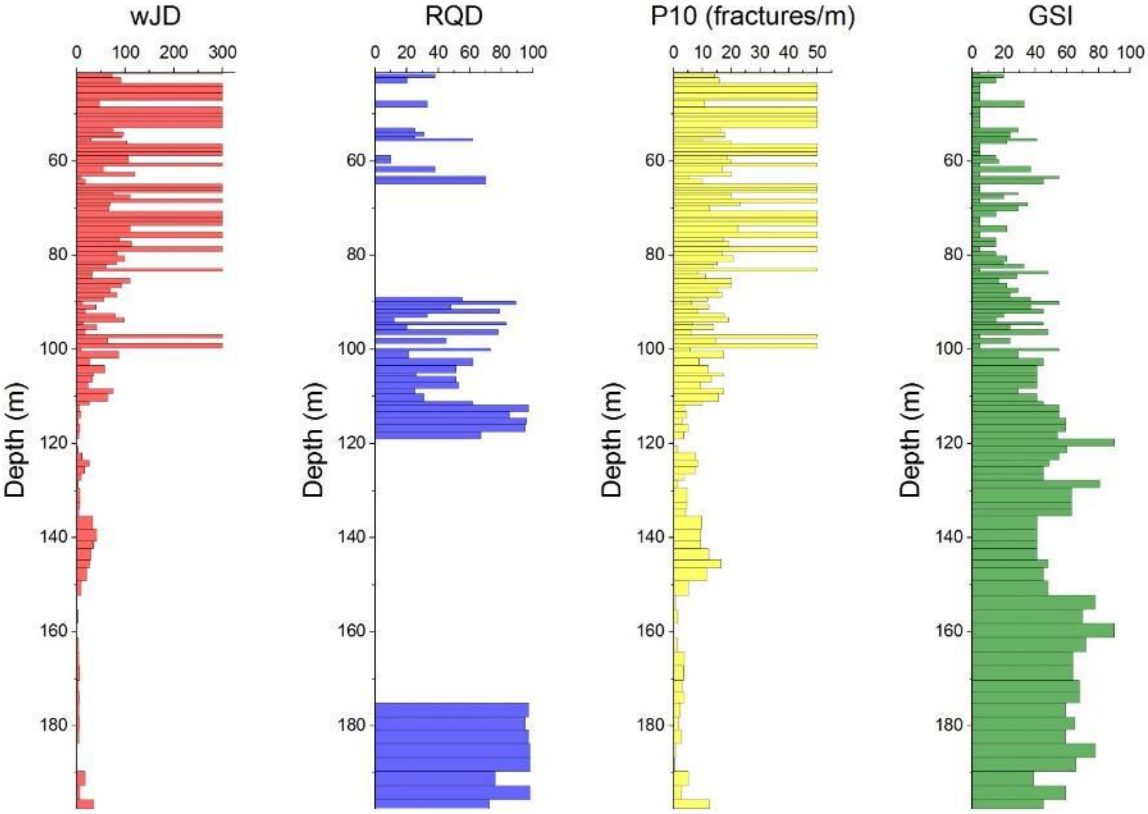

Figure 5.13: S113 characterization. Transition from a heterogeneous rock mass within the rockslide to more homogeneous one just below the unstable portion

S114 is located in the center of the slope, in the upper sector. The borehole investigates up to 95 m of depth, crossing several cataclatic levels with poor mechanical properties since the last meters of core, where an intensively fractured and brecciated level is encountered (Fig. 5.4), probably corresponding to basal shear band. Unfortunately, no clear evidences are collected, since the sampled material ends before entering good quality rock mass.

S115 is located at 1370 m a.s.l., just below the Upper Scarp. It is characterized by a first part in which fractured and coarse brecciated levels are frequently encountered. After around 60 m of depth, an increase in geotechnical properties is registered, with mean GSI values ranging from 60 to 80, probably corresponding to the shear zone associated with the occurrence of Upper Scarp. Unfortunately RQD was not available for this borehole.

S116 is the highest borehole drilled, located at 1680 m a.s.l. and investigating until 86 m of depth. The entire borehole log is characterized by the frequent occurrence of poor quality rock mass, with metric to plurimetric levels of brecciated material separating metric blocks of good-quality rock mass. Unfortunately RQD was not available for this borehole.

S117 is located in the slope toe, just above the valley bottom. The geotechnical log, which extends up to 32 m of depth, is constituted by good quality rock mass, with GSI always major than 60 and wJD and P_{10} almost equal to 0. This testify the emergence of basal shear band at a higher elevation, since the rock mass in this point appears undisturbed by rockslide occurrence.

S118 is located Northern from S117, and consists in a similar situation. The material crossed is of good quality with high values of GSI and low values of wJD and P_{10}. Unfortunately RQD was not available for this borehole.

S119 is located in the center of the slope, extending up to 97 m of depth. It consists of good quality rock mass crossed by intensively fractured levels with metric thickness, thus resembling the geotechnical pattern observed for other boreholes in medium sector of slope. The basal shear band is not clearly identified, even if below 83 m of depth slight increase in geotechnical properties is registered.

S122 is located in the village of Bedoglio, Northern from Spriana rockslide. It extends since 63 m of depth, showing a rock mass of good quality, with GSI comprised in the interval 60-80, P_{10} in the interval 0-5 and wJD in the interval 0-30 (Fig. 5.14). Notably, an intensively fractured level is encountered at 26 meters of depth, clearly emerging from borehole log. The occurrence of this level might be interpreted as evidence of prehistoric instability related to post-LGM readjustment.

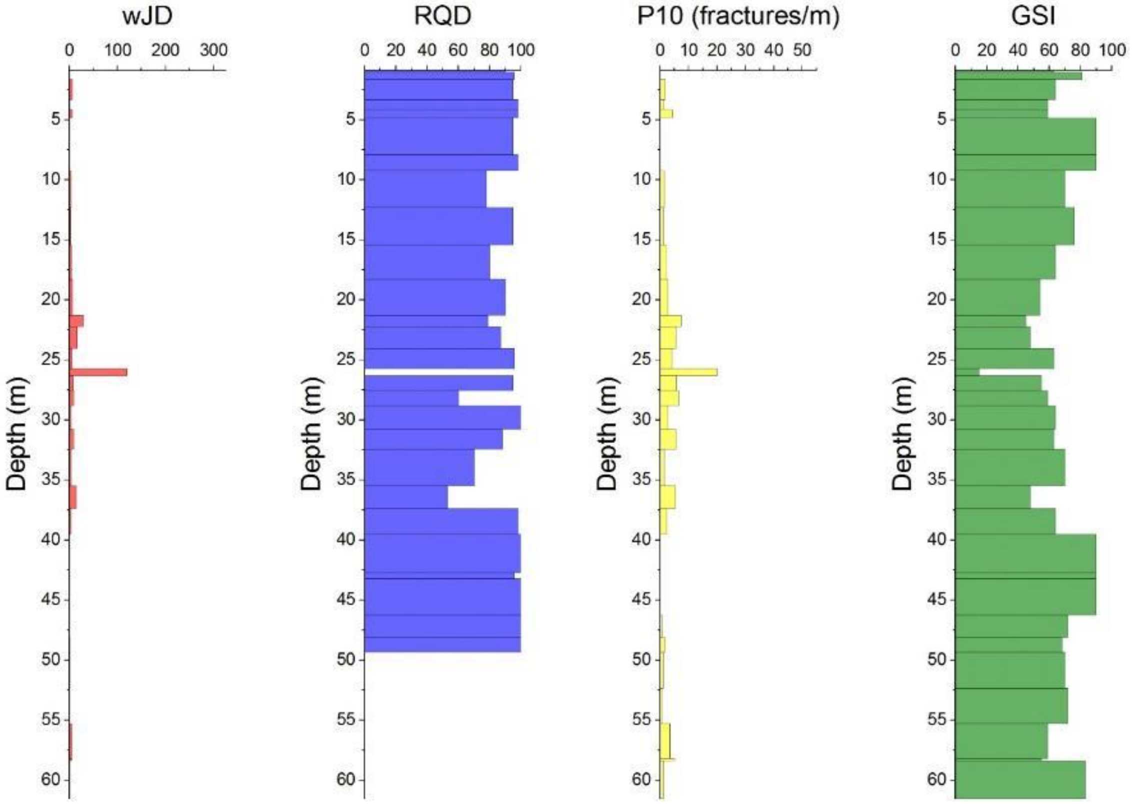

Figure 5.14: S122 characterization. Notably, a layer of breccias occurs at 26 meters from topographic surface.

5.4.1 *Analysis results*

Starting from the qualitative description obtained from borehole logs observation, the core runs were subdivided according to their position in respect to the rockslide. In this way, three different domains were identified:

- Within rockslide: S110, S114 and upper part of S106, S108, S109, S111, S112, S113, S115, S116, S119
- Below rockslide: lower part of S106, S108, S109, S111, S112, S113, S115, S116, S119
- Outside rockslide: S101, S103, S107, S117, S118, S122

The aim of this spatial criterion is, besides linking the damage state experienced by the rock mass with commonly-used geotechnical parameters, to reconstruct an evolutionary trend of damage and equivalent rock mass properties based on data coming from different sectors of slope, being also able to distinguish the effect of different processes (i.e. deglaciation, landslide displacement, landslide shear) on damage state. In this respect, differences in exploited geotechnical parameters clearly emerge between the highly-fractured zones within the rockslide and the less disturbed rock mass just beside or below the unstable body. Rockslide volume is crossed by several shear bands, in which rock has been crushed in breccias often filled with sand, silt and slight clay. The thickness of these highly fractured bands is variable and can range from tens of centimeter to more than 10 meters, being intercalated with good-quality remnants which were rigidly displaced downvalley, showing little damage joined with good mechanical properties. This dualism makes the geotechnical log within the rockslide very heterogeneous, consisting in the alternation of good and poor quality rock masses (i.e upper part of S113 in Fig. 5.13). Below the rockslide basal shear band, which sometimes is difficult to clearly identify in the borehole logs, the rock mass appears less fractured, with less weathered discontinuities occasionally crossed by submetric levels of breccias. Finally, outside the Spriana rockslide the rock mass appears of good mean quality with sparse submetric bands of intense fractured rock mass, while no breccias are encountered.

To investigate the occurrence of statistical trends in the different domains identified, we plotted the reclassified data in frequency histograms and tested the main used density functions with Goodness-of-fits test (modified Kolmogornov-Smirnov test). Below and outside the rockslide the GSI is fitted by a Gaussian distribution, which gives a mean value of 55 for the volume below landslide (SD=14.7; Fig. 5.15a) and of 65 for the volume outside the landslide (SD=14.1; Fig. 5.16a). For the rock mass interested by gravitational displacement, such distribution is no more recognizable, being the shape of the distribution largely disturbed by the repeated occurrence of brecciated levels with a GSI value of 0-5. Apart from this, a slightly Gaussian centered around 50 is identifiable, probably due to the rigid movement of rock-mass unfragmented portions inside the rockslide body (Fig. 5.17a).

The RQD proved not to be a good indicator of damage bear by rock mass, showing no clear trends or distribution of value. Only a rough translation of RQD values from high (outside rockslide) to medium (below rockslide) to low (within rockslide) can be inferred(Figs. 5.15b, 5.16b and 5.17b).

Regarding wJD, data show three different situations in the three exploited domains. Outside the rockslide, frequency histogram is well fitted by exponential distribution (λ=9.8, p-value=0.49) with the exception of an outlier value of 120 (Fig. 5.16c). In the rock mass below the Spriana rockslide, the lack of very low/null fractured rock masses and the distribution tail around 100 make Weibull distribution the only successfully tested (alpha=17.4, beta=0.77; Fig. 5.15c). Also for the wJD frequency, data collected within the rockslide are not reproducible with a simple statistical distribution: the peak at 300 is related to the widespread brecciated levels, while data for lower intensity of fractures reveals no correlations with normal, exponential or lognormal functions (Fig. 5.17c).

The fracture intensity value P_{10} follows similar trends in respect to the wJD for the three examined domains. Indeed, outside the landslide the distribution of frequencies is well fitted by an exponential distribution (λ=9.8; Fig. 5.16d) while below the basal shear band Weibull distribution successfully reproduce the observed values (Fig. 5.15d). Within the rockslide no clear distribution is observed and the striking features remains the peaks due to high frequency of highly damaged rock mass (Fig. 5.17d). Results of goodness-of-fits analysis are resumed in Table 5.2.

The statistical analysis of core runs population permitted the evaluation of “damage signatures” related to the different slope domains detected. This is true particularly for the GSI parameter that, considering also joint conditions and weathering, permitted to trace and quantify damage evolution for different portions of the slope. In the outside domain, the highest values of GSI are associated with good quality rock mass (Fig. 5.16a). The sparse layers of intense fractured material probably testify the damage imprint of deglaciation on slope. Instead, the domain below the Spriana rockslide is characterized by a higher degree of damage, testified by a lower mean value of GSI, which is mainly due to the occurrence of sparse brecciated level also below the basal shear zone and to a global increase in fracture density (Fig. 5.15a). Within the unstable body the frequent occurrence of intense fractured layers and breccias make the identification of statistical trends difficult (Fig. 5.17a). The consequence of deglaciation and following gravitational component due to the rockslide occurrence resulted in intense damage along the shear bands with the complete destruction of rock mass original structure also due to the shear deformation experienced. Regarding this domain, gravitational component acted also on rock mass remnants comprised between the main shear bands. Even if the GSI is not as low as in portion with localized damage, rock mass geotechnical characteristics are weaker in respect to the outside and below domains.

Domain	**Parameter**	**Distribution Type**	**Mean Value**	**St. Dev.**	**λ**	**P-Value**
Outside Landslide	GSI	Normal	65	14.1	-	0.083
	RQD	-	-	-	-	-
	wJD	Exponential	-	-	9.8	0.49
	P_{10}	Exponential	-	-	4.52	0.66
Below Landslide	GSI	Gaussian	55	14.7	-	0.052
	RQD	-	-	-	-	-
	wJD	Weibull	17.4	0.77	-	>0.1
	P_{10}	Exponential	-	-	6.48	0.07
Within Landslide	GSI	-	-	-	-	-
	RQD	-	-	-	-	-
	wJD	-	-	-	-	-
	P_{10}	-	-	-	-	-

Table 5.2: Results of statistical distribution fittings on the three domains identified.

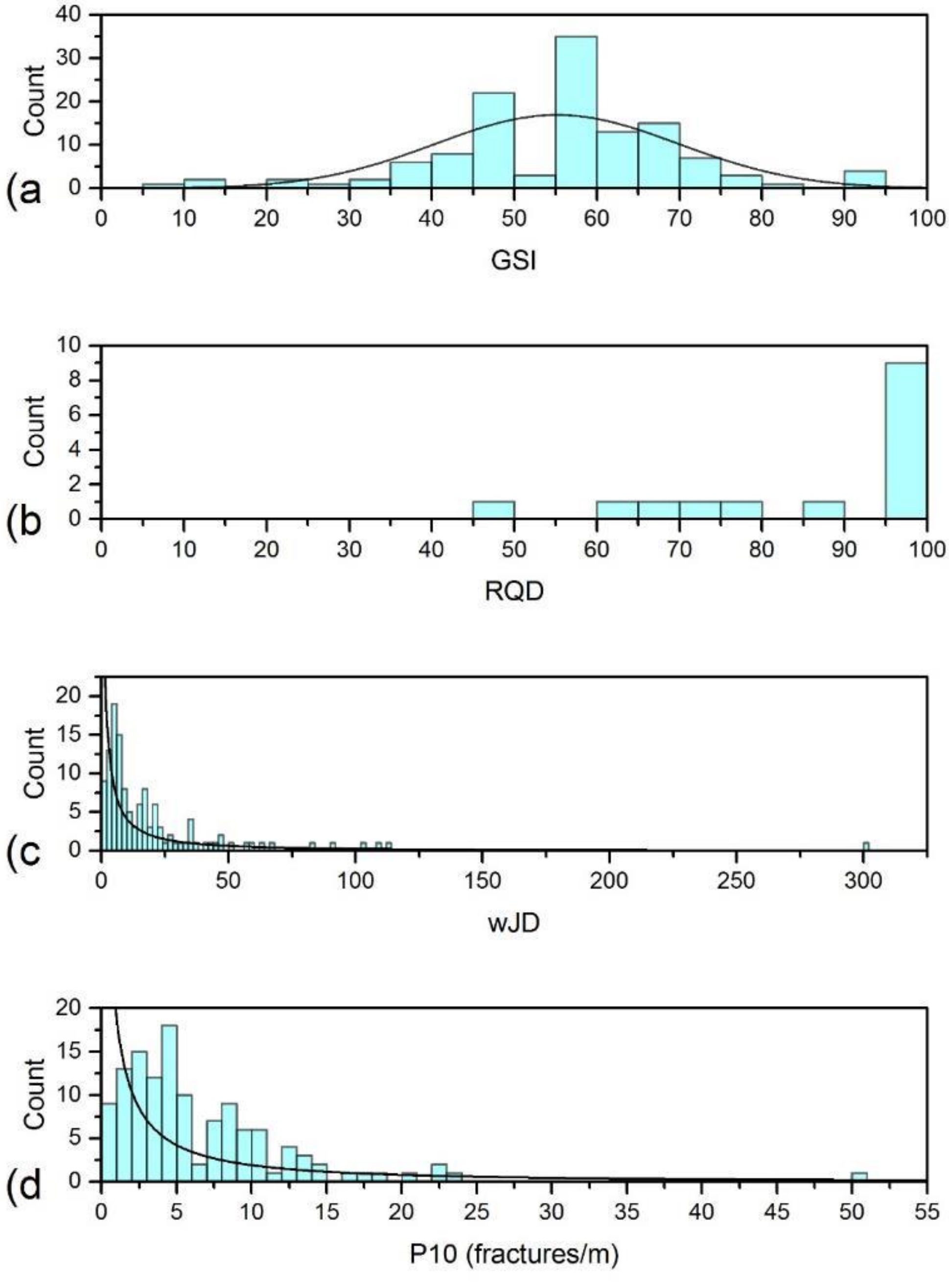

Figure 5.15: Frequency histograms for rock mass below the Spriana rockslide. GSI values are fitted by a Gaussian distribution, while wJD and P_{10} by log-normal trends.

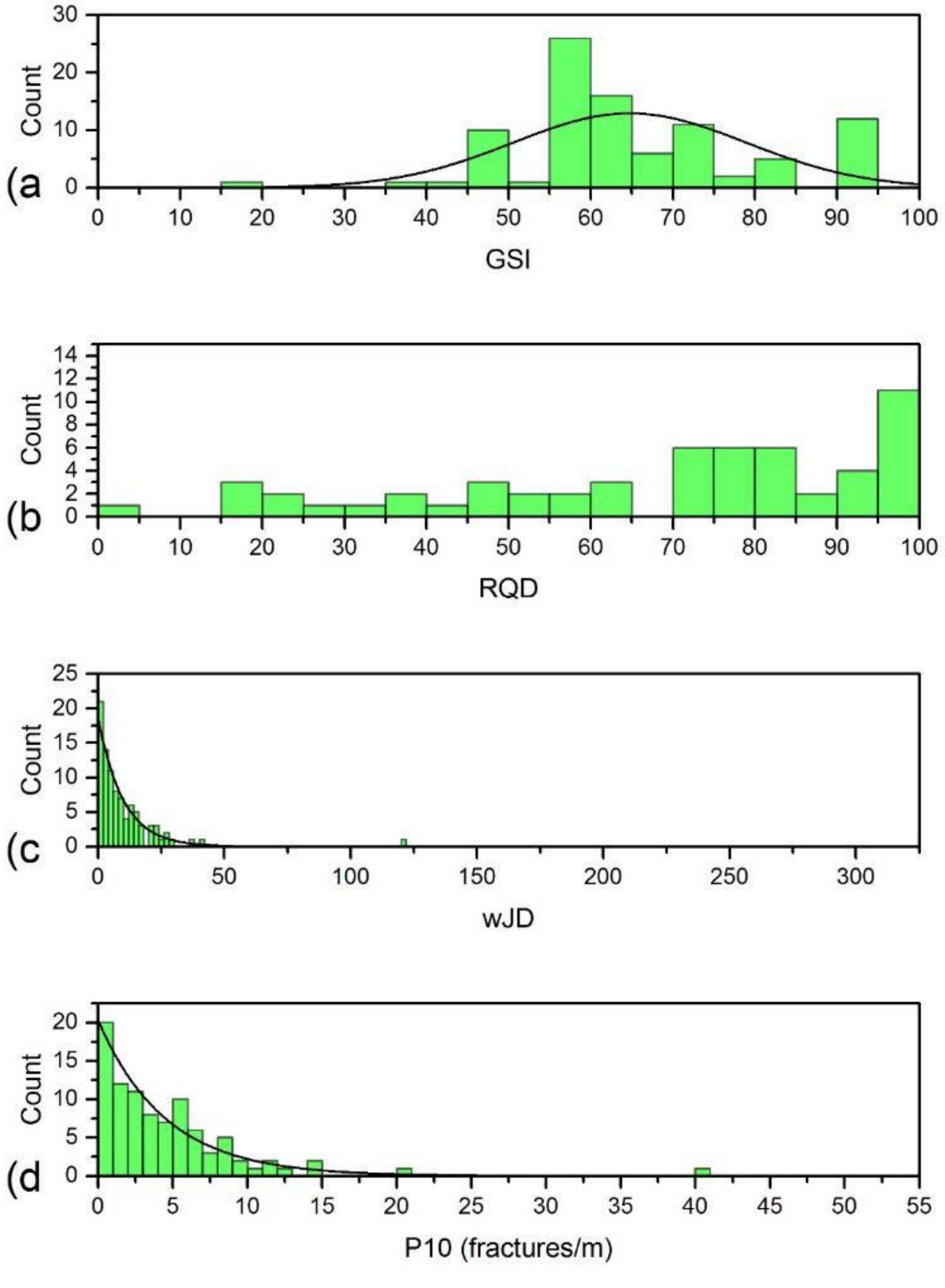

Figure 5.16: Frequency histograms for rock mass outside the Spriana rockslide. GSI values are fitted by a Gaussian distribution, while wJD and P_{10} by negative exponential trends.

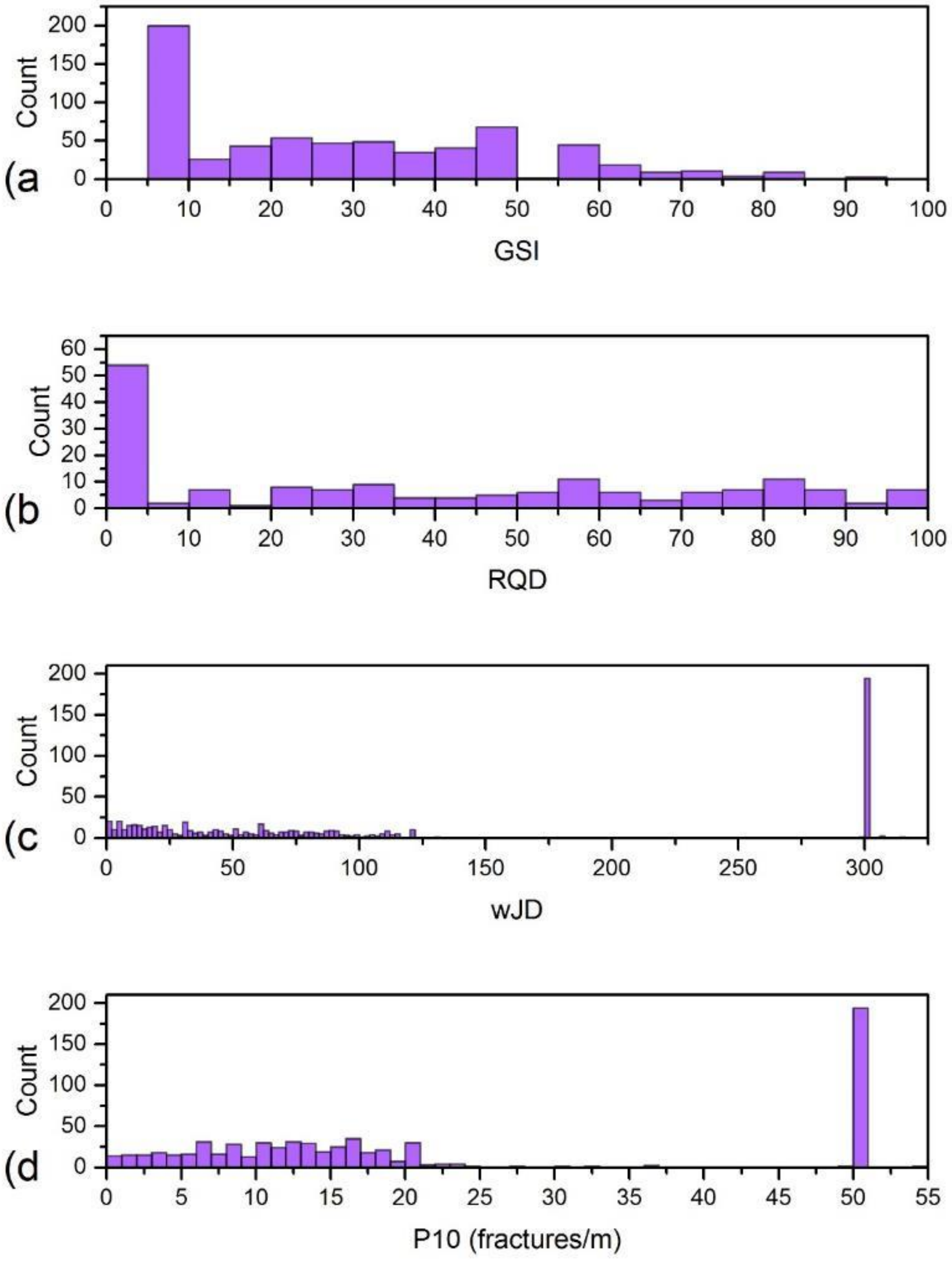

Figure 5.17: Frequency histograms for rock mass within the Spriana rockslide. The frequent occurrence of intense fractured levels and breccias makes the fitting of statistical distributions not possible for this domain.

5.5 NUMERICAL MODELLING

5.5.1 Model set-up and calibration

Numerical models of the Spriana slope were set up by discretizing the slope domain in a two-dimensional mesh of three-noded triangular finite elements with maximum edge size of 35 m, which roughly corresponds to 3% of the slope vertical size. The resulting mesh consisted in about 20,000 finite elements and 10,200 nodes (Fig. 5.18). Tests on mesh sensitivity performed for simplified slope profiles (Cf. chapter 4), suggested this value to provide the best compromise between computational time and consistency of results. The simulated profile (Fig. 5.18) was restored to Last Glacial Maximum conditions based on geomorphological field evidence: rockslide scarps were restored to their original configuration and bulging in the middle-lower sector of the slope caused by gravitational instability was removed. External mesh nodes along the bottom boundary were fixed in the x and y direction, whereas lateral ones were left free to move only in the y direction. The topographic profile was prolonged over the crest zone and, on the opposite side, ahead Mallero river to not introduce boundary effects within the numerical simulations.

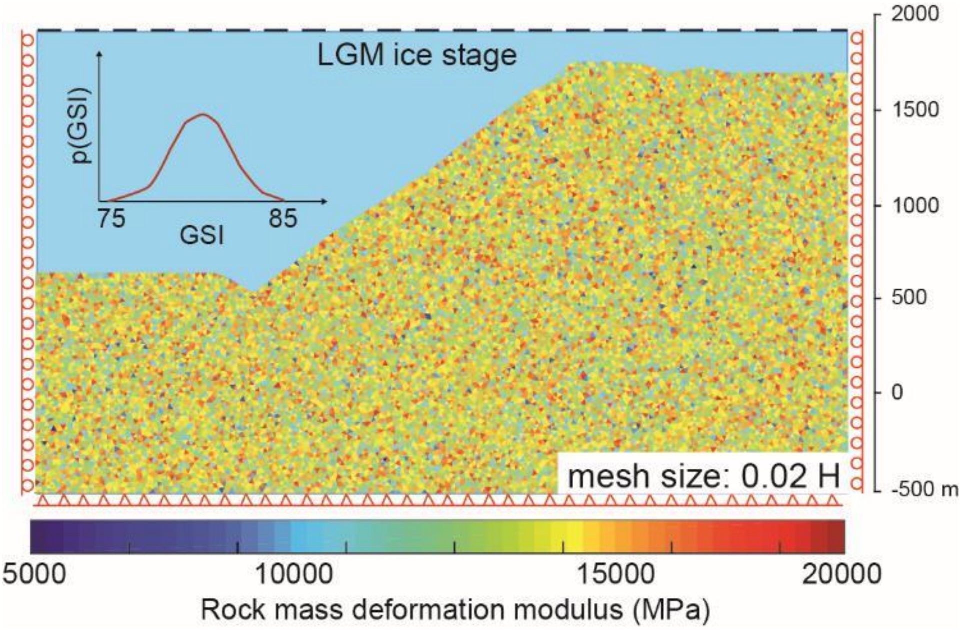

Figure 5.18: Model setup for the Spriana case study. Mesh size was established in 35 m, while rock mass heterogeneity was attributed assuming a GSI normal distribution with mean of 80 and standard deviation of 5. Corresponding values of rock mass deformation modulus are represented. Nodes along lateral boundary were constrained in x direction, while the model bottom was constrained also in y direction. The initial glacier height was derived from paleo-environmental and paleo-climatic data reported in literature.

The parameters *b* and *D*, governing the time-to-failure law and the damage law, respectively, were derived in the literature for intact rocks and laboratory conditions, then used for the simulation of static fatigue tests on synthetic specimens (Cf. chapter 4; Amitrano and Helmstetter, 2006). As stated in the previous chapter, the upscaling to rock mass value represent a concern, since no experimental data are available on large-scale sample. To further test this hypothesis also for real rock slope topographies, we performed an upscaling calibration to account for general rockslide features in Spriana slope. These preliminary simulations were conducted in extremely simplified conditions, without recurring to deglaciation and damage-dependent fluid pressure occurrence [Riva et al., 2016]. Parametric analysis performed on simplified rock slope set ups (Cf. chapter 4) indicates a limited scale effect (i.e. parameter upscaling from intact rock to rock mass) on *b*: in fact, damage patterns best representing commonly observed rockslide features are obtained wit b values falling in the lower range of available intact rock values, and in any case within the same order of magnitude. Simulation results indicate low values of *D* corresponding to less strain localization (i.e. shear band development), more diffused rock mass damage, and deeper rotational basal shear zone. Conversely, increase of *D* correspond to more localized and shallower shear strain, roto-translational rockslide kinematics and occurrence of multiple shear bands within the slope (Fig. 5.19). Regarding time-to-failure law, low values of *b* result in shallower rockslide basal shear bands and mainly translational kinematics, with two distinct scarps developing respectively at 1650 and 1400 m a.s.l. Instead, higher values of b result in deeper basal shear bands and more localized damage at depth in the rockslide (Fig. 5.20). The sensitivity to damage and time-to-failure parameters of the Spriana slope reflects what observed also in simulations on synthetic profiles. The analysis of displacement and damage patterns, localization and deformation moduli distributions of the different parametric models with respect to field data suggested the simulation with *D*=0.1 and *b*=30 as the best suitable to reproduce the Spriana rockslide features, meanwhile confirming the limited effect on *b* and *D* during the upscaling from intact rock to equivalent continuum rock mass.

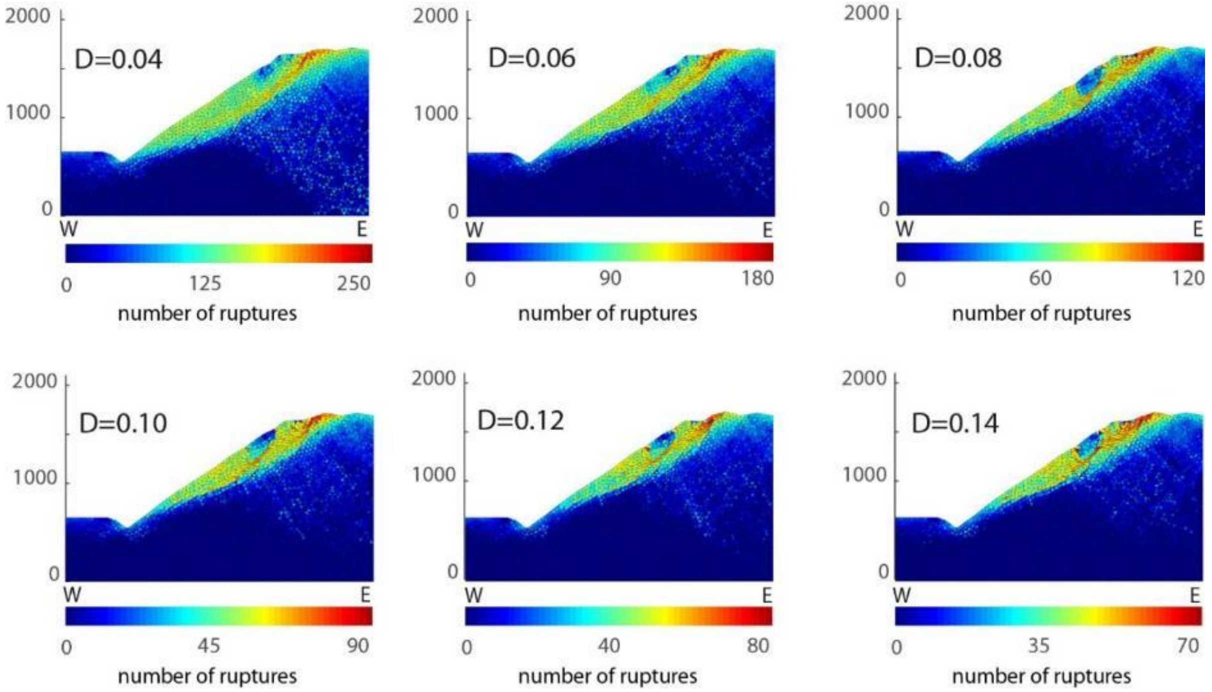

Figure 5.19: Spriana slope configuration and damage pattern for different values of the damage increment parameter *D*.

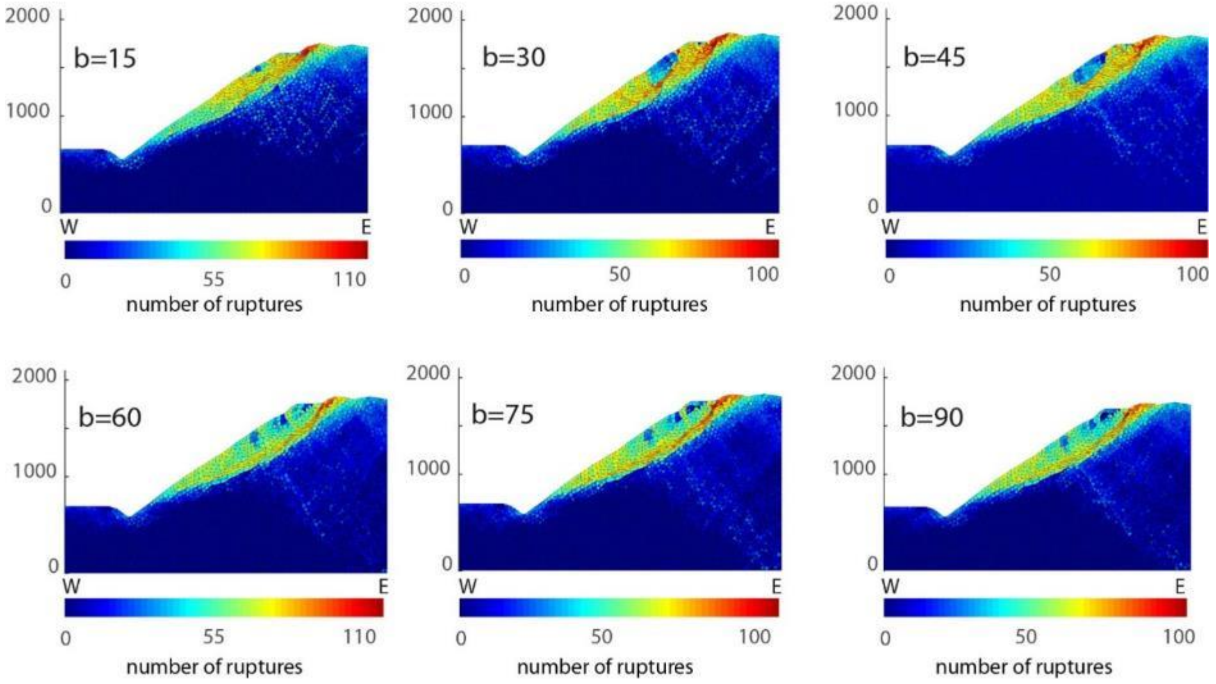

Figure 5.20: Spriana slope configuration and damage pattern for different values of the time-to-failure coefficient *b*.

Initial values of rock mass properties were derived from the analysis of site investigation regarding the "outside" damage domain (subsection 5.4), not affected by significant rockslide damage. To account for properties inherited from pre-model slope evolution yet considering relatively undisturbed "pre-damage" conditions, we imposed initial rock mass conditions corresponding to a mean GSI value to 80±5. This range corresponds to intact/blocky rock mass crossed by discontinuities with very good/good surface conditions (Fig. 2.2). According to the Hoek-Brown approach, GSI was used to upscale the strength and deformability of intact Monte Canale gneiss samples (Tab. 5.3), which mechanical parameters were derived through laboratory experiments by Agliardi et al. (2014).

Parameter	**Symbol**	**Mean**	**Interquartile range**
Uniaxial compressive strength UCS (MPa)	σ_c	60.1	56.4
Young Modulus (MPa)	ET_{50}	22.743	11.250
Tensile strength (MPa)	T	7.4	6.2
Cohesion (MPa)	S_0	21.3	10
Coefficient of internal friction	μ	0.67	0.1

Table 5.3: Monte Canale gneiss mechanical parameters derived from laboratory tests (from Agliardi et al., 2014)

Initial rock mass tensile strength, cohesion and coefficient of internal friction were imposed corresponding to a constant GSI value of 80. On the other hand, the initial deformation modulus E_0 was imposed to each element by assuming a random distribution of GSI, applying the relationship proposed by Hoek and Diederichs (2005) (Fig. 4.3). The upscaling of Poisson ratio was reasoned to take into account both ranges usually observed for rock mass values, which are higher in respect to corresponding intact rock (Gercek, 2007), and the increase of υ commonly observed during damage-controlled laboratory tests (Martin and Chandler, 1994; Eberhardt et al., 1999). Thus, we imposed $\nu=0.45$, which is a high value in respect to common modelling practice, but appears suitable for the DaDyn-RS approach.

Gravitational stress was initialized in the model and external ice load corresponding to the LGM ice stage applied. Then, modelling consisted in long-term simulation of the post-LGM deglaciation, through the Lateglacial and the Holocene until present day. The glacier LGM stage and the deglaciation time were constrained by the most updated paleo-environmental and chronological data available for the European Alps, including global trends inferred at alpine scale but also basin-scale observations and chronological data, particularly for valleys characterized by similar climatic, topographical and glaciological features with respect to the lower Malenco valley (Ivy-Ochs et al. 2006; Ivy-Ochs et al., 2008; Bini et al, 2009; Ivy-Ochs et al., 2015; Wirsig et al., 2016). Deglaciation was simulated starting from glacier elevation of 1950 m a.s.l. (Fig. 5.18) and lasting for a model time of about 700 yr, which is shorter with respect to deglaciation timing usually derived from absolute dating techniques, but coherent considering all the uncertainties related to the accurate assessment of LGM ice surface (Florineth 1998), start of deglaciation (Wirsig et al., 2016), downwasting rate and duration. However, the period we imposed corresponds to a mean ice downwasting of 2 m/yr, that is a rate commonly observed in present state retreating glacier in the Lombardy region (Bonardi et al., 2012).

The DaDyn-RS simulation stops when an imposed displacement value is reached. Here, we decided to monitor an observation point located at top of the observed prehistoric rockslide headscarp, which we supposed to be directly related with the post-LGM debuttressing. As field evidence constrained the vertical downthrown along this scarp in around 80 m, we decided to use this marker to represent the present slope state. Thus, the numerical model stopped when the vertical displacement reached 80 m at this point (Figs. 5.3 and 5.4).

To investigate the role of fluid pressure and deglaciation on the rockslide nucleation and development, we performed different model runs. The reference one was characterized by the account for both deglaciation and fluid pressure application, which were then excluded one at a time to constrain the influence on the slope evolution of the different processes. Regarding “dry” and “wet” conditions, we imposed values of permeable cluster filling by water of $w=0$ and $w=0.35$ respectively. Moreover, to assess the possible role of hydrologic pulses (i.e. medium-term groundwater fluctuations) on slope stability, we performed a simulation run characterized by time-dependent increase in permeable cluster filling. Static fluid pressures (i.e. no flow) were introduced in the model without specifying any pre-defined hydraulic boundary conditions, according to the adopted damage-based approach described in subsection 4.6. Model parameters were calibrated (Tab. 5.4) according to the multi-indicator approach described in subsection 4.8. To reduce uncertainties in model application to real slopes, correspondence between simulated and observed evidence of the following features were verified, including:

1) statistical distribution of simulated GSI values, back-calculated by distributions of effective deformation modulus in slope sectors corresponding to the different observed “damage domains” described in subsection 5.4;
2) slope geometry, in particular regarding unstable rockslide size, depth of basal shear band and correspondence between observed and simulated scarps;
3) spatial and mechanical patterns of damage, occurrence of localized and diffused damage in different slope sectors;
4) rockslide kinematics and patterns of surface and deep displacements;
5) time dependent behavior, slope life-cycle in respect to duration of deglaciation. Correspondence between the simulated displacement-time curve and the available absolute and relative chronological constraints.

Best fitting tensile strength and cohesion were imposed to 3.5 MPa and 7 MPa, respectively. Interestingly, these values fall in the range comprised between rock mass strength (no persistence of discontinuity accounted) and intact rock strength (Tab. 5.3). In the adopted damage-based modelling approach, calibrated strength values higher than those derived by empirical rock mass parametrization seem to reflect the importance of accounting for the occurrence of rock bridges when simulating the progressive failure of rock slopes (Einstein et al., 1983; Eberhardt et al., 1999; Stead and Eberhardt, 2013). The undamaged initial state is thus characterized by the occurrence of non-persistent fractures within rock mass, contributing to increase in strength at element scale.

In simulations with fluid pressure occurrence we also calibrated the parameter *w*, that regulates the permeable cluster filling. To do this, simulated rockslide depth, kinematics and degree of damage localization were compared to data coming from in situ characterization. The main rockslide features were correctly reproduced by imposing a filling degree of permeable element clusters equal to w=0.35. The calibrated parameters used for Spriana rockslide modelling are summarized in Table 5.4.

Parameter	**Symbol**	**Unit**	**Imposed value**
Unit Weight	γ	kN/m^3	27
Young Modulus (intact rock)	E_0	MPa	22,700
Tensile strength (rock mass)	T	MPa	3.5
Cohesion (rock mass)	C	MPa	7
Coefficient of internal friction (rock mass)	μ	-	1.1
Poisson ratio (rock mass)	ν	-	0.45
Damage increment parameter	D	-	0.10
Time-to-failure law parameter	b	-	30
Permeable cluster water filling	w	-	0.35

Table 5.4: Summary of calibrated numerical model parameters used in numerical simulations

5.6 MODEL RESULTS

5.6.1 Rockslide mechanisms

Calibrated model results accounting for upscaled material properties, time-dependent deglaciation and damage-dependent fluid pressure distributions provide a satisfactory account of the outcomes of long-term slope evolution ranging from post-LGM glacier downwasting to slope present-state. The model predicts the occurrence of a compound roto-translational rockslide suspended over the valley floor (Fig. 5.21). The rockslide overlies a band of localized damage extending from the rockslide toe at about 700 m a.s.l. up to the top of the slope, where it diffusely emerges in the upper, prehistoric top "scarp", indeed corresponding to the observed subdued slope sector above 1700 m a.s.l. The simulated rockslide depth, ranging between 100 and 180 m, is partially biased by the effect of mesh size, resulting in deeper unstable volume in respect to observation coming from borehole and inclinometric data (Fig. 5.22). Despite this, the spatial pattern reproduced by the simulation is coherent with the geological model of the slope and with the site investigations conducted on the rockslide, which highlighted the occurrence of damaged rock mass also below the basal shear zone (S113; Fig. 5.13). In any case, the preliminary parametric analyses conducted on mesh size effects had showed that predicted failure mechanisms and kinematics are affected in minor way by variations in element dimensions.

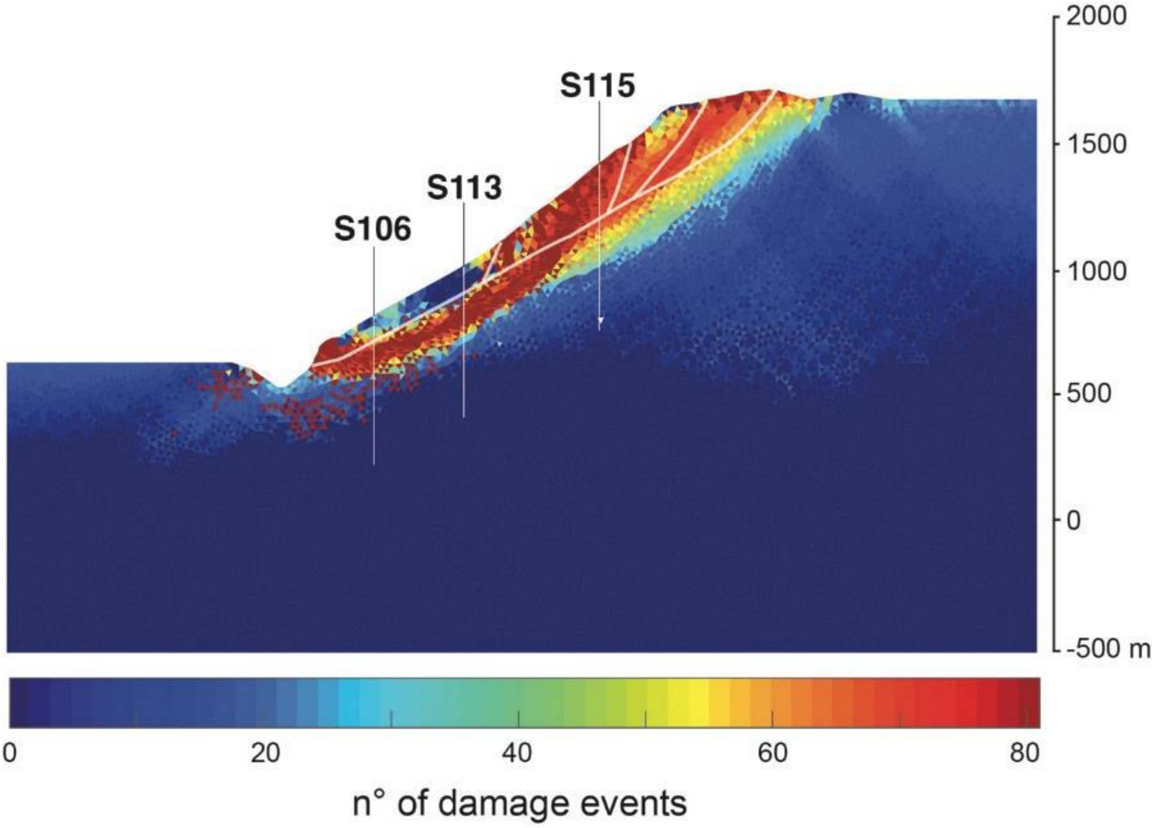

Figure 5.21: Pattern of damage registered for calibrated simulation, compared with observed rockslide features (white lines). The location of simulated boreholes is also reported.

We sampled vertical profiles of modelled horizontal displacement to simulate "virtual inclinometers" (white lines in Fig. 5.21 and 5.22): these were located corresponding to real boreholes drilled on the Spriana slope, particularly S106 (850 m a.s.l.; Fig. 5.12), S113 (1000 m a.s.l.; Fig. 5.13) and S115 (1370 m a.s.l.). Simulated profiles highlight slope horizontal displacement up to 120 m of depth in the lower portion of the slope, which is maintained constant moving upslope since S115. The transition to stable rock mass occurs gradually along the basal shear band, whose thickness grows moving from localized damage at toe to more diffused pattern in the upper portion. This accounts for a true rockslide mechanism associated to a deeper viscous deformation of damaged rock masses below. Notably, the rock mass within rockslide exhibit different behavior in respect to the slope sector analyzed. In the upper slope, rock mass displacement progressively decreases with depth, while in the lower and middle slope portions slight displacement increase with depth is registered, thus suggesting steering effect induced by deep movements and pushing from upper rockslide portions (Fig. 5.22).

The predicted spatial pattern of damage within the rockslide mass provides a satisfactory account of the borehole records, with generally diffuse damage close to the slope toe (where widespread shallow instabilities occurred since the late 19th century) and above the lower scarp (Fig. 5.21). Below the lower scarp, damage is far lower within the rockslide mass, but much more localized in a basal shear band. This is clear also in the vertical logs of simulated GSI, sampled along three vertical lines corresponding to boreholes S106, S113 and S115 (blue lines in Fig. 5.22): moving upward from S106, progressive deepening of the damaged rock mass is observed, ranging from 300 m up to 450 m in S116. Notably in S106 and S113 good-quality remnants overlies intensely fractured rock mass, with damage extending up to 300 m below. The different degree of damage and strain localization, simulated in the different parts of the basal shear band, mirror observed textural features of cataclastic breccias in the boreholes (Fig. 5.4), which are thicker and more comminuted in the lower part of the slope than in the upper.

Beside the spatial patterns simulation, the model is also able to quantify the impact of damage on rock mass mechanical properties for different slope sectors. Final values of rock mass deformation modulus were converted into corresponding value of GSI to be compared with observed data. This was done considering model elements up to depths of 150 m from the slope surface, to be representative of material sampled with boreholes.

Simulated GSI distributions are in close agreement with values derived from site geotechnical characterization (Fig. 5.23): starting from initial values in the narrow range 75-85 (green line in Fig. 5.23), progressive damage led to degradation of rock mass properties to GSI values in the range 55-65 below the rockslide (blue lines in Fig. 5.23). The simulated distribution, despite the good agreement for GSI values comprised in the interval 30-80, is characterized by the relative abundance of low values which were not collected through field observation. This could be ascribed to partial discordance between sampled domains and depth of the rockslide shear band, which is sampled recurring to constant depth all throughout the slope profile. Moreover, this effect could be related by an excessive rock mass damage reproduced by our simulation.

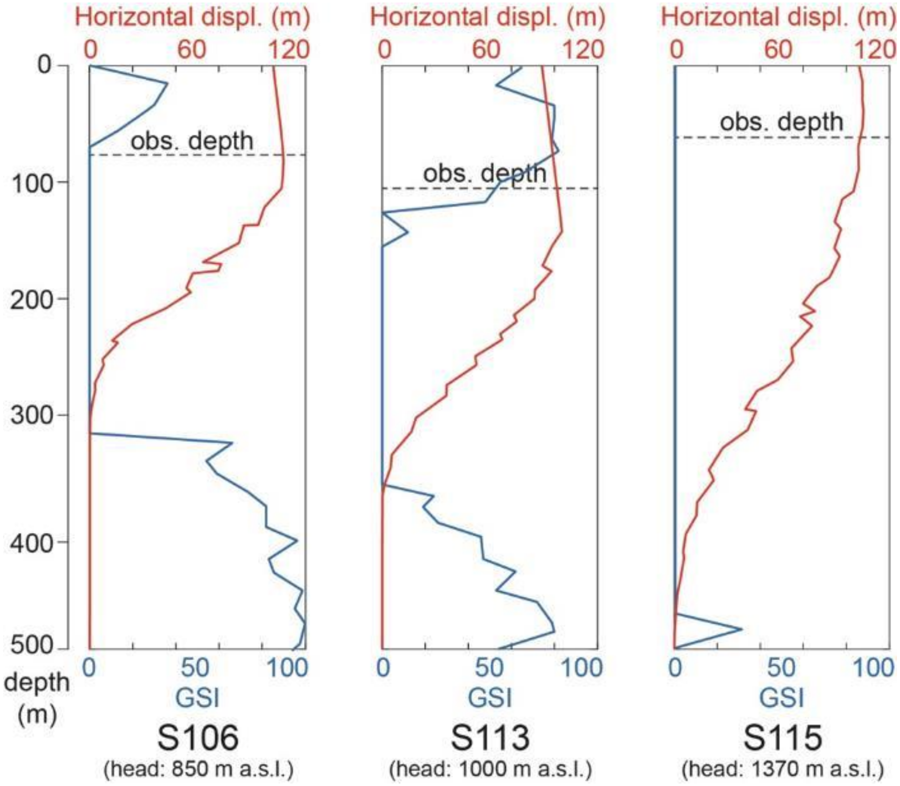

Figure 5.22: Logs of simulated horizontal displacement (i.e. virtual inclinometers) and GSI values (i.e. virtual borehole logs) along vertical lines corresponding to boreholes.

Inside the rockslide, gravitational deformation contributed to further damage and lower GSI values, accounting for observed loss of structure and intense fracturing (red lines in Fig. 5.23). Both simulated and observed distributions exhibit a peak for GSI values lower than 10 and sparse occurrence of rock mass of fair and good quality. The two relative peaks predicted by the simulation, which roughly correspond to GSI values of 30 and 65, are found also in observed dataset but with a light shift to values representative of better quality rock mass.

Interaction between fluid pressure occurrence and damage mechanisms during the entire simulation constrained the final (post-glacial) distribution of permeable element clusters, and thus of fluid pressure distribution within the slope. Here, three different permeable clusters form an almost fully interconnected perched aquifer in the slope portion below the lower scarp, within the rockslide and in the damage zone just below (clusters 3,4 and 5 in Fig. 5.24). Moreover, a shallower and spread aquifer occurs in the upslope portion, two hundred meters upslope the lower scarp, crossing the prehistoric rockslide headscarp, the prehistoric top scarp and extending over the slope crest until the model boundary (cluster 6). An additional cluster is predicted by the numerical model on the other side of the valley (cluster 1): its occurrence is purely artificial, since the real slope morphology was modified due to numerical and computational reasons. Results are consistent with borehole and piezometric evidence (ISMES, 1990; Belloni and Gandolfo, 1997; Agliardi and Crosta, 2014), thus supporting the present-day mechanical sensitivity of the rockslide to external hydrological inputs, especially in the lower part of the slope, where the largest displacements are cumulated (Figs. 5.4, 5.7 and 5.24).

Horizontal and vertical displacement patterns (Figs. 5.25a, b) emphasize the observed extent and compound kinematics of the rockslide, which is shallower than the damaged zone

(Fig. 5.22). The slope experienced large vertical displacements in the upper scarp region, where abrupt increase with respect to the upslope sector is collected. Moving throughout the headscarp surroundings, progressive decrease of displacement occurs, until a few meters cumulated on the prehistoric top scarp. On the other hand, dominant horizontal displacements occur between the upper scarp and the rockslide toe, accounting for the recent rockslide history, which indicates the major activity concentrated just in this slope sector. A little decrease in horizontal displacement magnitude is registered corresponding to the lower scarp while in the upper sector, as for vertical component, a progressive decrease is encountered until the portion immediately beneath the slope crest.

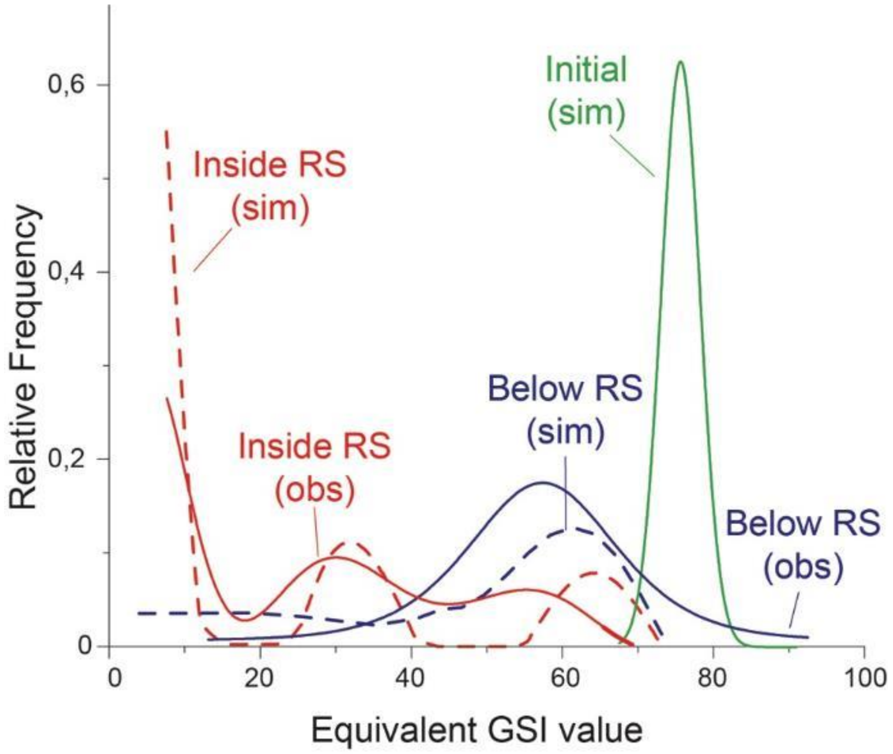

Figure 5.23: Observed versus simulated (dashed lines) frequency distributions of GSI values. Simulated value are back-calculated from distributions of simulated effective deformation moduli E_i.

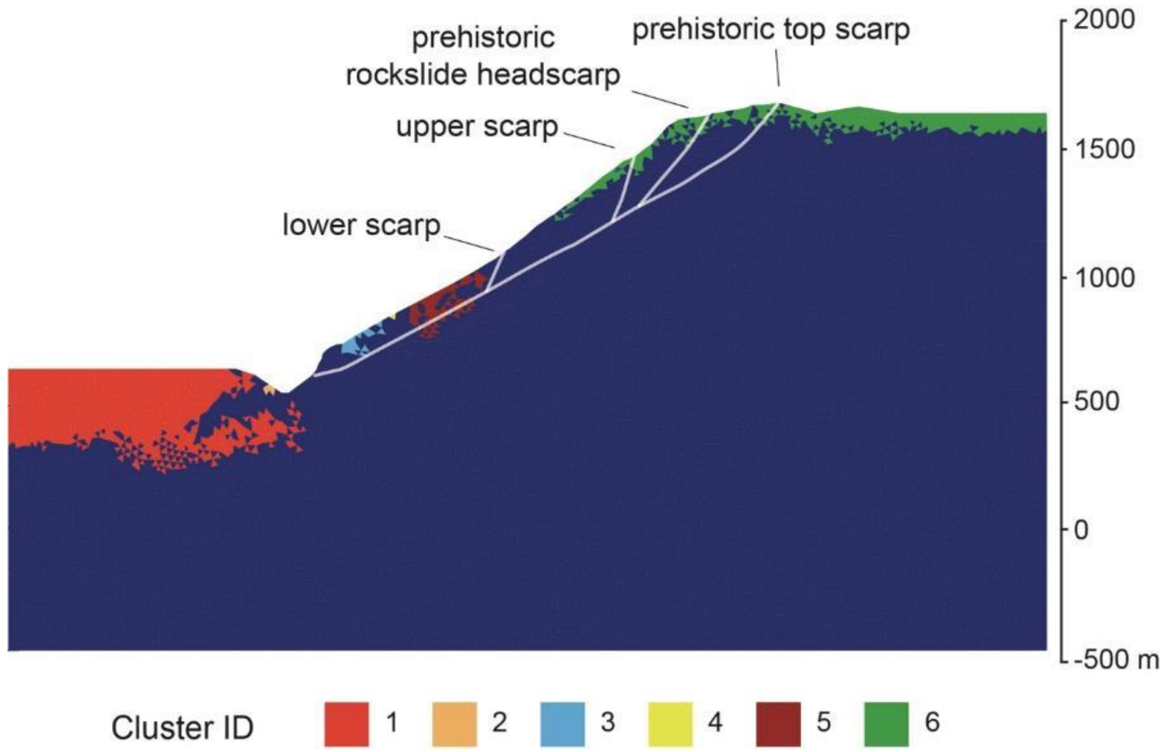

Figure 5.24: permeable element cluster distribution in the final state of simulation,outlining the occurrence of several perched aquifers in the differentiated rockslide body. The location of observed rockslide features is reported with white lines.

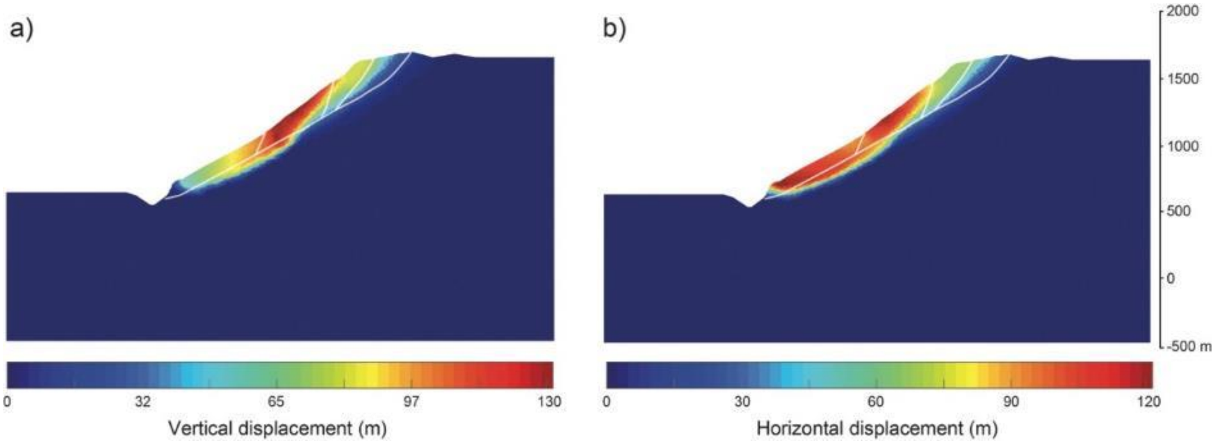

Figure 5.25: (a) Vertical and (b) horizontal displacement for calibrated simulation.

5.6.2 Time-dependent evolution

The explicitly time-dependent nature of our model provides the opportunity to explore the mechanism of slope damage, fluid occurrence, deformation and failure in an absolute chronological framework. Slope behavior was investigated through the storage of model partial states at predefined time intervals, thus providing frames of slope evolution through paraglacial and postglacial stages. Moreover, we tracked displacements simulated by numerical model for several observation points, in order to better constrain the temporal evolution of different slope sectors (Fig. 5.26). These were located along the slope corresponding to significant features of the rockslide, namely the prehistoric rockslide headscarp (point 1), the Lower Scarp (point 2) and the rockslide toe (point 3). We selected also 3 points in the upper (point 4), medium (point 5) and lower (point 6) sector of the basal shear band to monitor its evolution in respect to the superficial patterns. Displacement trends and location of the observation points are plotted in Figure 5.26.

Simulations begin with slope deglaciation, starting at about 21 kyr BP with an imposed total duration of 700 years. Five thousand years later, at 16 kyr BP, the effect of ice downwasting and rapid support removal caused minor scattered damage occurrence at slope toe (extension regime) and crest (compression regime), as a response to valley debuttressing (Fig. 5.27a). At this stage, fluid occurrence is limited to isolated clusters, mainly located at slope toe and in crest zone (Fig. 5.27b), while no considerable strain localization or permanent displacements occur (Fig. 5.27c and 5.26).

Major changes occur about 10 kyr after the end of deglaciation, in correspondence with the Holocene transition at 11000 yr BP. Initial damage localization occurs in the lower part of the slope, just above the valley bottom, ranging from 500 m to 700 m a.s.l.. Meanwhile, damage starts to propagate upslope, reaching the already damaged portion in the crest zone (Fig. 5.28a). Here, damage localization results in a dilatant damage zone, which strongly conditions permeable element clusters distribution. Indeed, a connected aquifer layer is hosted, linking the upper and lower portions of the slope (Fig. 5.29b). Although no shear strain localization occurs yet (Fig. 5.28c), a global increase of cumulative number of ruptures and velocity emerges from the analysis of time-displacement curves for the different observation points monitored during the simulation, especially for the prehistoric rockslide headscarp (point 1) and the upper part of the basal shear band, suggesting activation of the slope upper sector (Fig. 5.26).

After 12 kyr from the end of deglaciation (9000 yr BP), damage continues to progress upward from slope toe up to the middle slope sector (Fig. 5.29a). Moreover, progressive damage extends upwards, resulting in weakening and increased displacement rates also in middle and lower slope. Notably, damage at slope toe is followed by progressive strain localization, that initiates in the previously dilatant damaged zone and induce the transition of basal shear band to contractive behavior (Fig. 5.29c). Since one of the conditions imposed for permeable element cluster occurrence regards dilatancy, these modifications affect fluid pressure distribution through a progressive hydraulic sealing of the shear band (Fig. 5.29b). The observed displacement slowly cumulates within the entire slope, even if notable acceleration is not yet registered.

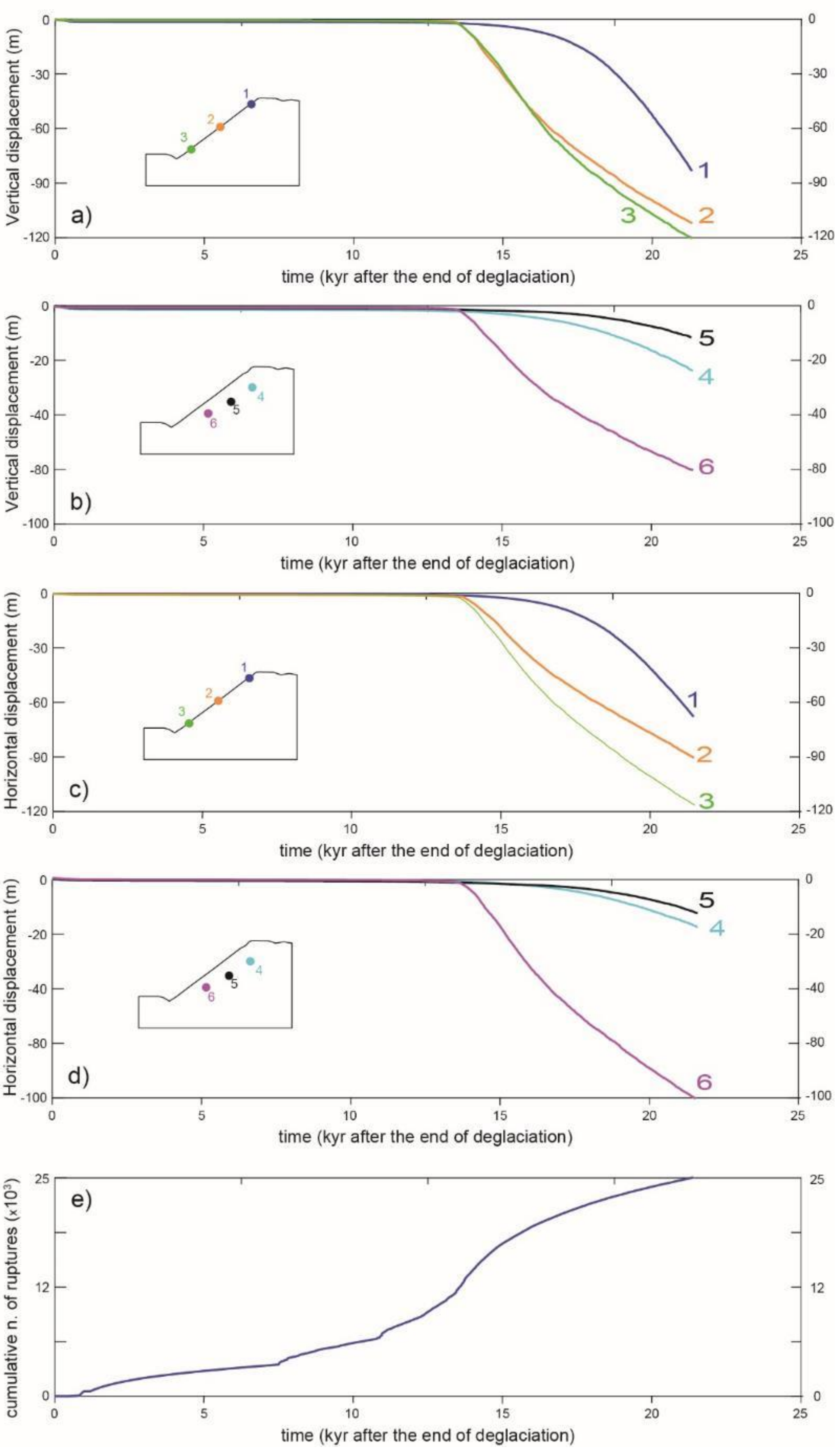

Figure 5.26: Vertical (a,b) and horizontal (c,d) displacements of selected observation points at key slope locations (insets) compared with cumulative number of ruptures (e).

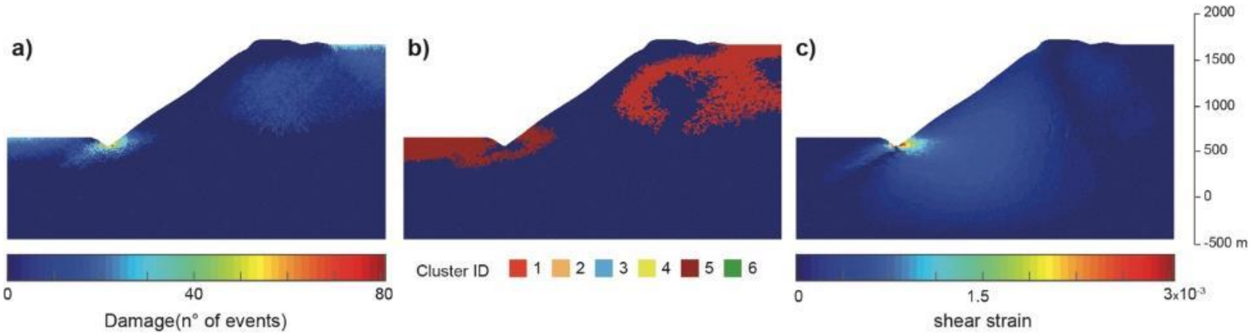

Figure 5.27: Damage pattern (a), permeable element cluster occurrence (b) and shear strain pattern (c) at 16 000 before present.

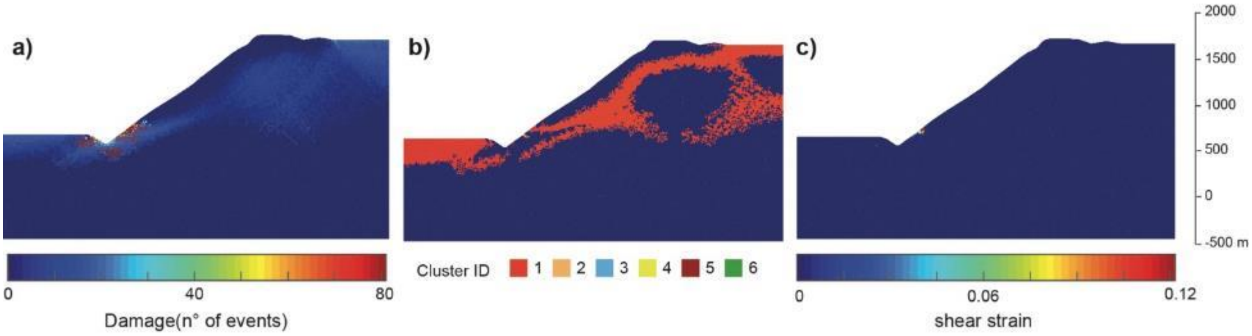

Figure 5.28: Damage pattern (a), permeable element cluster occurrence (b) and shear strain pattern (c) at 13 000 before present.

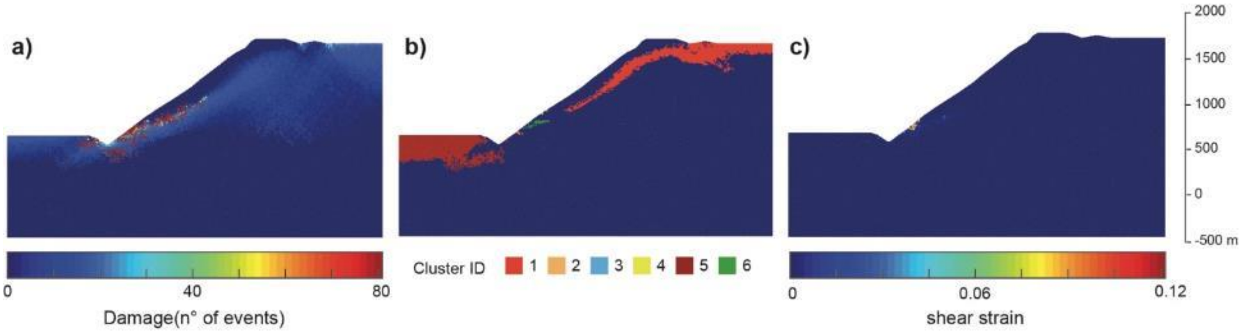

Figure 5.29: Damage pattern (a), permeable element cluster occurrence (b) and shear strain pattern (c) at 10 000 before present.

Complete rockslide differentiation is reached 6000 yrs BP, coinciding with the completion of damage bands extending from slope toe to the scarps located around 1400 m a.s.l.. At this stage, rockslide basal shear band consists in alternation of severe-damaged elements and less damaged portion, thus not yet exhibiting mature evolution (Fig. 5.30a). Intense strain localization along the present-day basal shear band, especially at slope toe and along upper scarp, is also registered, describing a roto-translational plane less inclined in respect to mean slope angle (Fig. 5.30c). The model suggests that the prehistoric headscarp and top scarp nucleated during this stage. Shear band contraction resulted in complete sealing and development of several little permeable element clusters within the rockslide, particularly in the lower and upper part of the rockslide (Fig. 5.30b). However, their dimension do not permit the complete interconnection at rockslide scale. Such evolution is associated to a one order-of-magnitude increase of rupture and displacement rates, especially at rockslide toe and in upper scarp sector (Figs. 5.26). At this stage, the entire basal shear band is activated, with displacement rates one order of magnitude higher in the lower portion with respect to the medium and upper sectors.

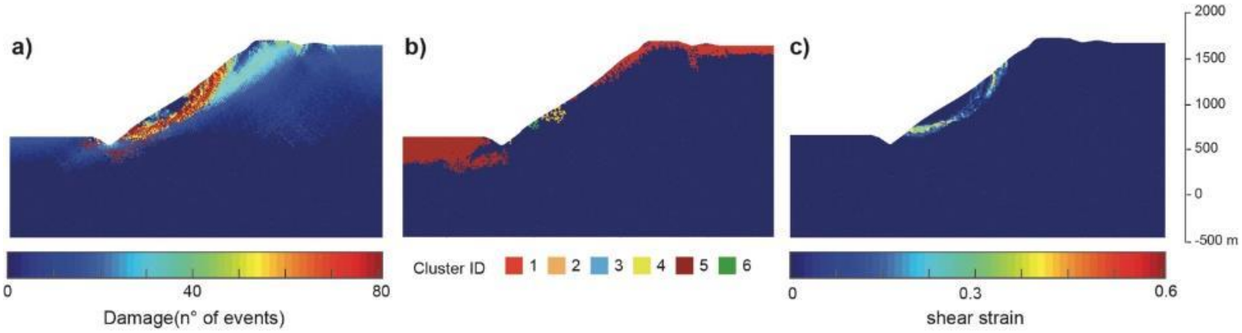

Figure 5.30: Damage pattern (a), permeable element cluster occurrence (b) and shear strain pattern (c) at 6 000 before present.

At 4000 yrs BP significant modifications take place along basal shear band, where further localization is registered in the sector comprised between the rockslide toe and the upper scarp (Fig. 5.31a). Meanwhile, also in the upper slope portion increase in damage occurs but with a different pattern, consisting in diffused damage expressed along a band almost 500 m wide. Shear strain distribution testify the shear band maturation in the lower sector, while in the upper slope diffused damage results in the extension of strain from the upper scarp to the upslope portion (Fig. 5.31c). Permeable element clusters within rockslide register a slight increase in dimensions, while in the upper slope the opposite trend is registered, with the upslope migration of crest zone cluster (Fig. 5.31b).

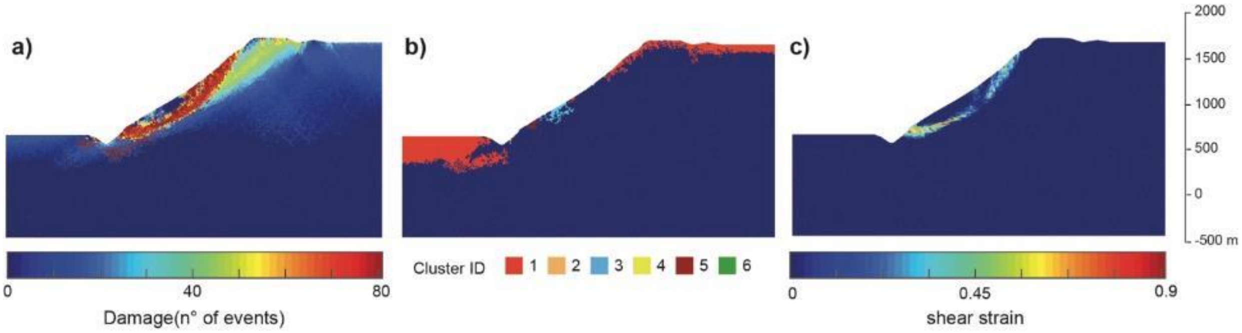

Figure 5.31: Damage pattern (a), permeable element cluster occurrence (b) and shear strain pattern (c) at 3 000 before present.

During the next 4000 yrs until present day conditions, intense damage occurrence is registered all throughout the slope particularly in the upper sector, where diffused damage is extended from 1300-1400 m a.s.l.. Meanwhile, several events are concentrated also along basal shear band, contributing to further localization (Fig 5.32a). Fluid pressure occurrence is diffused within the rockslide, especially in the lower part, where two almost interconnected clusters are simulated, resembling the present-day perched aquifer development. Another aquifer occurs in the upper rockslide portion and in the crest zone (Fig. 5.32b). Regarding strain, damage localization resulted in further shear along damaged band, which now exhibit a clear signature, especially in the lower portion of the rockslide (Fig. 5.32c). In the upper part of the slope and along main rockslide scarps strain pattern is less evident, also due to the diffuse nature of damage. Notably, evident changes occurred also in topographic profile, which now consists in lowered upper-part and bulging at rockslide toe. In monitored points, progressive failure and upslope growth of the basal shear band led to further non-linear increase of displacement rates until 20 mm/yr, sully consistent with present-day measured values.

Vertical displacement at the rockslide headscarp reached 80 m, progressively increasing moving downslope since 120 m collected at toe. Horizontal displacement follows the same trend, reaching 120 m in the lower sector and progressively decreasing since 70 m cumulated in the crest zone. The superficial displacement trend is reflected also by the shear band movements, with larger value up to 100 m collected in the lower portion for both vertical and horizontal components. In the middle and upper sectors, cumulated values are lower and with a minor velocity with respect to the rockslide toe.

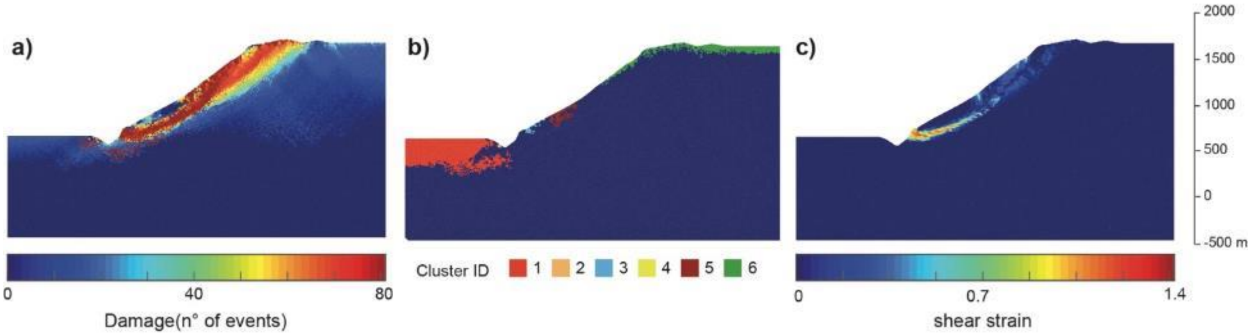

Figure 5.32: Damage pattern (a), permeable element cluster occurrence (b) and shear strain pattern (c) at the end of simulation

The displacement monitored in observation points located in different portions of the slope exhibits long-term smooth and regular trends (Fig. 5.26), which is not true for medium- and short-term periods. Indeed, examining a small span of time in slope history, the displacement rate results constituted by brittle acceleration phases, in which centimetric displacements are cumulated within a very short time, alternated with regressive periods, characterized by lower velocities and smoother displacement rates (Fig. 5.33).

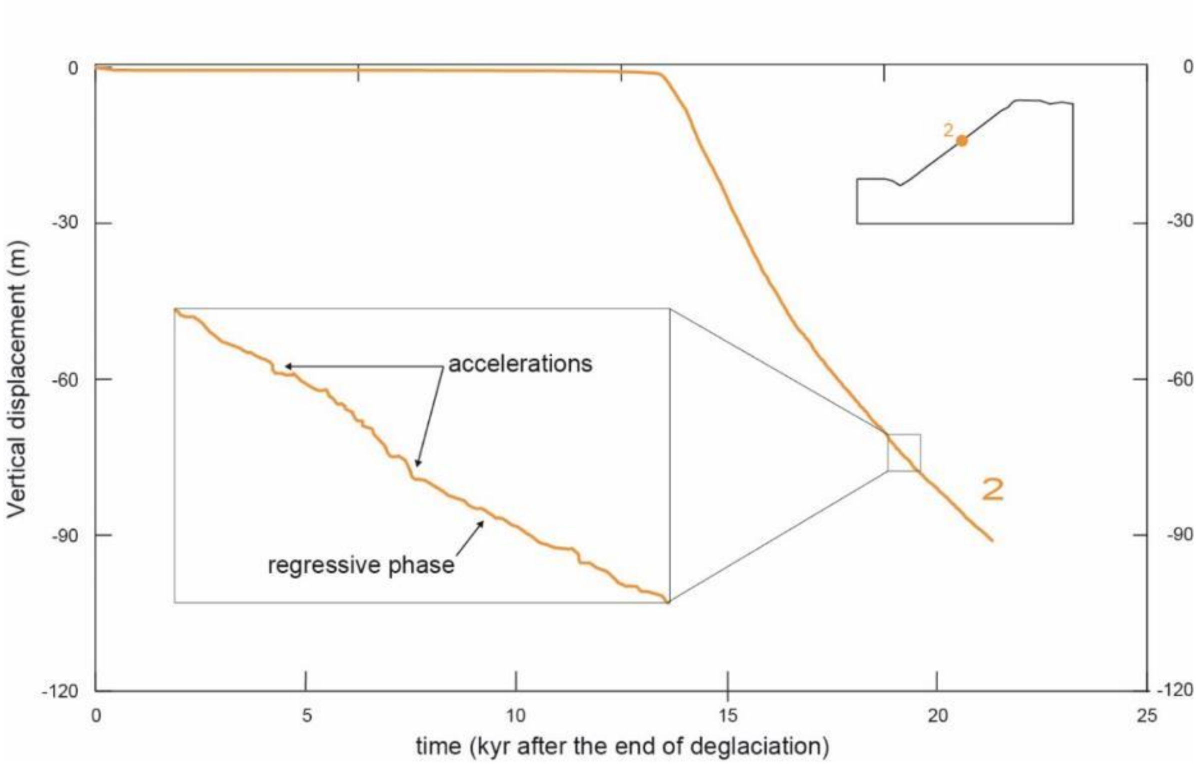

Figure 5.33: Vertical upper scarp displacement sampled in a 100 years period. Different stages are identified, showing the alternation of brittle acceleration phases with more smooth and long-lasting regressive phases.

5.6.3 Long-term effects of fluid pressure

The model results discussed in the previous paragraphs suggest a key role of fluid pressure occurrence in the long-term slope evolution, and confirm the realistic response of our damage-based fluid occurrence model, despite the simple hydrologic assumptions involved. This may also suggest that, in the long-term, mechanisms of brittle damage development are more influent than local-scale effects of hydro-mechanical coupling. The latter become increasingly important in mature stages of rockslide evolution, where hydro-mechanical coupling involve the response of well-developed shear bands made of soil-like material underlying weakened and permeable rockslide masses (Preisig et al., 2015; Crosta et al., 2014; Agliardi and Crosta, 2014).

To test this hypothesis, we further evaluate the effects of damage-based fluid distribution by running an additional model in “dry” conditions, setting the permeable element cluster filling to 0. Despite the extremely unlikely assumption of no groundwater occurrence on long-term large rock slope evolution, we were rather interested in evaluate the differences and similarities between the two simulations.

The dry simulation results in a sharply different geometry and kinematics of predicted rock slope failure, involving the entire slope with an inconsistent, deep rotational kinematics and an excess of damage localization along the simulated basal shear band, while the rock mass within the unstable volume exhibit minor damage and disturbance. The scarps observed along the slope profile are not reproduced by the dry model, which is also characterized by less strain without the rockslide body. The comparison between displacement patterns clearly highlight the difference in kinematics and depth of basal shear band (Fig. 5.34). In particular, the dry simulation under predict vertical displacement at the rockslide toe and results in sharper transition along the basal shear band.

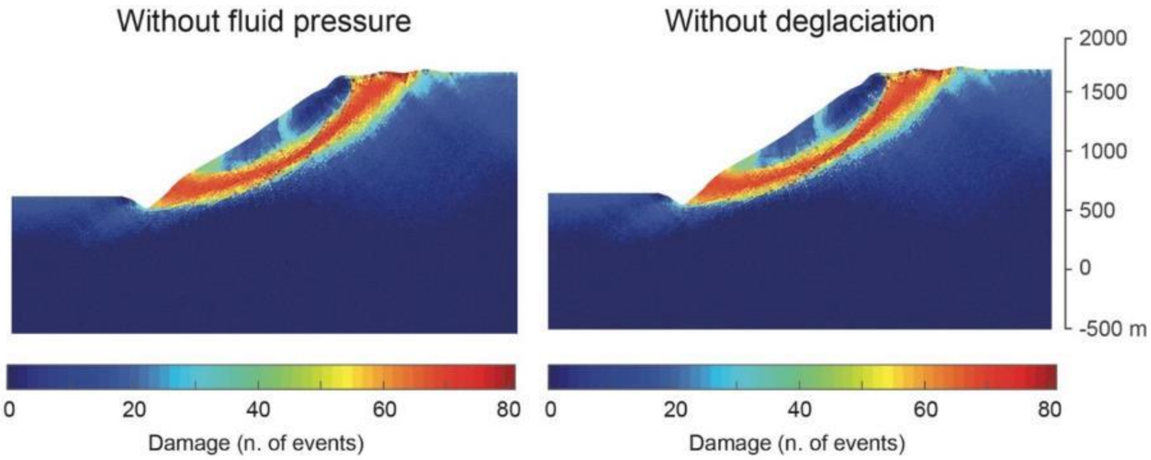

Figure 5.33: Comparison between final damage pattern for simulation with fluid pressure occurrence (a) and without (b).

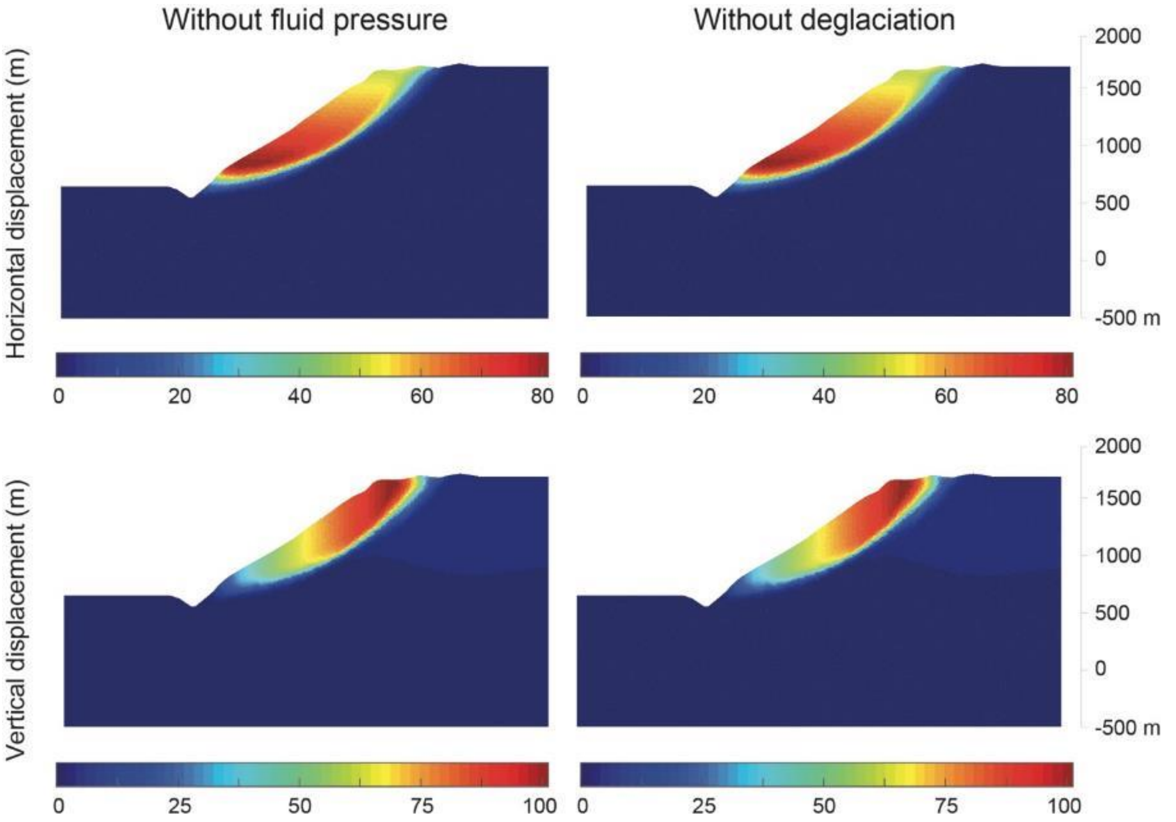

Figure 5.34: Comparison between vertical and horizontal displacement for simulation with fluid pressure occurrence (a and b) and without (c and d).

Simulations with and without fluid pressure occurrence are also extremely different regarding time-dependency. The dry model takes an excessively long time (>100 kyr) to reach observed cumulated displacement in prehistoric rockslide headscarp (Fig. 5.35a), meanwhile exhibiting very smooth acceleration during the entire slope life-cycle and avoiding the knee point clearly simulated in model with fluid pressure occurrence.

Accounting for permeable cluster filling also affect the long-term creep curve of the slope, here represented in terms of cumulative number of ruptures versus time (Fig. 5.35b). In fact, the model with fluid pressure results in a fluctuating trend: this is expressed by the superposition of long-term hydromechanical pulses, which are associated to major damage evolution stages, over a long-term material creep component. This trend is not reproduced by the dry model, which show a decelerating creep behavior upon deglaciation followed by a long-term steady state creep, which develops over a much longer time interval than in wet conditions.

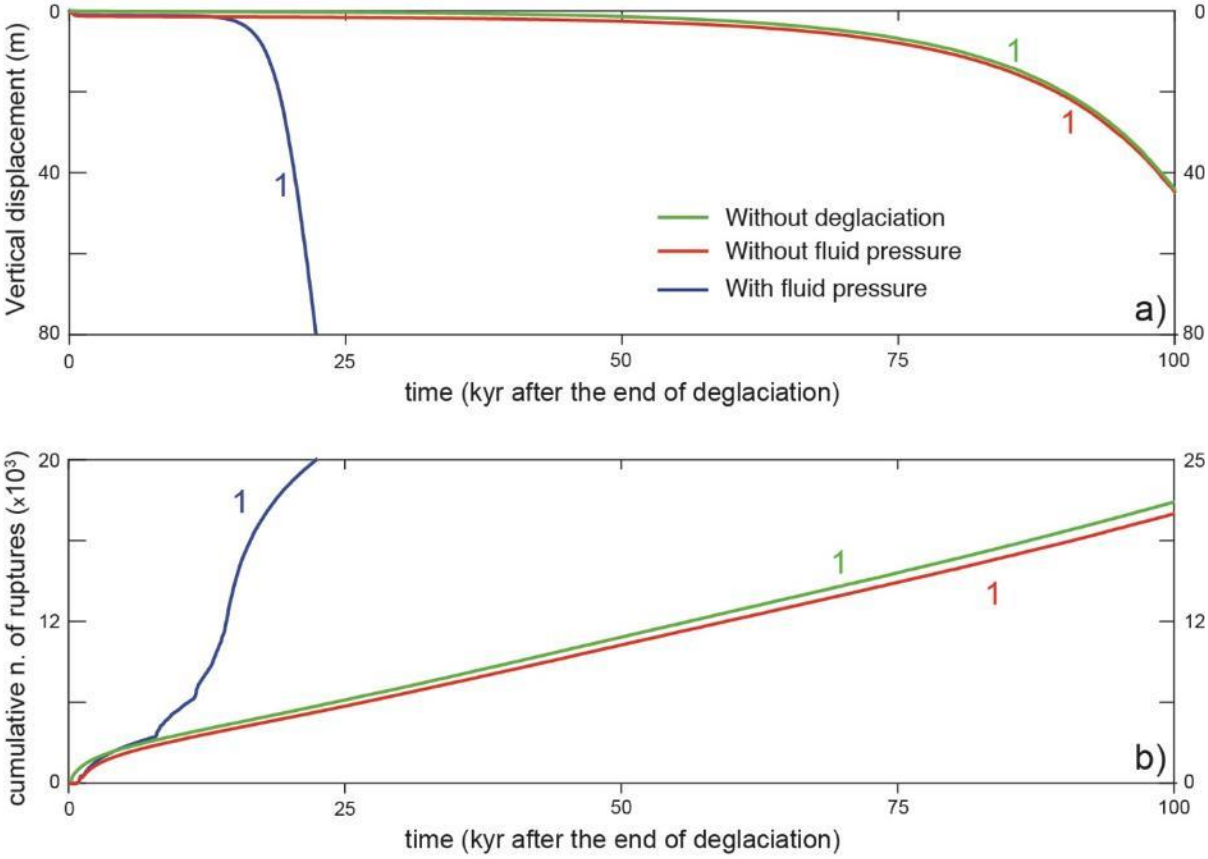

Figure 5.35: long-term displacement-time curves simulated with (blue) and without (red) accounting for fluid pressures (example for observation point 1); (d) long-term creep curves simulated with (blue) and without (red) accounting for fluid pressures, expressed in terms of cumulative numbers of ruptures.

To further investigate fluid pressure effect on slope behavior, we performed different models characterized by transient and progressively higher hydraulic loads. At this aim, we kept permeable cluster filling constant to *w*=0.35 until 5000 years from the present time (i.e. around 15-16 kyr BP), then we abruptly increase *w* to 0.50, 0.75 and 1. In every simulation, the increased filling degree was maintained until the end of simulation, i.e the reaching of threshold displacement in prehistoric rockslide headscarp (observation point 1). We decided to pick this particular period in slope history because, in paleo-climatic reconstructions, it is pointed out as characterized by wet conditions, abundance of meteoric water and widespread landslide temporal clustering all throughout the Alps (Magny et al., 2013; Zerathe et al., 2014).

Examining the damage patterns obtained from the different simulations, increase in fluid pressure within clusters resulted in consistent slope kinematics, basal shear band geometry and rockslide depth. In respect to the model with constant *w* (Fig. 5.36a), increase in clusters fluid pressure resulted in slightly upward migration of prehistoric top scarp, while the rock mass within the unstable volume appears more damaged, especially in the portion around 1000 m a.s.l. (Fig. 5.36e, g). Permeable element clusters within the rockslide show little variations regarding the number of elements constituting the perched aquifers: with respect to the constant simulation (Fig. 5.36b), increase in *w* to 0.5 (Fig. 5.36d) and 0.75 (Fig. 5.36f) corresponds to a slight growth in clusters dimension, while reaching complete clusters filling in a light decrease and fragmentation (Fig. 5.36h), due to the high strain occurring in the lower portion of rockslide.

Regarding the slope life-cycle, increase of fluid pressure resulted basically in shortening of the time to reach slope present state, except for the simulation with *w*=0.50, where an increase of around 500 years is reproduced (Fig. 5.37). For the other models, shortening in slope life-cycle up to 2000 years (10% of total slope lifetime) are obtained. The departure from constant simulation clearly appears since the variations in cluster filling, which immediately results in increased displacement rate (Figs. 5.37 and 5.38). Interestingly, the simulations with *w*=0.75 and *w*=1 encounter and unstable phase as a consequence of slope perturbed stress state, which in the latter occurs earlier, is longer and characterized by higher cumulated displacement. After that, a new equilibrium stage is reached, characterized by quasi-steady displacement rates ranging around 2.5/3.0 cm/year, consistent with data obtained from satellite interferometry on present-state Spriana slope (Agliardi and Crosta, 2014).

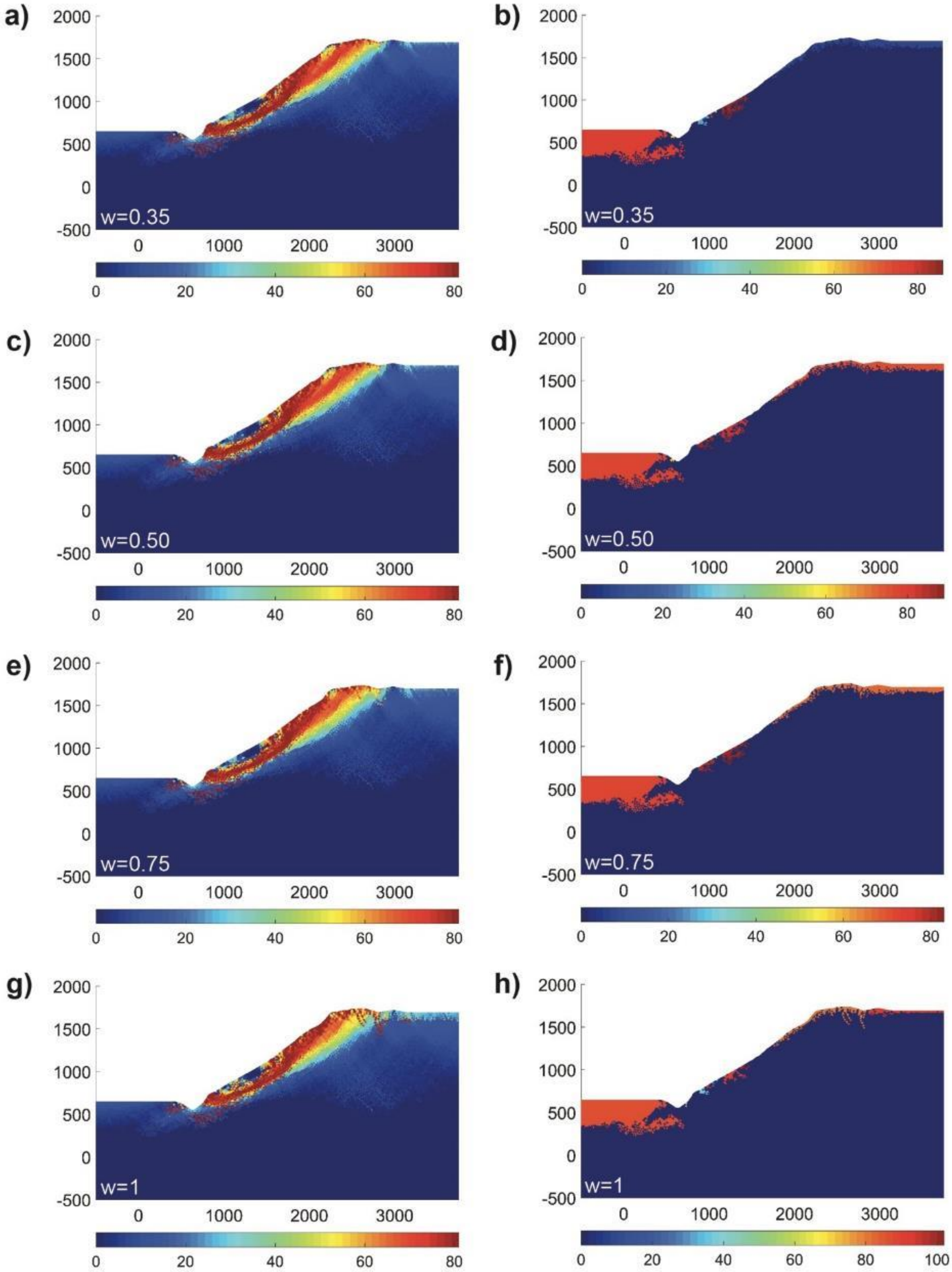

Figure 5.36: Comparison between damage patterns and permeable element clusters at the end of simulation for different increase in cluster filling, respectively (a, b) *w* constant to 0.35, (c, d) increase to 0.50, (e, f) increase to 0.75 and (g, h) increase to 1.

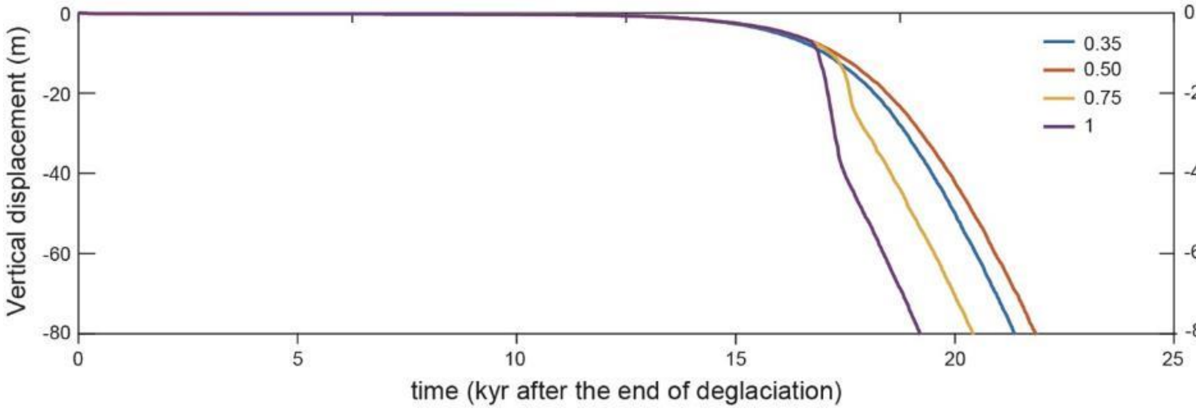

Figure 5.37: Vertical displacement of prehistoric rockslide headscarp (point 1 in Fig.5.26) for different values of permeable cluster filling increase. Increase of *w* to 0.75 and 1 results in shorter rockslide lifecycle.

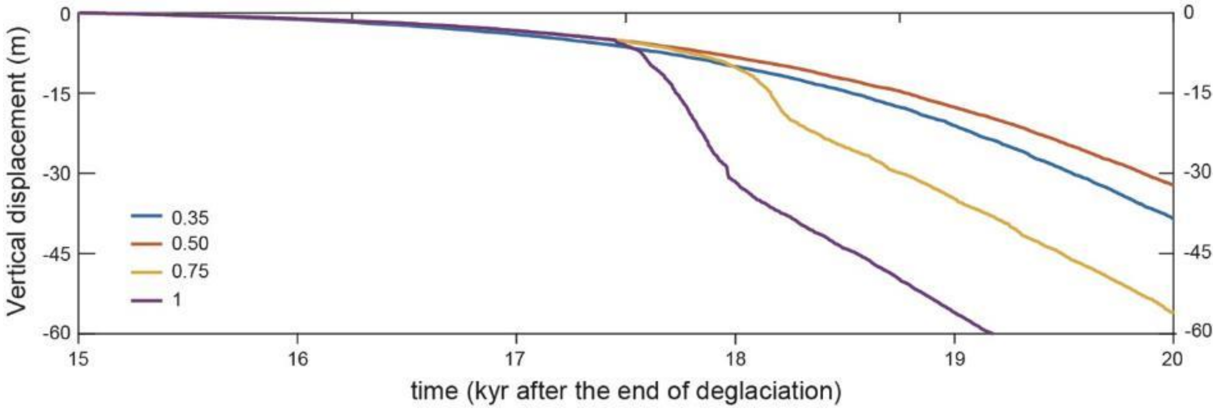

Figure 5.38: Detail of prehistoric rockslide headscarp vertical displacement (point 1 in Fig.5.26), just after the increase of cluster fluid pressure. Deviation from simulation with constant value of *w* and re-equilibrium for higher cluster fillings are represented.

5.6.4 Long-term effect of deglaciation

Deglaciation is often pointed as a major process in the long-term evolution of alpine slopes, largely conditioning the global stress pattern and the spatial and temporal damage distribution. To numerically evaluate its influence in our modelling framework, we run one simulation without including the effect of deglaciation, i.e. on a glacier-free slope. Regarding the other input values, model is characterized by the same time to failure, mechanical and fluid pressure parameters: the only difference consisted in the absence of ice buttress at the start of simulation.

Interestingly, the result is very similar with respect to the model without fluid pressure application, in terms of both damage (Fig. 5.33) and cumulated displacement (Fig. 5.34). Also in this case, deep rotational kinematics is reproduced, enclosing a rock mass poorly damage and deformed. The several scarps collected in the real slope are not reproduced, despite a little structure around 1500 m a.s.l., roughly corresponding to the upper scarp location.

The vertical and horizontal displacements exhibit only negligible contrasts with respect to the dry simulation, meanwhile being completely different if compared to the formerly glaciated model. In the latter, the effect of progressive debuttressing results into a soft but fundamental widespread damage all throughout the slope due to tensile rupture in shallower elements, particularly at toe, where the tensional release in greater. Nevertheless, the stress redistribution is often associated with the dilatancy regime, which in turn is strictly related to fluid pressure occurrence. In other words, the model without deglaciation results into a slope capable to host only small aquifers, thus almost neglecting the effect of fluid pressure application over the long-time. This is the reason why the model without deglaciation and the model without fluid pressure application are so similar, also regarding slope life-cycle and cumulated rupture events (Fig. 5.35). The little differences between the two curves are the visible effect of little permeable clusters, which nucleate within the glacier-free model. However, due to the limited spatial extension and the lack of interconnection, these permeable clusters are not able to condition the global evolution of the slope in the long-term period.

6 THE CRESTA DI SALINE DEEP SEATED GRAVITATIONAL SLOPE DEFORMATION

6.1 GEOLOGICAL AND GEOMORPHOLOGICAL SETTINGS

The Cresta di Saline Deep Seated Gravitational Slope Deformation is located in the upper part of Valtellina valley (Italian Central Alps), near Bormio village. The area belongs to the Austroalpine domain (Froitzheim et al., 2008) between two regional tectonic lines, respectively the Periadriatic lineament to the South and the Engadine line to the Northwest. The large-scale structure of the area consists in a series of stacked sedimentary units thrusted above Paleozoic basement units during the alpine orogeny (Fig. 6.1). According to the structural reconstruction of Frotzheim et al. (1994) and Conti (1997), the nappes emplacement, the exhumation of high-pressure units and at least two stages of post-nappe folding occurred since Upper Cretaceous. After that, an extensional regime contributed to a global extension consistent with the reactivation of existing faults during the Late Cretaceous as shallow normal faults postdating nappe stacking (Froitzheim et al. 1994). Following a subsequent compressive phase resulted in large scale nappe folding with axis oriented WNW-ESE (Eocene), Late Oligocene was characterized by N–S shortening synchronous with lateral continental extrusion along strike-slip and normal faults occurrence (i.e. Periadriatic, DAV, Brenner Lineament) marking the recent evolution of the belt (Conti 1997, Agliardi et al. 2009). The surroundings of the study area involves two main nappes: the Campo nappe and the Ortles nappe. The former consist of Pre-Mesozoic orthogneisses and phyllites in varisican amphibolitic facies, subsequently exposed to alpine greenschists retrogression and with minor occurrence of marbles and post-varisical magmatic intrusions. The latter is constituted by Permo-Triassic sedimentary carbonate covers deposed in platform zone (Dolomia Principale Fm.) and carbonates from Upper Triassic. The contact between these two nappes is defined by the Zebrù thrust, that gently dips to the E–SE along the Upper Val Venosta, where it outcrops in form of mylonitic bands. Moving westward toward Zebrù valley and Bormio area, the thrust dip direction rotate to North with a steeper angle and a transition to fragile and cataclastic behavior is recognized. This is interpreted as an evidence of a decreasing deformation temperature during the emplacement. For a detailed description of the litho-structural settings of the area, the reader can refer to Froitzheim et al. (1996), Conti (1997) and Mohn et al. (2012).

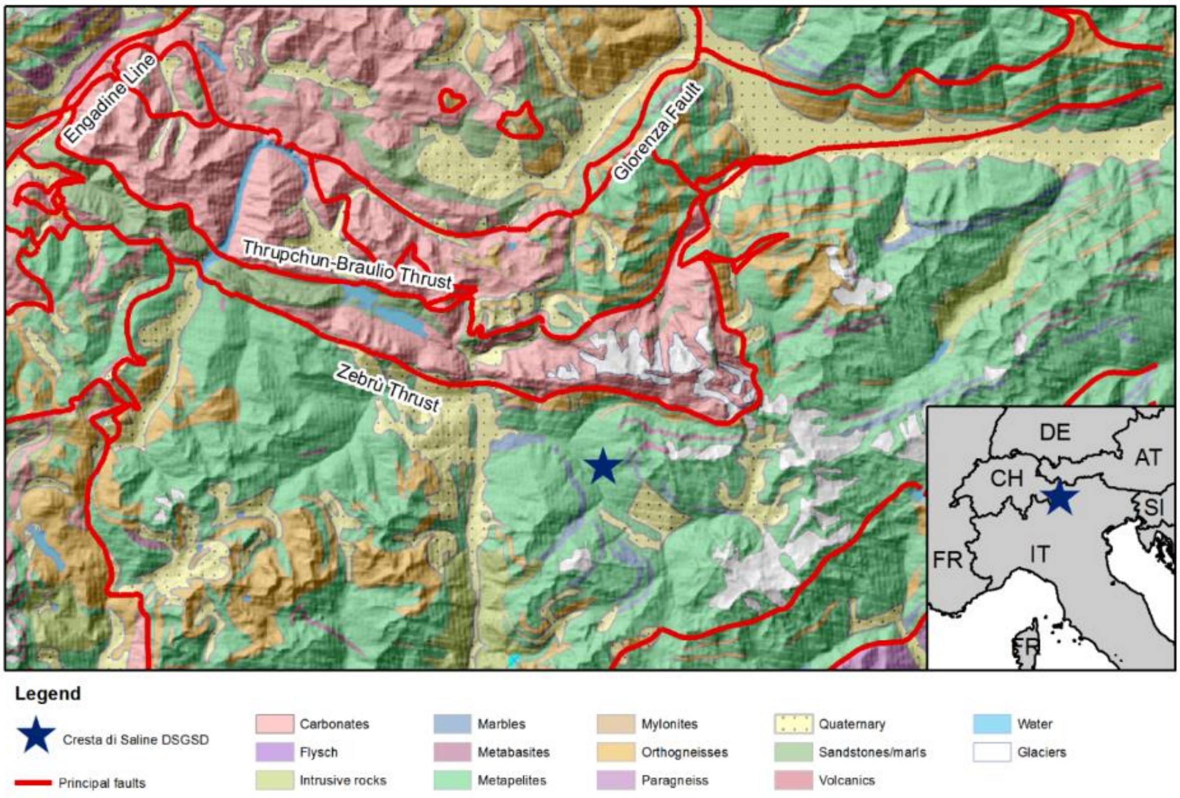

Figure 6.1: Geological sketch of the study area. The location of Cresta di saline DSGSD is indicated.

Phyllite constitutes the main lithotype in the study area, diffusely outcropping along Valfurva valley flanks (Fig. 6.2). This rock is mainly formed by quartz, chlorite and sericite, even if garnet, ilmenite and biotite are found as accessories, the latter often with evidence of metamorphic retrogression. Quartz content increase makes some portions switching to Phyllitic gneisses. Metric and decametric lenses of prasinites and marbles occur as interbedded layers, especially in the upper part of the slope. The former are mainly composed by chlorite, amphibole, epidote and quartz, while the latter consist of calcite with saccharoidal and microcrystalline structure, locally brecciated. Increase in chlorite content is registered locally, marking the transition to calcschists. Marble lens are also characterized by diffused weathering and karstic circulation: this is particularly evident near Confinale lake, where complex karstic groundwater network was recognized, and just upslope from Cavallaro Alta, where marble scarps exhibit weathering and enhanced dissolution (Fig. 6.3).

Figure 6.2: Centimetric-scale asymmetrical folding in phyllite rock outcrop near S. Antonio Valfurva

Figure 6.3: Marble lens near Cavallaro Alta. Rock mass appearance testify intense weathering and dissolution phenomena

Despite the Cresta di Saline DSGSD is entirely located in the Campo nappe, the occurrence of Zebrù thrust a few kilometers North partly affect the structural pattern of the slope. Indeed, at least four deformation events are recognized for the Campo nappe (Gregnanin, 1980). The first phase (D_1) was related to a foliation that after was completely transposed by the subsequent D_2. Relicts of original foliation were preserved in the hinge zone of centimetric-scale, isoclinal folds related to the phase D_2, highlighted by the orientation of quartz-rich levels. The resulting foliation S_{1+2}, in which the subscripts identify the contribute of both D_1 and D_2 phases, is expressed on the filed by alternation of millimetric, planar quartz-rich levels and centimetric, ondulated mica-rich domains. This schistosity was further rearranged by the occurrence of D_3 phase, which basically consisted in crenulation and large-scale asymmetrical folding with axial surfaces dipping to N-NE. Associated to this phase are also the centimetric chevron folds outcropping in the South-Western sector of the study area, probably related with a more ductile deformation in respect to the surrounding rock mass. The last phase D_4 is associated to gentle folding progressively decreasing moving away from Zebrù thrust, since it becomes no more recognizable at the bottom of Valfurva valley (Agliardi et al., 2001). It could be related to the huge displacement and strain cumulated during the emplacement of such regional tectonic structure.

The interpretation of aerial photos and Lidar DEM permitted to infer tectonic lineaments distribution and orientation in the surroundings of the study area (Fig. 6.4). From the exam of the rosette plot, sets orientated respectively NNE-SSW, NW-SE, N-S and E-W emerges. In particular, the systems NNE-SSW, NW-SE and N-S seems to be related to post-alpine fragile tectonics, caused by the readjustment subsequent to nappes emplacement (Gatto and Scolari, 1974). The NW-SE lineaments might be instead the fragile expression of the most recent stress field to which the area is subjected (Forcella et al., 1982; Forcella and Orombelli, 1984).

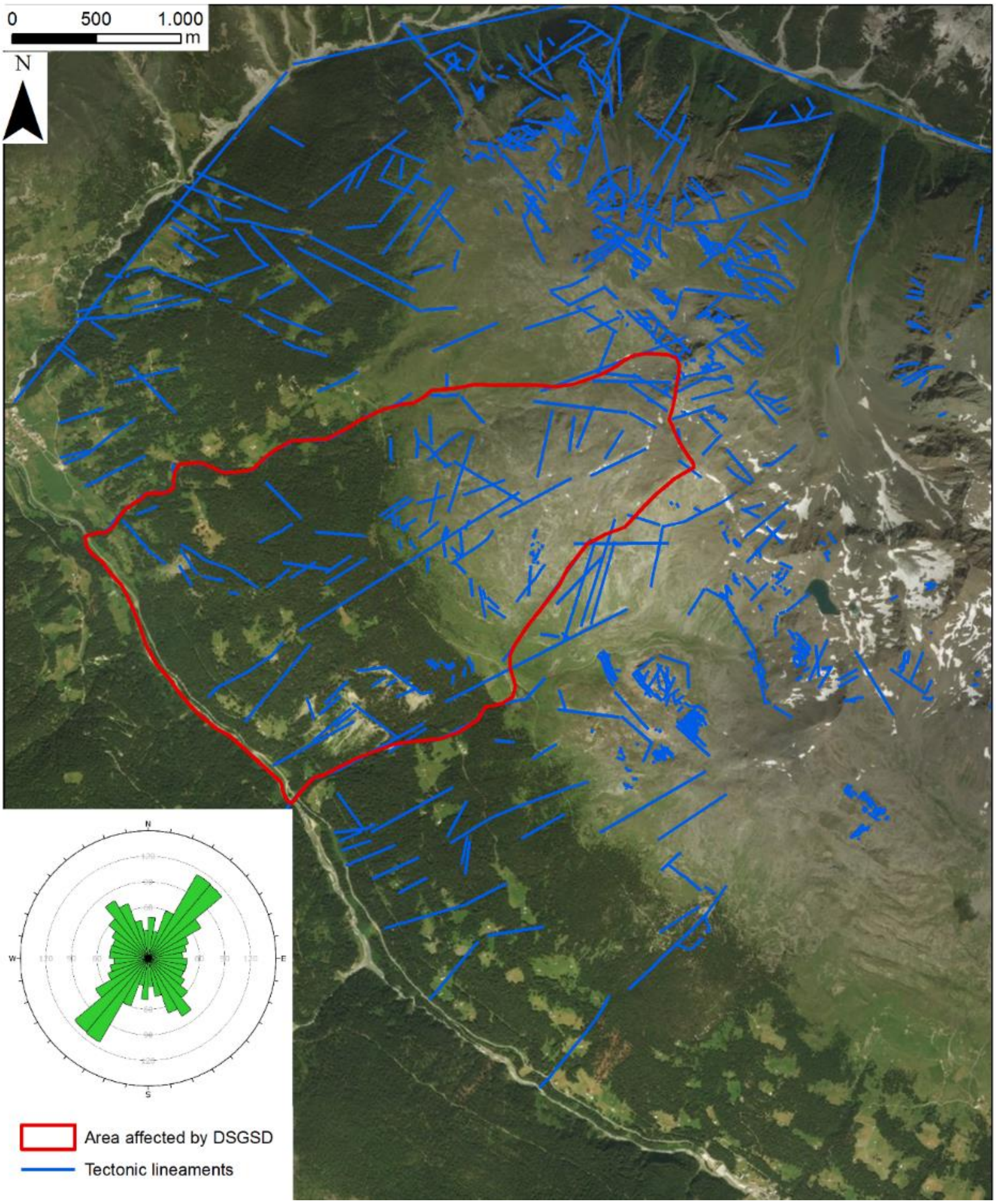

Figure 6.4: Tectonic lineaments recognized with mapping on aerial photos and Lidar DEM. The extension and the boundaries of DSGSD are clearly controlled by the structural pattern of the area.

6.2 THE CRESTA DI SALINE DEEP-SEATED GRAVITATIONAL SLOPE DEFORMATION

The Cresta di Saline slope ranges from 1350 m at the valley bottom to almost 3000 m in the crest zone, with a maximum width of around 2700 m. Lateral boundaries are represented respectively by the Confinale valley at SE and the Cavallaro valley at NW (Agliardi, 1999; Agliardi et al., 2001). The geomorphological settings of the study area are typical of Alpine environment, in which the carving operated by glaciers during the Last Glacial Maximum (LGM) greatly affected the valley flanks morphology, being still clearly recognizable on the landscape, with post-LGM evolution consisting in reshape by gravitational processes and minorly by fluvial erosion. Frequent glaciers, glacierets and cirques are clearly recognizable in the upper portions of tributaries, which are often perched on the Valfurva, as in the case of the Zebrù and Confinale valleys. At minor scale the action of glacial processes is testified by striated and moutonèe rock surfaces and widespread occurrence of glacial, rock glacier and talus deposits formed during Pleistocene and Holocene (Catasta and Smiraglia, 1978). Deposits mantle extended portion of the slope, mainly constituted by heterogeneous and poorly-sorted material deposed during the several advances of the Valfurva glacier and constituted by lithotypes transported from the upper portion of the valley. In the lower portion of the slope paleo-landslide accumulation are widely diffused, indicating catastrophic activity in the post-LGM period, contributing to valley damming and partial diversion of the Frodolfo river (Fig. 6.5).

Observing the study area and its morphology, two main sectors can be identified along slope profile: the first ranges from the crest area down to elevation of around 2300 m a.s.l., being characterized by relative low slope angle (mean value around 20°) and marked convexity. The lower portion, which extends from 2300 m a.s.l. to the valley bottom, is indeed characterized by steeper slope angle (from 30° to 35°) and more straightforward profile. The change in slope angle contributes to the occurrence of a knee point at the boundary between the two slope sectors.

The occurrence of long-term gravitational displacement experienced by the Cresta di Saline DSGSD is expressed by a wide-range of spectacular morphostructures, that are found all throughout the slope. In the crest zone, the cumulated movement resulted in ridge splitting of the Cresta di Saline, testified by the formation of a huge triangular scarp with downslope vertical component of around 150 m (1 in Figs. 6.5 and 6.6, fig. 6.7). Coherently with observed tectonic lineaments, the displacement vector is oriented to SSW. At the present state, the main scarp is extensively covered by rock blocks and listric counterscarps directly associated with its occurrence are recognized emerging from debris mantle (2 in Fig. 6.5 and 6.6, fig. 6.8), and accompanying the rotational component of DSGSD.

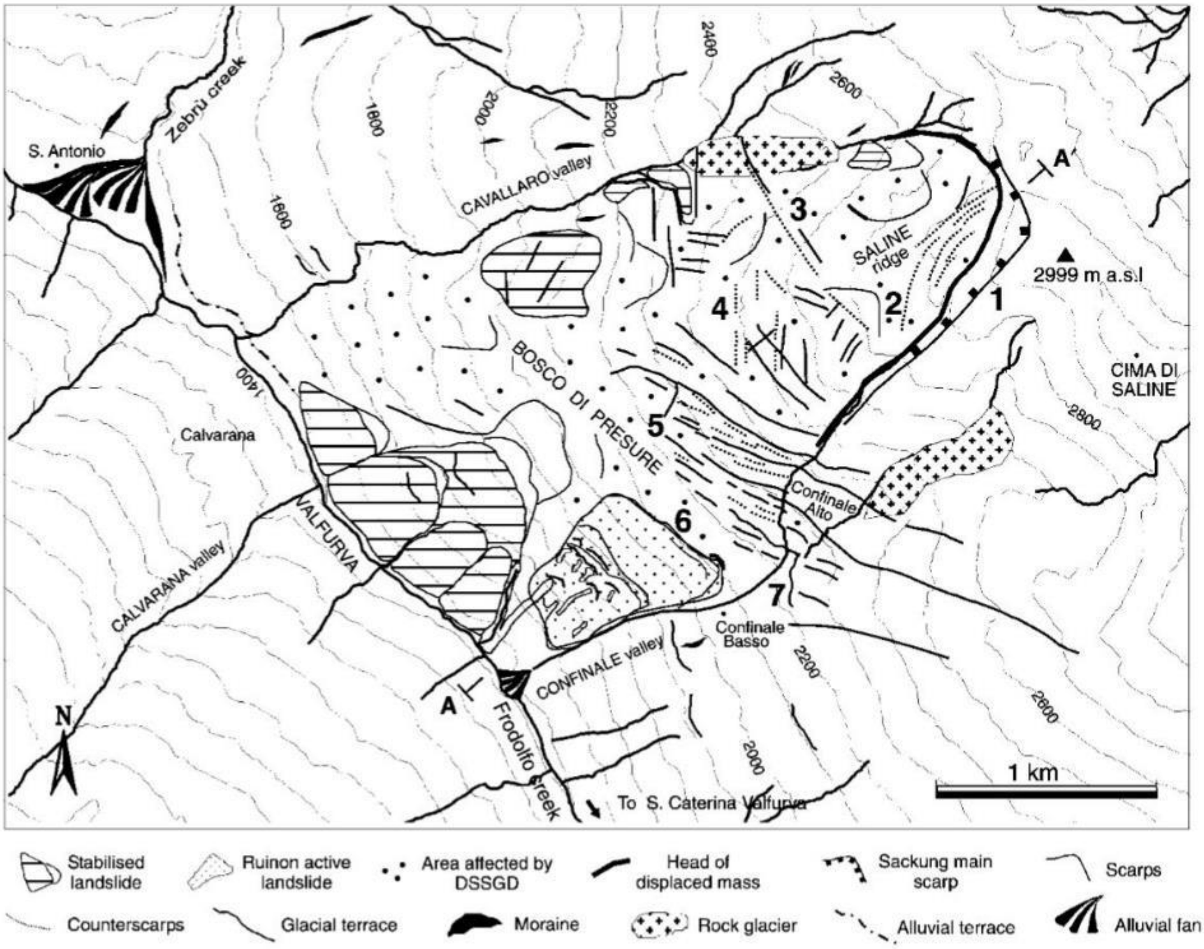

Figure 6.5: Geomorphological map of the Cresta di Saline DSGSD. For the meaning of numbers, please refer to the text (from Agliardi et al., 2001)

The kinematic of the upper slope sector is strongly conditioned also by the occurrence of a persistent tectonic lineament crossing the entire study area with direction WNW-WSE, steeply dipping downslope (3 in Figs. 6.5 and 6.6). This involve a swarm of fractures with individual lengths up to > 1km bounding the lower slope sector where it constrains the occurrence of an array of different past and ongoing rock slope instabilities (Agliardi et al., 2001).

Moving downslope, antithetic rectilinear counterscarps with length up to several hundred meters (4 in fig. 6.5 and 6.6, fig. 6.8) and vertical throw up to 3-4 m are encountered. These structures often exhibit well-preserved surfaces oriented N-S and NNW-SEE, representing the surficial expression of steeply-dipping shear zones (Agliardi et al., 1999).

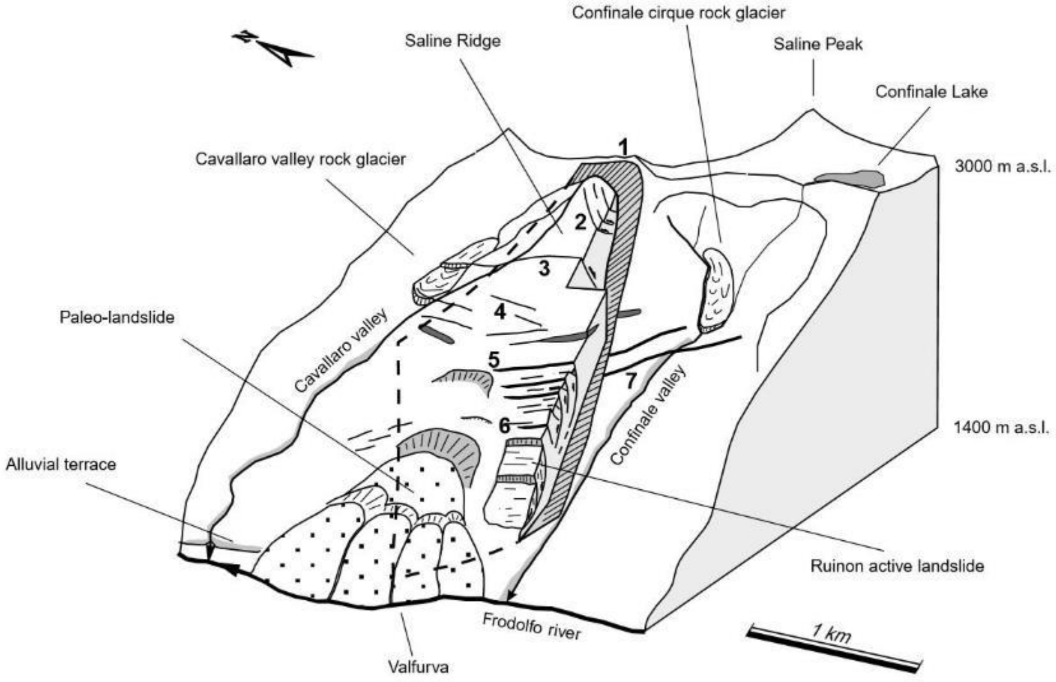

Figure 6.6: Three-dimensional sketch of the DSDSG kinematics. The main geomorphological features encountered throughout the slope are also reported. For the meaning of numbers, please refer to the text (from Agliardi et al., 2001)

Figure 6.7: Main scarp of the Cresta di Saline DSGSD. In the left part of the image, antithetic counterscarp related to the movement can be observed (2 in Fig. 6.5 and 6.6)

Figure 6.8: Counterscarp at around 2550 m a.s.l. in the middle slope sector.

Around 2300 m a.s.l., a swarm of synthetic scarps up to kilometric lengths is detected, often associated with counterscarps to form half-graben structures characterized by decametric width and blocks and debris filling (5 in fig. 6.5 and 6.6, fig. 6.9). Interestingly, these features involve cumulated displacement in the order of 20 m, along which glacial and periglacial landforms and deposits are cut, thus suggesting a relative chronology between the DSGSD state of activity in this slope sector and the deposition of material. Moving downslope transition to linear and convex scarps, trenches and traction fissures is encountered (6 in fig. 6.5 and 6.6, fig. 6.10), these range in dimension up to 5 meters in width and, most of all, are characterized by present state of activity, testified by three toppling and fresh rock surfaces outcropping. Interestingly, in this slope sector two marker levels occurs, being extremely useful in constraining the magnitude of displacement cumulated by DSGSD. The first one is represented by a marble lens located 2300 m a.s.l., near the Confinale Alto area. The DSGSD cut the lens in two different portions: one is located outside the main DSGSD at the divide with the Confinale cirque, while the other testifies the displacement of a significant part of the DSGSD. This marker testifies a vertical downthrown of about 80 m. The other marker level is constituted by a glacial terrace, located roughly in the same area, with a vertical downthrown of 30 m along a secondary scarp (7 in Fig. 6.5 and 6.6). P rehistoric rockslide accumulations cover the lower part of the slope (e.g. Scè rockslide), with estimated deposits thickness up to 100 m. These testify diffuse instability in the lower slope portion since paraglacial stages. Indeed, one of these deposits cuts an alluvial terrace near Sant'Antonio Valfurva, thus suggesting a post-Wurmian stage of slope instabilities. However, the most important element in the lower sector of the slope is represented by the "Ruinon", a nested rockslide threatening the bottom valley due to the risk of potential collapse.

Figure 6.9: Synthetic scarp in the middle slope portion (2475 m a.s.l.). At the bottom marble marker level can be recognized

Figure 6.10: Phillite scarp located just upslope Confinale Alto. The plurimetric thrown cumulated and the good surface condition makes this structure a key one in the comprehension of the DSGSD displacement trend.

6.2.1 The Ruinon rockslide

The Ruinon rockslide is located in the middle-lower portion of Cresta di Saline slope between 1700 and 2120 m a.s.l., and affects an area of about 250 000 m^2 with a maximum width of 580 (Fig. 6.11; Del Piccolo, 1998; Agliardi, 1999; Crosta and Agliardi, 2003; Agliardi et al., 2011). The rockslide is perched on the Valfurva valley bottom of around 200 m, involving estimated 13 Mm^3 of rock mass and debris. Surface evidence and borehole data suggest the occurrence of a compound basal surface, characterized by both translational and rotational component. Southeastern boundary corresponds to the DSGSD limit, which extends along the Confinale valley, depending on the local tectonic pattern. Debris cover is thick and extended especially in the lower portion, becoming thinner moving to the rockslide top. Two main scarps are detected on slope, classified in respect to the relative elevation in Upper scarp and Lower scarp (Fig. 6.11 and 6.12). The Upper scarp ranges from 2100 to 2120 m a.s.l., consisting in a 30 m high, disturbed rock mass outcrop, which can be followed for around 600 m along the slope. The lower scarp is located between 1890 and 1930 m a.s.l., mainly consisting of completely disrupted rock mass and slope debris. The orientation of the two scarps, which are parallel and directed WNW-ESE, is clearly influenced by the structural pattern, which conditions the instability development also for this slope sector. The geometry of basal shear band is mainly translational in the lower portion, becoming rotational linking with the Upper scarp. The potential for an upslope expansion of the unstable mass was detected, mainly consisting in the downslope pulling of rock mass located just above the Upper scarp. Nevertheless, due to the rockslide position in respect to valley bottom, transition from rockslide to rock avalanche is possible in case of slope complete collapse, making the assessment of stability condition crucial for civil protection purposes.

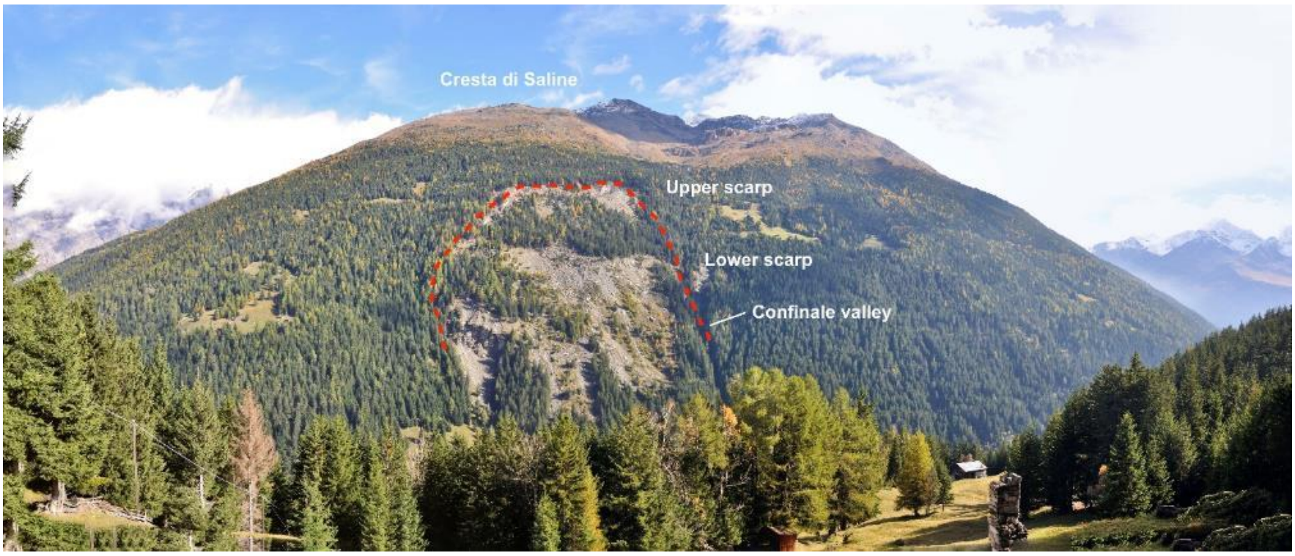

Figure 6.11: The Cresta di Saline slope in October 2014 as seen from the GB-InSAR point of view. Ruinon rockslide extension is represented by red dashed line.

The rockslide affected Valfurva valley since long time, as testified by the name "Ruinon", which in local vernacular literally means "great ruin". The first instability evidence dates back to 1891, when the Upper scarp is partially identifiable in a photo taken from the opposite valley side, near the summit of Cima Bianca (G. Cola, personal communication). In the last century, rockslide evolved mainly through diffused rockfalls, toppling and opening of large tension cracks, particularly in the Upper scarp portion. In the lower sector activity, which intensified starting from 1981, mainly consisted in rockfalls and mobilization of slope deposits in forms of debris flows, often reaching the underlying provincial road and the Frodolfo river as a consequence of intense or prolonged precipitations. Main activation events occurred particularly in 1960, 1983, 1987 and 1997, consequently to particularly intense and prolonged precipitation. The latter activation represented a marked evolution of the rockslide. Acceleration was registered in the Upper scarp, especially in the SE sector, where a toppling event involving around 2000 m^3 of rock mass occurred (Laffi et al., 1998). Meanwhile, in the lower sector an open steep fracture developed, dipping towards SE and bounding the NE boundary of rockslide body, probably indicating partial rotation of unstable rock mass volume. Further modifications were registered during 2001, with global acceleration of the Upper scarp and the regressive activity in the Lower one, testified by the formation of multiple scarps up to 30 m high. In the last decade, particularly from 2014, intense activity and velocity increase were registered, consisting in the further disintegration of rock mass constituting Lower scarp and cumulated displacements up to 12 m in the Upper scarp sector.

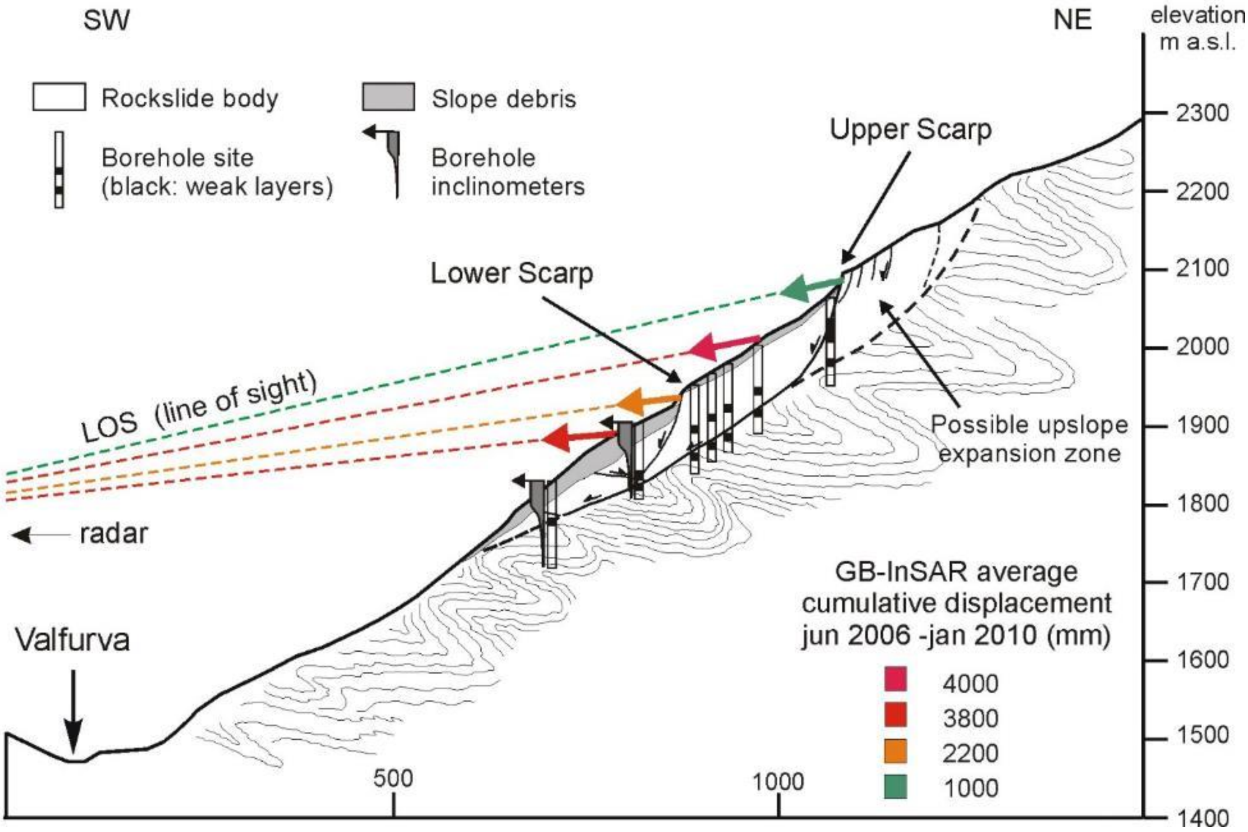

Figure 6.12: Geological cross-section of the Ruinon rockslide. Location of Upper and Lower scarps is reported, besides information and displacement derived from geotechnical investigation and monitoring (from Agliardi et al., 2011)

6.3 SLOPE INVESTIGATIONS AND GEOLOGICAL MODEL

Due to the large volumes involved and the depth of inferred basal shear band, precise assessment of DSGSD kinematics and geometry at depth is a difficult task. Geomorphological field observation permit to observe surficial expression of downslope movement through morphostructures mapping that, as illustrated in the previous chapter, are widespread on the Cresta di Saline slope. The kinematic interpretation morphostructural associationsallows drawing hypotheses on the kinematics, magnitude and relative chronology of displacements associated to different DSGSD sectors.. The cross-cutting relationships among DSGSD morpho-structuees and glacial and periglacial landforms and deposits provide constraints on the relative chronology of slope deformation when absolute chronological (dating) constraints are lacking.

During field activities carried out during the PhD, in October 2015 we performed rock sampling at kwy location for successive Cosmogenic Radionuclide Dating (CRE). In particular, we collected samples of phyllites (for ^{10}Be and ^{26}Al) and marbles (form ^{36}Cl) at the following locations:

- Antithetic counterscarp related to main scarp occurrence and represented in Figure 6.7 (2 in Fig. 6.5). For this structure two samples were performed, to infer also the displacement rate.
- Synthetic scarp located at 2475 m a.s.l., just above the aforementioned marble marker level (Fig. 6.9)
- Synthetic scarp located around 2300 m a.s.l., representative of displacement trend and magnitude in the middle portion of the slope. The structure is represented in Figure 6.10 (5 in Fig. 6.5) For this structure three samples were performed, to infer also the displacement rate.

Another evidence of the global slope movement is represented by data obtained with satellite interferometry. From the analysis of points obtained by PSInSAR and SqueeSAR for the period 2003-2009, downslope movement in the sector affected by Cresta di Saline DSGSD is evident. Mean annual displacement rates ranges from 10 mm/yr up to maximum values above 20-22 mm/yr. Unfortunately, the data are not homogenous: above the vegetation line points are densely distributed and permit clear trends analysis, while in vegetated areas, due to intrinsic limitation of the satellite interferometry technique, very few points are collected. However, the comparison at the entire DSGSD scale provide coherent displacement rates.

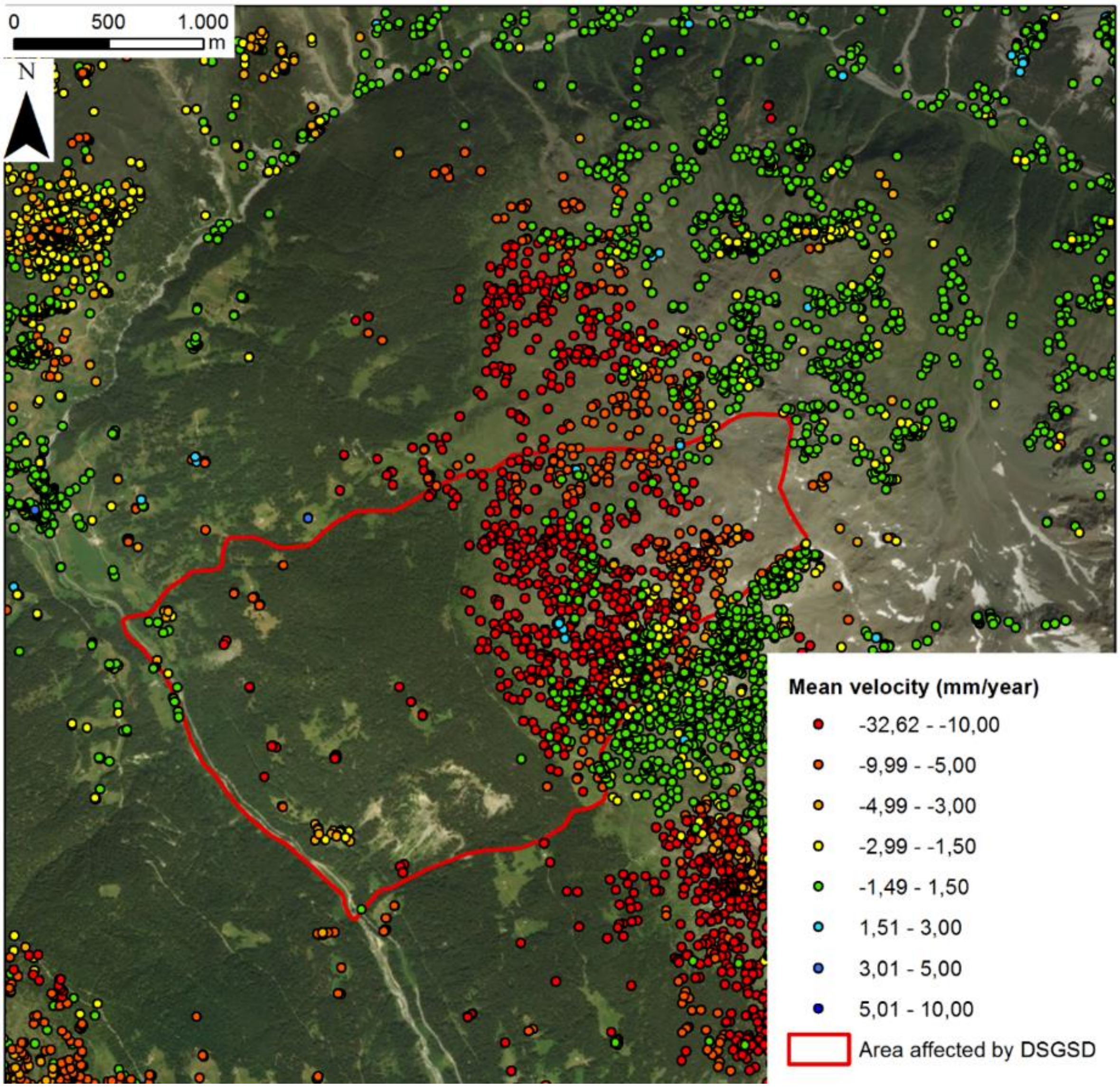

Figure 6.13: Mean displacements rates derived from satellite interferometry in the period 2003-2009. Global downslope movement is clearly detected, ranging in the upper sector from 10 up to more than 20 mm per year.

Geotechnical investigations, including drillings and full-core boreholes, piezometric and borehole inclinometer measurements, geophysical surveys and hydrogeological tracers tests, were carried out by Regione Lombardia and ARPA Lombardia in different stages (1988, 1998, 2004, 2013) mainly in the slope portion affected by and surrounding the Ruinon rockslide, motivated by its fast progressive behavior and potential catastrophic evolution. The borehole record, described in the following, allowed constraining rockslide geometry and the location and extent of basal shear zones. Infiltration from Confinale valley (Fig. 6.11) to rockslide body is detected in the upper sector, potentially constituting a trigger for the rock mass movement, particularly in periods characterized by snow-melting or intense precipitations. Moreover, several springs occur at the rockslide toe. The changing position and the intermittent activity of groundwater outflow along the same WNW-ESE alignments, possibly reflect the interaction between rockslide movement and structural control on the failure plane development.

Since almost 20 years, the Ruinon rockslide is subjected to geotechnical monitoring by the environmental agency of Lombardy region (ARPA Lombardia). The installed network consists of extensometers, inclinometers, piezometers and topographic benchmarks, mainly located in Upper and Lower scarps proximity (Fig. 6.14a). The analysis of data permitted to obtain a long time series, in which different displacement trends were distinguished depending on rockslide sector considered. Particularly, cumulative displacements result in periods characterized by global and progressive acceleration alternated with regressive phases, in which rockslide reach temporarily stable conditions, with low cumulated displacements and accelerations. The monitoring network was significantly updated since 2006, with the introduction of a Ground-Based InSAR located on the opposite valley side at a distance from the rockslide ranging from 800 m (rockslide toe) to 1100 m (Upper scarp). GB-InSAR observation point, from which the figure 6.11 was taken, permit to scan an approximately area of 1 km^2 approximately 5 times per hour, providing near real-time monitoring of global slope behavior. Analysis of slope displacement along GB-InSAR line of sight (Fig. 6.12) resulted in displacement trends coherent with the other monitoring devices located directly on the rockslide (Fig. 6.14b). Moreover, the application of such remote sensing technique permitted to reconstruct extremely accurate mid-term displacement series, which were particularly useful in constrain the rockslide behavior, in the determination of rockslide sub-areas (i.e. characterized by same displacement trends) and in the definition and the refinement of warning displacement thresholds for early warning and civil protection purposes (Crosta and Agliardi, 2003; Agliardi et al., 2011)Interestingly, the displacement pattern described by the monitoring network is reproduced also by a neightboring rockslide, the “Gembresca” one, which is located few kilometers NW from the Ruinon rockslide, despite consisting in a notable minor extension and volume involved. Manual measures performed in the last decade resulted in similarities regarding both acceleration and regressive phases (G. Cola, personal communication), testifying the role of hydrological triggers in determining instabilities occurrence at different scales.

Based on the summary of geological, geomorphological, morpho-structural and site investigation data, Agliardi et al. (2001) proposed the geological section in figure 6.15: here, the basal shear band runs with roto-translational kinematics up to 200 m of depth from topographical surface. Several synthetic structures in the middle slope portion permit strain accommodation, meanwhile displacing marker levels constituted by marble lenses (Fig. 6.9). The lower slope portion is dominated by the occurrence of the Ruinon rockslide.

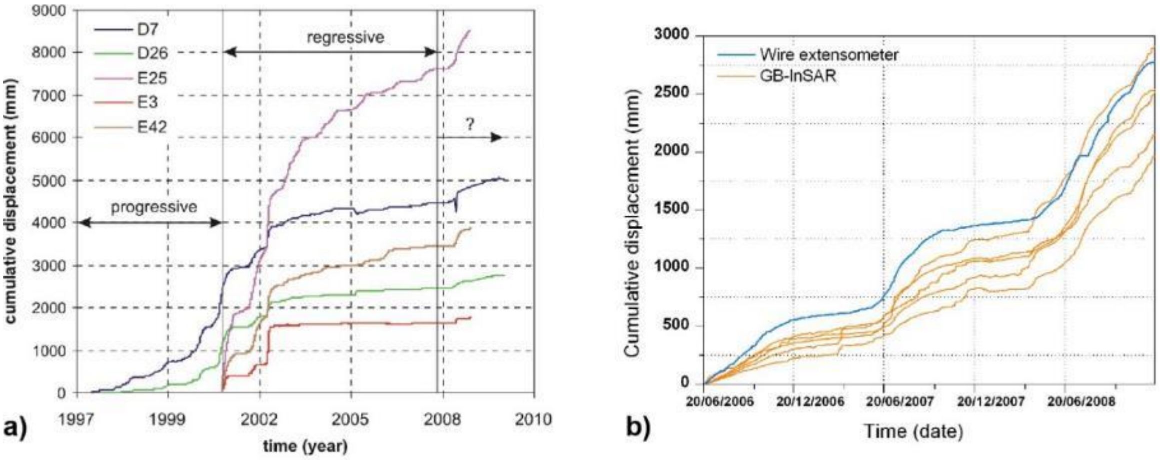

Figure 6.14: Ruinon rockslide cumulative displacement derived from monitoring devices in the period 2006-2008 (a) and 1997-2009 (b) (from Agliardi et al., 2011).

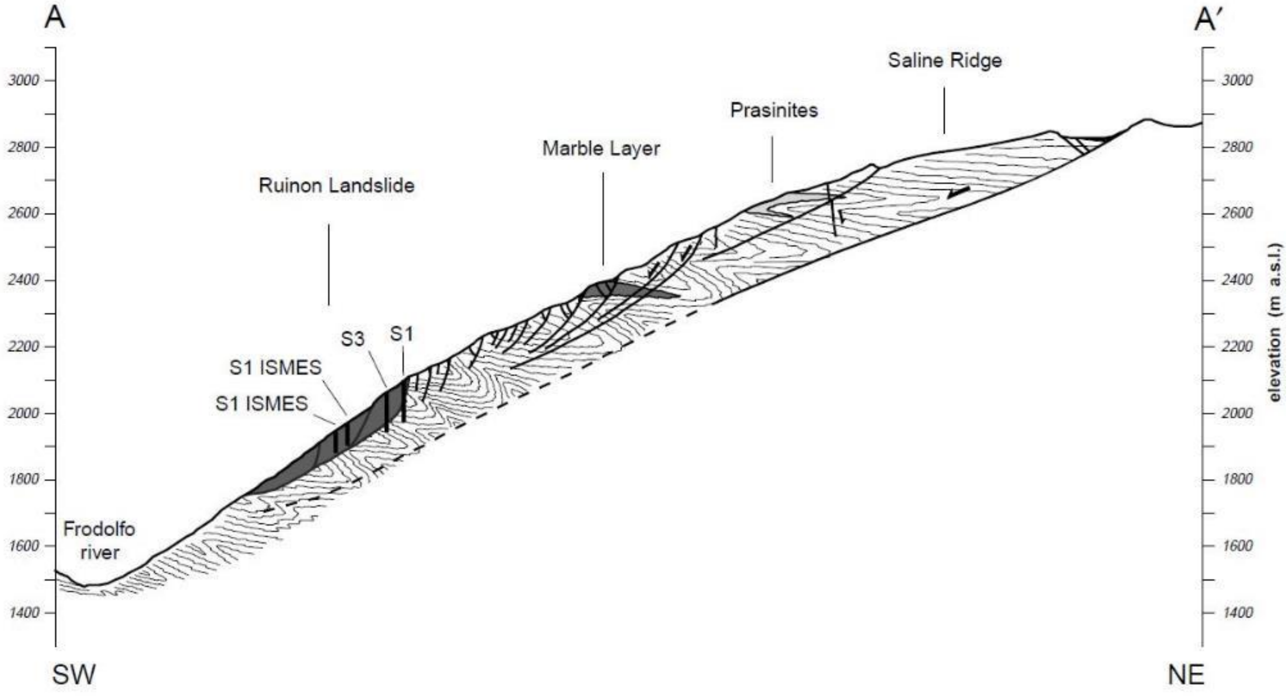

Fig. 6.15: Cresta di Saline DSGSD geological cross section (from Agliardi et al., 2001)

6.4 ROCK MASS CHARACTERIZATION

The characterization of the mechanical properties of rock masses involved by the Cresta di Saline DSGSD was carried out by the analysis and geomechanical classification of available drill cores, and by field discontinuity surveys at the less disturbed rock mass outcrops located outside the DSGSD area, integrated by data previously collected both inside and outside the DSGSD, available in the literature (Del Piccolo 1998; Agliardi et al., 2001, 2003; Del Ventisette et al., 2012)

Borehole data used for the geomechanical characterization of the DSGSD comes from two different investigation campaigns, performed respectively in 1988 and 2013 (Fig. 6.15). The two boreholes drilled in 1988 by ISMES, S1 and S2, investigate the material just below the Ruinon lower scarp, sampling rock mass entirely belonging to the rockslide and the underlying DSGSD. On the other hand, the cores of 2013, which are part of an engineering project investigation for a by-pass gallery of the unstable area, mainly focus on rock mass located below the DSGSD basal shear surface (Infrastrutture Lombarde, 2013). Despite 10 boreholes were drilled, only 6 were used for the classification, since the other 4 mainly investigates superficial deposits, not reaching the underlying bedrock. Notably the borehole SP06S crosses a 5 m thick layers of breccia (from 95 m to 100 m of depth), which could be related to the DSGSD basal shear zones. Detailed discontinuities logs were not available for the boreholes drilled in 1988, so only GSI and RQD were logged for each run. Regarding 2013 campaign, the original cores have been made available by the technical office of Valfurva municipality, and thus re-analyzed describing each discontinuity with regards to geotechnical classification purpose.

Data were analysed and plotted using the same methodology described for the Spriana case study (Cf. subchapter 5.4): for each core run, the weighted Joint Density (wJD), the P_{10}, the Gelogical Strength Index (GSI) and the Rock Quality Designation (RQD) were calculated and reported on geotechnical logs. For the 1988 boreholes, RQD was derived from borehole log attached to the original report while GSI from the exam of photographic documentation and from the data reported in Agliardi (1999). Total surveyed population resulted in 7 boreholes, consisting in 132 core runs for a total length of 235 m. Detailed profiles for each borehole are included in Annex 3.

S1-88 is located at the bottom of Ruinon lower scarp, at an elevation of 1823 m a.s.l.. Within the 91.5 m exploited by the drilling, the first 32 m consists of glacial deposits, constituted by gravel and sand with abundant fine-grained matrix, mainly clay and silt. After that, quartz-phyllites are encountered until the end of borehole. Sampled joints are mainly characterized by low-angle and low-roughness, even if some steep joints cross the borehole axis. The fracture intensity is approximately constant during the entire profile, even if local increase in rock mass fragmentation is encountered in a sub-metric level, localized from 50.5 to 51.0 m of depth. Regarding the collected geotechnical parameters, the GSI profile ranges between a maximum value of 70 and a minimum value of 30. RQD roughly follows the same trend, except when in correspondence with the aforementioned fractured level, which is clearly registered, resulting in a RQD of 0.

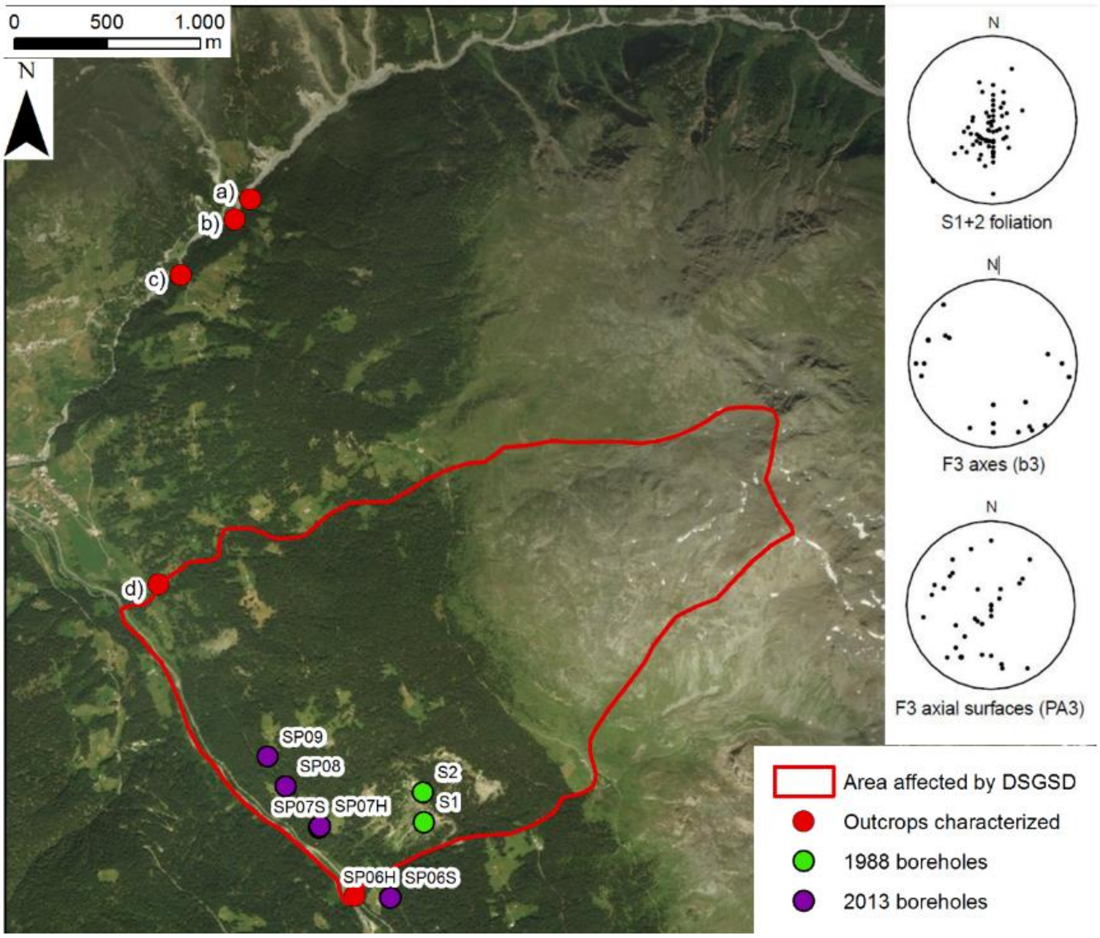

Figure 6.15: Geotechnical characterization of the Cresta di Saline DSGSD. The data comes from two different survey campaigns, performed in 1988 and 2013 and consisting of 7 boreholes. Data were integrated with field survey on outcropping rock mass outside the DSGSD area (red dots), and data previously reported in literature (Agliardi et al., 2001; Del Ventisette et al., 2012).

S2-88 was drilled in the central portion of the lower scarp at 1893 m a.s.l., extending until 94.6 m from the topographical surface. The collected material exhibit similar geotechnical characteristics in respect to the S1-88. It consists in glacial deposits up to 25 m, when transition to phyllite bedrock occurs. Here, the GSI profile ranges from 80 to 40 without intersecting any brecciated or intensively damaged level. However, local variations in fracture intensity are detected for sub-metric core portions, particularly at two depths: around 58 m and in the last decimeters before the borehole bottom (94 m).

Regarding 2013 campaign, SP06H was drilled in the central portion of the DSGSD, a few meters upslope from the valley bottom (1582 m a.s.l.). Here phyllites are encountered at 131 m of depth from topographical surface, characterized by fracture spacing ranging from 5 to 10 centimeters, with increase in density registered in the interval comprised between 131.8 and 132.0 m of depth. After that, increase in mean joint spacing is progressively collected until the end of borehole, where mean value rise up to 30-40 cm. The fractures crossed by SP06H show low weathering and low to medium roughness, even if local weathered joints are collected, with millimetric silt filling or calcite recrystallization. Evidence of water circulation was not collected. Geomechanical profiles resulted in roughly constant trend of GSI, with values of around 50. Instead, the other parameters characterized show a higher variability and sensitivity to local variation in fracture intensity, which sometimes is not so evident from the exam of GSI profile.

SP06S was drilled in the same position as SP06H, but with core axis orientation characterized by a dip direction of 053° and dip angle of 60°. Destruction drilling was performed until 90 m of depth, then rock cores were sampled until the end of borehole. The first meters of collected rock appear extremely weathered and disturbed by drilling operations, thus being hard to classify them as glacial deposits or brecciated and extremely weathered rock mass. After a few meters, in the interval 96-100 m, a brecciated level is clearly crossed, probably representing the DSGSD basal shear band (Fig. 6.16). This is constituted by angular to subangular rock fragments ranging in dimension from millimetric to pluricentimetric and sustained by clay-silty matrix (Fig. 6.17). Breccia occurrence is also registered for a thinner level localized at 104.85 m of depth. After these extremely fractured levels, transition to rock mass characterized by good mechanical properties and low fracture intensity is collected until the end of borehole. Rock cores are characterized by millimetric to submillimetric schistosity, with close to isoclinal centimetric folds highlighted by small quartz lenses Portions with mean spacing in the order of 10-15 centimeters alternating with more fractured decametric intervals were collected. Increase of mean spacing up to 40-50 cm is registered near the end of borehole. This trend is testified by progressive growth of GSI from 40 up to 75-80, meanwhile accompanied by decrease in wJD and P_{10} values.

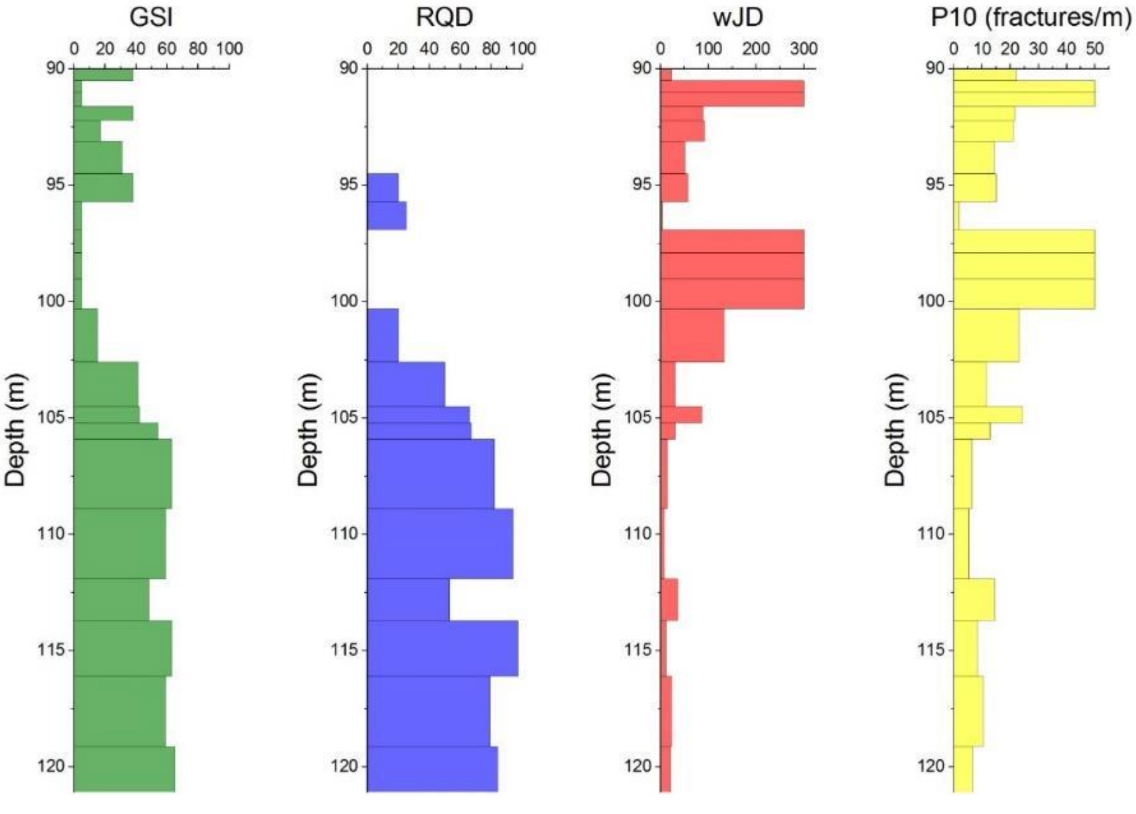

Figure 6.16: SP06S characterization. The occurrence of cataclastic breccia layers is reflected by correspond to abrupt parameters decrease in the interval 96-100 m, while the thinner level recognized around 105 m is not clear from geotechnical log.

SP07H is located in the central portion of the DSGSD, just downslope the Ruinon rockslide at 1546 m a.s.l.. The borehole axis follows a dip direction of 036° and a dip angle of 60°. The interval investigated with this borehole is restricted from 123 m to 130 m of depth, as the previous part was drilled recurring to core destruction. Sampled rock mass is characterized by millimetric schistosity and centimetric chevron folds locally moving to isoclinal, interrupted by low to medium fracture intensity pattern. Fractures are locally weathered and filled with silt and recrystallized calcite, for example at 128 m of depth, where a centimetric silt filling was sampled. The resulting geotechnical profile is characterized by only 3 core runs, which exhibit a progressive growth of GSI with depth from value of 40 to 60 at the borehole bottom. Meanwhile, wJD and P_{10} remains roughly constants and representative of poorly fractured rock mass.

Figure 6.17: Sample of cataclastic breccia layers sampled in SP06S. The occurrence of extremely damaged material is probably related to the occurrence of DSGSD basal surface.

SP07S is characterized by core axis oriented 036°/20°. This borehole was drilled starting from the same location of SP07H and protracted up to 191 m of depth. Unfortunately, also in this case only a small portion of rock mass was sampled, starting from 170 m of depth and including 21 m of rock cores. In this interval rock mass is intensively fractured, particularly between 170.0 and 171.2 m, where weathered discontinuities slightly filled with silt were crossed. After that, the rock mass appears characterized by low fracture intensity and centimetric open folds, with mean spacing of around 30-50 cm and GSI values around 60. Locally, steep angle discontinuities are crossed. All the geotechnical parameters testify a little increase of fracturing comprised in the range 177–182 m, caused by local increase in joint density not directly connected with DSGSD occurrence.

SP08 explores the NE lower portion of the DSGSD, with borehole head localized at 1563 m a.s.l.. It ranges in the interval 147-162.5 m of depth, which is entirely constituted by phyllites. Rock mass is characterized by the presence of centrimetric asymmetrical folding, from open to isoclinal. Regarding discontinuities the alternation of poorly fractured portion, with good geotechnical parameters and mean spacing of 30-40 cm, and more densely fractured, sometimes with silt centimetric filling and surface weathering, is registered (Fig. 6.18). As testified by other boreholes, the geotechnical characteristics are good at depth, with all the parameters investigated ranging in the usually-observed values.

Figure 6.18: Rock cores showing the alternation of portion at different fracture density. SP08 from 160.46 to 158.33 m

SP09 was drilled at the NE boundary of the DSGSD, starting from an elevation of 1600 m a.s.l.. The explored depth, which ranges from 144 to 167 m, resulted in rock mass with GSI values comprised in the interval 50-70, with little variations caused by oscillations in fracture intensity. Also for this borehole, alternation between good quality rock mass and submetric portion with increased fracture density is encountered. Geotechnical parameters reflect cores observation: GSI values maintain around 60 for the entire borehole, while wJD and P_{10} experienced slightly larger variations, however in the range for good-quality rock masses.

The low number of core runs joined with the limited spatial distribution of data, which totally lack for the middle and upper portion of the slope. result in a statistical population not robust and reliable as in the Spriana case study. Moreover, “damage imprint” between the different domains is not clear from the analysis of geotechnical logs and the only discerning criterion seems to be the spatial locations of core in respect to the hypothetical position of the basal shear band derived from the geological model. None of the investigated boreholes certainly cross the lower boundary of the DSGSD, but only fragmented information belonging to one or other domain were collected. Despite all these uncertainties, information about the structure in the recognized “damage domains” can be extrapolated. Here, two different types of rock mass were identified, respectively corresponding to within DSGSD and below DSGSD.

- Within DSGSD: S1_88, S2_88; upper part of SP06S_13
- Below DSGSD: SP06H_13, SP07S_13, SP07H_13, SP08_13, SP09_13, lower part of SP06S_13

Frequency histograms with fitted Probability Density Functions for both zones are presented in figures. 6.19 and 6.20. The goodness-of-fit was validated through modified Kolmogornov-Smirnov test.

Within the DSGSD domain, the goodness-of-fits tests performed resulted in the rejection of all the assumed distributions. Here, the presence of a more disturbed rock mass contributes to increase the count of lower value in both GSI and RQD logs (Fig. 6.19a, b). The occurrence of low values is often associated with the presence of brecciated or highly-fractured levels which cross the boreholes axis. However, from the analysis of GSI frequency histogram, normal distribution of values with mean at 55-60 can be inferred (Fig. 6.19a). The extremely limited size of wJD and P_{10} populations (Fig. 6.19c, d) doesn't permit any consideration about the statistical meaning of datasets.

Despite the limited sample size, GSI values belonging to the below domain are fitted by normal distribution characterized by mean value of 53 and standard deviation of 8 (Fig. 6.20a), while wJD values by lognormal distribution with mean of 3.1 and standard deviation of 0.8 (Fig. 6.20c). Also regarding the P_{10}, the lognormal distribution was successfully tested, with mean of 2.2 and standard deviation of 0.5 (Fig. 6.20d). RQD trend resulted in rejection for all the tested statistical distributions (Fig. 6.20b).

Domain	**Parameter**	**Distribution Type**	**Mean Value**	**St. Dev.**	**λ**	**P-Value**
Below Landslide	GSI	Gaussian	53	8.0	-	0.07
	RQD	-	-	-	-	-
	wJD	Lognormal	3.1	0.8	-	>0.15
	P_{10}	Lognormal	2.2	0.5	-	>0.15
Within Landslide	GSI	-	-	-	-	-
	RQD	-	-	-	-	-
	wJD	-	-	-	-	-
	P_{10}	-	-	-	-	-

Table 6.1: Results of statistical distribution fittings on the three domains identified.

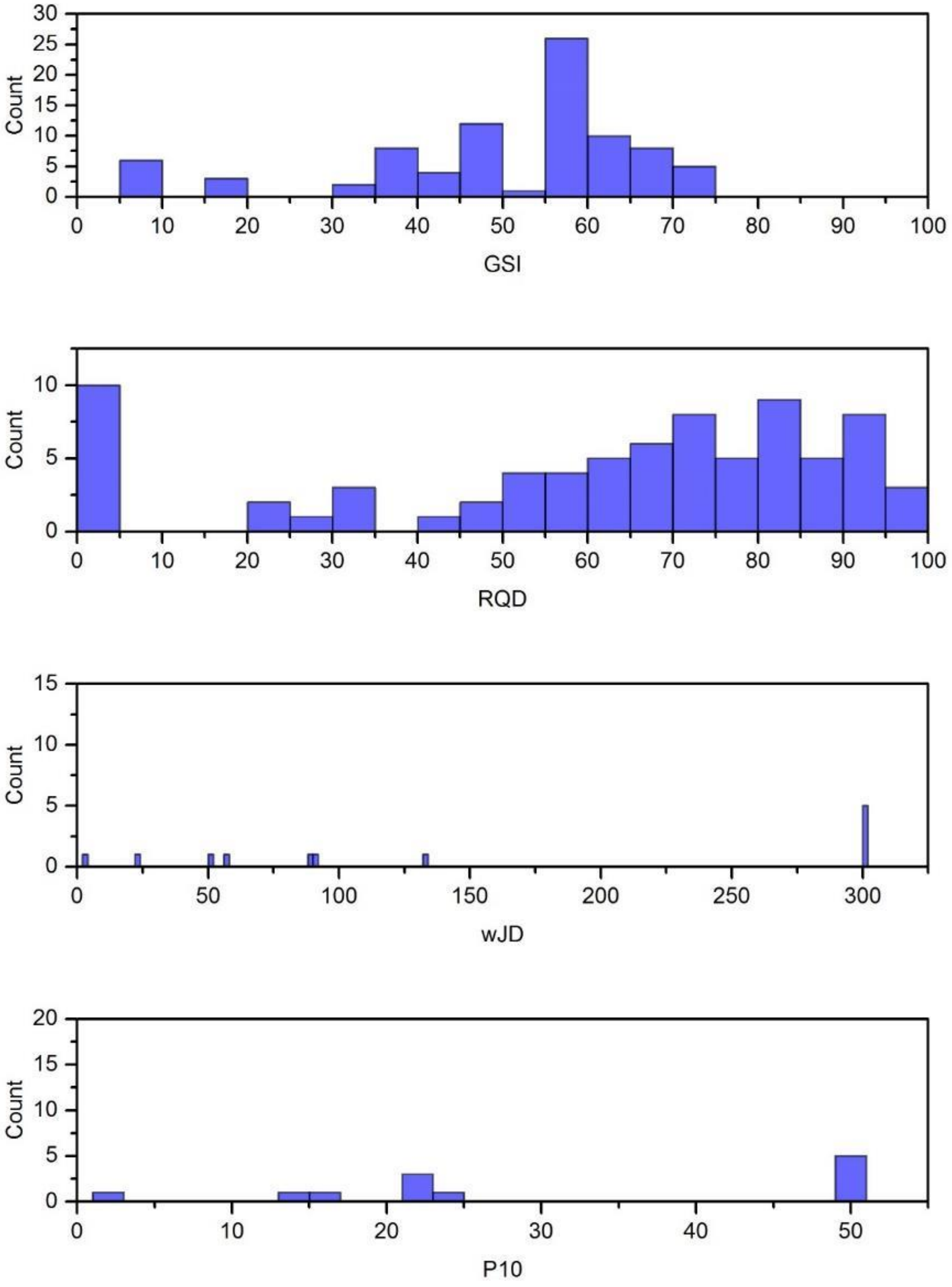

Figure 6.19: Frequency histograms for rock mass within the Cresta di Saline DSGSD. The frequent occurrence of intense fractured levels and breccias makes the fitting of statistical distributions not possible for this domain.

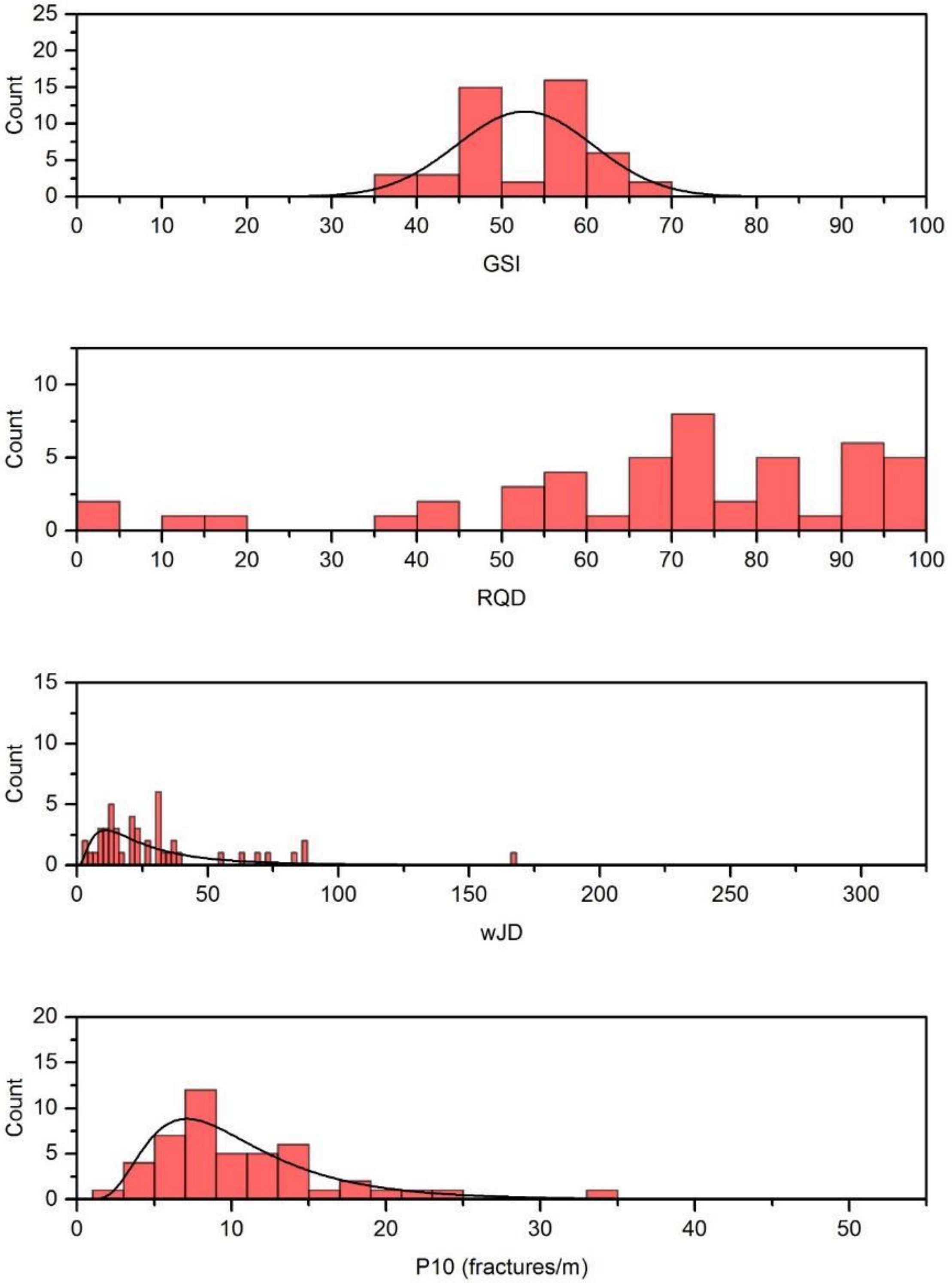

Figure 6.20: Frequency histograms for rock mass below the Cresta di Saline DSGSD. Here, normal distribution is fitted for GSI frequency histogram, while wJD and P10 are better described by lognormal functions.

To assess also the geotechnical conditions outside the DSGSD affected area, field survey was performed in selected rock mass outcrops. The choice of representative sample was limited by the large extension of deposits that mantle the study area, which result into scattered outcrops, mainly located along rivers and in correspondence to slope breaks. Moreover, due to the widespread occurrence of instability phenomena in the surroundings of the DSGSD, we wanted also to avoid sampling outcrops subjected to any type of gravitational "imprint" on rock mass damage state (Fig. 6.13). Finally, we focused on four outcrops (red dots in Fig. 6.15 and 6.21), located as close as possible to the DSGSD boundaries. Geomechanical characterization involved measuring of discontinuities sets regarding orientation, spacing, weathering, roughness and water occurrence. Moreover, to quantify the damage state in the surveyed outcrops, that we consider closer to the conditions of rock mass outside the DSGSD affected area, GSI was esteemed: values obtained for each outcrop are resumed in Table 6.2.

Outcrop	GSI
A	55-65
B	50-65
C	65-75
D	50-60

Table 6.2: GSI values obtained from the characterization of outcrops.

Values obtained are in the range encountered for fair-good quality rock mass, with minimum and maximum values of 50 and 75, respectively. Local decrease of rock mass mechanical properties and GSI is observed for densely fractured portions (lower portion of fig. 6.21b) or folded outcrops (Fig. 6.21d). With respect to the rock mass encountered below the DSGSD basal shear band, increase in mean GSI value of around 10-15 is obtained, even if direct trends comparison is difficult due to low amount of field data.

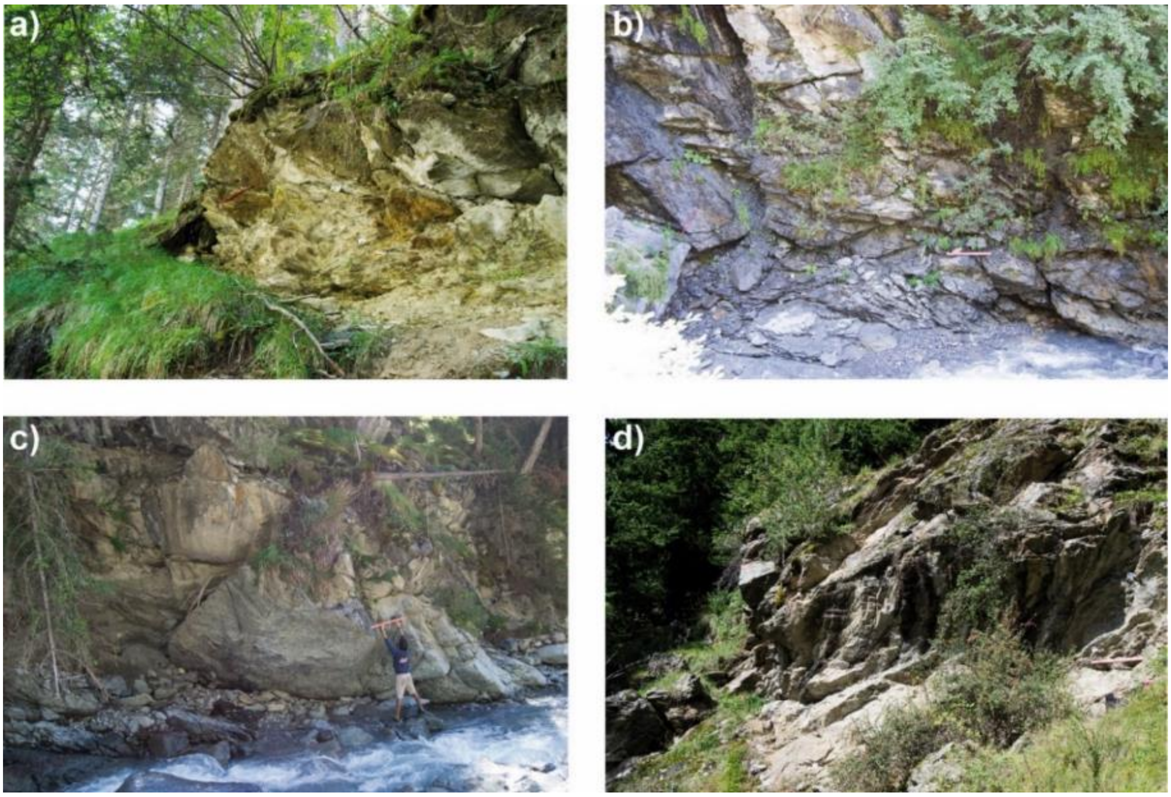

Figure 6.21: Rock mass outcrops surveyed near the DSGSD area. The 1 m-long red bar in photos serves as scale

6.5 NUMERICAL MODELLING

6.5.1 Model set-up and calibration

The numerical model of the Cresta di Saline slope was set up by discretizing the domain in a two-dimensional mesh of three-noded triangular finite elements with maximum edge size of 50 m, which roughly corresponds to 3% of the model vertical size, resulting in around 18000 finite elements and 9150 nodes (Fig. 6.22). The experience gained from mesh sensitivity tests performed for both simplified and real slope profiles, suggested this value as suitable for the adopted modelling approach in terms of computational time and reliability of simulation results. Also for this case study, the simulated profile (Fig. 6.22) was restored to Last Glacial Maximum conditions based on geomorphological field evidence: slope topography was retro-deformed to restore all the modifications induced by gravitational displacement, such as scarps, counterscarps, ridge splitting and toe bulging to nested rockslides in the lower slope sector. External mesh nodes along the bottom boundary were fixed in the x and y direction, whereas lateral ones were left free to move only in the y direction. The topographic profile was prolonged over the crest zone and, on the opposite side, ahead Frodolfo River, to not introduce boundary effects within the numerical simulations. To account for the occurrence of damaged rock masses associated with the swarm of tectonic lineaments crossing the middle slope sector (Cf. subsection 6.2), we introduced a 200 m wide band of finite elements dipping downslope with an angle of 75°, in which mechanical properties corresponding to weaker and more deformable rock mass was imposed. To investigate the influence of this weakened zone on DSGSD nucleation and development in the Dadyn_RS time-dependent framework, we ran two different simulations without (Fig. 6.22a) or with (Fig. 6.22b) including the weakened zone.

Based on the parametric tests performed for simplified slopes and for the Spriana case study, the initial value time-to-failure paramerter *b* was in the usual intact-rock range and calibrated based on simulation results to obtain the best possible fit between simulated and observed DSGSD features. Also in this case, we adopted a value of the damage increment parameter, *D*, equal to 0.1.

Initial values of rock mass properties were derived from the analysis of site investigation regarding the “outside” and “below” damage domains (subsection 6.4), not affected by significant DSGSD damage. To account for properties inherited from pre-deglaciation slope evolution we adopted increased initial rock mass conditions corresponding to a mean GSI value to 80±5. This range corresponds to intact/blocky rock mass crossed by discontinuities with very good/good surface conditions (Fig. 2.2). Instead, regarding the model subdomain representing the aforementioned weakened zone, mechanical properties were derived according to GSI lower values observed in the Gembresca area (outcrop “D” in Fig 6.21) where the weak zone outcrops, resulting in mean GSI value of 50±5 (Fig. 6.22a). According to the Hoek-Brown approach, GSI was used to upscale the strength and deformability of intact phyllite samples (Tab. 6.3), which mechanical parameters were derived through the review of laboratory experiments performed, by Agliardi et al. (1999), Agliardi et al. (2001) and Infrastrutture Lombarde (2013).

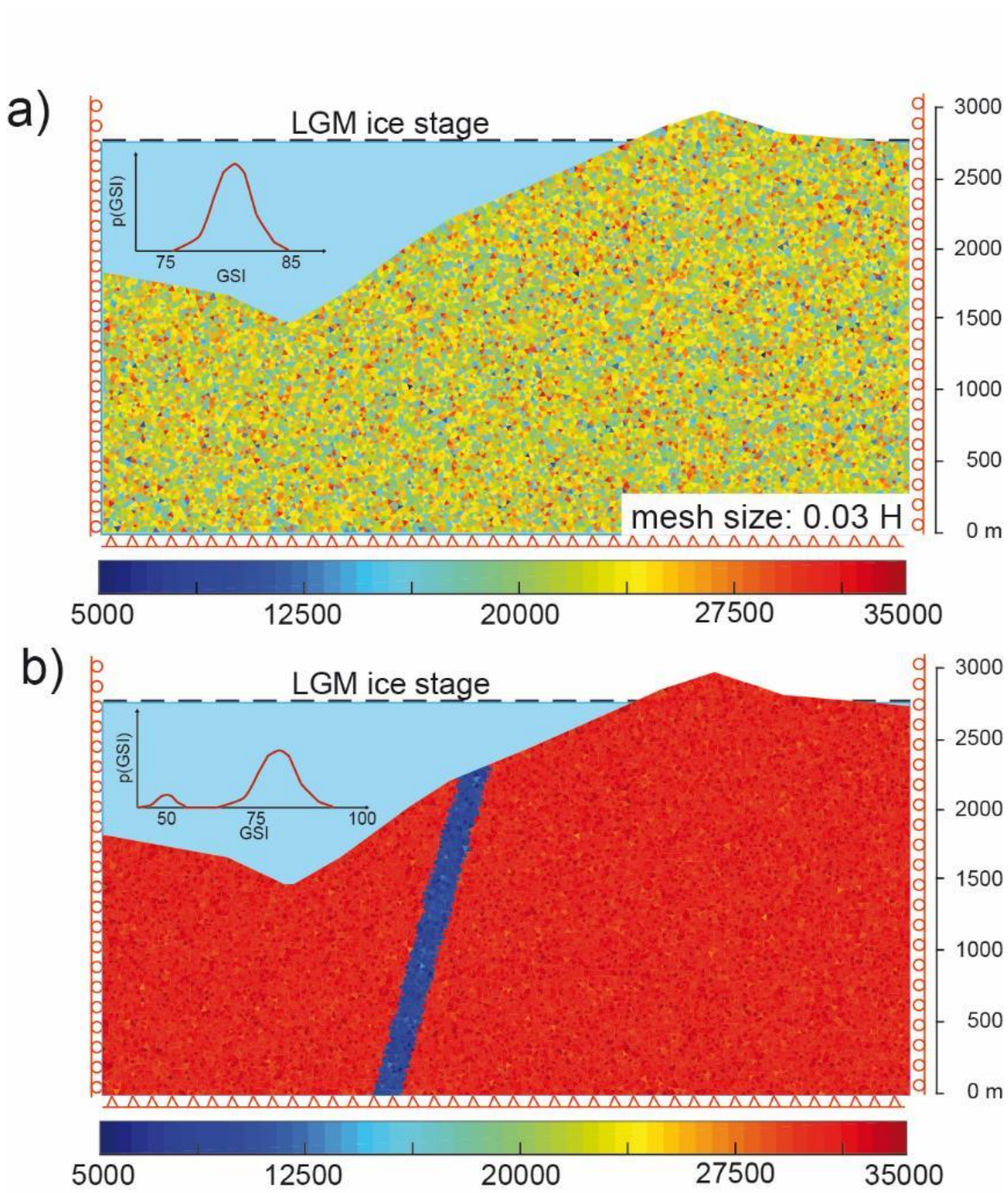

Figure 6.22: Model setup for the Cresta di Saline case study neglecting (a) or considering (b) the occurrence of a weakened band crossing the slope. Mesh size was established in 50 m, while rock mass heterogeneity was attributed assuming a GSI normal distribution with mean of 80 and standard deviation of 5, 50±5 for the weakened band. Corresponding values of rock mass deformation modulus are represented. Nodes along lateral boundary were constrained in x direction, while the model bottom was constrained also in y direction. The initial glacier height was derived from paleo-environmental and paleo-climatic data reported in literature.

Parameter	Symbol	Mean
Uniaxial compressive strength UCS (MPa)	σ_c	70
Young Modulus (MPa)	ET_{50}	35000
Tensile strength (MPa)	T	12
Cohesion (MPa)	S_0	0.6
Coefficient of internal friction	μ	0.65

Table 6.3: Intact phyllites mechanical parameters derived from laboratory tests, which resulted in great values variability depending on the load orientation with respect to rock fabric (from Agliardi et al. (1999), Agliardi et al. (2001) and Infrastrutture Lombarde (2013)).

Initial values of rock mass tensile strength, cohesion and coefficient of internal friction were derived imposing a constant GSI value of 80 (50 for the weakened band). On the other hand, the initial deformation modulus E_0 was assigned to each element by assuming a pseudo-random distribution of GSI, applying the relationship proposed by Hoek and Diederichs [2005] (Fig. 3.3). The upscaling of Poisson ratio was reasoned to take into account both ranges usually observed for rock mass values, which are higher in respect to corresponding intact rock [Gercek, 2007], and the increase of υ commonly observed during damage-controlled laboratory tests [Martin and Chandler, 1994; Eberhardt et al., 1999]. Thus, we imposed $\nu=0.45$, which is a high value in respect to common modelling practice, but appears suitable for the DaDyn-RS approach.

Gravitational stress was initialized in the model and external ice load corresponding to the LGM ice stage applied. Then, modelling consisted in long-term simulation of the post-LGM deglaciation, through the Lateglacial and the Holocene until present day. Taking into account the neighborhood of LGM accumulation zone, deglaciation was simulated in a model time corresponding to about 2000 yr, starting from an elevation of 2700 m a.s.l. (Fig. 6.22), thus corresponding to a mean deglaciation rate of 0.6 m/yr. The glacier LGM stage and the deglaciation time were constrained by the most updated available paleo-environmental and chronological data, taking into account the global trend inferred at alpine scale but also observing ice deglaciation at the scale of single basin, particularly for valleys characterized by similar climatic, topographical and glaciological features in respect to the Valfurva valley [Ivy-Oechs et al. 2006; Ivy-Oechs et al., 2008; Bini et al, 2009; Pelfini et al., 2014; Wirsig et al., 2016]. The DaDyn-RS simulation stops when an imposed displacement value is reached. Here, we decided to monitor the Cresta di Saline main scarp, which resulted in the spectacular ridge splitting observed on the field (Fig. 6.7) and is representative of the global DSGSD deformational history. As field evidence and DEM analysis constrained the vertical downthrown along the main DSGSD scarp in around 150 m, we decided to use this marker to represent the present slope state. Thus, the numerical model stopped when the vertical displacement reached 150 m at this point.

Model parameters were calibrated (Tab. 6.4) according to the multi-indicator approach described in subsection 4.8. To reduce uncertainties in model application to real slopes, correspondence between simulated and observed evidence of the following features were verified, including:

6) slope geometry, in particular regarding unstable DSGSD size, depth of basal shear band and correspondence between observed and simulated morphostructures;
7) spatial and mechanical patterns of damage, occurrence of localized and diffused damage in different slope sectors;
8) DSGSD kinematics and patterns of surface and deep displacements;
9) time dependent behavior, slope life-cycle in respect to duration of deglaciation. Correspondence between the simulated displacement-time curve and the available absolute and relative chronological constraints.

As a result of calibration process, tensile strength and cohesion were imposed to 5 MPa and 9 MPa, respectively. These values are comprised between the range described by the intact rock parameters (Tab. 6.3) and the upscaled rock mass values. The increase of mechanical properties in respect to the empirical Hoek and Brown scaling reflects the importance in accounting for the occurrence of rock bridges when simulating the progressive failure of rock slopes [Einstein et al., 1983; Eberhardt et al., 1999; Stead and Eberhardt, 2013]. The undamaged initial state is thus characterized by the occurrence of non-persistent fractures within rock mass, contributing to increase in strength at element scale.

In simulations with fluid pressure occurrence we also calibrated the parameter *w*, that regulates the permeable cluster filling. To do this, simulated rockslide depth, kinematics and degree of damage localization were compared to data coming from in situ characterization. The main rockslide features were correctly reproduced by imposing a filling degree of permeable element clusters equal to *w*=0.3. The calibrated parameters used for Cresta di Saline modelling are resumed in Table 6.4.

Parameter	Symbol	Unit	Imposed value
Unit Weight	γ	kN/m^3	27
Young Modulus (intact rock)	E_0	MPa	35000
Tensile strength (rock mass)	T	MPa	5
Cohesion (rock mass)	C	MPa	9
Coefficient of internal friction (rock mass)	μ	-	0.85
Poisson ratio (rock mass)	ν	-	0.45
Damage increment parameter	D	-	0.10
Time-to-failure law parameter	b	-	40
Permeable cluster water filling	w	-	0.30

Table 6.4: Summary of calibrated numerical model parameters used in Cresta di Saline numerical simulations

6.6 MODEL RESULTS

6.6.1 DSGSD mechanisms

The results obtained for simulation with weakened band occurrence (Fig. 6.22b), upscaled rock mass properties, time-dependent deglaciation and damage-dependent fluid pressure distribution reproduce the occurrence of a Deep Seated Gravitational Slope Deformation consistent with the geomorphological and geotechnical data available for the Cresta di Saline case study, thus providing a coherent long-term interpretation of post-LGM rock slope evolution. The predicted kinematics consists in a compound roto-translational unstable mass slightly suspended over the valley floor, whose lower boundary is constituted by a deep-seated basal shear band up to 300 m wide (Fig. 6.23). At the slope crest, the occurrence of such surface resulted in ridge splitting and lowering of downslope portion up to 150 m of vertical displacement, while at the slope toe shear band emerges in a slope portion intensively damaged located around 1550 m and 1700 m a.s.l.. The depth of DSGSD ranges between 100 m up to 500 m in the middle slope portion: even if no deep geotechnical data exists on this slope sector to constrain basal shear band thickness and location, also for this case study the simulated depth seems to be biased by the effect of mesh size, resulting in overestimation of depth with respect to the geological model of the slope, derived from the geological interpretation of Agliardi et al. (2001) and superimposed to damage pattern with the white lines in Fig. 6.23.

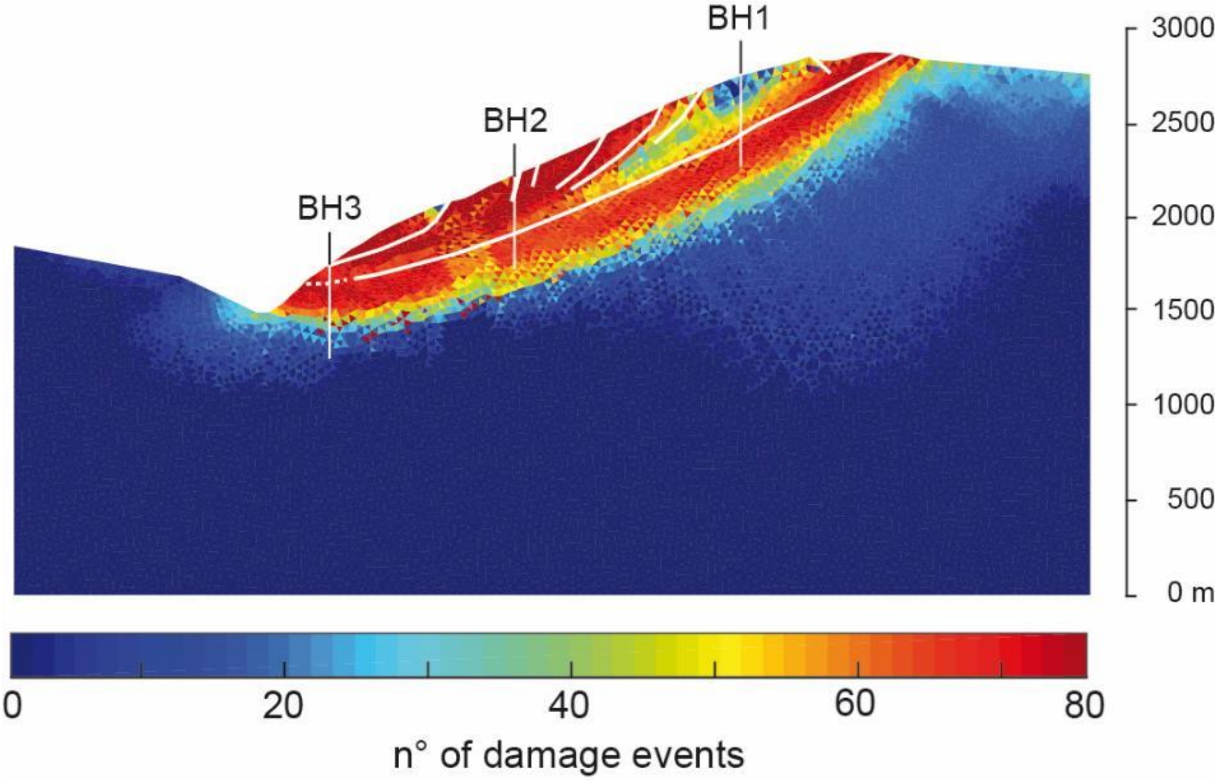

Figure 6.23: Pattern of damage registered for calibrated simulation, compared with observed and inferred DSGSD features (white lines, from Agliardi et al., 2001). The location of virtual boreholes is also reported.

The predicted spatial pattern of damage resulted in the occurrence of an intensively damaged zone, which extends from the slope toe up to an elevation of 2550 m a.s.l., resulting in the widespread extension of highly-fractured rock mass. The simulated behavior is coherent with the observation made on real slope, which indicates the occurrence of poor-quality rock mass in this sector, as testified by the occurrence of paleolandslide accumulations and of Ruinon rockslide. Moreover, just upslope the rockslide Upper Scarp, the widespread occurrence of synthetic scarps is recognized up to 2600 m a.s.l. (Fig. 6.15). Moving upslope, damage pattern is characterized by a progressive reduction of damage since crest zone, where the occurrence of quasi-undamaged rock mass surrounding the DSGSD basal shear zone is simulated.

Despite the lack of geotechnical deep data, we decided either way to simulate three "virtual inclinometers" (white lines in Fig. 6.23 and 6.24): respectively located at 1750 m a.s.l. (BH1), 2250 m a.s.l. (BH2) and 2750 m a.s.l. (BH3). Regarding the vertical logs of simulated GSI, BH1 is characterized by intense rock mass damage up to 350 m of depth, where the transition to undisturbed material is progressively reached. Moving upward to BH2, the same trend is observed, with damaged rock mass deepening up to 450 m. Notably, in BH3 good-quality remnants overlies intensely fractured rock mass, with damage extending up to 450 m below the slope surface. Vertical profiles of simulated horizontal displacements ("virtual inclinometers") outline slope displacement up to 250 m of depth in the lower portion of the slope, progressively increasing up to 400 m in BH3. Displacement vertical profiles suggest a significant internal deformation of the DSGSD, especially in the lower and middle portions, where progressive decrease of displacement is observed since slope surface. In the upper slope sector, the displacement profile in upper slope is characterized by a more abrupt transition and light steering effect, which suggest the rigid sliding of slightly deformed rock mass above a more localized basal shear zone (Fig. 6.24). This is consistent with the simulated patterns of damage and with the occurrence of large displacements associated to sharp morphostructures (e.g. DSGSD main scarp) mapped in the field.

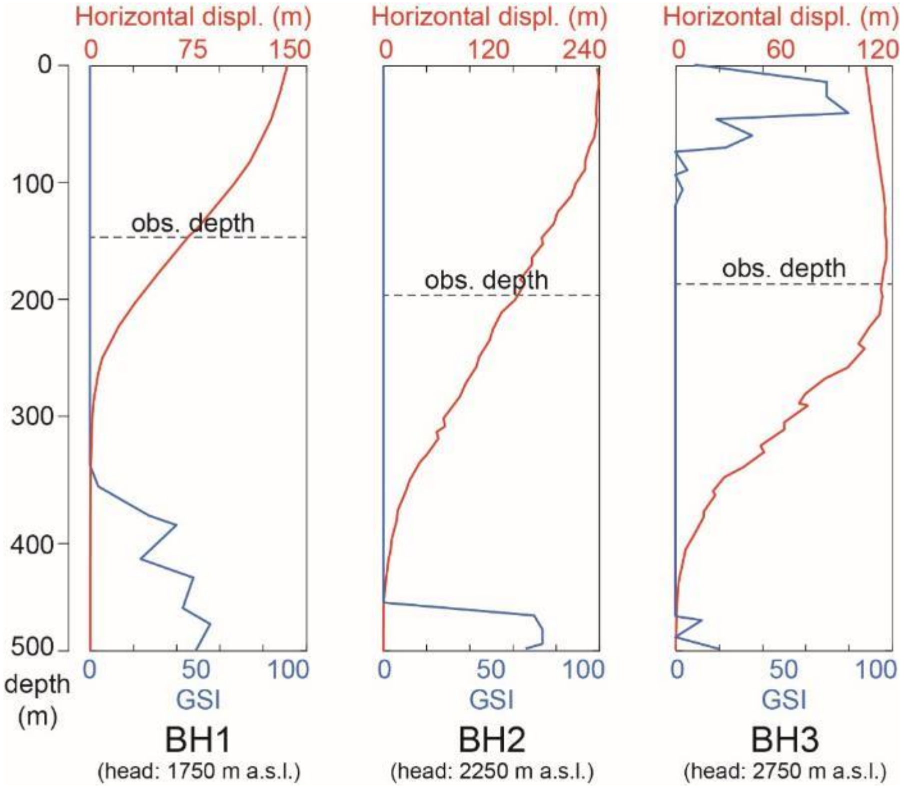

Figure 6.24: Logs of simulated horizontal displacement (i.e. virtual inclinometers) and GSI values (i.e. virtual borehole logs) along vertical lines corresponding to synthetic boreholes.

Due to the large rock mass volumes involved and the high depth of basal shear zones in DSGSDs, deep geotechnical data are rare, even though detailed investigation are often motivated by engineering purposes, regarding for example the interactions with hydropower reservoirs (Zangerl et al., 2010; Agliardi et al., 2012). With DaDy-RS, we tried to overcome these limitations and provide a robust assessment of mechanical properties for the entire slope domain, also considering deep rock masses, where direct investigations are usually not performed. To do this, final values of rock mass deformation modulus were converted into corresponding value of GSI to be compared with observed data. This was done considering model elements up to depths of 300 m from the slope surface, to be representative of material inside DSGSD.

Starting from initial values in the narrow range 75-85 (green line in Fig. 5.23), progressive damage led to degradation of rock mass properties, expressed by the decrease of GSI value down to 5, where a frequency peak is observed, probably associated to partial discordance between sampled domains and depth of the DSGSD basal shear zone, which is sampled recurring to constant depth all throughout the slope profile (blue lines in Fig. 5.23). Despite this, the simulated distribution resulted in good agreement for GSI values comprised in the interval 30-80. Inside the DSGSD, gravitational deformation contributed to damage accumulation and, consequently, to lower GSI values, which account for the intense fracturing, the loss of structure and the occurrence of cataclastic breccia layers (red lines in Fig. 5.23). Both simulated and observed distributions exhibit a peak for GSI values lower than 10, while the relative peak observed for GSI=50 is not simulated by the numerical model.

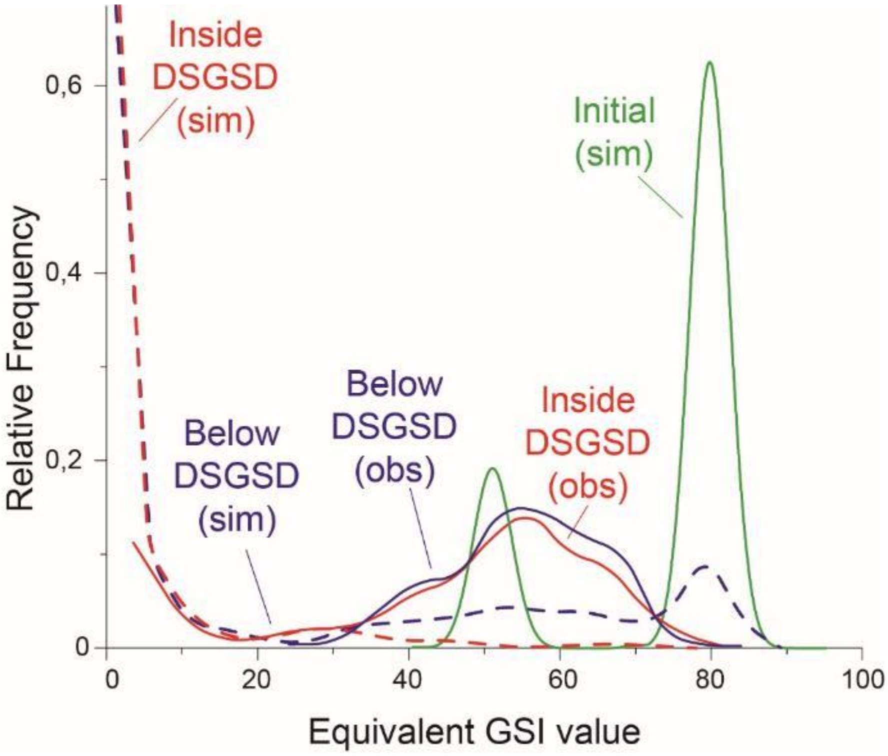

Figure 6.25: Observed versus simulated (dashed lines) frequency distributions of GSI values. Simulated value are back-calculated from distributions of simulated effective deformation moduli E_i.

Interaction between fluid pressure occurrence and damage mechanisms during the entire simulation influenced the final (post-glacial) distribution of permeable element clusters, and thus of fluid pressure distribution within the unstable portion of the slope. In the final model state (i.e. end of simulation at the attainment of the 150m displacement threshold at the main DSGSD scarp). Here, four different permeable clusters are recognized, extending close to the slope surface and constituting a shallower and almost interconnected aquifer ranging from crest to the slope sector immediately above the Ruinon (clusters 4, 5 and 6 in Fig. 6.26). In the rockslide, due to high strain and damage cumulated, only few permeable elements are simulated between the Upper and Lower scarps (clusters 2 and 3 in Fig. 6.26). An additional cluster is predicted by the numerical model on the other side of the valley (cluster 1): its occurrence is purely artificial, since the real slope morphology was modified due to numerical and computational reasons.

Horizontal and vertical displacement patterns (Figs. 6.27a, b) emphasize the observed extent of unstable (moving) rock mass, which also in this case is notably shallower than the damaged zone (Fig. 6.23). The slope experienced large vertical displacements in the middle-slope portion, particularly below 2550 m a.s.l., where abrupt increase in cumulated value is observed, while maximum values are reached for the Ruinon rockslide Upper Scarp. Another portion characterized by high vertical displacement is the crest zone, where displacement patterns mirroring the active wedge mapped in the field is quite well reproduced. Regarding horizontal displacements, the simulated pattern reflects what observed for the vertical component: main movements occur in the middle-lower slope sector, exhibiting the same increase below 2550 m a.s.l.. Starting from this elevation, high cumulated values of horizontal extends until 1700 m a.s.l., reaching maximum values in a range of altitudes and in a slope sector coherent with the Ruinon rockslide occurrence.

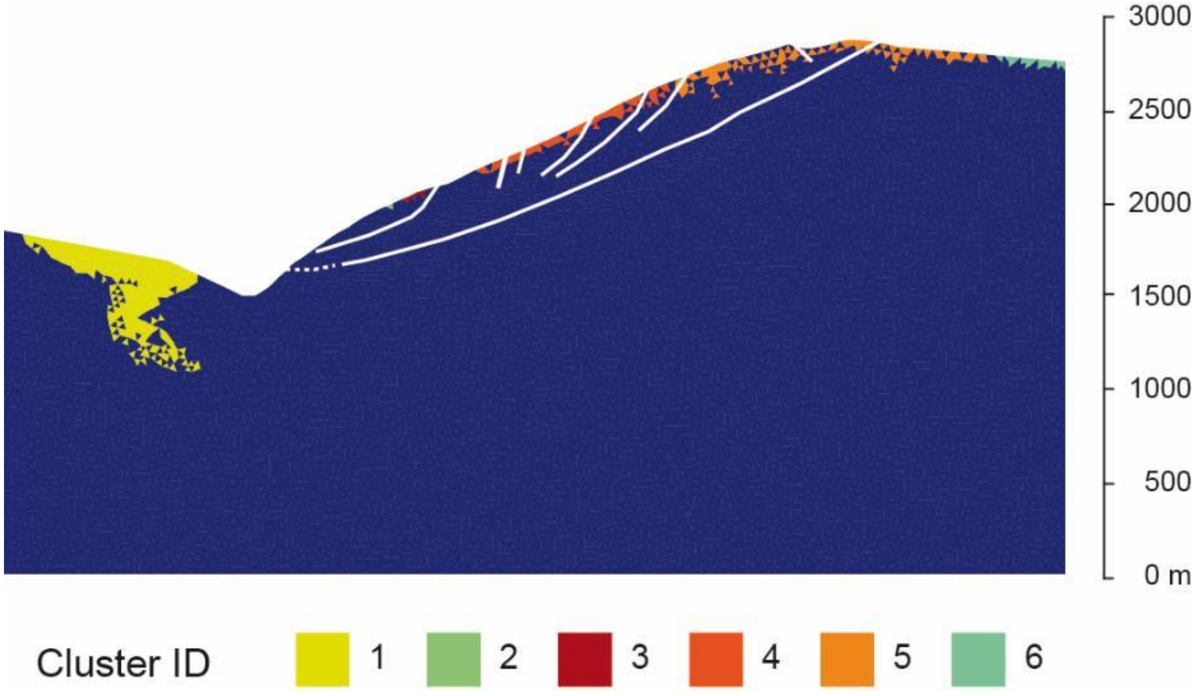

Figure 6.26: permeable element cluster distribution in the final state of simulation, outlining the occurrence of several shallow aquifers within the slope body. The location of observed or inferred DSGSD features is reported with white lines.

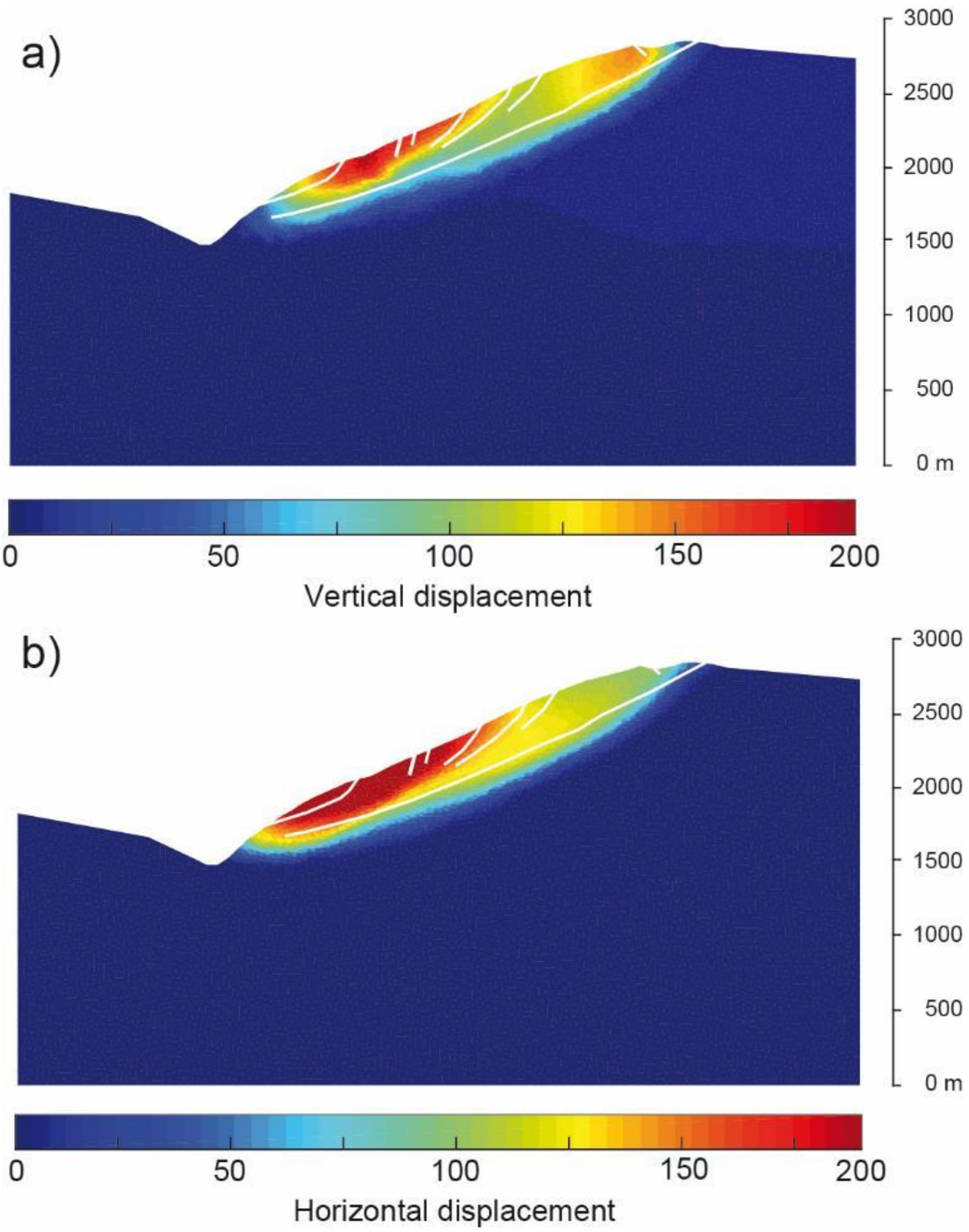

Figure 6.27: (a) Vertical and (b) horizontal displacement for calibrated simulation.

6.6.2 Time-dependent evolution

The explicitly time-dependent nature of our model provides the opportunity to explore the mechanism of slope damage, fluid occurrence, deformation and failure in an absolute chronological framework. The temporal evolution of the slope was analysed by a “time-lapse” comparison of model states at different stages between deglaciation and present timeMoreover, we continuously tracked displacements simulated by the model at several key observation points (Fig. 6.28). These were located along the slope corresponding to significant features of the DSGSD, namely the slope crest (point 1), the Confinale synthetic scarp (point 2, fig. 6.10) and the Ruinon Upper scarp (point 3) and Lower scarp (point 4). We selected also 3 points in the upper (point 5), medium (point 6) and lower (point 7) sector of the basal shear band to monitor its evolution in respect to the superficial patterns. Displacement trends and location of the observation points are plotted in Figure 6.28

Simulations begin with slope deglaciation, which onset was imposed at about 20 kyr BP with a total duration of 2000 years. At the end of deglaciation diffuse damage occurs especially at slope toe and in the rock mass underlying the crest (Fig. 6.29a). At this stage, widespread fluid occurrence can be already observed in the middle-lower slope, especially within the finite elements representing the weakened zone along the WNW-ESE tectonic lineament, which favored formation of an isolated aquifer extending from 1700 to 2200 m a.s.l. (Fig. 6.29b). Minor and scattered permeable clusters occur in the upslope portion. Apart from a little portion located at slope toe, no considerable strain localization or permanent displacements occur at this stage (Figs. 6.28 and 6.29c).

After 5 kyr the end of deglaciation (13000 yr BP), the slope experienced sharp changes in both damage pattern and permeable clusters distribution. At this stage, damage events occur mainly in two sectors, but with different spatial patterns: along the future DSGSD basal shear band, diffused damage occurs, homogeneously ranging from toe to crest, even if interrupted around 1500-1700 m a.s.l. by the occurrence of the weakened band with associated contrast in rock mass mechanical properties. On the other hand, sharp localization of damage is observed in the rock mass just surrounding the lower portion of basal shear band (1700 m to 1800 m a.s.l; Fig. 6.30a). At this stage, damage pattern and stress regime result in widespread fluid pressure occurrence, testified by the development of large and deep clusters all throughout the slope, especially in the middle and upper sectors (Fig. 6.30b). Shear strain increase at toe and upslope migration along basal shear band are observed, even if with low cumulated values, while a scarp nucleates in the slope portion affected by localized damage (Fig. 6.30c).

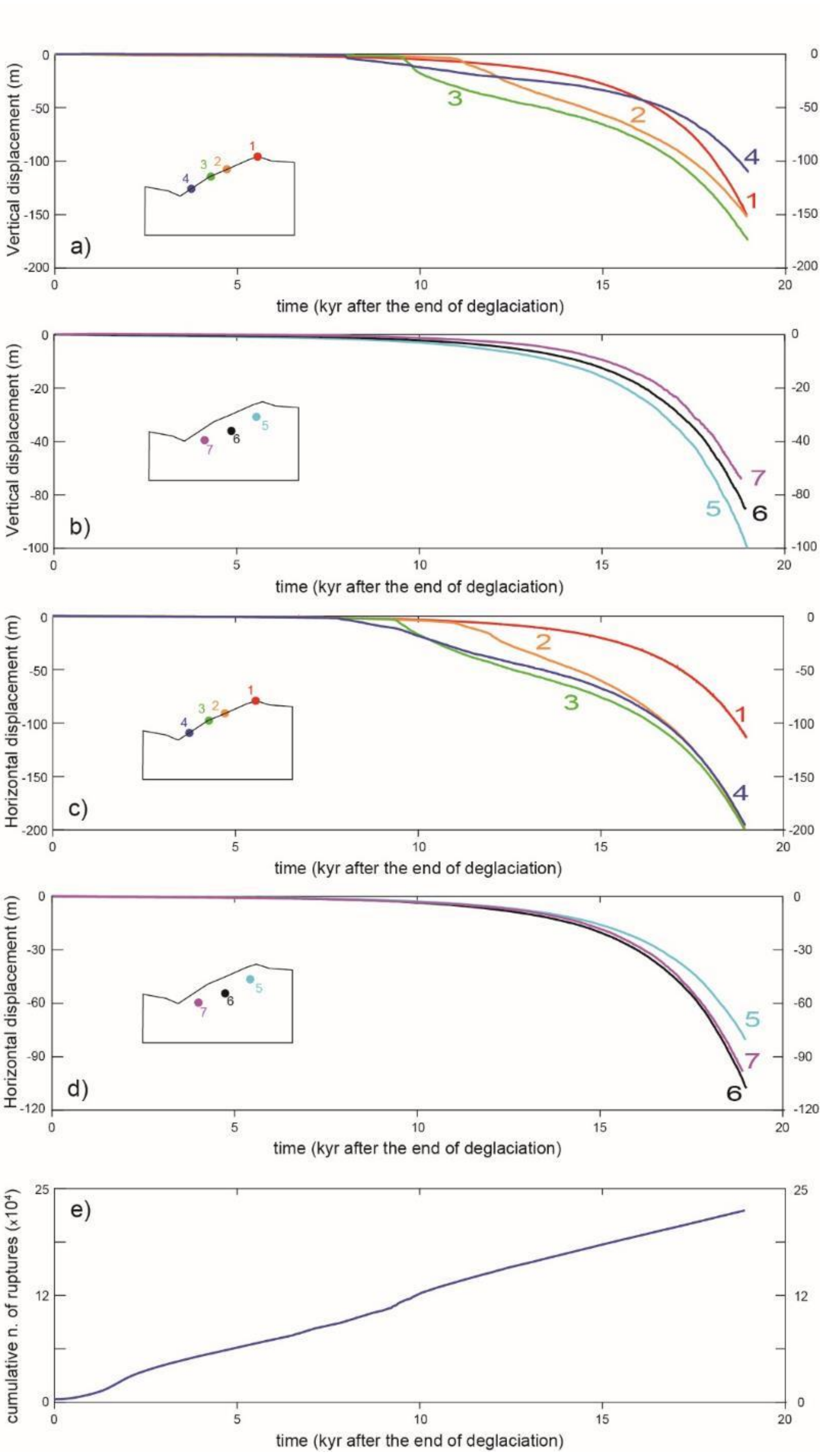

Figure 6.28: (a) and (b): vertical and horizontal displacements of selected observation points at key slope locations (insets).

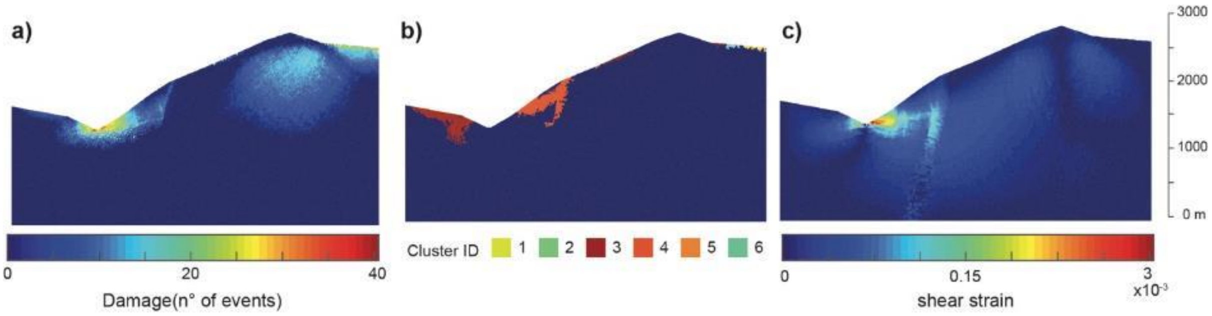

Figure 6.29: Damage pattern (a), permeable element cluster occurrence (b) and shear strain pattern (c) at the end of deglaciation (18 kyr BP).

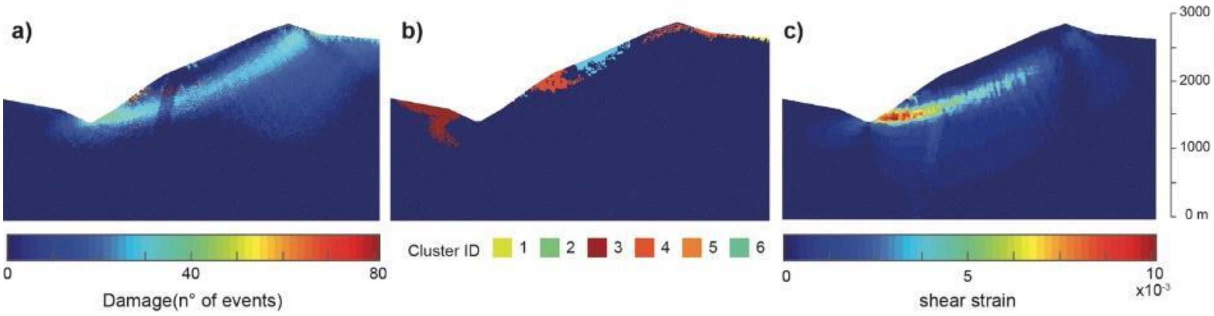

Figure 6.30: Damage pattern (a), permeable element cluster occurrence (b) and shear strain pattern (c) at 5 000 years after the end of deglaciation (13 kyr BP).

After 7 kyr from the end of deglaciation (11000 yr BP), a fundamental stage in slope evolution is reached. While damage keeps on localizing along the DSGSD basal shear zone, a second, shallower but much more intense localized damage (and shear strain) zone develops in the middle–lower slope sector daylighting between 1700 and 2100 m a.s.l., coincident with the position and depth of the collapsed Scè and the active Ruinon rockslide. (Fig. 6.31a,c) At this stage, damage and strain pattern influence the distribution of fluid pressure in the slope by strain accumulation along basal shear band and in the middle-lower slope sector: this causes notable permeable cluster reduction and the occurrence of a unique cluster ranging from crest down to 2200 m a.s.l. (Fig. 6.31c). Meanwhile, the observation points located along and within the slope testify the beginning of downslope displacement, especially in the low sector, where several meters are quickly cumulated (point 4 in fig. 6.28). Moreover, slope activation can be observed also for the entire basal shear band, with coherent trends for upper, middle and lower sectors (points 5, 6 and 7 in fig. 6.28).

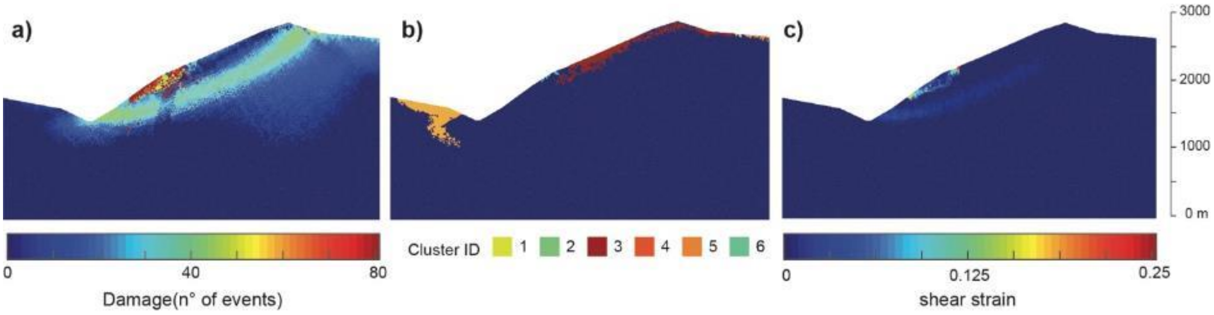

Figure 6.31: Damage pattern (a), permeable element cluster occurrence (b) and shear strain pattern (c) at 7 000 years after the end of deglaciation (11 kyr BP).

After 3 kyr (9 000 yr BP), the shallower damage zone extends upwards until 2400 m a.s.l. followed by retrogressive strain accumulation, leading to the development of a large roto-translational movement, nested within the DSGSD unstable mass and corresponding to the morpho-structures mapped in the field in the middle slope sector (Fig. 6.32a, c). The perched aquifer previously formed upslope does not experience significant changes during this period (Fig. 6.32b). Increase in displacement is collected for the entire slope, with higher rates in the observation point located in the Ruinon Upper scarp surroundings, which cumulated almost 50 m of vertical component in a few thousand years (point 3 in fig. 6.28).

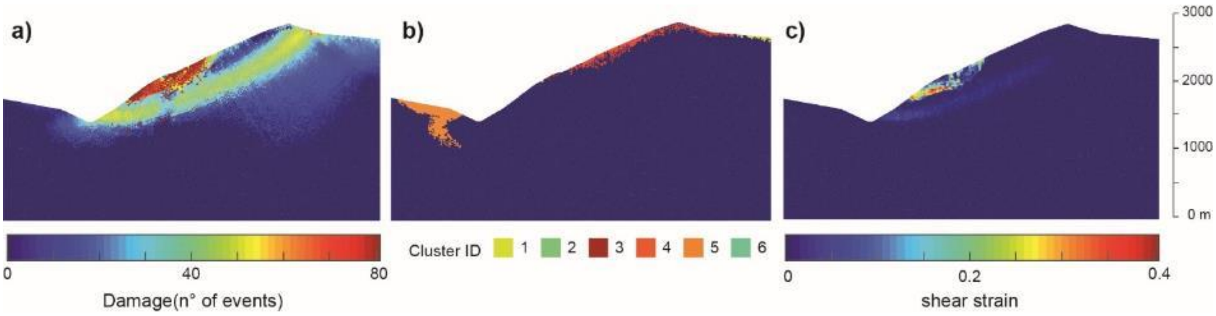

Figure 6.32: Damage pattern (a), permeable element cluster occurrence (b) and shear strain pattern (c) at 10 000 years after the end of deglaciation (8 kyr BP).

At 13 000 yr after the end of deglaciation (5 000 yrs BP), a significant evolution of the entire DSGSD is observed, with an increase in damage and strain localization along the basal shear zone, and an increase in accumulated displacement along the main scarp (Fig. 6.33a, c). This results in a significant reduction in permeable element clusters distribution, as fluid pressure occurrence is now localized only in the upper sector and in small and scattered aquifers in middle slope (Fig. 6.33b).

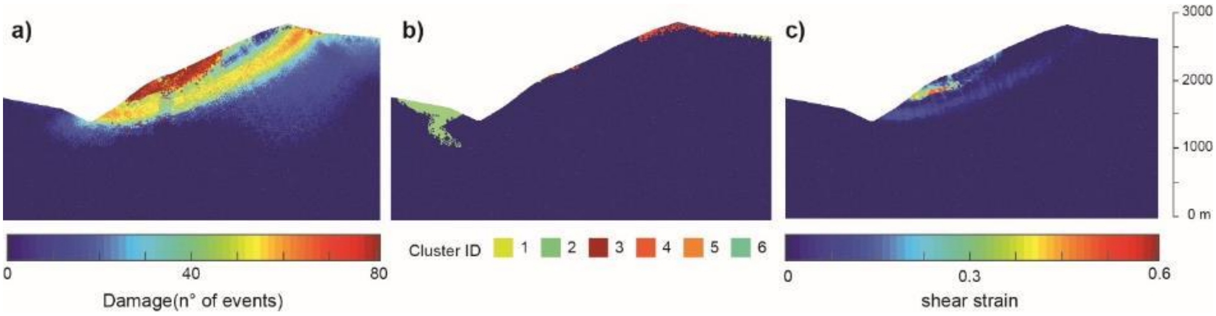

Figure 6.33: Damage pattern (a), permeable element cluster occurrence (b) and shear strain pattern (c) at 13 000 years after the end of deglaciation (5 kyr BP).

After 2000 yrs (4000 yrs BP), notable increase in damage is collected along basal shear band (Fig. 6.34a), resulting in global acceleration phase especially in crest zone and in the upper portion of basal shear band, testifying the complete maturation of DSGSD (Fig. 6.28). This is accompanied by further damage localization in shallow rock mass up to 2550 m a.s.l.. Permeable cluster distribution extended downslope, constituting a shallow interconnected aquifer that ranges from the middle sector the area immediately beneath the ridge crest (Fig.

6.34b). Strain pattern strongly increased along basal shear band, reaching appreciable cumulated values also in the crest zone, where ridge splitting is now evident (Fig. 6.34c).

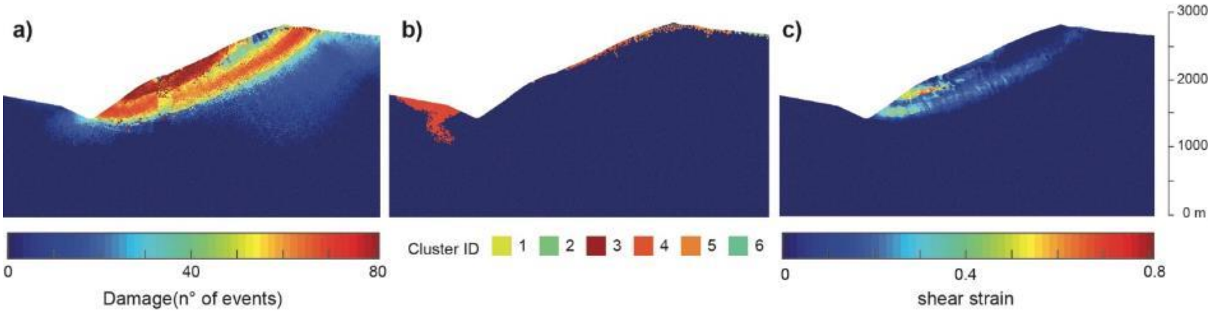

Figure 6.34: Damage pattern (a), permeable element cluster occurrence (b) and shear strain pattern (c) at 15 0000 years after the the end of simulation (3 kyr BP).

During the next 4000 yrs until present day conditions, further damage occurrence is registered along the basal shear band, particularly in the upper and lower sectors (Fig 6.35a). Regarding strain, damage localization results in further shear along basal shear band, which exhibit a clear signature, especially in the lower portion of the DSGSD, where it outlines diffused pattern coherent with the unstable conditions nowadays reported for this portion of the slope (Fig. 6.35c). Notably, evident changes occurred also in topographic profile, which now consists in ridge splitting and evident bulging in the lower part. In monitored points, progressive failure and upslope growth of the basal shear band led to further non-linear increase of displacement rates until 45 mm/yr in the Confinale area, lightly overrated with respect to data coming from satellite interferometry performed in this slope portion. Cumulated displacement reached maximum values in the Upper scarp sector, consisting in 175 m and 200 m of vertical and horizontal component, respectively, and testifying around 10 kyr of continuous activity.

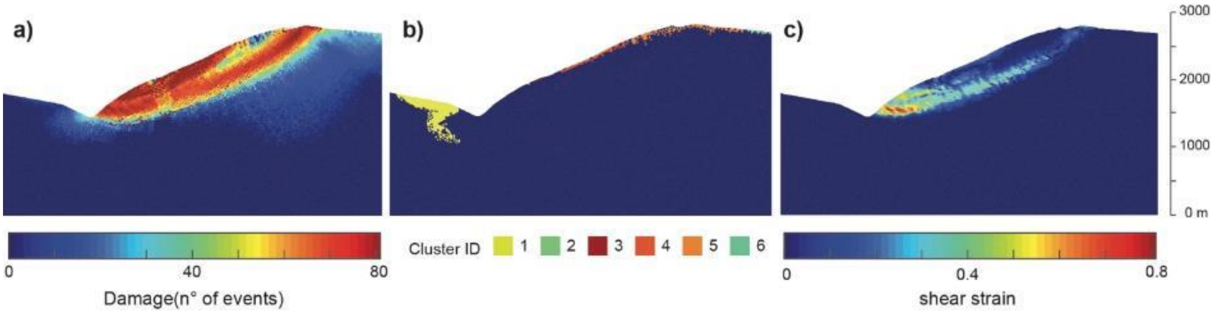

Figure 6.35: Damage pattern (a), permeable element cluster occurrence (b) and shear strain pattern (c) at the end of simulation.

6.6.3 *Long-term effects of brittle structures*

The model results discussed in the previous paragraphs suggest an important role of the weakened band in the long-term slope evolution, influencing both slope stress regime and permeable cluster distribution. To test this hypothesis, we ran an additional simulation without accounting for such zone (Fig. 6.22a) and maintaining all the other model parameters unchanged.

The simulation without weakened band results in a similar damage pattern excepts for the lower portion of basal shear zone, which develops more continuously and slightly lowered with respect to the previous simulation, resulting in deepening of DSGSD kinematics (Fig. 6.36).

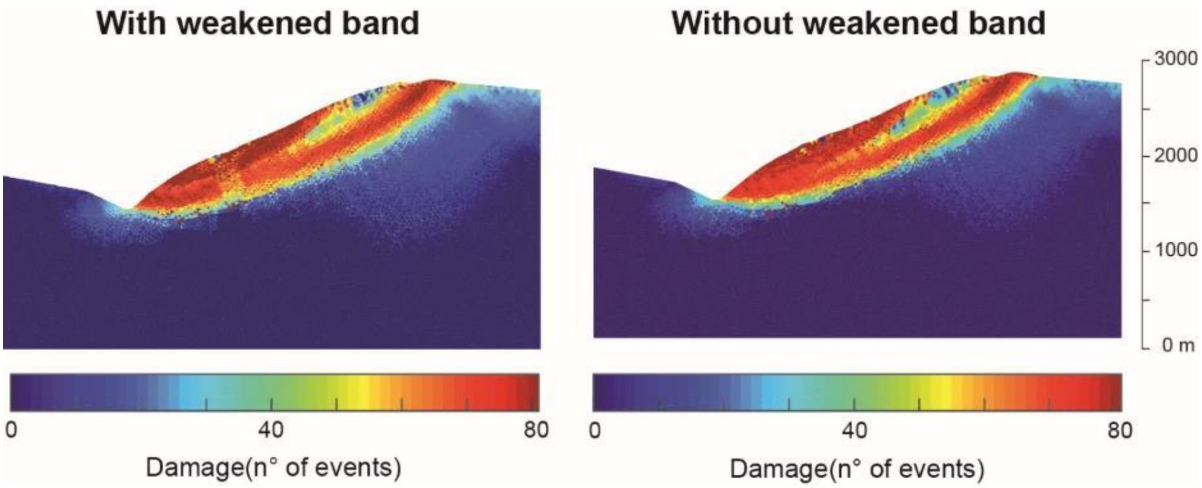

Figure 6.36: Comparison between final damage pattern for simulation with (a) and without (b) weakened band occurrence.

Despite the very similar damage distribution, displacement analysis outlines different patterns for the two tested configurations: the model with weakened band occurrence and associated contrast in rock mass mechanical properties is characterized by higher cumulated displacement in the middle-lower portion of the slope, regarding both vertical and horizontal component, which exceeds up to 50 m the correspondent values simulated without accounting for brittle structure occurrence (Fig. 6.37).

Moreover, the model without weakened band occurrecne takes a longer time (around 20% more) to reach observed cumulated displacement in DSGSD main scarp, even if displacement trends are coherent between the two simulations (Fig. 6.38a). The duration difference can be explained recurring to the analysis of cumulative number of ruptures: the behavior is quite similar until 10 kyr from the end of deglaciation, when an abrupt rate increase is observed for the model with weakened band occurrence (Fig. 6.38b). This stage corresponds to the nucleation of rockslide perched within the DSGSD and the consequent global slope acceleration (Fig. 6.32), which timing and occurrence are likely influenced by weakened band occurrence.

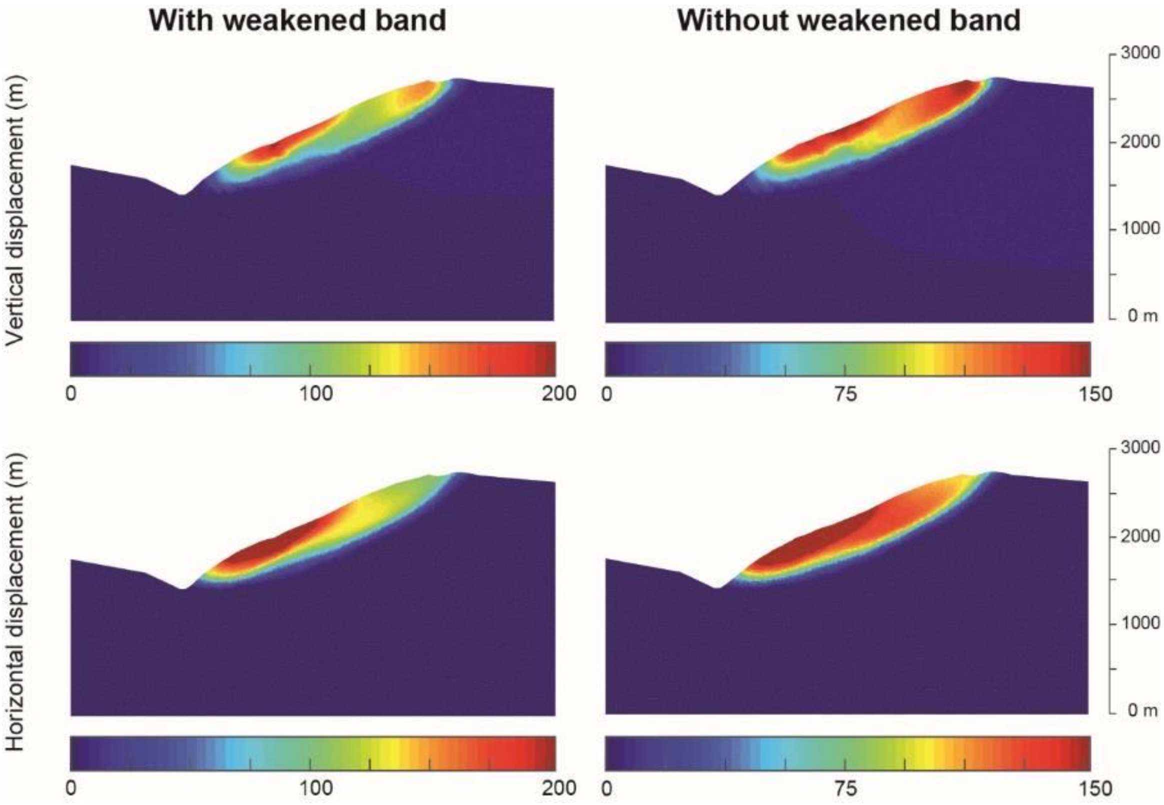

Figure 6.37: Comparison between vertical and horizontal displacement for simulation with and without weakened band occurrence.

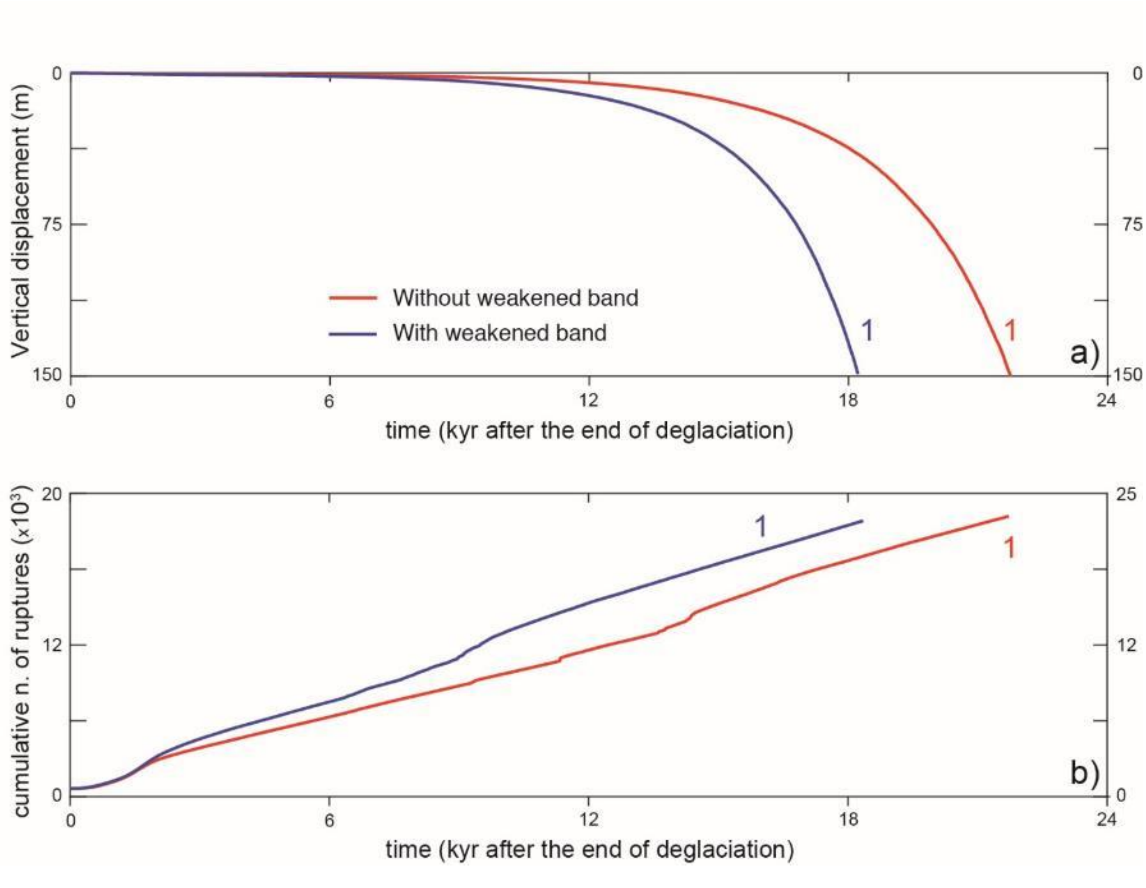

Figure 6.38: long-term displacement-time curves simulated with (blue) and without (red) accounting for weakened band occurrence (example for observation point 1); (d) long-term creep curves simulated with (blue) and without (red) accounting for weakened band occurrence, expressed in terms of cumulative numbers of ruptures.

7 DISCUSSION AND CONCLUSIONS

Starting from a damage-based, time-dependent approach originally conceived for laboratory creep tests, we developed novel model components making the numerical code suitable for application to real, large rock slopes. In particular, we included in the model upscaled relevant rock mass properties, time-dependent simulation of slope deglaciation and damage-based occurrence of fluid pressures in the slope.

DaDyn-RS was first tested on large slopes with simplified geometry (Cf. chapter 4) and then used to simulate the mechanics and timing of long-term evolution of two real slopes in the Italian Central Alps, namely the Spriana and Cresta di Saline slopes. They are affected by large rockslide and Deep-Seated Gravitational Slope Deformation (DSGSD) phenomena, respectively. The applications also allowed evaluating the computational performance of the model and reproducing in detail the key aspects of long-term alpine slope evolution, from glaciated to post-glacial (present-day) conditions through progressive deglaciation and a period of paraglacial readjustment.

The development of DaDyn-RS allowed proposing a novel approach to the numerical modelling of the long-term evolution of large rock slopes, able to account for all the key aspects of the problem: the damage mechanics, the time-dependent failure mechanisms, the effects of deglaciation, and the evolution (and mechanical aspects) of slope hydrology. In this chapter, we discuss the key points, outcomes, strengths and limitations of the proposed approach, and outline the contributions of damage-based, time-dependent modelling to the understanding of alpine slope evolution in a more general geomorphological, hydrological, geochronological and geohazard perspective.

7.1 ROCK MASS DAMAGE DISTRIBUTION IN REAL ROCK SLOPES

Establishing robust links between observed and simulated slope damage patterns is a key point in the set-up, calibration and validation stages of modelling with DaDyn-RS. The amount and spatial distribution of rock mass damage in a slope provides a picture of the cumulative impacts of different physical processes associated to long-term slope evolution. Rock mass damage is closely related to changes in fracture density associated to the loading history experienced by the slope over the long-term. Thus, in situ "damage states" conditions can be quantified using fracture abundance measures commonly adopted in rock engineering, that can be derived from boreholes and outcrops.

The data derived from site investigations, especially for the Spriana case study, were thus re-classified in terms of RQD, Weighted Joint Density (wJD), linear fracture density (P_{10}) and Geological Strength Index (GSI), and represented in logs. This allowed identifying different "damage domains", depending on the spatial continuity of damage conditions and their relationships with rock slope instabilities. In particular, rock mass properties estimated below rock slope instabilities (i.e. deeply inside the slope) are inferred to be closer to initial "pre-deglaciation" properties, depending on rock mass structure and discontinuity condition inherited from the tectonic history and from previous landscape evolution (green line in fig. 7.1). At the same time, the conditions of rock masses outcropping outside areas affected by rockslides or DSGSD are considered representative of deglaciation-induced damage (blue line in fig. 7.1). Finally, rock masses inside rockslide and DSGSD suffered the damage imprint of large rock slope deformations, including diffuse damage and localized damage along cataclastic shear zones (red line in fig. 7.1).

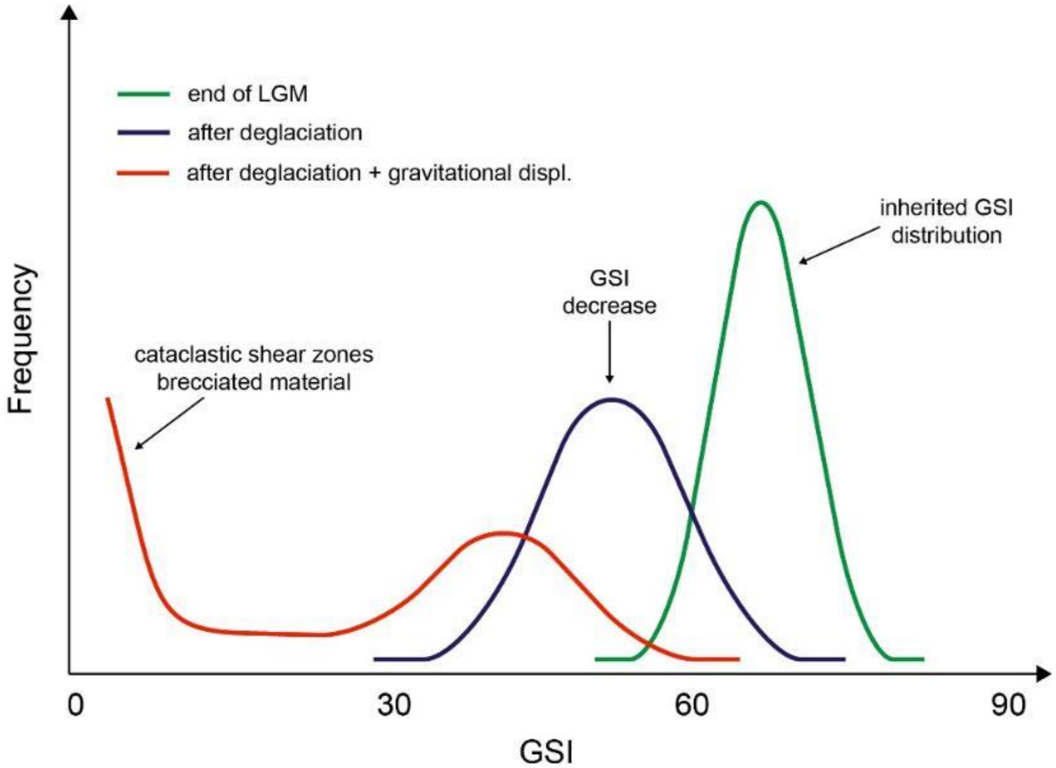

Figure 7.1: Conceptual model of the evolution of rock mass properties, as a consequence of damage related to deglaciation and gravitational deformation.

The analysis of the statistical distributions of fracture abundance measure in each damage domain also provides estimates of rock mass heterogeneity in pre- and post-failure conditions and consistent sets of input parameters to DaDyn-RS model set ups, as well as more robust model validation constraints. Among the different parameters tested, the Geological Strength Index (GSI) proved to be the most suitable to account for the main geological features responsible to rock mass strength (i.e. structure and joint conditions; Hoek and Brown, 1997) and establish a two-way link between reality and modelling. In fact, GSI allows the direct application of the widely used Hoek-Brown criterion to parametrize rock masses for modelling purposes and to derive the initial distribution of deformation moduli (input dataset) required by DaDyn-RS, using the empirical approach of Hoek and Diederichs (2005). At the same time, model damage states computed by DaDyn-RS for each finite element in terms of reduced deformation moduli can be easily converted into GSI distributions to be compared with field data for different observed damage domains (validation dataset).

On the other hand, RQD resulted in biased and frequency distributions, poorly representative of the damage patterns observed in the drillcore records. Despite the large use in engineering practice, we considered RQD not suitable for rock mass damage classification. Finally, P_{10} and wJD demonstrated a good performance in the classification of rock mass damage state, particularly regarding the higher sensitivity with respect to GSI in the detection of thin and intense fractured intervals, which clearly appear in geotechnical logs. The disadvantage of using these parameters is represented by the difficult linking between obtained distributions and rock mass mechanical parameters, i.e. deformation modulus, cohesion, tensile strength and friction angle.

The uncertainties associated with a slope-scale rock mass damage assessment mainly derive from the quality, spatial availability and statistical significance of investigation or field data. In real rock masses, which are characterized by heterogeneity and possible anisotropy, the quantification of parameters can be largely affected by orientation bias, scale effects, scattered investigations (especially for deep rock masses) and collected information representative only of a point-like portion of slope. Moreover, site investigation regards only the slope present state, and no constraints can be imposed regarding the long-term slope conditions. Using statistical distribution of rock mass properties typical of different damage domains allows (at least in part) accounting for these sources of problem uncertainty.

7.2 TIME-DEPENDENT DAMAGE MODELLING OF LARGE SLOPES: PARAMETER UPSCALING

The damage- and time-dependent model (Amitrano and Helmstetter, 2006) on which DaDyn-RS has been built is able to reproduce the progressive failure of large rock slopes in real rock masses, and to describe the spatial and temporal changes of material properties throughout the entire "life cycle" of a slope. The model has an explicit time-dependent formulation, allowing tracking the full slope history from glaciated conditions (e.g. LGM or different stadials) to the present time. Such history can be rescaled to real time based on geomorphological, morpho-structural or dating constraints. The long-term behavior is simulated starting from initial conditions which, regarding rock mass properties, only assume a distribution of deformation modulus (and related heterogeneity) observed in real slopes and inherited from previous geological processes (Cf. subsection 3.4), thus avoiding strong assumptions on basal shear band geometry and rheology. Elastic interactions among finite elements (and resulting stress distributions) allow reproducing progressive damage localization, shear band formation and complete description of creep curve at the macroscopic (slope) scale as model emerging properties, eventually leading to the differentiation of large rock slope instabilities. This represents a fundamental achievement of our modelling approach, which overcomes both the limitations of time-dependent rheological approaches, usually requiring strong assumptions on the geometry and properties of localized shear zones (Crosta et al., 2014), and the inability of most elasto-plastic model of accounting for time-dependence (Preisig et al., 2016).

The damage accumulation occurring in finite elements at successive model stages is controlled by stress conditions and initial values of the deformation modulus, depending on the value of the incremental damage parameter *D*. The latter is defined according to a continuum damage mechanics approach (Kachanov, 1958; Amitrano et al., 1999; Murakami, 2012), and represents a proxy of the increase of fracture abundance/density occurring in a model a consequence of a brittle failure event (Cf. subsection 3.1.1). Thus, *D* modulate the amount of damage accumulated in a given element (and in surrounding elements during an avalanche) in a sequence of damage events (Fig. 3.1a). Since no experimental data is available to constrain the optimal values of D on the rock mass (slope) scale, we performed parametric tests on simple slopes to investigate how *D* controls the style of damage accumulation within the slope (i.e. diffused vs. localized). For low values of *D*, diffused damage dominated, whereas high *D* values result in more localized damage. No significant scale effects on the parameter D were suggested by simulations, since the kinematics and damage patterns observed for real rock slopes in "damage domains" are best reproduced for values of *D* similar to those previously calibrated for simulations of laboratory experiments on intact rocks (*D*=0.1; Amitrano et al., 1999; Amitrano and Helmstetter, 2006; Lacroix and Amitrano, 2013). The sensitivity analysis performed showed a significant dependency of *D* on finite element mesh size. Decreasing the nominal mesh size and maintaining the damage increment parameter constant (or *vice-versa*), results in a lower portion of the model damaged in each event, resulting in a smoother degradation of rock mass properties which favors diffused damage.

The time-dependent component of the model is based on an exponential time-to-failure law (Cf. subsection 3.1.2) mainly controlled by the parameter *b*. This was empirically determined by Amitrano and Helmstetter (2006) for problems and scales involving intact rocks, through the statistical analysis of the results of laboratory creep tests on rock samples of different lithology. Again, moving from the intact rock (lab) to rock mass (field) scale, the impossibility to directly measure *b* in the field makes calibration necessary (Lacroix and Amitrano, 2013). There are no studies or theoretical arguments supporting the occurrence or absence of scale effects on *b*, thus we performed several calibration tests for both simplified slopes (Cf. chapter 4) and real rock slopes (Cf. chapters 5 and 6). We observed that upscaling has a limited effect on *b*, as typical geometries and kinematics observed in real rock slopes are reproduced by DaDyn-RS for time-to-failure parameter in the same order of magnitude of those observed for intact rock in laboratory tests, with calibrated *b* values in lower range of intact rock experimental values. In our modelling exercises, we kept the time-to-failure parameter constant with respect to changes in water content, temperature and confining pressure, despite laboratory tests highlight variations of *b* for changes in such boundary conditions (Kranz et al., 1980; Kranz et al., 1982). We assumed this simplified condition due to the scarce data available on stress corrosion effects, poroelastic properties of fractures rock masses and boundary condition effects (Tab. 3.1 and fig. 3.2), to avoid introducing excessive additional uncertainty in the analysis at this stage of model development.

The adopted time-to-failure law implies that the model develops into a continuous sequence of failure events, preventing the reaching of equilibrium state, also for mobilized stress very low with respect to instantaneous strength. To overcome this limitation, threshold value has to be imposed, to stop the calculation loop and produce the simulation outputs. Among the different parameters (e.g. strain, time, number of damage events) we decided to impose displacement-related threshold, in particular the vertical component monitored in a specific mesh node, which can be compared with displacements easily detected in the field. The mechanical properties of rock masses strongly control the occurrence, geometry and damage patterns of slope instability, as well as their timing (Cf. subsection 3.1.4). As previously outlines by Lacroix and Amitrano (2013), results are strongly affected by rock mass cohesion and tensile strength, the calibrated values of which fall in the range between intact rock and equivalent-continuum rock mass values. This is consistent with a contribution of intact rock bridges in brittle rock masses, which are commonly characterized by non-persistent discontinuities on different scales (Eberhardt et al., 2004; Frayssines and Hantz, 2006; Stead et al., 2006; Brideau et al., 2009; Elmo and Stead 2009).

7.3 WHY STARTING FROM GLACIATED CONDITIONS?

The transition from glacial to postglacial conditions represents a key point in the evolution of alpine slopes, resulting in stress redistribution and rock mass damage (Cf. subsection 1.2; Ballantyne, 2002; Eberhardt et al., 2004; McColl, 2012; Deline et al., 2015). The long-term slope history simulated by DaDyn-RS starts from the end of the Last Glacial Maximum (LGM), which was recognized as the last extensive alpine glacial pulse, in which glaciers filled main valleys under several hundred meters of ice thickness. Nevertheless, due to the intense carving and erosion operated by LGM glaciers, almost every valley morphologies and deposits related to previous large-scale stadials were obliterated (Kelly et al., 2004; Preusser et al., 2011), making the reconstruction of paleoenvironmental and geomorphological settings before the LGM extremely difficult. Even starting from the LGM, the assessment of rock mass mechanical (and hydraulic) properties is a difficult task due to the lack of data constraining slope conditions at that time (Preusser et al., 2011; Gianotti et al., 2015): we tried to overcome this limitation recurring to the assessment of rock mass damage state as discussed in subsection 7.1.

At the Last Glacial Maximum conditions (around 20 kyr ago), rock masses constituting slopes had already accumulated damage related to their previous tectonic and geomorphological history (previous cycles of glacial and fluvial erosion Fig. 7.1). Therefore, an ambitious reconstruction of the entire rock mass damage history (e.g. from orogenic exhumation to Holocene) would be impossible and biased by a large number of unconstrained assumptions, introducing more uncertainty than information in the model set up. Existing studies on long-term effect of erosion, active tectonics and repeated glaciation cycles provide interesting insights on their effects on slopes evolution (Leith, 2012; Leith et al., 2014; GIschig et al., 2015). Nevertheless, these studies are performed for simplified slopes in simplified environmental conditions. We choose a compromise between a long-term modelling effort and the availability of constraints on long-term evolution of slope topography, material properties and external actions, thus starting our modelling from LGM glaciated conditions and accounting for inherited damage imprints through material properties.

7.4 INSIGHTS INTO THE MECHANICS AND LONG-TERM EVOLUTION OF ROCKSLIDES AND DSGSD

Despite the simplified assumptions discussed in the previous sections, DaDyn-RS proved able to reproduce different key aspects of the long-term evolution of large alpine rock slopes, and in particular the mechanisms and processes which controlling the entire slope lifecycle and the onset of different types of large instabilities, from their initial nucleation to mature ("differentiated") stages.

During simulations, different stages of evolution were systematically outlined, preparing the ground for the onset of potential global slope instabilities. In this perspective, deglaciation has a major role on the stress and damage evolution of simulated slopes during the Lateglacial and following periods. Therefore, slope debuttressing induces a strong stress redistribution, reinforcing the effect of topographical component observed in unglaciated slopes and resulting in high mobilized stress and tensile rupture in shallow rock mass. Consequently, damage, mechanical properties degradation and stress redistribution starts to occur within the rock mass. Initially, rupture events are usually observed in the lower portion of the slope, which not necessarily corresponds with the toe, as exact location depends on different factors such as rock mass mechanical properties, deglaciation timing and slope morphology. This could result in damage localization at bottom slope (Cresta di Saline slope) or slightly above the valley floor (Spriana slope), as confirmed by observation on real large rock slope instabilities (Cappa et al., 2004; Agliardi et al., 2012; Crosta et al., 2014). Damage localization is a progressive process, since stress redistribution caused by damage induces higher stress in the surroundings, thus promoting further failure in the neighborhood rock mass. Damage localization is followed by the onset of shear strain localization. In continuum materials (i.e. no structural controls), this usually starts from the lower portion and extending upslope, leading to the progressive development of a basal shear zone. Notably, damage and strain localization do not occur simultaneously, but a time lag is inferred from the analysis of strain patterns and time-displacement curves. During slope differentiation, depending on mechanical properties and morphology, one or more secondary scarps can develop, connecting the topographical surface and the basal shear band.

In the simulated case studies, namely a rockslide (Cf. chapter 5) and a DSGSD (Cf. chapter 6), initial topographic conditions and material properties (i.e. gneiss vs metapelite) resulted in different damage and strain distributions, leading to different slope kinematics supported by field evidence. In the case of Spriana, a relatively sharp and narrow basal shear zone (considering the effect of mesh size) is simulated, especially in the lower part of the slope, where quasi-undamaged rock mass is crossed. Moving upslope, increase of rock mass damage and the emergence of two shear bands occurs, located in correspondence to rockslide upper scarp and prehistoric top scarp (Fig. 7.2a). On the other hand, the basal shear zone simulated for the Cresta di Saline corresponds to a broader localized damage zone, with a smoother "damage transition" to surrounding rock mass. Moving upslope, an opposite trend with respect to Spriana is observed, testified by the progressive reduction of damage and the occurrence of ridge splitting (Fig. 7.2b).

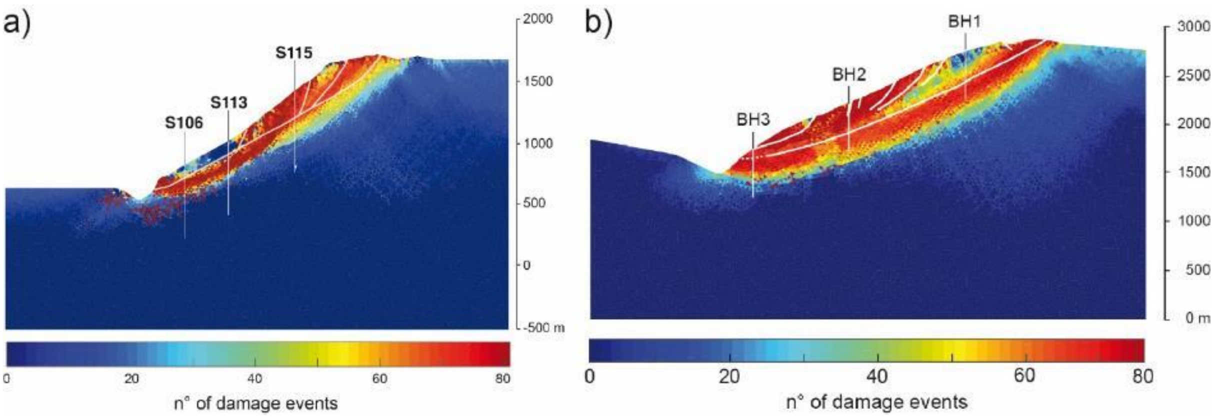

Figure 7.2: Pattern of damage simulated for (a) Spriana slope and (b) Cresta di Saline slope. Features observed or inferred on slopes are reported with white lines.

Besides the spatial patterns, the model is also able to quantify the impact of damage on rock mass properties in different slope sectors. Simulated GSI distributions are coherent with values observed or inferred on the slopes, thus quantitatively accounting for the progressive damage and degradation of rock mass properties, also in portions characterized by loss of structure and intense fracturing (Figs. 5.23 and 6.25). Moreover, the different degree of damage and strain localization, simulated in the different parts of the basal shear zone, mirror observed textural features of cataclastic breccias in the boreholes, which for the Spriana slope are more comminuted in the lower part of the slope than in the upper.

The explicitly time-dependent nature of our model provides an opportunity to explore the mechanism of slope damage, fluid occurrence, deformation and failure in an absolute chronological framework. Simulations begin with deglaciation, causing rapid slope debuttressing and initial occurrence of diffused damage, which occurs at slope toe (compression) and crest (extension), as a response to stress redistribution. At this stage, fluid occurrence is limited to isolated clusters, and no considerable strain localization or permanent displacements are observed (Figs. 5.27 and 6.29). Major changes occur few thousand years after the end of deglaciation, near the Holocene transition (13-10 yr BP; Figs. 5.28 and 6.30), when initial damage localization occurs in the lower part of the slope, resulting in a dilatant damage zone hosting a connected aquifer layer. Although no strain localization occurs yet, a global increase of velocity and rupture rates is evident from the time-displacement curves in Figs. 5.26 and 6.28. After that, strain localization initiates in the previously dilatant damaged band and leads to the evolution of a contractive deep shear zone, in turn affecting fluid pressure distribution through a progressive hydraulic sealing of the shear zone. At this stage, progressive damage extends upwards, resulting in weakening and increased displacement rates in the middle-lower portion of slope (Figs. 5.29 and 6.32). Complete slope differentiation and basal shear zone maturation is then reached (Figs. 5.30 and 6.33), marked by the upward migration of intense strain localization into the present-day basal shear zone. At this stage, shear zone contraction resulted in complete sealing and the development of permeable connected element clusters within the unstable rock mass. During the next thousands of years until present day (Fig. 5.32 and 6.35), progressive failure and upslope growth of basal shear zone led to further non-linear increase of displacement rates.

DaDyn-RS is able to distinguish the different features and temporal evolutions associated to rockslides and DSGSDs, respectively. Indeed, the simulations of Spriana and Cresta di Saline slopes differ by some key points, which are coherent with field observations on real slopes, and more generally, with the main features that characterize these two types of large rock instabilities. The Cresta di Saline DSGSD is characterized by a different timing, since after a few thousand years, significant evolution and damage localization has already undergone (Fig. 6.29), while the Spriana slope maintained little scattered damage (Fig. 5.27), suggesting different behaviors with respect to stress perturbation and rock mass material properties. Also observing the different behavior collected with respect to cumulative number of ruptures, differences in timing for Cresta di Saline and Spriana slopes are clear: while the former exhibit a more linear and progressive trend, interrupted by only one break at 9 kyr BP (Fig. 6.28e). the latter is characterized by strong increase in rupture rate in the period 5-10 kyr BP (Fig. 5.26e), ascribed to basal shear zone progressive sealing and rockslide differentiation. Regarding permeable element clusters, Cresta di Saline DSGSD is characterized by widespread occurrence of fluid pressure in early stages, progressively decreasing due to strain and damage accumulation until the present state, when clusters are detected only in the upper slope sector. On the other hand, in Spriana slope fluid pressure occurrence takes more time to develop at slope scale but, reaching mature stages, it is preserved, especially in the lower part of the slope, where the brittle basal shear zone results in the progressive aquifer sealing and the formation of a perched “damage reservoir” consistent with field observation.

The explicitly time-dependent nature of our model provides the opportunity to explore the mechanism of slope damage, deformation and failure in an absolute chronological framework. Simulations begin with slope deglaciation, causing rapid debuttressing and scattered damage occurrence at toe and crest. At this stage, fluid occurrence is limited to isolated clusters, and no considerable strain localization or permanent displacements occur. The aforementioned considerations allow us to contribute to a more general discussion of the timing and controls of large alpine rock slope instabilities, in the framework of postglacial evolution of Alpine landscapes. Two different temporal clusters of rockslide instability events (including both initiation/reactivation and catastrophic collapse) have been documented in the literature using absolute dating techniques, especially radiocarbon and Cosmic Ray Exposure (Fig. 1.10; Hormes et al., 2008; Prager et al., 2008; Le Roux et al., 2009; Zerathe et al., 2014 and reference therein). The first cluster, between 11 and 8 kyr BP, has been suggested as possibly related to paraglacial readjustment, by progressive failure at the transition with the Holocene (Prager et al., 2008). The second, concerning the period 5-3 kyr BP, was mainly suggested to be related to seismicity (Prager et al., 2008) and/or paleo-hydrologic pulses during Middle-Holocene climatic transition (Prager et al., 2008; Zerathe et al., 2014). Interestingly, both age clusters correspond with two major evolutionary steps predicted by our model for two different case studies, characterized by different morphological and topographical settings. The first cluster (10 kyr BP) corresponds to initial damage localization and dilatancy, while the second (5 kyr BP) to rockslide differentiation and significant increase in displacement rate. Thus we suggest, and submit to further testing, the hypothesis that progressive damage processes in subcritical stress conditions may have contributed to both age clusters in a unique post-deglaciation evolutionary frame, with different outcomes (slow deformations or catastrophic collapse) depending on site-specific topographic, lithological and structural features. In this view, particular assumptions on paleo-hydrologic conditions may not be required to explain Mid-Holocene rockslide clustering, although wet periods would have positively contributed to rockslide differentiation.

7.4 LONG-TERM EVOLUTION OF SLOPE HYDROLOGY AND FLUID PRESSURE DISTRIBUTIONS

The main issue we faced in the development of DaDyn-RS fluid pressure component regarded the almost completely unknown hydrological and hydrogeological regime at the end of Last Glacial Maximum and during paraglacial and postglacial stages. To overcome this limitation and considering that, detailed reconstruction of paleo-hydrogeological conditions is nearly impossible, we decided to use simplified boundary conditions, thus avoiding strong assumptions on imposed hydraulic loads, fluxes and recharge rates. The fluid pressure application is self-regulated by the stress and strain states of each element and by the parameter *w*, which expresses the filling degree of permeable clusters and simulates equilibrium conditions between recharge and discharge, resulting in a constant and partial filling, depending on cluster size and depth. With this respect, constant value of *w* might represent an oversimplification in respect to real conditions, as we basically assume constant water circulation throughout around 20 kyr. On the other hand, no evidence exists permitting to assess or quantify the magnitude of hydrological variations, which are subject to regional trends but also to site-specific effects. Nevertheless, assuming that no fluid pressure acts on the slope before the start of simulation, DaDyn-RS provide a minimum esteem of the fluid pressure occurrence within the slope, as open fractures and slope aquifers could either exist before the LGM deglaciation. Furthermore, DaDyn-RS ability to predict the effects of water-slope interactions on long- and short-term displacements is expected to sharply decrease after rockslide differentiation, due to different concerns. First, with the progressive evolution of slope, shear bands occur within the modelled slope, along which, due to the high damage and strain cumulated, a soil-like material is expected. Our brittle creep model is not conceived to deal with such material rheology, regarding hydraulic but also mechanical behavior, thus resulting in biased representation. Indeed, for specific rock types, material weakening/softening could evolve through strongly different mechanisms (e.g. chemical effects in clay-rich rocks). Moreover, the static formulation we introduced do not account for recharge and flow processes within the slope, which becomes fundamental in mature rockslides, where aquifers layers become interconnected.

The model results discussed in the previous chapters suggest a key role of water in the long-term slope evolution, confirming the realistic response of our simplified damage-based fluid occurrence model despite the lack of knowledge regarding hydrological conditions at the end of LGM and during Lateglacial. Nevertheless, with this simplified implementation (Cf. subsection 3.6), which represents a novel approach to this aspect of long-term numerical modelling, we gained insights on hydro-mechanical controls on instability development. The static formulation we adopted allows including the fluid pressure effect and relating brittle failure processes with rock mass hydraulic properties on the large scale and under changing stress conditions typical of rock slopes. Model results show the ability of DaDyn-RS to capture the changes in slope hydrology related to progressive damage and strain accumulation. These changes are mainly driven by the evolution of localized shear zones, with a progressive transition from permeable localized damage zones to sealing cataclastic layers, able to support perched water table within rockslide bodies. This model behavior can be regarded as another emergent behavior of DaDyn-RS, which is able to track complex macro-scale phenomena starting from rather simple yet physically based element scale rules.

When fluid pressure is imposed to occur within the evolving slope (Fig 5.28), the progressive aquifers nucleation develops from slope dilatant portions, since interconnection at slope-scale is reached. Fluid pressure distribution during the slope lifecycle is strongly influenced by damage and strain patterns, as testified by the progressive aquifer sealing consistent with the development of contracting basal shear band. As a result, perched aquifers are built within unstable rock mass, particularly in less damaged portions, as further increase in damage and strain results in highly-deformed rock mass and unfavorable conditions for fluid pressure occurrence. This may also suggest that, in the long-term, mechanisms of brittle damage development set the framework for local-scale effects of hydro-mechanical coupling. The latter become increasingly important in mature stages of rockslide evolution, where hydro-mechanical coupling involve the response of well-developed shear bands made of soil-like material underlying weakened and permeable rockslide masses (Crosta et al., 2014; Agliardi and Crosta, 2014; Preisig et al., 2015). Damage mechanisms constrained the final (post-glacial) distribution of permeable element clusters, and thus of fluid pressure occurrence in the slopes, suggesting a minor sensitivity to fluid pressure in the DSGSD rather than in the rockslide. Indeed, in Cresta di Saline slope a progressive reduction of fluid pressure occurrence within DSGSD body is observed through time, due to the diffused patterns of damage and strain and resulting, for the present state, in a shallow aquifer located in the upper slope portion, while in the lower part the slope is substantially dry (Fig. 6.26). In the Spriana slope, final fluid pressure distribution resulted into a fully interconnected (i.e. one cluster) perched aquifer in the lower rockslide portion, with less connected perched aquifers upslope the rockslide base and at slope crest (Fig. 5.24), which supports the present-day mechanical sensitivity of the rockslide to external hydrological inputs, especially in the lower part of the slope.

We further evaluated the effects of damage-based fluid distribution by running additional model in dry conditions (Cf. subsection 5.6.3). This results in sharply different geometry and kinematics of predicted rock slope failure, involving the entire slope with deep rotational kinematics and excess of damage localization with respect to kinematics and damage patterns usually observed in real rock slopes (Figs. 5.33 and 5.34). Simulations with and without fluid pressure are also characterized by a sharply different lifetime. The “dry” model takes an excessively long time (>100 kyr) to collect observed cumulated displacement, which is reached with a smoother transition to tertiary creep phase (Fig. 5.35). Timing is strongly affected by fluid pressure occurrence, as higher amounts of water within slope corresponds to shorter lifetime, sometimes occurring with abrupt transition to acceleration phase resulting in slope collapse (Figs. 4.10, 5.37 and 5.38). Accounting for fluid occurrence also affect the long-term creep curve of the slope, represented in terms of cumulative number of ruptures versus time. In fact, the models with fluid pressure result in a fluctuating trend, derived from the superposition of long-term hydromechanical pulses (associate to major damage evolution stages) over a long-term material creep component. In any case, these trends are not reproduced by the dry simulation, which show decelerating creep behavior upon deglaciation followed by a long-term steady state creep, which develops over a much longer time interval than in wet conditions.

7.5 THE INFLUENCE OF DEGLACIATION

Time-dependent deglaciation was introduced within the model to simulate the influence of glacial to postglacial transition on stress state, mechanical properties and stability of large rock slopes. Based on the simulations we conducted, deglaciation has a strong influence on both slope tensional and mechanical states. Indeed, progressive debuttressing triggers a sequence of hydromechanical processes within the entire slope, which in the long-term deeply condition its evolution (Cf. subsections 7.4 and 7.5). Neglecting the effects of deglaciation, fluid pressure occurrence is strongly limited, as rock mass results in lower density of closer fractures, without the development of an interconnected slope aquifer. This, in the long-term perspective, bring to nearly dry conditions, as demonstrated through the simulation with fluid pressure but no deglaciation conducted for the Spriana slope (subsection 5.6.4 and fig.5.36). As the effect of deglaciation involve chain-reaction processes that protract for the entire slope lifecycle, paraglacial readjustment can be ideally extended up to slope collapse or reaching of ultimate stability conditions, although, during the long-term evolution and particularly after slope differentiation, it assumes a secondary influence with respect to climatic and hydrologic forcing, which strongly condition stress regime through hydromechanical coupling.

Glacier buttress has also a fundamental role in delaying long-term progressive failure, as deglaciation coincides with stress mobilization, time-to-failure shortening and triggering of progressive failure events, which timing strongly depends on slope angle and mechanical properties of the rock mass constituting the slope. We observed that for steep and weak slopes, glacier removal can trigger slope instability during or just after deglaciation, with potential for short-time catastrophic evolution. On the other hand, for stronger and/or less inclined slopes deglaciation can be followed by slow creep deformation, delayed catastrophic failure or regressive phases with ultimate slope stability condition.

Glacier occurrence is simulated assuming transient "hydrostatic" ice load on FE mesh nodes at slope surface through the approach described in subsection 3.5. The maximum height of ice surface during LGM was reconstructed in literature by the analysis of geomorphological, geochronological and paleoclimatic evidence (Florineth, 1998; Bini et al., 2009; Wirsig et al., 2016) but, despite the multidisciplinary approach, uncertainties associated with precise assessment of ice surface climax are up to tens of meters (Florineth and Schlucter, 1998). Deglaciation duration and onset represent other sources of uncertainties, as the most accurate information comes from absolute chronological constraints obtained through surface exposure dating on formerly glaciated bedrock portion. However, the typical uncertainty associated with the application of this technique usually ranges around 1-2 Kyr (Ivy-Ochs et al., 2006; Ivy-Ochs et al., 2008; Ivy-Ochs et al., 2015; Wirsig et al., 2016 and references therein). Glacier load in DaDyn-RS is calculated assuming a constant ice density of 916 kg/m^3, which represent the upper boundary among typical values for temperate glaciers, where a progressive density increase is encountered with depth (Cuffey and Paterson, 2010). This assumption introduces overestimation of glacier weight, especially in slope upper portion, where ice is lighter, even if the error introduced is negligible in comparison with the aforementioned uncertainties. Glacier mass balance depends on the interaction between flow regime, climatic forcing and morphology of accumulation basin, thus resulting in complex behavior as a response to disequilibrium conditions (Cuffey and Paterson, 2010 and references therein). As a consequence of post-LGM deglaciation, DaDyn-RS simulates a linear trend of ice thickness reduction, which represent a strong simplification with respect to the complex conditions observed in glaciated and formerly glaciated basins. However, since no geochronological or paleo-glaciological data were available for our case studies neither accurate reconstruction of glacier dynamics cover the purpose of this thesis, we decided to consider linear trend as a reasonable approximation for slope stability modelling.

7.6 CONCLUDING REMARKS

We implemented a damage-based, time-dependent modelling approach to reproduce the entire life-cycle of large alpine rock slopes, starting from the Last Glacial Maximum to the present time. The application of continuum damage mechanics to real, large rock slope instabilities provided the opportunity to evaluate the performance, advantages and limitations of the adopted modelling approach and investigate the mechanisms and timing of long-term evolution of alpine slopes from deglaciation to modern conditions.

Main large features of both rockslides and DSGSDs (e.g. geometry, damage and strain localization, perched aquifers) were reproduced by DaDyn-RS without the need of strong assumptions on shear band geometry, rock mass strength and hydraulic boundary conditions. The model is able to reproduce both localized and diffuse patterns of brittle damage, depending on the combination of material properties and water pressure distribution. Damage-dependent fluid pressure distributions strongly affect the geometry and the timing of instability, resulting in the commonly observed interplay between creep (up to tertiary regime) and hydrological forcing, which becomes more and more important throughout slope evolution. The localization of damage is a pre-requisite for water circulation in hydraulically interconnected slope sector, further damage and, subsequently, strain localization and slope deformation. The model simulates a contractive behavior of shear zone as an emerging property, and allows accounting for the hydraulic barrier effect leading to the development of perched aquifers and the "differentiation" of rockslides characterized by a high sensitivity to external triggers.

The model is able to link slopes evidence and processes, commonly observed in real case studies, in the framework of a continuous mechanical history, unfolding since the post-LGM. Models suggest that stress perturbations and modifications induced by deglaciation last for the entire slope lifecycle, suggesting a novel interpretation of paraglacial readjustment in large alpine rock slopes, much longer then postulated by most authors (Cruden and Hu, 1994; Le Roux et al., 2009; Ballantyne et al., 2014). The continuous development of large slope instabilities is conditioned by discrete steps of enhanced evolution, related to damage and subsequent development of strain localization and slope differentiation. Since these stages affect different slope sectors in different time, with delays up to some thousands of years, this outcome may be fundamental when performing and interpreting absolute dating on real rock slopes. Nevertheless, the simulated timing of evolutionary steps is coherent with geomorphological, geomechanical, hydrological and geochronological constraints available for real case studies, suggesting a major role of long-term progressive damage in the development of Holocene rockslides and present-day geohazards.

8 REFERENCES

- Agliardi F. (1999). Deformazioni gravitative profonde e grandi frane, rilevamento geologico e geomorfologico, studio geomeccanico e modellazione numerica del versante destro della media Valfurva (SO). MsC thesis.
- Agliardi, F., Crosta, G., & Zanchi, A. (2001). Structural constraints on deep-seated slope deformation kinematics. Engineering Geology, 59(1), 83-102.
- Agliardi, F., Zanchi, A., & Crosta, G. B. (2009). Tectonic vs. gravitational morphostructures in the central Eastern Alps (Italy): constraints on the recent evolution of the mountain range. Tectonophysics, 474(1), 250-270.
- Agliardi, F., Crosta, G. B., & Frattini, P. (2012). 18 Slow rock-slope deformation. Landslides: Types, Mechanisms and Modeling, 207.
- Agliardi, F., Crosta, G. B., Frattini, P., & Malusà, M. G. (2013a). Giant non-catastrophic landslides and the long-term exhumation of the European Alps. Earth and Planetary Science Letters, 365, 263-274.
- Agliardi, F., Crosta, G. B., Meloni, F., Valle, C., & Rivolta, C. (2013b). Structurally-controlled instability, damage and slope failure in a porphyry rock mass. Tectonophysics, 605, 34-47.
- Agliardi, F., Crosta, G. B., Sosio, R., Rivolta, C., & Mannucci, G. (2013c). In situ and remote long term real-time monitoring of a large alpine rock slide. In Landslide Science and Practice (pp. 415-421). Springer Berlin Heidelberg.
- Agliardi, F., & Crosta, G. B. (2014a). Long-and short-term controls on the Spriana rockslide (Central Alps, Italy). In Landslide Science for a Safer Geoenvironment (pp. 243-249). Springer International Publishing.
- Agliardi, F., Zanchetta, S., & Crosta, G. B. (2014b). Fabric controls on the brittle failure of folded gneiss and schist. Tectonophysics, 637, 150-162.
- Agliardi, F., Sapigni, M., & Crosta, G. B. (2016). Rock Mass Characterization by High-Resolution Sonic and GSI Borehole Logging. Rock Mechanics and Rock Engineering, 49(11), 4303-4318.
- Alzo’ubi, A. K., Martin, C. D., & Cruden, D. M. (2010). Influence of tensile strength on toppling failure in centrifuge tests. International Journal of Rock Mechanics and Mining Sciences, 47(6), 974-982.

- Ambrosi, C., & Crosta, G. B. (2006). Large sackung along major tectonic features in the Central Italian Alps. Engineering Geology, 83(1), 183-200.
- Ambrosi, C., & Crosta, G. B. (2011). Valley shape influence on deformation mechanisms of rock slopes. Geological Society, London, Special Publications, 351(1), 215-233.
- Amitrano, D., Grasso, J. R., & Hantz, D. (1999). From diffuse to localised damage through elastic interaction. Geophysical Research Letters, 26(14), 2109-2112.
- Amitrano, D., & Helmstetter, A. (2006). Brittle creep, damage, and time to failure in rocks. Journal of Geophysical Research: Solid Earth, 111(B11).
- Angeli, M. G., Gasparetto, P., Menotti, R. M., Pasuto, A., & Silvano, S. (1996). A visco-plastic model for slope analysis applied to a mudslide in Cortina d'Ampezzo, Italy. Quarterly Journal of Engineering Geology and Hydrogeology, 29(3), 233-240.
- Atkinson, B. K., & Meredith, P. G. (1981). Stress corrosion cracking of quartz: a note on the influence of chemical environment. Tectonophysics, 77(1), T1-T11.
- Atkinson, B. K. (1984). Subcritical crack growth in geological materials. Journal of Geophysical Research: Solid Earth, 89(B6), 4077-4114.
- Atkinson, B. K., & Meredith, P. G. (1987). The theory of subcritical crack growth with applications to minerals and rocks. Fracture mechanics of rock, 2, 111-166.
- Augustinus, P. C. (1995). Glacial valley cross-profile development: the influence of in situ rock stress and rock mass strength, with examples from the Southern Alps, New Zealand. Geomorphology, 14(2), 87-97.
- Bäckblom, G., & Martin, C. D. (1999). Recent experiments in hard rocks to study the excavation response: implications for the performance of a nuclear waste geological repository. Tunnelling and underground space technology, 14(3), 377-394.
- Ballantyne, C. K. (2002). Paraglacial geomorphology. Quaternary Science Reviews, 21(18), 1935-2017.
- Ballantyne, C. K., Sandeman, G. F., Stone, J. O., & Wilson, P. (2014). Rock-slope failure following Late Pleistocene deglaciation on tectonically stable mountainous terrain. Quaternary Science Reviews, 86, 144-157.
- Barbarano, M., Agliardi, F., Crosta, G. B., & Zanchi, A. (2015). Inherited and Active Tectonic Controls on the Piz Dora DSGSD (Val Müstair, Switzerland). In Engineering Geology for Society and Territory-Volume 2 (pp. 605-608). Springer International Publishing.
- Barton, N., Lien, R., & Lunde, J. (1974). Engineering classification of rock masses for the design of tunnel support. Rock mechanics, 6(4), 189-236.
- Barton, N. (1976). The shear strength of rock and rock joints. In International Journal of rock mechanics and mining sciences & Geomechanics abstracts (Vol. 13, No. 9, pp. 255-279). Pergamon.
- Barton, N., & Choubey, V. (1977). The shear strength of rock joints in theory and practice. Rock mechanics, 10(1-2), 1-54.
- Baud, P., & Meredith, P. G. (1997). Damage accumulation during triaxial creep of Darley Dale sandstone from pore volumometry and acoustic emission. International Journal of Rock Mechanics and Mining Sciences, 34(3), 24-e1.

- Belloni, L., & Gandolfo, M. (1997). La frana di Spriana. Geologia tecnica ed ambientale, 3, 7-36.
- Benko, B., & Stead, D. (1998). The Frank slide: a reexamination of the failure mechanism. Canadian Geotechnical Journal, 35(2), 299-311.
- Bense, V. F., Gleeson, T., Loveless, S. E., Bour, O., & Scibek, J. (2013). Fault zone hydrogeology. Earth-Science Reviews, 127, 171-192.
- Bieniawski, Z. T. (1974). Geomechanics classification of rock masses and its application in tunnelin. In Proc. 3rd Int. Cong. Rock Mech. (Vol. 2, pp. 27-32).
- Bieniawski, Z. T., & Van Heerden, W. L. (1975, April). The significance of in situ tests on large rock specimens. In International Journal of Rock Mechanics and Mining Sciences & Geomechanics Abstracts (Vol. 12, No. 4, pp. 101-113). Pergamon.
- Bieniawski, Z. T. (Ed.). (1976). Exploration for rock engineering: proceedings of the Symposium on Exploration for Rock Engineering, Johannesburg, 1-5 November 1976 (Vol. 1). AA Balkema.
- Bieniawski, Z. T. (1989). Engineering rock mass classifications: a complete manual for engineers and geologists in mining, civil, and petroleum engineering. John Wiley & Sons.
- Bigi, G., Cosentino, D., Parotto, M., Sartori, R., Scandone, P., 1990. Structural model of Italy 1:500,000. PFG-CNR, Quad. Ric. Sci, 114.
- Bini, A., Buoncristiani, J. F., Coutterand, S., Ellwanger, D., Felber, M., Florineth, D., ... & Schoeneich, P. (2009). La Svizzera durante l'ultimo massimo glaciale (LGM), 1: 500'000.
- Biot, M. A. (1941). General theory of three-dimensional consolidation. Journal of applied physics, 12(2), 155-164.
- Bjerrum, L. (1967). Progressive failure in slopes of overconsolidated plastic clay and clay shales. Journal of Soil Mechanics & Foundations Div.
- Bonardi, L., Rovelli, E., Scotti, R., Toffaletti, A., Urso, M., & Villa, F. (2012). I ghiacciai della Lombardia, evoluzione ed attualità. Milan, Hoepli.
- Bonzanigo, L. (1999). Lo slittamento di Campo Vallemaggia (Doctoral dissertation, Diss. Naturwissenschaften ETH Zürich, Nr. 13387, 2000).
- Bonzanigo, L., Eberhardt, E., & Loew, S. (2007). Long-term investigation of a deep-seated creeping landslide in crystalline rock. Part I. Geological and hydromechanical factors controlling the Campo Vallemaggia landslide. Canadian Geotechnical Journal, 44(10), 1157-1180.
- Boulton, G. S., & de Marsily, G. (1997). Hydrogeological aspects of glaciation. Glaciation and Hydrogeology, SKI Rep. 97, 13, 33-44.
- Boulton, G.S. 2005. Britain's glacial past and its climatic future. Teaching Earth Sciences, 30(2), 14-18.
- Bovis, M. J. (1982). Uphill-facing (antislope) scarps in the Coast Mountains, southwest British Columbia. Geological Society of America Bulletin, 93(8), 804-812.
- Brace, W. F. (1984). Permeability of crystalline rocks: New in situ measurements. Journal of Geophysical Research: Solid Earth, 89(B6), 4327-4330.

- Brantut, N., Baud, P., Heap, M. J., & Meredith, P. G. (2012). Micromechanics of brittle creep in rocks. Journal of Geophysical Research: Solid Earth, 117(B8).
- Brantut, N., Heap, M. J., Meredith, P. G., & Baud, P. (2013). Time-dependent cracking and brittle creep in crustal rocks: A review. Journal of Structural Geology, 52, 17-43.
- Brideau, M. A., Yan, M., & Stead, D. (2009). The role of tectonic damage and brittle rock fracture in the development of large rock slope failures. Geomorphology, 103(1), 30-49.
- Broadbent, C. D., & Zavodni, Z. M. (1982). Influence of rock structure on stability. Stability in Surface Mining, 3.
- Brocklehurst, S. H., & Whipple, K. X. (2004). Hypsometry of glaciated landscapes. Earth Surface Processes and Landforms, 29(7), 907-926.
- Brook, M. S., Kirkbride, M. P., & Brock, B. (2004). Rock strength and development of glacial valley morphology in the Scottish Highlands and northwest Iceland. Geografiska Annaler: Series A, Physical Geography, 86(3), 225-234.
- Brückl, E., & Parotidis, M. (2005). Prediction of slope instabilities due to deep-seated gravitational creep. Natural Hazards and Earth System Science, 5(2), 155-172.
- Cai, M., Kaiser, P. K., Uno, H., Tasaka, Y., & Minami, M. (2004). Estimation of rock mass deformation modulus and strength of jointed hard rock masses using the GSI system. International Journal of Rock Mechanics and Mining Sciences, 41(1), 3-19.
- Caine, N. (1971). A conceptual model for Alpine slope process study. Arctic and Alpine Research, 319-329.
- Caine, J. S., Evans, J. P., & Forster, C. B. (1996). Fault zone architecture and permeability structure. Geology, 24(11), 1025-1028.
- Cancelli, A. (1980). The monitoring of the Spriana landslide. In Proceedings international symposium on land-slides (pp. 7-11).
- Cappa, F., Guglielmi, Y., Soukatchoff, V. M., Mudry, J., Bertrand, C., & Charmoille, A. (2004). Hydromechanical modeling of a large moving rock slope inferred from slope levelling coupled to spring long-term hydrochemical monitoring: example of the La Clapiere landslide (Southern Alps, France). Journal of Hydrology, 291(1), 67-90.
- Carlsson, A., Olsson, T., 1982. High rock stresses as a consequence of glaciation. Nature 298, 739–742.
- Casagli, N., Catani, F., Del Ventisette, C., & Luzi, G. (2010). Monitoring, prediction, and early warning using ground-based radar interferometry. Landslides, 7(3), 291-301.
- Chaboche, J. L. (1977). Viscoplastic constitutive equations for the description of cyclic and anisotropic behaviour of metals. Bull. Acad. Polon. Sci., Ser. Sci. Tech., 25(1), 33-42.
- Chester, F. M., & Logan, J. M. (1986). Implications for mechanical properties of brittle faults from observations of the Punchbowl fault zone, California. Pure and Applied Geophysics, 124(1-2), 79-106.
- Chigira, M. (1992). Long-term gravitational deformation of rocks by mass rock creep. Engineering Geology, 32(3), 157-184.
- Chigira, M., & Kiho, K. (1994). Deep-seated rockslide-avalanches preceded by mass rock creep of sedimentary rocks in the Akaishi Mountains, central Japan. Engineering Geology, 38(3-4), 221-230.

- Church, M., & Ryder, J. M. (1972). Paraglacial sedimentation: a consideration of fluvial processes conditioned by glaciation. Geological Society of America Bulletin, 83(10), 3059-3072.
- Clague, J. J., & Stead, D. (2012). Landslides: types, mechanisms and modeling. Cambridge University Press.
- Clark, P. U., Dyke, A. S., Shakun, J. D., Carlson, A. E., Clark, J., Wohlfarth, B., ... & McCabe, A. M. (2009). The last glacial maximum. science, 325(5941), 710-714.
- Corominas, J., Moya, J., Ledesma, A., Lloret, A., & Gili, J. A. (2005). Prediction of ground displacements and velocities from groundwater level changes at the Vallcebre landslide (Eastern Pyrenees, Spain). Landslides, 2(2), 83-96.
- Cossart, E., Braucher, R., Fort, M., Bourlès, D. L., & Carcaillet, J. (2008). Slope instability in relation to glacial debuttressing in alpine areas (Upper Durance catchment, southeastern France): evidence from field data and 10 Be cosmic ray exposure ages. Geomorphology, 95(1), 3-26.
- Crosta, G. (1996). Landslide, spreading, deep seated gravitational deformation: analysis, examples, problems and proposals. Geografia fisica e dinamica quaternaria, 19(2), 297-313.
- Crosta, G., & Zanchi, A. (2000). Landslides in Research, Theory and Practice.
- Crosta, G. B., & Agliardi, F. (2003). Failure forecast for large rock slides by surface displacement measurements. Canadian Geotechnical Journal, 40(1), 176-191.
- Crosta, G. B., Agliardi, F., Frattini, P., & Sosoi, R. (2012). SafeLand Deliverable 1.1: landslide triggering mechanisms in Europe—overview and state of the art. Identification of mechanisms and triggers.
- Crosta, G. B., Frattini, P., & Agliardi, F. (2013). Deep seated gravitational slope deformations in the European Alps. Tectonophysics, 605, 13-33.
- Crosta, G. B., Di Prisco, C., Frattini, P., Frigerio, G., Castellanza, R., & Agliardi, F. (2014a). Chasing a complete understanding of the triggering mechanisms of a large rapidly evolving rockslide. Landslides, 11(5), 747-764.
- Crosta, G. B., Frattini, P., Pena Reyes, F., & Riva, F. (2014b). Groundwater flow and hydrochemistry in mountain areas affected by DSGSDs. In EGU General Assembly Conference Abstracts (Vol. 16, p. 15947).
- Cruden, D. M., & Hu, X. Q. (1993). Exhaustion and steady state models for predicting landslide hazards in the Canadian Rocky Mountains. Geomorphology, 8(4), 279-285.
- Cruden, D. M., & Hu, X. Q. (1994). Topples on underdip slopes in the Highwood Pass, Alberta, Canada. Quarterly Journal of Engineering Geology and Hydrogeology, 27(1), 57-68.
- Cuffey, K. M., & Paterson, W. S. B. (2010). The physics of glaciers. Academic Press.
- Cundall, P. A. (1971). The measurement and analysis of accelerations in rock slopes (Doctoral dissertation, University of London).
- Das, S., & Scholz, C. H. (1981). Theory of time-dependent rupture in the earth. Journal of Geophysical Research: Solid Earth, 86(B7), 6039-6051.
- De Caro, M., Crosta, G. B., Castellanza, R., Agliardi, F., Volpi, G., & Alberti, S. (2016). 2D De Caro M., Crosta G.B. , Castellanza R., Agliardi F., Volpi G. and Alberti S.(2016). 2D Modelling of rockslide displacements by non-linear time dependent relationships.

In Landslides and Engineered Slopes. Experience, Theory and Practice. Proceedings of the 12th International Symposium on Landslides (Napoli, Italy, 12-19 June 2016),

- Deere, D. U., Hendron, A. J., Patton, F. D., & Cording, E. J. (1966, January). Design of surface and near-surface construction in rock. In The 8th US Symposium on Rock Mechanics (USRMS). American Rock Mechanics Association.
- Del Ventisette, C., Casagli, N., Fortuny-Guasch, J., & Tarchi, D. (2012). Ruinon landslide (Valfurva, Italy) activity in relation to rainfall by means of GBInSAR monitoring. Landslides, 9(4), 497-509.
- Deline, P., Gruber, S., Delaloye, R., Fischer, L., Geertsema, M., Giardino, M., ... & McColl, S. (2015). Ice loss and slope stability in high-mountain regions. Snow and Ice-Related Hazards, Risks, and Disasters, edited by: Haeberli, W., Whiteman, C., and Shroder, JF, Elsevier Science, Saint Louis, 521-561.
- Dershowitz, W. S., & Herda, H. H. (1992, January). Interpretation of fracture spacing and intensity. In The 33th US Symposium on Rock Mechanics (USRMS). American Rock Mechanics Association.
- Dershowitz, W. (2015, April). Characterizing Fractured Rock with Geo-structural and Micro-structural Models. In EGU General Assembly Conference Abstracts (Vol. 17, p. 7667).
- Dortch, J. M., Owen, L. A., Haneberg, W. C., Caffee, M. W., Dietsch, C., & Kamp, U. (2009). Nature and timing of large landslides in the Himalaya and Transhimalaya of northern India. Quaternary Science Reviews, 28(11), 1037-1054.
- Eberhardt, E., Stead, D., & Stimpson, B. (1999). Quantifying progressive pre-peak brittle fracture damage in rock during uniaxial compression. International Journal of Rock Mechanics and Mining Sciences, 36(3), 361-380.
- Eberhardt, E., Stead, D., & Coggan, J. S. (2004). Numerical analysis of initiation and progressive failure in natural rock slopes—the 1991 Randa rockslide. International Journal of Rock Mechanics and Mining Sciences, 41(1), 69-87.
- Eberhardt, E., Bonzanigo, L., & Loew, S. (2007). Long-term investigation of a deep-seated creeping landslide in crystalline rock. Part II. Mitigation measures and numerical modelling of deep drainage at Campo Vallemaggia. Canadian Geotechnical Journal, 44(10), 1181-1199.
- Edelbro, C. (2004). Evaluation of rock mass strength criteria. Luleå University of Technology. Licentiate thesis, 72, 153.
- Ehlers, J., & Gibbard, P. L. (2004). Quaternary glaciations-extent and chronology: part I: Europe (Vol. 2). Elsevier.
- Einstein, H. H., Veneziano, D., Baecher, G. B., & O'reilly, K. J. (1983). The effect of discontinuity persistence on rock slope stability. In International journal of rock mechanics and mining sciences & geomechanics abstracts (Vol. 20, No. 5, pp. 227-236). Pergamon.
- Elmo, D. (2006). Evaluation of a hybrid FEM/DEM approach for determination of rock mass strength using a combination of discontinuity mapping and fracture mechanics modelling, with particular emphasis on modelling of jointed pillars (Doctoral dissertation, University of Exeter).

- Elmo, D., & Stead, D. (2010). An integrated numerical modelling–discrete fracture network approach applied to the characterisation of rock mass strength of naturally fractured pillars. Rock Mechanics and Rock Engineering, 43(1), 3-19.
- Elmo, D., Rogers, S., Stead, D., & Eberhardt, E. (2014). Discrete Fracture Network approach to characterise rock mass fragmentation and implications for geomechanical upscaling. Mining Technology, 123(3), 149-161.
- Elmo, D., Stead, D., & Rogers, S. (2015). Guidelines for the Quantitative Description of Discontinuities for use in Discrete Fracture Network Modelling. In 13th ISRM International Congress of Rock Mechanics. International Society for Rock Mechanics.
- Emery, J. J., & Finn, W. L. (1972). Creep Problems in Soil Mechanics. In Applications of solid mechanics: proceedings of the symposium held at the University of Waterloo, June 26 and 27, 1972 (No. 7, p. 417). Solid Mechanics Division, University of Waterloo].
- Evans, S. G., & Clague, J. J. (1994). Recent climatic change and catastrophic geomorphic processes in mountain environments. Geomorphology, 10(1), 107-128.
- Fairhurst, C. (1964). On the validity of the 'Brazilian'test for brittle materials. In International Journal of Rock Mechanics and Mining Sciences & Geomechanics Abstracts (Vol. 1, No. 4, pp. 535-546). Pergamon.
- Faoro, I., Vinciguerra, S., Marone, C., Elsworth, D., & Schubnel, A. (2013). Linking permeability to crack density evolution in thermally stressed rocks under cyclic loading. Geophysical Research Letters, 40(11), 2590-2595.
- Feng, X. T., Chen, S., & Zhou, H. (2004). Real-time computerized tomography (CT) experiments on sandstone damage evolution during triaxial compression with chemical corrosion. International Journal of Rock Mechanics and Mining Sciences, 41(2), 181-192.
- Fischer, L., Amann, F., Moore, J. R., & Huggel, C. (2010). Assessment of periglacial slope stability for the 1988 Tschierva rock avalanche (Piz Morteratsch, Switzerland). Engineering Geology, 116(1), 32-43.
- Florineth, D., & Schlüchter, C. (1998). Reconstructing the Last Glacial Maximum (LGM) ice surface geometry and flowlines in the Central Swiss Alps. Eclogae Geologicae Helvetiae, 91, 391-407.
- Flowers, G. E., & Clarke, G. K. (2002). A multicomponent coupled model of glacier hydrology 1. Theory and synthetic examples. Journal of Geophysical Research: Solid Earth, 107(B11).
- Forcella, F., & Orombelli, G. (1984). Holocene slope deformations in Valfurva, central Alps, Italy. Geografia Fisica e Dinamica Quaternaria, 7, 41-48.
- Fortin, J., Stanchits, S., Vinciguerra, S., & Guéguen, Y. (2011). Influence of thermal and mechanical cracks on permeability and elastic wave velocities in a basalt from Mt. Etna volcano subjected to elevated pressure. Tectonophysics, 503(1), 60-74.
- Frayssines, M., & Hantz, D. (2006). Failure mechanisms and triggering factors in calcareous cliffs of the Subalpine Ranges (French Alps). Engineering Geology, 86(4), 256-270.
- Frei, C., Schär, C. (1998). A precipitation climatology of the Alps from high-resolution rain-gauge observations. International Journal of Climatology 18, 873–900.

- Fukuzono, T. (1985, August). A new method for predicting the failure time of a slope. In Proceedings of the 4th International Conference and Field Workshop in Landslides, Tokyo (pp. 145-150).
- Gercek, H. (2007). Poisson's ratio values for rocks. International Journal of Rock Mechanics and Mining Sciences, 44(1), 1-13.
- Gianotti, F., Forno, M. G., Ajassa, R., Cámara, F., Costa, E., Ferrando, S., ... & Perotti, L. (2015). The Ivrea Morainic Amphitheatre as a well preserved record of the Quaternary climate variability (PROGEO-Piemonte Project, NW Italy). In Engineering Geology for Society and Territory-Volume 8 (pp. 235-238). Springer International Publishing.
- Gischig, V., Amann, F., Moore, J. R., Loew, S., Eisenbeiss, H., & Stempfhuber, W. (2011). Composite rock slope kinematics at the current Randa instability, Switzerland, based on remote sensing and numerical modeling. Engineering Geology, 118(1), 37-53.
- Gischig, V. S., Eberhardt, E., Moore, J. R., & Hungr, O. (2015). On the seismic response of deep-seated rock slope instabilities—Insights from numerical modeling. Engineering Geology, 193, 1-18.
- Gleeson, T., & Manning, A. H. (2008). Regional groundwater flow in mountainous terrain: Three-dimensional simulations of topographic and hydrogeologic controls. Water Resources Research, 44(10).
- Griffith, A. A. (1921). The phenomena of rupture and flow in solids. Philosophical transactions of the royal society of london. Series A, containing papers of a mathematical or physical character, 221, 163-198.
- Griffith, A.A. 1924. Theory of rupture. Proc. First Int. Cong. Applied Mech (eds Bienzo and Burgers). 55-63. Delft: Technische Boekhandel and Drukkerij.
- Gruber, S., Peter, M., Hoelzle, M., Woodhatch, I., & Haeberli, W. (2003, July). Surface temperatures in steep alpine rock faces—a strategy for regional-scale measurement and modelling. In Proceedings of the 8th International Conference on Permafrost (Vol. 1, pp. 325-330).
- Hydrogeochemistry: an investigation tool to evaluate infiltration into large moving rock masses (case study of La Clapière and Séchilienne alpine landslides). Bulletin of Engineering Geology and the Environment, 61(4), 311-324.
- Guglielmi, Y., & Cappa, F. (2010). Regional-scale relief evolution and large landslides: Insights from geomechanical analyses in the Tinée Valley (southern French Alps). Geomorphology, 117(1), 121-129.
- Guglielmi, Y., Vengeon, J., Bertrand, C., Mudry, J., Follacci, J., & Giraud, A. (2002).
- Hamdi, P. (2015). Characterization of Brittle Damage in Rock from the Micro to Macro Scale (Doctoral dissertation, Science: Department of Earth Sciences).
- Hansmann, J., Loew, S., & Evans, K. F. (2012). Reversible rock-slope deformations caused by cyclic water-table fluctuations in mountain slopes of the Central Alps, Switzerland. Hydrogeology Journal, 20(1), 73-91.
- Harbor, J. M. (1992). Numerical modeling of the development of U-shaped valleys by glacial erosion. Geological Society of America Bulletin, 104(10), 1364-1375.
- Harbor, J. M. (1995). Development of glacial-valley cross sections under conditions of spatially variable resistance to erosion. Geomorphology, 14(2), 99-107.

- Havaej, M., Wolter, A., & Stead, D. (2015). The possible role of brittle rock fracture in the 1963 Vajont Slide, Italy. International Journal of Rock Mechanics and Mining Sciences, 78, 319-330.
- Heap, M. J., Baud, P., & Meredith, P. G. (2009). Influence of temperature on brittle creep in sandstones. Geophysical Research Letters, 36(19).
- Heap, M. J., Faulkner, D. R., Meredith, P. G., & Vinciguerra, S. (2010). Elastic moduli evolution and accompanying stress changes with increasing crack damage: implications for stress changes around fault zones and volcanoes during deformation. Geophysical Journal International, 183(1), 225-236.
- Heiland, J. (2003). Laboratory testing of coupled hydro-mechanical processes during rock deformation. Hydrogeology Journal, 11(1), 122-141.
- Helmstetter, A., & Garambois, S. (2010). Seismic monitoring of Séchilienne rockslide (French Alps): Analysis of seismic signals and their correlation with rainfalls. Journal of Geophysical Research: Earth Surface, 115(F3).
- Herman, F., Beaud, F., Champagnac, J. D., Lemieux, J. M., & Sternai, P. (2011). Glacial hydrology and erosion patterns: a mechanism for carving glacial valleys. Earth and Planetary Science Letters, 310(3), 498-508.
- Hinderer, M., Kastowski, M., Kamelger, A., Bartolini, C., & Schlunegger, F. (2013). River loads and modern denudation of the Alps—a review. Earth-Science Reviews, 118, 11-44.
- Hippolyte, J. C., Bourlès, D., Braucher, R., Carcaillet, J., Léanni, L., Arnold, M., & Aumaitre, G. (2009). Cosmogenic 10 Be dating of a sackung and its faulted rock glaciers, in the Alps of Savoy (France). Geomorphology, 108(3), 312-320.
- Hippolyte, J. C., Bourlès, D., Léanni, L., Braucher, R., Chauvet, F., & Lebatard, A. E. (2012). 10 Be ages reveal> 12ka of gravitational movement in a major sackung of the Western Alps (France). Geomorphology, 171, 139-153.
- Hoek, E., & Brown, E. T. (1980). Underground excavations in rock (No. Monograph).
- Hoek, E., & Bray, J. D. (1981). Rock slope engineering. CRC Press.
- Hoek, E. (1988). The Hoek-Brown failure criterion-a 1988 update. In Proc. 15th Canadian Rock Mech. Symp (pp. 31-38). Toronto, Dept. Civil Engineering, University of Toronto.
- Hoek, E., & Brown, E. T. (1997). Practical estimates of rock mass strength. International Journal of Rock Mechanics and Mining Sciences, 34(8), 1165-1186.
- Hoek, E., Carranza-Torres, C., & Corkum, B. (2002). Hoek-Brown failure criterion-2002 edition. Proceedings of NARMS-Tac, 1, 267-273.
- Hoek, E., & Diederichs, M. S. (2006). Empirical estimation of rock mass modulus. International Journal of Rock Mechanics and Mining Sciences, 43(2), 203-215.
- Hoek, E. (2007). Rock mass properties. Practical rock engineering. Available at www. rocscience. com/learning/hoek-s-corner.
- Hormes, A., Ivy-Ochs, S., Kubik, P. W., Ferreli, L., & Michetti, A. M. (2008). 10 Be exposure ages of a rock avalanche and a late glacial moraine in Alta Valtellina, Italian Alps. Quaternary International, 190(1), 136-145.
- Hudson, J. A., & Harrison, J. P. (1997). Engineering rock mechanics, vol. I.

- Infrastrutture Lombarde (2013). Progetto preliminare: intervento di protezione e valorizzazione dei territori dell'Alta Valtellina attraverso la difesa degli abitati e delle infrastrutture della frana del Ruinon di Valfurva (SO). Technical report
- ISMES (1990). Indagini nel corpo frana, Indagini geognostiche. Progetto 8.2. Ministero dei lavori pubblici, provveditorato alle Opere Pubbliche per la Lombardia, Milano
- Itasca, P. F. C., & PFC3D, R. (2003). 3.0, Itasca Consulting Group. Inc., Minneapolis.
- Itasca, U. D. E. C. (2012). 5.0. Manual. Itasca Consulting Group Inc., Minneapolis (United States).
- Ivy-Ochs, S., Kerschner, H., Kubik, P. W., & Schlüchter, C. (2006). Glacier response in the European Alps to Heinrich Event 1 cooling: the Gschnitz stadial. Journal of Quaternary Science, 21(2), 115-130.
- Ivy-Ochs, S., Kerschner, H., Reuther, A., Preusser, F., Heine, K., Maisch, M. & Schlüchter, C. (2008). Chronology of the last glacial cycle in the European Alps. Journal of Quaternary Science, 23(6-7), 559-573.
- Ivy-Ochs, S. (2015). Glacier variations in the European Alps at the end of the last glaciation. Cuadernos de investigación geográfica, 41(41), 295-315.
- Jing, L., & Hudson, J. A. (2002). Numerical methods in rock mechanics. International Journal of Rock Mechanics and Mining Sciences, 39(4), 409-427.
- Jing, L. (2003). A review of techniques, advances and outstanding issues in numerical modelling for rock mechanics and rock engineering. International Journal of Rock Mechanics and Mining Sciences, 40(3), 283-353.
- Kachanov, L. M. (1958). Time of the rupture process under creep conditions. Isv. Akad. Nauk. SSR. Otd Tekh. Nauk, 8, 26-31.
- Kachanov L., A microcrack model of rock inelasticity: Part I. frictional sliding on microcracks. J . Mech. Mater., 1(1), 19-29 (1982) .
- Kachanov, M. (1986). On crack-microcrack interactions. International Journal of Fracture, 30(4), R65-R72.
- Katz, O., & Reches, Z. E. (2004). Microfracturing, damage, and failure of brittle granites. Journal of Geophysical Research: Solid Earth, 109(B1).
- Kelly, M. A., Buoncristiani, J. F., & Schlüchter, C. (2004). A reconstruction of the last glacial maximum (LGM) ice-surface geometry in the western Swiss Alps and contiguous Alpine regions in Italy and France. Eclogae Geologicae Helvetiae, 97(1), 57-75.
- Kemeny, J. M., & Cook, N. G. (1987, January). Determination of rock fracture parameters from crack models for failure in compression. In The 28th US Symposium on Rock Mechanics (USRMS). American Rock Mechanics Association.
- Kirchner, J. W., Finkel, R. C., Riebe, C. S., Granger, D. E., Clayton, J. L., King, J. G., & Megahan, W. F. (2001). Mountain erosion over 10 yr, 10 ky, and 10 my time scales. Geology, 29(7), 591-594.
- Korup, O., Clague, J. J., Hermanns, R. L., Hewitt, K., Strom, A. L., & Weidinger, J. T. (2007). Giant landslides, topography, and erosion. Earth and Planetary Science Letters, 261(3), 578-589.
- Krajcinovic, D., & Fonseka, G. U. (1981). The continuous damage theory of brittle materials, part 1: general theory. Journal of applied Mechanics, 48(4), 809-815.

- Kranz, R. L. (1980). The effects of confining pressure and stress difference on static fatigue of granite. Journal of Geophysical Research: Solid Earth, 85(B4), 1854-1866.
- Kranz, R. L., Harris, W. J., & Carter, N. L. (1982). Static fatigue of granite at 200 C. Geophysical Research Letters, 9(1), 1-4.
- Kranz, R. L. (1983). Microcracks in rocks: a review. Tectonophysics, 100(1-3), 449-480.
- Krauland, N., Söder, P., & Agmalm, G. (1989). Determination of rock mass strength by rock mass classification—Some experiences and questions from Boliden mines. In International Journal of Rock Mechanics and Mining Sciences & Geomechanics Abstracts (Vol. 26, No. 1, pp. 115-123). Pergamon.
- Lacroix, P., & Amitrano, D. (2013). Long-term dynamics of rockslides and damage propagation inferred from mechanical modeling. Journal of Geophysical Research: Earth Surface, 118(4), 2292-2307.
- Le Roux, O., Schwartz, S., Gamond, J. F., Jongmans, D., Bourles, D., Braucher, R., ... & Leanni, L. (2009). CRE dating on the head scarp of a major landslide (Séchilienne, French Alps), age constraints on Holocene kinematics. Earth and Planetary Science Letters, 280(1), 236-245.
- Lebrouc, V., Schwartz, S., Baillet, L., Jongmans, D., & Gamond, J. F. (2013). Modeling permafrost extension in a rock slope since the Last Glacial Maximum: Application to the large Séchilienne landslide (French Alps). Geomorphology, 198, 189-200.
- Leith, K. J. (2012). Stress development and geomechanical controls on the geomorphic evolution of alpine valleys (Doctoral dissertation, Diss., Eidgenössische Technische Hochschule ETH Zürich, Nr. 20566, 2012).
- Leith, K., Moore, J. R., Amann, F., & Loew, S. (2014). Subglacial extensional fracture development and implications for Alpine Valley evolution. Journal of Geophysical Research: Earth Surface, 119(1), 62-81.
- Lemaitre J., Dufailly J. , Modelization and identification of endommagement plasticity of material. In: Proceedings of the 3rd French Congress of Mechanics, Grenoble, France, pp.17-21 (1977).
- Lemaitre, J. (1984). How to use damage mechanics. Nuclear engineering and design, 80(2), 233-245.
- Lemaitre, J., & CHABOCHE, J. L. (1978). Aspect phénoménologique de la rupture par endommagement. J Méc Appl, 2(3).
- Li, Y., Liu, G., & Cui, Z. (2001). Glacial valley cross-profile morphology, Tian Shan Mountains, China. Geomorphology, 38(1), 153-166.
- Lockner, D. (1993, December). The role of acoustic emission in the study of rock fracture. In International Journal of Rock Mechanics and Mining Sciences & Geomechanics Abstracts (Vol. 30, No. 7, pp. 883-899). Pergamon.
- Loew S, Strauhal T (2013) Pore pressure distributions in brittle transla- tional rockslides. In: Int. Conf. on Vajont 1963–2013. Proceedings: thoughts and analyses after 50 years since the catastrophic landslide. Ital. J. Eng. Geol. Environ., Book Series 6, pp 181–191.
- Lorig, L. J., Cundall, P. A., Damjanac, B., & Emam, S. (2010). A three-dimensional model for rock slopes based on micromechanics. In 44th US Rock Mechanics

Symposium and 5th US-Canada Rock Mechanics Symposium. American Rock Mechanics Association.

- Magny, M., Combourieu-Nebout, N., De Beaulieu, J. L., Bout-Roumazeilles, V., Colombaroli, D., Desprat, S. & Sadori, L. (2013). North-south palaeohydrological contrasts in the central Mediterranean during the Holocene: tentative synthesis and working hypotheses. Climate of the Past Discussions, 9, 1901-1967.
- Makurat, A., Barton, N., Vik, G., & Tunbridge, L. (1990). Site Characterization and Validation: Coupled Stress-flow Testing of Mineralized Joints of 200 Mm and 1400 Mm Length in the Laboratory and in Situ: Stage III. SKB.
- Marinos, P., & Hoek, E. (2000, November). GSI: a geologically friendly tool for rock mass strength estimation. In ISRM International Symposium. International Society for Rock Mechanics.
- Marinos, V., Marinos, P., & Hoek, E. (2005). The geological strength index: applications and limitations. Bulletin of Engineering Geology and the Environment, 64(1), 55-65.
- Martin, C. D., & Chandler, N. A. (1994). The progressive fracture of Lac du Bonnet granite. In International Journal of Rock Mechanics and Mining Sciences & Geomechanics Abstracts (Vol. 31, No. 6, pp. 643-659). Pergamon.
- Martin, E., Leguillon, D., & Lacroix, C. (2001). A revisited criterion for crack deflection at an interface in a brittle bimaterial. Composites science and technology, 61(12), 1671-1679.
- Masuda, K. (2001). Effects of water on rock strength in a brittle regime. Journal of Structural Geology, 23(11), 1653-1657.
- MATLAB and Statistics Toolbox Release 2012b, The MathWorks, Inc., Natick, Massachusetts, United States.
- Matsuoka, N. (1994). Continuous recording of frost heave and creep on a Japanese alpine slope. Arctic and alpine research, 245-254.
- McCalpin, J. P., & Irvine, J. R. (1995). Sackungen at the Aspen Highlands ski area, Pitkin County, Colorado. Environmental & Engineering Geoscience, 1(3), 277-290.
- McCalpin, J. P. (1999). Criteria for determining the seismic significance of sackungen and other scarplike landforms in mountainous regions. Techniques for Identifying Faults and Determining their Origins. US Nuclear Regulatory Commission, Washington, 2-55.
- McColl, S. T. (2012). Paraglacial rock-slope stability. Geomorphology, 153, 1-16.
- McSaveney, M. J. (1993). Rock avalanches of 2 May and 6 September 1992, Mount Fletcher, New Zealand. Landslide News, 7, 2-4.
- Meigs, A., & Sauber, J. (2000). Southern Alaska as an example of the long-term consequences of mountain building under the influence of glaciers. Quaternary Science Reviews, 19(14), 1543-1562.
- Meinzer, O. E. (1928). Compressibility and elasticity of artesian aquifers. Economic Geology, 23(3), 263-291.
- Miller, D. J., & Dunne, T. (1996). Topographic perturbations of regional stresses and consequent bedrock fracturing. Journal of Geophysical Research: Solid Earth, 101(B11), 25523-25536.

- Mitchell, T. M., and D. R. Faulkner (2008), Experimental measurements of permeability evolution during triaxial compression of initially intact crystalline rocks and implications for fluid flow in fault zones, J. Geophys. Res.-Solid Earth, 113, B11412,
- Molnar, P. (2004). Interactions among topographically induced elastic stress, static fatigue, and valley incision. Journal of Geophysical Research: Earth Surface, 109(F2).
- Mortara, G., & Sorzana, P. F. (1984). Slope instability in high mountain environments: deep seated gravitational deformation in western Alps Italy. In Proc. CNR-PAN Meeting on Progress in Mass Movements and sediment transport study.
- Murakami, S., & Ohno, N. (1981). A continuum theory of creep and creep damage. In Creep in structures (pp. 422-444). Springer Berlin Heidelberg.
- Murakami, S. (2012). Continuum damage mechanics: a continuum mechanics approach to the analysis of damage and fracture (Vol. 185). Springer Science & Business Media.
- Murrell, S. A. F. (1958). The strength of coal under triaxial compression. Mechanical properties of non-metallic brittle materials, 123-153.
- Neuzil, C. E. (2003). Hydromechanical coupling in geologic processes. Hydrogeology Journal, 11(1), 41-83.
- Nichol, S. L., Hungr, O., & Evans, S. G. (2002). Large-scale brittle and ductile toppling of rock slopes. Canadian Geotechnical Journal, 39(4), 773-788.
- Nur, A., & Byerlee, J. (1971). An exact effective stress law for elastic deformation of rock with fluids. Journal of Geophysical Research, 76(26), 6414-6419.
- Oda, M., Konishi, J., & Nemat-Nasser, S. (1982). Experimental micromechanical evaluation of strength of granular materials: effects of particle rolling. Mechanics of materials, 1(4), 269-283.
- Olsson, R., & Barton, N. (2001). An improved model for hydromechanical coupling during shearing of rock joints. International Journal of Rock Mechanics and Mining Sciences, 38(3), 317-329.
- Olvmo, M., & Johansson, M. (2002). The significance of rock structure, lithology and pre-glacial deep weathering for the shape of intermediate-scale glacial erosional landforms. Earth Surface Processes and Landforms, 27(3), 251-268.
- Oppikofer, T., Jaboyedoff, M., & Keusen, H. R. (2008). Collapse at the eastern Eiger flank in the Swiss Alps. Nature Geoscience, 1(8), 531-535.
- Orowan, E. (1941). Origin and spacing of slip bands. Nature, 147, 452-453.
- Palmstrom, A. (1985). Application of the volumetric joint count as a measure of rock mass jointing. In Int. Symp. on Fundamentals of Rock Joints, Björkliden (pp. 103-110).
- Palmström, A., & Singh, R. (2001). The deformation modulus of rock masses—comparisons between in situ tests and indirect estimates. Tunnelling and Underground Space Technology, 16(2), 115-131.
- Palmstrom, A. (2005). Measurements of and correlations between block size and rock quality designation (RQD). Tunnelling and Underground Space Technology, 20(4), 362-377.
- Paterson, M. S., & Wong, T. F. (2005). Experimental rock deformation-the brittle field. Springer Science & Business Media.

- Patton, F. D. (1966). Multiple modes of shear failure in rock. In 1st ISRM Congress. International Society for Rock Mechanics.
- Pedrazzini, A. (2012). Characterization of gravitational rock slope deformations at different spatial scales based on field, remote sensing and numerical approaches.
- Pelfini, M., Leonelli, G., Trombino, L., Zerboni, A., Bollati, I., Merlini, A., ... & Diolaiuti, G. (2014). New data on glacier fluctuations during the climatic transition at~ 4,000 cal. year BP from a buried log in the Forni Glacier forefield (Italian Alps). Rendiconti Lincei, 25(4), 427-437.
- Pollard, D. D., and A. Aydin (1988), Progress in understanding jointing over the past century, Geol. Soc. Am. Bull., 100, 1181–1204
- Prager, C., Zangerl, C., Patzelt, G., & Brandner, R. (2008). Age distribution of fossil landslides in the Tyrol (Austria) and its surrounding areas. Natural Hazards and Earth System Sciences, 8, 377-407.
- Preisig, G., Eberhardt, E., Smithyman, M., Preh, A., & Bonzanigo, L. (2015). Hydromechanical rock mass fatigue in deep-seated landslides accompanying seasonal variations in pore pressures. Rock Mechanics and Rock Engineering, 1-19.
- Preusser, F., Graf, H. R., Keller, O., Krayss, E., & Schlüchter, C. (2011). Quaternary glaciation history of northern Switzerland. E&G Quaternary Science Journal, 60, 282-305.
- Rabotnov, Y. N. (1968). Creep rapture. In Proc. XII IUTAM Congress (p. 137). Springer.
- Rabotnov, I. N. (1969). Creep problems in structural members (Vol. 7). North-Holland Pub. Co..
- Radbruch-Hall, D. H. (1978). Gravitational creep of rock masses on slopes. Rockslides and avalanches, 1, 607-657.
- Ray, S. K., Sarkar, M., & Singh, T. N. (1999). Effect of cyclic loading and strain rate on the mechanical behaviour of sandstone. International Journal of Rock Mechanics and Mining Sciences, 36(4), 543-549.
- Ritter, W. (1879). Die statik der tunnelgewölbe. J. Springer.
- Riva F., Agliardi, F., Amitrano, D., Crosta, G.B. (2016). Damage-based long term modelling of a large alpine rock slope. In Landslides and Engineered Slopes. Experience, Theory and Practice. Proceedings of the 12th International Symposium on Landslides (Napoli, Italy, 12-19 June 2016),
- Riva, F., Agliardi, F., Crosta, G. B., & Zanchi, A. (2016). Numerical investigation of the long-term influence of seismicity on the development of the Piz Dora DSGSD (Val Mustair, Switzerland). Rendiconti online Societa Geologica Italiana, 41, 187-190.
- Romana, M. (1995). The geomechanical classification SMR for slope correction. In 8th ISRM Congress. International Society for Rock Mechanics.
- Rose, N. D., & Hungr, O. (2007). Forecasting potential rock slope failure in open pit mines using the inverse-velocity method. International Journal of Rock Mechanics and Mining Sciences, 44(2), 308-320.
- Rutqvist, J. (1995). Determination of hydraulic normal stiffness of fractures in hard rock from well testing. In International journal of rock mechanics and mining sciences & geomechanics abstracts (Vol. 32, No. 5, pp. 513-523). Pergamon.

- Rutqvist, J., & Stephansson, O. (2003). The role of hydromechanical coupling in fractured rock engineering. Hydrogeology Journal, 11(1), 7-40.
- Rutqvist, J. (2015). Fractured rock stress-permeability relationships from in situ data and effects of temperature and chemical-mechanical couplings. Geofluids, 15(1-2), 48-66.
- Saito, M., & Uezawa, H. (1961, July). Failure of soil due to creep. In Fifth International Conference of Soil Mechanics and Foundation Engineering (pp. 315-318).
- Savage, W. Z., & Swolfs, H. S. (1986). Tectonic and gravitational stress in long symmetric ridges and valleys. Journal of Geophysical Research: Solid Earth, 91(B3), 3677-3685.
- Schmid, S.M., Fogenschuh, B., Kissling, E., Schuster, R. (2004). Tectonic map and overall architecture of the Alpine orogen. Eclogae Geologicae Helvetiae 97, 93–117.
- Scholz, C., Molnar, P., & Johnson, T. (1972). Detailed studies of frictional sliding of granite and implications for the earthquake mechanism. Journal of geophysical research, 77(32), 6392-6406.
- Schulze, O., Popp, T., & Kern, H. (2001). Development of damage and permeability in deforming rock salt. Engineering Geology, 61(2), 163-180.
- Secondi, M. M., Crosta, G., di Prisco, C., Frigerio, G., Frattini, P., & Agliardi, F. (2013). Landslide motion forecasting by a dynamic visco-plastic model. In Landslide science and practice (pp. 151-159). Springer Berlin Heidelberg.
- Sheorey, P. R., Biswas, A., & Choubey, V. D. (1989). An empirical failure criterion for rocks and jointed rock masses. Engineering Geology, 26(2), 141-159.
- Sigurdsson, O., & Williams Jr, R. S. (1991). Rockslides on the Terminus of" Jökulsárgilsjökull", Southern Iceland. Geografiska Annaler. Series A. Physical Geography, 129-140.
- Stanchitz et al. (2006)
- Stead, D., & Eberhardt, E. (2013). Understanding the mechanics of large landslides. Ital. J. Eng. Geol. Environ. Book Ser, 6, 85-112.
- Sternai, P., Herman, F., Fox, M. R., & Castelltort, S. (2011). Hypsometric analysis to identify spatially variable glacial erosion. Journal of Geophysical Research: Earth Surface, 116(F3).
- Strauhal, T., Loew, S., Holzmann, M., & Zangerl, C. (2016). Detailed hydrogeological analysis of a deep-seated rockslide at the Gepatsch reservoir (Klasgarten, Austria). Hydrogeology Journal, 24(2), 349-371.
- Sturzenegger, M., Keegan, T., Wen, A., Willms, D., Stead, D., & Edwards, T. (2015). LiDAR and Discrete Fracture Network Modeling for Rockslide Characterization and Analysis. In Engineering Geology for Society and Territory-Volume 6 (pp. 223-227). Springer International Publishing.
- Tapponnier, P., & Brace, W. F. (1976, April). Development of stress-induced microcracks in Westerly granite. In International Journal of Rock Mechanics and Mining Sciences & Geomechanics Abstracts (Vol. 13, No. 4, pp. 103-112). Pergamon.
- Terzaghi, K. V. (1923). Die berechnung der durchlassigkeitsziffer des tones aus dem verlauf der hydrodynamischen spannungserscheinungen. Sitzungsberichte der

Akademie der Wissenschaften in Wien, Mathematisch-Naturwissenschaftliche Klasse, Abteilung IIa, 132, 125-138.

- Terzaghi, K. (1946). Rock defects and loads on tunnel supports.
- Terzaghi, K. (1962). Stability of steep slopes on hard unweathered rock. Geotechnique, 12(4), 251-270.
- Thorpe, R. K., Hanson, M. E., Anderson, G. D., & Shaffer, R. J. (1982). Step cracks: Theory, experiment, and field observation. In The 23rd US Symposium on Rock Mechanics (USRMS). American Rock Mechanics Association.
- Tomkin, J. H., & Braun, J. (2002). The influence of alpine glaciation on the relief of tectonically active mountain belts. American Journal of Science, 302(3), 169-190.
- Trigila, A., Iadanza, C., & Spizzichino, D. (2010). Quality assessment of the Italian Landslide Inventory using GIS processing. Landslides, 7(4), 455-470.
- Trommsdorff, V., Montrasio, A., Hermann, J., Muntener, O., Spillmann, P., & Giere, R. (2007). The geological map of Valmalenco.
- Tsang, C. F. (1991). Coupled hydromechanical-thermochemical processes in rock fractures. Reviews of geophysics, 29(4), 537-551.
- Turcotte, D. L., Newman, W. I., & Shcherbakov, R. (2003). Micro and macroscopic models of rock fracture. Geophysical Journal International, 152(3), 718-728.
- Vallet, A., Charlier, J. B., Fabbri, O., Bertrand, C., Carry, N., & Mudry, J. (2015). Functioning and precipitation-displacement modelling of rainfall-induced deep-seated landslides subject to creep deformation. Landslides, 1-18.
- Varnes, D. J., Radbruch-Hall, D. H., & Savage, W. Z. (1989). Topographic and structural conditions in areas of gravitational spreading of ridges in the western United States. United States Geological Survey, Professional Paper;(USA), 1496.
- Violay, M., Gibert, B., Mainprice, D., & Burg, J. P. (2015). Brittle versus ductile deformation as the main control of the deep fluid circulation in oceanic crust. Geophysical Research Letters, 42(8), 2767-2773.
- Vogler, M., Loew, S., Glueer, F., & Grämiger, L. (2016, April). Glacial Debutressing and Displacement History of the Driest Rockslide (Central Alps, Switzerland). In EGU General Assembly Conference Abstracts (Vol. 18, p. 8040).
- Voight, B., & Pariseau, W. G. (1978). Rockslides and avalanches: an introduction. Rockslides and avalanches, 1.
- Voight, B. (1988). A method for prediction of volcanic eruptions. Nature, 332(6160), 125-130.
- Voight, B. (1989). A relation to describe rate-dependent material failure. Science, 243(4888), 200-203.
- Vyazmensky, A., Stead, D., Elmo, D., & Moss, A. (2010). Numerical analysis of block caving-induced instability in large open pit slopes: a finite element/discrete element approach. Rock mechanics and rock engineering, 43(1), 21-39.
- Welch, L. A., & Allen, D. M. (2012). Consistency of groundwater flow patterns in mountainous topography: Implications for valley bottom water replenishment and for defining groundwater flow boundaries. Water Resources Research, 48(5).

- Welch, L. A., & Allen, D. M. (2014). Hydraulic conductivity characteristics in mountains and implications for conceptualizing bedrock groundwater flow. Hydrogeology Journal, 22(5), 1003-1026.
- Wiederhorn, S. M., & Bolz, L. H. (1970). Stress corrosion and static fatigue of glass. Journal of the American Ceramic Society, 53(10), 543-548.
- Wienhöfer, J., Lindenmaier, F., Ihringer, J., Zehe, E., & Marks, D. (2009). Characterization of soil hydraulic properties on a creeping alpine slope. In Proceedings of the International Commission on Snow and Ice Hydrology" Hydrology in Mountain Regions: Observations, Processes and Dynamics", Perugia, Italy, July 2007. (pp. 3-10). IAHS Press.
- Wirsig, C., Zasadni, J., Christl, M., Akçar, N., & Ivy-Ochs, S. (2016). Dating the onset of LGM ice surface lowering in the High Alps. Quaternary Science Reviews, 143, 37-50.
- Witherspoon, P. A., Wang, J. S., Iwai, K., & Gale, J. E. (1980). Validity of cubic law for fluid flow in a deformable rock fracture. Water resources research, 16(6), 1016-1024.
- Witherspoon, P. A. (2000). The Stripa project. International Journal of Rock Mechanics and Mining Sciences, 37(1), 385-396.
- Xu, T., Tang, C. A., Zhao, J., Li, L., & Heap, M. J. (2012). Modelling the time-dependent rheological behaviour of heterogeneous brittle rocks. Geophysical Journal International, 189(3), 1781-1796.
- Yuan, S. C., & Harrison, J. P. (2006). A review of the state of the art in modelling progressive mechanical breakdown and associated fluid flow in intact heterogeneous rocks. International Journal of Rock Mechanics and Mining Sciences, 43(7), 1001-1022.
- Zangerl, C., Eberhardt, E., & Perzlmaier, S. (2010). Kinematic behaviour and velocity characteristics of a complex deep-seated crystalline rockslide system in relation to its interaction with a dam reservoir. Engineering Geology, 112(1), 53-67.
- Zerathe, S., Lebourg, T., Braucher, R., & Bourlès, D. (2014). Mid-Holocene cluster of large-scale landslides revealed in the Southwestern Alps by 36 Cl dating. Insight on an Alpine-scale landslide activity. Quaternary Science Reviews, 90, 106-127.
- Zhang W.H., Numerical Analysis of Continuum Damage Mechanics. Ph.D.Thesis, University of New South Wales, Australia (1992).
- Zischinsky, U. (1969). Über sackungen. Rock Mechanics, 1(1), 30-52.
- Zoback, M. D., & Byerlee, J. D. (1975). The effect of cyclic differential stress on dilatancy in Westerly granite under uniaxial and triaxial conditions. Journal of Geophysical Research, 80(11), 1526-1530.

9 ANNEX 1: PARAMETRIC ANALYSIS

In this Annex, extended results of parametric analysis on DaDyn-RS are reported. First, main parameters imposed for each model are summarized in Table A1, then graphical outputs comprehending number of damage events, strain on xy plane and summit vertical displacement versus time are listed for each simulation.

Model number	Slope angle	b	D	Cluster filling	Slope failure time
33-1-1	33	15	0.1	0.25	
33-1-2	33	15	0.1	0.5	
33-1-3	33	15	0.1	0.75	
33-1-4	33	15	0.1	0	
33-1-5	33	30	0.1	0.25	
33-1-6	33	30	0.1	0.5	
33-1-7	33	30	0.1	0.75	
33-1-8	33	30	0.1	0	
33-1-9	33	45	0.1	0.25	
33-1-10	33	45	0.1	0.5	
33-1-11	33	45	0.1	0.75	
33-1-12	33	45	0.1	0	
33-5-1	33	15	0.05	0.25	
33-5-2	33	15	0.05	0.5	
33-5-3	33	15	0.05	0.75	
33-5-4	33	15	0.05	0	
33-5-5	33	30	0.05	0.25	
33-5-6	33	30	0.05	0.5	
33-5-7	33	30	0.05	0.75	
33-5-8	33	30	0.05	0	

Model number	**Slope angle**	**b**	**D**	**Cluster filling**	**Slope failure time**
33-5-9	33	45	0.05	0.25	
33-5-10	33	45	0.05	0.5	
33-5-11	33	45	0.05	0.75	
33-5-12	33	45	0.05	0	
33-15-1	33	15	0.15	0.25	
33-15-2	33	15	0.15	0.5	
33-15-3	33	15	0.15	0.75	
33-15-4	33	15	0.15	0	
33-15-5	33	30	0.15	0.25	
33-15-6	33	30	0.15	0.5	
33-15-7	33	30	0.15	0.75	
33-15-8	33	30	0.15	0	
33-15-9	33	45	0.15	0.25	
33-15-10	33	45	0.15	0.5	
33-15-11	33	45	0.15	0.75	
33-15-12	33	45	0.15	0	
45-1-1	45	15	0.1	0.25	
45-1-2	45	15	0.1	0.5	
45-1-3	45	15	0.1	0.75	
45-1-4	45	15	0.1	0	
45-1-5	45	30	0.1	0.25	
45-1-6	45	30	0.1	0.5	
45-1-7	45	30	0.1	0.75	
45-1-8	45	30	0.1	0	
45-1-9	45	45	0.1	0.25	
45-1-10	45	45	0.1	0.5	
45-1-11	45	45	0.1	0.75	
45-1-12	45	45	0.1	0	
45-5-1	45	15	0.05	0.25	
45-5-2	45	15	0.05	0.5	
45-5-3	45	15	0.05	0.75	
45-5-4	45	15	0.05	0	
45-5-5	45	30	0.05	0.25	
45-5-6	45	30	0.05	0.5	
45-5-7	45	30	0.05	0.75	
45-5-8	45	30	0.05	0	
45-5-9	45	45	0.05	0.25	

Model number	Slope angle	b	D	Cluster filling	Slope failure time
45-5-10	45	45	0.05	0.5	
45-5-11	45	45	0.05	0.75	
45-5-12	45	45	0.05	0	
45-15-1	45	15	0.15	0.25	
45-15-2	45	15	0.15	0.5	
45-15-3	45	15	0.15	0.75	
45-15-4	45	15	0.15	0	
45-15-5	45	30	0.15	0.25	
45-15-6	45	30	0.15	0.5	
45-15-7	45	30	0.15	0.75	
45-15-8	45	30	0.15	0	
45-15-9	45	45	0.15	0.25	
45-15-10	45	45	0.15	0.5	
45-15-11	45	45	0.15	0.75	
45-15-12	45	45	0.15	0	

Table A1: Input parameters imposed for each simulation.

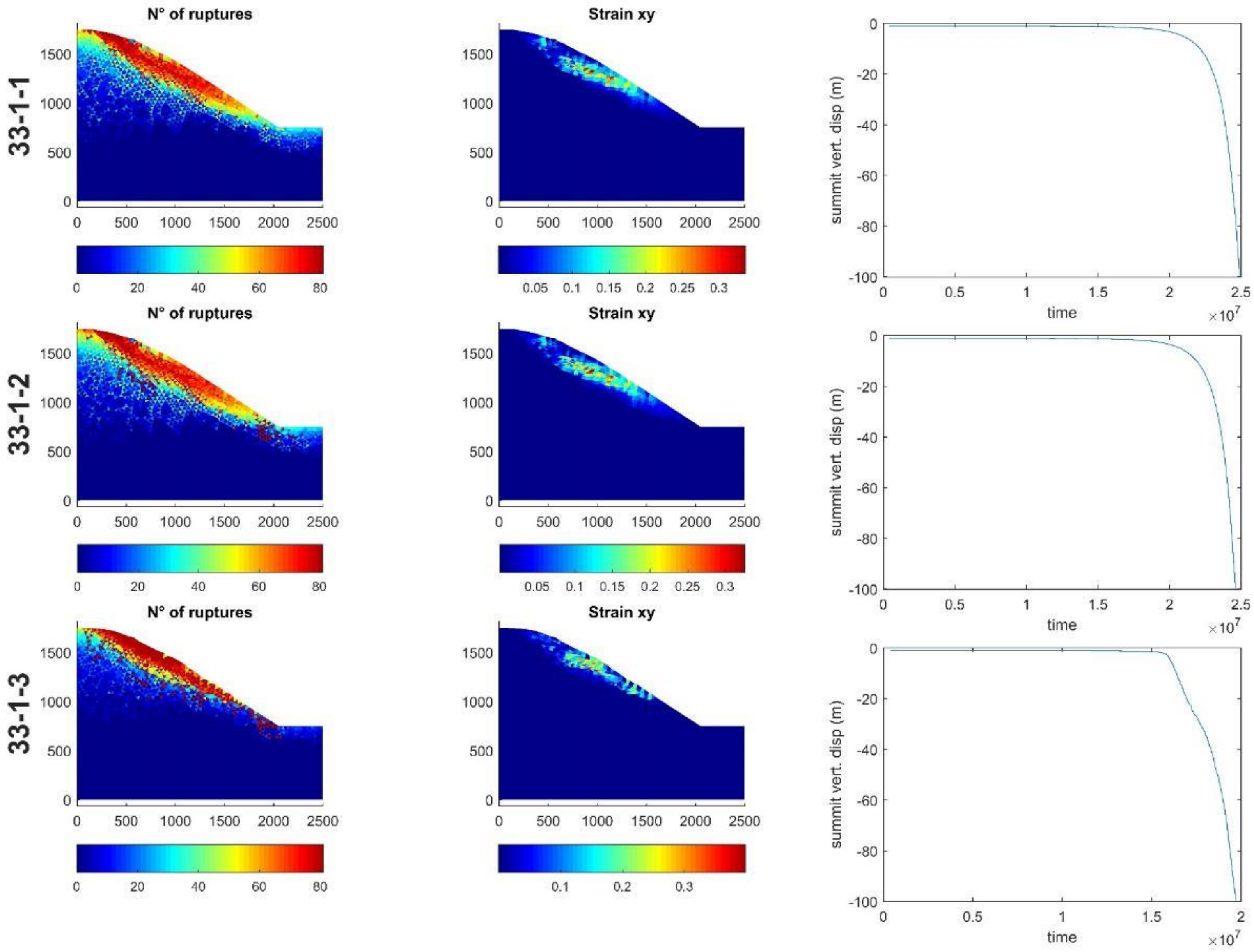
33-1-1
33-1-2
33-1-3
N° of ruptures
Strain xy
0
500
1000
1500
2000
2500
0
20
40
60
80
0.05
0.1
0.15
0.2
0.25
0.3
summit vert. disp (m)
0
-20
-40
-60
-80
-100
0.5
1
1.5
2
2.5
time
$\times 10^7$

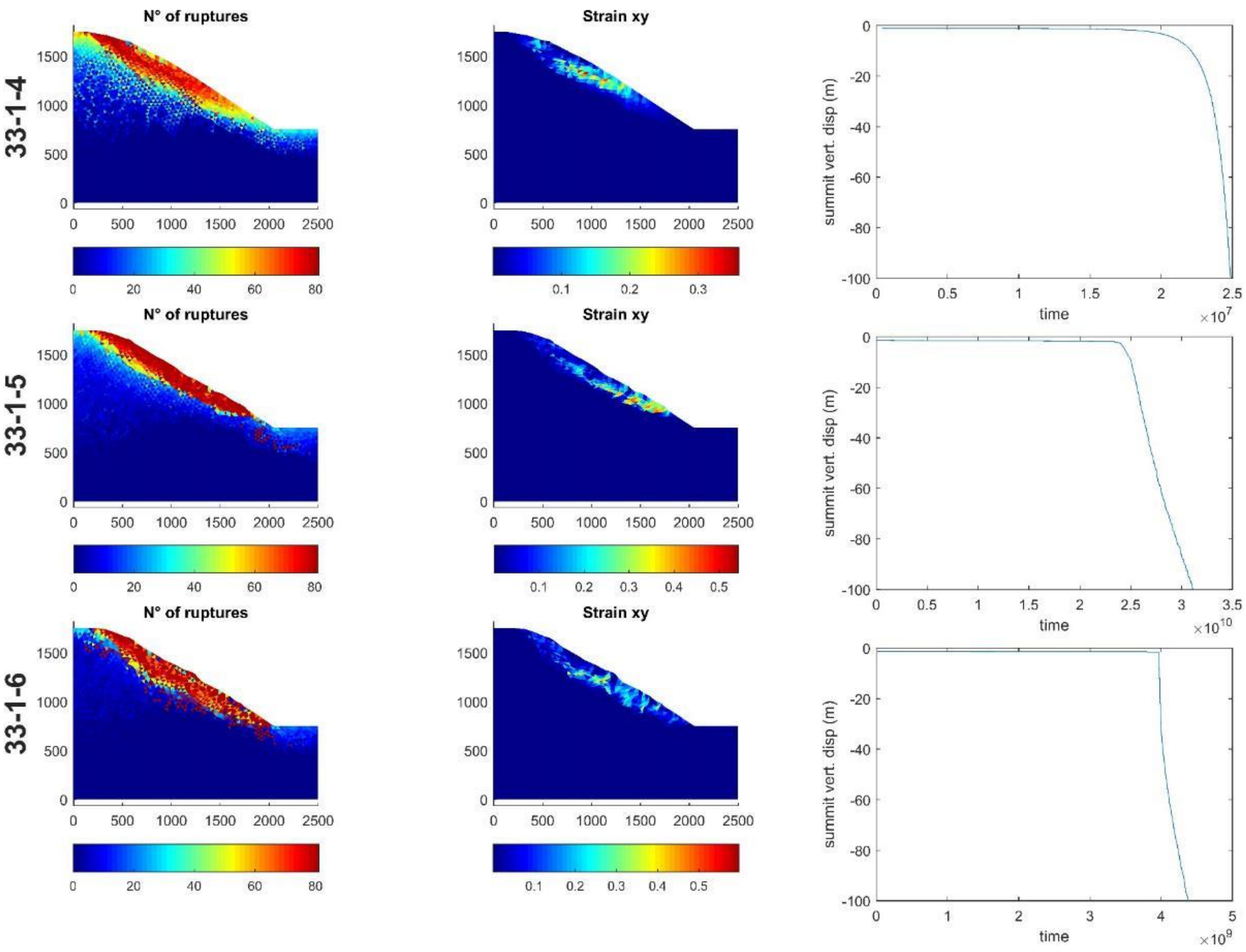
33-1-4
33-1-5
33-1-6
N° of ruptures
Strain xy
summit vert. disp (m)
time
0
500
1000
1500
2000
2500
0
20
40
60
80
0.1
0.2
0.3
0.4
0.5
-100
-80
-60
-40
-20
×10^7
×10^10
×10^9

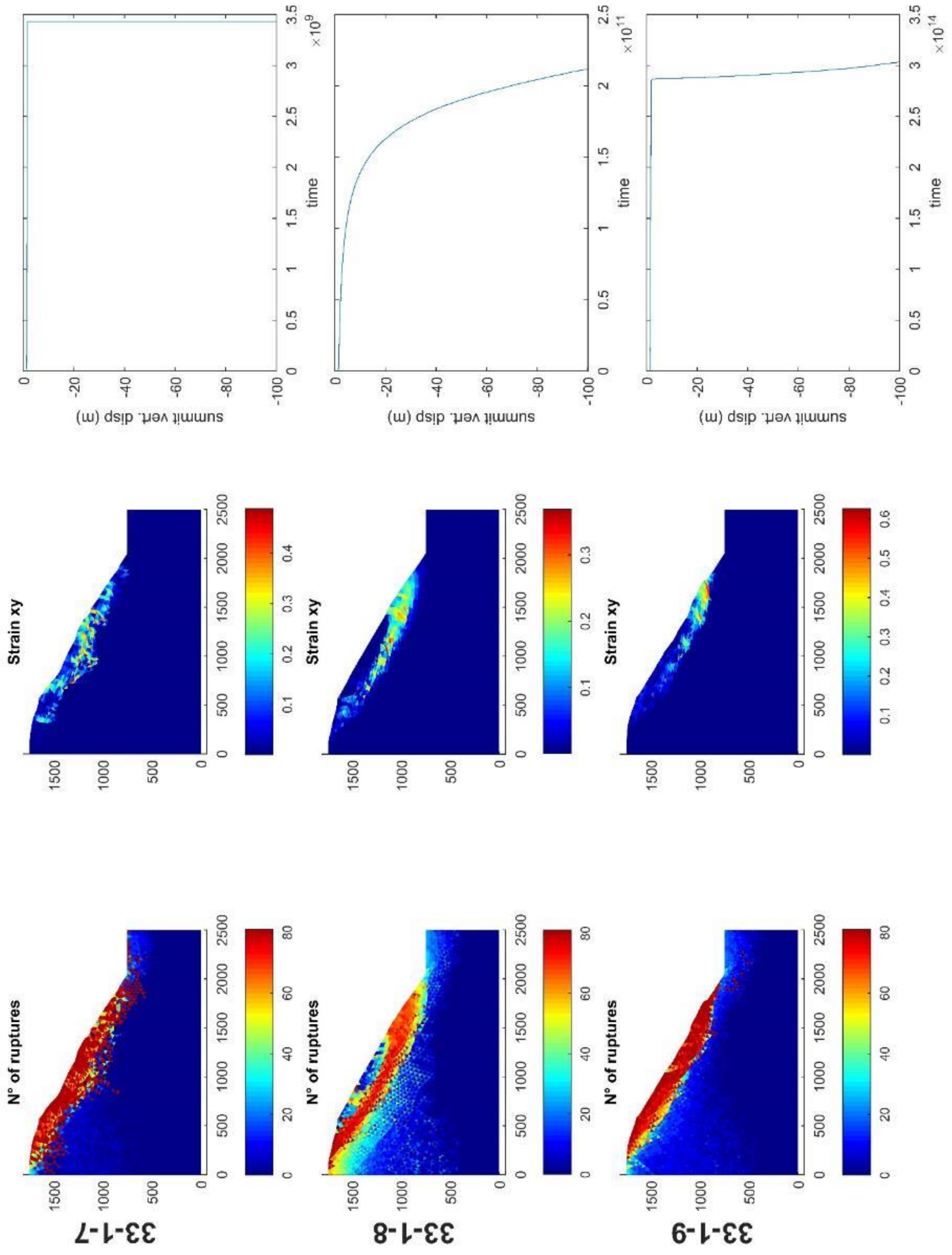
33-1-7
33-1-8
33-1-9
N° of ruptures
Strain xy
summit vert. disp (m)
time
×10^9
×10^11
×10^14
0
-20
-40
-60
-80
-100
0
500
1000
1500
2000
2500
0.1
0.2
0.3
0.4
0.5
0.6
20
40
60
80
0.5
1
1.5
2
2.5
3
3.5

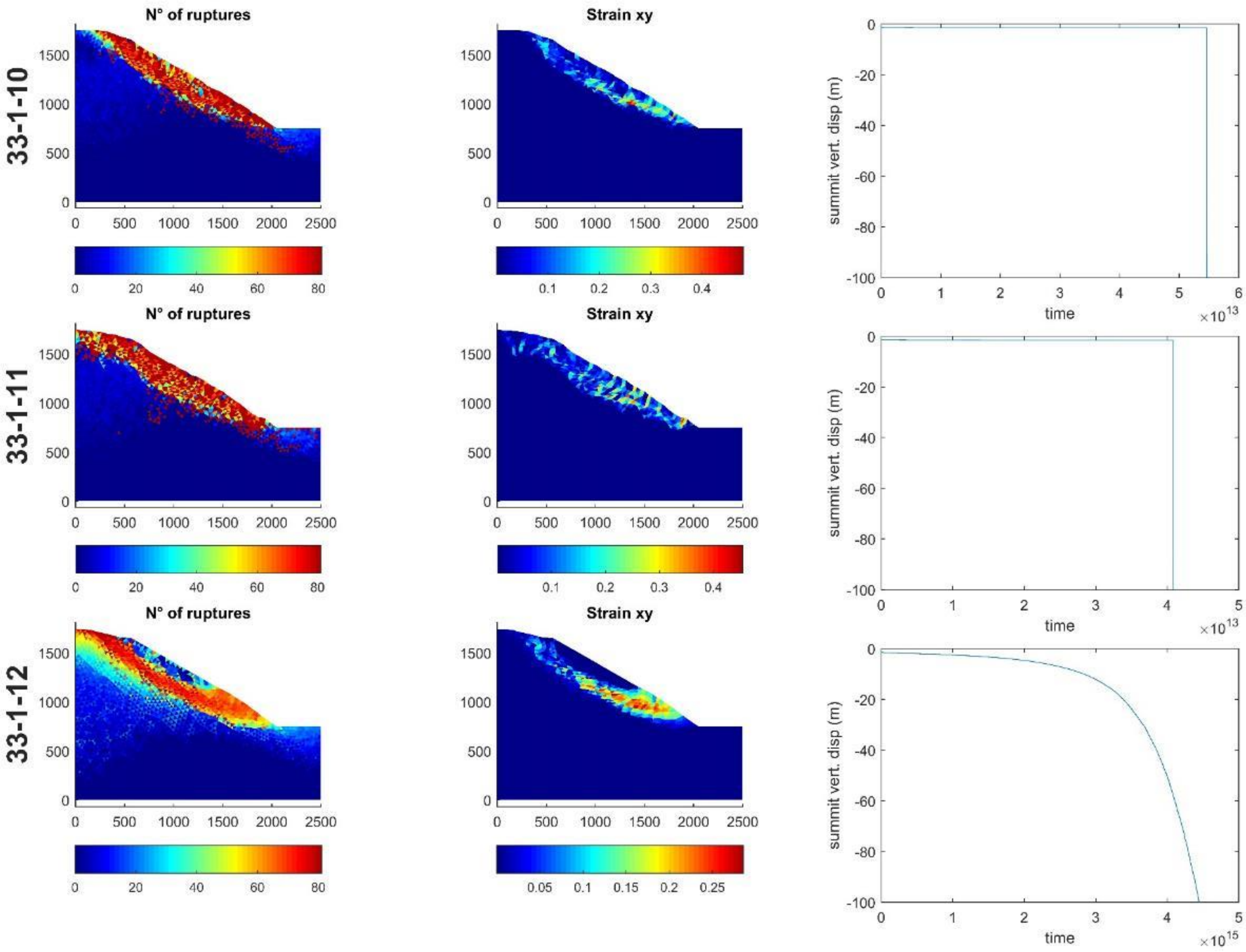
33-1-10
33-1-11
33-1-12
N° of ruptures
Strain xy
0
500
1000
1500
2000
2500
0
20
40
60
80
0.05
0.1
0.15
0.2
0.25
0.3
0.4
summit vert. disp (m)
0
-20
-40
-60
-80
-100
time
1
2
3
4
5
6
×10^13
×10^15

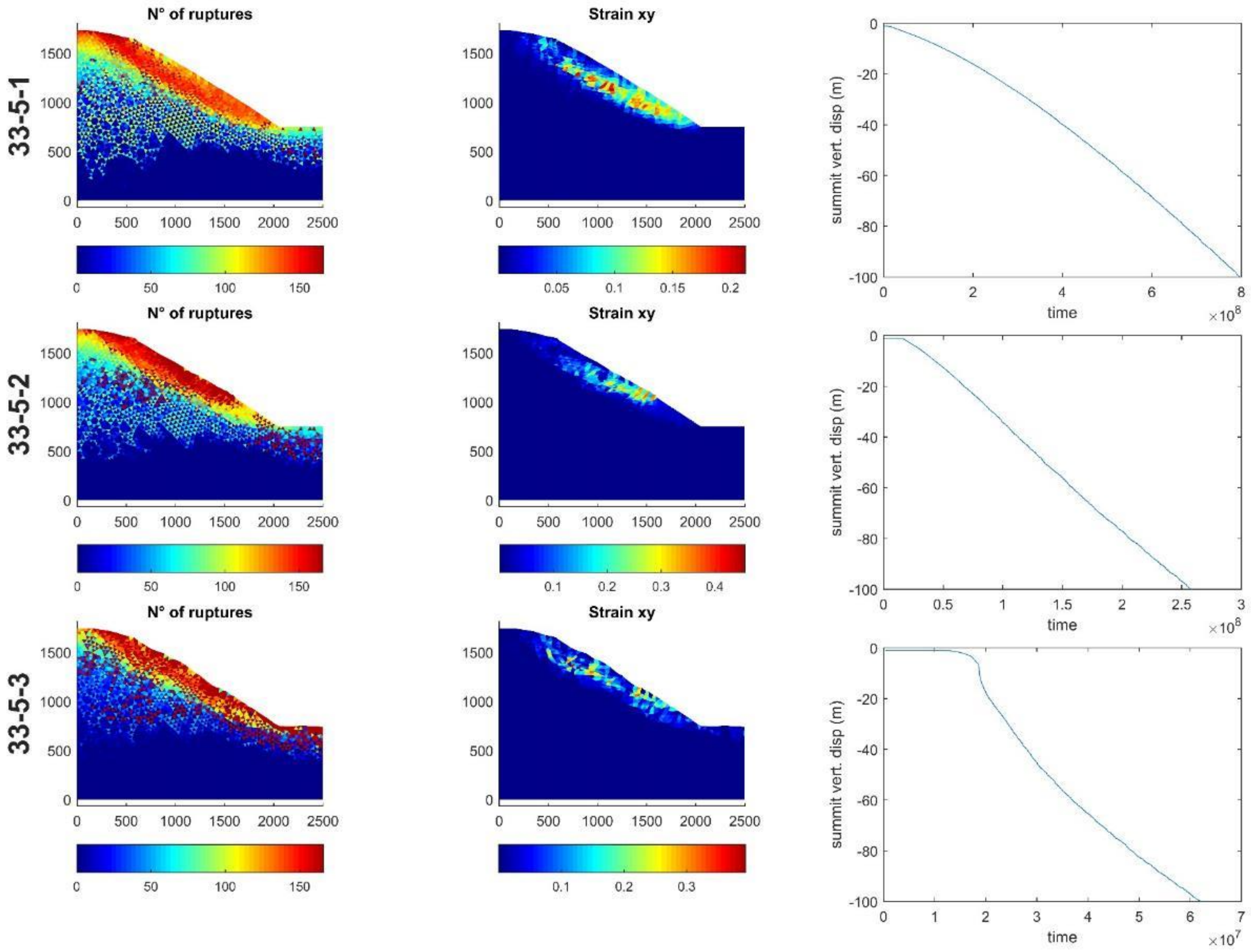
33-5-1
33-5-2
33-5-3
N° of ruptures
Strain xy
summit vert. disp (m)
time
0
500
1000
1500
2000
2500
50
100
150
0.05
0.1
0.15
0.2
0.3
0.4
-20
-40
-60
-80
-100
×10^8
×10^7

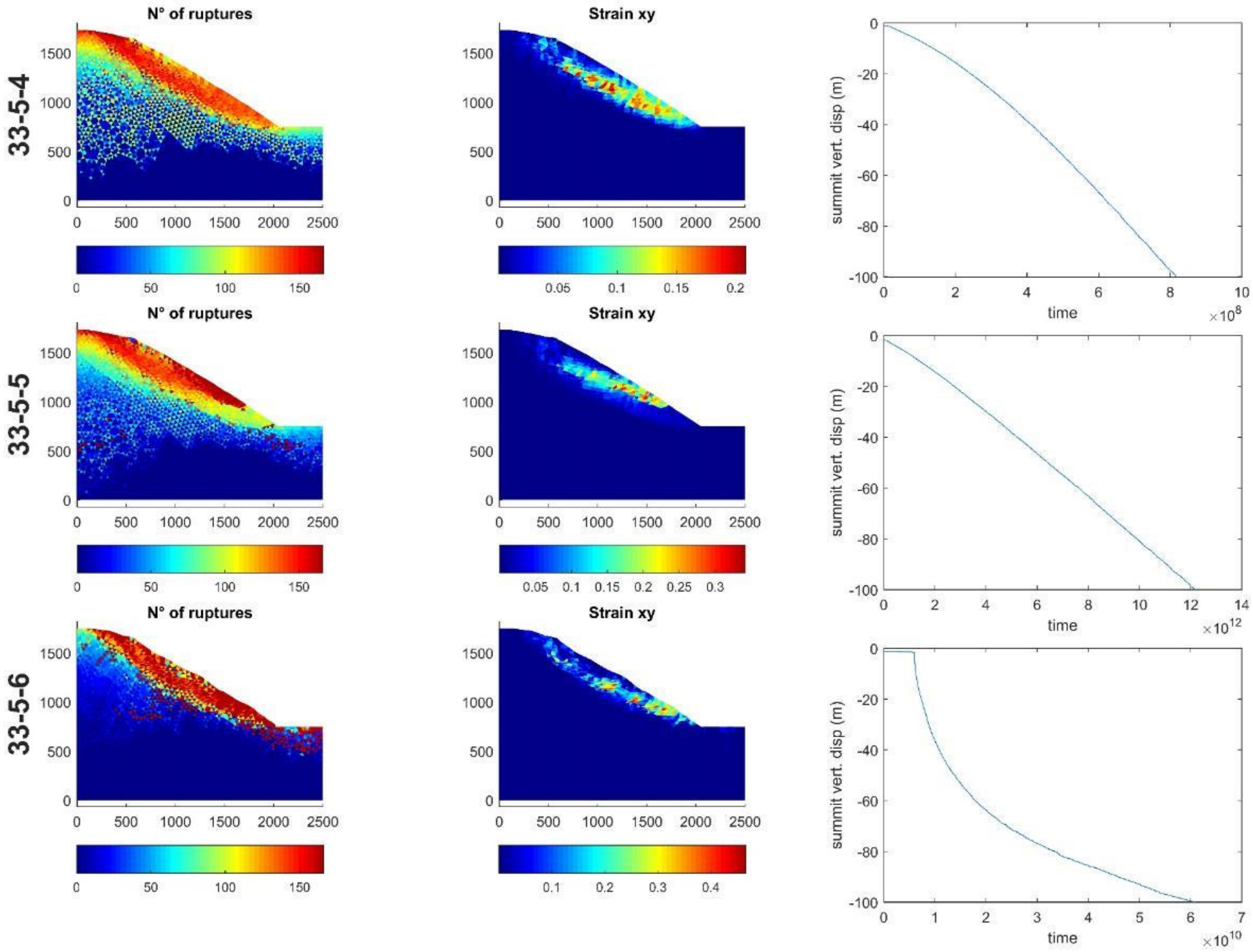
33-5-4
33-5-5
33-5-6
N° of ruptures
Strain xy
summit vert. disp (m)
time
×10^8
×10^12
×10^10

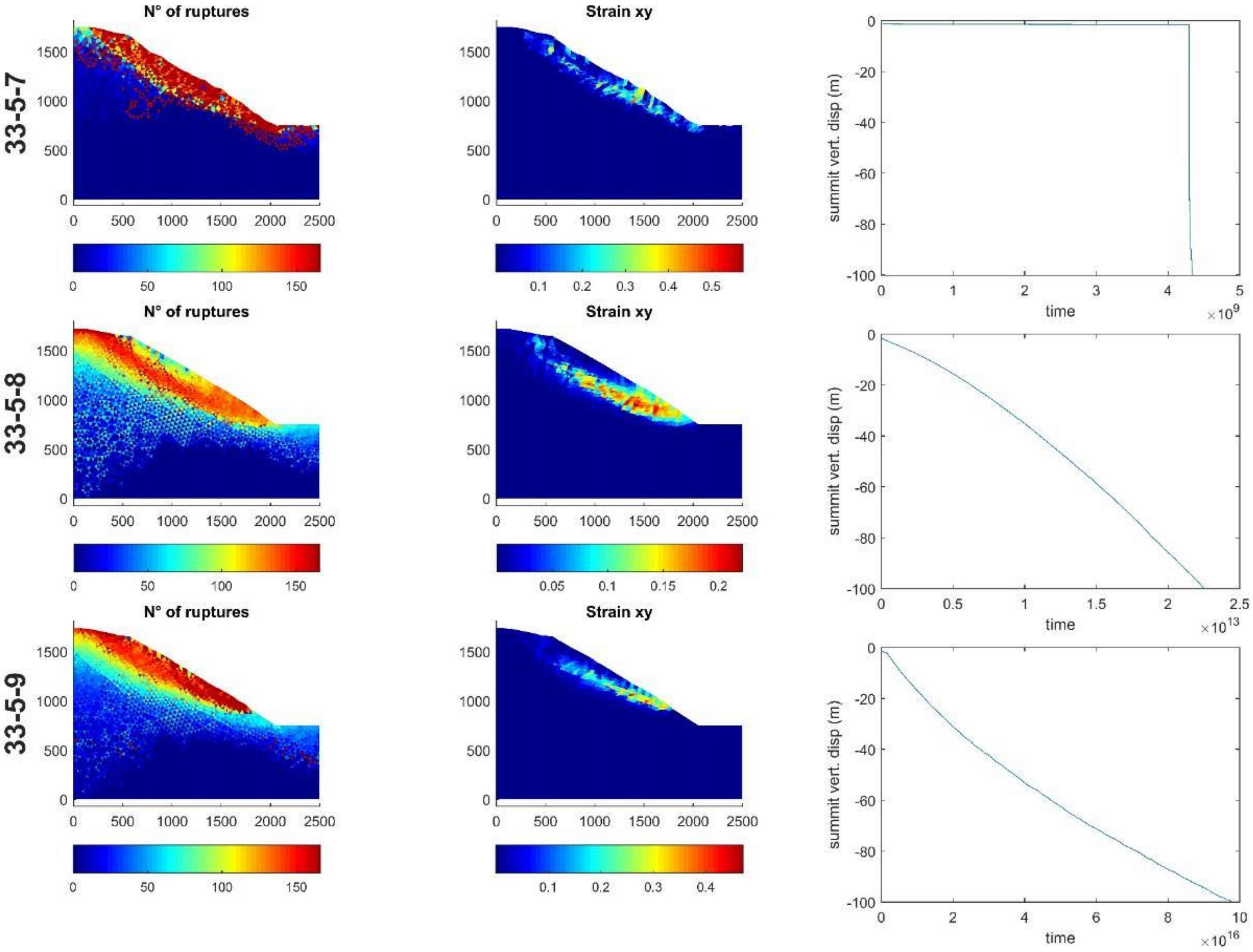
33-5-7
33-5-8
33-5-9
N° of ruptures
Strain xy
0
500
1000
1500
2000
2500
0
50
100
150
0.05
0.1
0.15
0.2
0.2
0.3
0.4
0.5
summit vert. disp (m)
0
-20
-40
-60
-80
-100
time
$\times 10^{9}$
$\times 10^{13}$
$\times 10^{16}$
0.5
1
1.5
2
2.5
3
4
5
6
8
10

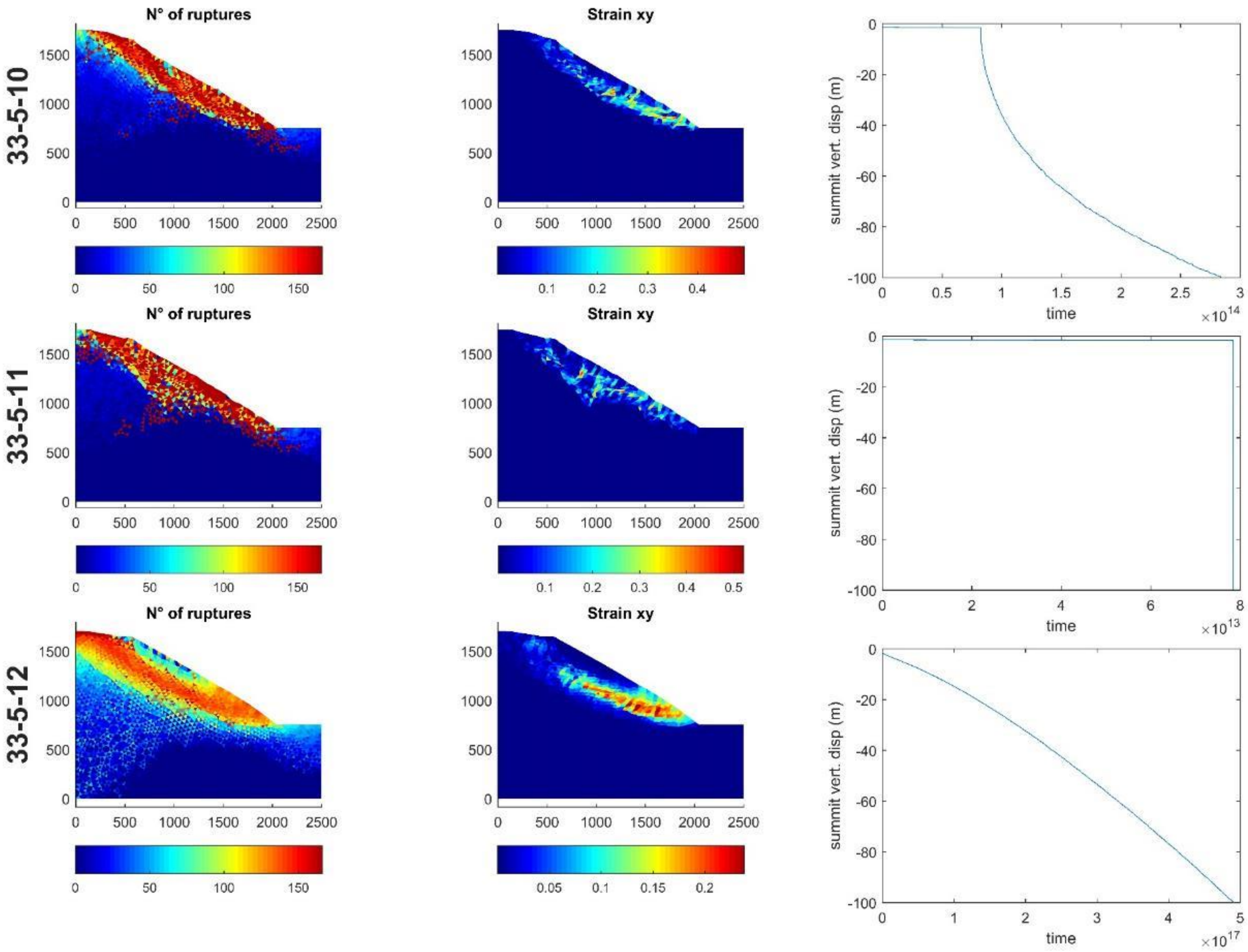
33-5-10
33-5-11
33-5-12
N° of ruptures
Strain xy
summit vert. disp (m)
time
×10^14
×10^13
×10^17
0
500
1000
1500
2000
2500
50
100
150
0.05
0.1
0.15
0.2
0.3
0.4
0.5
-20
-40
-60
-80
-100

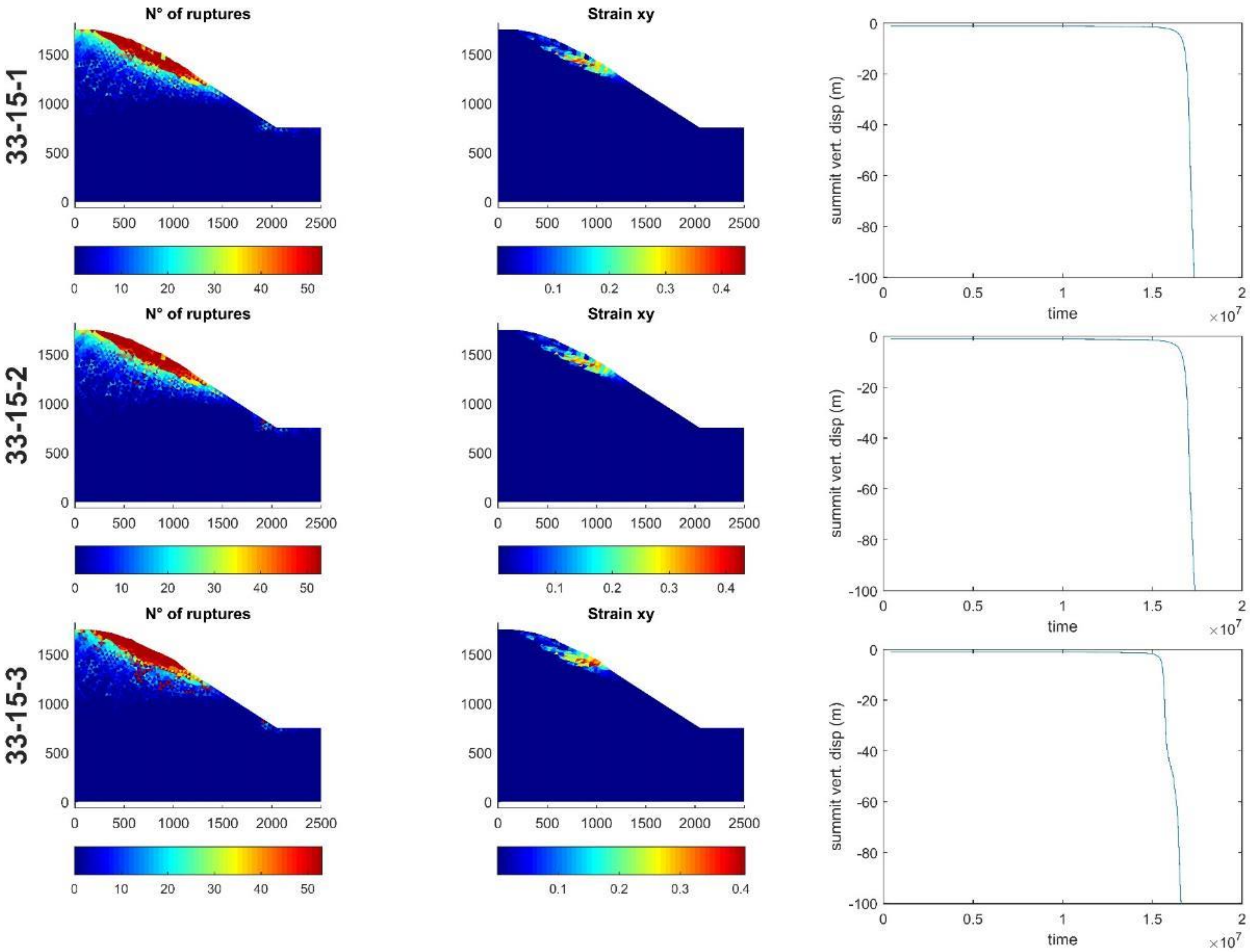
33-15-1
33-15-2
33-15-3
N° of ruptures
Strain xy
summit vert. disp (m)
time
×10^7
0
500
1000
1500
2000
2500
0
10
20
30
40
50
0.1
0.2
0.3
0.4
0
-20
-40
-60
-80
-100
0.5
1
1.5
2

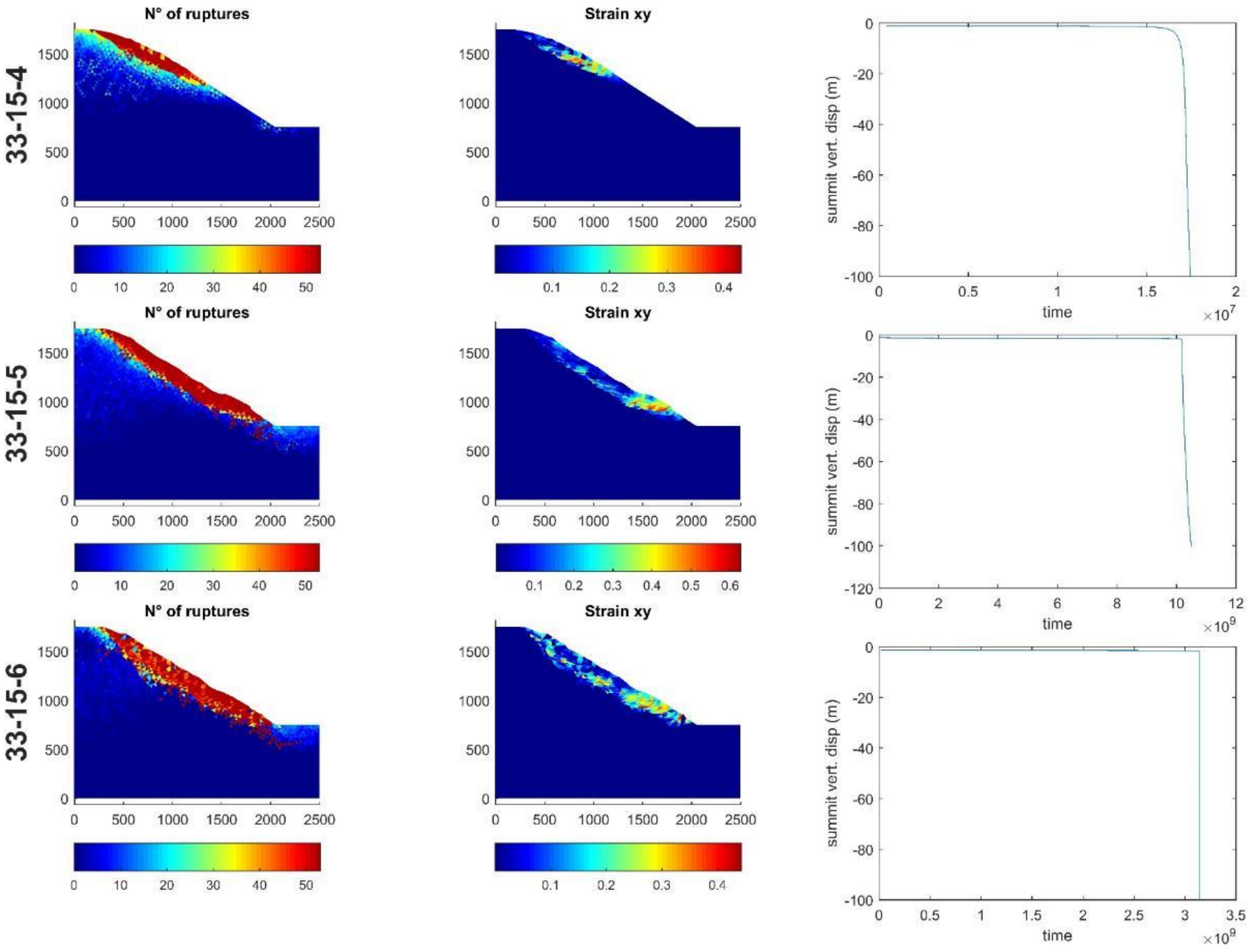
33-15-4
33-15-5
33-15-6
N° of ruptures
Strain xy
summit vert. disp (m)
time
×10^7
×10^9
0
500
1000
1500
2000
2500
0
10
20
30
40
50
0.1
0.2
0.3
0.4
0.5
0.6
-20
-40
-60
-80
-100
-120
0.5
1
1.5
2
2.5
3
3.5
4
6
8
10
12

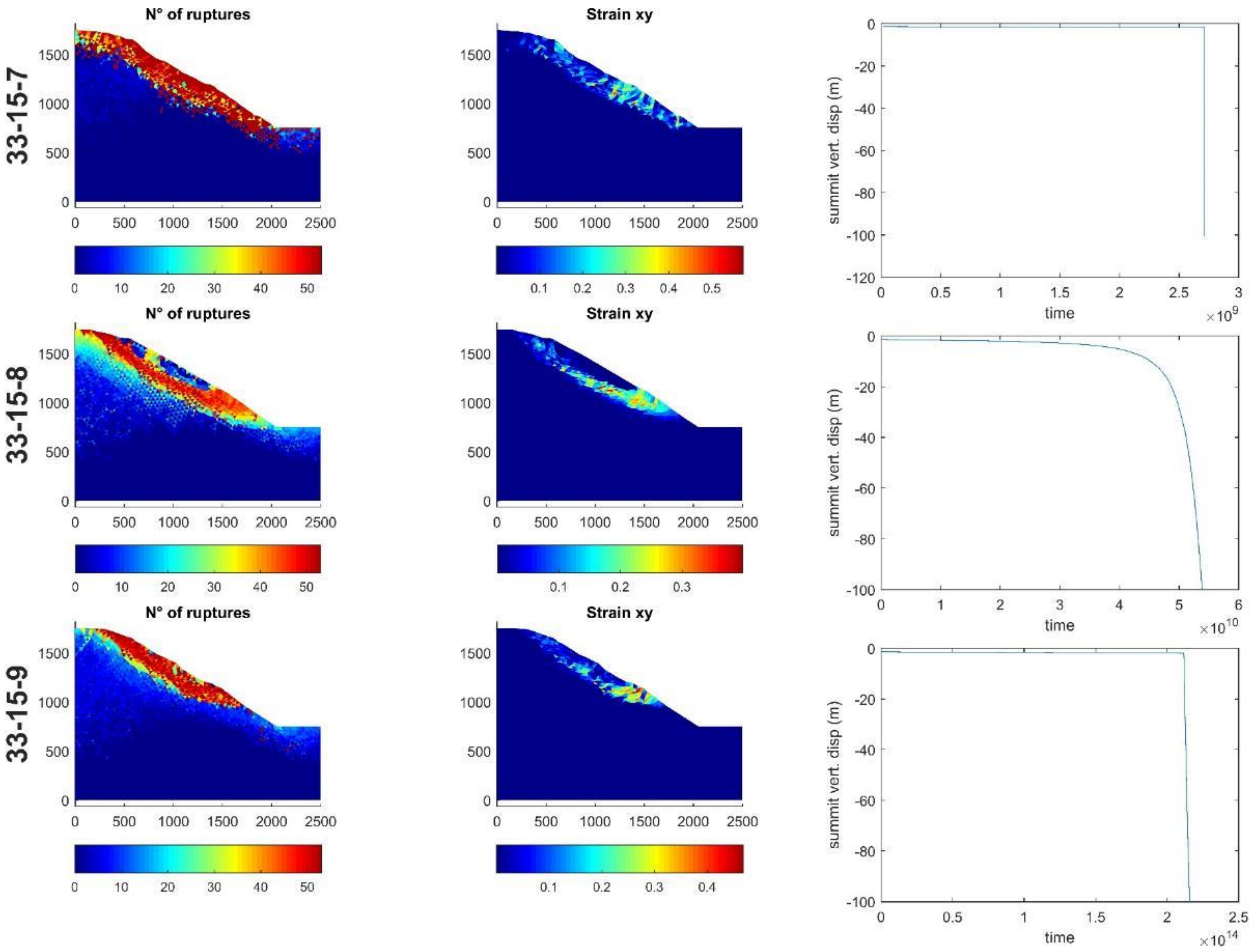
33-15-7
33-15-8
33-15-9
N° of ruptures
Strain xy
summit vert. disp (m)
time
×10^9
×10^10
×10^14
0
500
1000
1500
2000
2500
10
20
30
40
50
0.1
0.2
0.3
0.4
0.5
-20
-40
-60
-80
-100
-120

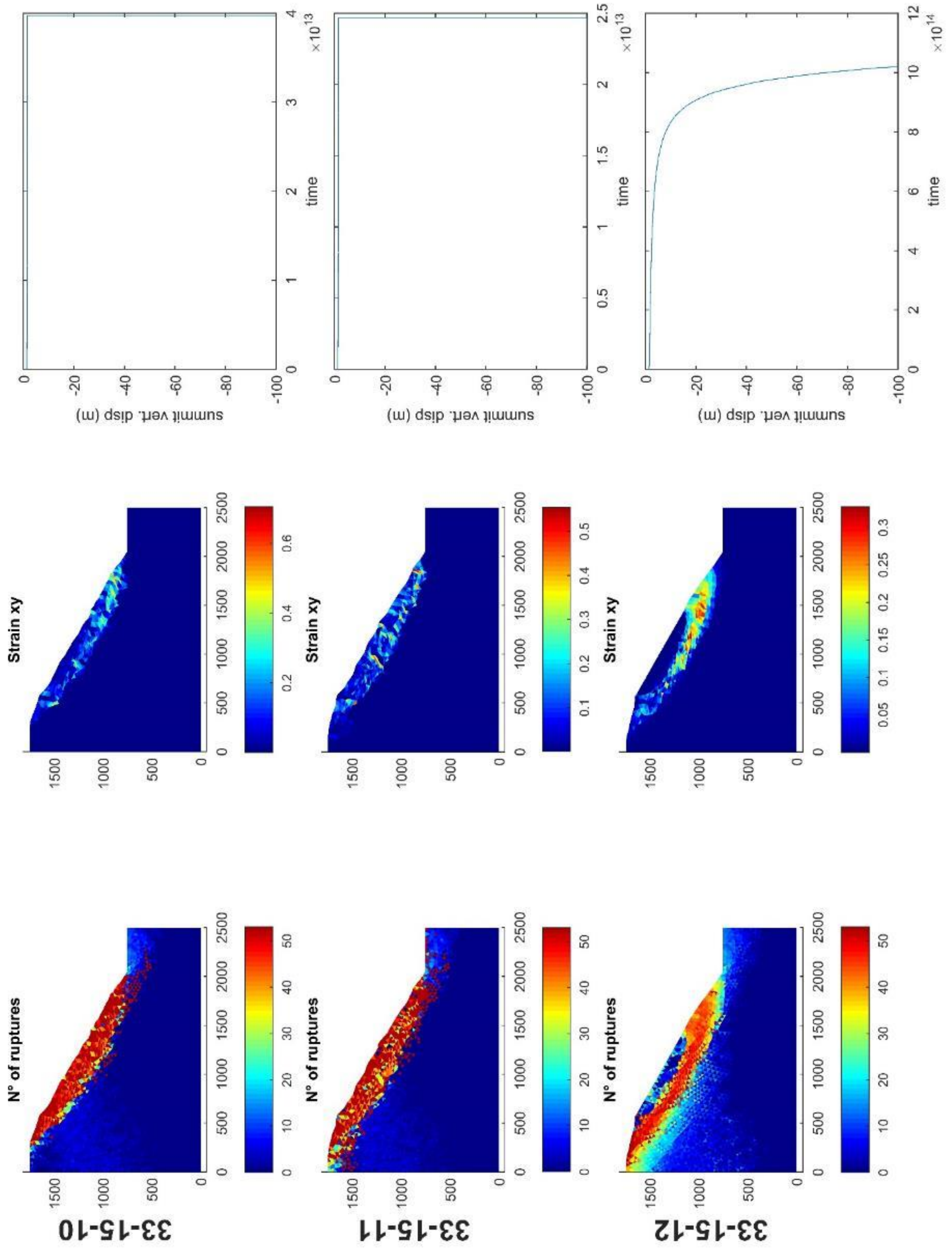
33-15-10
33-15-11
33-15-12
N° of ruptures
Strain xy
summit vert. disp (m)
time
×10^13
×10^14
0
500
1000
1500
2000
2500
10
20
30
40
50
0.2
0.4
0.6
0.1
0.3
0.5
0.05
0.15
0.25
-20
-40
-60
-80
-100

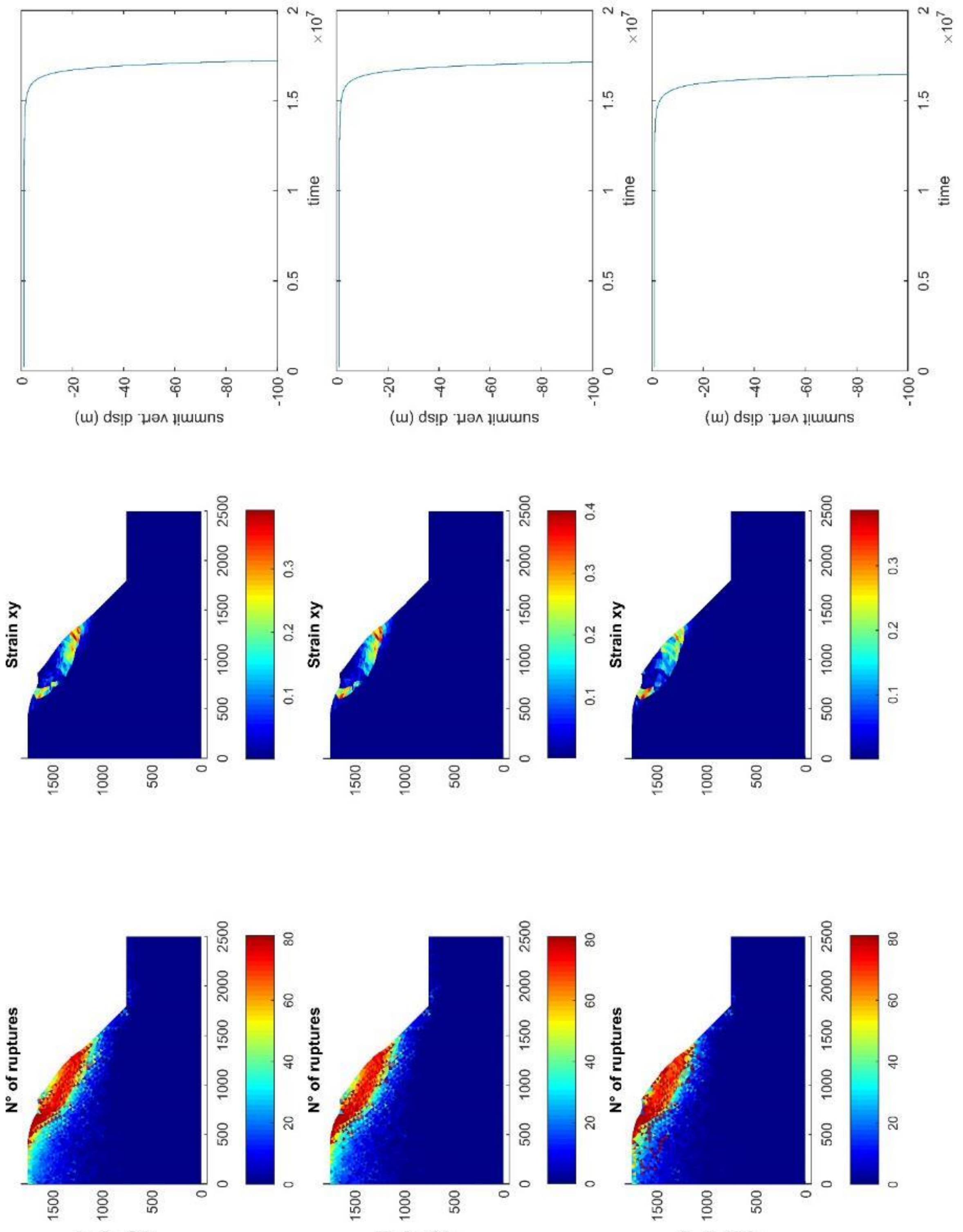
45-1-1
45-1-2
45-1-3
N° of ruptures
Strain xy
summit vert. disp (m)
time
$\times 10^7$
0
500
1000
1500
2000
2500
0
20
40
60
80
0.1
0.2
0.3
0.4
0
-20
-40
-60
-80
-100
0
0.5
1
1.5
2

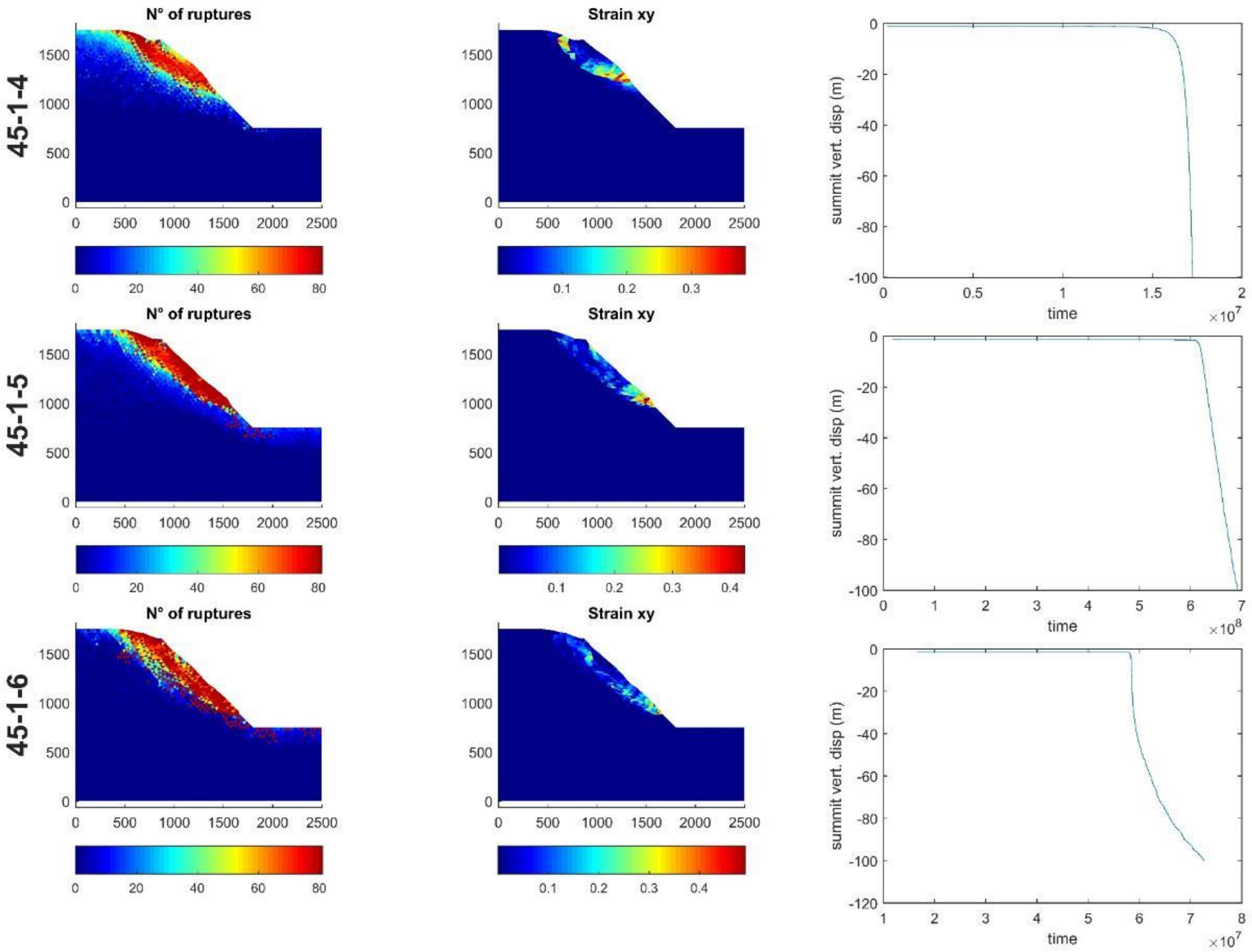
45-1-4
45-1-5
45-1-6
N° of ruptures
Strain xy
0
500
1000
1500
2000
2500
0
20
40
60
80
0.1
0.2
0.3
0.4
summit vert. disp (m)
0
-20
-40
-60
-80
-100
-120
time
0.5
1
1.5
2
$\times 10^7$
$\times 10^8$
$\times 10^7$

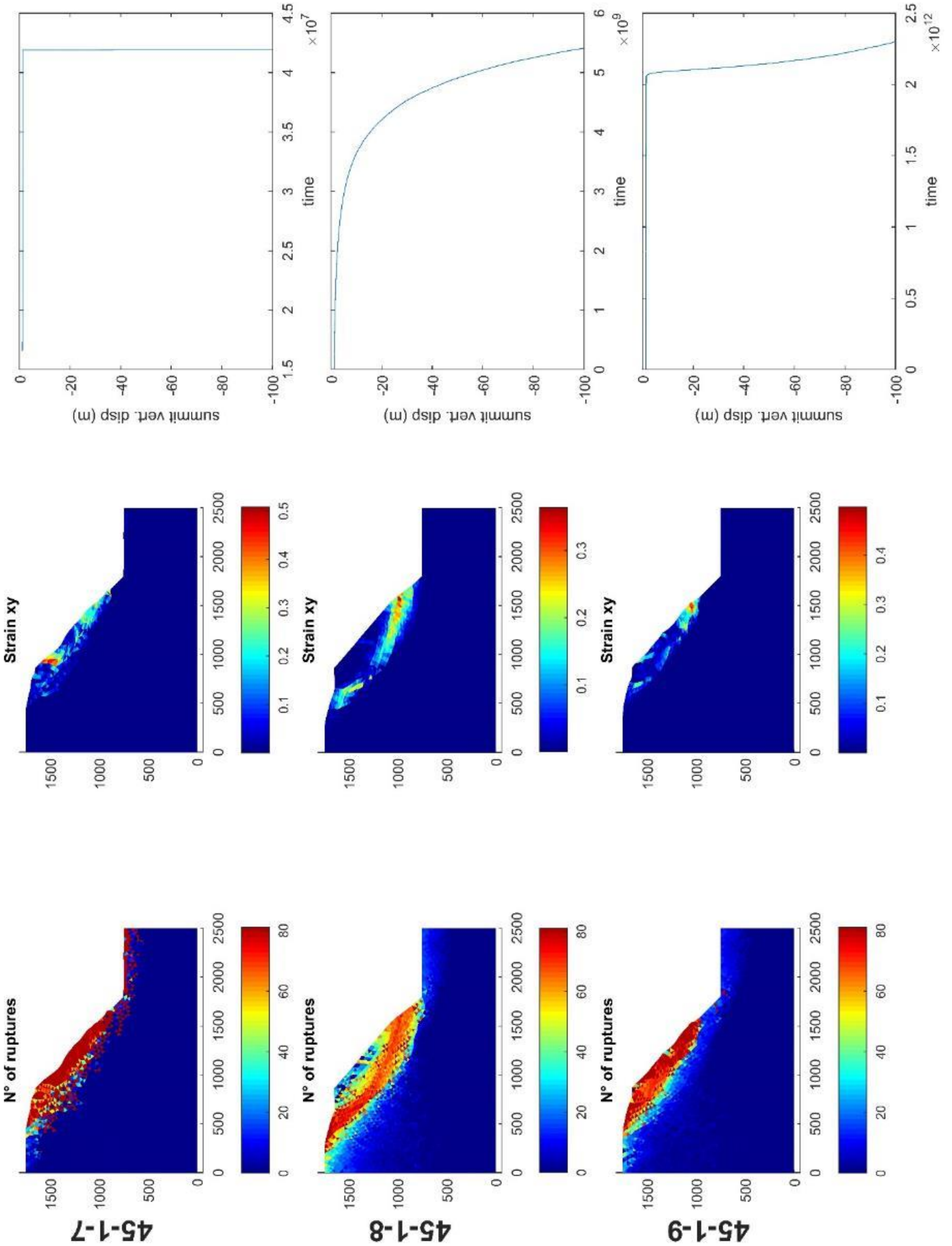
45-1-7
45-1-8
45-1-9
N° of ruptures
Strain xy
summit vert. disp (m)
time
$\times 10^7$
$\times 10^9$
$\times 10^{12}$

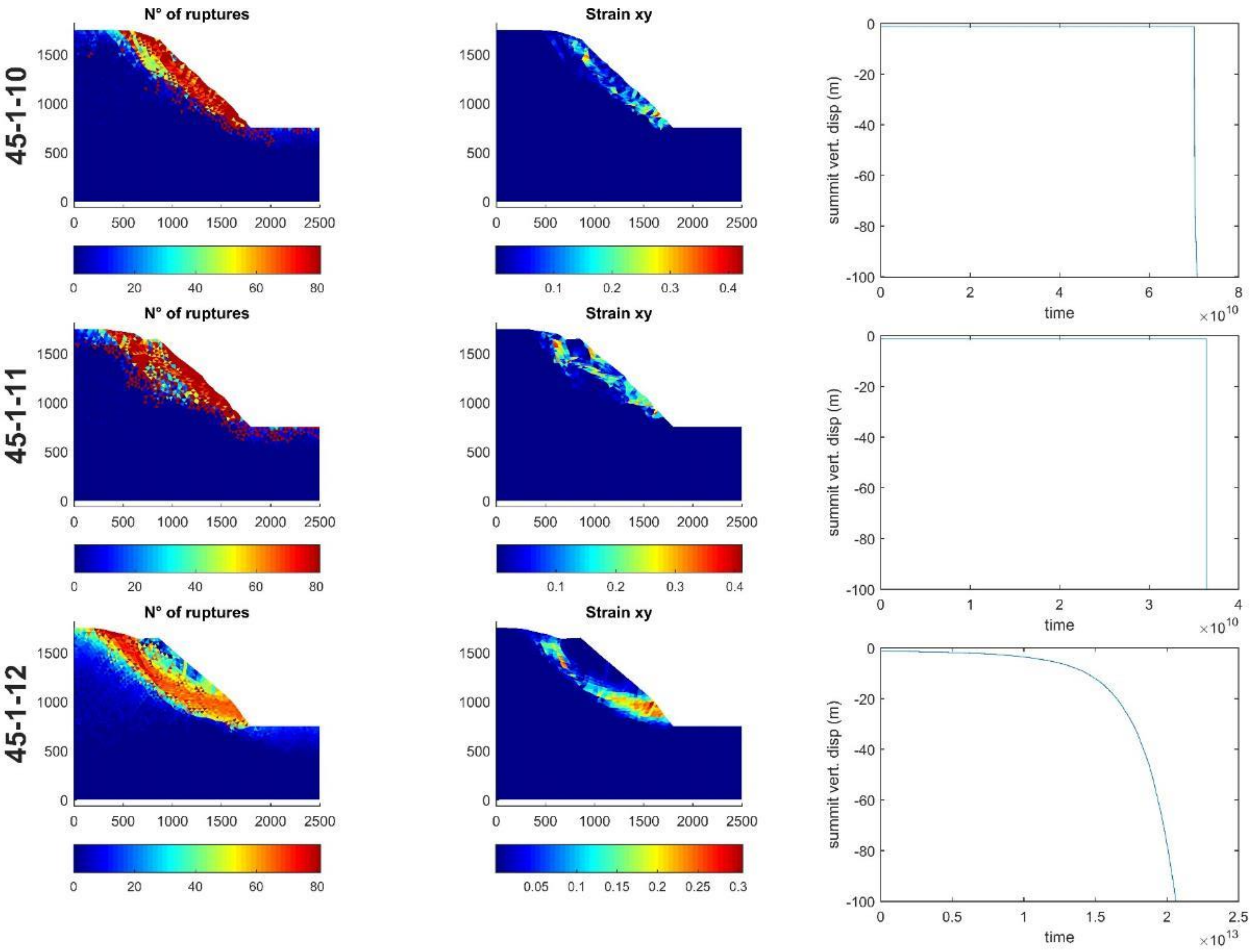
45-1-10
45-1-11
45-1-12
N° of ruptures
Strain xy
0
500
1000
1500
2000
2500
0
20
40
60
80
0.05
0.1
0.15
0.2
0.25
0.3
0.4
summit vert. disp (m)
-100
-80
-60
-40
-20
time
$\times 10^{10}$
$\times 10^{13}$
0.5
1.5
2.5

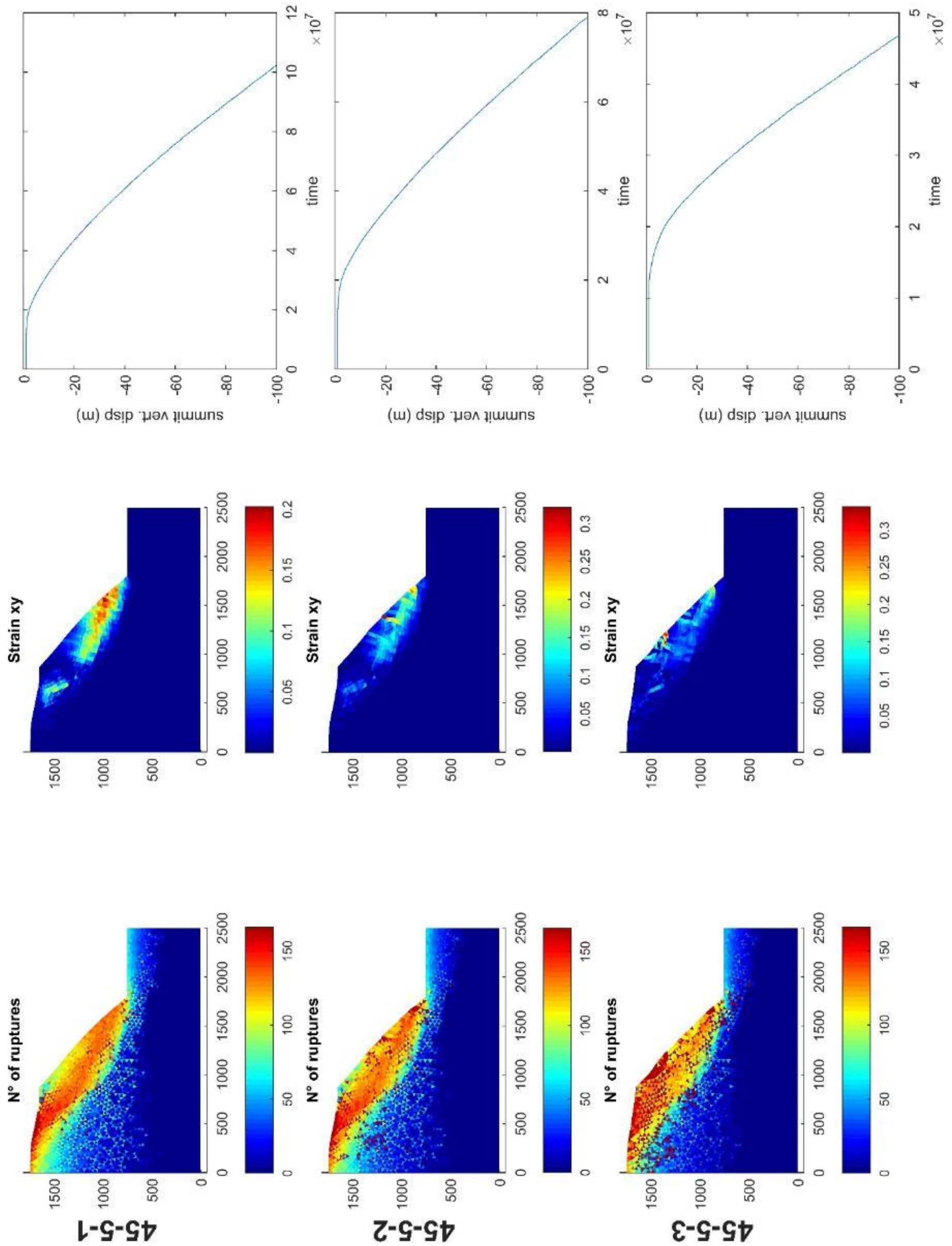
45-5-1
45-5-2
45-5-3
N° of ruptures
Strain xy
summit vert. disp (m)
time
×10^7
0
500
1000
1500
2000
2500
0.05
0.1
0.15
0.2
0.25
0.3
50
100
150
0
-20
-40
-60
-80
-100
2
4
6
8
10
12

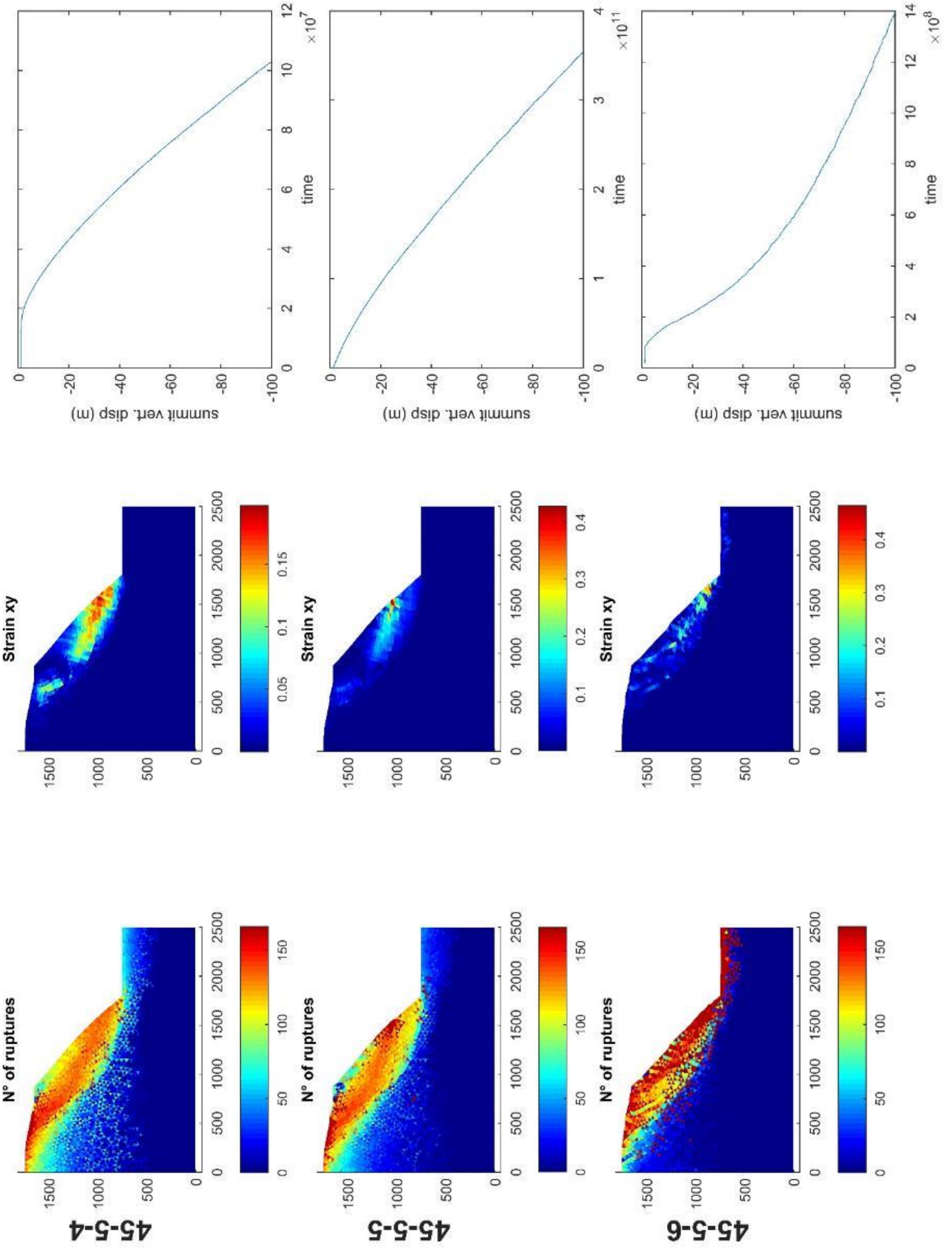
45-5-4
45-5-5
45-5-6
N° of ruptures
Strain xy
summit vert. disp (m)
time
$\times 10^7$
$\times 10^{11}$
$\times 10^8$

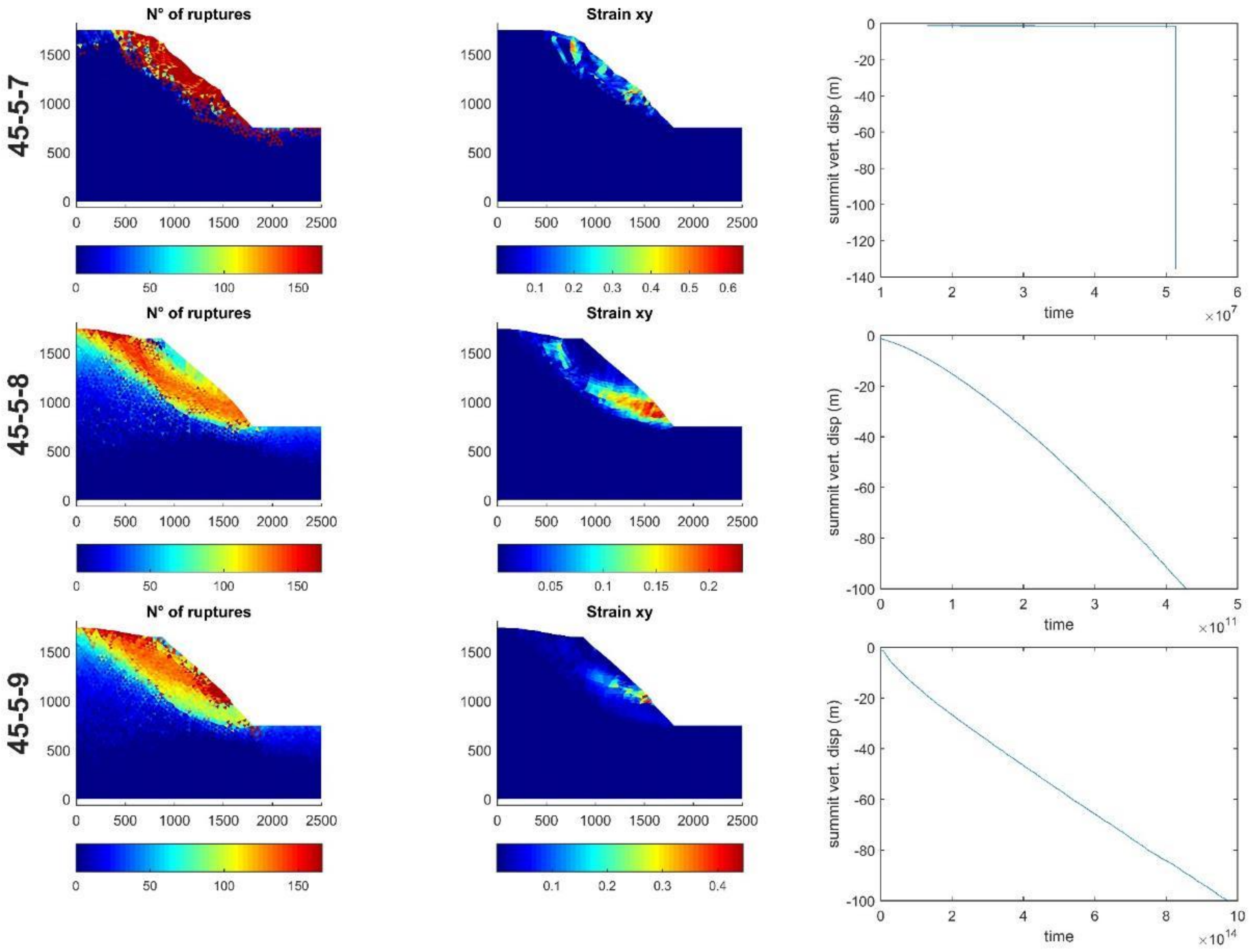
45-5-7
45-5-8
45-5-9
N° of ruptures
Strain xy
summit vert. disp (m)
time
×10^7
×10^11
×10^14
0
500
1000
1500
2000
2500
50
100
150
0.05
0.1
0.15
0.2
0.3
0.4
0.5
0.6
-20
-40
-60
-80
-100
-120
-140

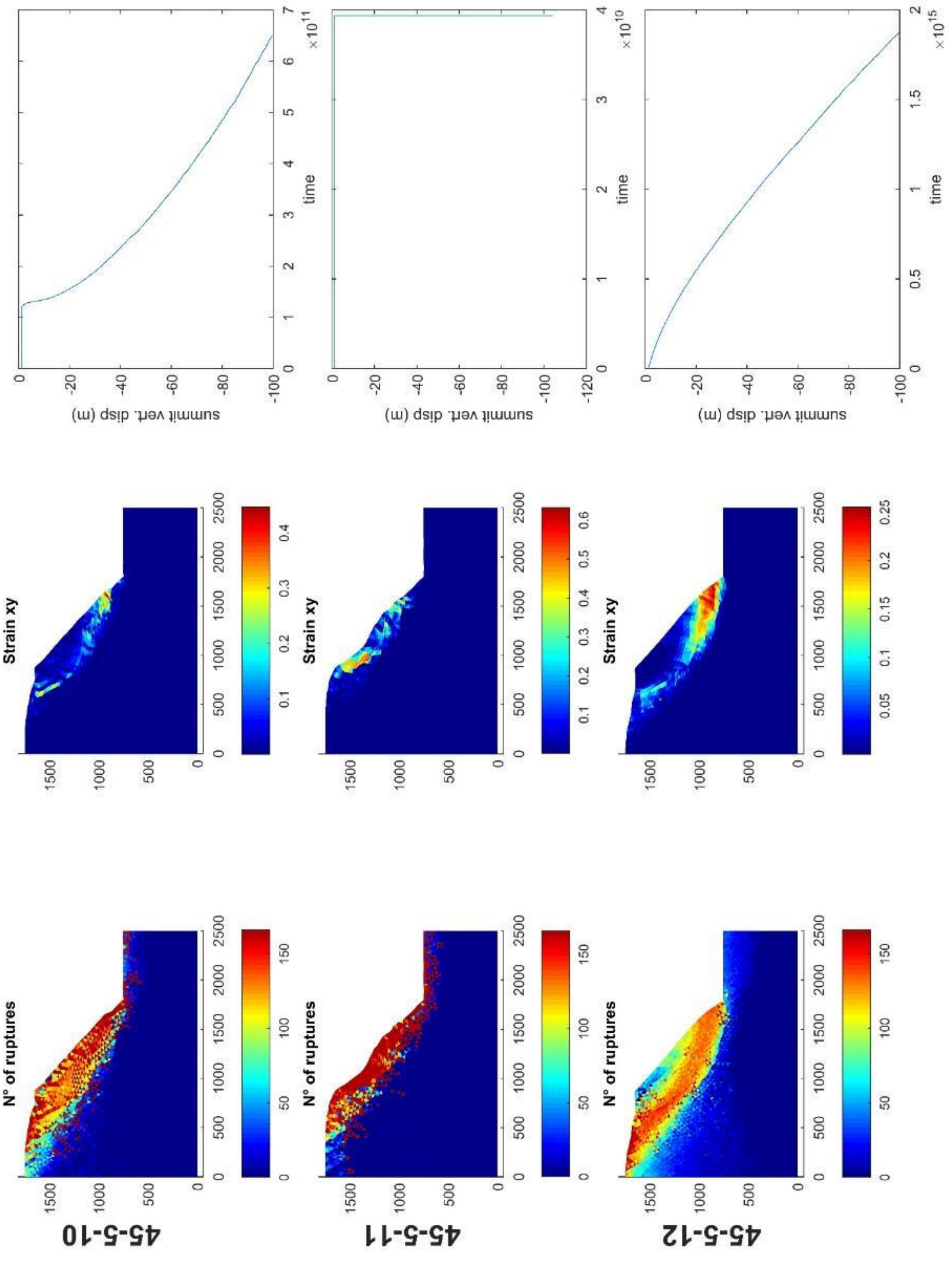
45-5-10
45-5-11
45-5-12
N° of ruptures
Strain xy
summit vert. disp (m)
time
$\times 10^{11}$
$\times 10^{10}$
$\times 10^{15}$

45-15-1

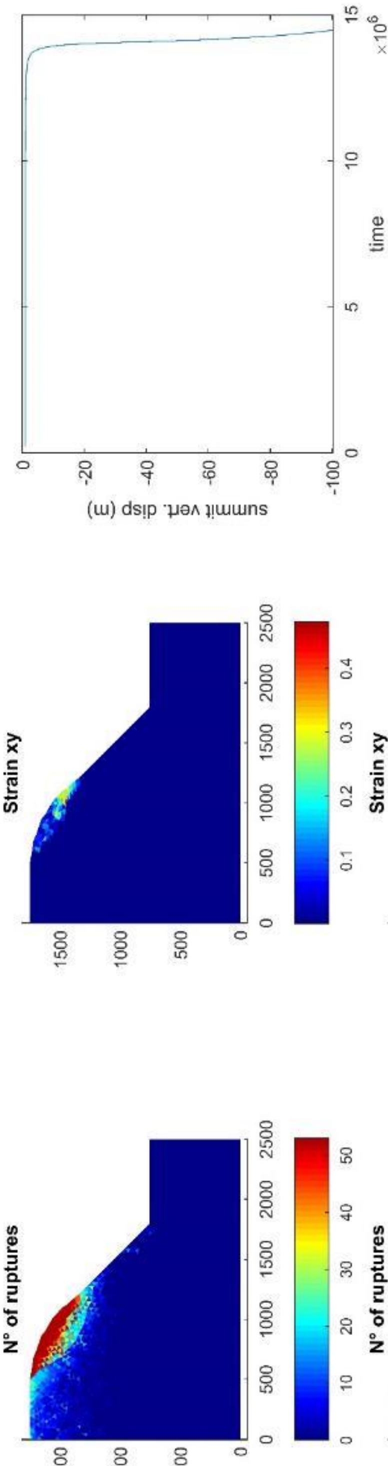

45-15-2

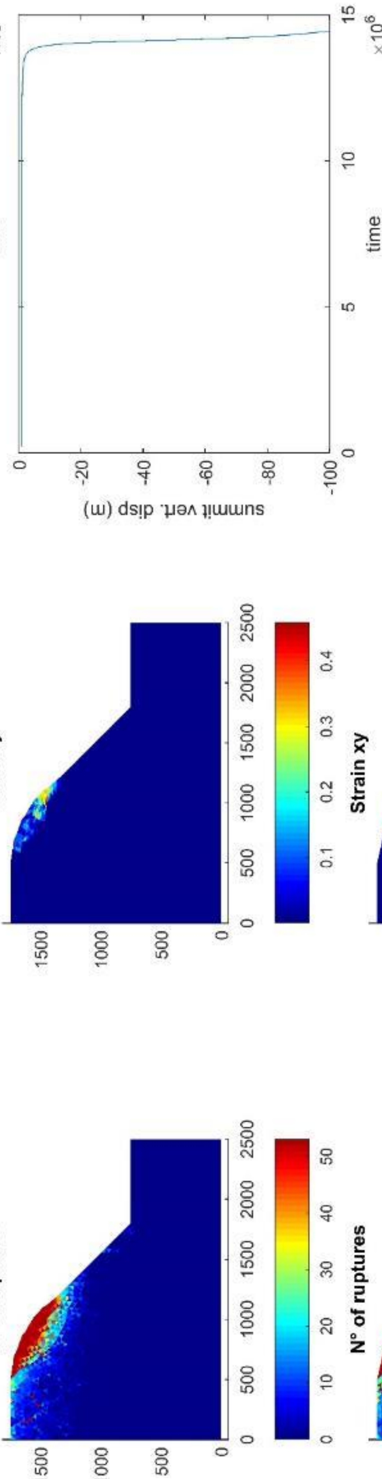

45-15-3

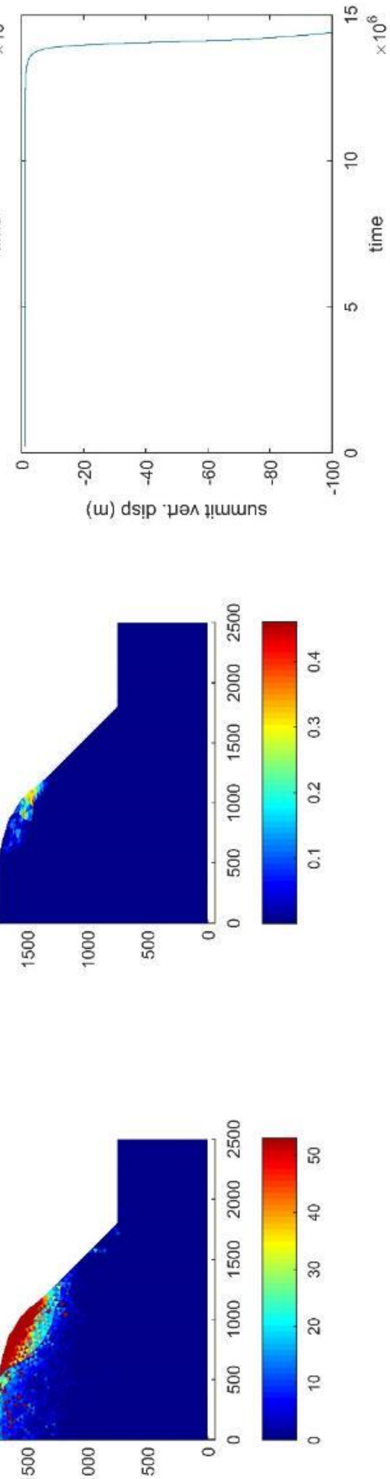

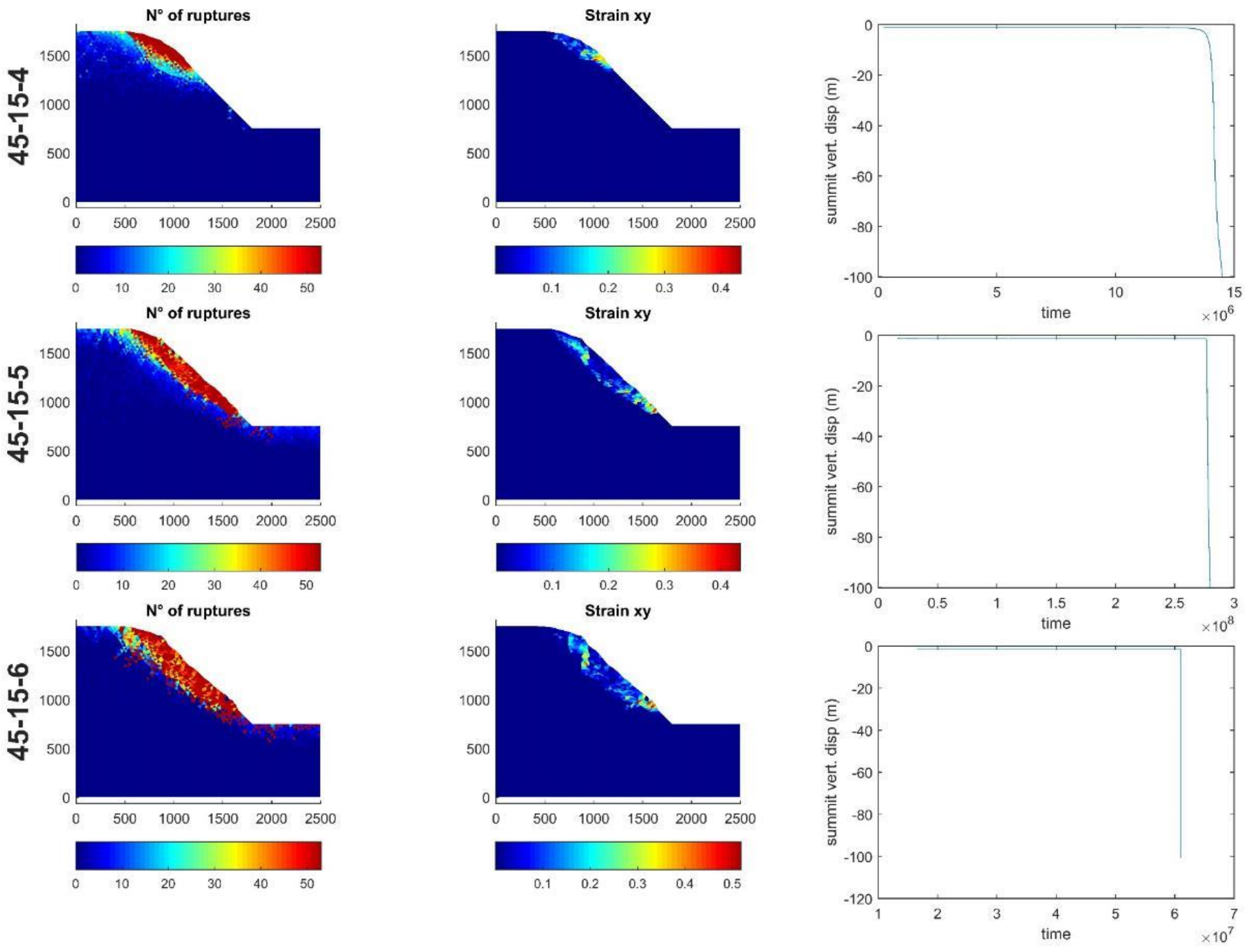
45-15-4
45-15-5
45-15-6
N° of ruptures
Strain xy
0
500
1000
1500
2000
2500
10
20
30
40
50
0.1
0.2
0.3
0.4
0.5
summit vert. disp (m)
-20
-40
-60
-80
-100
-120
time
$\times 10^6$
$\times 10^8$
$\times 10^7$

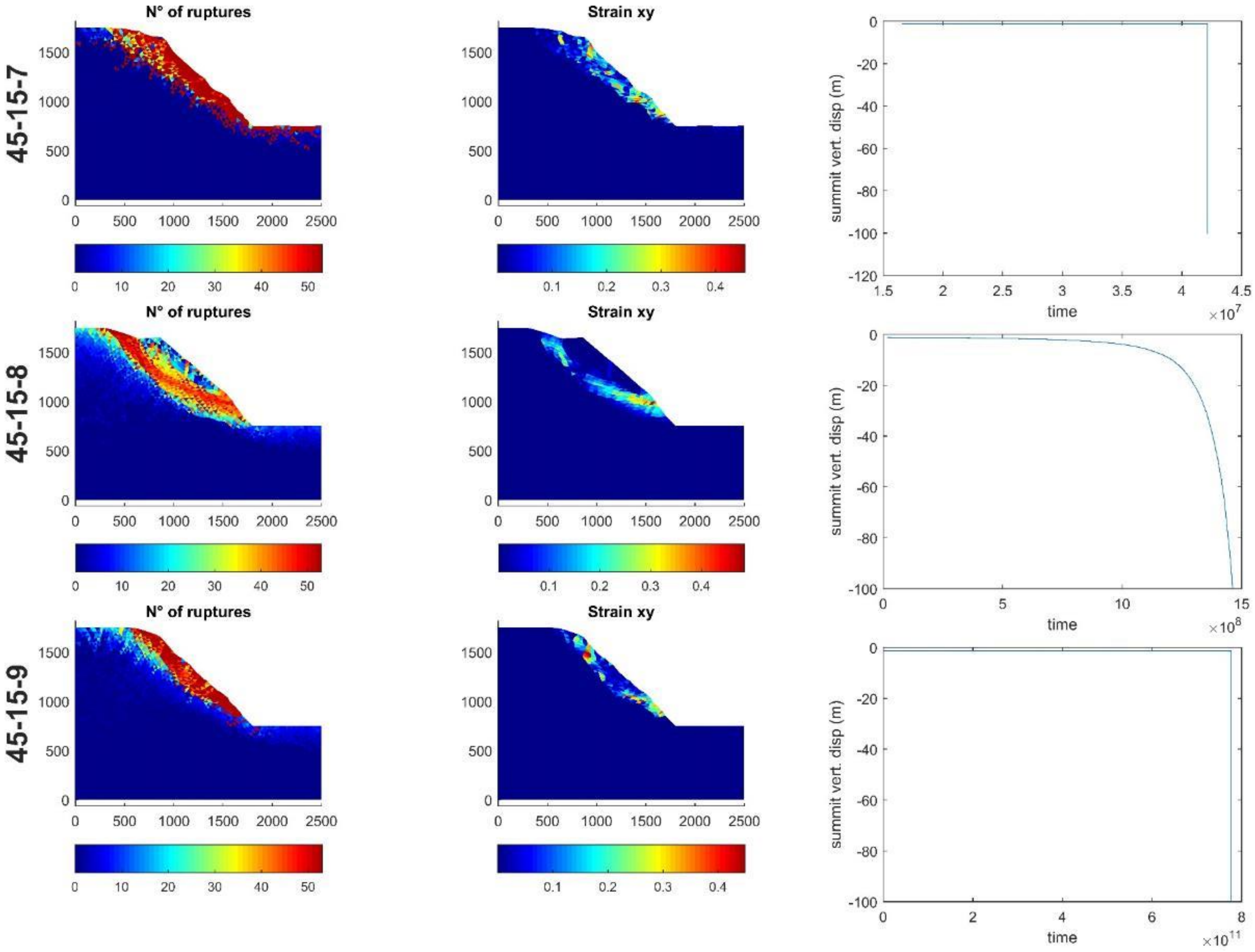
45-15-7
45-15-8
45-15-9
N° of ruptures
Strain xy
summit vert. disp (m)
time
×10^7
×10^8
×10^11
0
500
1000
1500
2000
2500
10
20
30
40
50
0.1
0.2
0.3
0.4
-20
-40
-60
-80
-100
-120
1.5
2
2.5
3
3.5
4
4.5
5
15
4
6
8

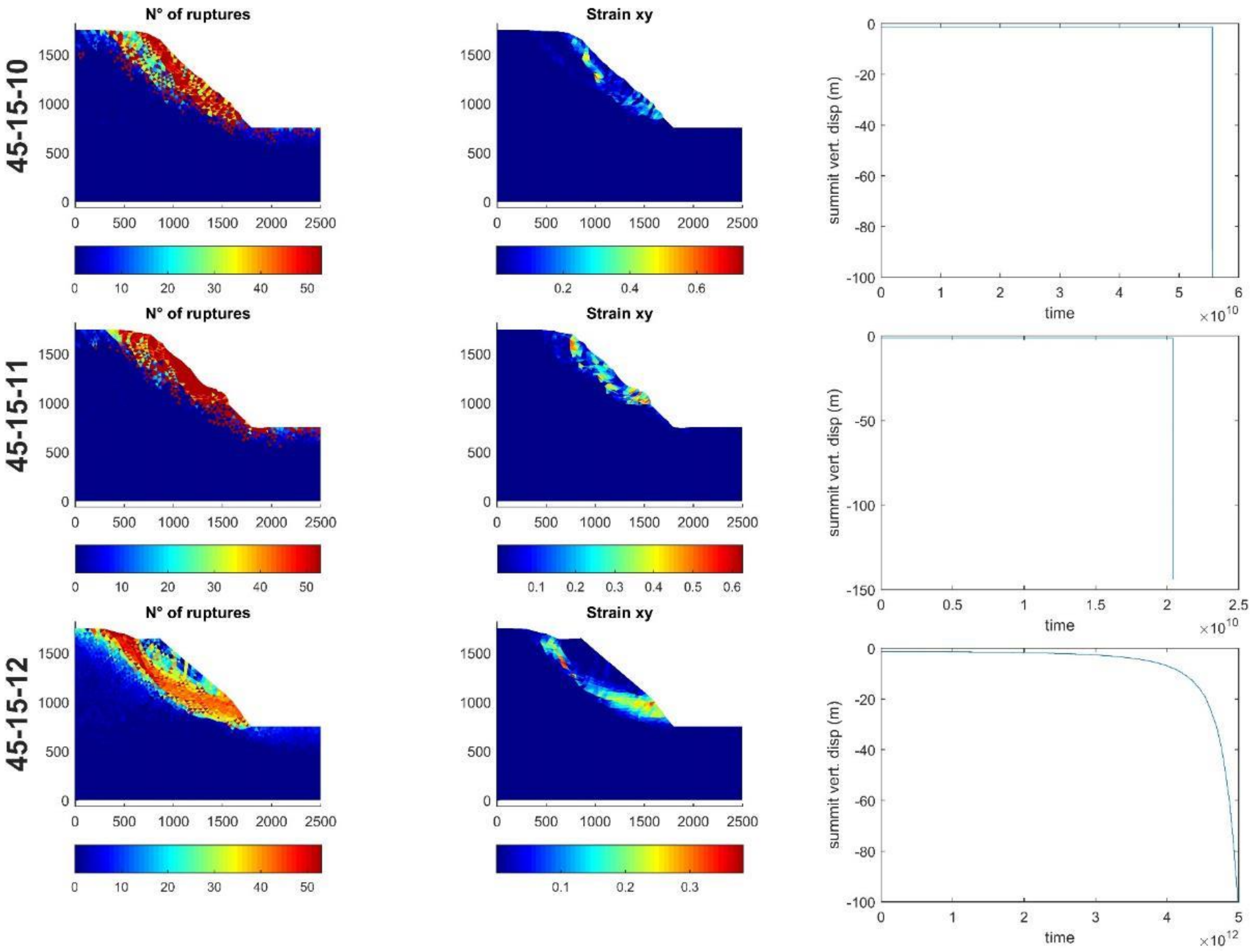
45-15-10
45-15-11
45-15-12
N° of ruptures
Strain xy
0
500
1000
1500
2000
2500
0
10
20
30
40
50
0.1
0.2
0.3
0.4
0.5
0.6
summit vert. disp (m)
0
-20
-40
-60
-80
-100
-50
-150
time
0.5
1
1.5
2
2.5
3
4
5
6
$\times 10^{10}$
$\times 10^{12}$

10 ANNEX 2: SPRIANA BOREHOLES CHARACTERIZATION

S101

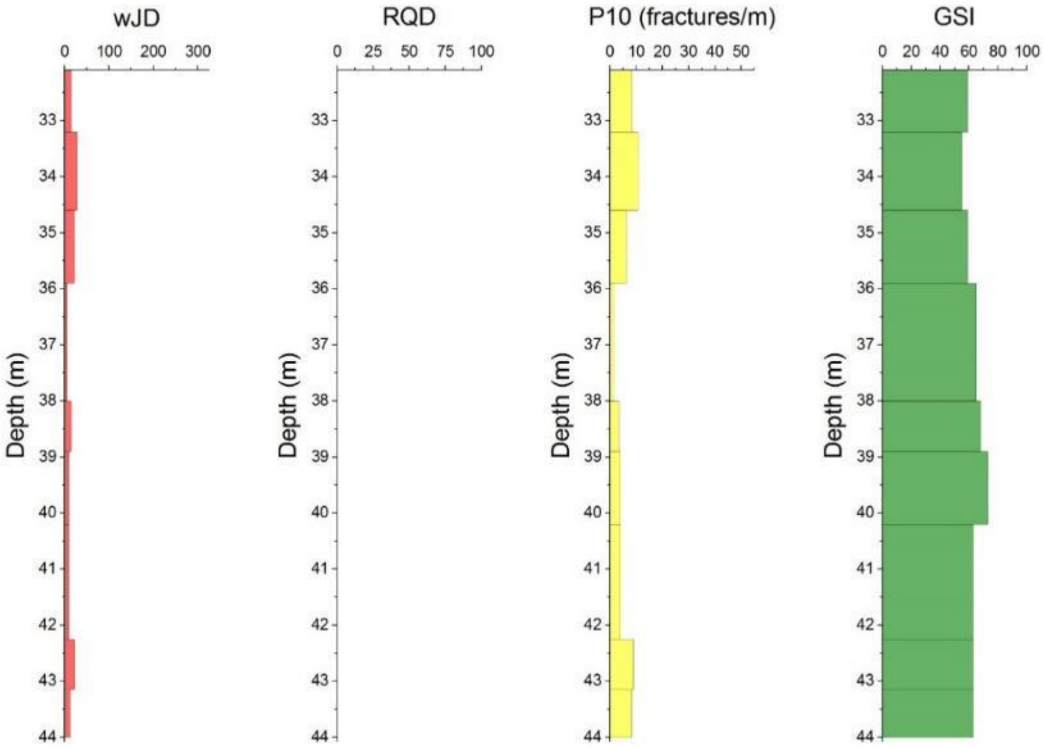

S103

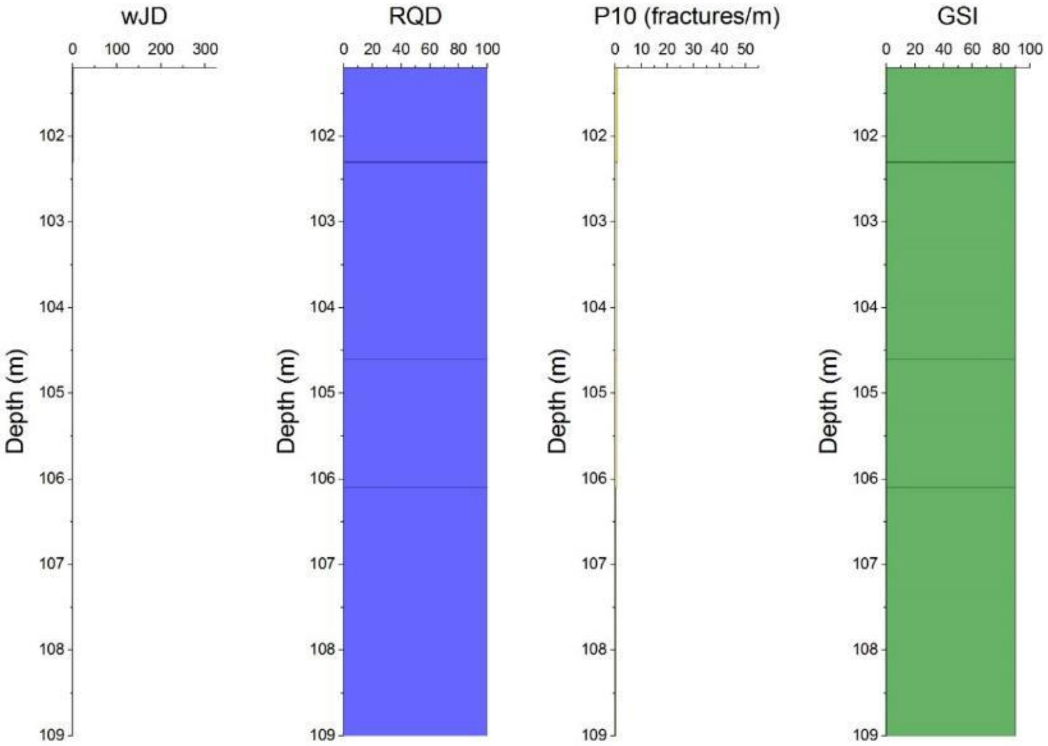
wJD
0 100 200 300
RQD
0 20 40 60 80 100
P10 (fractures/m)
0 10 20 30 40 50
GSI
0 20 40 60 80 100
Depth (m)
102
103
104
105
106
107
108
109

S106

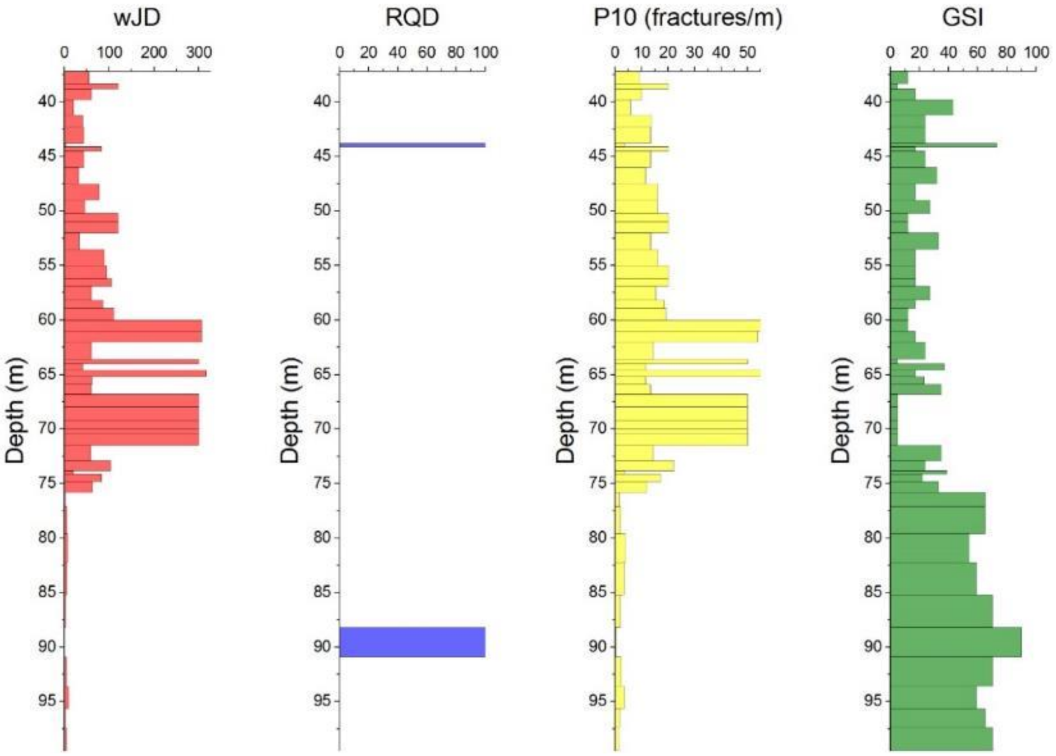
wJD
0 100 200 300
RQD
0 20 40 60 80 100
P10 (fractures/m)
0 10 20 30 40 50
GSI
0 20 40 60 80 100
Depth (m)
40
45
50
55
60
65
70
75
80
85
90
95

S107

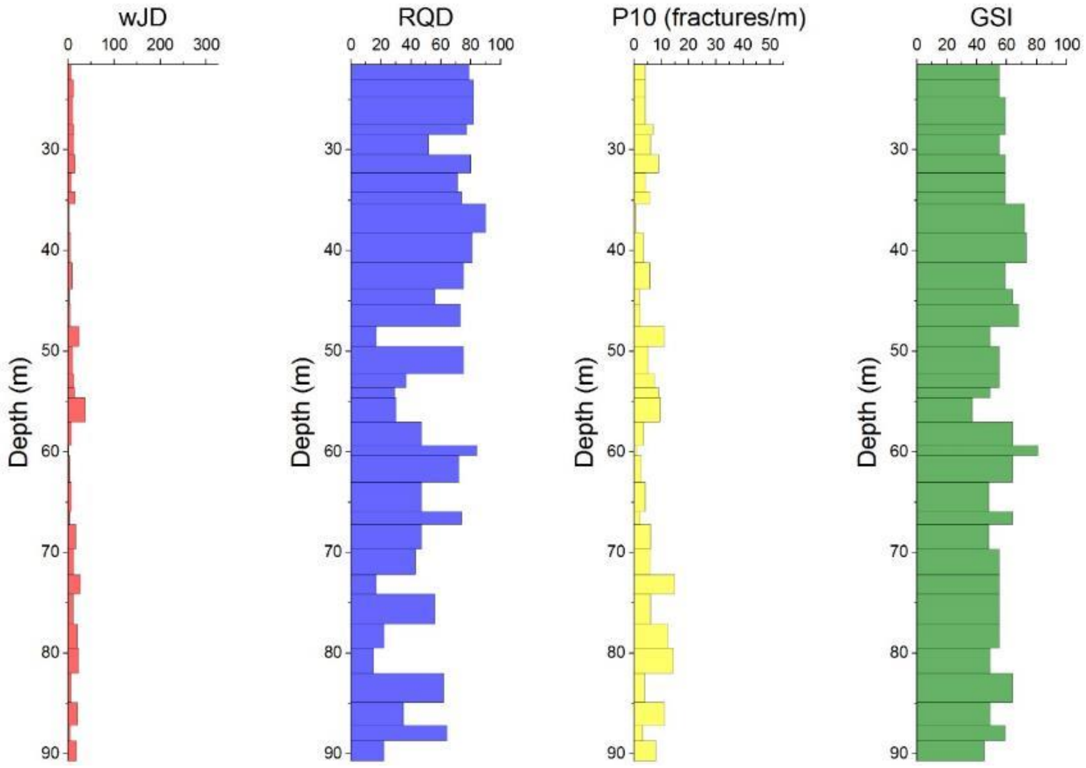
wJD
0
100
200
300
RQD
0
20
40
60
80
100
P10 (fractures/m)
0
10
20
30
40
50
GSI
0
20
40
60
80
100
Depth (m)
30
40
50
60
70
80
90

S108

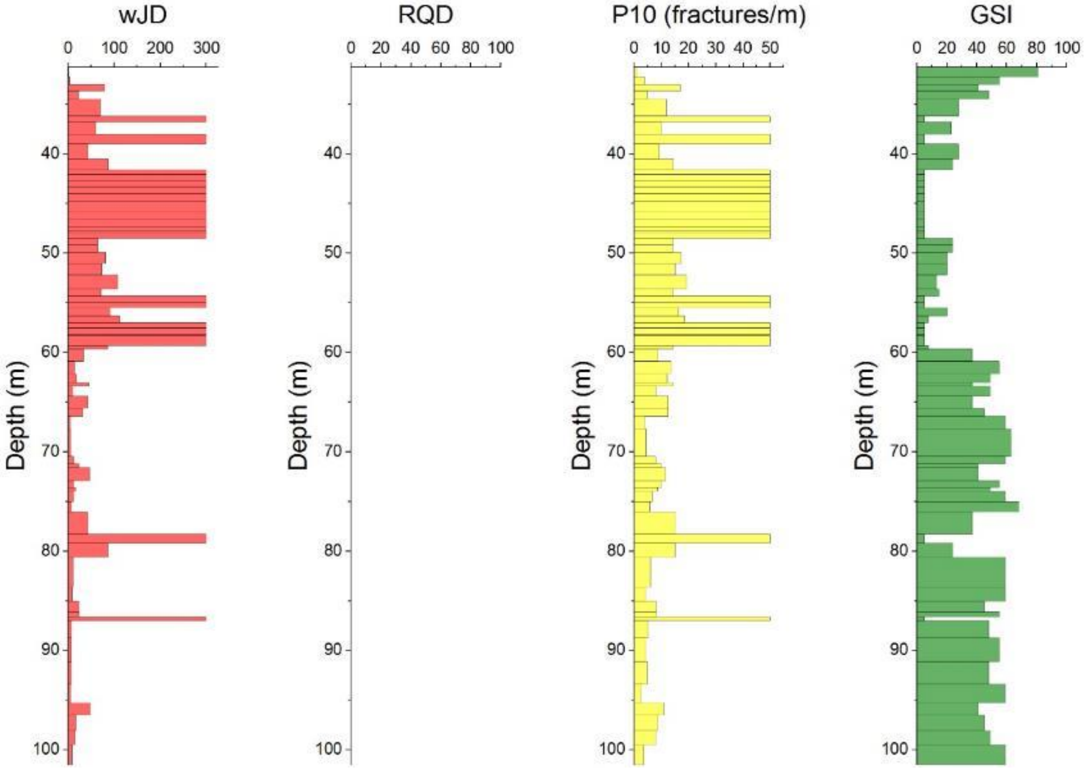
wJD
0
100
200
300
RQD
0
20
40
60
80
100
P10 (fractures/m)
0
10
20
30
40
50
GSI
0
20
40
60
80
100
Depth (m)
40
50
60
70
80
90
100

S109

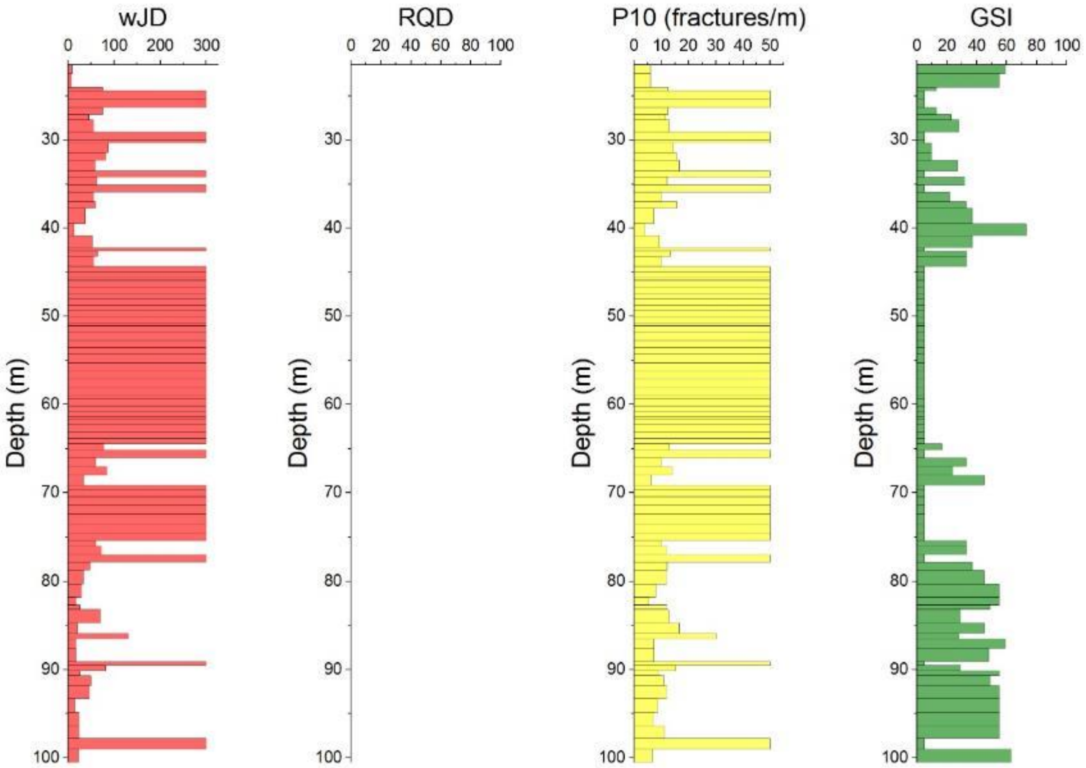
wJD
0 100 200 300
RQD
0 20 40 60 80 100
P10 (fractures/m)
0 10 20 30 40 50
GSI
0 20 40 60 80 100
Depth (m)
30
40
50
60
70
80
90
100

S110

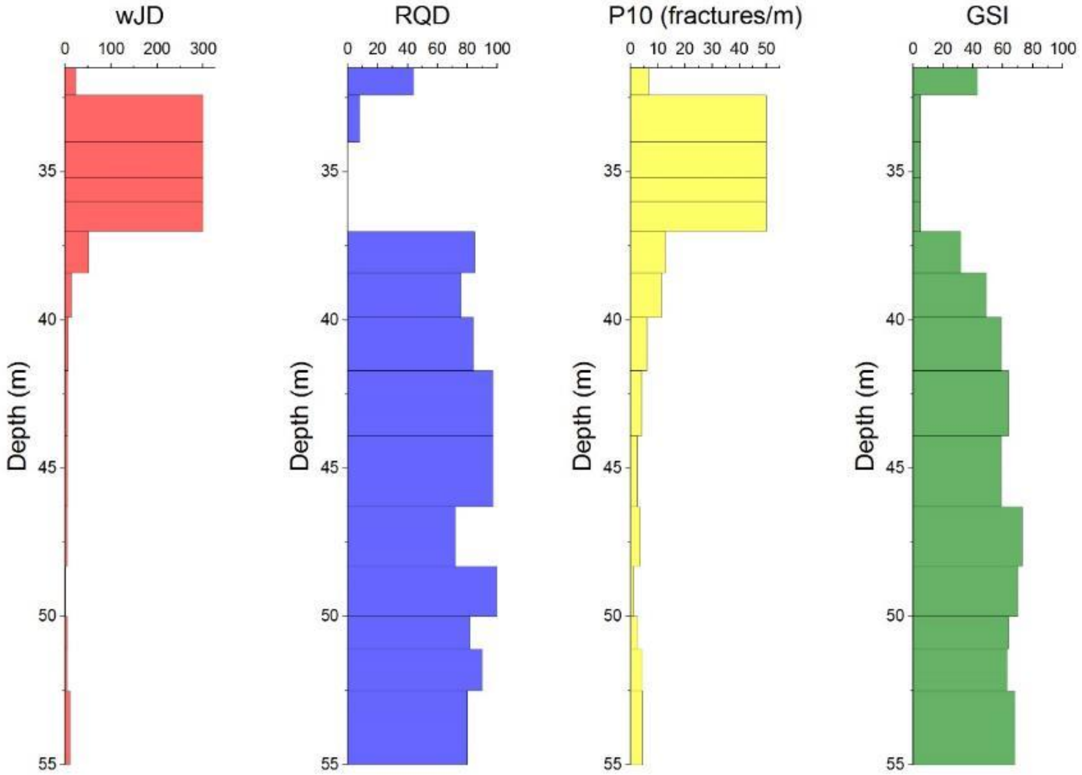
wJD
0 100 200 300
RQD
0 20 40 60 80 100
P10 (fractures/m)
0 10 20 30 40 50
GSI
0 20 40 60 80 100
Depth (m)
35
40
45
50
55

S111

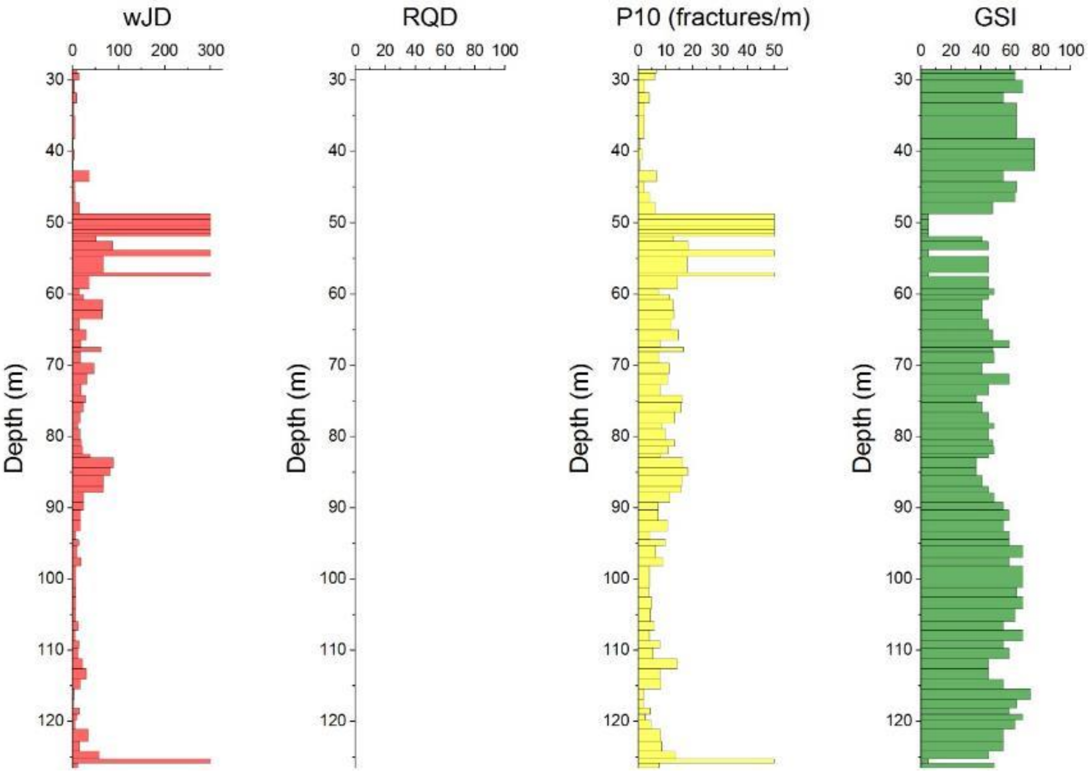
wJD
0
100
200
300
RQD
0
20
40
60
80
100
P10 (fractures/m)
0
10
20
30
40
50
GSI
0
20
40
60
80
100
Depth (m)
30
40
50
60
70
80
90
100
110
120

S112

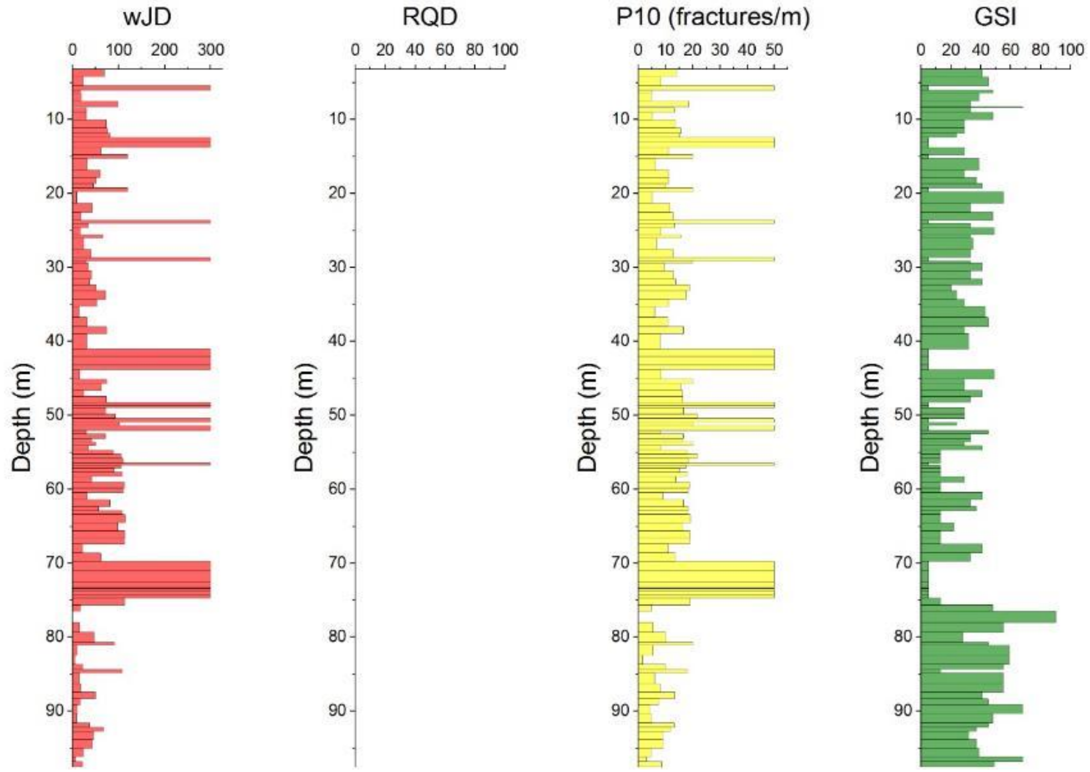
wJD
0
100
200
300
RQD
0
20
40
60
80
100
P10 (fractures/m)
0
10
20
30
40
50
GSI
0
20
40
60
80
100
Depth (m)
10
20
30
40
50
60
70
80
90

S113

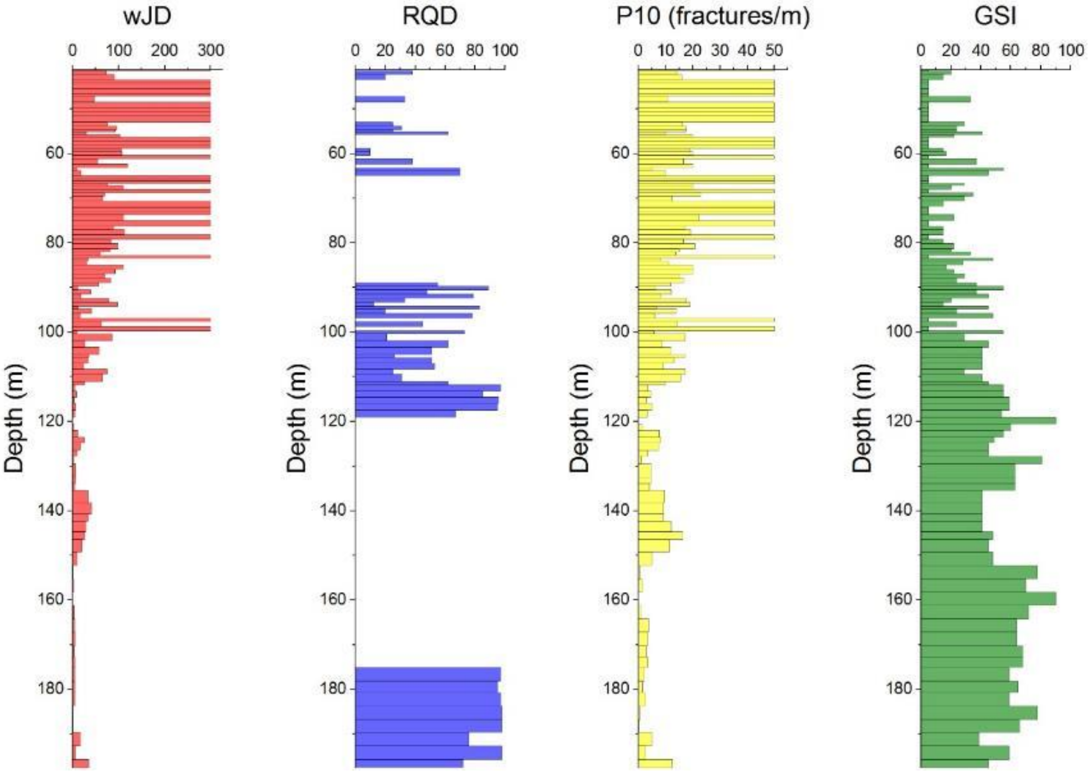
wJD
0 100 200 300
RQD
0 20 40 60 80 100
P10 (fractures/m)
0 10 20 30 40 50
GSI
0 20 40 60 80 100
Depth (m)
60
80
100
120
140
160
180

S114

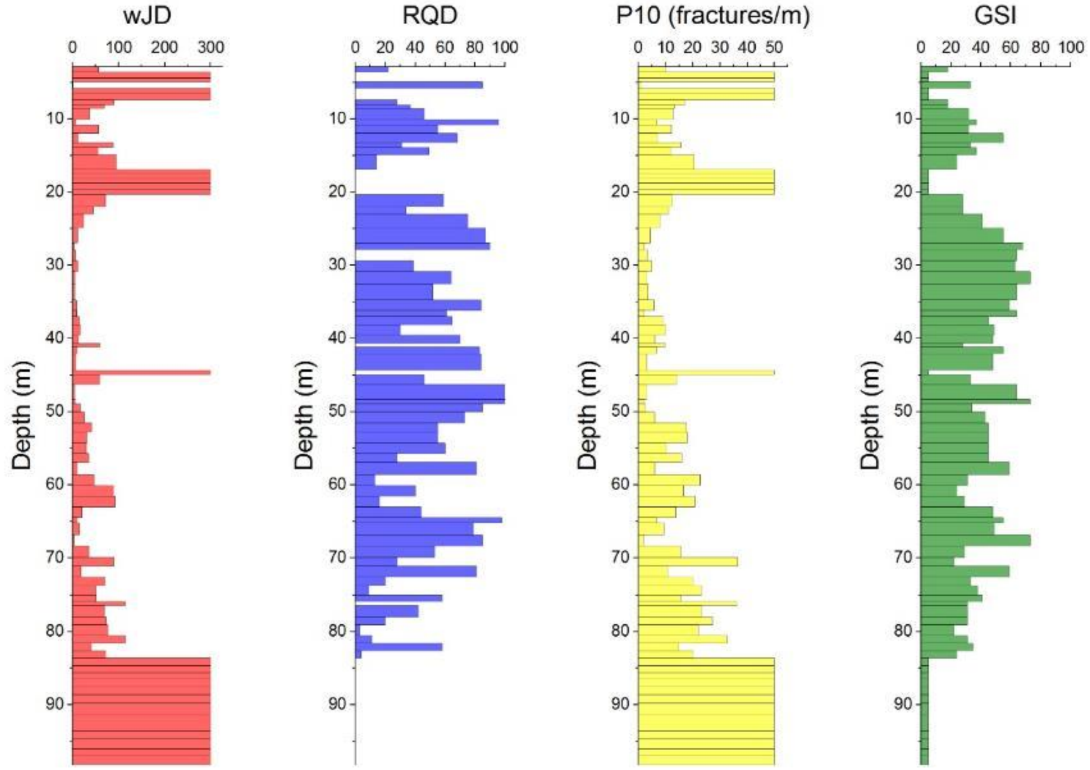
wJD
0 100 200 300
RQD
0 20 40 60 80 100
P10 (fractures/m)
0 10 20 30 40 50
GSI
0 20 40 60 80 100
Depth (m)
10
20
30
40
50
60
70
80
90

S115

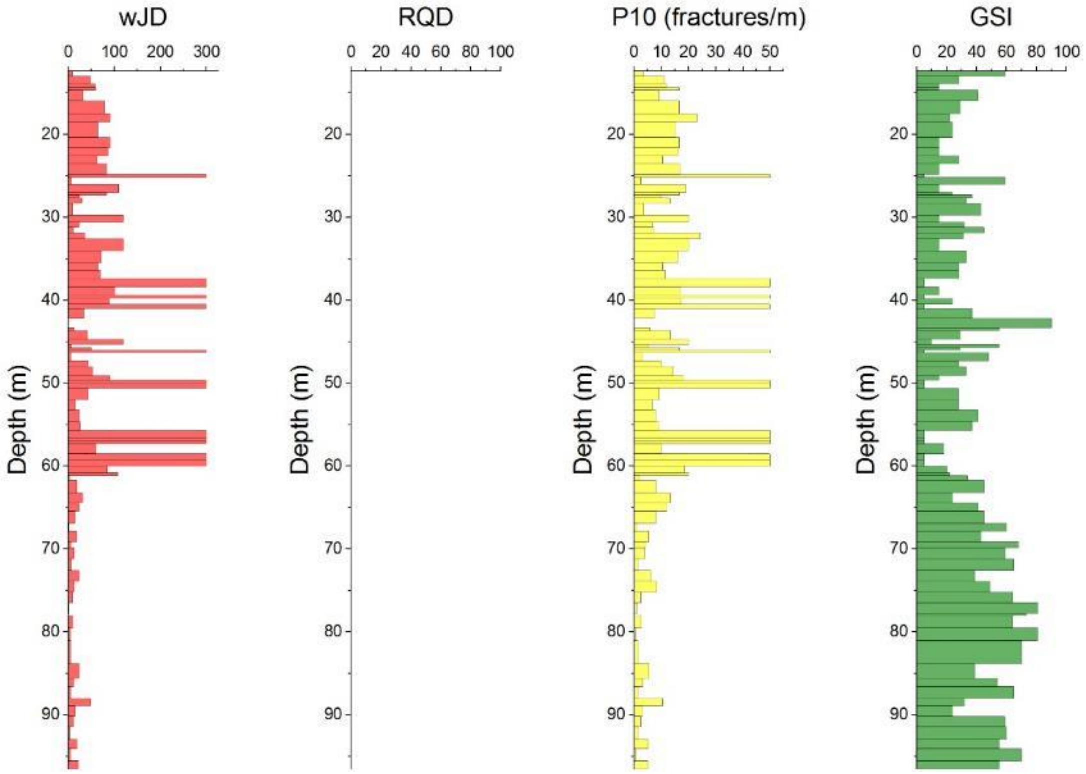
wJD
0 100 200 300
RQD
0 20 40 60 80 100
P10 (fractures/m)
0 10 20 30 40 50
GSI
0 20 40 60 80 100
Depth (m)
20
30
40
50
60
70
80
90

S116

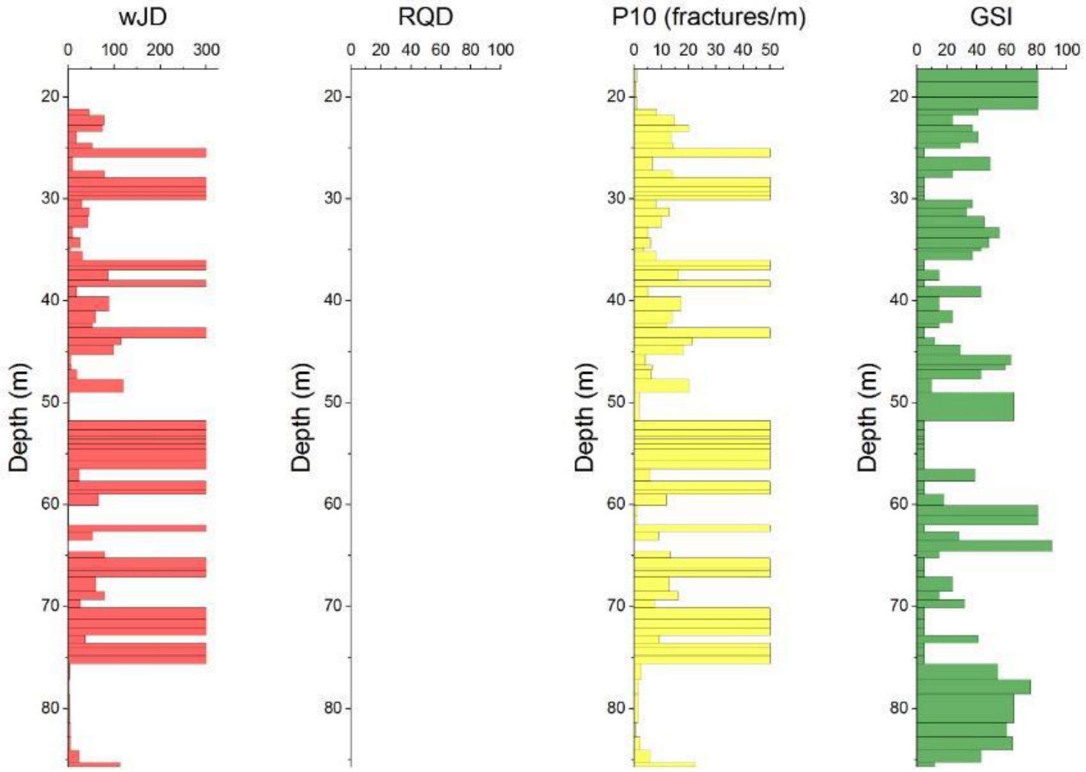
wJD
0 100 200 300
RQD
0 20 40 60 80 100
P10 (fractures/m)
0 10 20 30 40 50
GSI
0 20 40 60 80 100
Depth (m)
20
30
40
50
60
70
80

S117

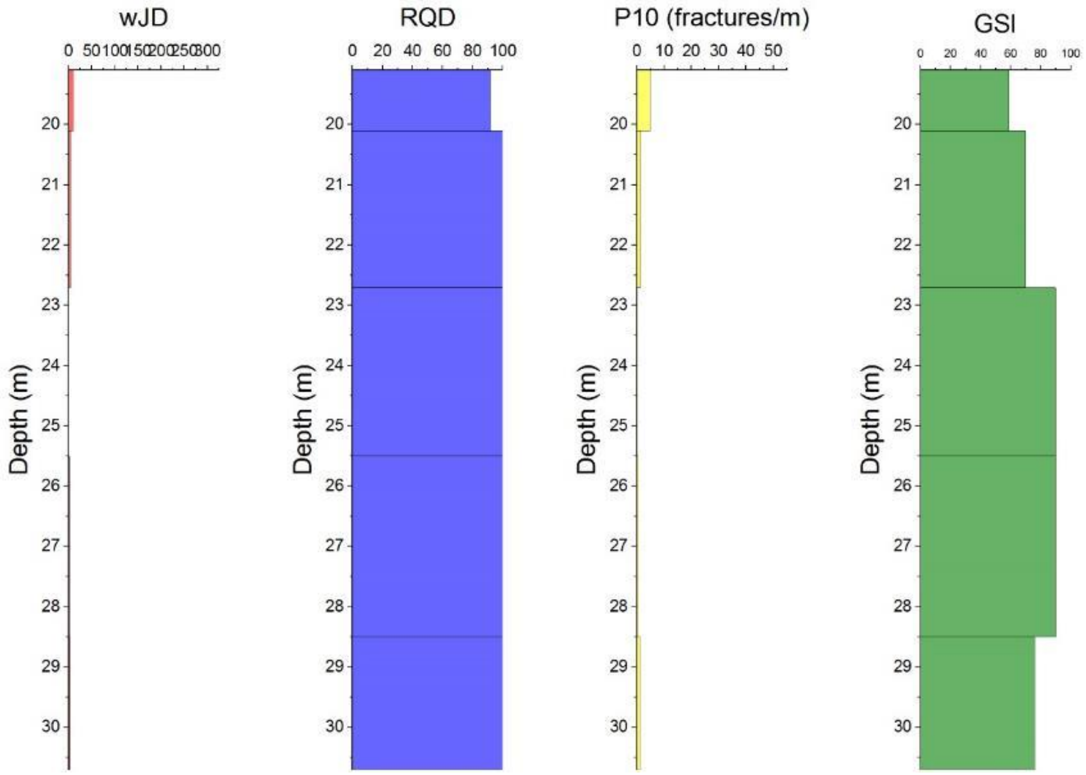
wJD
0 50 100 150 200 250 300
RQD
0 20 40 60 80 100
P10 (fractures/m)
0 10 20 30 40 50
GSI
0 20 40 60 80 100
Depth (m)
20
21
22
23
24
25
26
27
28
29
30

S118

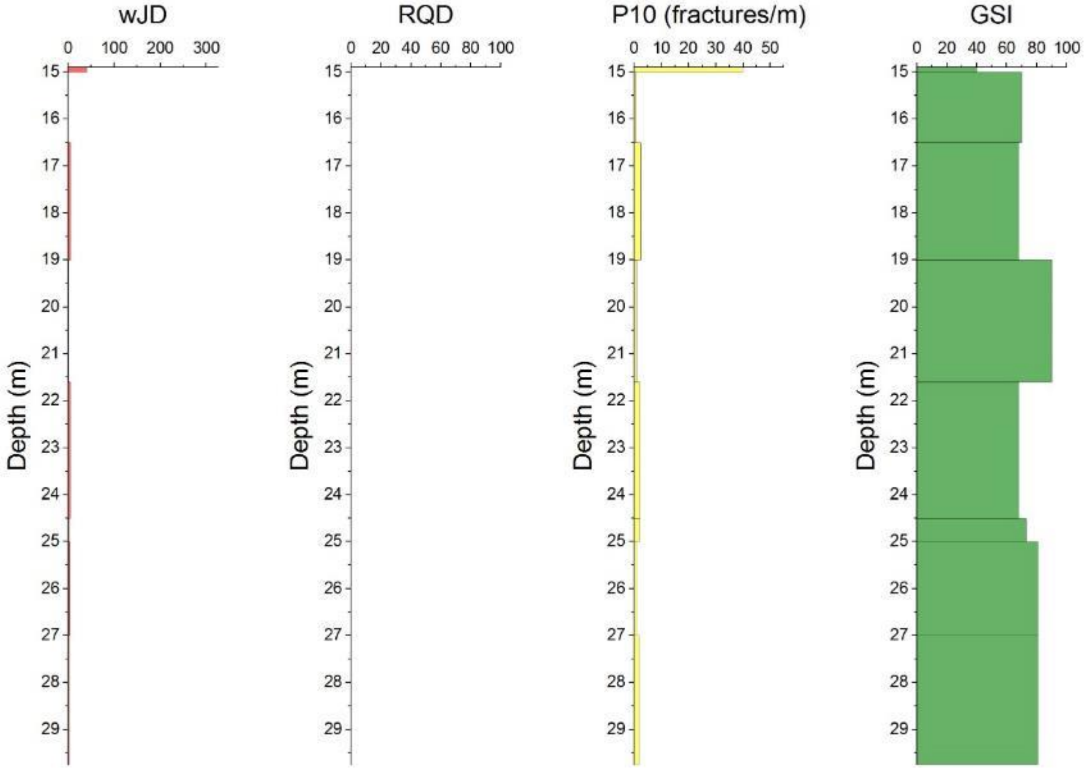
wJD
0 100 200 300
RQD
0 20 40 60 80 100
P10 (fractures/m)
0 10 20 30 40 50
GSI
0 20 40 60 80 100
Depth (m)
15
16
17
18
19
20
21
22
23
24
25
26
27
28
29

S119

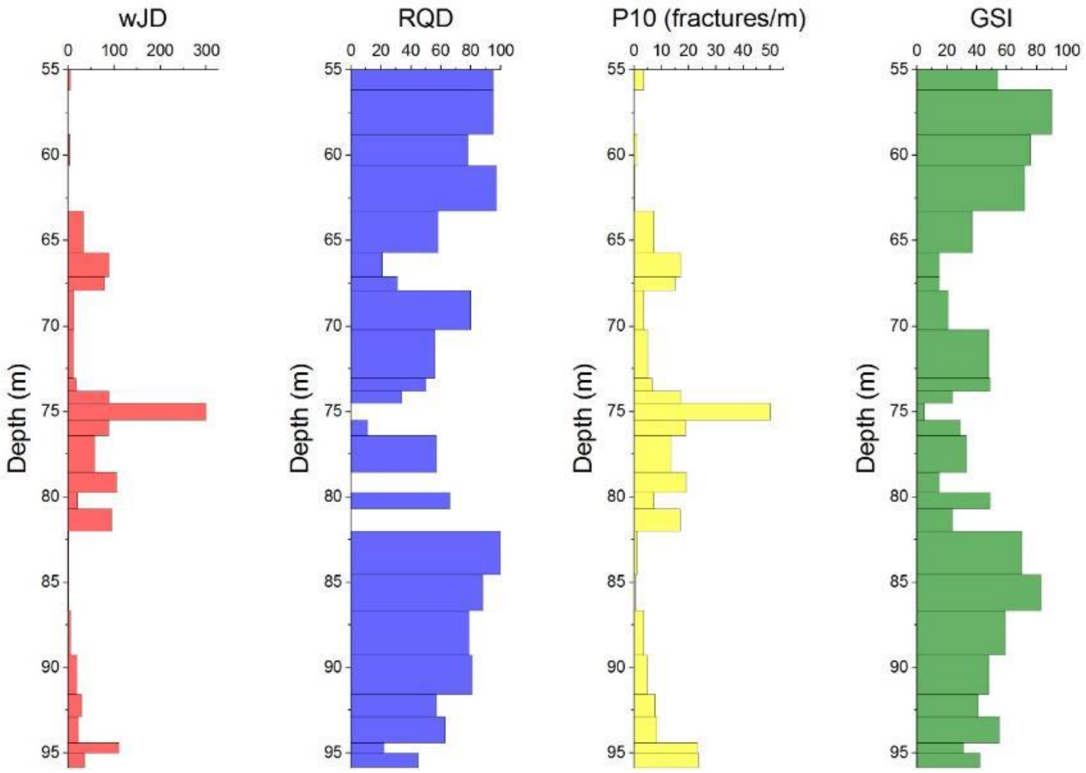
wJD
0
100
200
300
Depth (m)
55
60
65
70
75
80
85
90
95
RQD
0
20
40
60
80
100
Depth (m)
55
60
65
70
75
80
85
90
95
P10 (fractures/m)
0
10
20
30
40
50
Depth (m)
55
60
65
70
75
80
85
90
95
GSI
0
20
40
60
80
100
Depth (m)
55
60
65
70
75
80
85
90
95

S122

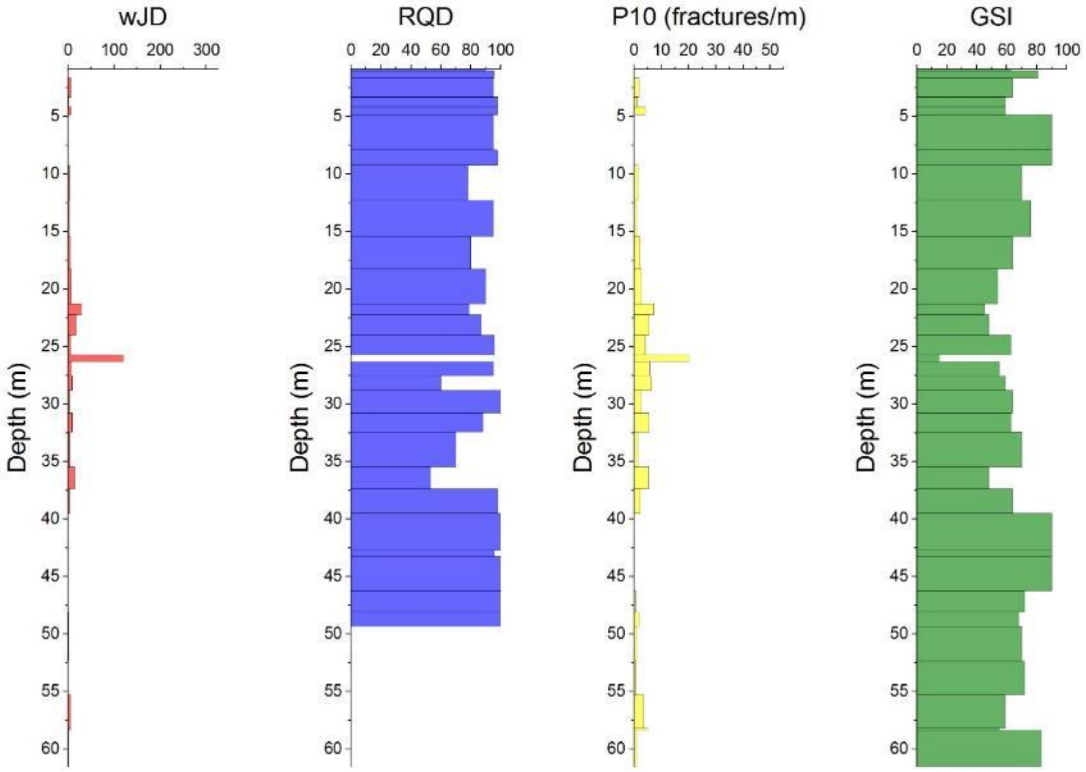
wJD
0
100
200
300
Depth (m)
5
10
15
20
25
30
35
40
45
50
55
60
RQD
0
20
40
60
80
100
Depth (m)
5
10
15
20
25
30
35
40
45
50
55
60
P10 (fractures/m)
0
10
20
30
40
50
Depth (m)
5
10
15
20
25
30
35
40
45
50
55
60
GSI
0
20
40
60
80
100
Depth (m)
5
10
15
20
25
30
35
40
45
50
55
60

11 **ANNEX 3: CRESTA DI SALINE BOREHOLES CHARACTERIZATION**

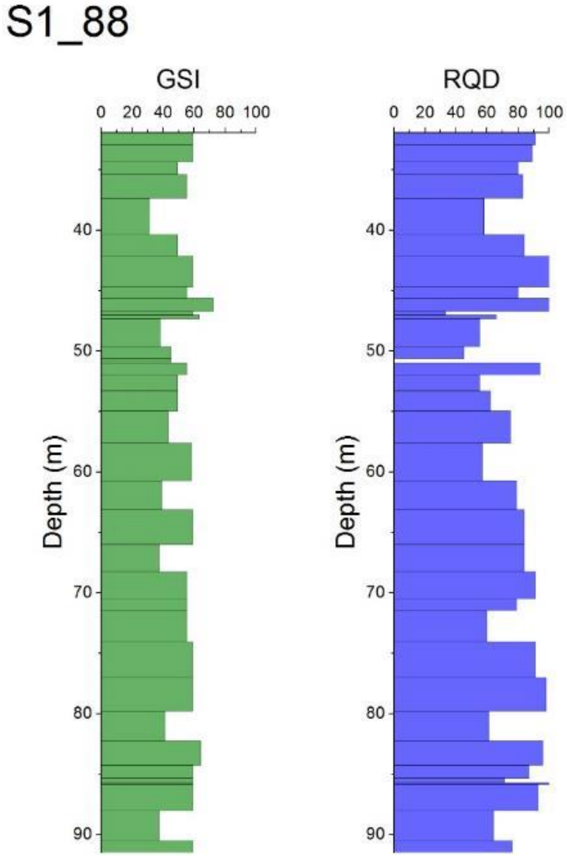

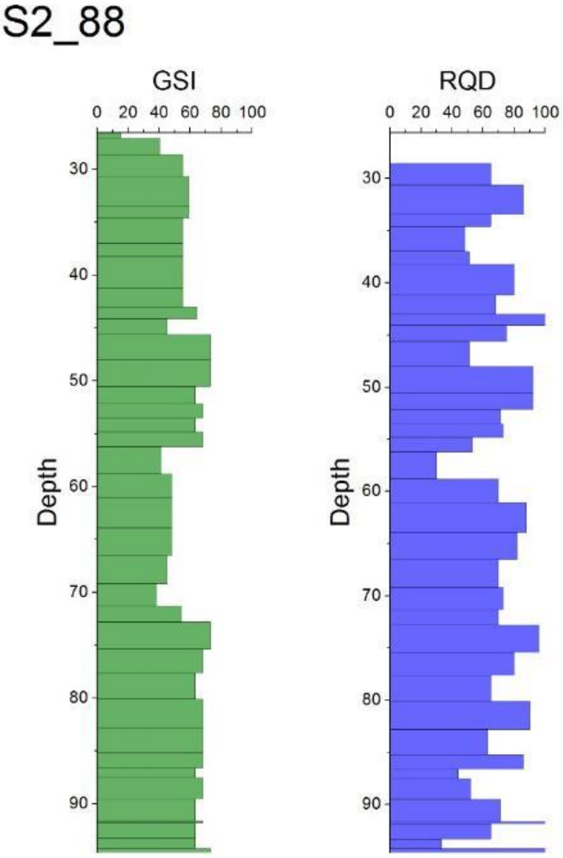
S2_88
GSI
0 20 40 60 80 100
RQD
0 20 40 60 80 100
Depth
30
40
50
60
70
80
90

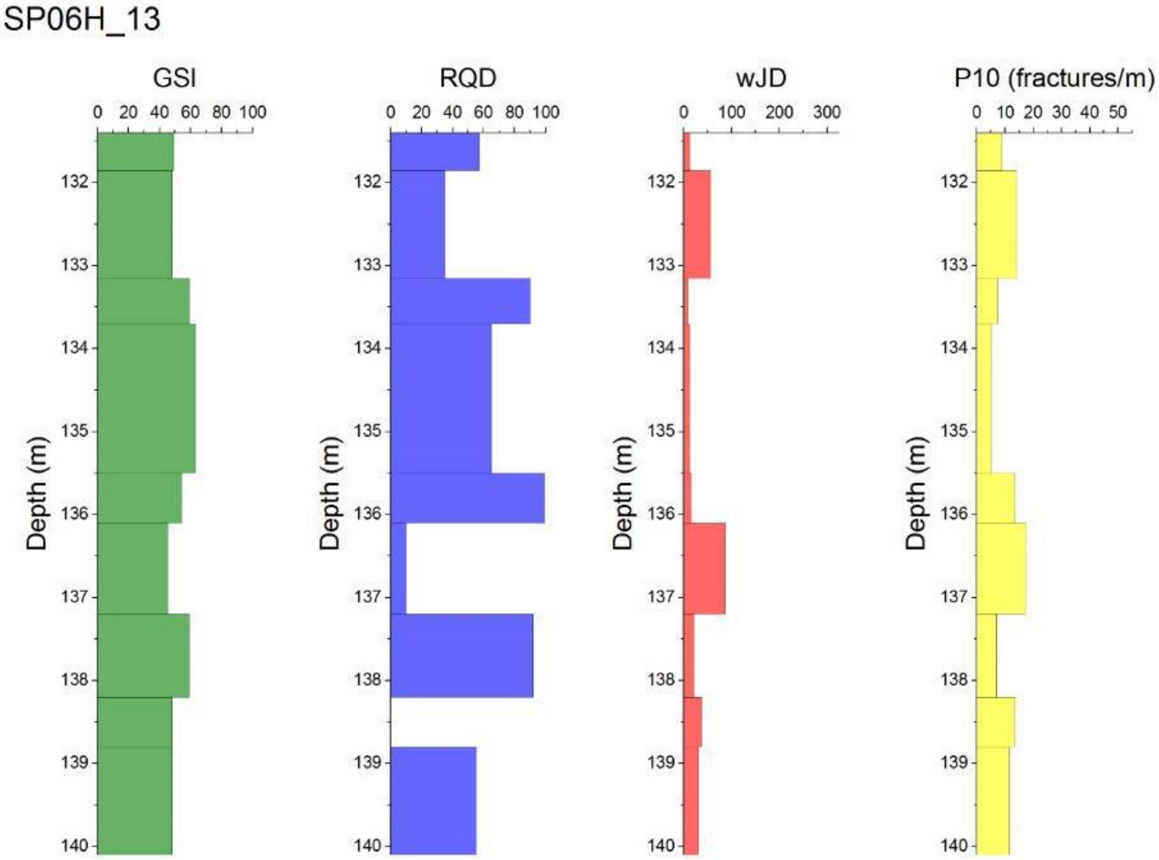
SP06H_13
GSI
0 20 40 60 80 100
RQD
0 20 40 60 80 100
wJD
0 100 200 300
P10 (fractures/m)
0 10 20 30 40 50
Depth (m)
132
133
134
135
136
137
138
139
140

SP06S_13

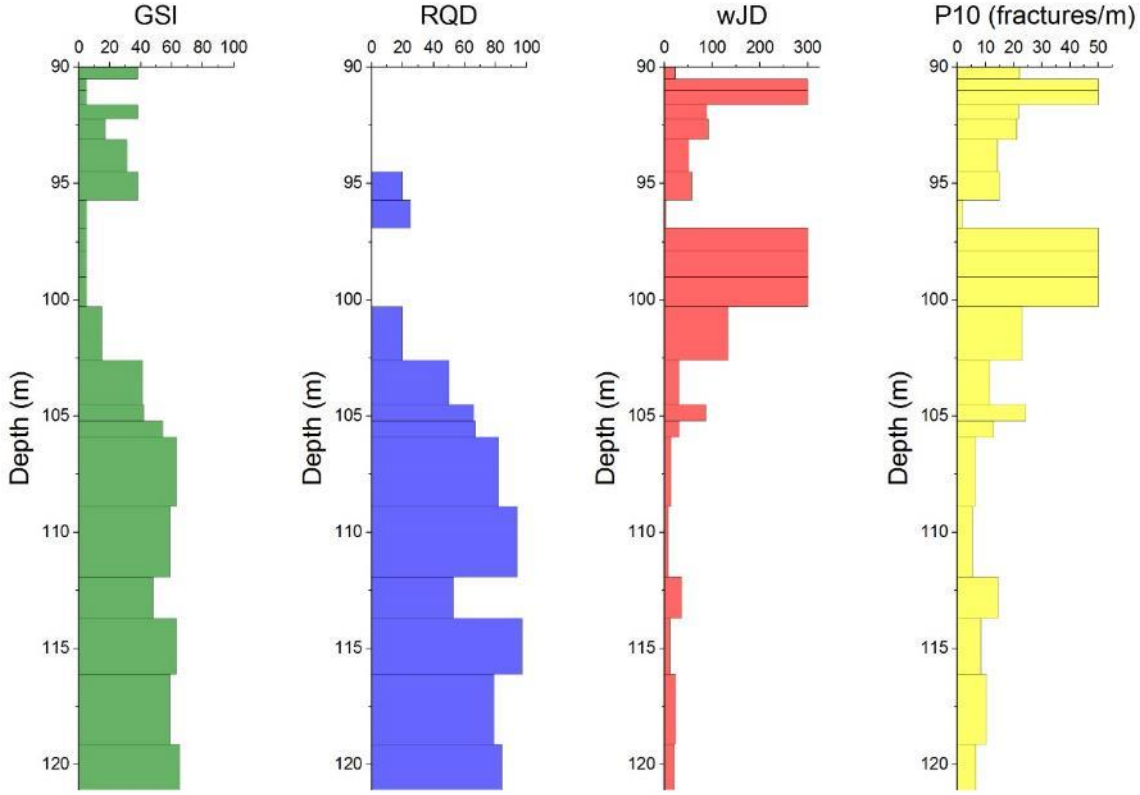

SP07H_13

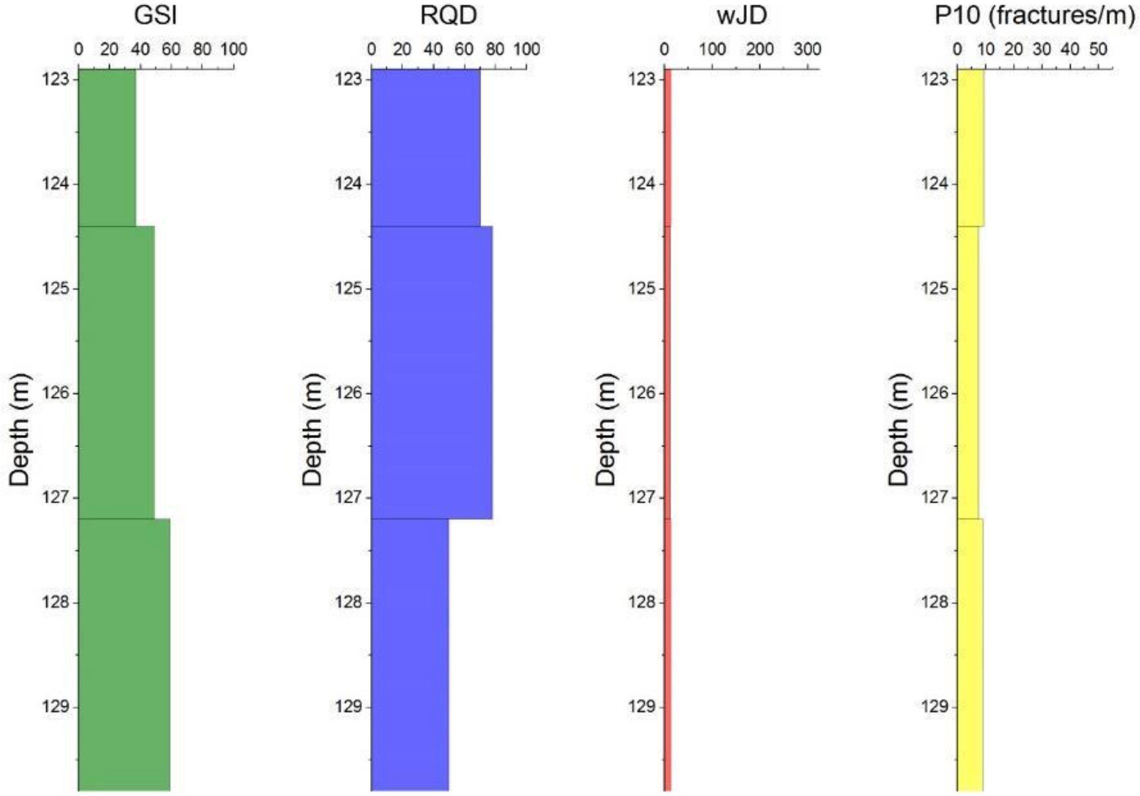

SP07S_13

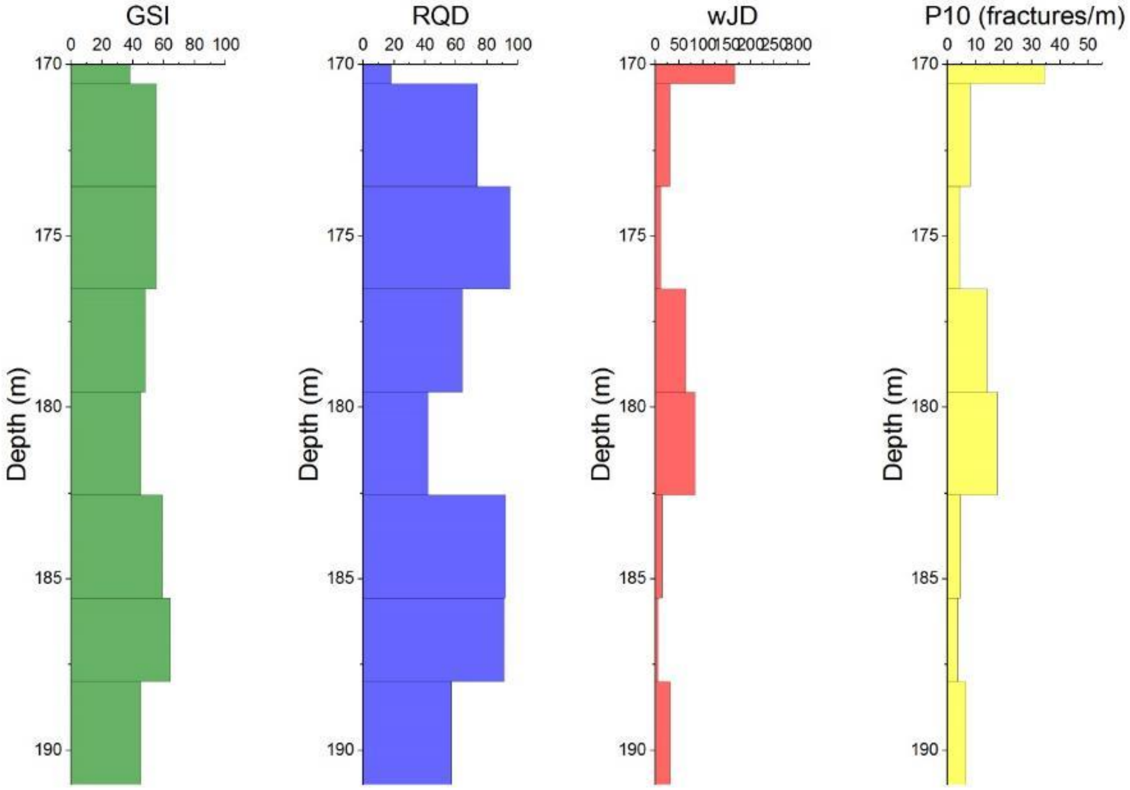

SP08_13

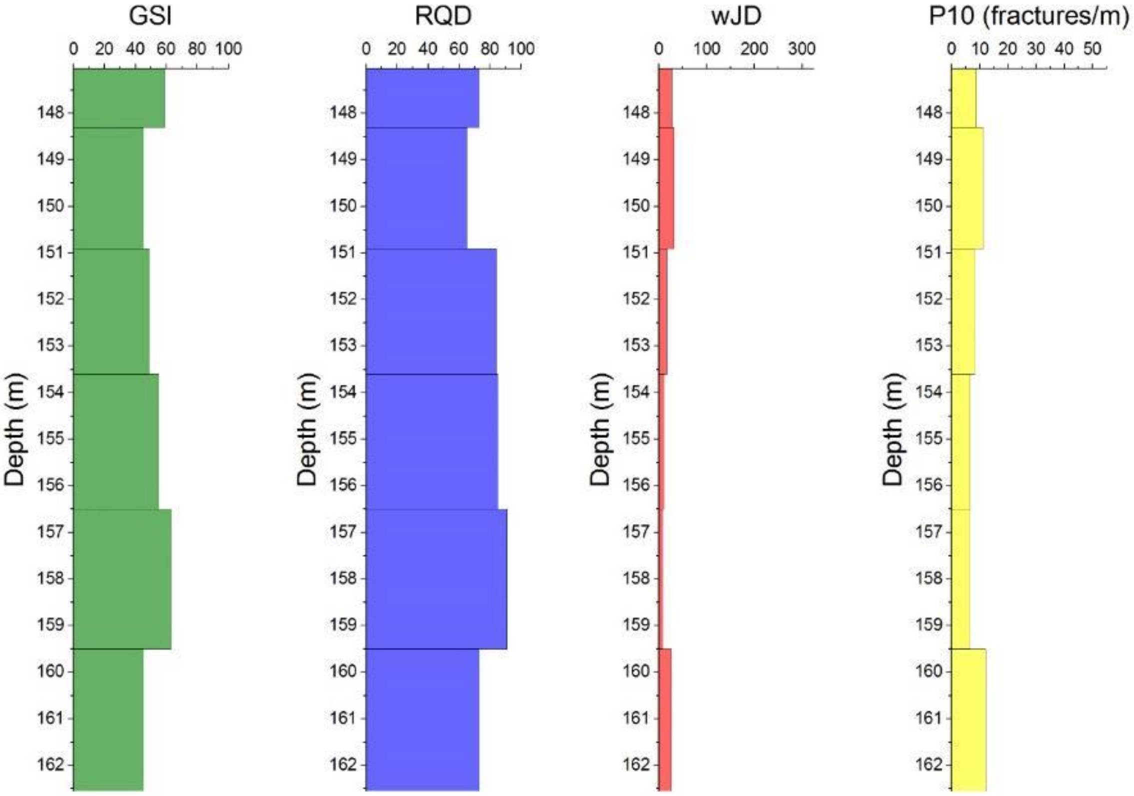

SP09_13

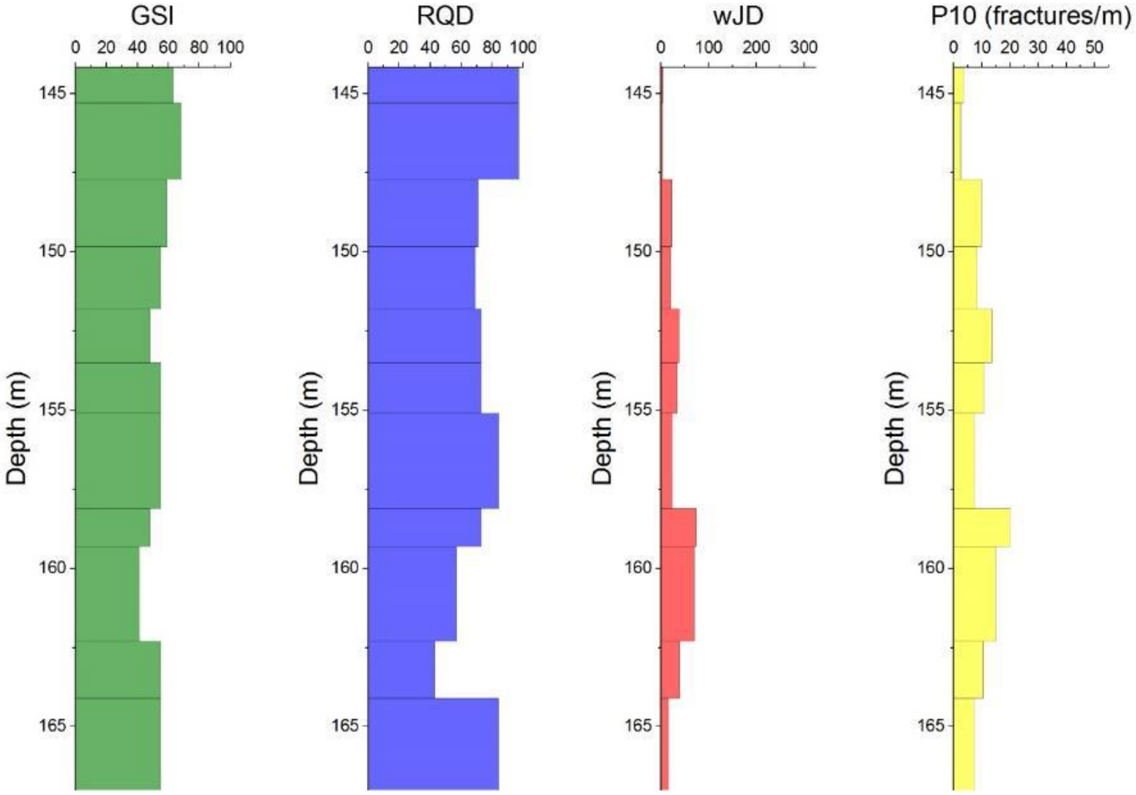
GSI
0 20 40 60 80 100
RQD
0 20 40 60 80 100
wJD
0 100 200 300
P10 (fractures/m)
0 10 20 30 40 50
Depth (m)
145
150
155
160
165